NASA/CP-1999-209691/VOL1/PT2

1997 NASA High-Speed Research Program Aerodynamic Performance Workshop

Volume I—Configuration Aerodynamics

Edited by
Daniel G. Baize
Langley Research Center, Hampton, Virginia

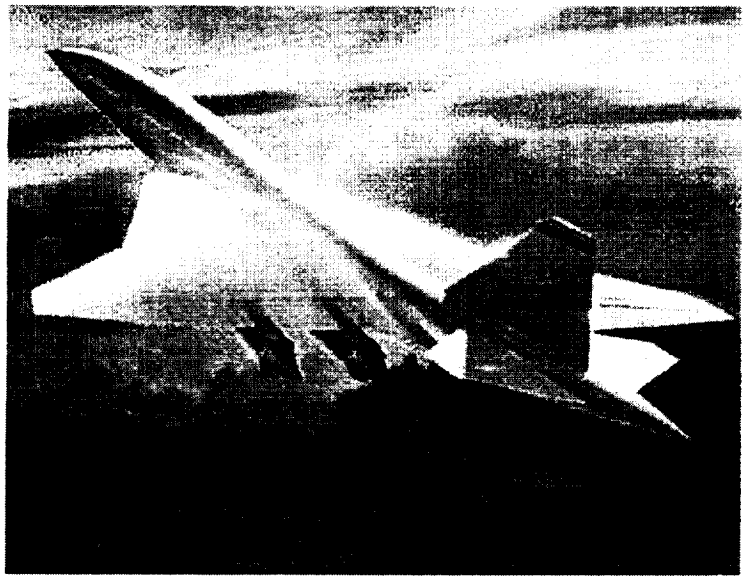

December 1999

The NASA STI Program Office . . . in Profile

Since its founding, NASA has been dedicated to the advancement of aeronautics and space science. The NASA Scientific and Technical Information (STI) Program Office plays a key part in helping NASA maintain this important role.

The NASA STI Program Office is operated by Langley Research Center, the lead center for NASA's scientific and technical information. The NASA STI Program Office provides access to the NASA STI Database, the largest collection of aeronautical and space science STI in the world. The Program Office is also NASA's institutional mechanism for disseminating the results of its research and development activities. These results are published by NASA in the NASA STI Report Series, which includes the following report types:

- TECHNICAL PUBLICATION. Reports of completed research or a major significant phase of research that present the results of NASA programs and include extensive data or theoretical analysis. Includes compilations of significant scientific and technical data and information deemed to be of continuing reference value. NASA counterpart of peer-reviewed formal professional papers, but having less stringent limitations on manuscript length and extent of graphic presentations.

- TECHNICAL MEMORANDUM. Scientific and technical findings that are preliminary or of specialized interest, e.g., quick release reports, working papers, and bibliographies that contain minimal annotation. Does not contain extensive analysis.

- CONTRACTOR REPORT. Scientific and technical findings by NASA-sponsored contractors and grantees.

- CONFERENCE PUBLICATION. Collected papers from scientific and technical conferences, symposia, seminars, or other meetings sponsored or co-sponsored by NASA.

- SPECIAL PUBLICATION. Scientific, technical, or historical information from NASA programs, projects, and missions, often concerned with subjects having substantial public interest.

- TECHNICAL TRANSLATION. English-language translations of foreign scientific and technical material pertinent to NASA's mission.

Specialized services that complement the STI Program Office's diverse offerings include creating custom thesauri, building customized databases, organizing and publishing research results . . . even providing videos.

For more information about the NASA STI Program Office, see the following:

- Access the NASA STI Program Home Page at ***http://www.sti.nasa.gov***

- Email your question via the Internet to help@sti.nasa.gov

- Fax your question to the NASA STI Help Desk at (301) 621-0134

- Telephone the NASA STI Help Desk at (301) 621-0390

- Write to:
  NASA STI Help Desk
  NASA Center for AeroSpace Information
  7121 Standard Drive
  Hanover, MD 21076-1320

NASA/CP-1999-209691/VOL1/PT2

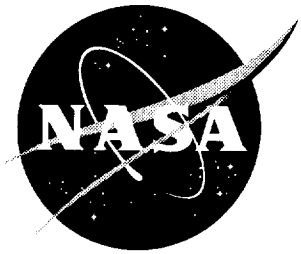

1997 NASA High-Speed Research Program Aerodynamic Performance Workshop

Volume I—Configuration Aerodynamics

Edited by
Daniel G. Baize
Langley Research Center, Hampton, Virginia

Proceedings of a workshop held at
Langley Research Center,
Hampton, Virginia
February 25–28, 1997

National Aeronautics and
Space Administration

Langley Research Center
Hampton, Virginia 23681-2199

December 1999

Available from:

NASA Center for AeroSpace Information (CASI)
7121 Standard Drive
Hanover, MD 21076-1320
(301) 621-0390

National Technical Information Service (NTIS)
5285 Port Royal Road
Springfield, VA 22161-2171
(703) 605-6000

PREFACE

The High-Speed Research Program and NASA Langley Research Center sponsored the NASA High-Speed Research Program Aerodynamic Performance Workshop on February 25–28, 1997. The workshop was designed to bring together NASA and industry High-Speed Civil Transport (HSCT) Aerodynamic Performance technology development participants in areas of Configuration Aerodynamics (transonic and supersonic cruise drag prediction and minimization), High-Lift, Flight Controls, Supersonic Laminar Flow Control, and Sonic Boom Prediction. The workshop objectives were to (1) report the progress and status of HSCT aerodynamic performance technology development; (2) disseminate this technology within the appropriate technical communities; and (3) promote synergy among the scientist and engineers working HSCT aerodynamics. In particular, single- and multi-point optimized HSCT configurations and HSCT high-lift system performance predictions were presented along with executive summarizes for all the Aerodynamic Performance technology areas.

The workshop was organized in three sessions as follows:

Session I	Plenary Session
Session II	Independent Session
Session III	Executive Summaries

The proceedings are published in two volumes:

Volume I, Parts 1 and 2	Configuration Aerodynamics
Volume II	High Lift

Conference Chairmen: Daniel G. Baize and Robert L. Calloway
NASA Langley Research Center

CONTENTS

Volume I, Part 2—Configuration Aerodynamics

Volume II—High Lift

Adams, Jr.
William M.
NASA Langley Research Center
Mail Stop 489
Hampton VA 23681-0001
Ph. 757-864-4013
fax 757-864-7795
eMail: w.m.adams@larc.nasa.gov

Agrawal
Shreekant
McDonnell Douglas Aerospace Co.
Mail Code 71-35
2401 E. Wardlow Road
Long Beach CA 90807-5309
Ph. 562-593-3436
fax 562-593-7593
eMail: agrawal@mdta.mdc.com

Allen
Jerry M.
NASA Langley Research Center
Mail Stop 499
Hampton VA 23681-0001
Ph. 757-864-5592
fax 757-864-4869
eMail: j.m.allen@larc.nasa.gov

Anders
Scott G.
NASA Langley Research Center
Mail Stop 170
Hampton VA 23681-0001
Ph. 757-864-8044
fax 757-864-8801
eMail: s.g.anders@larc.nasa.gov

Anderson
W. Kyle
NASA Langley Research Center
Mail Stop 128
Hampton VA 23681-0001
Ph. 757-864-2164
fax 757-864-8816
eMail: w.k.anderson@larc.nasa.gov

Antani
Tony
McDonnell Douglas Aerospace Co.
Mail Code 71-35
2401 E Wardlow Road
Long Beach CA 90807-5309
Ph. 562-593-3920
fax 562-593-7593
eMail: C362247@mdcpo05.lb.mdc.com

Applin
Zac
NASA Langley Research Center
Mail Stop 286
Hampton VA 23681-0001
Ph. 757-864-5062
fax 757-864-8192
eMail: z.t.applin@larc.nasa.gov

Arslan
Alan
McDonnell Douglas Aerospace Co.
Mail Code 71-35
2401 E. Wardlow Road
Long Beach CA 90807-5309
Ph. 562-593-8535
fax 562-593-7593
eMail: aea@indigo1.mdc.com

Bailey
F. Alan
The Boeing Company
Mail Stop 6H-FK
P.O. Box 3707
Seattle WA 98124-2207
Ph. 206-965-2699
fax 206-234-4543
eMail: frazier.a.bailey@boeing.com

Bailey
Mel
Lockheed Engineering & Sciences Co
NASA Langley Research Center
Mail Stop 389
Hampton VA 23681-0001
Ph. 757-864-4030
fax 757-864-7795
email: m.l.bailey@larc.nasa.gov

Bailey
Randall
Calspan Advanced Tech Center
P.O. Box 400
4455 Genesee Street
Buffalo NY 14225-0400
Ph. 716-631-6939
fax 716-631-6990
eMail: bailey@calspan.com

Baize
Dan
NASA Langley Research Center
Mail stop 119
Hampton VA 23681-0001
Ph. 757-864-1071
fax 757-864-8852
eMail: d.g.baize@larc.nasa.gov

Ball
Doug
The Boeing Company
Mail Stop 6H-FK
P.O. Box 3707
Seattle WA 98124-2207
Ph. 206-965-2151
fax 206-234-4543
eMail: baldnb00@ccmail.ca.boeing.com

Barrett
Mike
Honeywell Inc.
MS: MN65-2810
3660 Technology Drive
Minneapolis MN 55418
Ph. 612-951-7286
fax 612-951-7438
eMail: mike_barrett@htc.honeywell.com

Belcastro
Christine
NASA Langley Research Center
Mail Stop 161
Hampton VA 23681-0001
Ph. 757-864-4035
fax 757-864-7795
eMail:christine.m.belcastro@larc.nasa.go

Bencze
Dan
NASA Ames Research Center
Mail Stop 227-6
Moffett Field CA 94035-1000
Ph. 415-604-6618
fax 415-604-0737
eMail: dbencze@mail.arc.nasa.gov

Bengston
Robert
Pratt & Whitney
Mail Stop 165-21
400 Main St.
East Eartford CT 06108
Ph. 860-565-2080
fax 860-565-0123
eMail: bengtsrj@pweh.com

Bharadvaj
Bala
McDonnell Douglas Aerospace Co.
Mail Code 71-35
2401 E Wardlow Road
Long Beach CA 90807-5309
Ph. 562-593-3514
fax 562-982-7787
eMail: c336381@mail.mdc.com

Borland
Chris
The Boeing Company
Mail Stop 6H-FK
P.O. Box 3707
Seattle WA 98124-2207
Ph. 206-965-0336
fax 206-234-4543
eMail: christopher.j.borland@boeing.com

Bunin
Bruce
McDonnell Douglas Aerospace Co.
Mail Code 71-30
2401 E. Wardlow Road
Long Beach CA 90807-5309
Ph. 562-593-0629
fax 562-982-7383
eMail: bunin@mdta.mdc.com

Buning
Pieter G.
NASA Langley Research Center
Mail Stop 280
Hampton VA 23681-0001
Ph. 757-864-3093
fax 757-864-8195
eMail: p.g.buning@larc.nasa.gov

Burner
Alpheus W.
NASA Langley Research Center
Mail Stop 236
Hampton VA 23681-0001
Ph. 757-864-4635
fax 757-864-7607
eMail: a.w.burner@larc.nasa.gov

Buttrill
Carey
NASA Langley Research Center
Mail Stop 132
Hampton VA 23681-0001
Ph. 757-864-4016
fax 757-864-7795
eMail: c.s.buttrill@larc.nasa.gov

Calloway
Robert
NASA Langley Research Center
Mail Stop 119
Hampton VA 23681-0001
Ph. 757-864-2960
fax 757-864-8852
eMail: r.l.calloway@larc.nasa.gov

Camache
Peter
McDonnell Douglas Aerospace Co.
Mail Code 71-30
2401 E. Wardlow Road
Long Beach CA 90807-5309
Ph. 562-593-7012
fax 562-982-7787
eMail: camacho@mdta.mdc.com

Campbell
Brian A.
NASA Langley Research Center
Mail Stop 286
Hampton VA 23681-0001
Ph. 757-864-5069
fax 757-864-8192
eMail: b.a.campbell@larc.nasa.gov

Campbell
James F.
NASA Langley Research Center
Mail Stop 499
Hampton VA 23681-0001
Ph. 757-864-2866
fax 757-864-8469
eMail: j.f.campbell@larc.nasa.gov

Campbell
Richard L.
NASA Langley Research Center
Mail Stop 499
Hampton VA 23681-0001
Ph. 757-864-2872
fax 757-864-8469
eMail: r.l.campbell@larc.nasa.gov

Capone
Fran J.
NASA Langley Research Center
Mail Stop 280
Hampton VA 23681-0001
Ph. 757-864-3004
fax 757-864-8195
eMail: f.j.capone@larc.nasa.gov

Cappuccio
Mina
NASA Ames Research Center
Mail Stop 227-6
Moffett Field CA 94035-1000
Ph. 415-604-1313
fax 415-604-0737
eMail: mcappuccio@mail.arc.nasa.gov

Chaney
Steve R.
The Boeing Company
Mail Stop 6H-FK
P.O. Box 3707
Seattle WA 98124-2207
Ph. 206-237-2878
fax 206-234-4543
eMail:

Chang
Bor-Chin
Drexel University
Dept. Mechanical Engineering
Philadelphia PA 19104
Ph. 215-895-1790
fax 215-895-1478
eMail: bchang@coe.drexel.edu

Chen
Allen W.
The Boeing Company
Mail Stop 6H-FK
P.O. Box 3707
Seattle WA 98124-2207
Ph. 206-965-3490
fax 206-234-4543
eMail: awc@hsctaero.ca.boeing.com

Cheung
Samson
McDonnell Douglas Aerospace Co.
Mail Code 71-35
2401 E. Wardlow Road
Long Beach CA 90807-5309
Ph. 562-593-9025
fax 562-593-7593
eMail: shc@indigo1.mdc.com

Christhilf
David M.
Lockheed Engineering & Sciences Co.
NASA Langley Research Center
Mail Stop 389
Hampton VA 23681-00
Ph. 757-864-4029
fax 757-864-8838
eMail: d.m.christhilf@larc.nasa.gov

Chu
Julio
NASA Langley Research Center
Mail Stop 248
Hampton VA 23681-0001
Ph. 757-864-5136
fax 757-864-3553
eMail: j.chu@larc.nasa.gov

Clark
Roger
McDonnell Douglas Aerospace Co.
Mail Code 71-35
2401 E Wardlow Road
Long Beach CA 90807-5309
Ph. 562-982-5334
fax 562-593-7593
eMail: c08375@mdcpo17.lb.mdc.com

Cliff
Susan
NASA Ames Research Center
Mail Stop 227-6
Moffett Field A 94035-1000
Ph. 415-604-3907
fax 415-604-0737
eMail: cliff@ra-iris.arc.nasa.gov

Coen
Peter
NASA Langley Research Center
Mail Stop 248
Hampton VA 23681-0001
Ph. 757-864-5991
fax 757-864-3553
eMail: p.g.coen@larc.nasa.gov

Conner
Roy S.
The Boeing Company
Mail Stop 6H-FK
P.O. Box 3707
Seattle WA 98124-2207
Ph. 206-965-3774
fax 206-234-4543
eMail: rsc7463@hsctaero.ca.boeing.com

Cuthbertson
R. D.
The Boeing Company
Mail Stop 6H-FR
P.O. Box 3707
Seattle WA 98124-2207
Ph. 206-237-7594
fax 206-234-4543
eMail: robert.d.cuthbertson@boeing.com

Darden
Christine
NASA Langley Research Center
Mail Stop 119
Hampton VA 23681-0001
Ph. 757-864-5258
fax 757-864-8852
eMail: c.m.darden@larc.nasa.gov

Deere
Karen A.
NASA Langley Research Center
Mail Stop 280
Hampton VA 23681-0001
Ph. 757-864-8986
fax 757-864-8195
eMail: k.a.deere@larc.nasa.gov

DeLoach
Richard
NASA Langley Research Center
Mail Stop 236
Hampton VA 23681-0001
Ph. 757-864-4657
fax 757-864-7607
eMail: r.deloach@larc.nasa.gov

Derry
Steve
NASA Langley Research Center
Mail Stop 125B
Hampton VA 23681-0001
Ph. 757-864-7412
fax 757-864-8837
eMail: s.d.derry@larc.nasa.gov

Domack
Christopher S.
Lockheed Engineering & Sciences Co.
NASA Langley Research Center
Mail Stop 248
Hampton VA 23681-0001
Ph. 757-864-6504
fax 757-864-3553
eMail: domack@avd00.larc.nasa.gov

Duffy
Keith S.
The Boeing Company
Mail Stop 6H-FA
P.O. Box 3707
Seattle WA 98124-2207
Ph. 206-965-0116
fax 206-234-4543
eMail: keith@brazil.ca.boeing.com

Ebner
N. Keith
The Boeing Company
Mail Stop 6H-FK
P.O. Box 3707
Seattle WA 98124-2207
Ph. 206-965-0198
fax 206-234-4543
eMail: keith.ebner@boeing.com

Elgersma
Mike
Honeywell Inc.
MS: MN 65-2810
3660 Technology Drive
Minneapolis MN 55418
Ph. 612-951-7208
fax 612-951-7438
eMail: mike_elgersma@htc.honeywell.com

Erickson
Gary E.
NASA Langley Research Center
Mail Stop 413
Hampton VA 23681-0001
Ph. 757-864-2886
fax 757-864-8095
eMail: g.e.erickson@larc.nasa.gov

Fan
Xuetong
ASE Technologies Inc.
Suite 203
4015 Exeuctive Park Drive
Cincinnati OH 45241
Ph. 513-563-8855
fax 513-563-8865
eMail: fan@mars.asetach.com

Feifel
Winfried M.
The Boeing Company
Mail Stop 6H-FK
P.O. Box 3707
Seattle WA 98124-2207
Ph. 206-965-0561
fax 206-234-4543
eMail:

Fenbert
James W.
NASA Langley Research Center
Mail Stop 248
Hampton VA 23681-0001
Ph. 864-5973
fax
eMail: j.w.fenbert@larc.nasa.gov

Funk
Joan G.
NASA Langley Research Center
Mail Stop 119
Hampton VA 23681-0001
Ph. 757-864-3092
fax 757-864-8852
eMail: j.g.funk@larc.nasa.gov

Garg
Sanjay
NASA Lewis Research Center
Mail Stop 77-1
21000 Brookpark Road
Cleveland OH 44135
Ph. 216-433-2685
fax 216-433-8643
eMail: sanjay.garg@lerc.nasa.gov

Ghaffari
F.
NASA Langley Research Center
Mail Stop 499
Hampton VA 23681-0001
Ph. 757-864-2856
fax 757-864-8469
eMail: f.ghaffari@larc.nasa.gov

Giesy
Dan
Lockheed Engineering & Sciences Co.
NASA Langley Research Center
Mail Stop 389
Hampton VA 23681-0001
Ph. 757-864-4006
fax 757-864-8838
eMail: d.p.giesy@larc.nasa.gov

Gilbert
Bill
NASA Langley Research Center
Mail Stop 119
Hampton VA 23681-0001
Ph. 757-864-6392
fax 757-864-8852
eMail: w.p.gilbert@larc.nasa.gov

Glaab
Louis
Lockheed Engineering & Sciences Co.
NASA Langley Research Center
Mail Stop 343
Hampton VA 23681-0001
Ph. 757-864-1159
fax 757-864-7722
eMail: l.j.glaab@larc.nasa.gov

Goldberg
Perry
McDonnell Douglas Aerospace Co.
Mail Code 71-35
2401 E. Wardlow Road
Long Beach CA 90807-5309
Ph. 562-982-2126
fax 562-593-7593
eMail: goldbet@citm.mdc.com

Gracey
Chris
NASA Langley Research Center
Mail Stop 161
Hampton VA 23681-0001
Ph. 757-864-4019
fax 757-864-7795
eMail: c.gracey@larc.nasa.gov

Green
Lawrence L.
NASA Langley Research Center
Mail Stop 159
Hampton VA 23681-0002
Ph. 757-864-2228
fax 757-864-9713
eMail: l.l.green@larc.nasa.gov

Gregory
Irene
NASA Langley Research Center
Mail Stop 132
Hampton VA 23681-0001
Ph. 757-864-4075
fax 757-864-7795
eMail: i.m.gregory@larc.nasa.gov

Greiner
Glenn P.
George Washington University
NASA Langley Research Center
Mail Stop 132
Hampton VA 23681-0001
Ph. 757-864-4086
fax 757-864-7795
eMail: g.p.greiner@larc.nasa.gov

Griffiths
Robert C.
The Boeing Company
Mail Stop 6H-FK
P.O. Box 3707
Seattle WA 98124-2207
Ph. 206-965-3465
fax 206-234-4543
eMail: robert.c.griffiths@boeing.com

Gumbert
Clyde R.
NASA Langley Research Center
Mail Stop 159
Hampton VA 23681-0001
Ph. 757-864-2221
fax 757-864-9713
eMail: c.r.gumbert@larc.nasa.gov

Hager
James
McDonnell Douglas Aerospace Co.
Mail Code 71-35
2401 E. Wardlow Road
Long Beach CA 90807-5309
Ph. 562-982-9217
fax 562-593-7593
eMail: joh@indigo1.mdc.com

Hahne
Dave
NASA Langley Research Center
Mail Stop 153
Hampton VA 23681-0001
Ph. 757-864-1162
fax 757-864-7722
eMail: d.e.hahne@larc.nasa.gov

Halberg
Eric N.
Naval Postgraduate School
Mail Code 31
Halligan Hall
Monterey CA 93940
Ph. 408-656-5040
fax 408-656-2313
eMail: hallberg@aa.nps.navy.mil

Hamner
Marvine P.
McDonnell Douglas Aerospace Co.
Mail Code S1022272
P.O. Box 516
St Louis MO 63166-0516
Ph. 314-233-1600
fax 314-777-2984
eMail: mph@indigo1.mdc.com

Hartwich
Peter M.
McDonnell Douglas Aerospace Co.
Mail Code 71-35
2401 E. Wardlow Road
Long Beach CA 90807-4418
Ph. 562-593-2965
fax 562-593-7593
eMail: pmh@indigo1.mdc.com

Henderson
Dennis K.
McDonnell Douglas Aerospace Co.
Mail Code 71-35
2401 E Wardlow Road
Long Beach CA 90807-5309
Ph. 562-982-9269
fax 562-593-7593
eMail: dhenderson@c17m.mdc.com

Hickey
Paul K.
ASE Technologies, Inc.
Suite 203
4015 Executive Park Drive
Cincinnati OH 45241
Ph. 513-563-8855
fax 513-563-8865
eMail: phickey@asetech.com

Hines
Dick
Pratt & Whitney
Mail Stop 165-22
400 Main St.
East Hartford CT 06108
Ph. 860-565-7239
fax 860-565-0168
eMail: hinesrw@pwfl.com

Jackson
Bruce
NASA Langley Research Center
Mail Stop 132
Hampton VA 23681-0001
Ph. 757-864-4060
fax 757-864-7795
eMail: e.b.jackson@larc.nasa.gov

Jackson
Mike
Honeywell Inc.
MS: MN 65-2810
3660 Technology Drive
Minneapolis MN 55418
Ph. 612-951-7748
fax 612-951-7438
eMail: mike_jackson@htc.honeywell.com

Jager
Merle L.
McDonnell Douglas Aerospace Co.
Mail Code 71-30
2401 E. Wardlow Road
Long Beach CA 90807-5309
Ph. 562-593-4003
fax 562-982-7787
eMail: C391818@mdcpo10.lb.mdc.com

Joshi
Suresh
NASA Langley Research Center
Mail Stop 132
Hampton VA 23681-0001
Ph. 757-964-6608
fax 757-864-7795
eMail: s.m.joshi@larc.nasa.gov

Joslin
Ron
NASA Langley Research Center
Mail Stop 170
Hampton VA 23681-0001
Ph. 757-864-2234
fax 757-864-8801
eMail: r.d.joslin@larc.nasa.gov

Kaminer
Issac I.
Naval Postgraduate School
Mail Code AA/KA
Monterey CA 93943
Ph. 408-656-5040
fax 408-656-2313
eMail: kaminer@aa.nps.navy.mil

Kandula
Max
Dynacs Engineering Co., Inc.
Building 3, Suite B
258 S.W. 43rd
Renton WA 98055
Ph. 206-251-8692
fax 206-251-9564
eMail: kandula@vm.nas.gov

Kemmerly
Guy T.
NASA Langley Research Centr
Mail Stop 286
Hampton VA 23681-0001
Ph. 757-864-5070
fax 757-864-8192
eMail: g.t.kemmerly@larc.nasa.gov

Kennelly
Robert A.
NASA Ames Research Center
Mail Stop 227-6
Moffett Field CA 94035-1000
Ph. 415-604-5860
fax 415-604-0737
eMail: rakennelly@mail.arc.nasa.gov

Kinard
Tom A.
Lockheed Martin
86 South Cobb Drive
Mail Code 0685
Marietta GA 30063-0685
Ph. 770-494-8588
fax 770-494-3055
eMail: kinard@mar.lmco.com

Klopter
Goetz H.
MCAT, Inc.
NASA Ames Research Center
Mail Stop 258-1
Moffett Field CA 94035-1000
Ph. 415-604-3993
fax 415-604-2238
eMail: klopter@nas.nasa.gov

Kobayashi
Takahisa
NASA Lewis Research Center
Mail Stop 77-1
21000 Brookpark Road
Cleveland OH 44135-3191
Ph. 216-433-3739
fax 216-433-8643
eMail: tak@lerc.nasa.gov

Krause
Fred
General Electric
Mail Drop T34
1 Neumann Way
Cincinnati OH 45215-1988
Ph. 513-552-4279
fax 513-552-4350
eMail: fred.h.krause@ae.ge.com

Krist
Steven E.
NASA Langley Research Center
Mail Stop 280
Hampton VA 23681-0001
Ph. 757-864-3046
fax
eMail: s.e.krist@larc.nasa.gov

Kubiatko
Paul
McDonnell Douglas Aerospace Co.
Mail Code 71-35
2401 E. Wardlow Road
Long Beach CA 90807-5309
Ph. 562-982-7850
fax 562-593-7593
eMail: kubiatko@mdta.mdc.com

Kulfan
Bob
The Boeing Company
Mail Stop 6H-FK
P.O. Box 3707
Seattle WA 98124-2207
Ph. 206-965-3779
fax 206-234-4543
eMail: robert.m.kulfan@boeing.com

Kwatny
Harry
Drexel University
Dept Mechanical Engineering
Philadelphia PA 19104
Ph. 215-895-2356
fax 215-895-1478
eMail: hkawtny@coe.drexel.edu

Lawrence
Scott
NASA Ames Research Center
Mail Stop T27-B-2
Moffett Field CA 94035-1000
Ph. 415-604-4050
fax 415-604-1095
eMail: lawrence@nas.nasa.gov

Leavitt
Larry
NASA Langley Research Center
Mail Stop 280
Hampton VA 23681-0001
Ph. 757-864-3017
fax 757-864-8195
eMail: l.d.leavitt@larc.nasa.gov

Lessard
Victor R.
VIGYAN
30 Research Drive
Hampton VA 23666-1325
Ph. 757-864-5072
eMail: v.r.lessard@larc.nasa.gov.

Lessard
Wendy
NASA Langley Research Center
Mail Stop 286
Hampton VA 23681-0001
Ph. 757-864-1165
fax 757-864-8192
eMail: w.b.lessard@larc.nasa.gov

Light
Bruce A.
The Boeing Company
Mail Stop 6H-FP
P.O. Box 3707
Seattle WA 98124-2207
Ph. 206-965-1934
fax 206-234-4543
eMail:

Lin
Kyong
NASA Langley Research Center
Mail Stop 161
Hampton VA 23681-0001
Ph. 757-864-4342
fax 757-864-7797
eMail: k.b.lim@larc.nasa.gov

Liu
Tianshu
High Technology Corporation
28 Research Drive
Hampton VA 23666
Ph. 757-865-6766
eMail: tianshu@htc.tech.com

Ludas
Kevin
McDonnell Douglas Aerospace Co.
Mail Code 71-30
2401 E Wardlow Road
Long Beach CA 90807-5309
Ph. 562-593-2889
fax 562-982-7383
eMail: ludas@mdta.mdc.com

Lund
David W.
The Boeing Company
Mail Stop 6H-FK
P.O. Box 3707
Seattle WA 98124-2207
Ph. 206-965-2151
fax 206-234-4543
eMail: david.w.lund@boeing.com

MacKinnon
Malcolm I.K.
The Boeing Company
Mail Stop 6H-FM
P.O. Box 3707
Seattle WA 98124-2207
Ph. 206-237-0339
fax 206-234-4543
eMail: malcolm.i.mackinnon@boeing.com

MacWilkinson
Derek G.
McDonnell Douglas Aerospace Co.
Mail Code 71-30
2401 E. Wardlow Road
Long Beach CA 90807-5309
Ph. 562-496-8723
fax 562-982-7383
eMail: dmacw@mdta.mdc.com

Maddalon
Dal V.
NASA Langley Research Center
Mail Stop 170
Hampton VA 23681-0001
Ph. 757-864-1909
fax 757-864-8801
eMail: d.v.maddalon@larc.nasa.gov

Martin
Grant L.
McDonnell Douglas Aerospace Co.
Mail Code 71-35
2401 E. Wardlow Road
Long Beach CA 90807-5309
Ph. 562-593-0040
fax 562-593-7593
eMail: glm@indigo1.mdc.com

McMillin
S. Naomi
NASA Langley Research Center
Mail Stop 499
Hampton VA 23681-0001
Ph. 757-864-5581
fax 757-864-8469
eMail: s.n.mcmillin@larc.nasa.gov

McMinn
Dana
NASA Langley Research Center
Mail Stop 132
Hampton VA 23681-0001
Ph. 757-864-4069
fax 757-864-7795
eMail: j.d.mcminn@larc.nasa.gov

Mejia
Kevin K.
The Boeing Company
Mail Stop 6H-FK
P.O. Box 3707
Seattle WA 98124-2207
Ph. 206-965-3773
fax 206-234-4543
eMail: devin.m.mejia@boeing.com

Meredith
Paul T.
The Boeing Company
Mail Stop 6H-FK
P.O. Box 3707
Seattle WA 98124
Ph. 206-965-3468
fax 206-234-4543
eMail: paul.t.meredith@ca.boeing.com

Morgenstern
John
McDonnell Douglas Aerospace Co.
Mail Code 71-30
2401 E Wardlow Road
Long Beach CA 90807-5309
Ph. 562-982-9276
fax 562-982-7787
eMail: morgenstern@mdta.mdc.com

Morris
Martin J.
McDonnell Douglas Aerospace Co.
Mail Code 106-7126
P.O. Box 516
St. Louis MO 63166-0516
Ph. 314-232-6939
fax 314-777-1328
eMail: mmorris@mdc.com

Mortlock
Alan
McDonnell Douglas Aerospace Co.
Mail Code 71-30
2401 E Wardlow Road
Long Beach CA 90807-5309
Ph. 562-593-3937
fax 562-982-7787
eMail: mortlock@mdta.mdc.com

Narducci
Robert
McDonnell Douglas Aerospace Co.
Mail Code 71-35
2401 E. Wardlow Road
Long Beach CA 90807-5309
Ph. 562-593-0171
fax 562-593-7593
eMail: rpn@indigo1.mdc.com

Nelms, Jr.
Pres
NASA Ames Research Center
Mail Stop 237-2
Moffett Field CA 94035-1000
Ph. 415-604-6093
fax 415-604-6990
eMail: p_nelms@qmgate.arc.nasa.gov

Nelson
Chester P.
The Boeing Company
Mail Stop 6H-FK
P.O. Box 3707
Seattle WA 98124-2207
Ph. 206-965-5514
fax 206-234-4543
eMail: chester.p.nelson@boeing.com

Newman
Brett
Old Dominion University
Ph. 757-683-3720
fax 757-683-3200

Owens
Lewis
NASA Langley Research Center
Mail Stop 286
Hampton VA 23681-0001
Ph. 757-864-5127
fax 757-864-8192
eMail: l.r.owens@larc.nasa.gov

Ozoroski
L. P.
NASA Langley Research Center
Mail Stop 248
Hampton VA 23681-0001
Ph. 757-864-5992
fax 757-864-3553
eMail: l.p.ozoroski@larc.nasa.gov

Pao
S. Paul
NASA Langley Research Center
Mail Stop 280
Hampton VA 23681-0001
Ph. 757-864-3044
fax 757-864-8195
eMail: s.p.pao@larc.nasa.gov

Patton
Robert E.
The Boeing Company
Mail Stop 6H-FK
P.O. Box 3707
Seattle WA 98124-2207
Ph. 206-965-1425
fax 206-234-4543
eMail: robert.e.patton@boeing.com

Peavey
Charles C.
Northrop Grumman Corp.
Mail Code 9B52/GK
8900 E. Washington Blvd.
Pico Rivera CA 90660
Ph. 562-948-8937
fax 562-948-8068
eMail: cpeavey@world.northgrum.com

Pittman
James L.
NASA Langley Research Center
Mail Stop 395
Hampton VA 23681-0001
Ph. 757-864-1361
fax 757-864-8193
eMail:

Polito
Ryan C.
McDonnell Douglas Aerospace Co.
Mail Code 71-35
2401 E. Wardlow Road
Long Beach CA 90807-5309
Ph. 562-593-0048
fax 562-593-7593
eMail: rp@indigo1.mdc.com

Popernack, Jr.
Thomas G.
NASA Langley Research Center
Mail Stop 267
Hampton VA 23681-0001
Ph. 757-864-5163
fax
eMail: t.g.popernack.jr@larc.nasa.gov

Pototzky
Anthony S.
NASA Langley Research Center
Mail Stop 389
Hampton VA 23681-0001
Ph. 757-864-2827
fax 757-864-8838
eMail: a.s.pototzky@larc.nasa.gov

Powell
Art
McDonnell Douglas Aerospace Co.
Mail Code 71-35
2401 E. Wardlow Road
Long Beach CA 90807-5309
Ph. 562-593-3225
fax 562-593-7593
eMail: C306624@mdcpo11.lb.md.com

Proffitt
Melissa
Lockheed Engineering and Sciences Co.
NASA Langley Research Center
Mail Stop 389
Hampton VA 23681-0001
Ph. 757-864-4024
fax 757-864-7795
eMail: m.s.proffitt@larc.nasa.gov

Radeztsky
Ronald
High Technology Corporation
28 Research Drive
Hampton VA 23666
Ph. 757-865-0818
fax 757-865-6766
eMail: ron@htc.tech.com

Raney
David
NASA Langley Research Center
Mail Stop 489
Hampton VA 23681-0001
Ph. 757-864-4033
fax 757-864-7795
eMail: d.l.raney@larc.nasa.gov

Ray
James K.
The Boeing Company
Mail Stop 6H-FA
P.O. Box 3707
Seattle WA 98124-2207
Ph. 206-965-1997
fax 206-234-4543
eMail: james.k.ray@.boeing.com

Reuther
James
RIACS
NASA Ames Research Center
Mail Stop 227-6
Moffett Field CA 94035-1000
Ph. 415-604-1516
fax 415-604-0737
eMail: reuther@ra.iris-arc.nasa.gov

Ricketts
Rodney H.
NASA Langley Research Center
Mail Stop 119
Hampton VA 23681-0001
Ph. 757-864-1209
fax 757-864-8852
eMail: r.h.ricketts@larc.nasa.gov

Rimlinger
Mark J.
Sterling Software, Inc.
NASA Ames Research Center
Mail Stop 227-6
Moffett Field CA 94035-1000
Ph. 757-864=5944
fax 757-864-0737
eMail: rimlinge@ra-iris.arc.nasa.gov

Rivers
Melissa B.
NASA Langley Research Center
Mail Stop 499
Hampton VA 23681-0001
Ph. 757-864-5161
fax 757-864-7892
eMail: m.b.rivers@larc.nasa.gov

Rivers
Rob
NASA Langley Research Center
Mail Stop 132
Hampton VA 23681-0001
Ph. 757-864-3917
fax 757-864-8549
eMail: r.a.rivers@larc.nasa.gov

Roberts
Thomas W.
NASA Langley Research Center
Mail Stop 128
Hampton VA 23681-0001
Ph. 757-864-6804
fax 757-864-8166
eMail: t.w.roberts@larc.nasa.gov

Rossitto
Ken
McDonnell Douglas Aerospace Co.
Mail Code 36-41
2401 E Wardlow Road
Long Beach CA 90807-5309
Ph. 562-593-3870
fax 562-593-7593
eMail: rossitto@mdta.mdc.com

Saladino
Anthony J.
Dynacs Engineering Co., Inc.
Building 3, Suite B
258 S.W. 43rd Street
Renton WA 98055
Ph. 206-251-8692
fax 206-251-9564
eMail: saladino@indyl.dynacsgen.com

Sawyer
Wallace C.
NASA Langley Research Center
Mail Stop 119
Hampton VA 23681-0001
Ph 757-864-2267
fax 757-864-8852
Email: w.c.sawyer@larc.nasa.gov

Scott
Michael
NASA Langley Research Center
Mail Stop 132
Hampton VA 23681-0001
Ph. 757-864-6618
fax 757-864-7795
eMail: michael.allen.scott@larc.nasa.gov

Shaw
Joe
NASA Lewis Research Center
Mail Stop 60-2
21000 Brookpark Road
Cleveland OH 44135-3191
Ph. 216-977-7135
fax 216-977-7133
eMail: robert.j.shaw@lerc.nasa.gov

Shields
Bill
Lockheed Engineering & Sciences Co.
NASA Langley Research Center
Mail Stop 248
Hampton VA 23681-0001
Ph. 757-864-5958
fax 757-864-5958
eMail: c.w.shields@larc.nasa.gov

Siclari
Michael J.
Northrop Grumman Corp.
Mail Stop KO8-14
South Oyster Bay Road
Bethpage NY 11714
Ph. 516-575-8067
fax 516-346-2937
eMail: siclari@gateway.grumman.com

Smith
Brian
NASA Ames Research Center
Mail Stop 247-2
Moffett Field CA 94035-3191
Ph. 415-604-6669
fax 415-604-3489
eMail: bsmith@mail.arc.nasa.gov

Snyder
Phil
NASA Ames Research Center
Mail Stop 237-2
Moffett Field CA 94035-1000
Ph. 415-604-4592
fax 415-604-6990
eMail: p.t.snyder@mail.arc.gov

Sundaram
Pichuraman
McDonnell Douglas Aerospace Co.
Mail Code 71-35
2401 E. Wardlow Road
Long Beach CA 90807-5309
Ph. 562-496-9787
fax 562-593-7593
ps@indigo1.mdc.com

Tamrat
Befecadu
Boeing North American Inc.
Mail Code Sk12
2600 Westminster Blvd.
Seal Beach CA 90740
Ph. 310-797-4948
fax 310-797-4854
eMail: bftamrat@naa.boeing.com

Thomas
James L.
NASA Langley Research Center
Mail Stop 128
Hampton VA 23681-0001
Ph. 757-864-2163
fax 757-864-8816
eMail: j.l.thomas@larc.nasa.gov

Thomas
Scott D.
Sterling Software, Inc.
NASA Ames Research Center
Mail Stop 237-2
Moffett Field CA 94035-1000
Ph. 415-604-6387
fax 415-604-6990
eMail: thomas@nas.nasa.gov.

Troha
William A.
NASA Lewis Research Center
Mail Stop 86-1
21000 Brookpark Road
Cleveland OH 44135-3191
Ph. 216-433-3195
fax 216-433-6624
eMail: william.a.troha@lerc.nasa.gov

Unger
Eric R.
McDonnell Douglas Aerospace Co.
Mail Code 71-35
2401 E. Wardlow Road
Long Beach CA 90807-5309
Ph. 562-593-3037
fax 562-593-7593
eMail: c386821@hc1038.mdc.com

Vasquez
Moises
George Washington University
NASA Langley Research Center
Mail Stop 286
Hampton VA 23681-0001
Ph.
Fax
eMail: vasquez@ab80.larc.nasa.gov

Vatsa
Veer N.
NASA Langley Research Center
Mail Stop 128
Hampton VA 23681-0001
Ph. 757-864-2236
fax 757-864-8816
eMail: v.n.valsa@larc.nasa.gov

Viars
Philip
General Electric
Mail Drop T34
1 Neumann Way
Cincinnati OH 45215-1988
Ph. 513-552-4132
fax 513-552-4350
eMail: Philip.Viars@ae.ge.com

Wahls
Richard A.
NASA Langley Research Center
Mail Stop 499
Hampton VA 23681-0001
Ph. 757-864-5108
fax 757-864-8469
eMail: r.awahls@larc.nasa.gov

Wallace
Hoyt
McDonnell Douglas Aerospace Co.
Mail Code S270-2370
P.O. Box 516
St Louis MO 53166-0516
Ph. 314-233-7712
fax 314-234-7210
eMail: hwallace@mdc.com

Walsh
Michael J.
NASA Langley Research Center
Mail Stop 170
Hampton VA 23681-0001
Ph. 757-864-5542
fax 757-864-7897
eMail: m.j.walsh@larc.nasa.gov

Wechsler
Jim
McDonnell Douglas Aerospace Co.
Mail Code 71-35
2401 E. Wardlow Road
Long Beach CA 90807-5309
Ph. 562-496-7627
fax 562-982-7787
eMail: jwex@mdta.mdc.com

Westra
Bryan W.
Northrop Grumman Corp.
Mail Code 9B52/GK
8900 E. Washington Blvd.
Pico Rivera CA 90660
Ph. 562-948-7560
fax 562-948-8068
eMail: bwestra@world.northgrum.com

Whitehead
Allen H. Jr.
NASA Langley Research Center
Mail Stop 119
Hampton VA 23681-0001
Ph. 757-864-7800
fax 757-864-8852
eMail: allen.h.whitehead@larc.nasa.gov

Wilhite
Alan W.
NASA Langley Research Center
Mail Stop 119
Hampton VA 23681-0001
Ph. 757-864-2982
fax 757-864-8852
eMail: a.w.wilhite@larc.nasa.gov

Williams
Todd
McDonnell Douglas Aerospace Co.
Mail Code 71-12
2401 E. Wardlow Road
Long Beach CA 90807-5309
Ph. 562-496-8795
fax 562-496-9244
eMail: twilliams@mdta.mdc.com

Wilson
Doug
The Boeing Company
Mail Stop 6H-FK
P.O. Box 3707
Seattle WA 98124-2207
Ph. 206-965-3458
fax 206-234-4543
eMail: douglas.l.wilson@boeing.com

Wittenberg
K. Robyn
The Boeing Company
Mail Stop 6H-FK
P.O. Box 3707
Seattle WA 98124-2207
Ph. 206-965-1091
fax 206-234-4543
eMail:

Woan
Chung-Jin
Boeing North American, Inc.
Mail Code SK07
P.O. Box 3644
Seal Beach CA 90740-7644
Ph.
fax
eMail

Wood
Rick
NASA Langley Research Center
Mail Stop 499
Hampton VA 23681-0001
Ph. 757-864-6174
fax 757-864-8469
eMail:

Wyatt
Greg
The Boeing Company
Mail Stop 6H-FK
P.O. Box 3707
Seattle WA 98124-2207
Ph. 206-965-3466
fax 206-234-4543
eMail: douglas.l.wilson@boeing.com

Yaghmaee
Sasan S.
The Boeing Company
Mail Stop 6H-FK
P.O. Box 3707
Seattle WA 98124-2207
Ph. 206-965-3777
fax 206-234-4543
eMail: sasan.yagmaee@boeing.com

Yaros
Steven
NASA Langley Research Center
Mail Stop 286
Hampton VA 23681-0001
Ph. 757-864-3050
fax 757-864-8192
eMail: s.f.yaros@larc.nasa.gov

Yeh
David T.
McDonnell Douglas Aerospace Co.
Mail Code 71-35
2401 E. Wardlow Road
Long Beach CA 90807-5309
Ph. 562-496-9113
fax 562-593-7593
eMail: dty@indigo1.mdc.com

Zuniga
Fanny
NASA Ames Research Center
Mail Stop 247-2
Moffett Field CA 94035-1000
Ph. 415-604-2017
fax 415-604-3489
eMail: fzuniga@mail.arc.nasa.gov

Overview Of CA Activities at Boeing

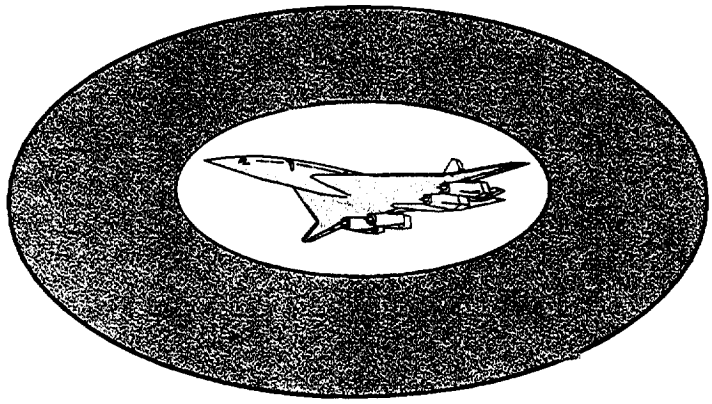

Aerodynamics Performance Workshop

NASA Langley
February 25 - February 28, 1997

Robert M. Kulfan
Boeing Commercial Airplane Group

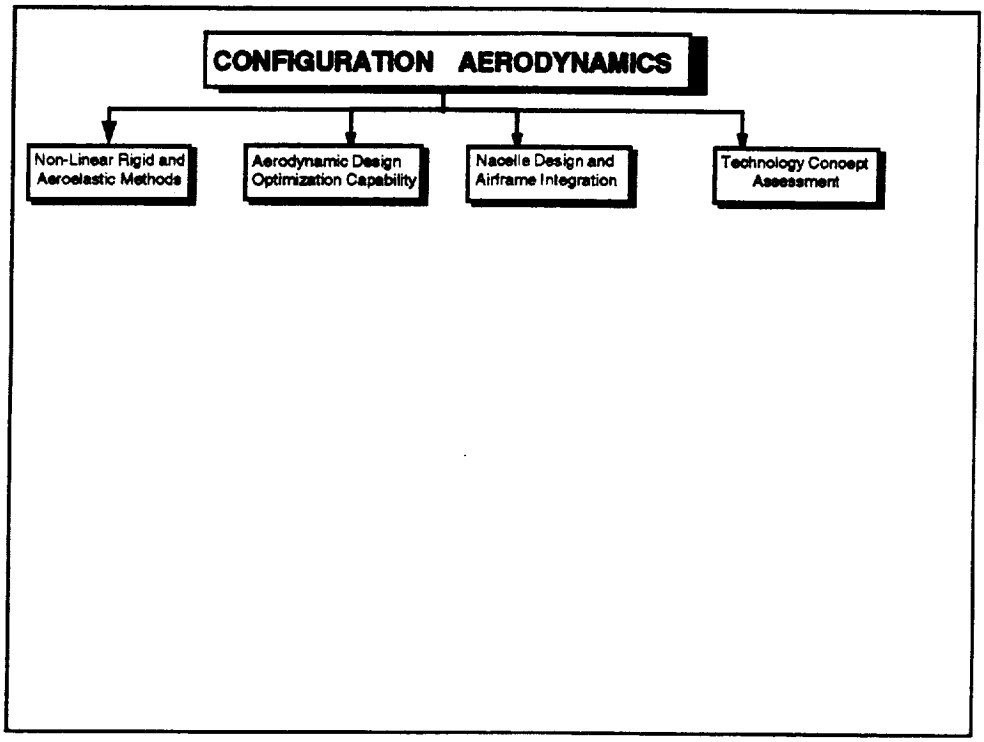

The Configuration Aerodynamics technology development activities consist of four primary subtasks. These include:

1. Non-linear rigid and aeroelastic methods adaption and validation.
2. Developing and validation non-linear aerodynamic design optimization capability.
3. Nacelle design and airframe integration studies.
4. Assessments of the baseline TCA configuration and determining the benefits of the Configuration Aerodynamics technology development activities.

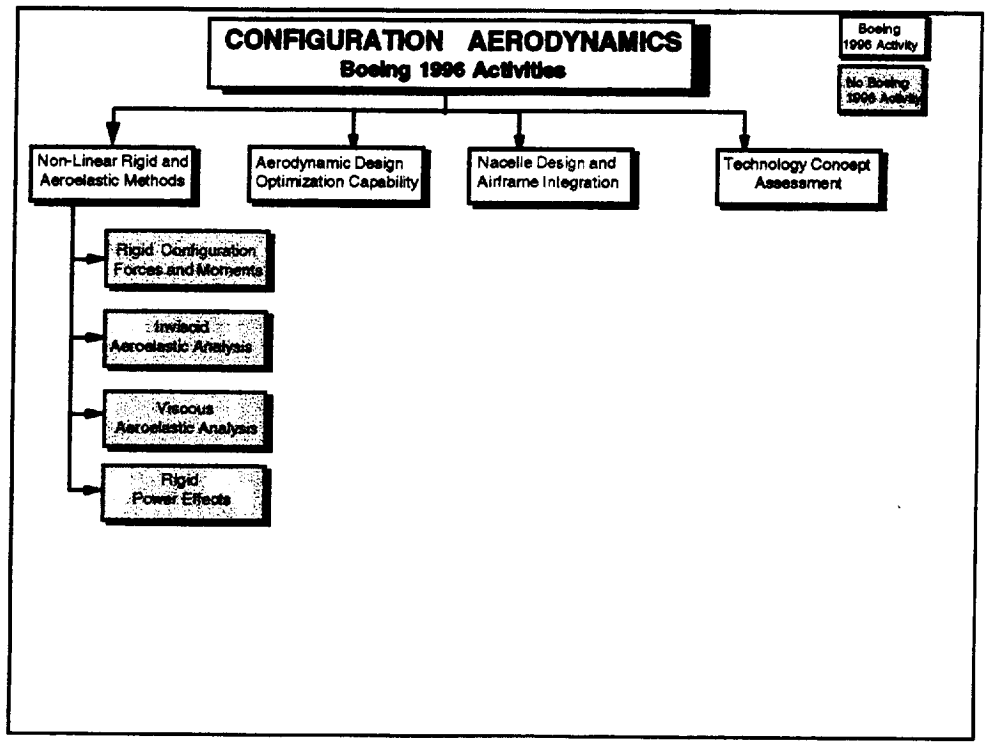

The Non-Linear Rigid and Aeroelastic Methods subtask activities consist for four primary task elements. These Include:

1. Prediction of complete configuration forces and moments.
2. Inviscid aeroelastic analysis methods development.
3. Viscous aeroelastic analysis methods development.
4. Prediction of power induced effects on the complete rigid configuration.

The overall objective is to adapt, apply and validate non-linear aerodynamic analysis methods for prediction of the forces, moments and pressure distributions on complete HSCT type configurations including elastic and propulsion system power induced effects. The CFD methods are used as critical elements in then other three subtasks.

Also included in the subtask are experimental activities conducted to validate the analysis tools.

Boeing did not have any activity in this subtask in 1996

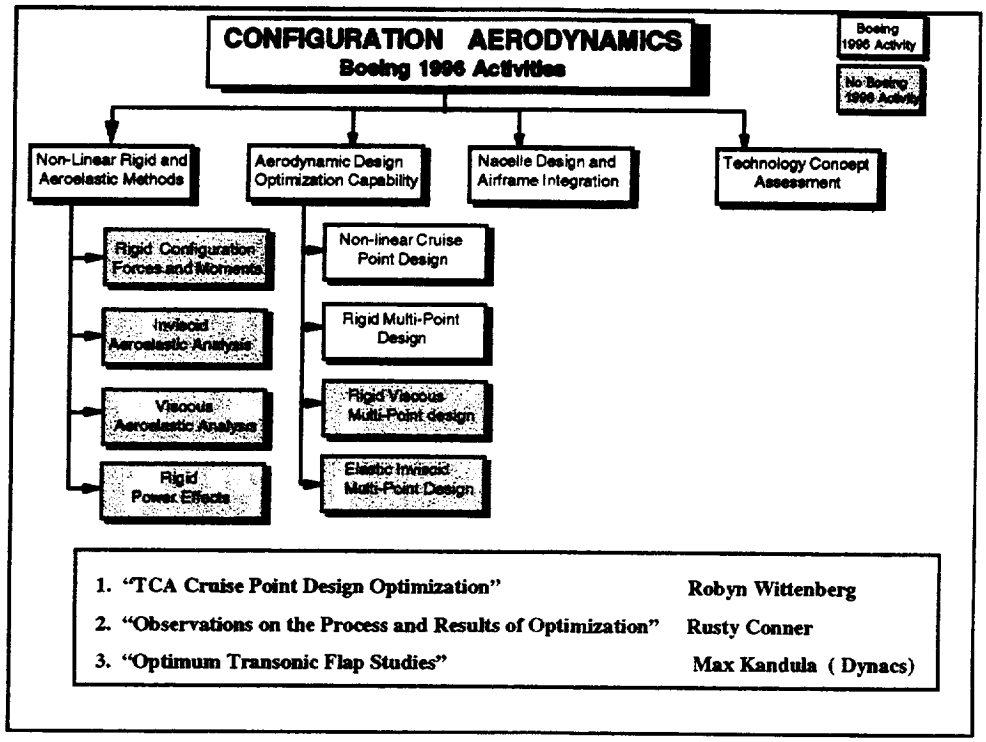

The Aerodynamic Design Optimization Capability subtask consists of four subtask elements. These are the four essential sequential steps necessary to develop the ultimate capability of non-linear aerodynamic design optimization including both viscous and aeroelastic effects.

The Boeing Non-linear cruise point activities were focused on including typical realistic design constraints in the TRANAIR non-linear optimization process and assessing the potential cruise performance benefits when applied to the TCA linear design baseline configuration. Robyn Wittenburg and Rusty Conner will discuss the Boeing point design optimization work.

The Boeing rigid multi-point design optimization activity was focused on transonic flap optimization of the TCA configuration. An important element is to understand the nature of the flow over the flaps for the optimum condition. This is a prelude for developing multi-point design optimization capability. Max Kandula will summarize the work performed by Dynacs for Boeing in this area.

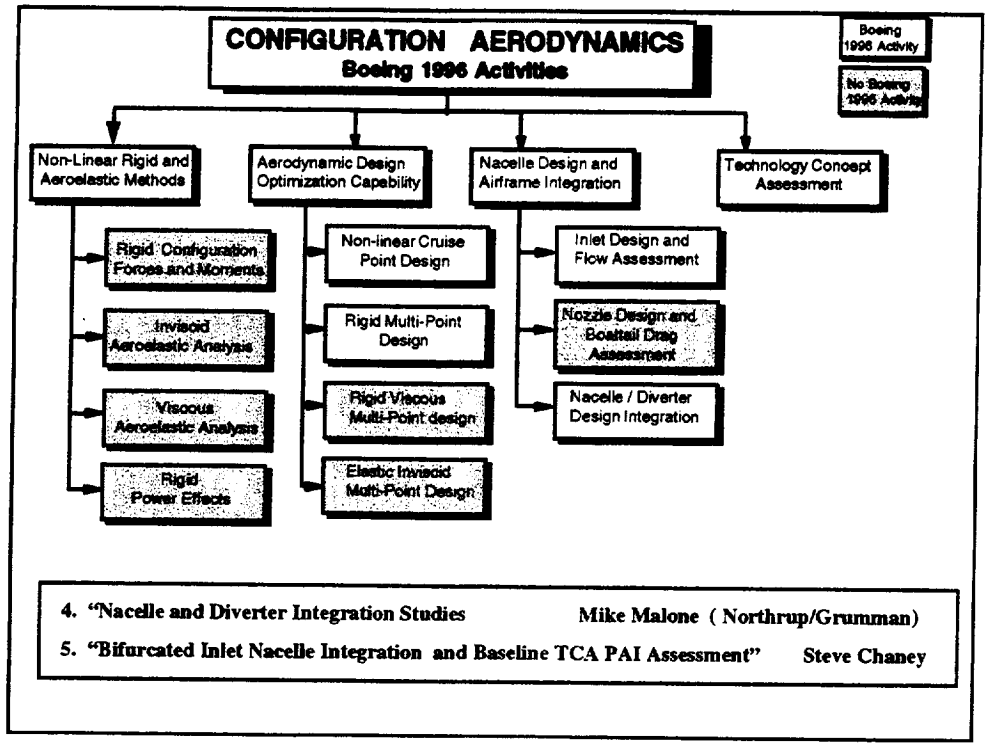

The Nacelle Design and Airframe Integration subtask consists of four three subtasks elements:

- Inlet design and flow assessment
- Nozzle design and boattail drag assessment
- Nacelle / Diverter design integration

Mike Malone will summarize the nacelle and diverter integration studies conducted by Northrup/Grumann for Boeing.

Steve Chaney will discuss the bifurcated inlet nacelle integration studies and the assessments of the nacelle / diverter installation on the baseline TCA configuration.

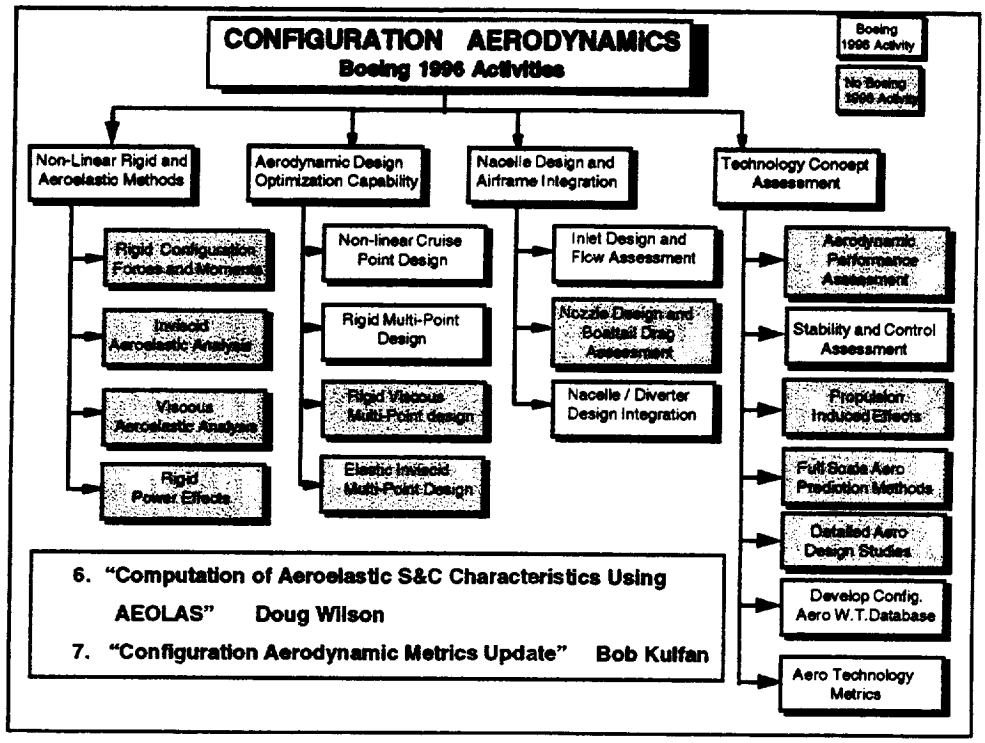

The Technology Concept Assessment subtask consists of:

- Aerodynamic performance assessments of the baseline TCA configuration
- Stability and control assessments of the TCA
- Propulsion induced effects test programs and related prediction methods validation activities.
- Developing methods for predicting full scale aerodynamic predictions.
- Fundamental aerodynamic design studies
- Development of wind tunnel database for the TCA
- Aerodynamic technology metrics developments and tracking the technology process.

Doug Wilson will summarize results of computing aeroelastic S&C characteristics using the Boeing AEOLAS program.

Bob Kulfan will review the metrics development and tracking activities during the plenary session of the workshop.

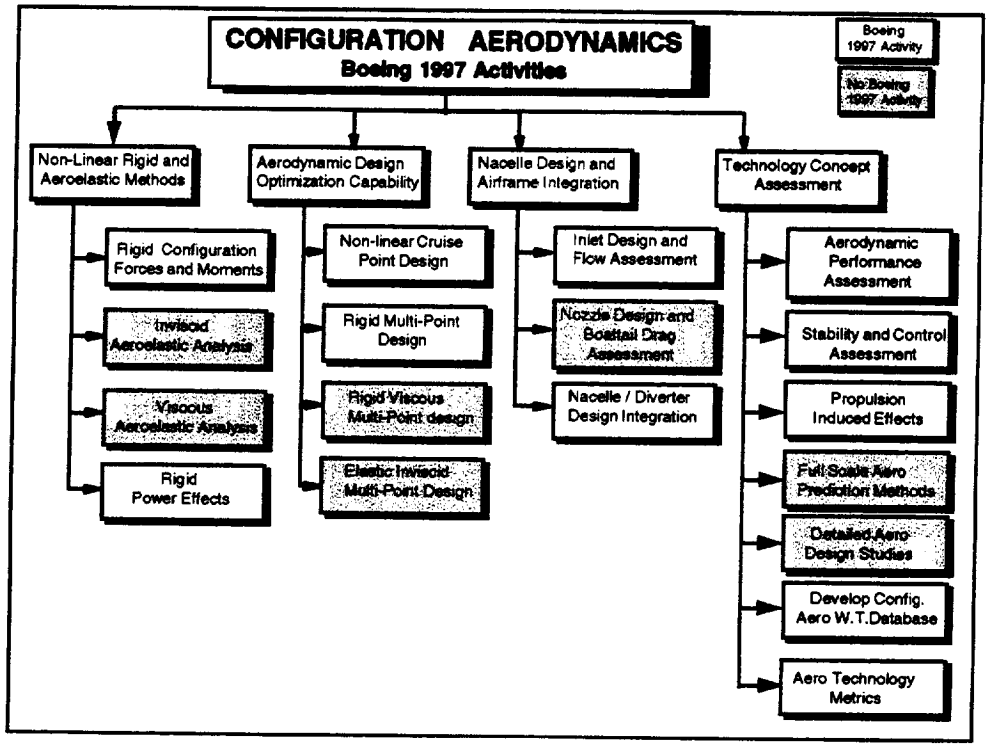

The Boeing technology development areas in 1997 will be expanded relative to 1996.

Rigid Configuration Forces and Moments: The focus will be on prediction on complete configuration forces and moments including aftbody / empennage and trim drag. This will support the planned aft-body closure wind tunnel test program planned for later this year.

Rigid Power Effects: The objective of this activity is to develop CFD modeling and analysis capability to represent Propulsion Induced Effects (PIE) on the TCA configuration, Inlet spillage, bleed, bypass and nozzle flow effects will be included. The initial focus will be on identifying the magnitude of these effects in support of the planned Configuration Aerodynamics PIE wind tunnel test program. This work will be conducted by Northrup/ Grumann

Non-Linear Cruise Point Design: .The TRANAIR design optimization method will be enhanced to include optimization with viscous effects, Complete configuration including trim drag effects, and inlet flow quality constraints. The enhanced methodology will be applied to the TCA configuration.

Rigid Multi-Point Design: Techniques will be explored to determine if TRANAIR can be used to conduct meaningful off-design flap optimization. A strategy for conducting multi-point design optimization with TRANAIR will be formulated.

Inlet Design and Flow Assessment: Studies are underway to develop techniques to model inlet spillage effects with the OVERFLOW Navier Stokes CFD code. The objective is to develop and validate the capability to model actual flight spillage rates so that the axi-symmetric and bifurcated nacelles can be accurately compared at the transonic acceleration flight conditions. This work is in support of inlet downselect decisions.

Nacelle/Diverter Design Integration: This will be an extension of the detailed nacelle design integration studies currently underway. The planned wind tunnel test programs of various nacelle integration concepts on the TCA will be supported.

Aerodynamic Performance Assessment: Wind tunnel performance data obtained with the TCA configuration will be evaluated especially at the off-design conditions in which the outboard flaps are deflected.

Stability and Control Assessments: Stability and control assessments of the TCA configuration will be continued.

Propulsion Induced Effects: Efforts to support the planned PIE wind tunnel test program are currently under way.

Develop Configuration Aero Wind Tunnel Database: Boeing will participate in supporting the development of the wind tunnel database for the TCA configuration.

Aerodynamic Technology Metrics: The L/D projection processes will continue to be refined. These metrics will be used through the year to track the technology development progress.

Boeing Presentation Schedule

8:00 - 8:10	"Overview of CA Activities at Boeing	Bob Kulfan
8:10 - 8:50	"TCA Cruise Point Design Optimization"	Robyn Wittenberg
8:50 - 9:30	"Observations on the Process and Results of Optimization"	Rusty Conner
9:30 - 10:00	"Optimum Transonic Flap Studies"	Max Kandula
10:00 - 10:15	Break	
10:15 - 10:45	"Nacelle and Diverter Integration Studies	Mike Malone
10:45 - 11:45	"Bifurcated Inlet Nacelle Integration and Baseline TCA PAI Assessment"	Steve Chaney
11:45-12:00	"Computation of Aeroelastic S&C Characteristics Using AEOLAS"	Doug Wilson

This is the schedule for the Boeing Presentations.

TCA Configuration
Cruise Point Design Optimization

Configuration Aerodynamics Task 32
Design Optimization Capability
(W.B.S. 4.3.1.2)

K. R. Wittenberg
25–28 February 1997

TCA Configuration Cruise Point Design Optimization

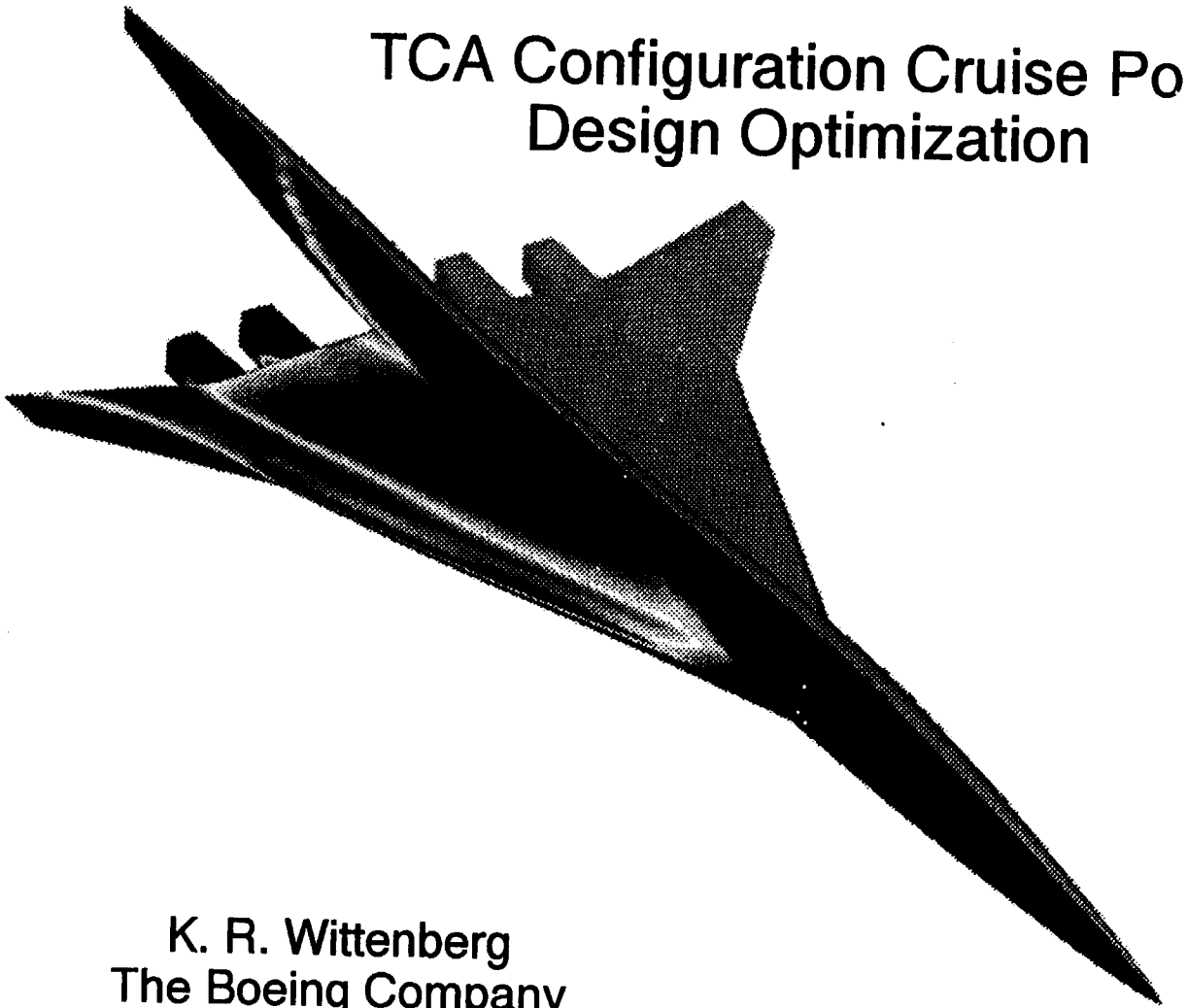

K. R. Wittenberg
The Boeing Company

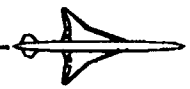

HSCT TCA Optimization : Outline

- Objective
- Approach
- Problem Definition
- Progress
- Future Work

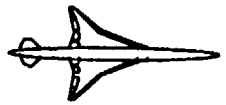

HSCT TCA Optimization : Objective

The 1996 objective was to produce and validate a non–linear CFD design, at the TCA cruise point, which met project constraints and yielded a reasonable drag reduction. The optimization was to be based upon the linear–design TCA configuration.

HSCT TCA Optimization : Objective

To develop and apply the capability to produce a realistic, non-linear, point-designed, optimized configuration, with reduced drag, based upon the TCA configuration.

HSCT TCA Optimization : Approach

The approach is to limit the design space through implementation of both the specified project constraints plus other geometric constraints which past experience had shown to be effective in ushering the design toward acceptable geometry. The method permits emphasis on acceptable geometric solutions. By attending to the locations of active constraints, we may still choose to compromise on the constraints for more attractive possible solutions.

The TRANAIR code was chosen as the optimization tool. This selection was made for several reasons. First, TRANAIR has repeatedly demonstrated that the full potential equation contains all the physics, except viscosity, necessary to accurately calculate the flow about the supersonic cruise point of efficient HSCT configurations. Integrated forces, in particular drag, are accurately predicted. Second, the optimization implementation is very efficient. Finally, the ability to handle arbitrary geometry allows accurate and faithful representation of as much of the configuration as desired.

We have continued to build the capability of our optimization in steps or building blocks. This approach was chosen because it is much simpler to assess the success and effect of a single, decoupled step. Considering the complexity of the optimization process, it is too unpredictable to proceed without understanding each successive step. This method allows us to evaluate further how each step contributes to the whole.

There are clear advantages to constraining the optimizer to the smoothest solution that it can find. The improvement in flow time to create a final loft can be dramatic if starting from a relatively smooth optimization product. While some final smoothing will always be required, and since we are limited to a finite number of controlling variables, we can eliminate the larger excursions that are more difficult to smooth.

The resulting TRANAIR non–linearly optimized configuration is taken, as the final step, into the OVERFLOW code for Navier–Stokes analysis of the inviscid design. During the optimization, checks are made of parameters which we have found can indicate potential viscous problems.

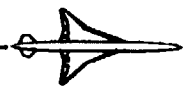

HSCT TCA Optimization : Approach

- Validate Implementation of Project Constraints
- Use TRANAIR for Optimization
- Reduce Post-Optimization Smoothing Effort
- Verify Result Using OVERFLOW (NS)

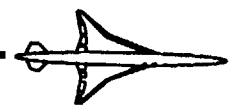

HSCT TCA Optimization : Problem Definition

The following sections will describe the overall TRANAIR optimization problem definition. This definition includes wing, body, and wing–to–body project prescribed constraints and other constraints included based on past non–linear design experience. The layout of the design variables during the optimization phases is also described.

HSCT TCA Optimization : Problem Definition

- Constraints
- TRANAIR Variable Layout

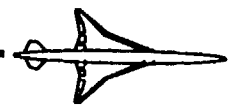

HSCT TCA Optimization – Wing Project Constraints

The project constraints implemented this year are listed here. All have been verified as working as expected. The subsonic leading edge is enforced, not for manufacturing, but for off–design concerns. The trailing edge closure angle and spar thickness constraints are for manufacturing. The wing volume is for fuel requirements.

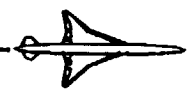

TCA Optimization : Wing Project Constraints

- Subsonic Leading Edge Radius
- Trailing Edge Closure Angle
- Wing Thickness at Spars
- Maximum Wing t/c
- Wing Volume
- Supersonic Wing Leading Edge Closure Angle

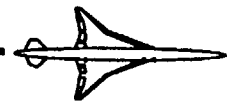

TCA Wing Constraints

This graphic shows the wing constraints on the TCA planform.

TCA Wing Constraints

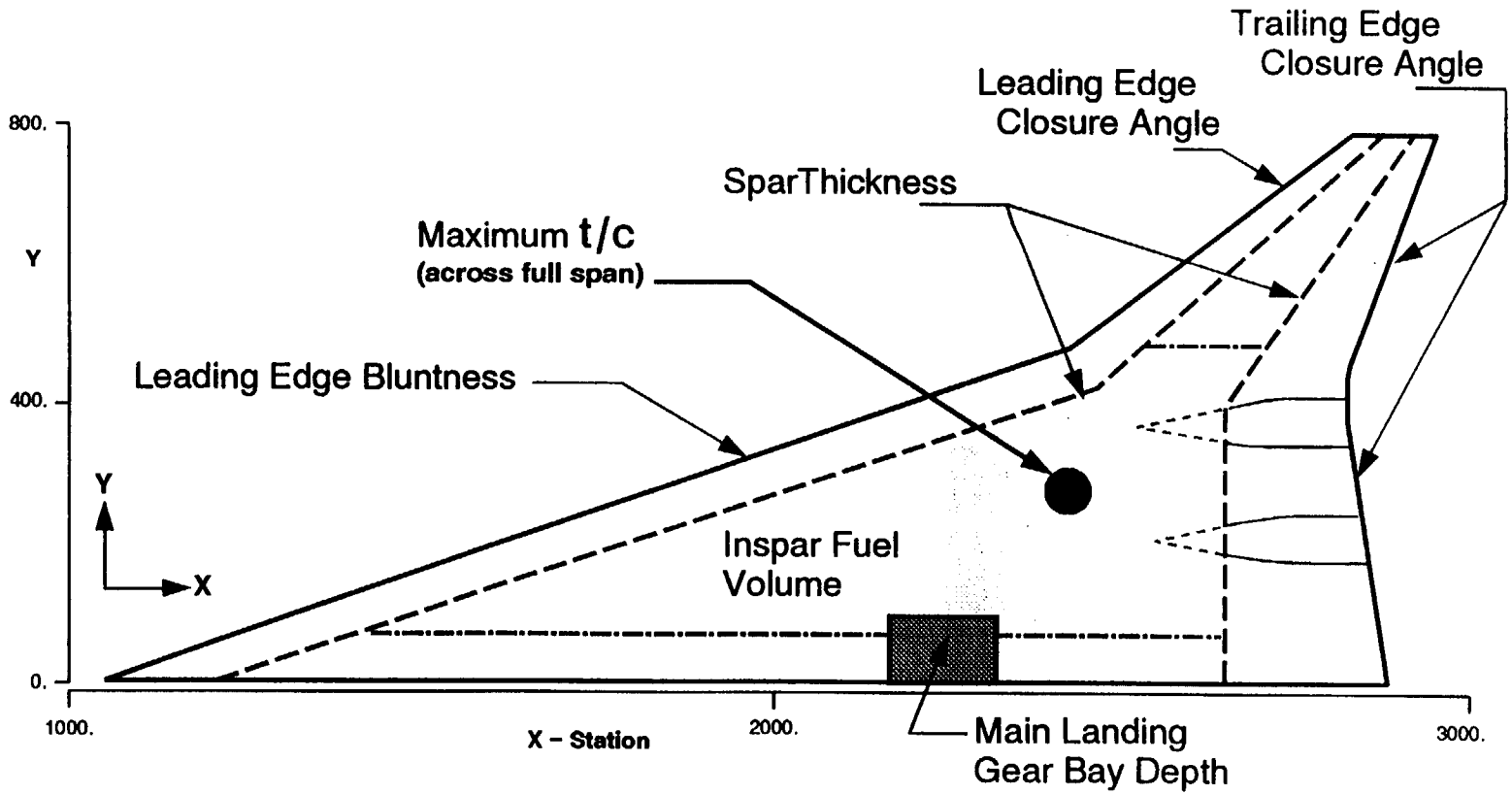

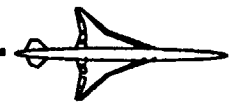

HSCT TCA Optimization – Body Project Constraints

The project constraints implemented this year are listed here. All have been verified as working as expected. The internal polygon shapes are for passenger and cargo clearances. The separation of front spar and cabin floor is required for systems clearance. Also the primary and auxiliary box clearances are for systems. The overwing emergency exit door clearance is an airplane certification requirement. Both the main cabin floor angle and the floor kink angles are requirements for in–flight cart handling and passenger safety and comfort.

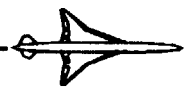

TCA Optimization :

Body Project Constraints

- Body Internal Polygon Shapes
- Front Spar / Cabin Floor Separation
- Primary & Auxiliary Box Clearance
- Minimum/Maximum Radius of Cross Section
- Main Cabin Floor Angle of Attack
- Floor Kink Angles
- Pilot Location Area
- Horizontal Tail Carry Through Structure

TCA Body Constraint Sections

This figure shows a side view of the TCA baseline body with internal polygons for the various sections added. The nose gear bay and the cargo bay are also sketched. This figure indicates how much of the body is controlled via the internal constraints.

TCA Body Constraint Sections

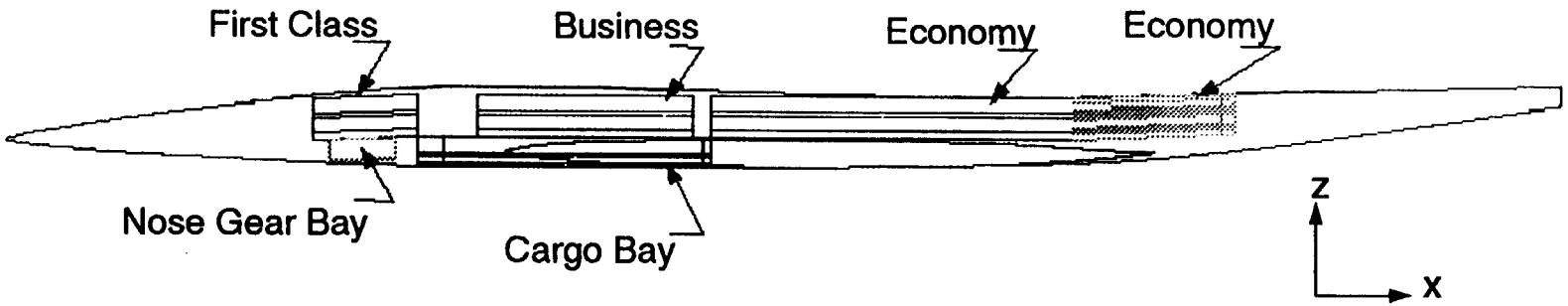

Internal Polygon Clearances
MLGB Thickness
Primary & Auxilliary Box Clearances
Body Radius of Curvature (X-section)
Pilot Area
Main Cabin Floor Angle of Attack
Floor Kink Angles

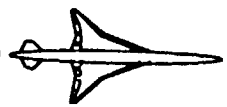

HSCT TCA Optimization – Wing–to–Body Project Constraints

The project constraints implemented this year are listed here. All have been verified as working as expected. The lift coefficient is an overall constraint as the design is allowed to trade wing and body lift and drag. The main landing gear bay thickness affects both the wing and the body by virtue of their interconnectedness in this configuration.

TCA Optimization : Wing-to-Body Project Constraints

- Main Landing Gear Bay Thickness
- Front Spar / Cabin Floor Separation
- Overwing Emergency Exit Door Clearance
- Body Keel to Rear Spar Depth Provision

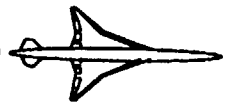

HSCT TCA Optimization – Other Constraints

In order to encourage the optimizer to create pleasing shapes and to hold certain areas inviolate, we implemented a series of constraints unrelated to project requirements.

Spanwise curvature constraints were implemented to cause the optimizer to look for solutions with more reasonable contours in the spanwise direction and certain regions were controlled with chordwise constraints. Allowed to go free, the optimizer opted for wing designs that engineering judgement said was too wavy. The body curvature was limited in both the length and circumference curvatures.

In order to keep within the building block approach discussed earlier, we implemented several constraints requiring the geometry in the nacelle/diverter region to remain relatively fixed. This region was specifically targeted by the final optimization cycle. In the future, greater local design tailoring will be available to work on the nacelle/diverter increment. This year's work was restricted to wing and body optimization in the presence of the nacelles and diverters.

With just the incorporation of the full–up project constraints, recent designs meet the cross flow criterion, developed during 1995, although at each intermedicate step this criterion was checked to ensure that no surprises would be found during Navier–Stokes verification.

As in previous design cycles, the wing maximum Mach number was limited. This constraint was also a viscous effect additional constraint to avoid strong expansions and compressions.

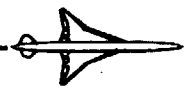

TCA Optimization : Other Constraints

- Smoothness
  - Wing Surface Chordwise Curvature
  - Wing Surface Spanwise Curvature
  - Body Lengthwise Curvature
- Consistent Nacelle/Diverter Placement
  - Diverter LE/TE Height
  - Allow for Boundary Layer Clearance to Inlet
- Viscous Effects
  - Maximum Mach Number
- Lift Coefficient

TCA Tranair Optimization Problem Posed

The figure shows the full thickness/camber/twist variable layout on the TCA planform. The variables are shown as circles. The spars are shown with dashed lines. A total of 298 wing variables were used for the optimization (more were used for the body camber and area – discussed later). The variables are arranged in a rectangular grid. The camber and thickness variables were located at the same percent chord.

Future plans are to allow the belts to have varying distributions to use the limited number of variables in a more efficient manner.

TCA Optimization Problem Posed

Variables:

- 11 Spanwise Node Belts
- 12 Camber Nodes per Belt
- 13 Thickness Nodes per Belt
- 1 Shear Node per Belt
- 1 Twist Node per Belt
- 1 Alpha

Objective Function:
Minimize C_D

27 wing variables per belt X 11 belts = 298 wing variables

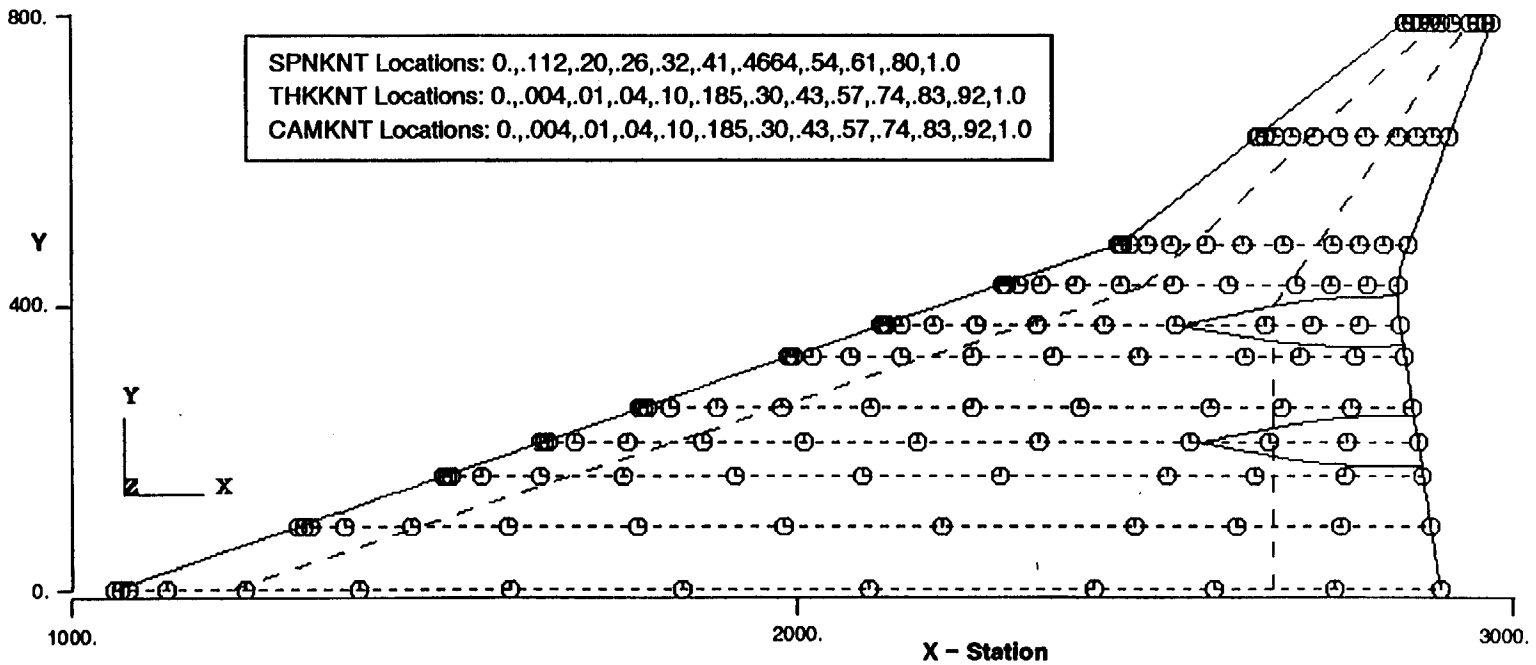

TCA Tranair Optimization – Body Variables

The figure shows the layout of the body variables on the TCA configuration. The camber variables are shown as squares. The area variables are shown as diamonds. The cabin floor is shown as a series of straight segments with the floor kink locations shown with circles. The area variables are shown on the lower sketch with five nodes distributed radially. A total of 118 body variables were used for the simultaneous full wing/body optimization.

TCA Optimization – Body Variables

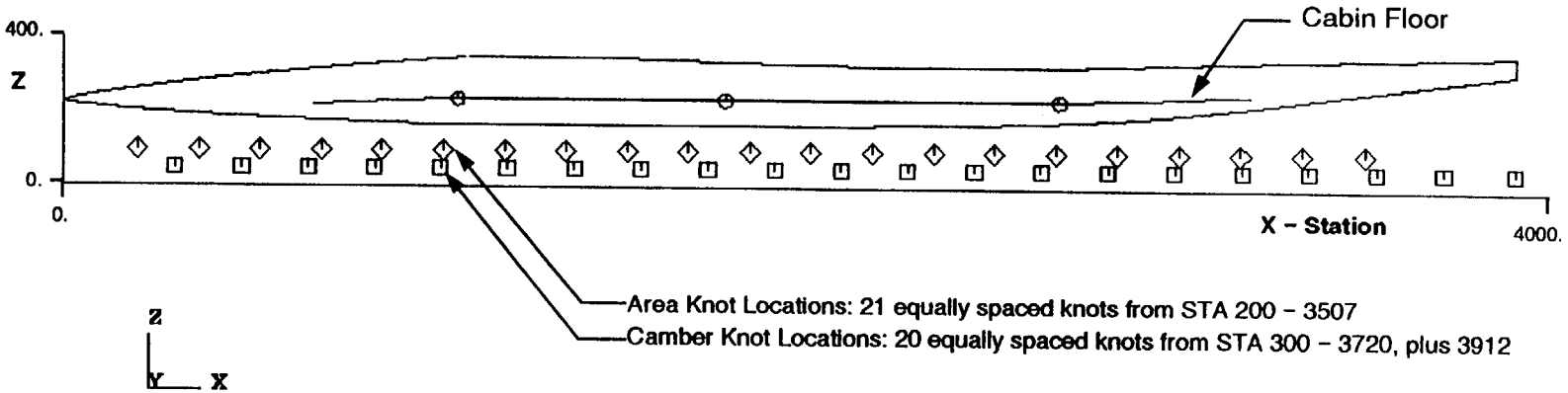

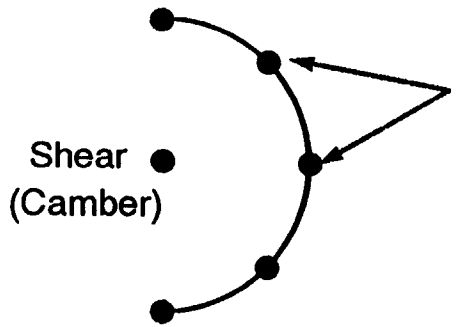

Five Cross Section Variables per Station

19 Locations * 6 variables = 115
3 Floor Kink Variables = 3
118

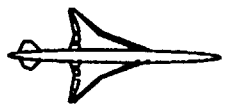

TCA Tranair Optimization Problem Posed – Nacelle Tune–Up

The figure shows the adjusted and compressed variable layout on the TCA planform which was used for the final cycle to get more detailed design adjustments in the local nacelle/diverter region. The variables are shown as circles. The spars are shown with dashed lines. A total of 384 wing variables were used for the optimization, with 20 body camber–only variables, plus alpha and floor kink nodes to bring the total to 408 variables for the tune–up run. The variables are arranged in a rectangular grid. The camber and thickness variables were located at the same percent chord.

Future plans are to allow the belts to have varying distributions to use the limited number of variables in a more efficient manner.

TCA Optimization Problem Posed – Nacelle Tune–up

Wing Variables:
- 12 Spanwise Node Belts
- 16 Camber Nodes per Belt
- 16 Thickness Nodes per Belt

32 wing variables per belt X 12 belts = 384 wing variables
+ 20 body camber variables
+ 1 alpha + 3 floor variables => 408 variables

Objective Function:
Minimize C_D

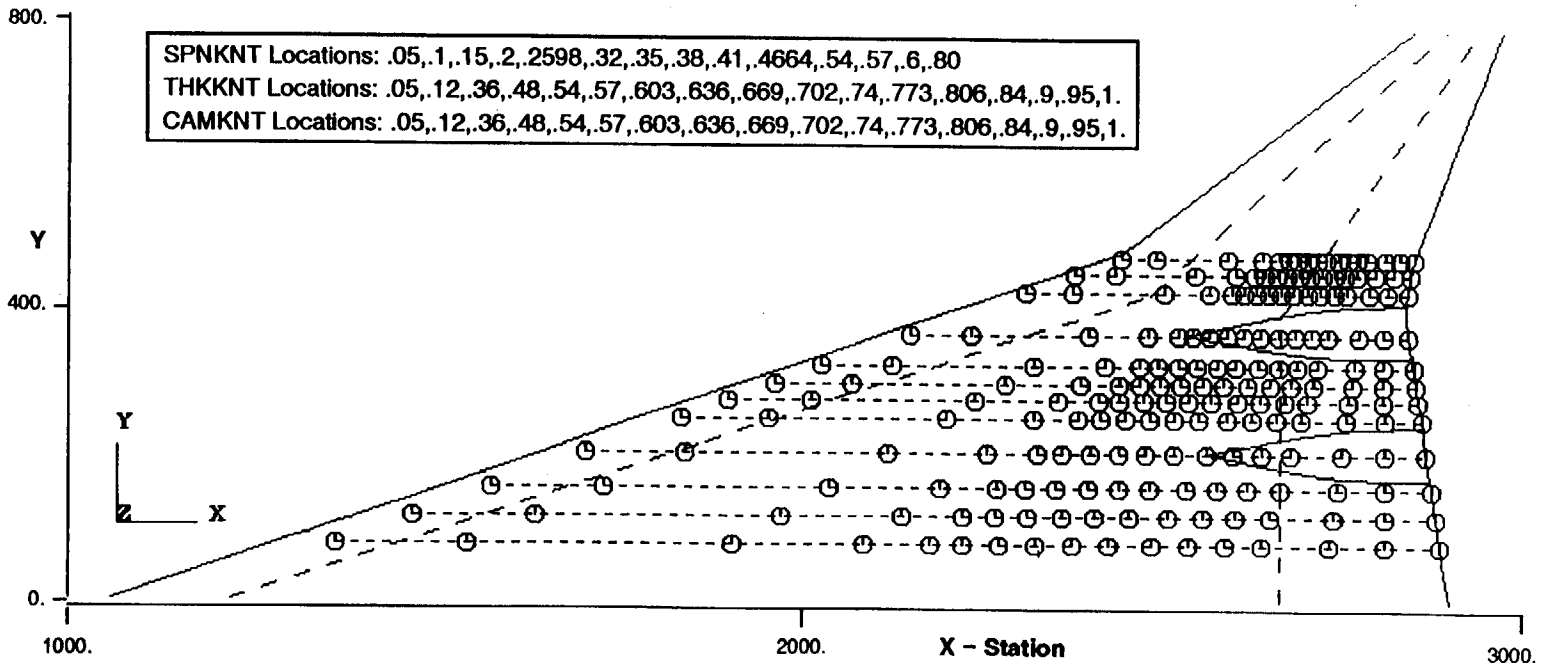

HSCT TCA Optimization : Progress

The following section presents the TCA optimization summary, discusses the TRANAIR design process, and presents the results of the TRANAIR optimization.

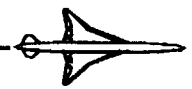

HSCT TCA Optimization : Progress

- TCA Optimization Summary
- TRANAIR Design Process
- Results

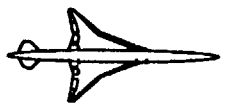

Tranair TCA Optimization Summary –1

TRANAIR is a full potential code for arbitrary geometries. Complex wing/body/diverter/nacelle geometries can be accurately modeled subject to specific boundary conditions.

TRANAIR uses adaptive grid refinement methodology. This method allows grid to be concentrated in regions where something is happening, and allows the solution to move additional grid to regions where features are appearing. The wing optimization study used both first and second order upwinding, and one and two term transpiration. The less accurate, but less computationally expensive, first order upwinding and one term transpiration are used in cycle 1 to get the majority of the movement toward the solution. The second order upwinding and two term transpiration are used in cycle 2 to fine tune the design for more accurate shocks and peaks.

TRANAIR's design capability to formulate and solve constrained aerodynamic problems is also quite general. We were able to tailor the constraints as needed for our airplane using FORTRAN subroutines. In the design mode, TRANAIR relates surface movement to the mass flow boundary conditions on the original surfaces. These transpiration methods were discussed briefly above. Two term transpiration has been found to be most capable when the movements specified by design are fairly small. Furthermore, a linearized version was required toward years end due to increasing problem sizes and limitations of the NAS C–90 queue.

Despite the absence of boundary layer capability at this time, the code has many unique features which lend themselves to the optimization problem.

Years of experience, on multiple configurations, have shown that except for viscous effects, TRANAIR's full potential formulation accurately predicts the flow about and forces on HSCT geometries at supersonic cruise.

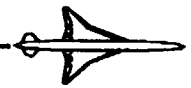

Tranair TCA Optimization Summary -1

- Tranair Full Potential Code for Optimization
- Transpiration Boundary Condition
- Sensitivity Method
- Fixed Lift Constraint

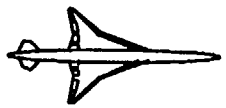

Tranair TCA Optimization Summary –2

As described previously, TRANAIR's capability in geometry modeling allowed us to do these designs with the actual nacelle/diverter geometry included. The wing was optimized with thickness, camber, and twist all active simultaneously. The body optimization included simultaneous camber and area changes. With one exception, all cycles were simultaneous wing and body design runs, the exception had no body area variables. For the full case, a total of 416 variables and 36000 constraints were used to control the design. The TCA configuration, with the highly integrated wing and body, responded best with the simultaneous wing and body optimization.

Tranair TCA Optimization Summary – 2

- Wing & Body Design with Diverters/Nacelles Included
- Wing : Thickness + Camber + Twist + Shear
- Body : Camber + Cross Section

- For the Wing and Body Simultaneous Optimization:
  - 35,000 Linear Constraints
  - 416 Variables

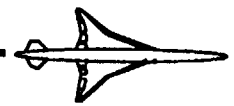

TRANAIR TCA Optimization – Process

In running several initial optimization series with the TCA configuration, it became clear that the simultaneous design of wing and body was quite important. It was nearly impossible to separate the wing and body constraints in order to do separate optimizations as was done with the RefH geometry. It also became obvious that, with the way we have implemented the detailed constraints, that the optimization process itself is rather configuration dependent. Methods that had been developed with the decoupled RefH geometry were not effective with this highly integrated TCA configuration.

It was learned that it was important to set up the initial flow with a simultaneous cycle with 2nd order upwinding and 2–Term transpiration. This run started the wing/body on a more pleasing path than setting up with 1–Term which allowed the wing to move quickly. A single cycle–1 run was then used to allow a reasonable amount of wing movement, with only body camber changes. This run was then followed by multiple cycle–2 runs until the design was complete.

During various cycles, selected variables had their allowed movement limited to prevent excursions that were deemed too radical and hard to recover from.

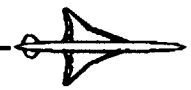

Tranair TCA Optimization Process

- Configuration Dependent Process
- Start with Simultaneous Cycle to Set Up W/B Flow
- Follow with Single Wing 1-Term Cycle for Shear
- Continue with Simultaneous Cycles to End
- Limiting Variable Movements as Required

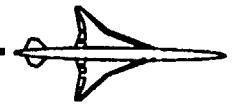

TRANAIR TCA Optimization Process –1

The design cycle described here is referred to as a simultaneous cycle or a cycle–2.

This cycle allows full wing and body movement, subject to the constraints. The wing is allowed thickness, camber, twist, and shear changes. The body is allowed camber and cross section movements. These movements are input at the 416 variable locations, with spline fits between, and subject to 35000 constraints placed on the problem.

The TRANAIR features of this cycle are the use of 2nd order upwinding to sharpen and capture shock locations, and the use of 2–Term transpiration which is more like a boundary layer model of transpiration than the classic 1–Term model. The higher order transpiration, a 2nd order formula expansion about the local velocity (which is non– constant), while less robust like any higher order function, allows a derivative effect so that transpiration will be more accurate in regions where local velocities are rapidly changing. The other feature of 2–Term transpiration is that it allows, on the body, a more realistic simulation of body cross section changes (1–Term allows only a "breathing" movement change of area, i.e., just grow everywhere in girth).

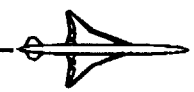

Tranair TCA Optimization Process -1

Simultaneous Cycle :

- 2-Term Transpiration
- 2nd Order Upwinding
- Wing : Thickness / Camber / Twist / Shear
- Body : Camber / Cross Section

- 416 Variables
- 35000 Constraints

TRANAIR TCA Optimization Process –2

The design cycle described here is referred to as an alternate cycle or a cycle–1.

This cycle allows full wing and partial body movement, subject to the constraints. The wing is allowed thickness, camber, twist, and shear changes. The body is allowed only camber movements. These movements are input at the 321 variable locations, with spline fits between, and subject to 31000 constraints placed on the problem.

The TRANAIR features of this cycle are the use of 2nd order upwinding to sharpen and capture shock locations, and the use of 1–Term transpiration, "classic" transpiration, which is more stable and allows greater movements than the 2–Term model. The 1–Term transpiration is a 1st order formula linearizing about the freestream velocity (which is constant). The body cross section changes may only be a "breathing" movement change of area, i.e., just growth everywhere in girth.

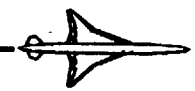

Tranair TCA Optimization Process –2

Alternate Cycle :

- 1–Term Transpiration
- 2nd Order Upwinding
- Wing : Thickness / Camber / Twist / Shear
- Body : Camber

- 321 Variables
- 30981 Constraints

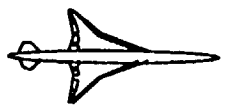

TRANAIR TCA Optimization Process –3

The design cycle described here is referred to as a nacelle/diverter tune–up cycle or a cycle–3.

This cycle allows partial wing and full body movement, subject to the constraints. The wing is allowed only thickness and camber changes (no twist). The body is allowed camber and cross section movements. These movements are input at the 408 variable locations, with spline fits between, and subject to 27000 constraints placed on the problem.

As with the cycle–1, this cycle uses 2nd order upwinding and 2–Term transpiration. The variables are clustered about the nacelle/diverter region, and the wing leading edge is left untouched. This cycle is used as the final cycle of the design, hence "tune–up". In the future, it is planned that this cycle will be done with the boundary layer turned on over the wing and body. Only a single cycle is run with this definition.

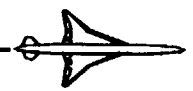

Tranair TCA Optimization Process –3

Nacelle/Diverter Tune–Up Cycle :

- 2–Term Transpiration
- 2nd Order Upwinding
- Wing : Thickness / Camber
- Body : Camber

- 408 variables
- 26544 constraints

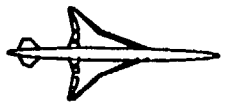

TRANAIR TCA Optimization Process –4

This page describes the actual series of cycles used to generate the Tranair TCA optimized configuration. An initial simultaneous cycle is run (cycle–2). This run series is followed by a single alternate cycle (cycle–1). Three simultaneous cycles are then completed. The nacelle/diverter cycle is run on the resultant geometry from the design.

Tranair TCA Optimization Process –4

Actual Optimization Series :

- Simultaneous Cycle
- Alternate Cycle
- Simultaneous Cycle
- Simultaneous Cycle
- Simultaneous Cycle
- Nacelle/Diverter Tune–Up Cycle

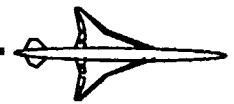

HSCT TCA Configuration Optimization

The final TRANAIR wing/body optimization was performed on the TCA wbdn configuration. The full project constraint set was obeyed during the design with up to 36000 linear constraints and 416 variables. The inboard nacelle/diverter was toed-out by 1 degree per the Northrup-Grumman study. No optimization work was done on the nacelle/diverter placement for the optimized geometry. One cycle required three to four runs to complete and, with NAS C-90 special queue allowance, the flow time was typically three to four days. The design was optimized at the cruise point, Cl=0.08556 , Mach=2.4, and was inviscid.

The results were quite promising. At the cruise point, Cl=.08556, an inviscid design drag improvement of 7.05 counts was achieved. When this geometry was analyzed at the evaluation point, Cl=0.100, the drag benefit of 8.18 counts was seen.

The resulting geometry was notably smooth as optimized, although not featureless. Significant efforts were made later to generate a wind-tunnel smoothed loft and will be discussed in the following paper by Rusty Conner.

HSCT TCA Configuration Optimization

- TCA Based Study at C_L=0.08556 and C_L=0.1000

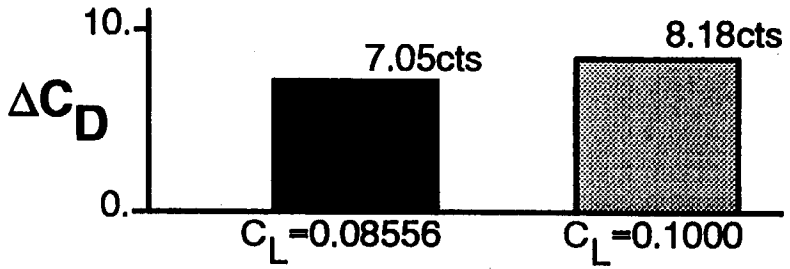

- Smoothness of Wing Dramatically Improved.
- Body Cross Section Responding Simultaneously to Wing Movement.
- Inboard Nacelle/Diverter Toe–Out 1 degree per Northrup–Grumman Study.

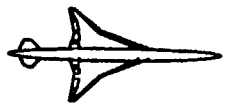

TRANAIR Optimized TCA Configuration
Shaded Graphics Image

This design is a result of a simultaneous design of the TCA wing, using Thickness/Camber/Twist, with body, using Camber/Area. This design used, in it's final cycle, 35000 constraints and 416 variables. The design required five design cycles, with a nacelle/diverter tune–up cycle as the last pass. The optimization was run at Mach=2.4, Cl=.08556, with α~4.0 degrees. The resultant inviscid design showed a 8.2 count drag improvement at the evaluation Cl=0.10. The geometry was pleasantly smooth and showed again the gentle gull tendency that was seen in previous RefH design efforts.

Tranair Optimized TCA Configuration

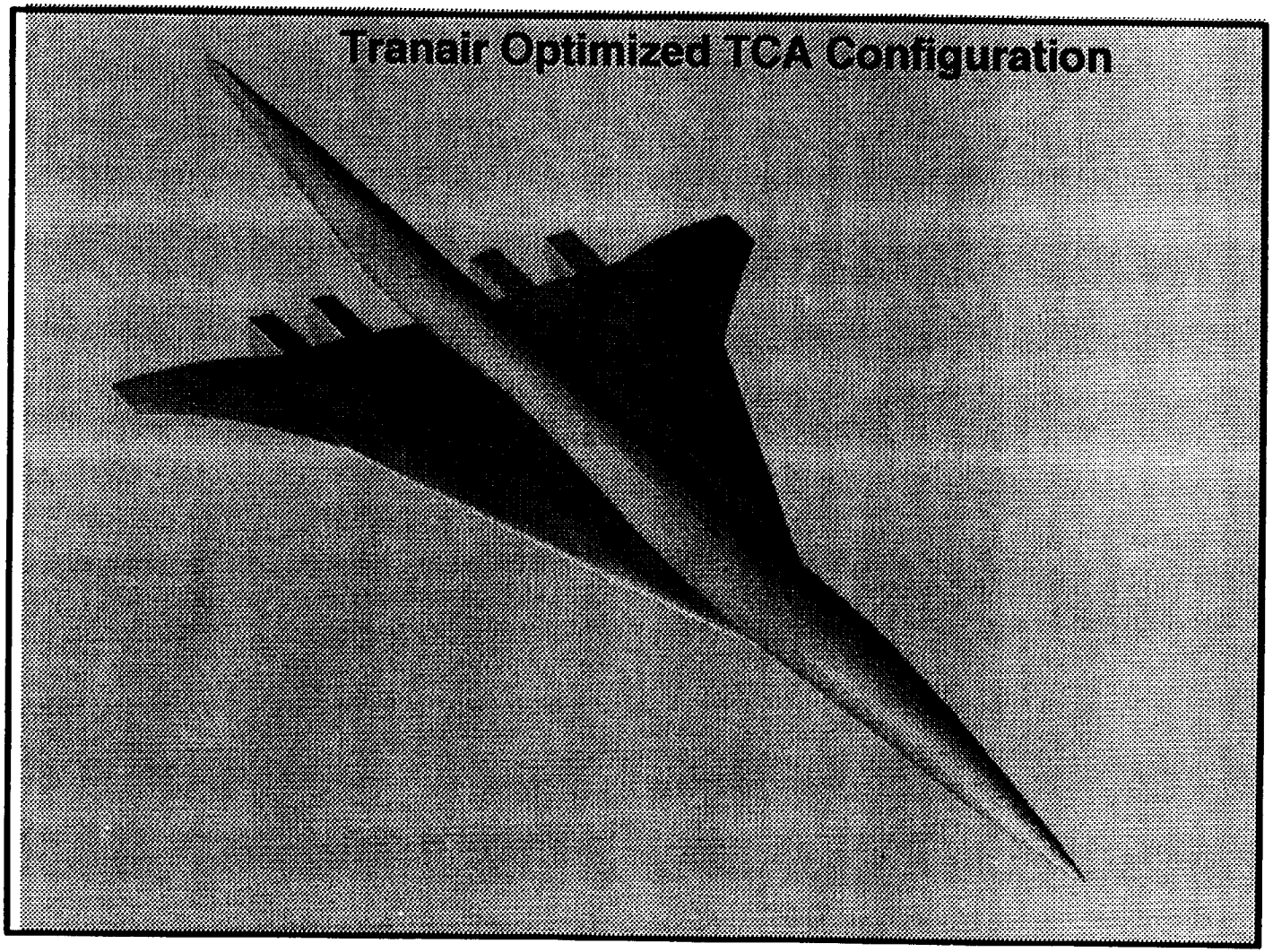

d2fmagic

Baseline TCA Configuration

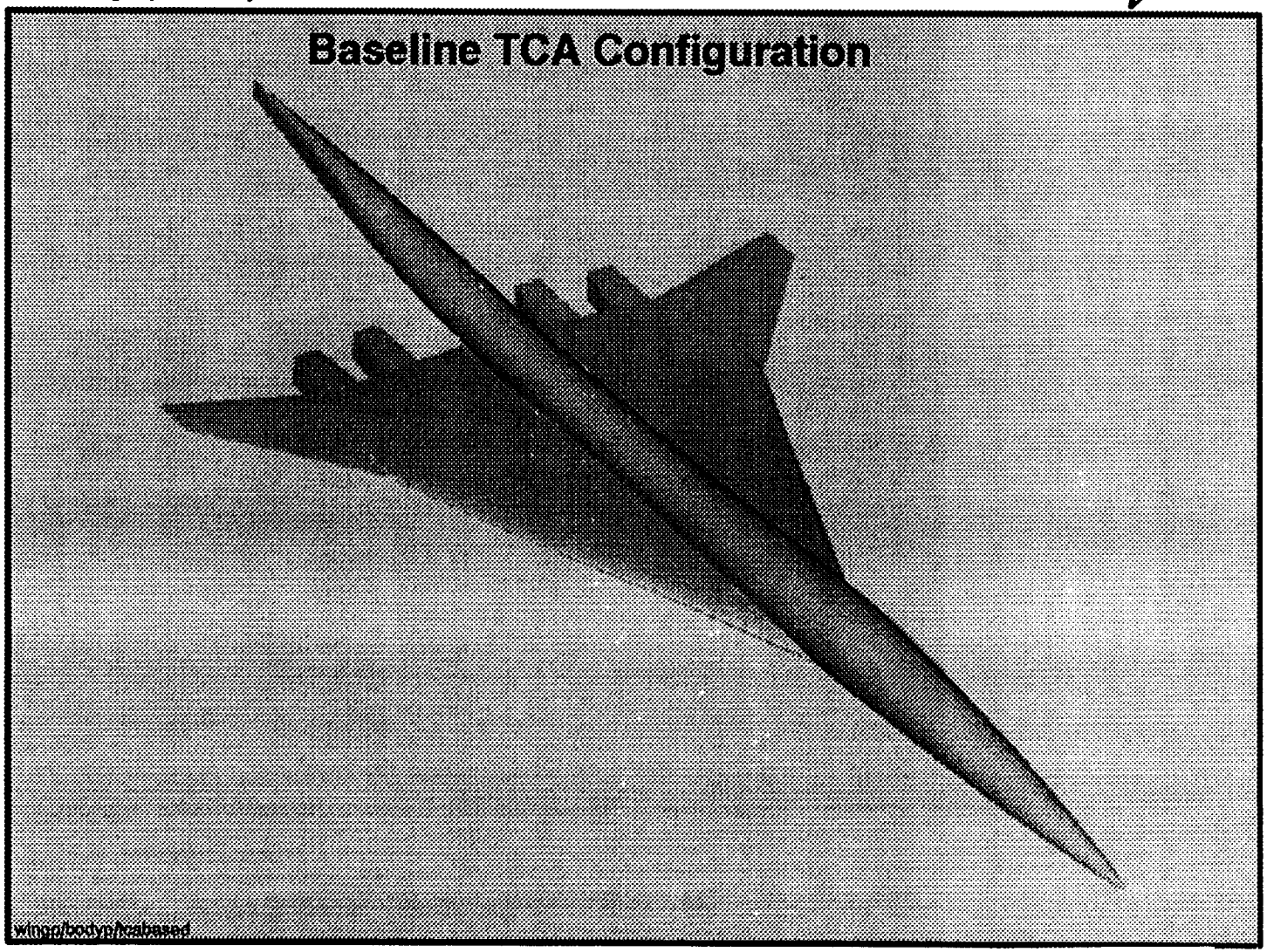

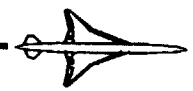

Tranair Optimized TCA Configuration

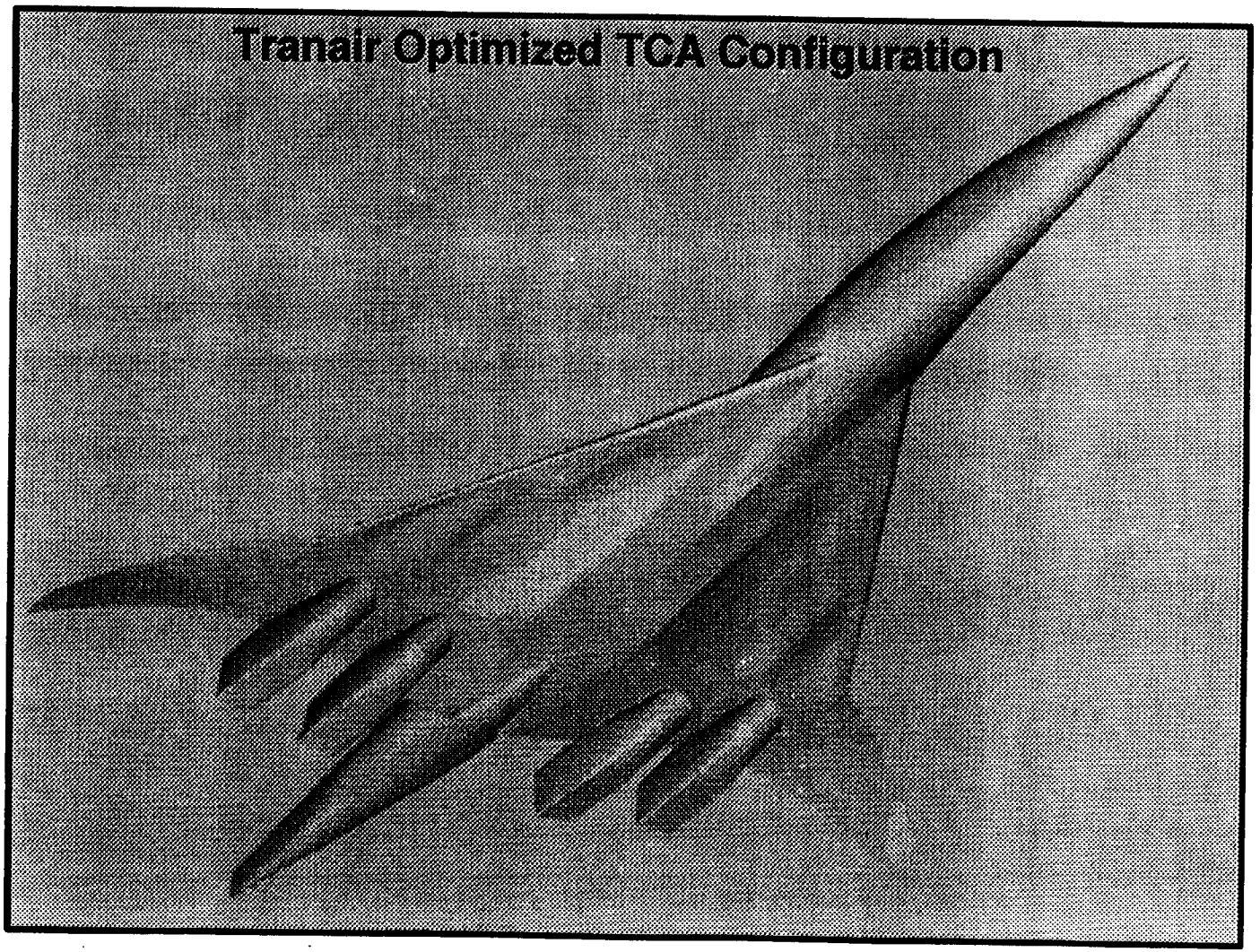

d2fmagic

Baseline TCA Configuration

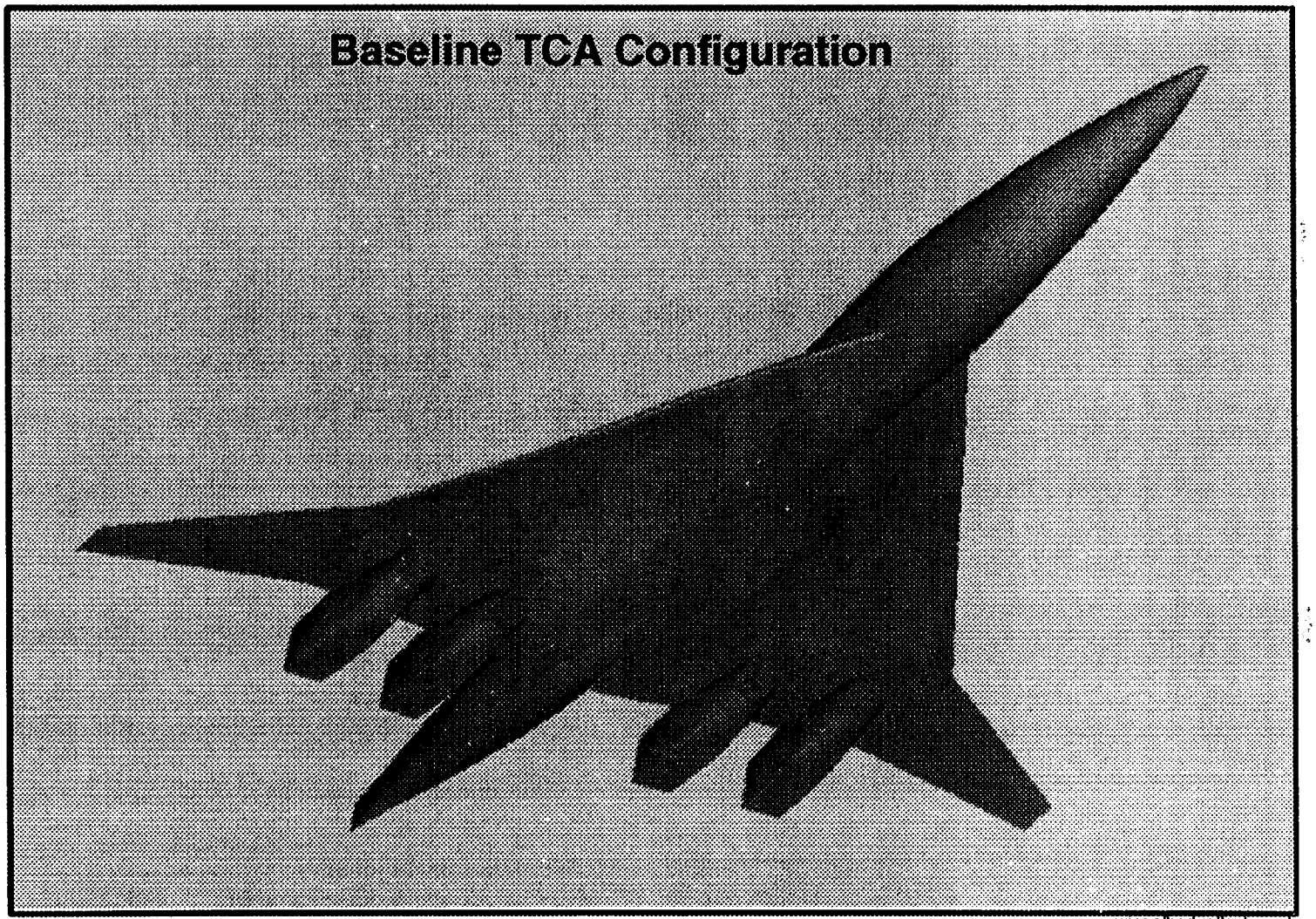

wingp/bodyp/tcabased

Tranair Optimized TCA Configuration

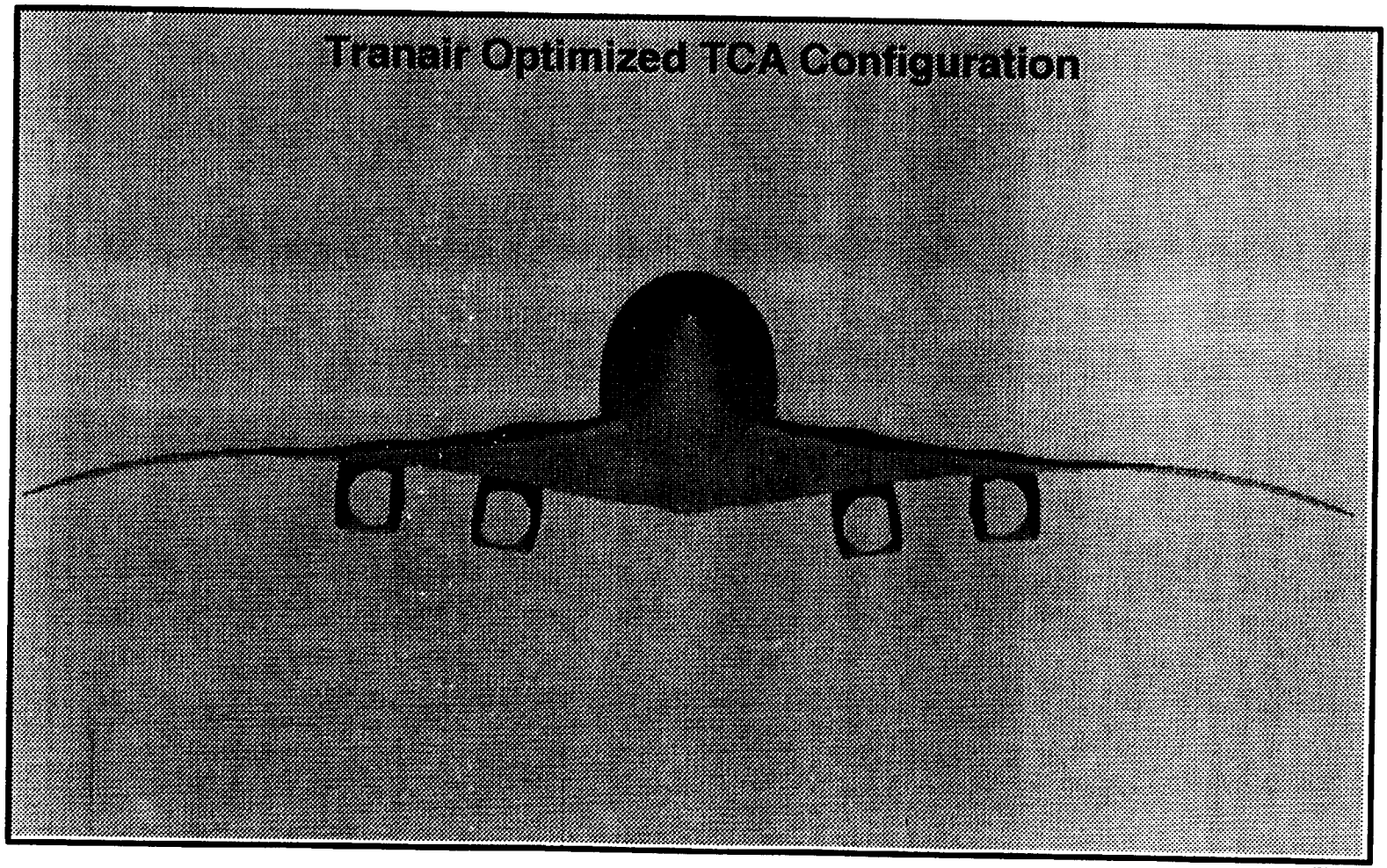

d2fmagic

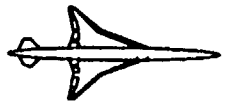

TCA Configuration Optimization

This shaded graphics image shows the baseline TCA geometry (bottom) compared with the TRANAIR inviscid design geometry (top). Both models are pitched to their respective cruise attitudes for Cl=.08556.

TCA Configuration Optimization

Optimized Geometry

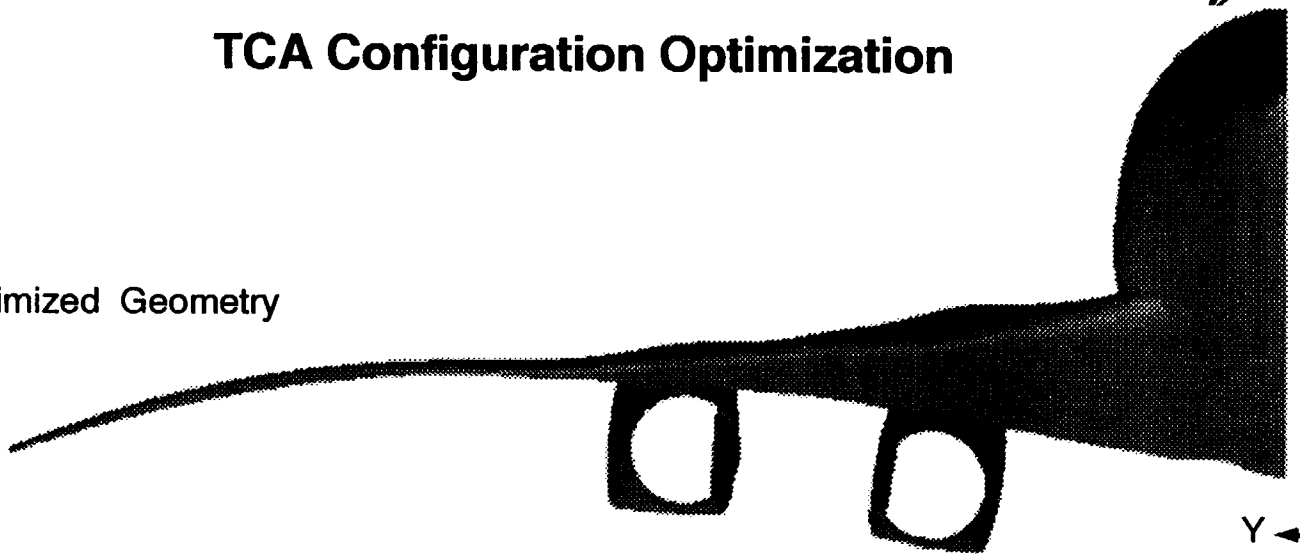

Front View
at Cruise Attitude

Baseline TCA Geometry

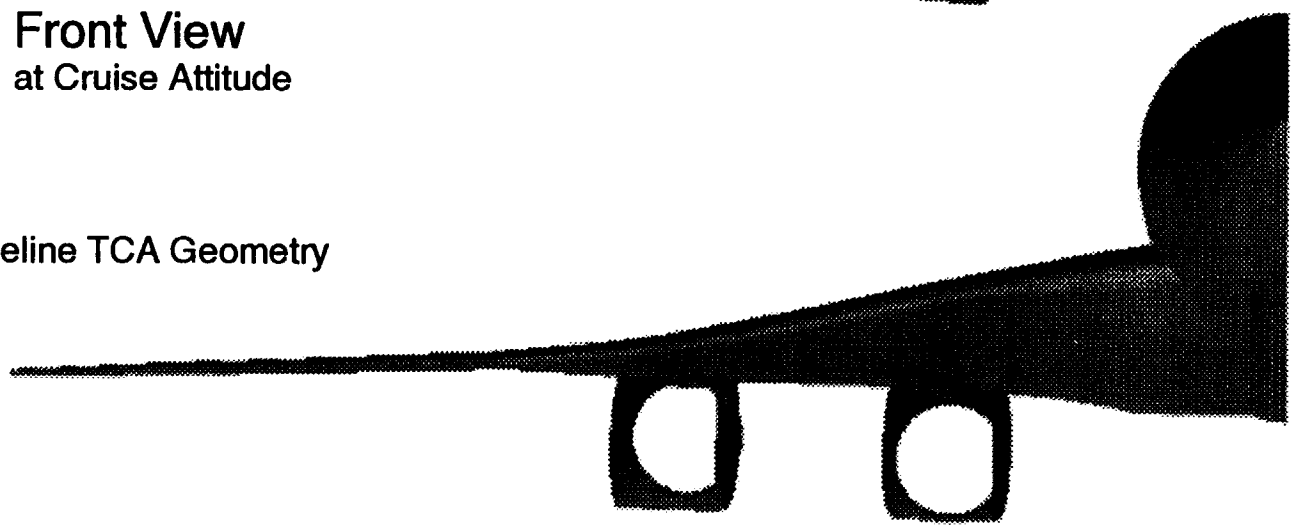

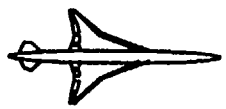

TCA Configuration : Area Distribution Baseline and Optimized

This image shows the baseline area distribution for wing, body, and wing+body as a dashed line. The optimized geometry result is shown solid. It can be seen that the optimization increased the area, except at the body waist, while decreasing the drag.

TCA Area Distribution : Baseline and Optimized

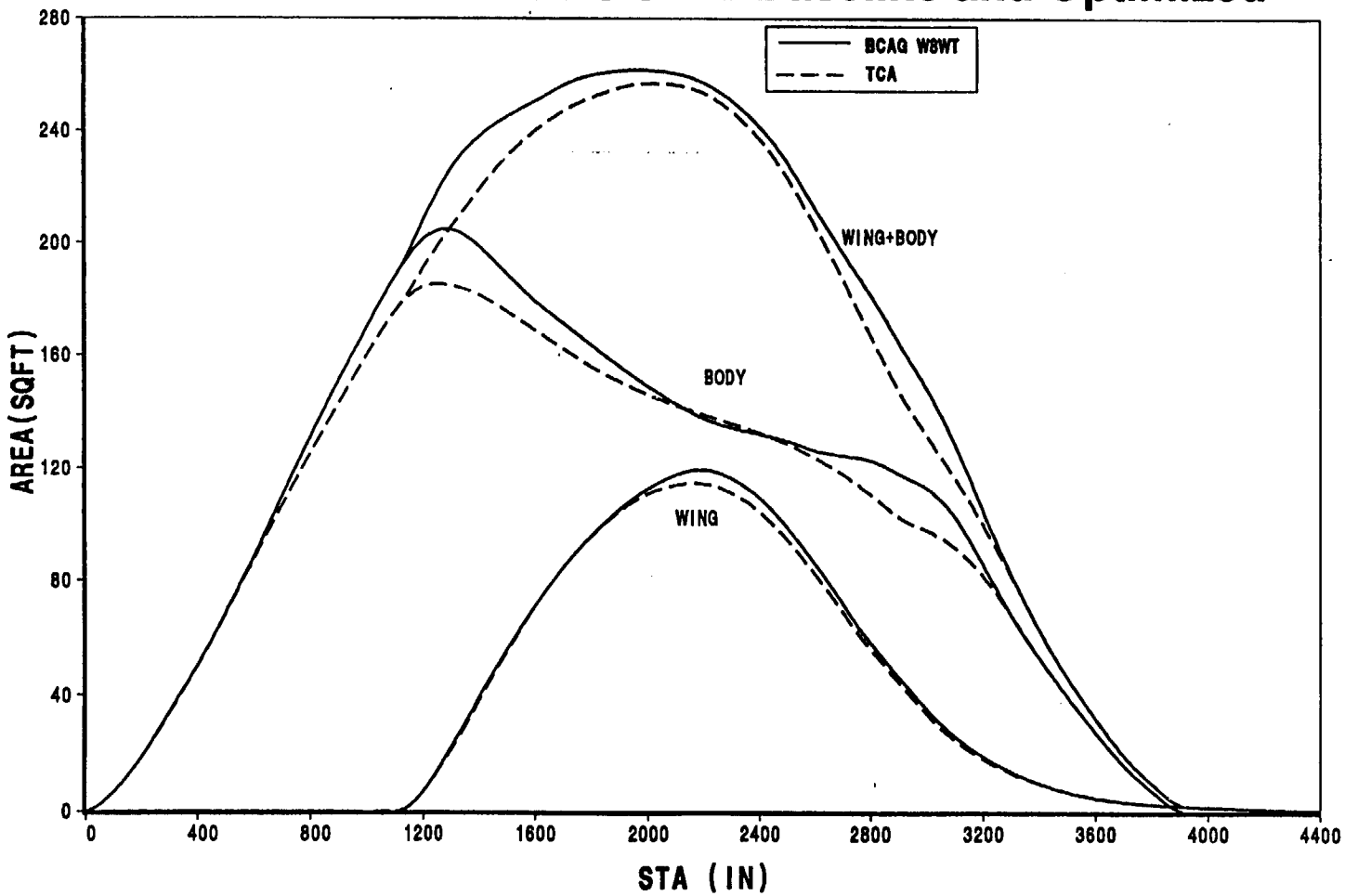

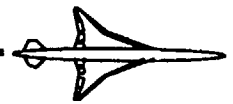

TRANAIR TCA Configuration Optimization – Upper Surface

These images compare the upper surface Mach distribution for the TCA baseline (lower) to the optimized (upper) configuration.

The drag benefit for optimization is 7.05 counts from the baseline TCA. The optimized wing's upper surface Mach number distribution shows a generally steepened shock with more high speed flow concentrated forward and inboard on the wing.

Tranair TCA Configuration Optimization

Upper Surface Solution Mach=2.4 C_L=.08556

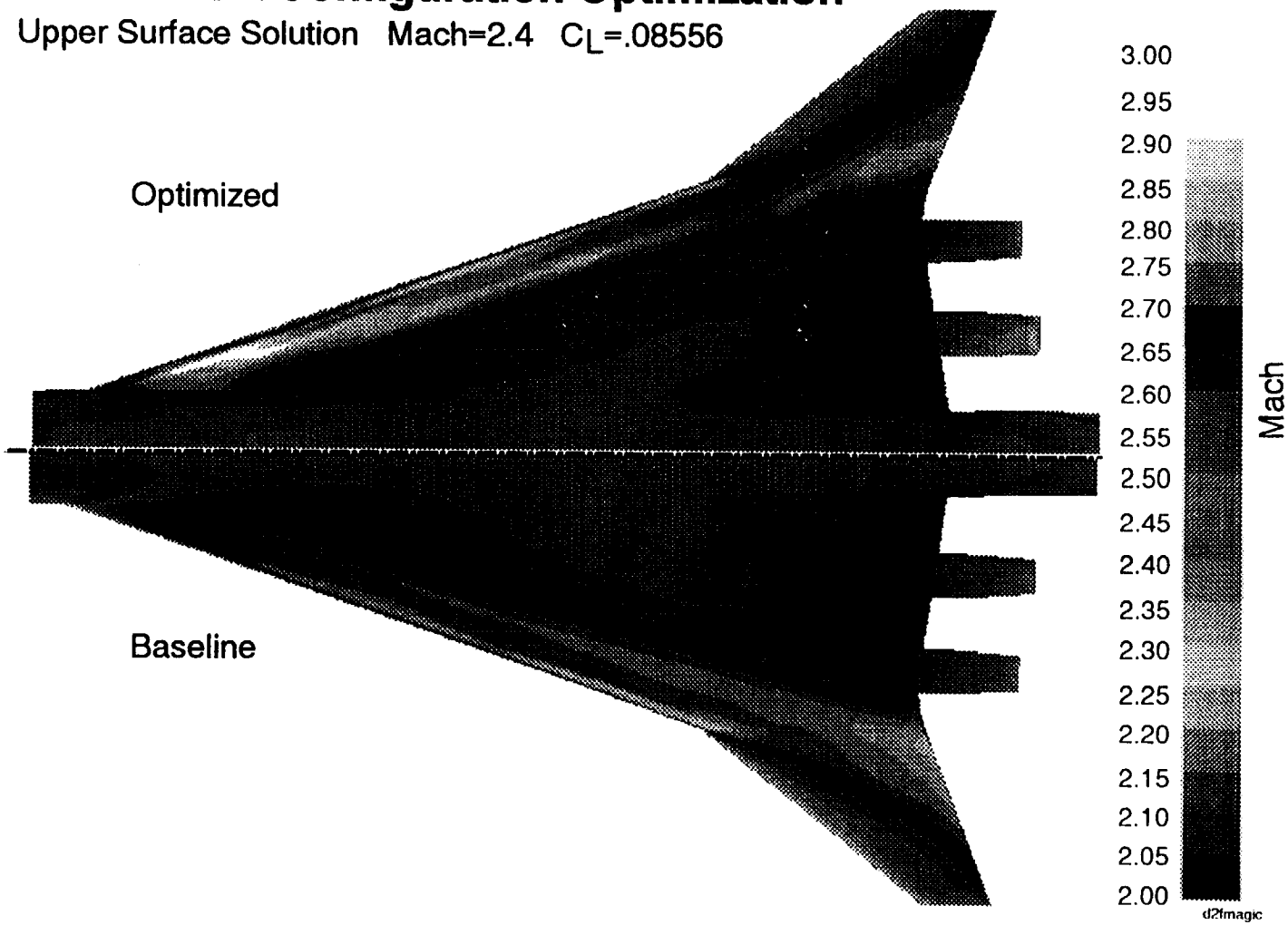

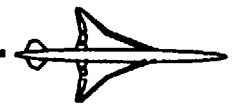

TRANAIR TCA Configuration Optimization – Lower Surface

These images compare the lower surface Mach distribution for the TCA baseline (lower) to the optimized (upper) configuration.

The drag benefit for optimization is 7.05 counts from the baseline TCA. The optimized wing's lower surface Mach number distribution shows a dramatic diminishing of the nacelle high speed flows on the wing. Also noted should be the sculpted features which the optimizer put on the wing lower surface to enhance the flow into the nacelle/diverter region to improve the interference.

Tranair TCA Configuration Optimization

Lower Surface Solution Mach=2.4 C_L=.08556

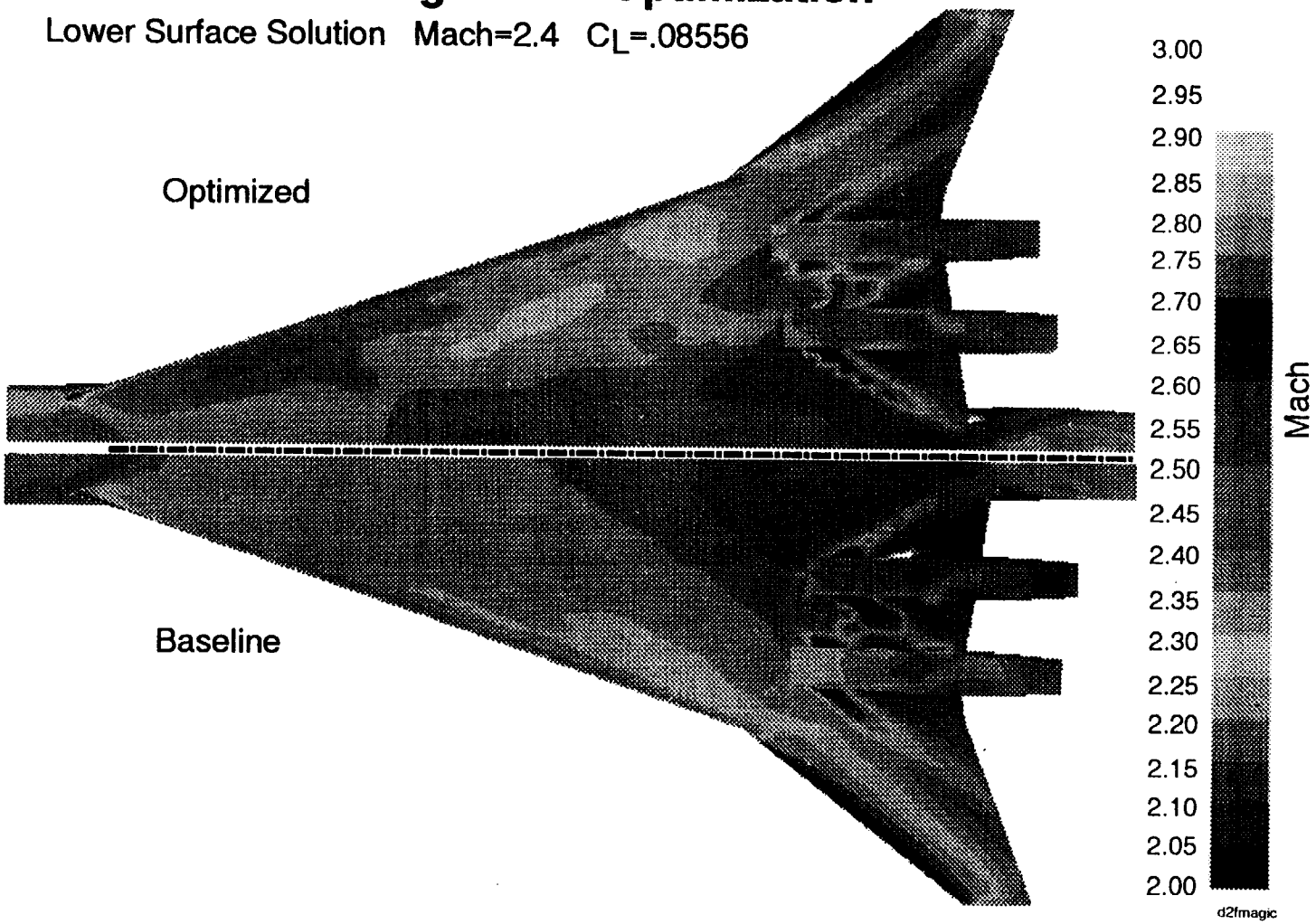

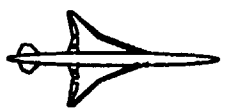

HSCT TCA Configuration Optimization
Viscous Verification

The chart shows the comparison for both the cruise point and evaluation point for the 'Navier–Stokes smoothed' lofts as analyzed in TRANAIR and OVERFLOW(NS). At both lift conditions, 80% of the predicted inviscid drag improvement is realized in the Navier–Stokes analysis.

HSCT TCA Configuration Optimization
Viscous Verification

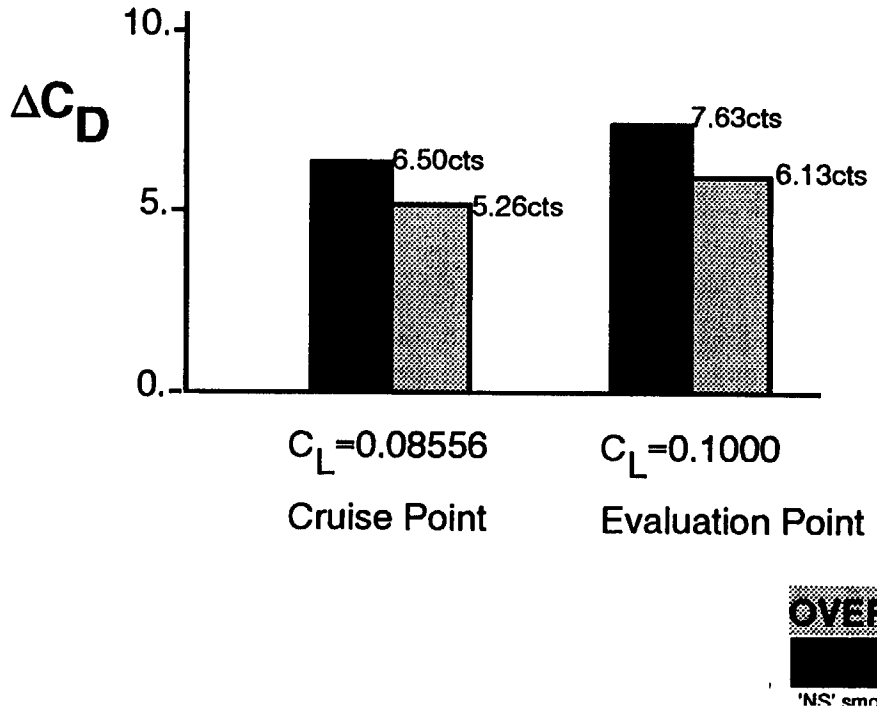

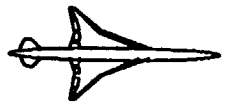

HSCT TCA Configuration Optimization
Viscous Verification – Upper Surface

This image compares the upper surface pressure distributions for the full model TRANAIR (inviscid) and for the OVERFLOW (Navier–Stokes) solutions based upon the "NS smoothed" lofts. At the cruise point, 80% of the inviscid predicted drag improvement is verified by the Navier Stokes analysis.

It can be seen from the images that the TRANAIR and OVERFLOW solutions agree quite well.

TCA Configuration Optimization – Viscous Verification

Upper Surface Solution Mach=2.4

Tranair (Invisicd)
Optimized TCA
C_L=0.0855

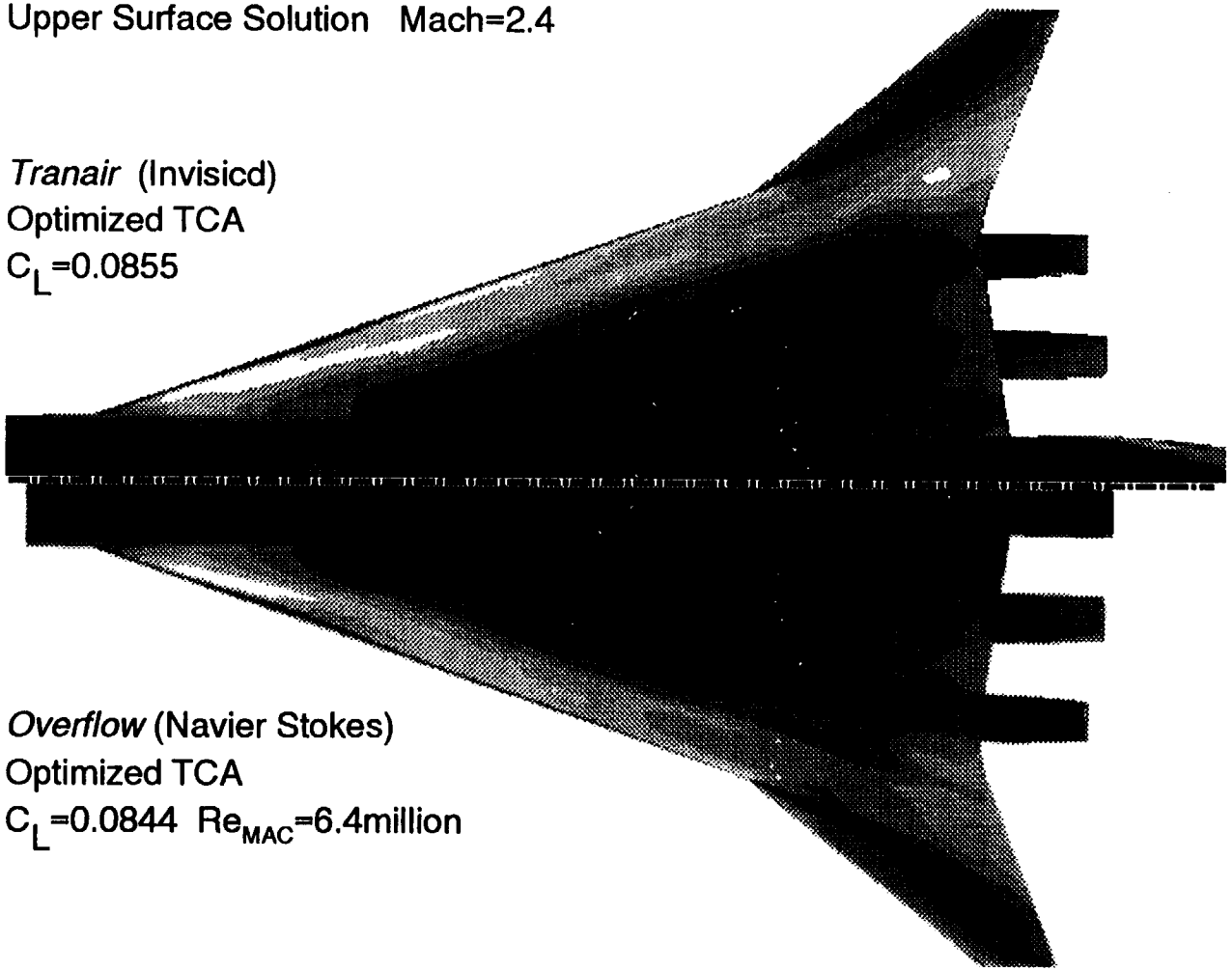

Overflow (Navier Stokes)
Optimized TCA
C_L=0.0844 Re_{MAC}=6.4million

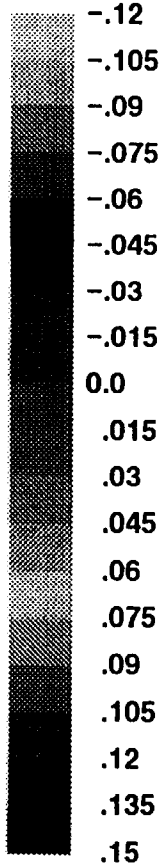

nsw8ctop2.i565

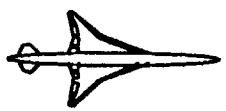

HSCT TCA Configuration Optimization
Viscous Verification – Lower Surface

The image compares the lower surface pressure distributions for the full model TRANAIR (inviscid) and OVERFLOW (Navier–Stokes) solutions based upon the "NS smoothed" lofts. At the cruise point, analysis using Navier–Stokes verifies that 80% of the inviscid drag improvement prediction is realized.

It can be seen from the images that the TRANAIR and OVERFLOW solutions agree quite well.

TCA Configuration Optimization – Viscous Verification Cp

Lower Surface Solution Mach=2.4

Tranair (Invisicd)
Optimized TCA
C_L=0.0855

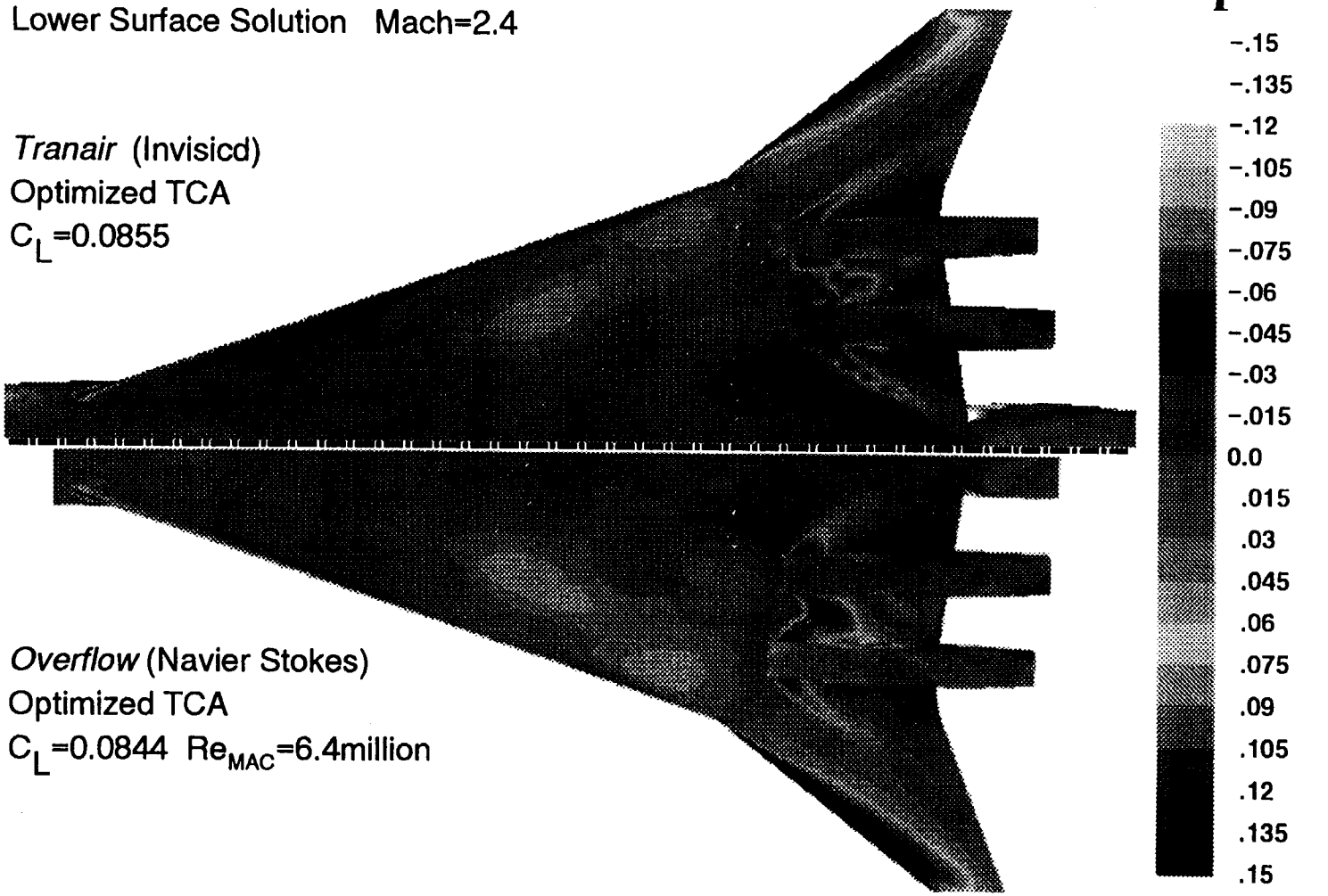

Overflow (Navier Stokes)
Optimized TCA
C_L=0.0844 Re_{MAC}=6.4million

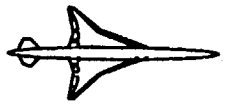

HSCT Wing Optimization – Summary

The extensive project constraints are effective as implemented in TRANAIR. The optimization was able to attend to all of them as it proceeded, with little or no intervention from the engineer. Smoothness has improved with implementation of the project constraints. The rear spar depth constraint appeared to be the most constraining of the wing constraints. The body floor kink constraint was also quite restricting.

The Tranair inviscid prediction was verified by Navier–Stokes analysis. The impact of smoothing the loft was also noted in inviscid increment.

TCA Configuration Optimization Summary

- Project Constraints are Implemented Effectively
- Smoothness Improved with All Constraints
- Beneficial Effect of Tranair Optimization Confirmed by Navier–Stokes

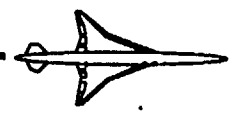

TCA Configuration Optimization – Future Work

In the upcoming period, we plan to test the newly implemented TRANAIR supersonic boundary layer, both in analysis and in design. We would hope to take advantage of the boundary layer especially in the nacelle/diverter region. The use of boundary layer may impact the number of available variables as well as the cycle time.

We have the capability to do sub–optimizations with OVERFLOW for the inlet flow problem. This optimization can make small changes on the wing lower surface from an input geometry in the presence of full viscous effects to improve the inlet flows.

We will begin the effort on transonic cruise / transonic acceleration / supersonic cruise multi–point optimization. We expect to add the effects of horizontal tail and exhaust plume into these optimizations.

Near the end of the TCA optimization, we got the capability to do mixed transpiration cycles. This mixed cycle would use 1–Term transpiration on the wing, while allowing the body to take advantage of the more realistic (for bodies) 2–Term transpiration. This new capability has great potential for allowing the simultaneous nature of the interaction to develop freely, while allowing the wing to have more freedom to move in the initial stages of the design. It is not time–wise practical to use the more accurate, and less robust, 2–Term transpiration for the entire design series.

TCA Configuration Optimization
Future Work

- TRANAIR Viscous Design Effort
- Couple Process with Local OVERFLOW for Inlet Flow
- Proceed onto Multi-Point / Applicability
- Investigate Alternate Process Steps
- Add Vertical and Horizontal Tails
- Thrust Vector / Plume Effects

TCA Configuration Cruise Point Design Optimization

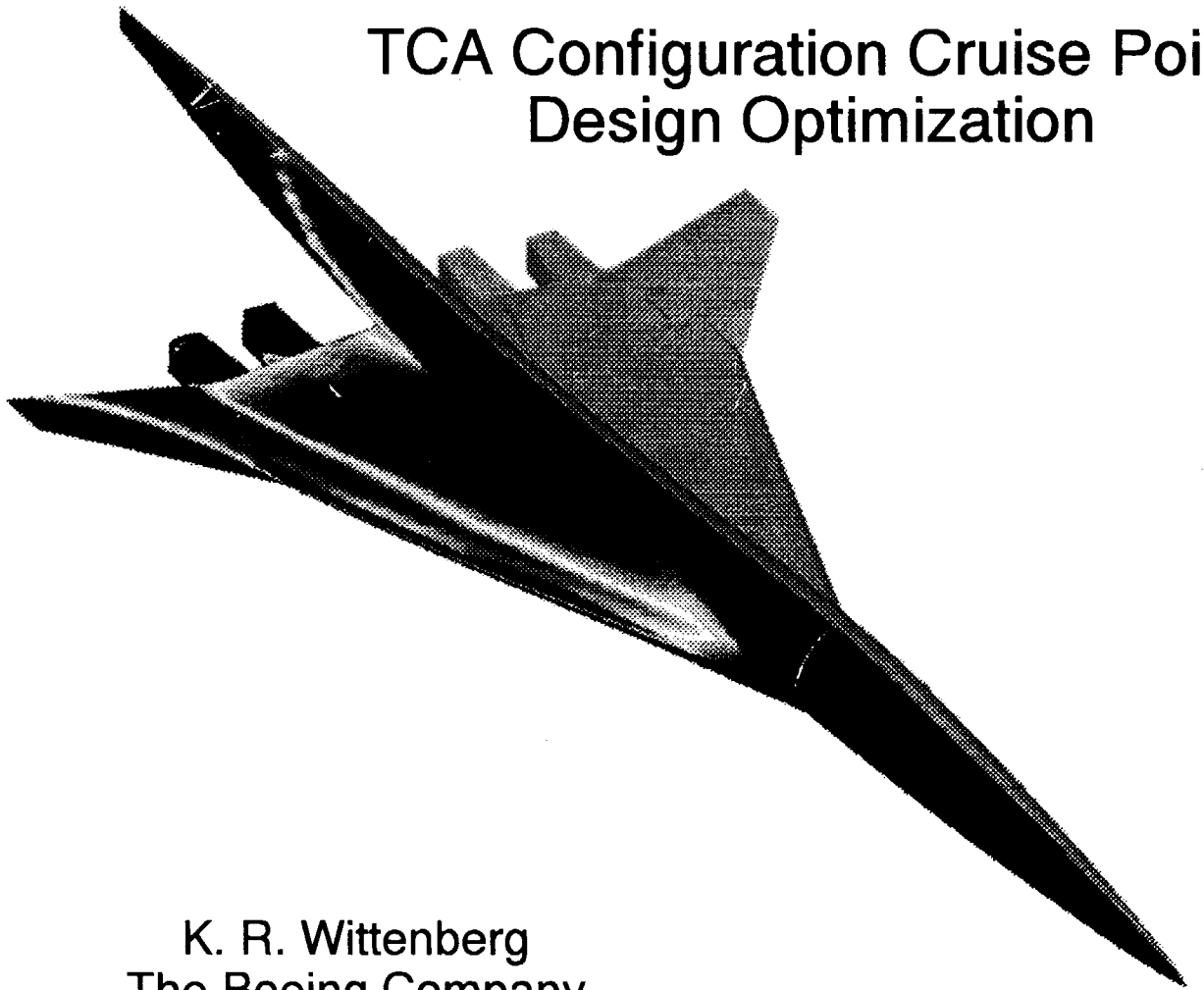

K. R. Wittenberg
The Boeing Company

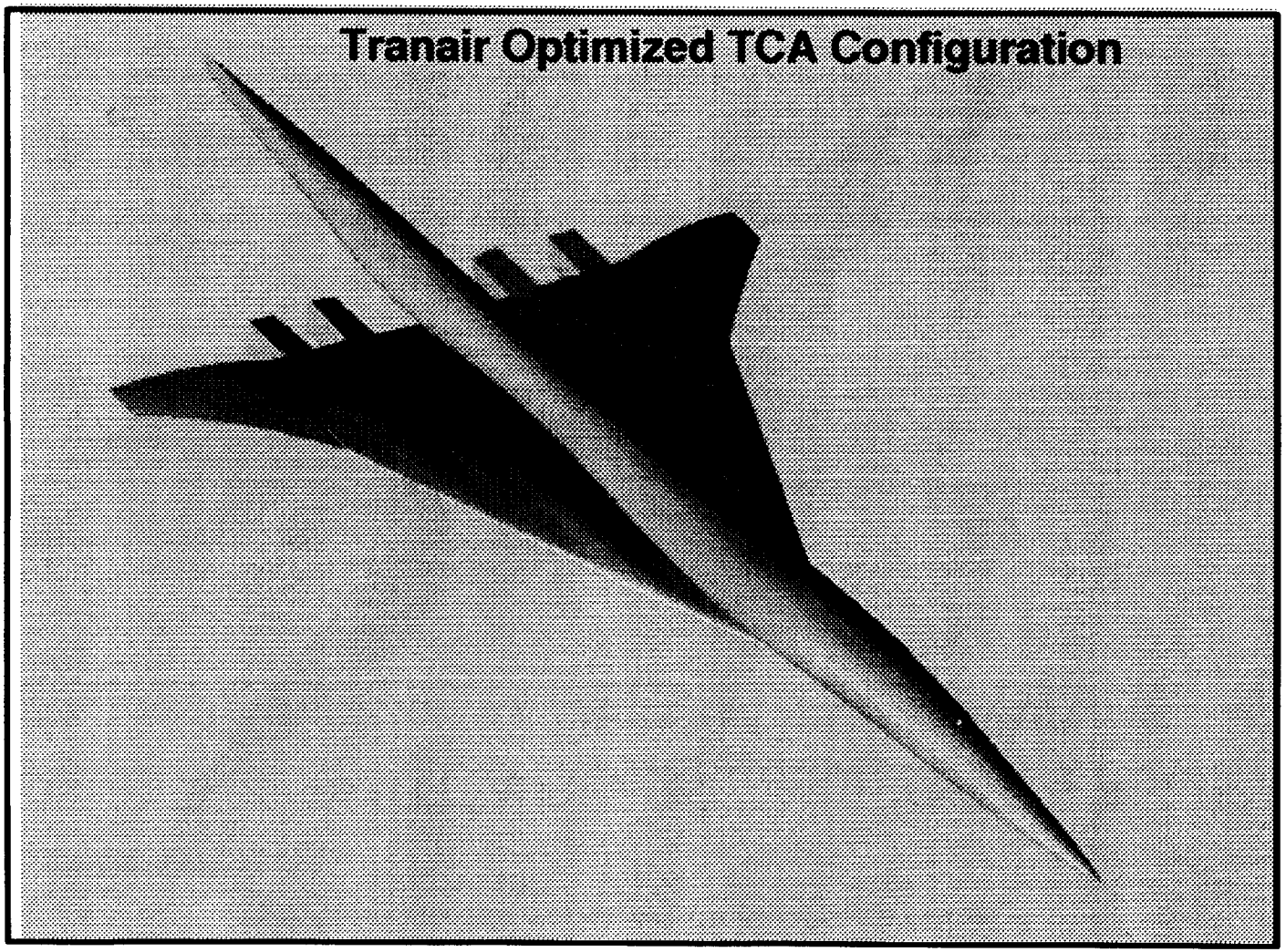
Tranair Optimized TCA Configuration
d2fmagic

Baseline TCA Configuration

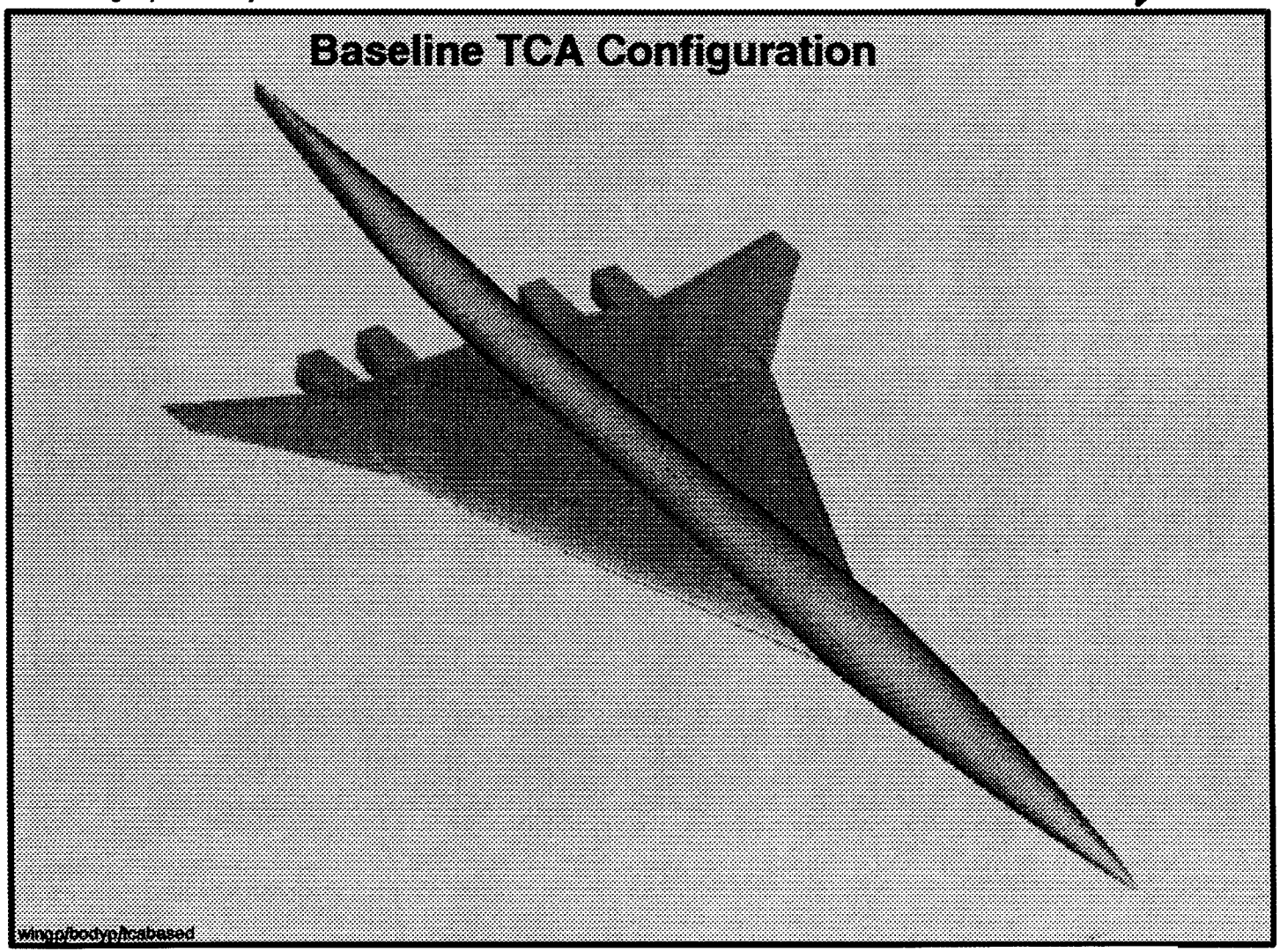

Tranair Optimized TCA Configuration

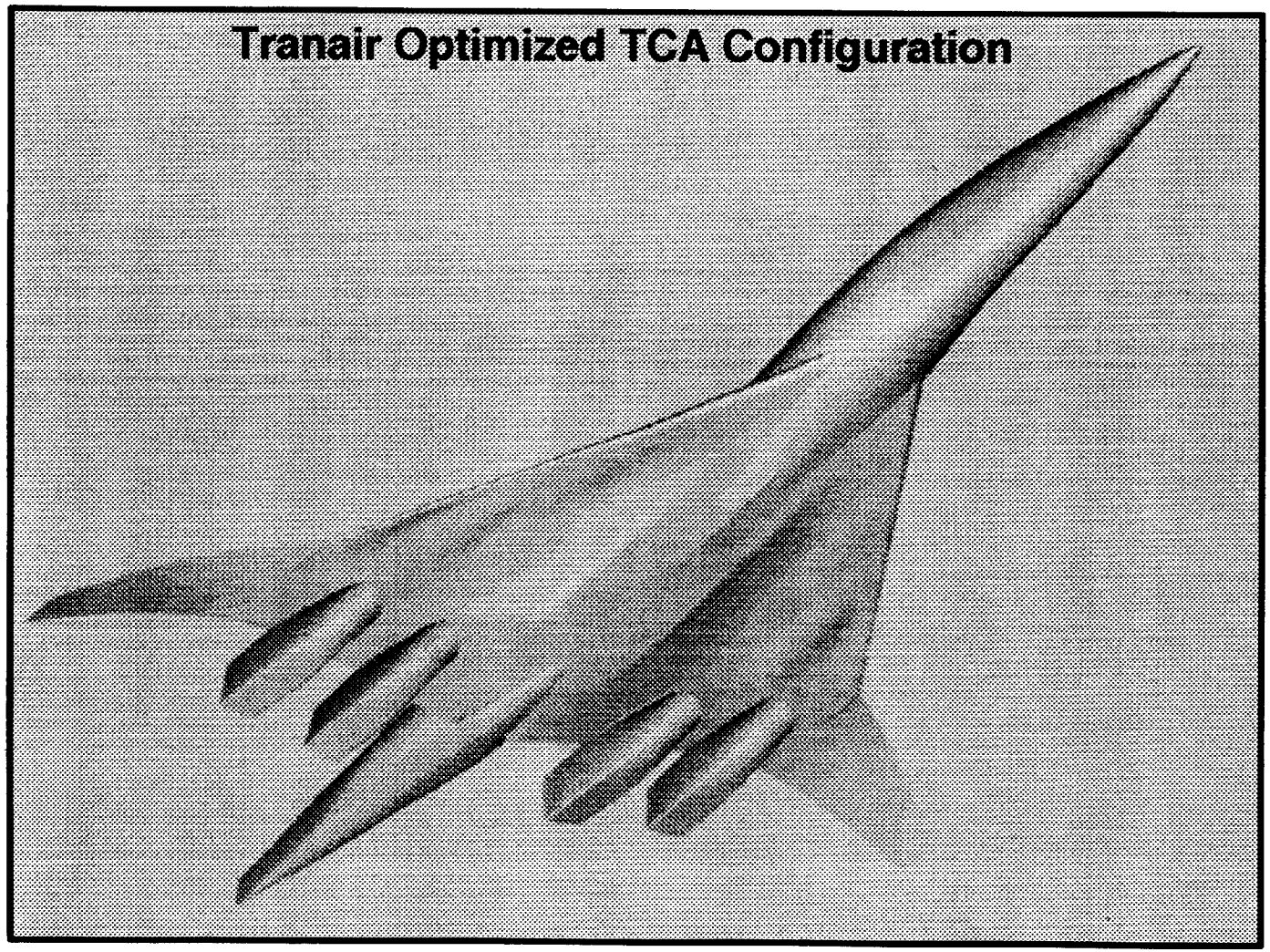

Baseline TCA Configuration

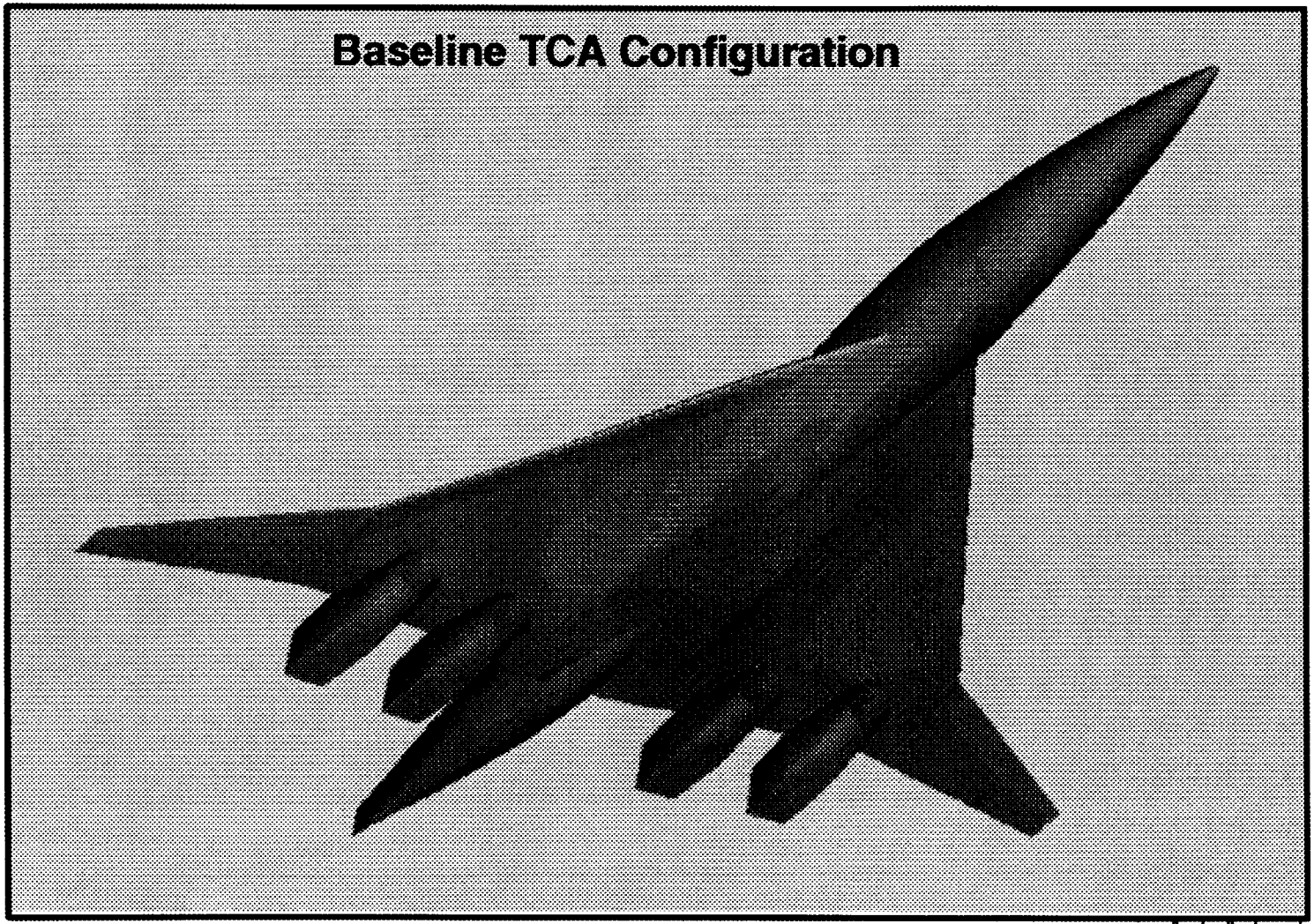

wingp/bodyp/tcabased

Tranair Optimized TCA Configuration

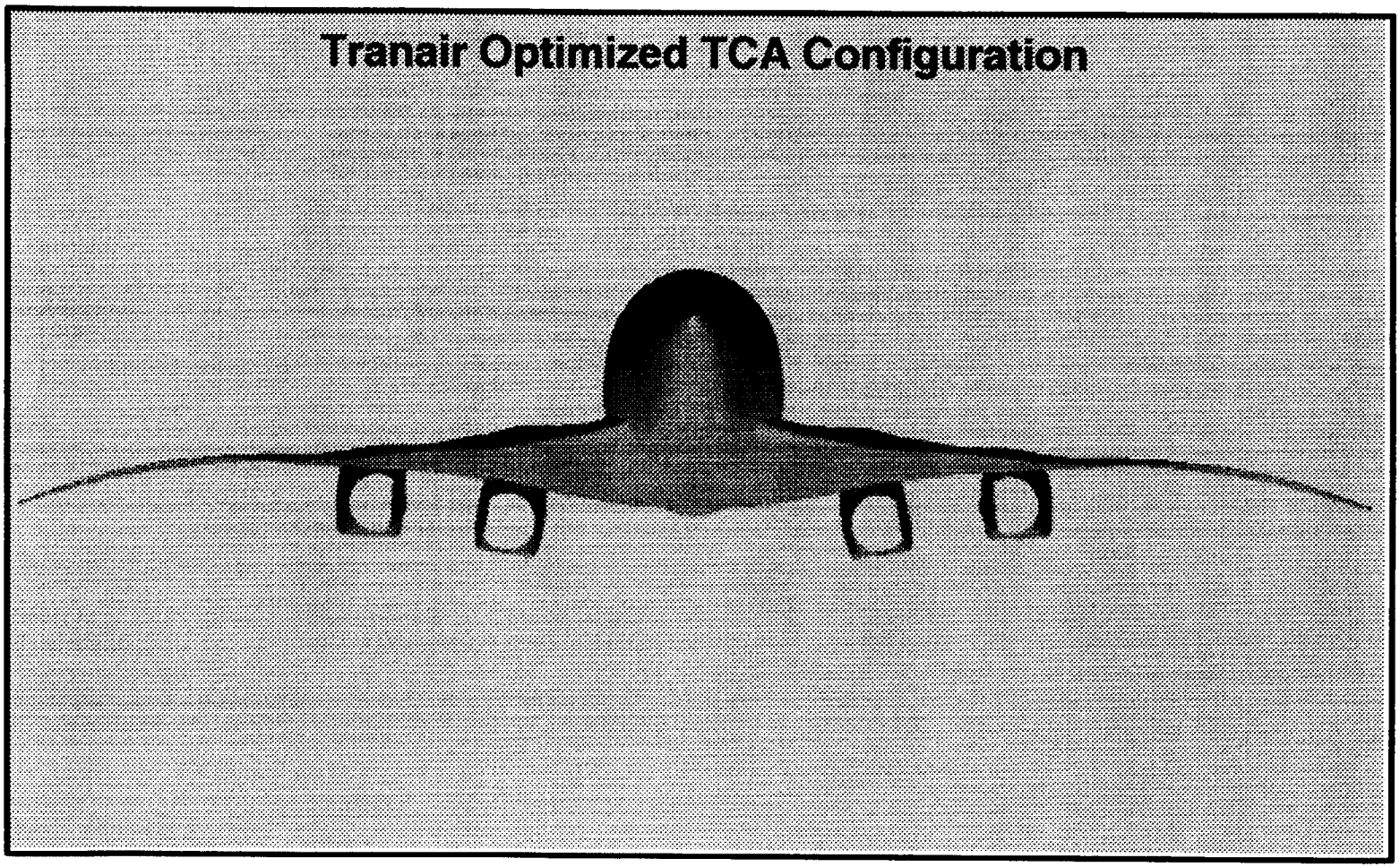

d2fmagic

TCA Configuration Optimization

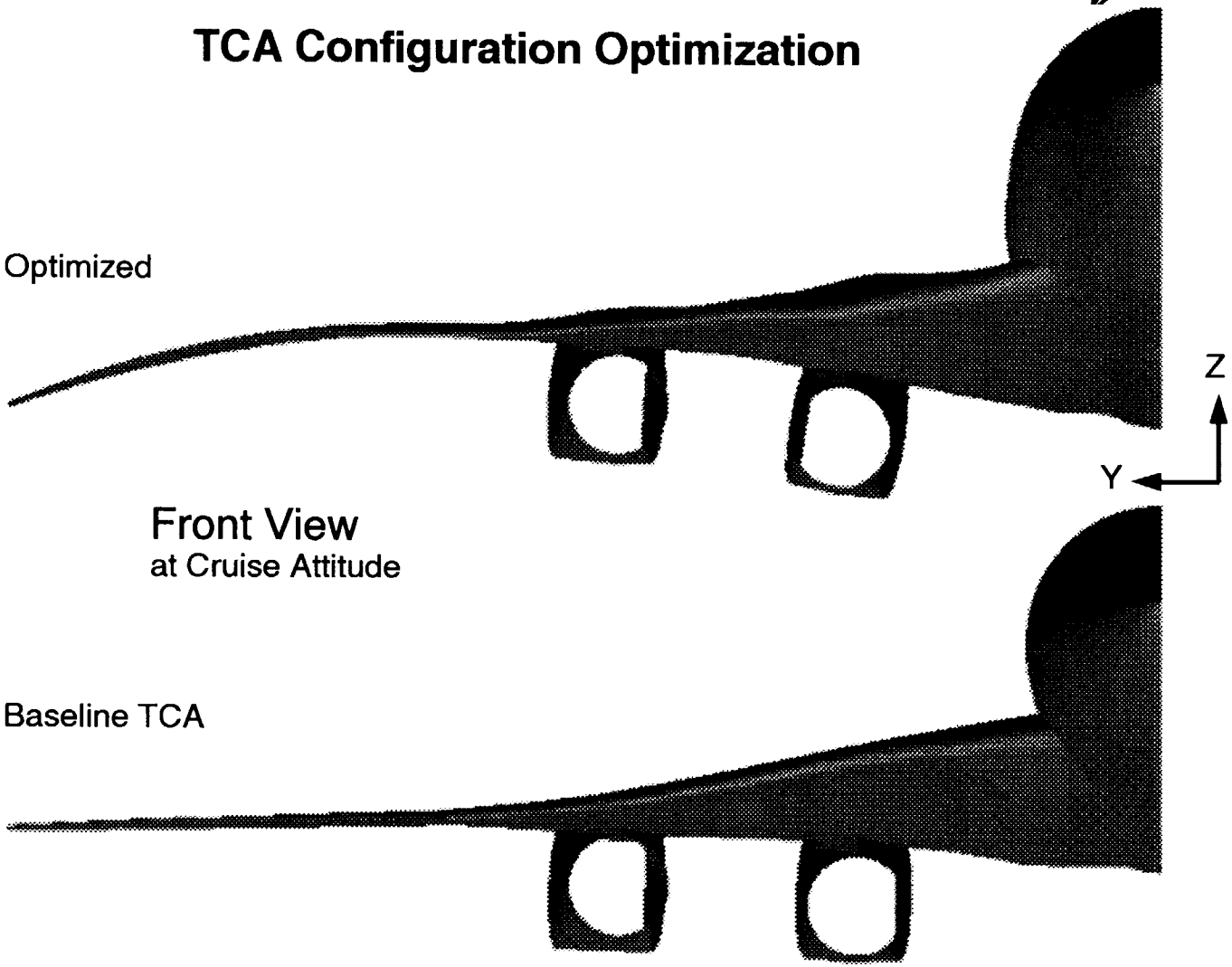

TCA Body Constraint Sections

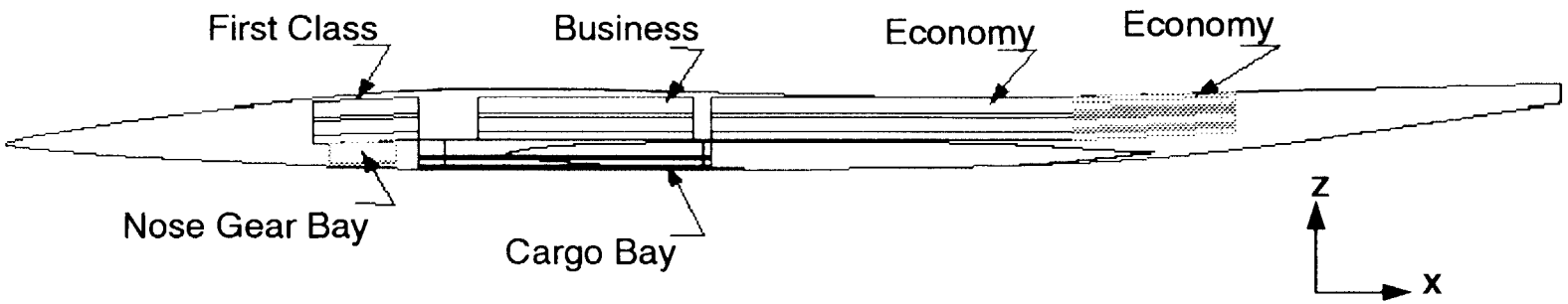

Internal Polygon Clearances
MLGB Thickness
Primary & Auxilliary Box Clearances
Body Radius of Curvature (X-section)
Pilot Area
Main Cabin Floor Angle of Attack
Floor Kink Angles

TCA Wing Constraints

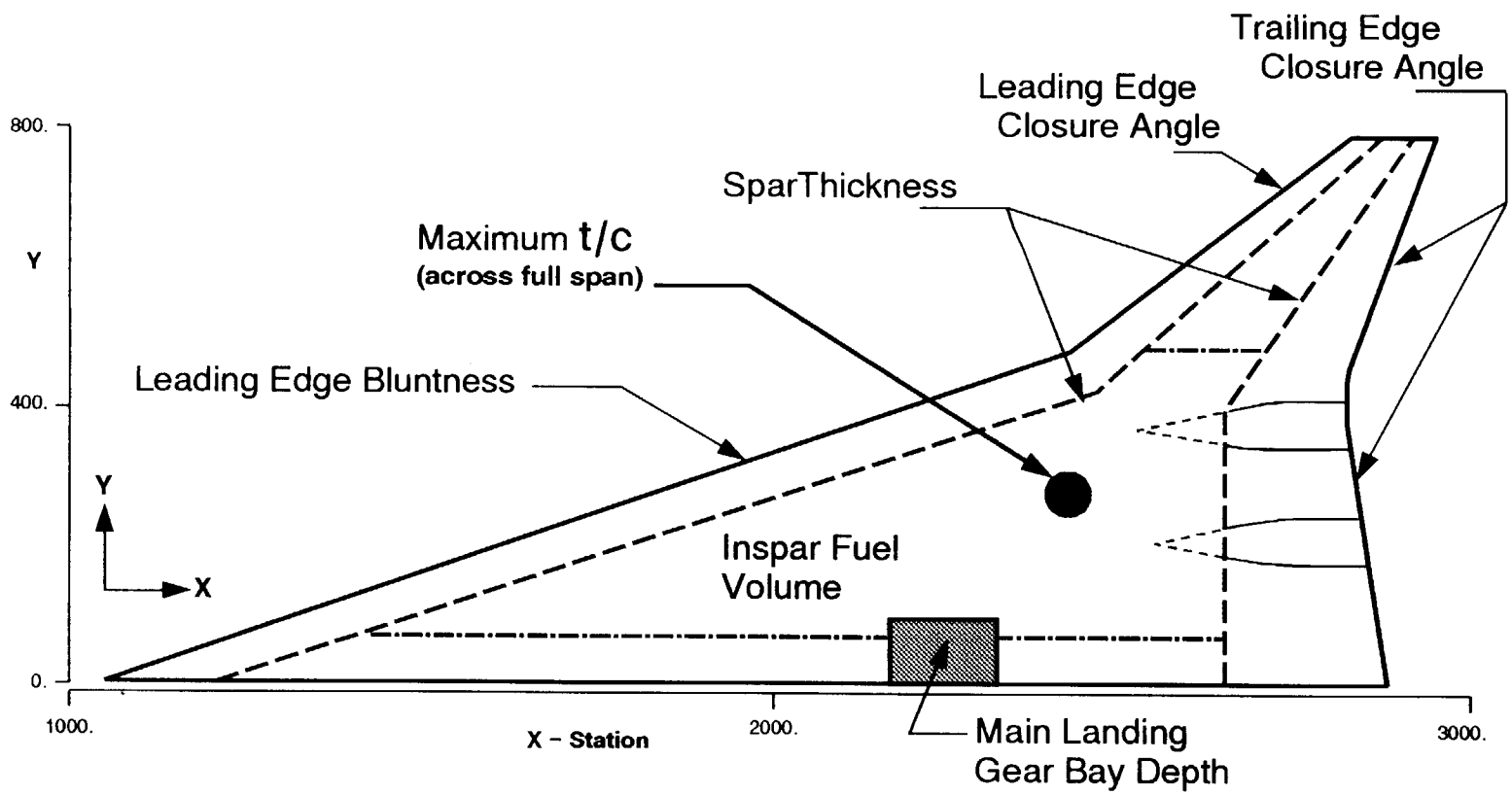

TCA Optimization Problem Posed

Variables:

- 11 Spanwise Node Belts
- 12 Camber Nodes per Belt
- 13 Thickness Nodes per Belt
- 1 Shear Node per Belt
- 1 Twist Node per Belt
- 1 Alpha

Objective Function:
Minimize C_D

27 wing variables per belt X 11 belts = 298 wing variables

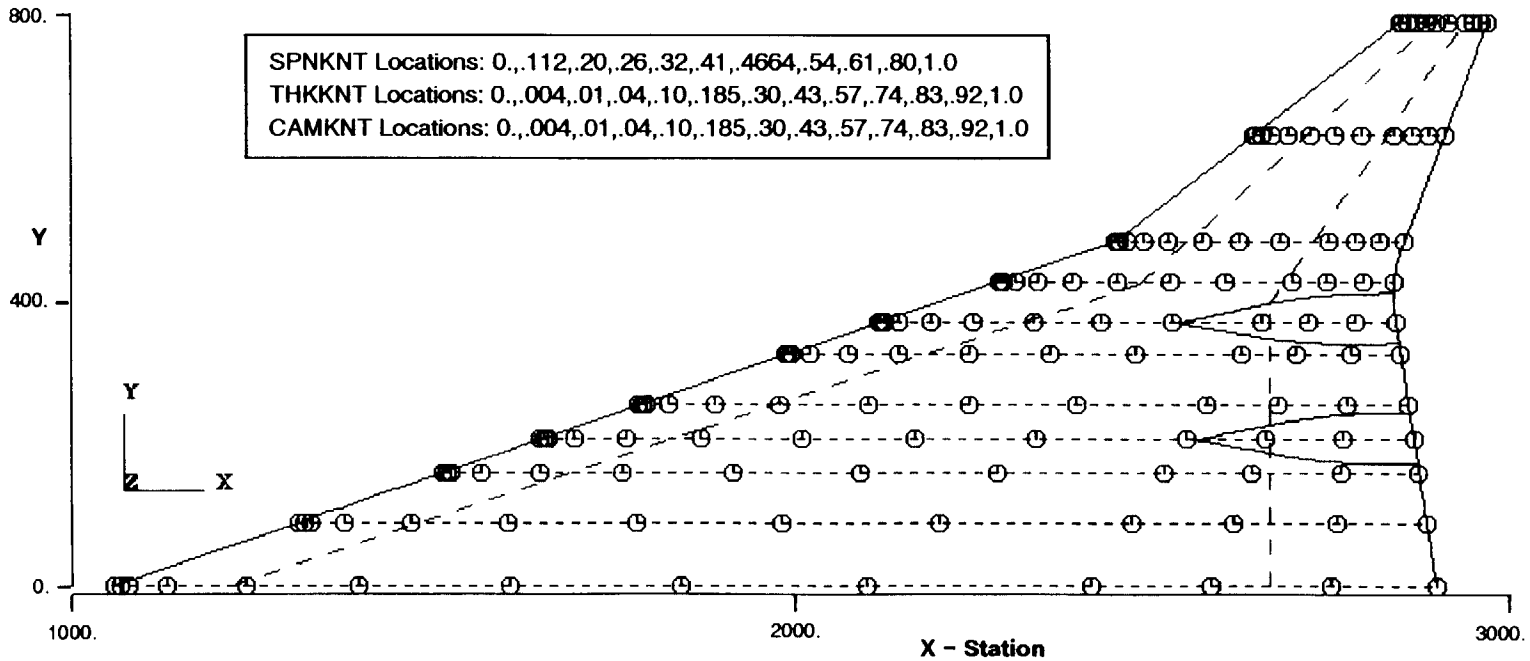

TCA Optimization – Body Variables

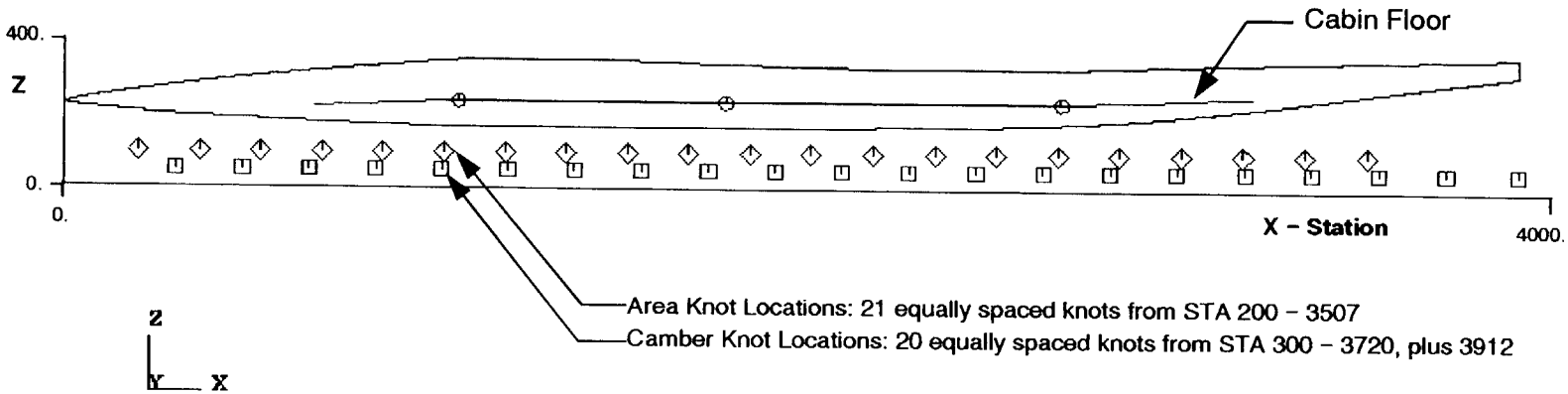

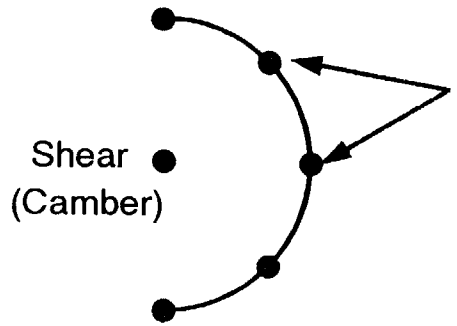

Five Cross Section Variables per Station

19 Locations * 6 variables = 115
3 Floor Kink Variables = 3
118

TCA Optimization Problem Posed – Nacelle Tune-up

Wing Variables:
- 12 Spanwise Node Belts
- 16 Camber Nodes per Belt
- 16 Thickness Nodes per Belt

32 wing variables per belt X 12 belts = 384 wing variables
+ 20 body camber variables
+ 1 alpha + 3 floor variables => 408 variables

Objective Function:
Minimize C_D

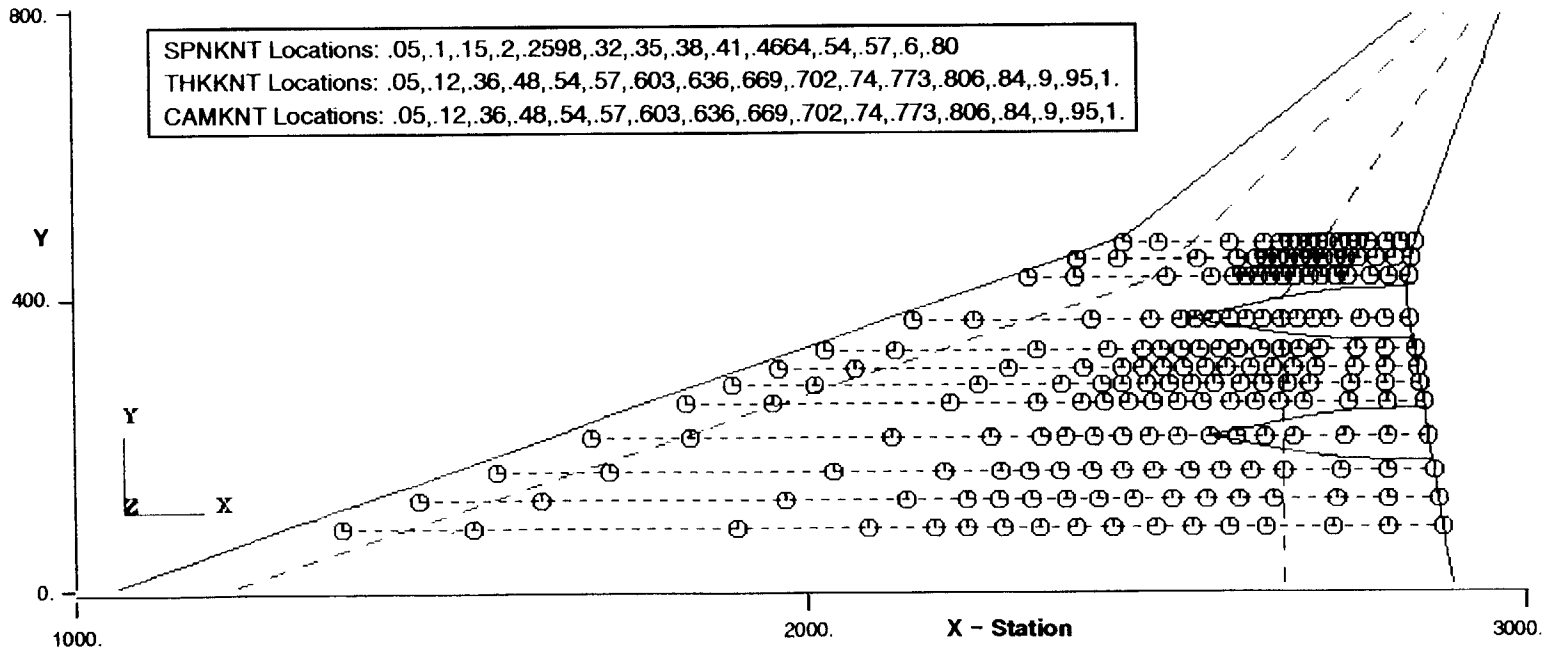

Tranair TCA Configuration Optimization

Upper Surface Solution Mach=2.4 C_L=.08556

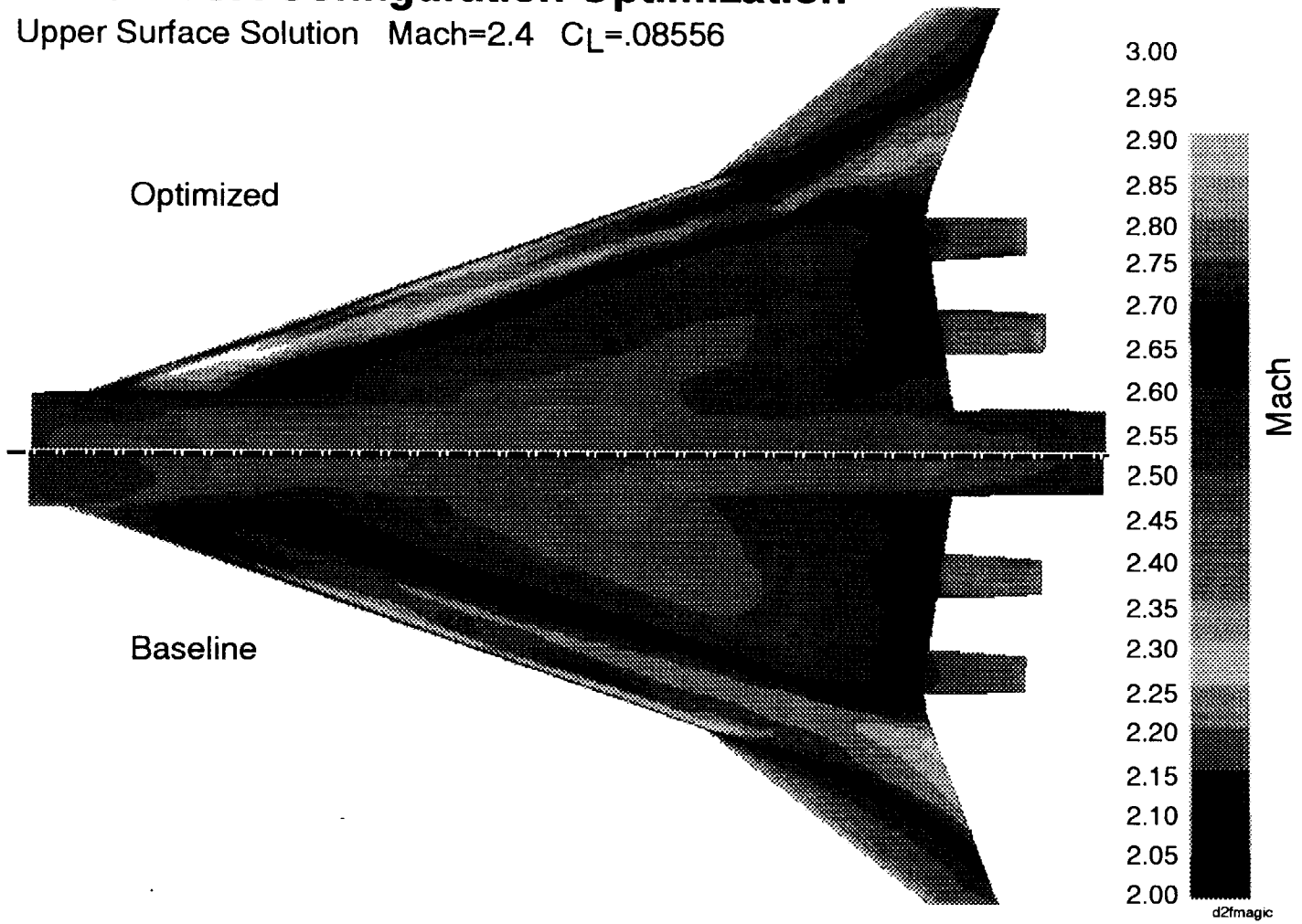

Tranair TCA Configuration Optimization

Lower Surface Solution Mach=2.4 C_L=.08556

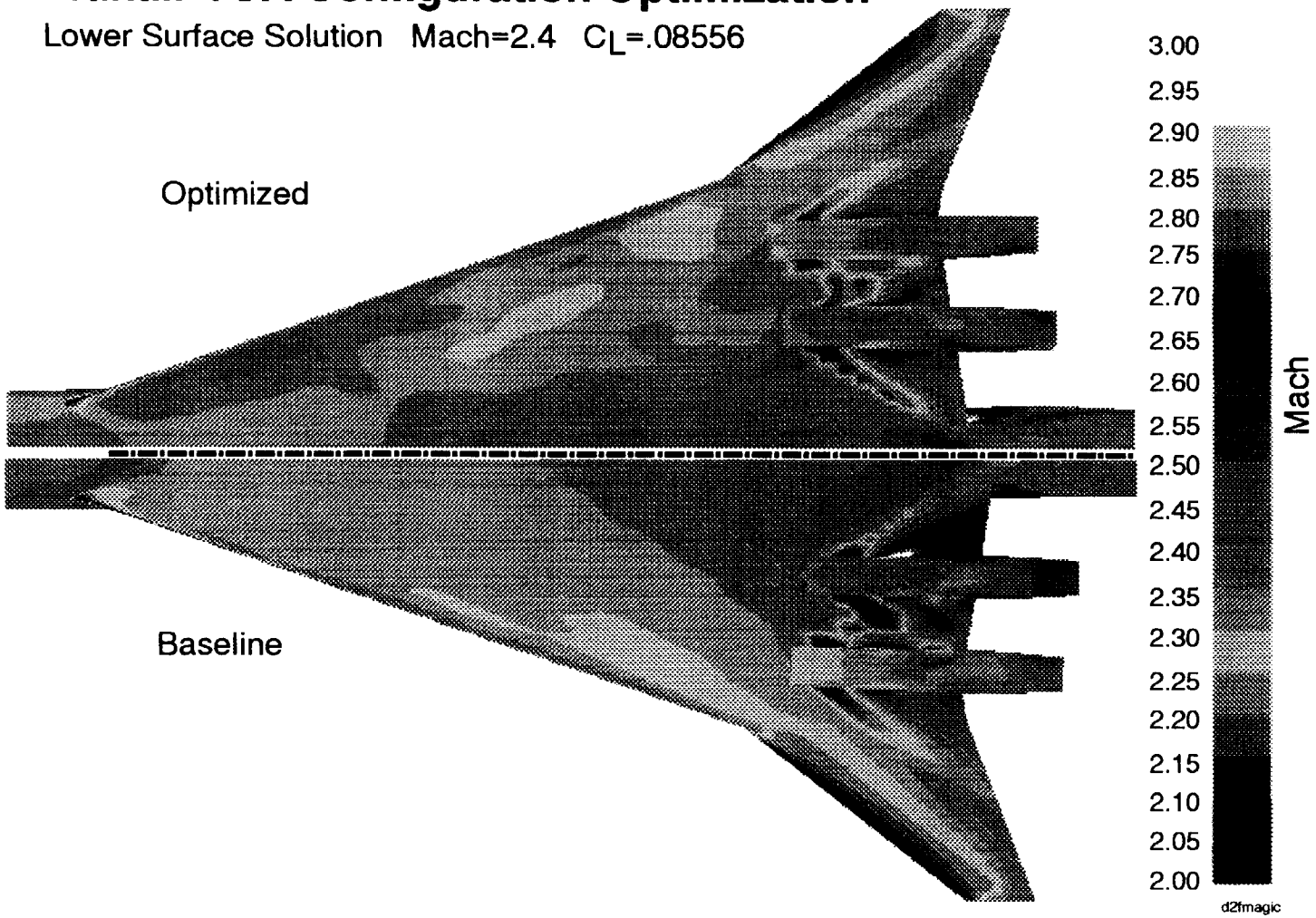

TCA Configuration Optimization – Viscous Verification

Upper Surface Solution Mach=2.4

Tranair (Invisicd)
Optimized TCA
C_L=0.0855

Overflow (Navier Stokes)
Optimized TCA
C_L=0.0844 Re_{MAC}=6.4million

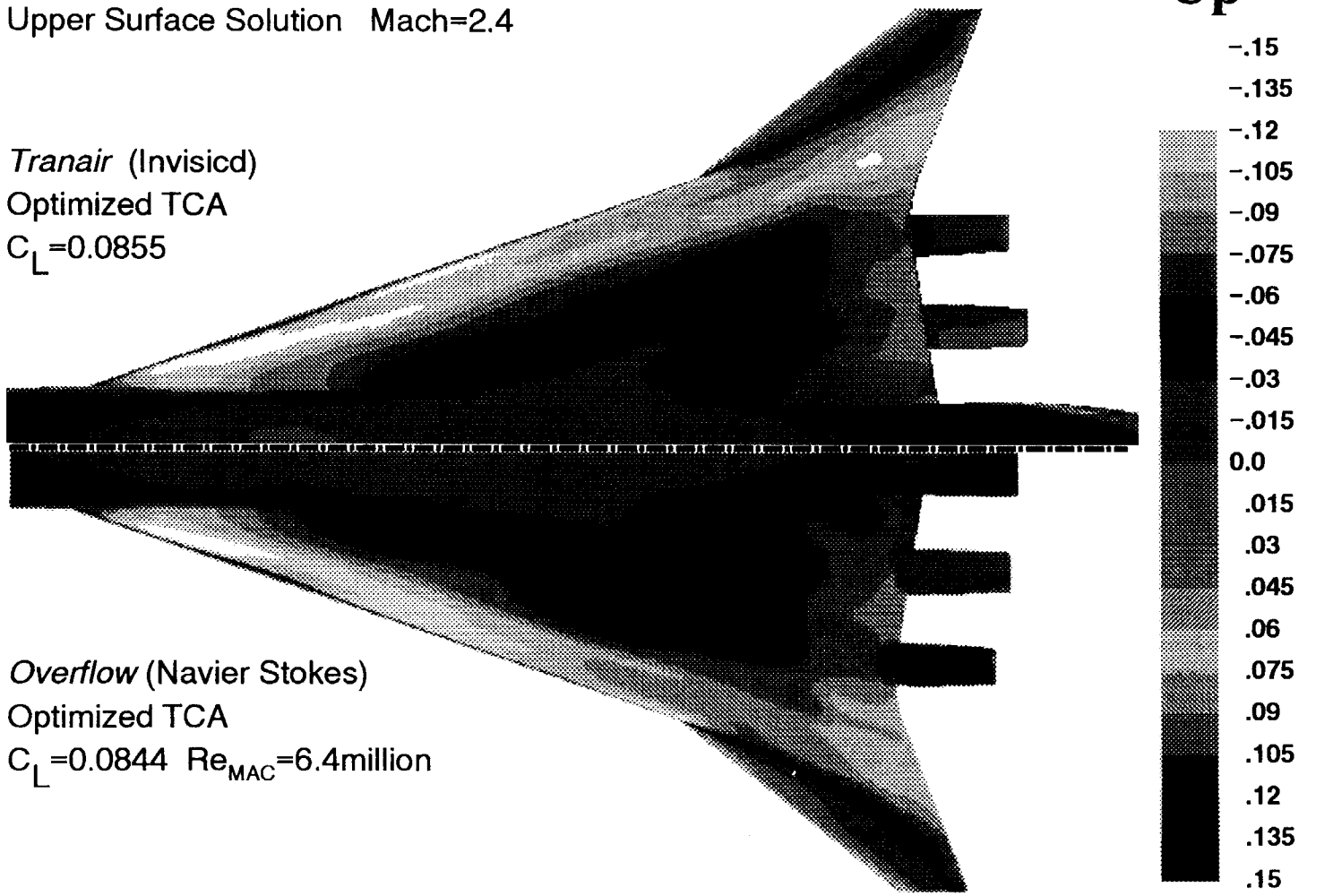

nsw8ctop2.i565

TCA Configuration Optimization – Viscous Verification Cp

Lower Surface Solution Mach=2.4

Tranair (Invisicd)
Optimized TCA
C_L=0.0855

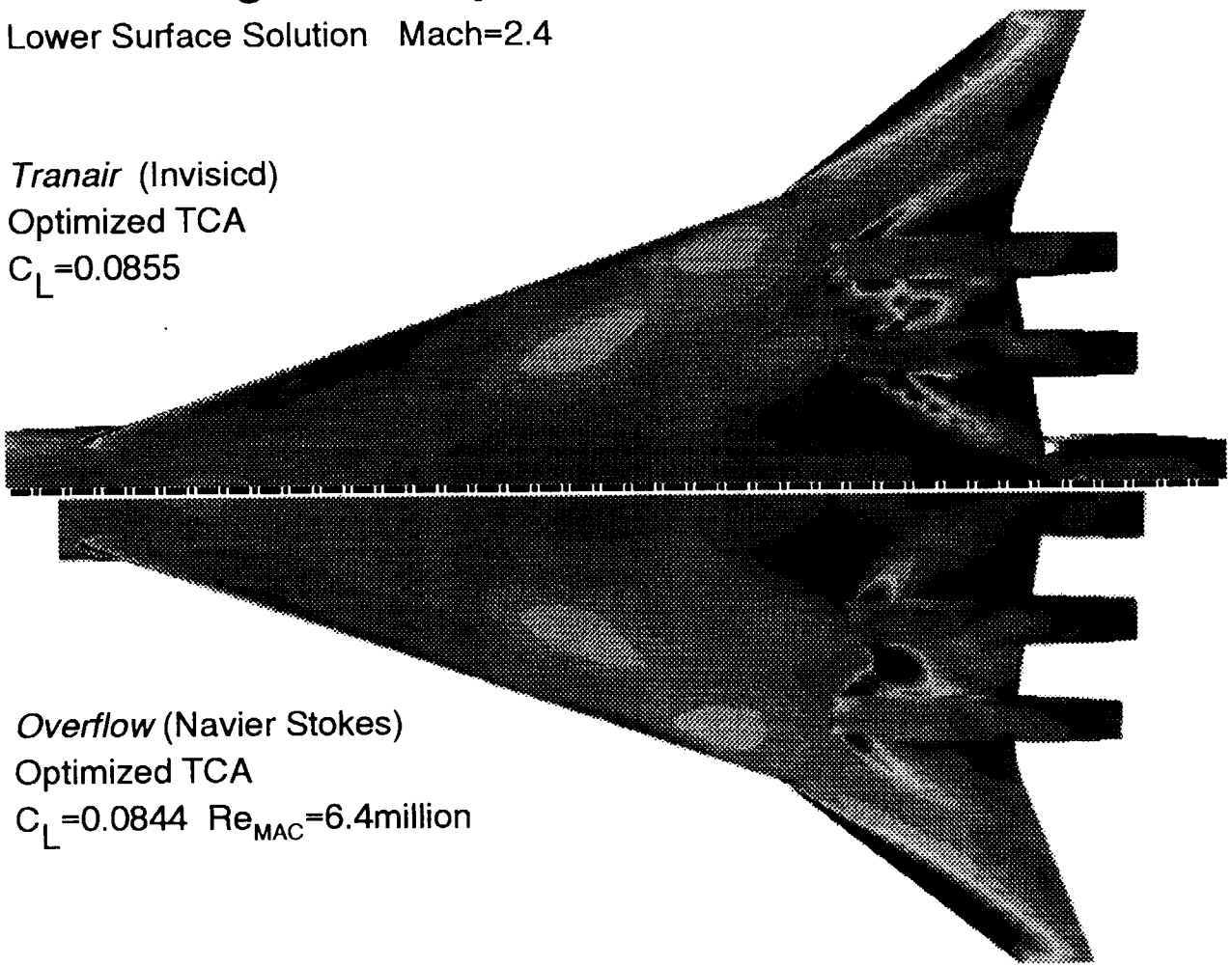

Overflow (Navier Stokes)
Optimized TCA
C_L=0.0844 Re_{MAC}=6.4million

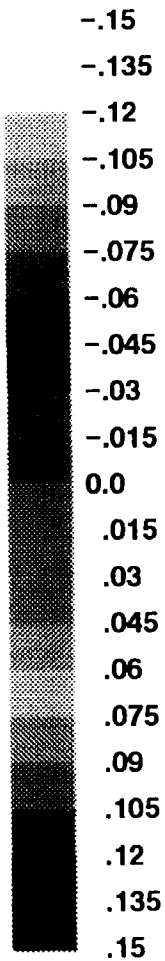

nsw8ctop2.i565

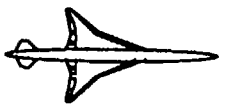

Observations on the Process and Results of Optimization

Configuration Aerodynamics Task 32
Aerodynamic Design Optimization Capability
(W.B.S. 4.3.1.2)

R. S. Conner

25–28 February 1997

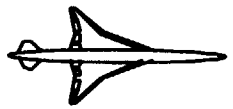

Acknowledgements

The results shown in this presentation are the combination of substantial amounts of work on the part of several people. The main team members are listed here with their contributions. Robyn Wittenberg performed not only the optimization reported here, but the prior TCA optimizations which lead to this result. She was also responsible for all the inviscid analyses. Bill Huffman is our optimization expert and is responsible for the optimization routines used. Steve Chaney and Steve Ogg performed all the viscous analyses shown and not shown. Eric Adamson is my Technology Integration counterpart and has acted as TI guide for this and previous such exercises. Finally, Bob Patton is lead of the Configuration Aerodynamics group and contributes on all levels from resource management to technical consultant.

Acknowledgements

- **Robyn Wittenberg**
  - Optimization Application, Inviscid Analysis, ...
- **Bill Huffman**
  - Optimization Development, Consultation, ...
- **Steve Chaney and Steve Ogg**
  - Viscous Analysis
- **Eric Adamson**
  - TI, Geometric Analysis, ...
- **Bob Patton**
  - Lead, Consultation, ...

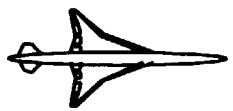

Outline

The outline of this presentation is shown here. The smoothing process will be described and some visual examples of the results of the activity will be shown. This is followed by a discussion of the constraint behavior of the optimization. Active and inactive constraints are listed and some interesting examples are shown. The next section illustrates the effect of optimization on the spanwise aerodynamic properties of the TCA configuration. It is prefaced with the effects of nacelle/diverters on the TCA. The presentation concludes with a broad discussion of some of the drag reduction mechanisms which appear to be exploited by the optimization. Examples of each mechanism are given. This presentation follows, and assumes the contents of, the presentation "TCA Configuration Cruise Point Design Optimization" by Robyn Wittenberg.

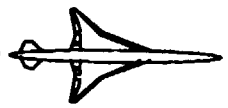

Outline

- Smoothing Process
- Constraint Results
- Spanwise Properties
- Drag Reduction Mechanisms

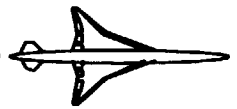

Smoothing Process

An essential step in all the current optimization processes is post–optimization smoothing. None of the current optimization tools create geometries that are of sufficient surface quality to permit direct use by wind tunnel model design. Some additional work is required prior to defining a wind tunnel model of the design.

In the current Boeing process, smoothing occurs after the optimization proper is complete. Ideally, this would be a cycled smoothing, wherein the results of the smoothing would be evaluated in an appropriate analysis tool. The schedule for this optimization exercise did not allow for cycling, therefore, the results of the initial round of smoothing were committed to wind tunnel model design.

The geometry produced by the TRANAIR optimization met all the TCA project constraints. As a result, the smoothing process was limited to removing undesirable surface behavior. The goal was to limit the changes so as to retain as much of the character of the optimization as possible. Specifically, large features due to optmization were retained and areas were modified only when particular undesirable surface quality was noticed. These areas of concern typically were characterized by higher frequency, lower amplitude deviations from the general surface. They were referred to as noise.

The smoothing was performed interactively. Specific areas were located by visual inspection of shaded images, 2–D cuts and curvature displays. These areas were then treated on a case by case basis, where the cure was specifically tailored to that area. One by one, undesirable surface behaviors were located and removed. The process was based on subjective opinion as to what looked right. The wing and body lofts were smoothed by different individuals but were coordinated for consistency of approach and result.

Shaded images of before and after are shown next.

Smoothing Process

- Unsmoothed Design Met All Constraints
- Philosophy : Minimum Changes
  - Retain Features
  - Remove Noise
- Interactive, Constrained Smoothing
  - Search & Destroy
  - Eyeball Criterion

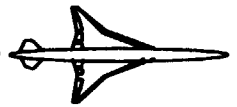

Tranair Optimized TCA

An upper surface isometric view of the Tranair Optimized TCA is shown here. This is the shape as defined by the optimization process, prior to smoothing. Comparing it to a similar view of the smoothed configuration, shown next, reveals the kinds of changes that were made by the smoothing process.

On the wing, there are several changes apparent. There is a series of spanwise waves that run outboard from the leading edge planform break region that were removed. One can also see a smaller chordwise bump between the two larger ones. A last wing change is the spanwise wave that can be seen near the leading edge of the retained inboard bump.

The body smoothing on the upper surface tended to be limited to removing areas of concentrated circumferential curvature that appear here as longitudinal creases.

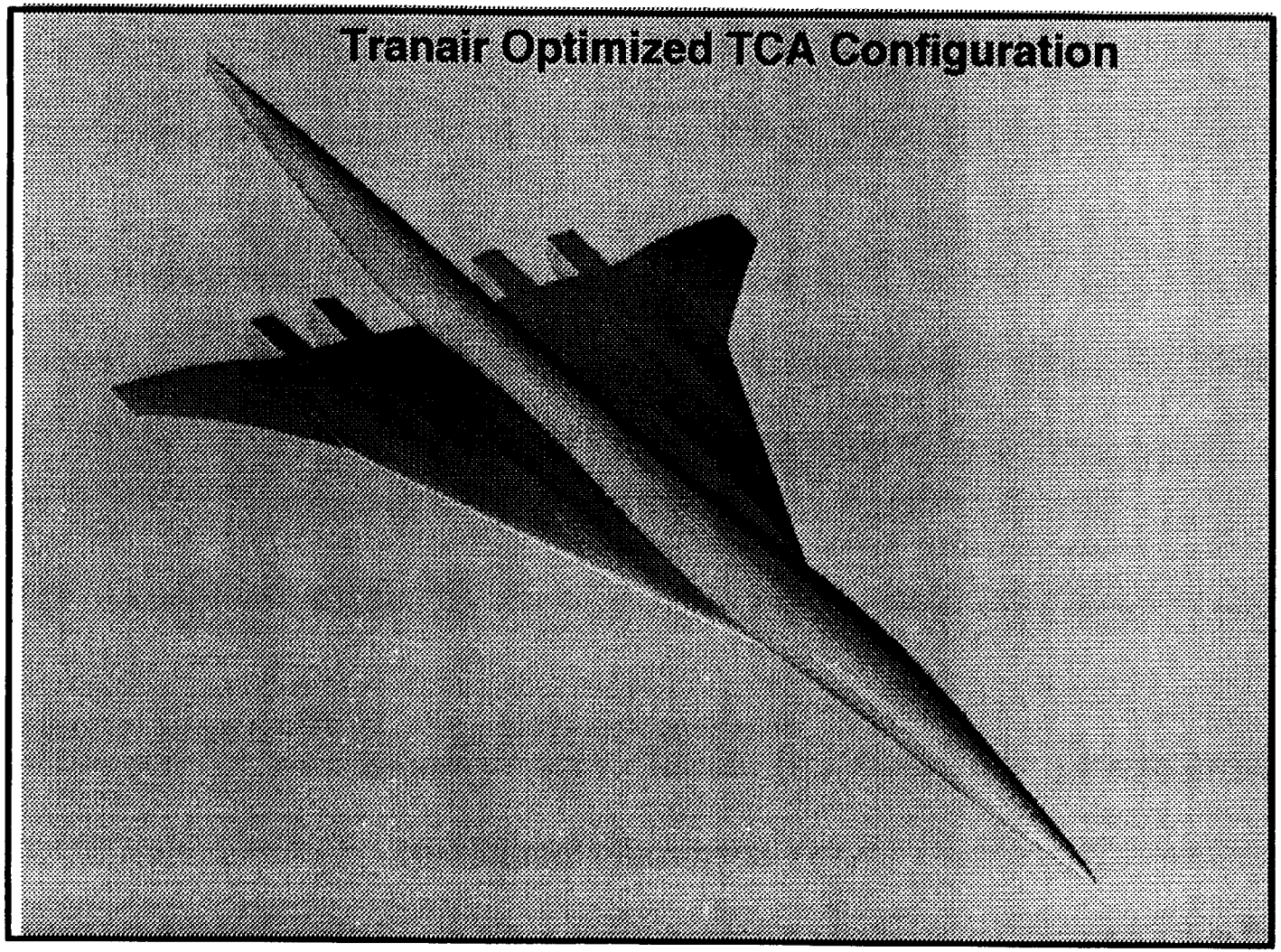
Tranair Optimized TCA Configuration
12fmagic

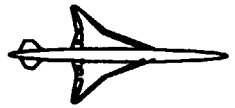

Smoothed, Optimized TCA

An upper surface isometric view of the final smoothed, Optimized TCA is shown here. These are the lofts that were transmitted to Model Design for wind tunnel model fabrication.

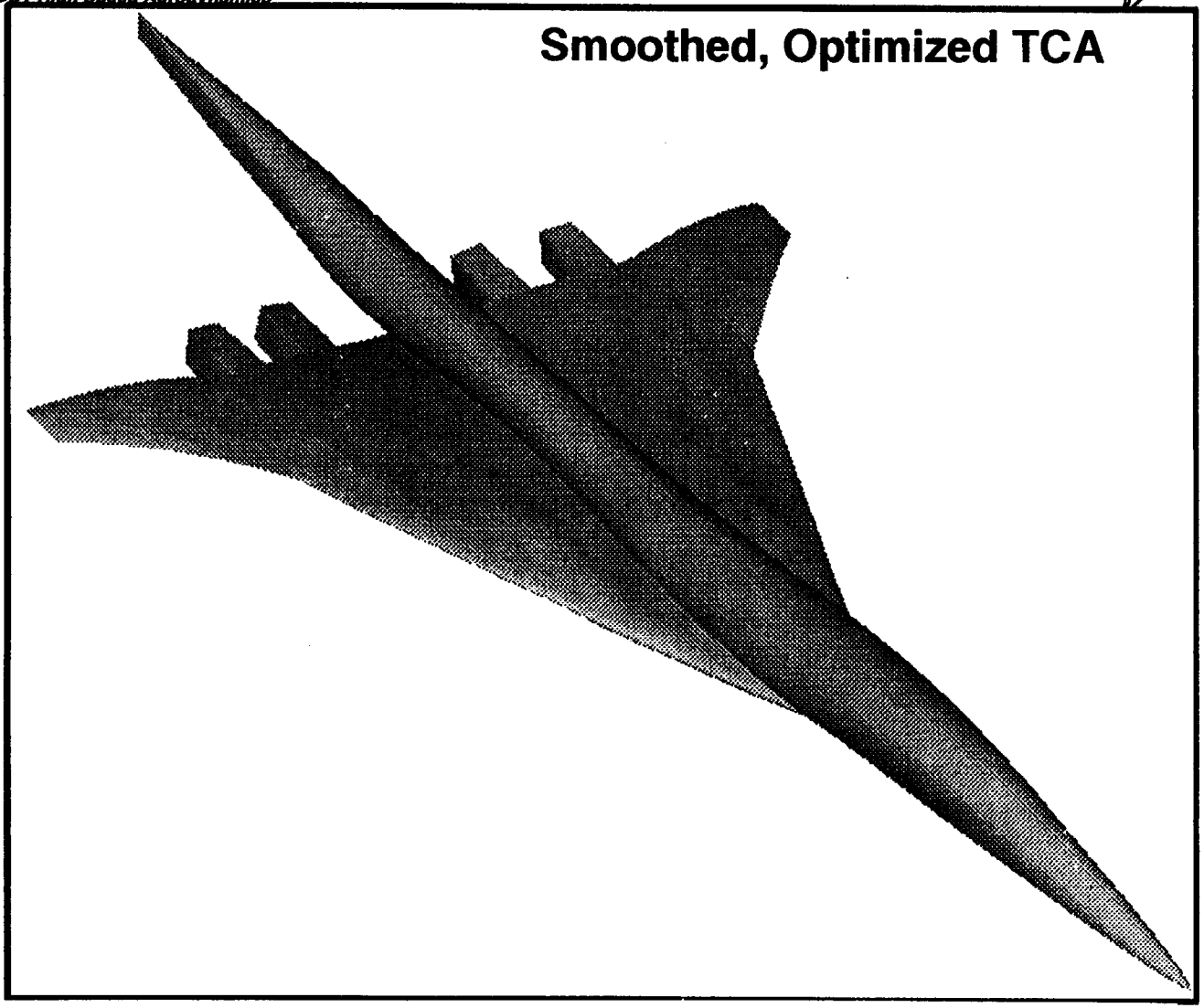
Smoothed, Optimized TCA
tca8wt

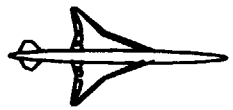

Tranair Optimized TCA

A lower surface isometric view of the Tranair Optimized TCA is shown here. This is the shape as defined by the optimization process, prior to smoothing. Comparing it to a similar view of the smoothed configuration, shown next, reveals the kinds of changes that were made by the smoothing process.

The most obvious change apparent in this view is the plane of symmetry crease in the wing loft at the forward end of the wing/body intersection. A plane of symmetry condition has been added to the optimization routine to prevent this behavior in the future.

The only other change shown here is another small spanwise wave near the leading edge of the inboard trough. Recall that a similar feature was noted on the upper surface.

Tranair Optimized TCA Configuration

d2fmagic

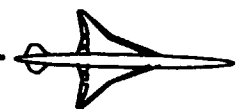

Smoothed, Optimized TCA

A lower surface isometric view of the final smoothed, Optimized TCA is shown here. These are the lofts that were transmitted to Model Design for wind tunnel model fabrication.

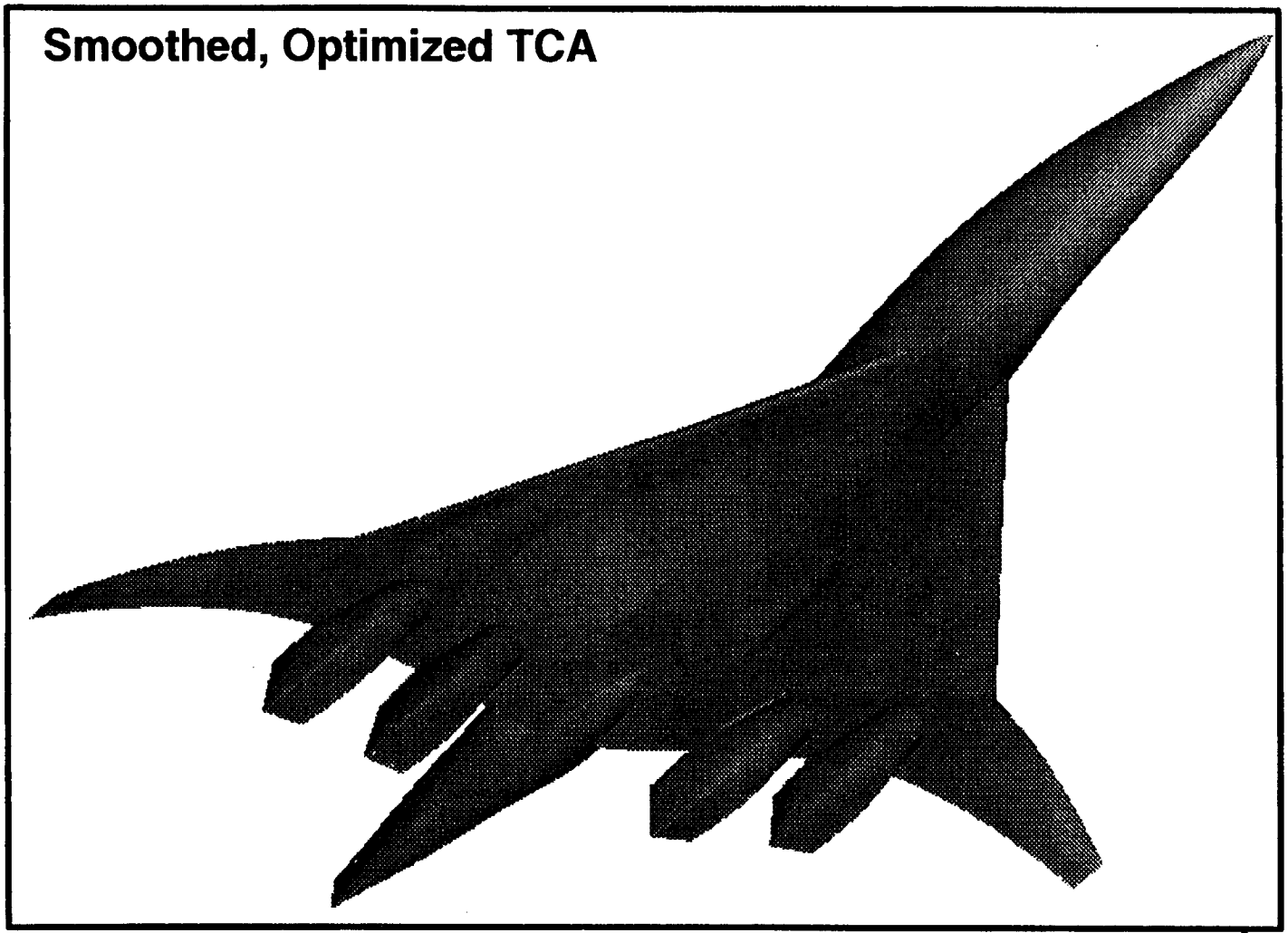
Smoothed, Optimized TCA
tca8wt

Active Wing Constraints

The active wing constraints are listed here. Note that the inboard wing is almost exclusively defined by the leading edge bluntness and the rear spar. The outboard wing is strongly constrained by thickness: both spars and the maximum thickness constraints are all active. There is an interesting single defining section of the inboard wing which is also against the t/c constraint. This is described more in the following slide. The trailing edge included angle constraint was only active on the first two defining sections outboard of the leading edge planform break.

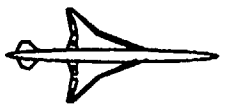

Active Wing Constraints

- LE Bluntness : Entire Inboard Wing
- Rear Spar Thickness : Entire Wing
- LE Spar Thickness : Outboard Wing
- Maximum t/c : y = 256, and y ~ 600 to 700
- TE Closure Angle : y = 485 to 514

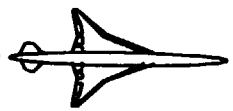

Effect of Optimization on the Maximum t/c

These two plots compare the value and location of the maximum local thickness–to–chord ratio of the TCA and the Optimized TCA. The two curves, solid and dashed, are piecewise linear curves through the spanwise locations of the twenty–nine defining sections of the optimized wing loft. Of particular interest is the point at Y=256 where the optimization is against the constraint value of 2.4 percent. This indicates a local but sensitive area of the configuration. The second plot show how the location of maximum t/c moves fore and aft as a function of span. The constrained station of the inboard wing corresponds to the return of the maximum thickness to the aft location just outboard of the inboard nacelle.

Effect of Optimization on the Maximum t/c

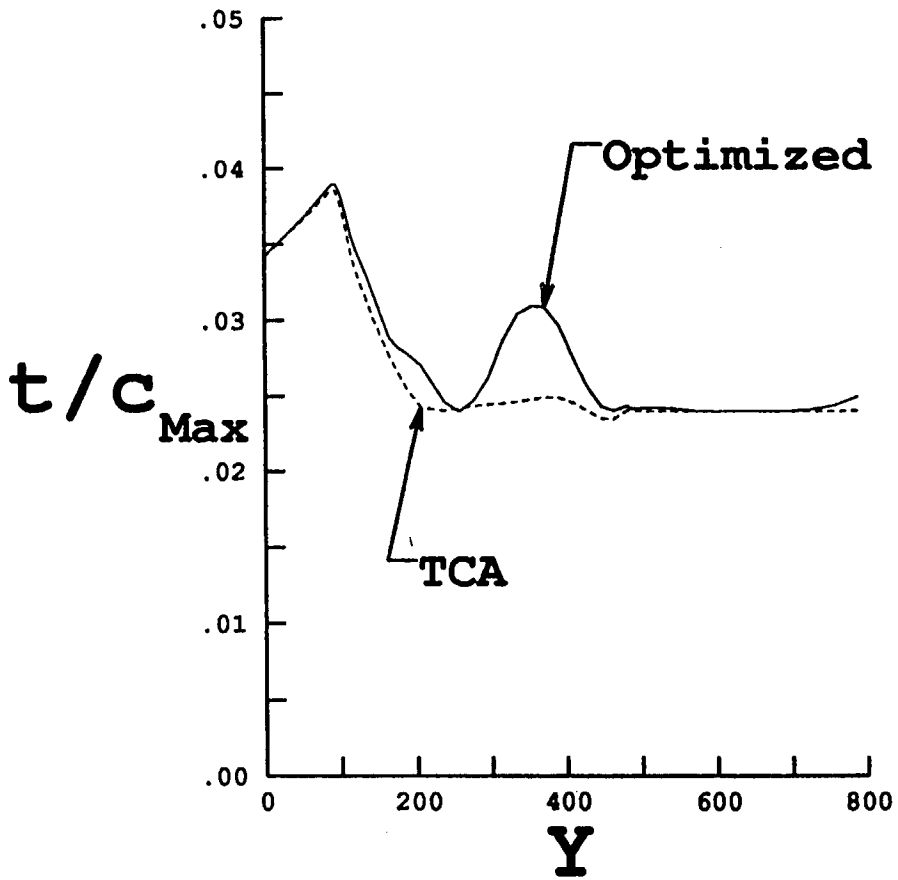

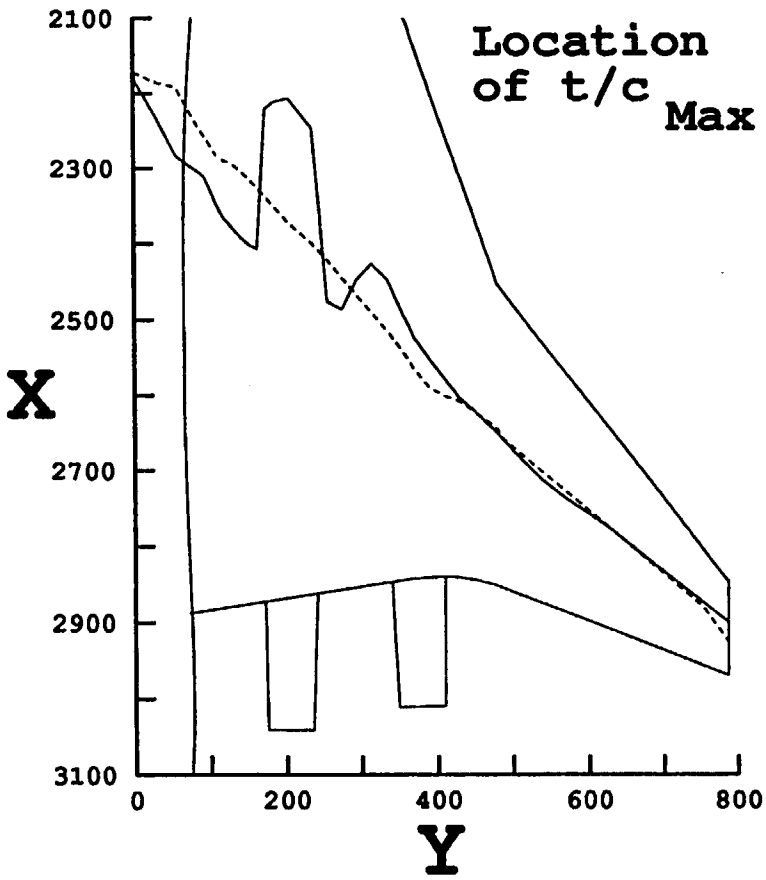

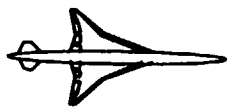

Active Body Constraints

The active body constraints are listed here. They are illustrated in more detail in the slides which follow.

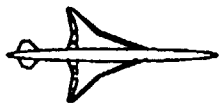

Active Body Constraints

- **Cross Section Max Radius of Curvature :** Four Places
- **Cabin Floor Angle at Cruise**
- **Cabin Envelope :** Two Places
- **Primary Wing Box / Floor Clearance :** Forward Edge
- **MLG Bay :** Forward Top Edge and Rear Bottom Edge
- **Rear Spar / Body Keel Clearance**

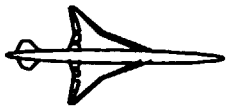

Body Cross Section Examples

The four regions where the body cross section maximum radius of curvature constraint was active are indicated by the four station cuts shown on the fuselage side view at the top of the slide. These cuts are only representative locations within regions which extend fore and aft from the cuts. The regions are roughly as long as the fuselage is thick. Cross sections from the first two regions are shown below the fuselage. The dashed polygons are the interior envelope constraint at the same station. The symbols further indicate that these are defining stations of the interior envelope.

The first section, station 780, is a forebody cut and is representative of the optimized forebody shape. The lower lobe has been pulled in to the curvature constraint. The forebody is flying in compression field.

The second section, station 1730, is representative of the fuselage cross section exposed to the accelerated wing upper surface flow. Here the upper lobe is pulled in to the radius of curvature constraint. One can also see that this is one of the two locations where the interior envelope constraint is active. The symbol is the head clearance constraint at the aft end of the business class section.

Body Cross Section Examples

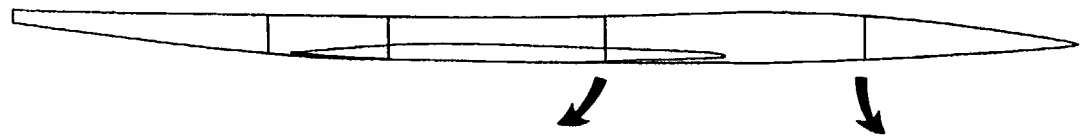

Curvature Constrained

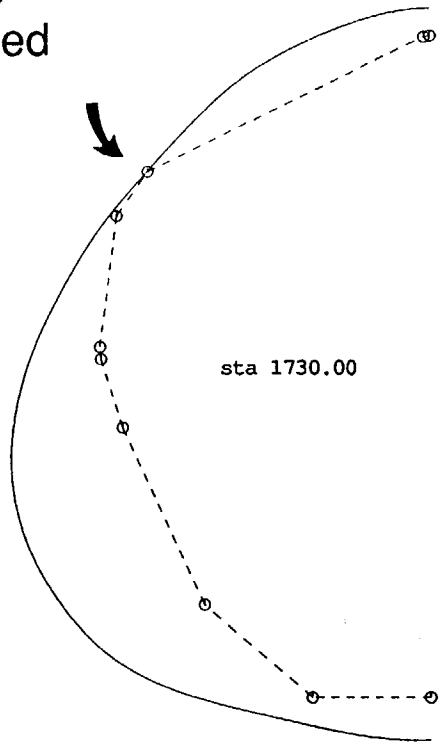

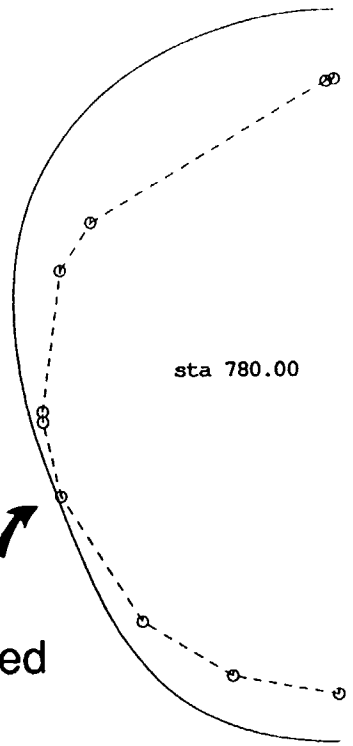

Curvature Constrained

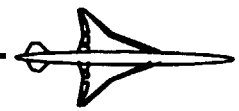

More Body Cross Section Examples

Representative cuts of the last two curvature constrained regions are shown here.

The first section, station 2531.88, is in the compressed flow region of the upper wing and is very similar to the forebody cut shown previously. Again, the lower lobe is pulled in against the curvature constraint.

The second section, station 2977.29, is representative of the fuselage cross section exposed to the expansion field emanating from the wing trailing edge. It bears a striking resemblance to the second cut of the previous slide. Here also, the upper lobe is pulled in to the radius of curvature constraint.

Both these sections illustrate the second location where the interior envelope constraint is active. This is the aisle of the forward portion of the economy class section. This is also shown in the next slide.

More Body Cross Section Examples

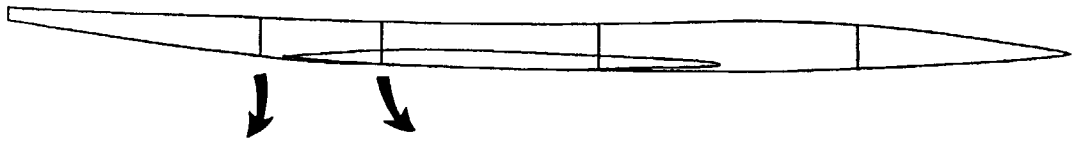

Curvature
Constrained

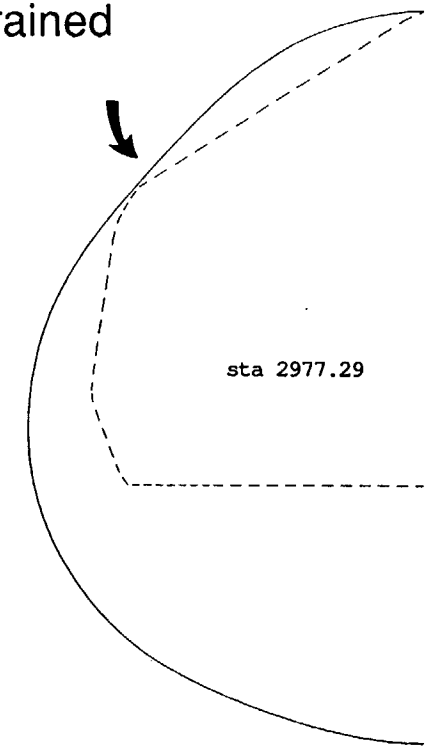

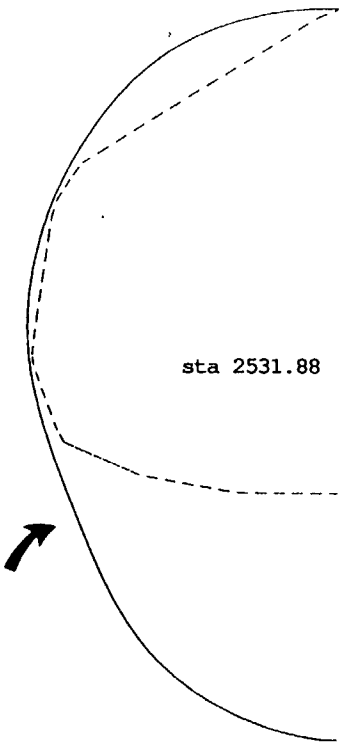

Curvature
Constrained

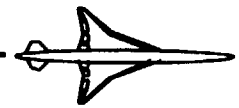

Optimized Plane–of–Symmetry Constraints

This image illustrates how several of the body constraints are both active and interconnected. The unlabeled collection of rectangles, parallelograms and triangles inside the body is the interior envelope constraint. The cabin floor is the middle, somewhat horizontal line of the set. Starting at the top of the body, the crown is constrained by the aisle of the forward portion of the economy class section of the interior envelope. Moving down, the primary wing box clearance is active between the floor and the wing/body intersection curve. The plane of symmetry wing shape is the same in this view as the wing/body intersection in the region of the primary wing box and the main landing gear bay. The wing thickness is set by the main landing gear bay constraint. Finally, the body keel is set by the rear spar to keel clearance requirement. Although not as obvious as the rest, the relationship between the floor and the wing/body intersection is being further controlled by the cabin floor cruise angle constraint.

Optimized Plane-of-Symmetry Constraints

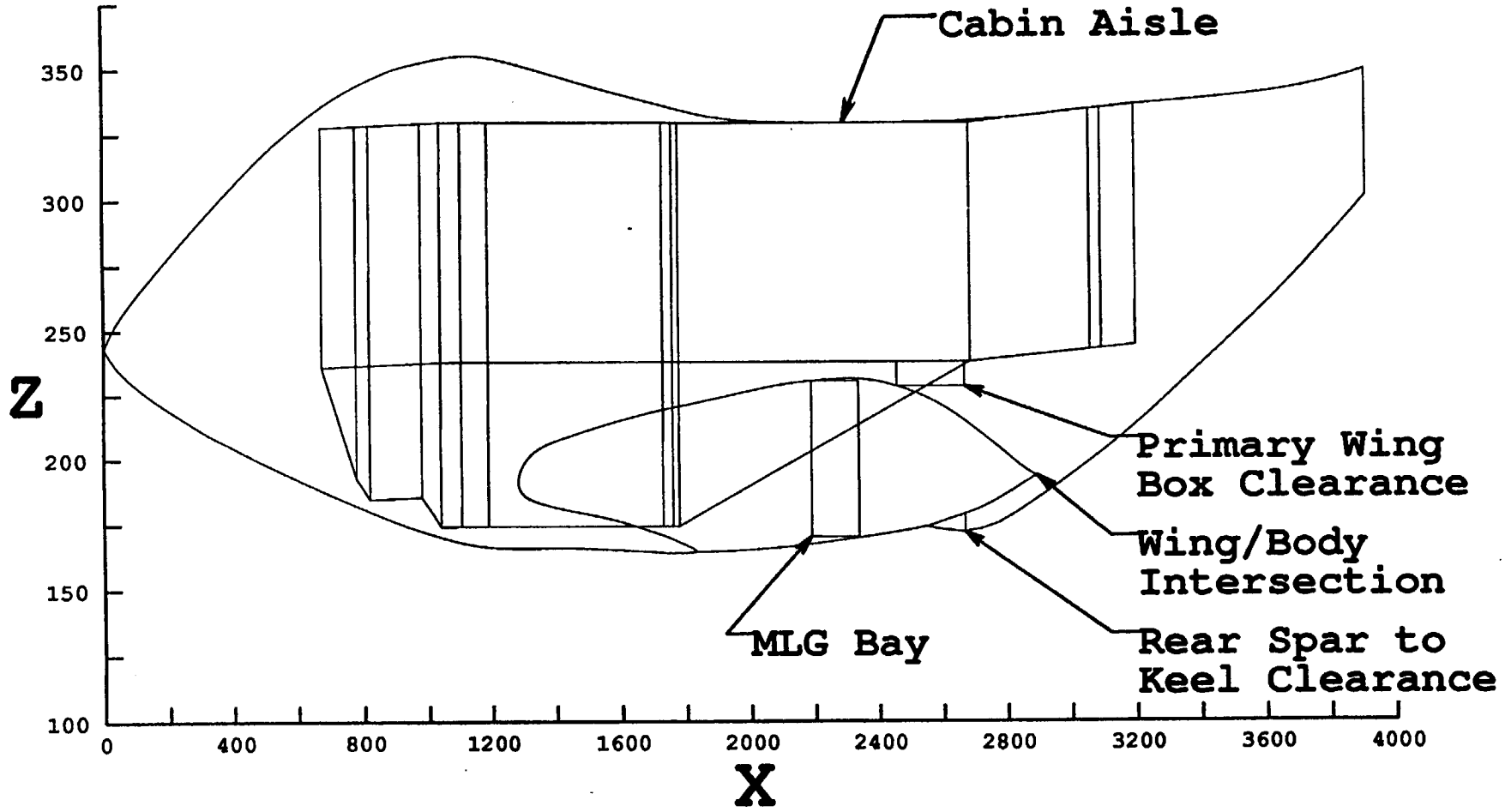

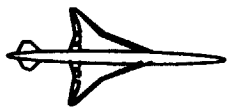

Inactive Constraints

The list of inactive constraints is shown here. It appears that the leading edge bluntness and rear spar constraints are so dominant that wing volume and minimum inspar thickness naturally fall out. Since the body tended to increase in alpha relative to the wing, until stopped by the cabin floor constraint, the auxiliary wing box clearance and overwing exit constraint were not issues. Finally, the pilot's eye cross section ended up larger than the TCA, as was the case for much of the body, as shown in the preceding presentation.

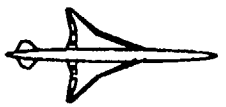

Inactive Constraints

- Inspar Wing Volume (Fuel)
- Minimum Inspar Thickness
- Auxiliary Wing Box / Floor Clearance
- Overwing Exit Door Clearance
- Pilot's Eye Cross Section Area

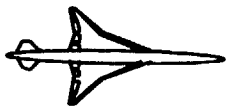

Comparison of TCA Pressure Forces

Fundamental to the ability to optimize with an inviscid method is the ability to accurately, inviscidly predict the pressure forces that will be realized in viscous flow. This ability has been demonstrated by every HSR group for many configurations. A comparison of the Boeing's inviscid optimization tool, Tranair, and viscous analysis tool, Overlfow, are shown here for the TCA at the cruise Mach number. The plots are the lift curve and drag polar. The curves are fitted to the Overflow data, the small diamonds, and the Tranair data is show only as symbols, the larger squares. As with comparisons for other configurations, correlation is excellent. Matching both the lift curve and drag polar indicates that the interaction between geometry and flow at the heart of pressure drag optimization is being predicted. Based on this and previous correlations, the following analysis of inviscid results are suggested to be true of the corresponding viscous flow, at least in large part.

Comparison of TCA Pressure Forces

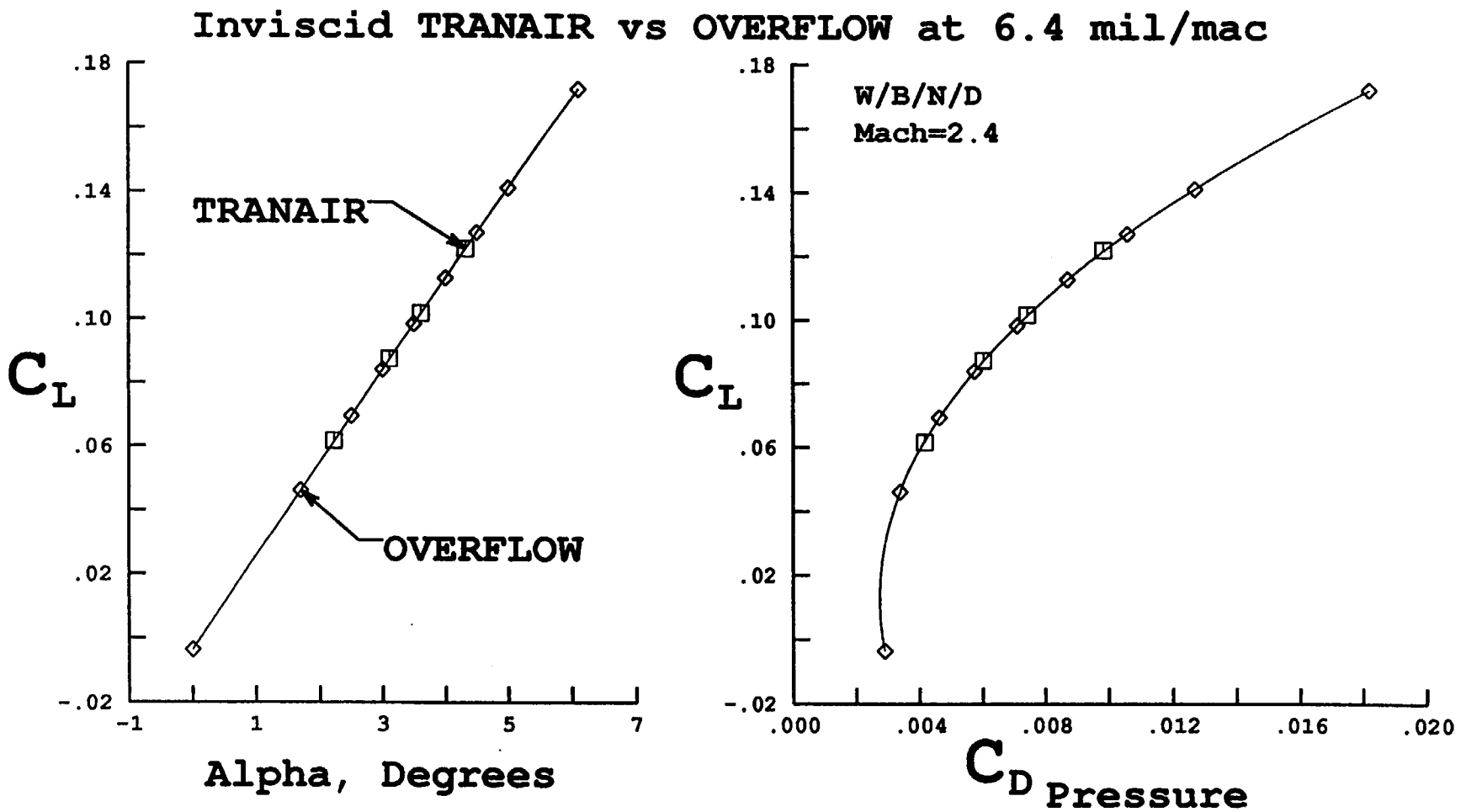

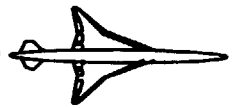

Effect of Nacelle/Diverters on Spanload

Prior to considering the effect of optimization on spanwise properties, it is useful to establish what aspects of the distributions are due to the nacelle/diverters. The effect on spanload is shown here. Note that the angle of attack is matched, not the total lift coefficient. Note also that these and the following companion plots are straight line connections between about seventy locations from the plane of symmetry to the wing tip. Cuts are made through the body and through the nacelle diverters. As a result, the plots are not as smooth as are the properties near these components but, are still representative of the data and provide useful comparisons.

The first plot is of local lift coefficient verses semispan. At constant angle of attack, the nacelle/diverters show up as notable regions of increased local lift with accompanying regions of some lift reduction. The second plot is of nondimensional spanload verse semispan. This plot can be misleading since the total lift coefficients are different. This will not be the case when considering the effect of optimization where lift is matched. Even for comparison shown here, the second plot illustrates where and how the nacelle/diverters add lift.

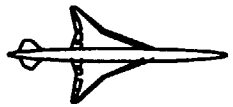

Effect of Nacelle/Diverters on Spanload

Inviscid TRANAIR: Wing/Body/Nacelle/Diverter vs Wing/Body

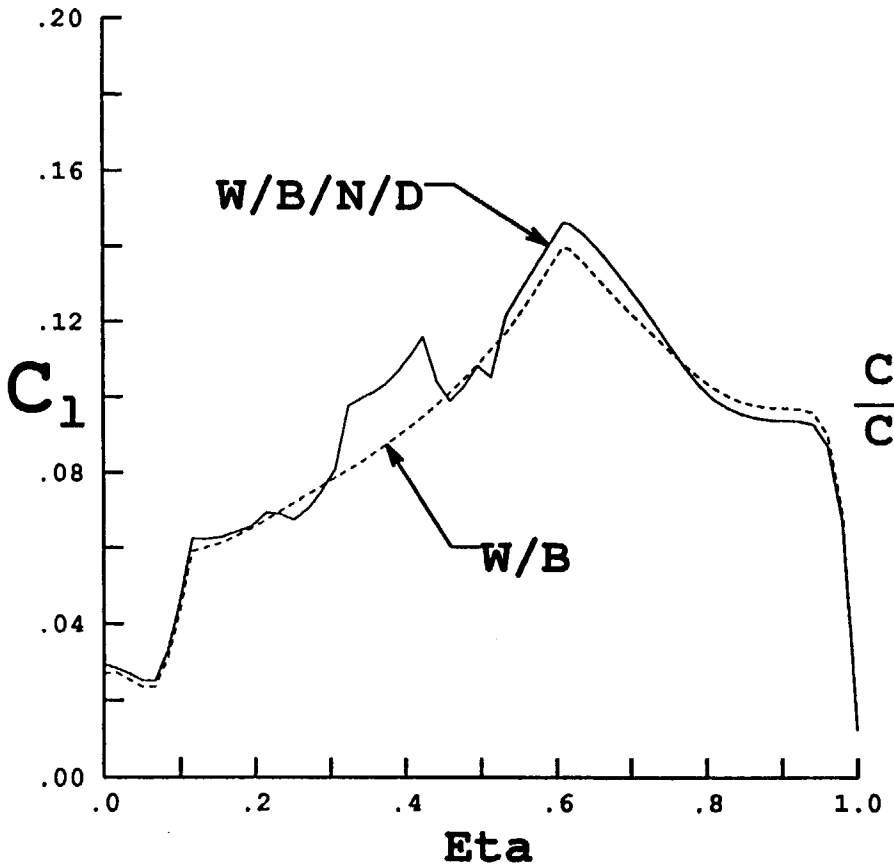

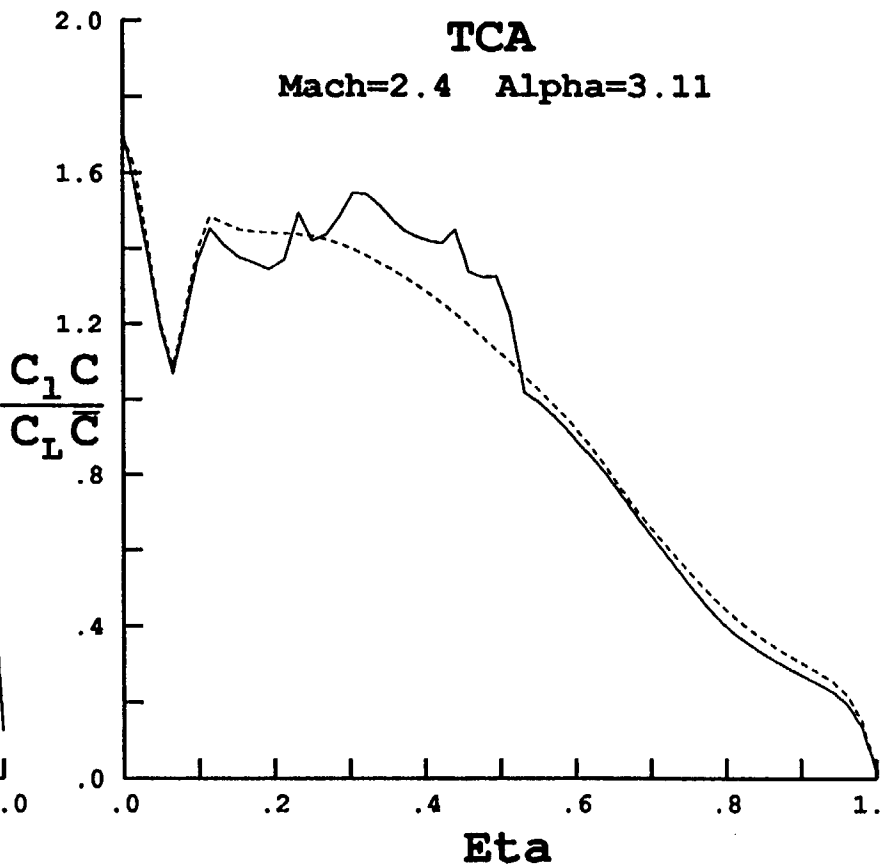

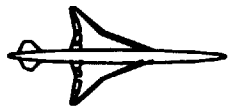

Effect of Nacelle/Diverters on Spandrag

These are drag versions of the previous slide's plots, local drag coefficient and nondimensional spandrag, respectively. Here the nacelle/diverters clearly show up as local drag increases. The wing/body intersection also shows up as a local drag increase.

Effect of Nacelle/Diverters on Spandrag

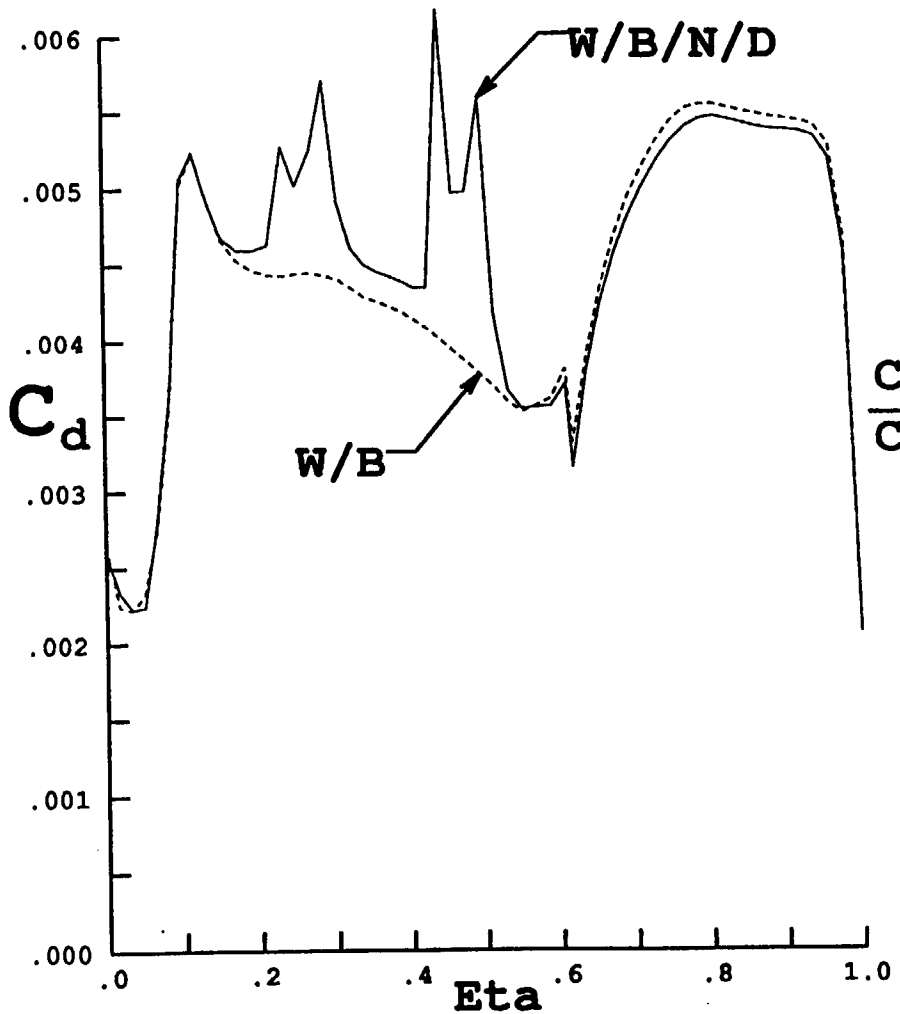

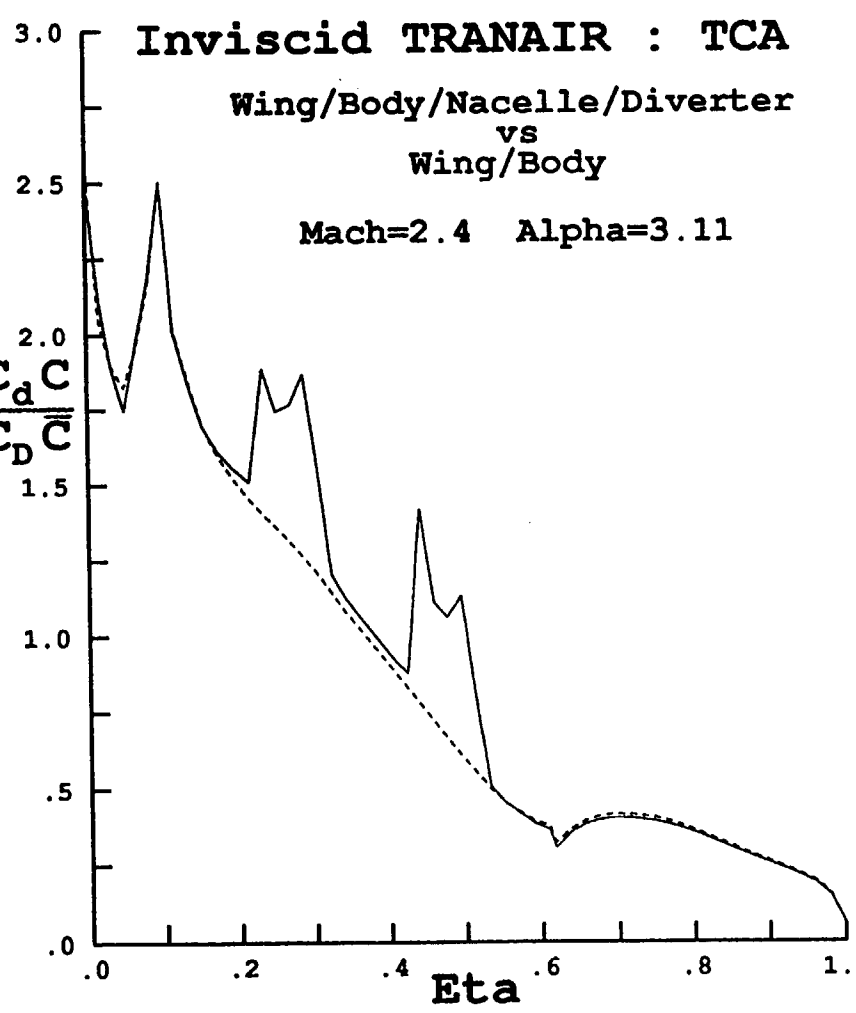

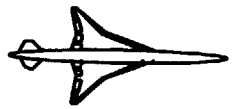

Effect of Optimization on Spanload

These plots show the effect of TCA optimization on spanwise loading at constant lift.. In terms of local lift, the first plot, one can see that load has been increased on the body and inboard wing, and decreased on most of the wing. The second plot illustrates how the relatively large chords of the body and inboard wing are able to offload the rest of the wing.

Effect of Optimization on Spanload

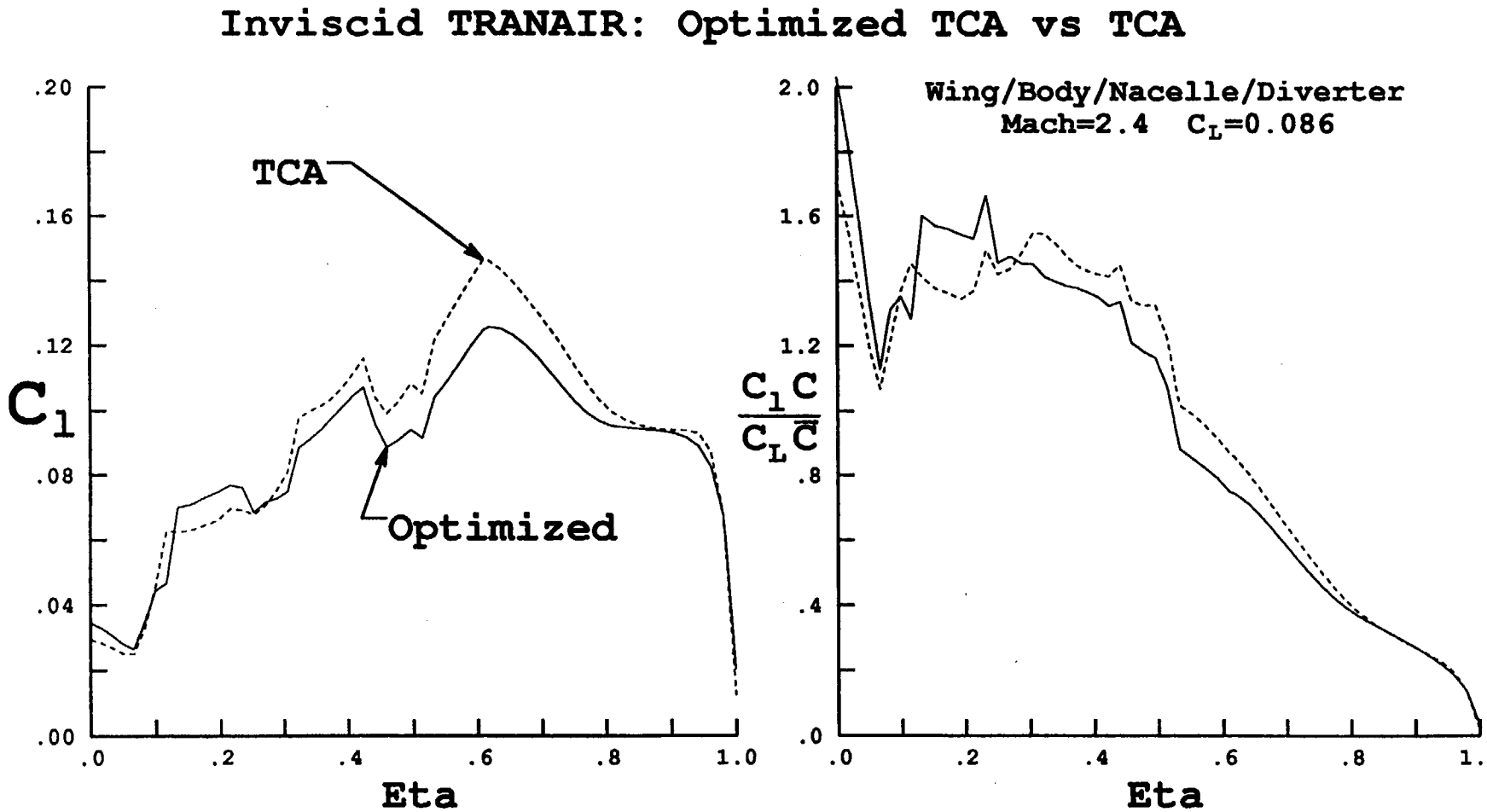

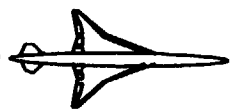

Effect of Optimization on Spandrag

These plots of the effect of optimization on spanwise drag indicate several interesting features of the optimization. First, increased body drag was traded for decreased drag on essentially the entire wing. Second, the increased loading of the inboard wing, shown on the previous slide, is shown here to be accompanied by a local decrease in drag. Next, the second plot indicates that the drag reduction on the inboard wing is almost constant at all locations, even at the nacelle /diverters. Finally, at the leading edge planform break, Eta=.61, the local inviscid drag of the optimized configuration approaches zero.

Effect of Optimization on Spandrag

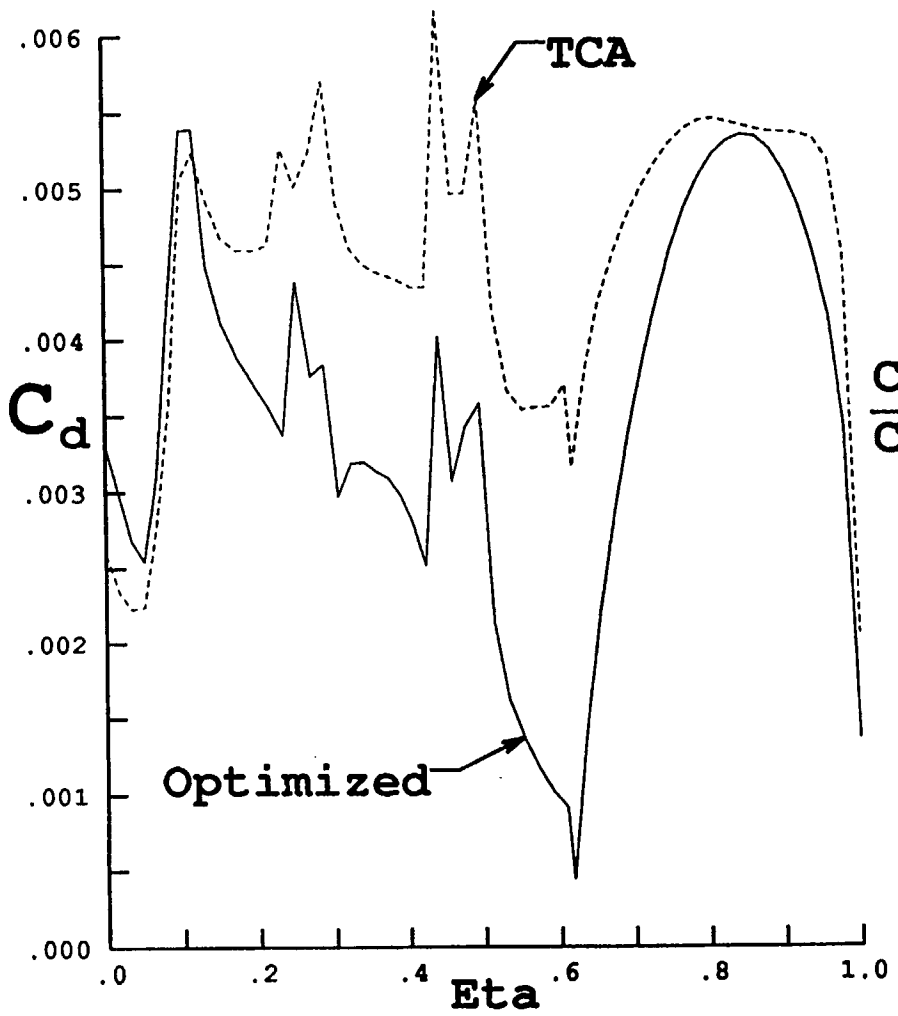

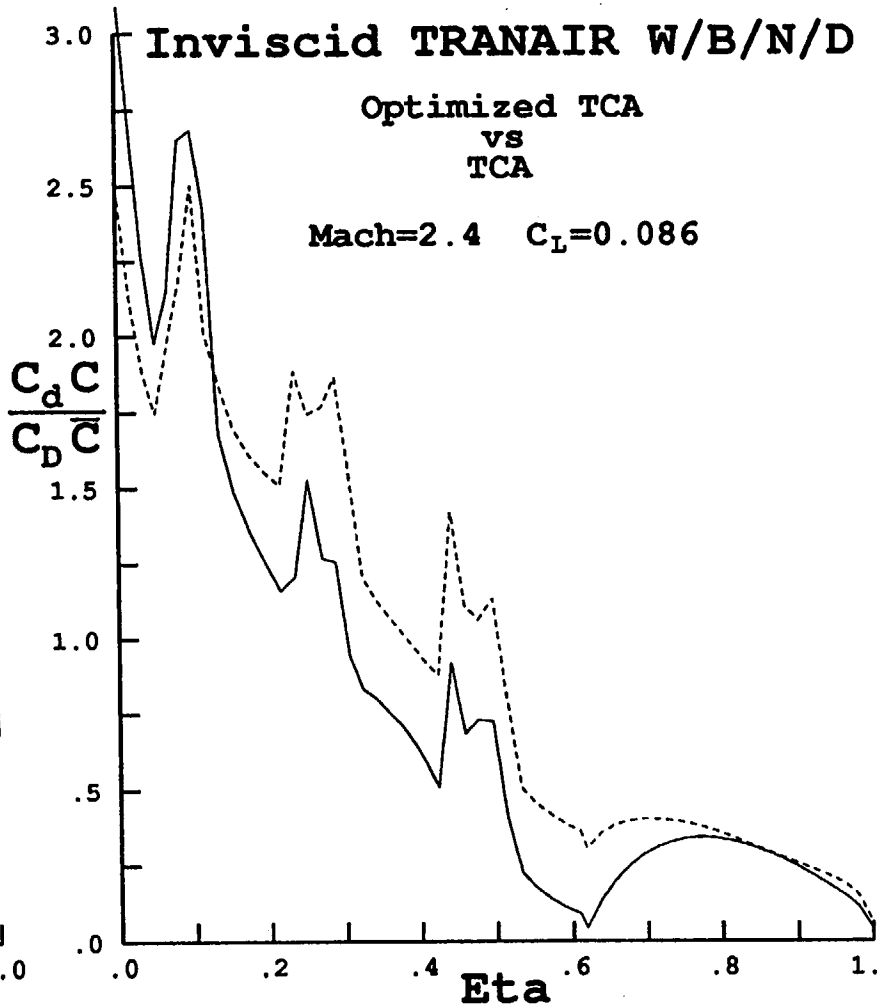

TCA Navier–Stokes Solutions

This comparison of the upper surface solutions of the TCA and optimized TCA, and the lower surface comparison which follows, helps illustrate the complexity of the optimized result. The optimized flow has far more character than that of the TCA. The next section will suggest reasons why the optimization produces such a result.

TCA Navier–Stokes Solutions

Wing Upper Surface

Mach=2.4 C_L=0.10 Re_{MAC}=6.4million

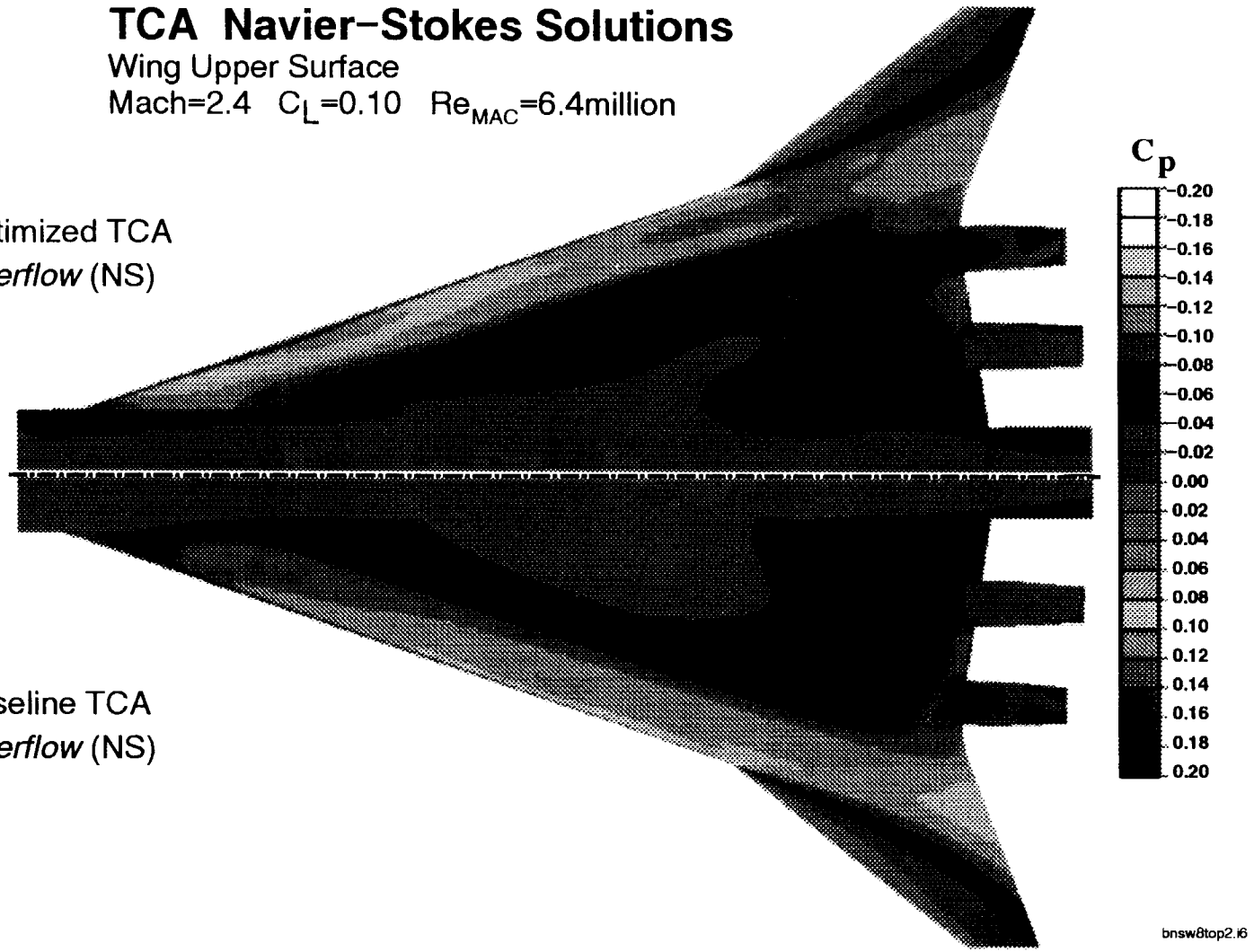

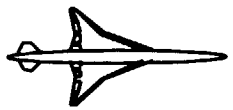

TCA Navier–Stokes Solutions

This is a comparison of the lower surface solutions of the TCA and optimized TCA.

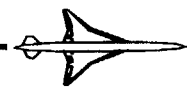

TCA Navier–Stokes Solutions

Wing Lower Surface

Mach=2.4 C_L=0.10 Re_{MAC}=6.4million

Optimized TCA

Overflow (NS)

Baseline TCA

Overflow (NS)

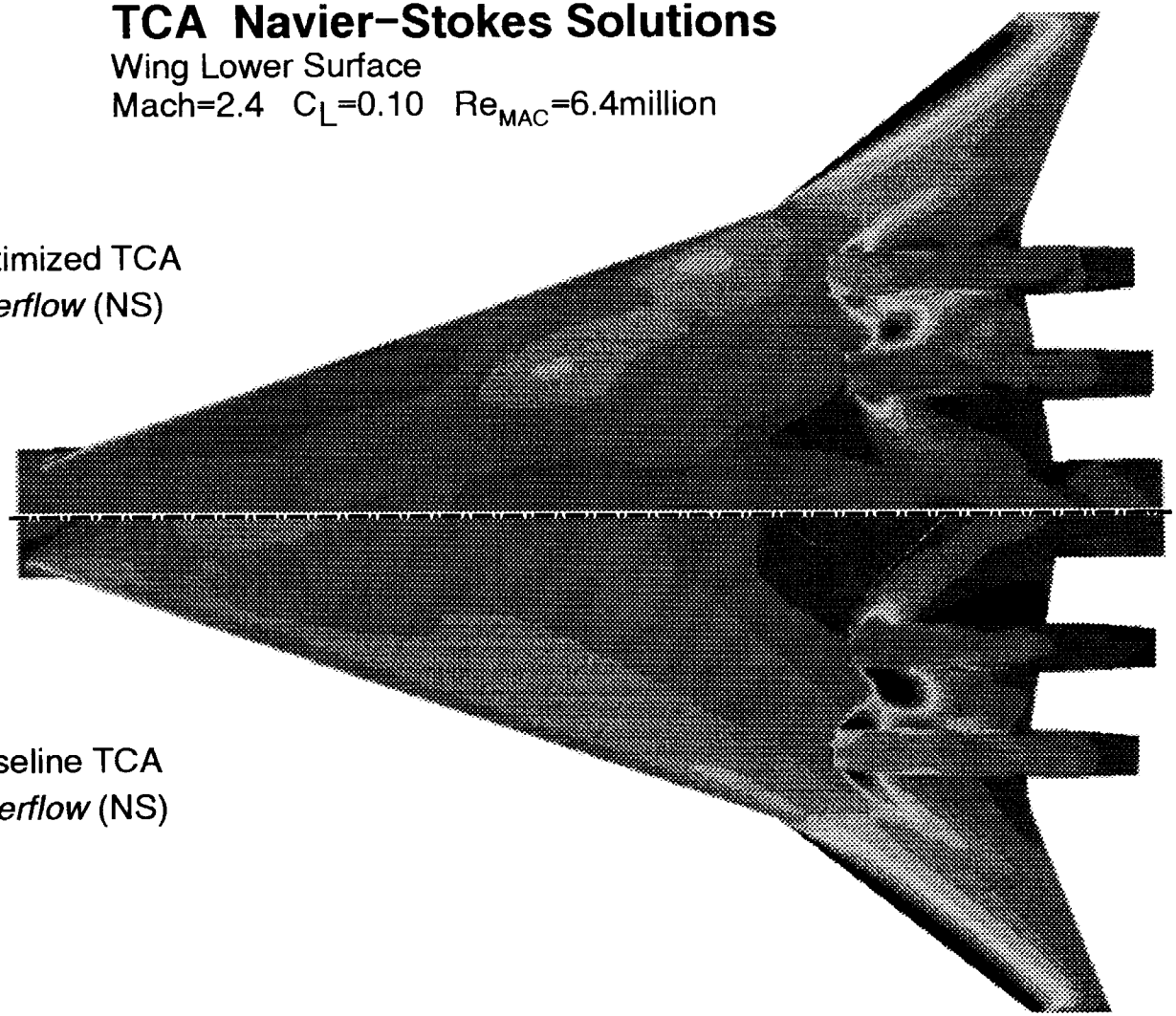

bnsw8bot2.i6

bnstcabot2.i6

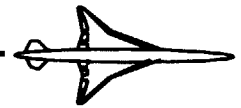

Drag Reduction Mechanisms

The drag reduction realized by the TCA optimization appears to be the result of many different mechanisms. Several are listed here and are followed with examples to illustrate each. Frequently the mechanisms are interelated, sometimes in a complementary fashion and sometimes in conflict. This section is not intended to be definitive but is offered as the point we are at. Taken as a whole, it does tend to explain why the resulting flow is more complex than the baseline condition and also seems to suggest why a simultaneous optimization produces results that will not occur during piecemeal optimization. This list of mechanisms is not complete. There are others suggested by the data but not prepared for this presentation.

Drag Reduction Mechanisms

- Lift Redistribution
- Lift Recovery
- Shock Strength Reduction
- Pressure / Contour Manipulation
- Upflow Enhancement and Exploitation

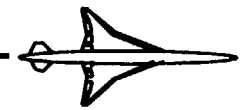

TCA Configuration : Navier–Stokes Solution

Comparison of this upper surface isometric view of the viscous solution of the TCA, with the following slide of the optimized TCA, illustrates the lift redistribution drag reduction mechanism. In particular, they show how the optimization increased the lift on the forebody. This is deduced from the isobar patterns which show a larger vertical differential on the optimized forebody. In supersonic flow, drag can be reduced by spreading the lift longitudinally. That appears to be the case here. Forebody loading also appears to enhance upwash, as will be shown later.

TCA Configuration : Navier–Stokes Solution

Overflow (NS)
TCA Configuration Isometric View
Mach=2.4 C_L=0.10 Re_{MAC}=6.4million

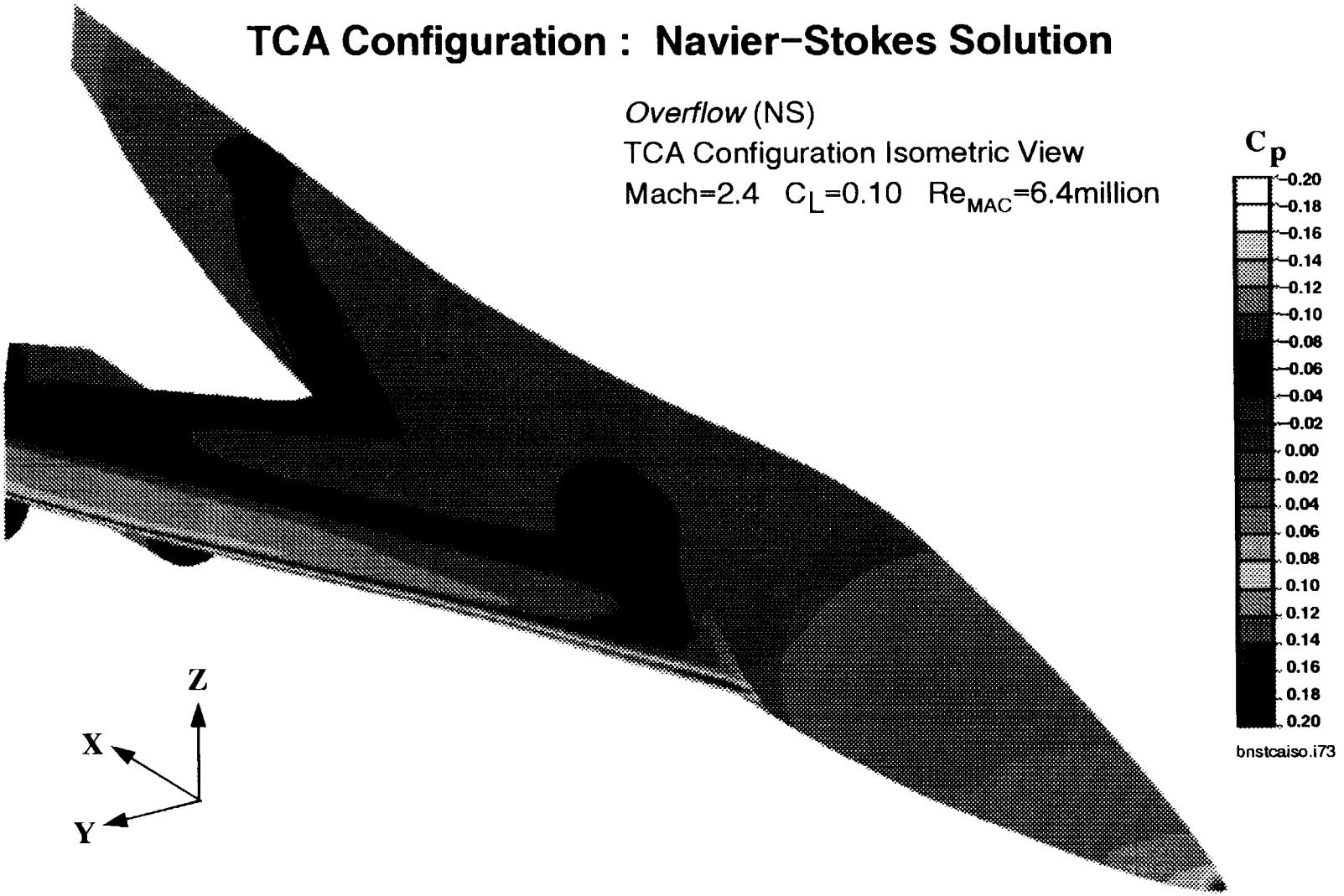

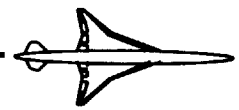

Optimized TCA Configuration : Navier–Stokes Solution

This is the optimized TCA companion to the previous slide and helps illustrate the lift redistribution drag reduction mechanism. The forebody is carrying more lift than is the case for the TCA.

Optimized TCA Configuration : Navier–Stokes Solution

Overflow (NS) Optimized TCA
Isometric View
Mach=2.4 C_L=0.10 Re_{MAC}=6.4million

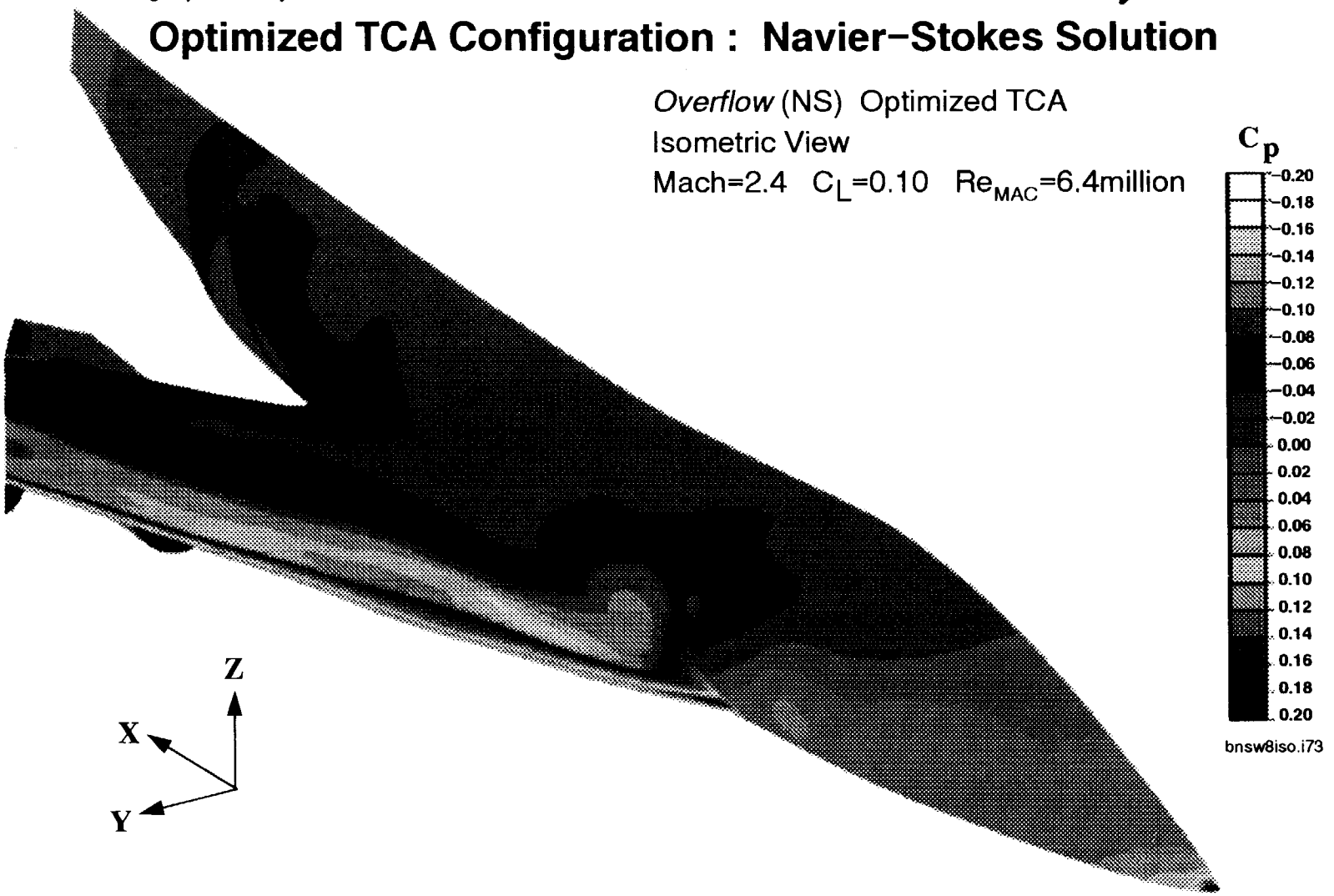

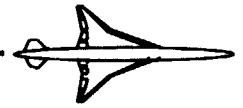

TCA Configuration : Navier–Stokes Solution

Comparison of this lower surface view of the viscous solution of the TCA, with the following slide of the optimized TCA, illustrates the next two drag reduction mechanisms. First, examination of the wing flow on the inboard side of the inboard nacelle shows lift recovery occurring on the optimized configuration. This is indicated by the reduction in velocity and the accompanying increase in local pressure. It should be noted however, that there are many other regions where the velocities are increased on the optimized configuration.

The next drag reduction mechanism, shock strength reduction, can be seen in terms of the nacelle/diverter shocks. Notice that the resulting compressions are weaker on the optimized configuration. This is also an example of conflicting interaction between mechanisms. Reducing the shock strength also reduces lift. Here the optimization is required to trade wave drag for lift.

TCA Configuration : Navier–Stokes Solution

Overflow (NS)
TCA Wing Lower Surface
Mach=2.4 C_L=0.10 Re_{MAC}=6.4million

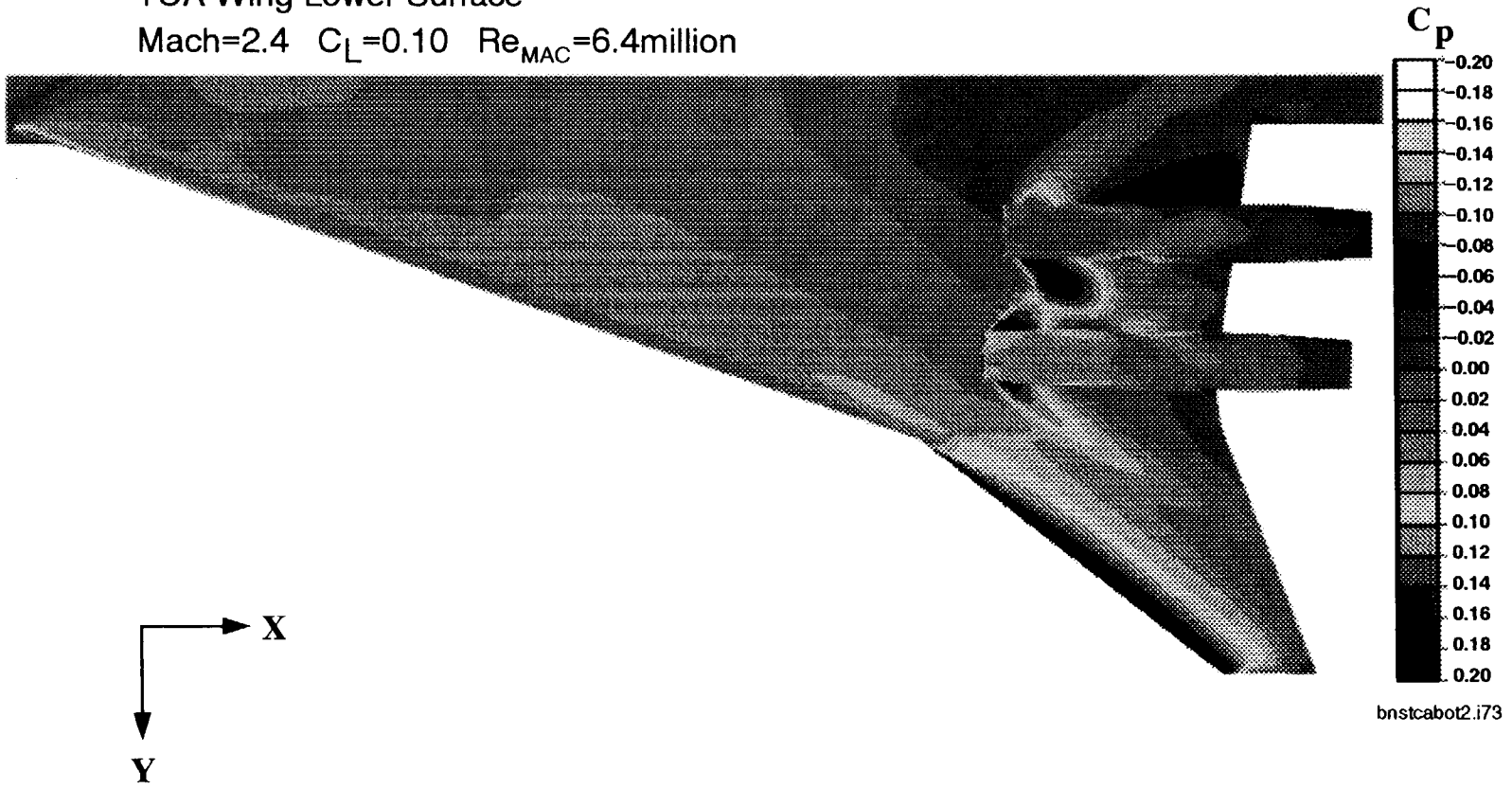

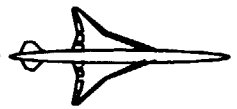

Optimized TCA Configuration : Navier–Stokes Solution

This is the optimized TCA companion to the previous slide and helps illustrate both the lift recovery and shock strength reduction drag reduction mechanisms. Some lower surface supervelocities and the nacelle/diverter shock strength are reduced compared to the TCA.

Optimized TCA Configuration : Navier–Stokes Solution

Overflow (NS) Optimized TCA
Wing Lower Surface
Mach=2.4 C_L=0.10 Re_{MAC}=6.4million

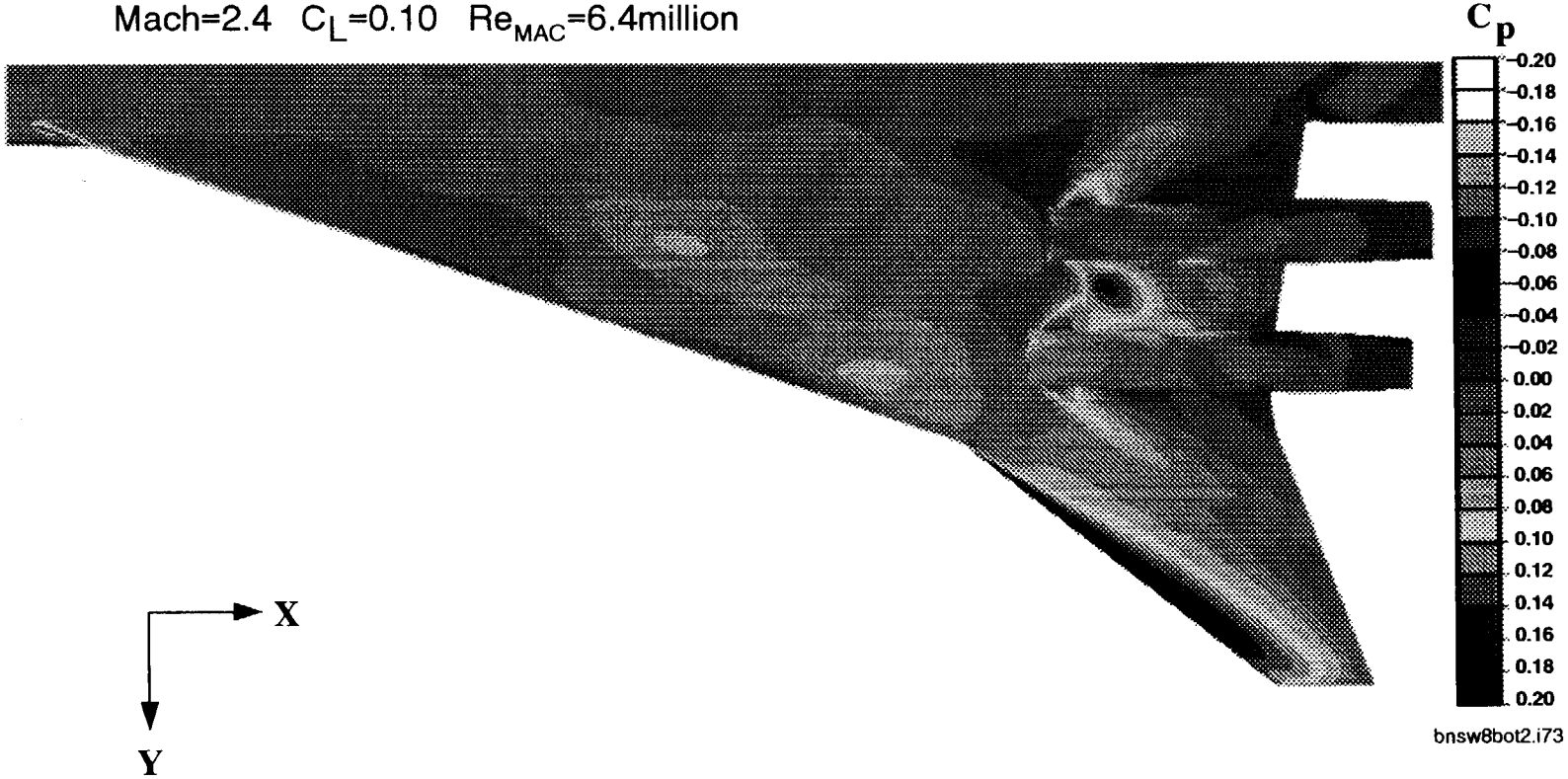

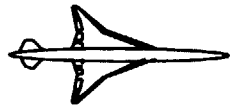

TCA Configuration : Navier–Stokes Solution

Comparison of this upper surface view of the viscous solution of the TCA, with the following slide of the optimized TCA, also illustrates the shock strength reduction drag reduction mechanism. It also illustrates that the optimization may chose to increase shock strength. Examination of the two images show many places where the isobars in the recompression of the optimized solution are either closer or further apart than for the TCA.

TCA Configuration : Navier–Stokes Solution

Overflow (NS)
TCA Wing Upper Surface
Mach=2.4 C_L=0.10 Re_{MAC}=6.4million

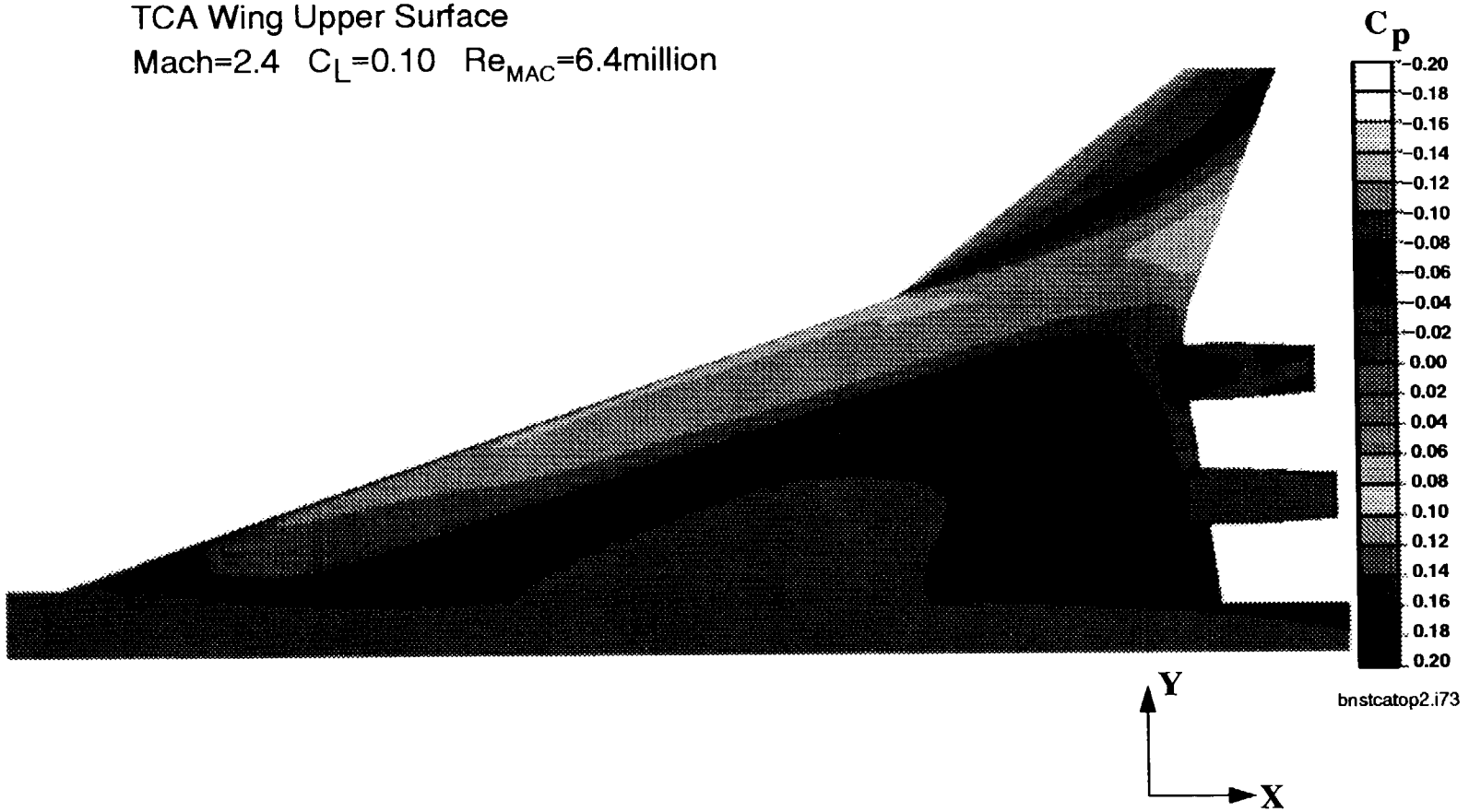

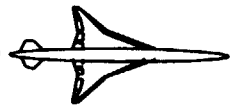

Optimized TCA Configuration : Navier–Stokes Solution

This is the optimized TCA companion to the previous slide and helps illustrate the shock strength reduction drag reduction mechanism. Some recompressions are reduced compared to the TCA.

Optimized TCA Configuration : Navier–Stokes Solution

Overflow (NS) Optimized TCA
Wing Upper Surface
Mach=2.4 C_L=0.10 Re_{MAC}=6.4million

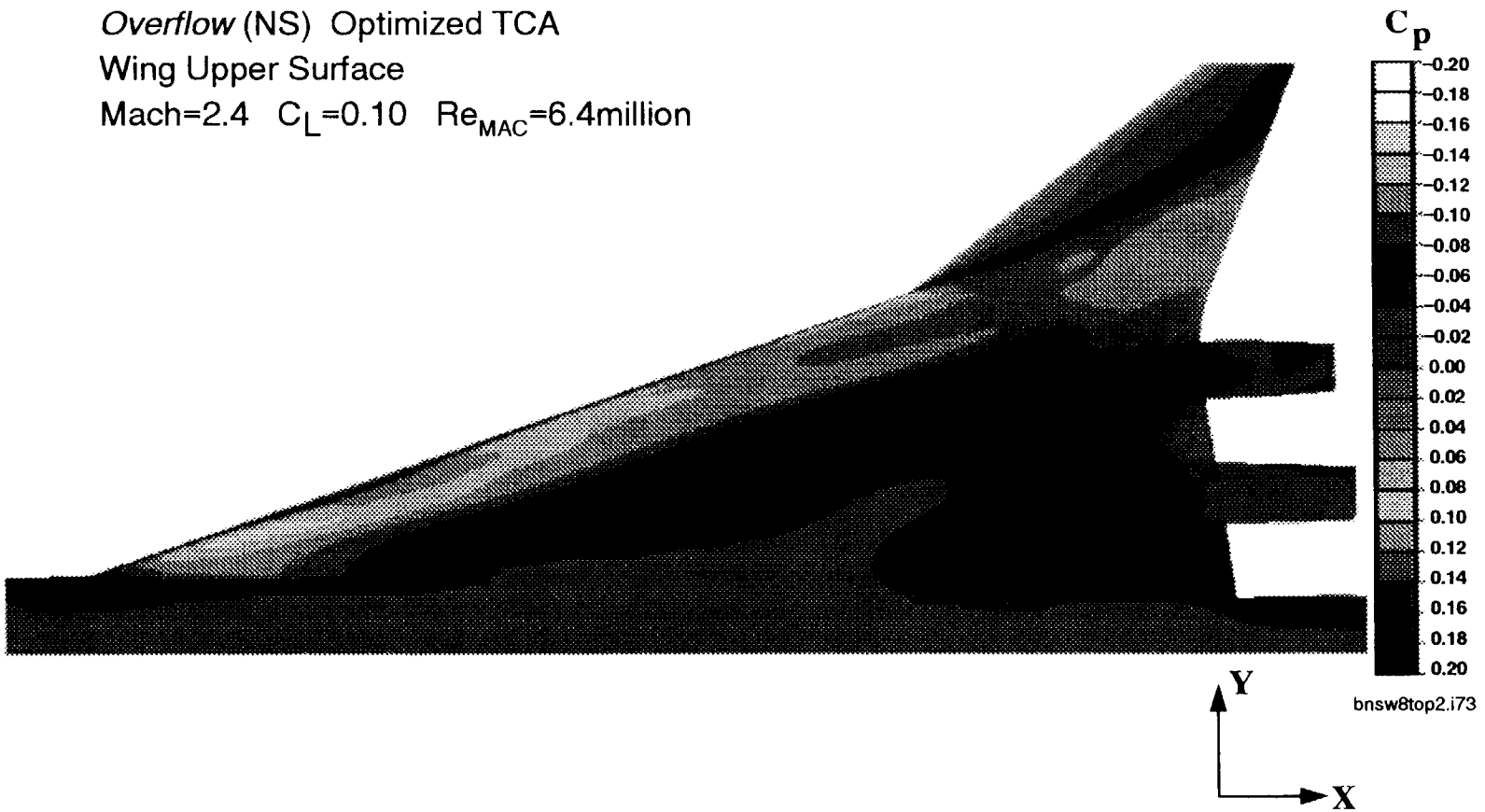

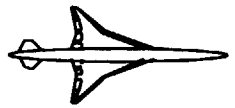

TCA Configuration : Navier–Stokes Solution

Comparison of this front view at angle of attack of the viscous solution of the TCA, with the following slide of the optimized TCA, illustrates the pressure/contour manipulation drag reduction mechanism. The basic mechanism is to arrange for lower pressures to act on forward facing surfaces and for higher pressures to act on aft facing surfaces. A related concept is to arrange for a surface to face normal to the freestream so as to eliminate its effect on pressure drag.

Pressure/contour manipulation can be seen on both the upper and lower surfaces of the wing and on the side of the body in these images. On the wing upper surface, particularly on the bumps and at the leading edge planform break, low pressure is apparent on more exposed area on the optimized TCA than for the TCA. On the wing lower surface, the optimized TCA has reduced the forward exposure of the nacelle/diverter shocks.

The lower pressure on a forward facing surface of the optimized TCA can also be seen on the side of the body.

TCA Configuration : Navier–Stokes Solution

Overflow (NS)
TCA shown at 3 deg angle of attack
Mach=2.4 C_L=0.10 Re_{MAC}=6.4million

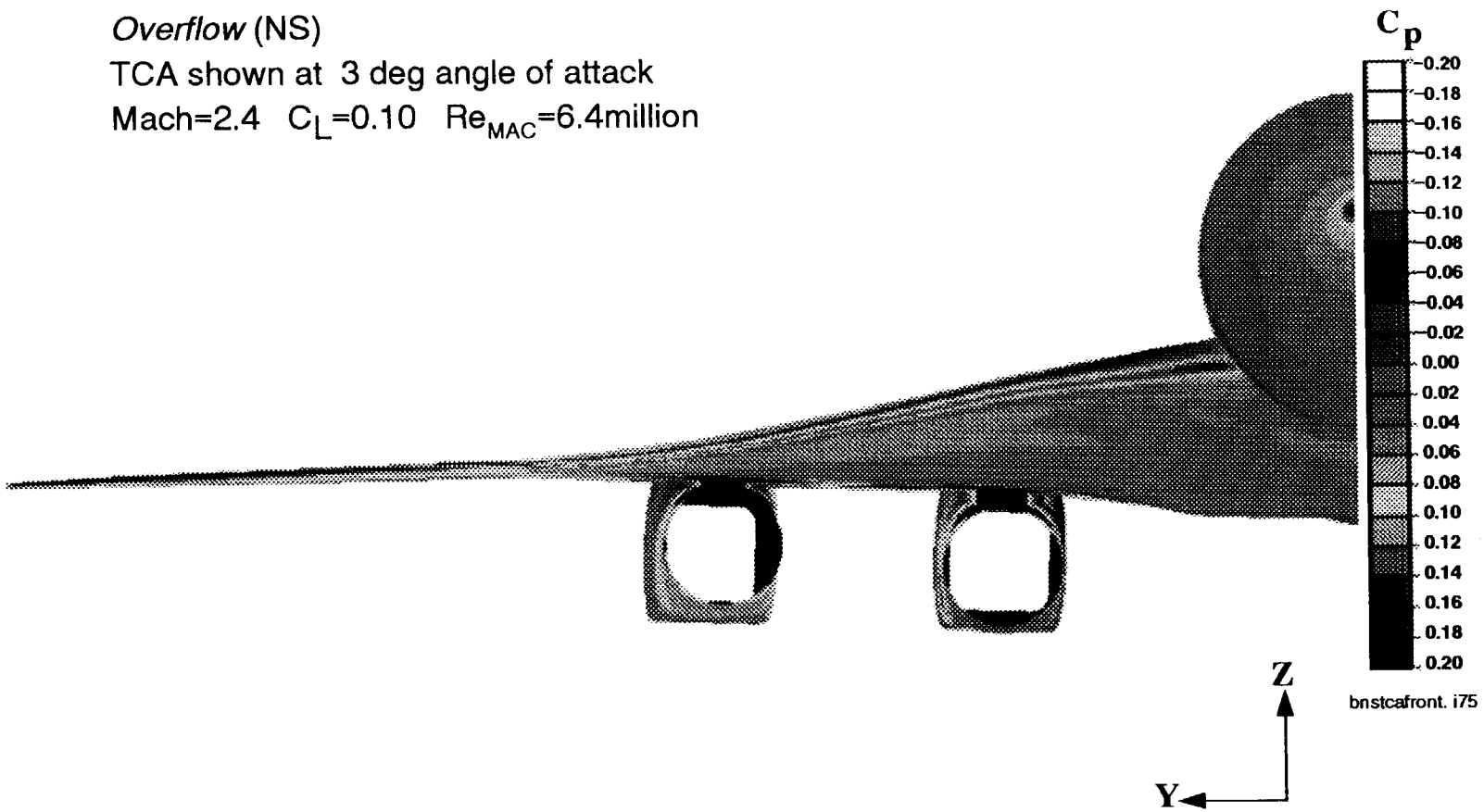

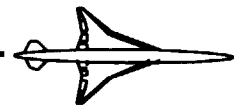

Optimized TCA Configuration : Navier–Stokes Solution

This is the optimized TCA companion to the previous slide and helps illustrate the pressure/contour manipulation drag reduction mechanism. The effect is apparent on both surfaces of the wing and the body.

Optimized TCA Configuration : Navier–Stokes Solution

Overflow (NS) Optimized TCA
shown at 4 deg angle of attack
Mach=2.4 C_L=0.10 Re_{MAC}=6.4million

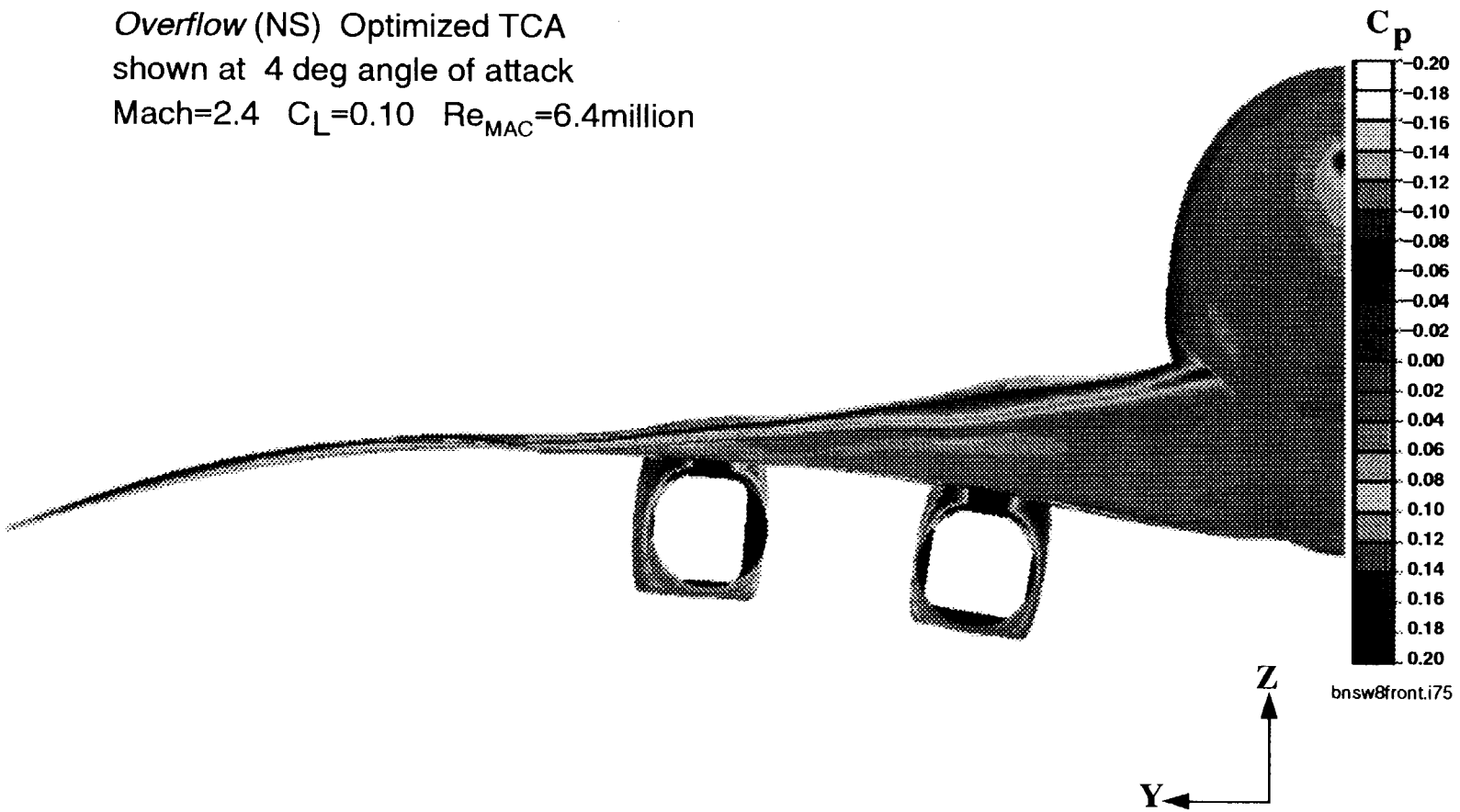

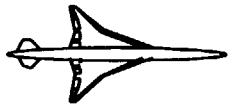

Effect of Optimization on Eta=0.215

This and the following five slides illustrate the pressure/contour manipulation effect at specific spanwise locations. They also show the effect of optimization on the airfoil shapes and the pressure distributions.

The airfoils are shown in a nondimensional transformed coordinate system, the vertical dimension of which is designated as Z'/C. The transformation rotates the airfoil to its correct angle of attack for the condition and, in the case shown here, places all the trailing edges to the same location. This helps illustrates differences in local angle of attack but, eliminates differences in shear between the two configurations. Strictly speaking, the airfoils should be plotted verses the corresponding longitudinal dimension, X'/C, however, for the angles shown here, the difference is indistinguishable on the plot.

The suction loops plotted in the lower right hand corner are just the pressure coefficient verses the transformed height, Z'/C. In this way, the area within the curve is the local drag, just as the area in the standard pressure distribution is the local lift. When the suction loop curve crosses over itself, as is the case for the optimized TCA, a thrust loop is formed.

This airfoil comparison shows the cambering and thickening due to optimization that lead to the upper surface wing bumps. The pressure distributions illustrate lift recovery and shock strength reduction. The suction loops illustrate pressure/contour manipulation.

Effect of Optimization on Eta=0.215

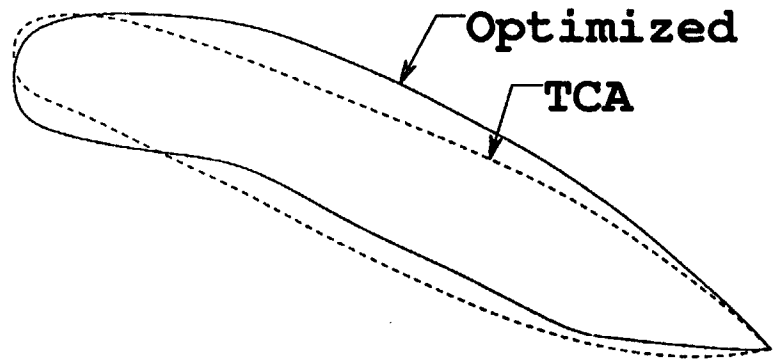

Inviscid TRANAIR W/B/N/D

Optimized TCA vs TCA

Mach=2.4 C_L=0.086

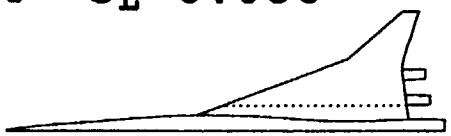

Airfoils at
Angle of Attack
(Common Trailing Edge)

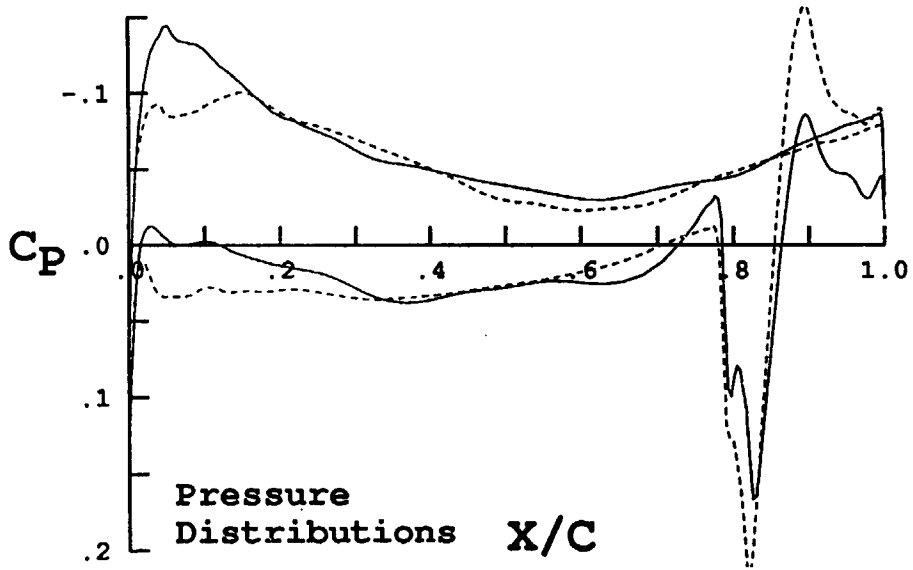

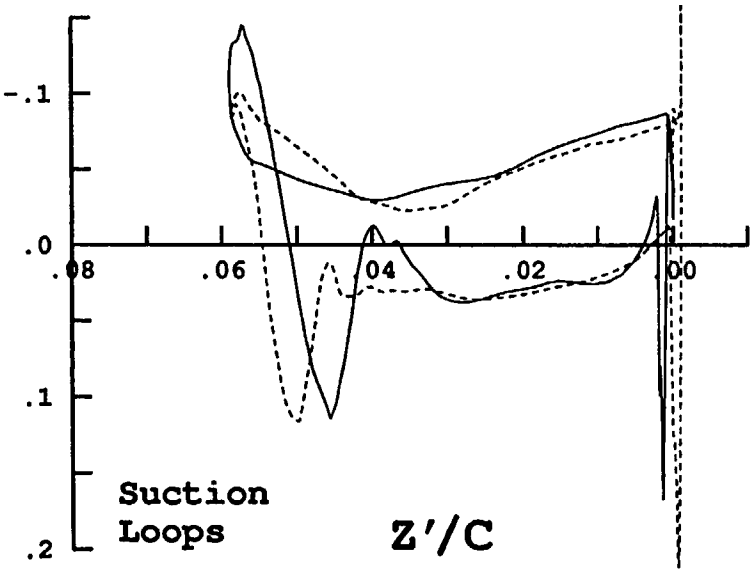

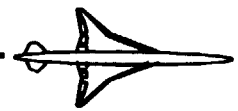

Effect of Optimization on Eta=0.424

This comparison illustrates the drag reduction value of trading camber for angle of attack. It also show that the TCA has small thrust loops and that peaky pressure distributions are not necessary in order to form thrust loops. Another effect apparent in the suction loops is how the optimization reduced the local pressure drag due to the nacelle/diverter shocks by aligning the airfoil local surface with the freestream vector.

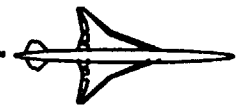

Effect of Optimization on Eta=0.424

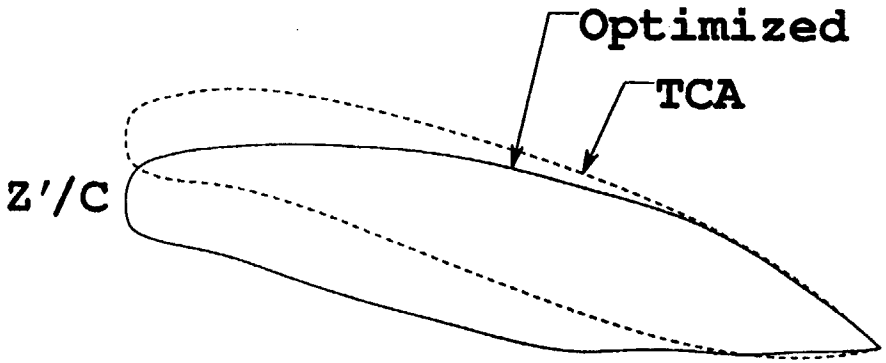

Inviscid TRANAIR W/B/N/D

Optimized TCA vs TCA

Mach=2.4 C_L=0.086

Airfoils at
Angle of Attack
(Common Trailing Edge)

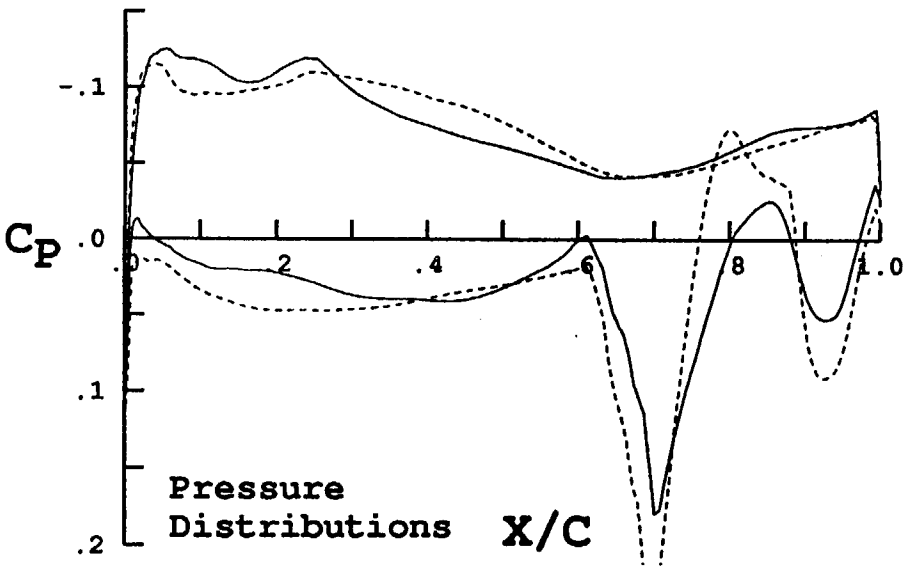

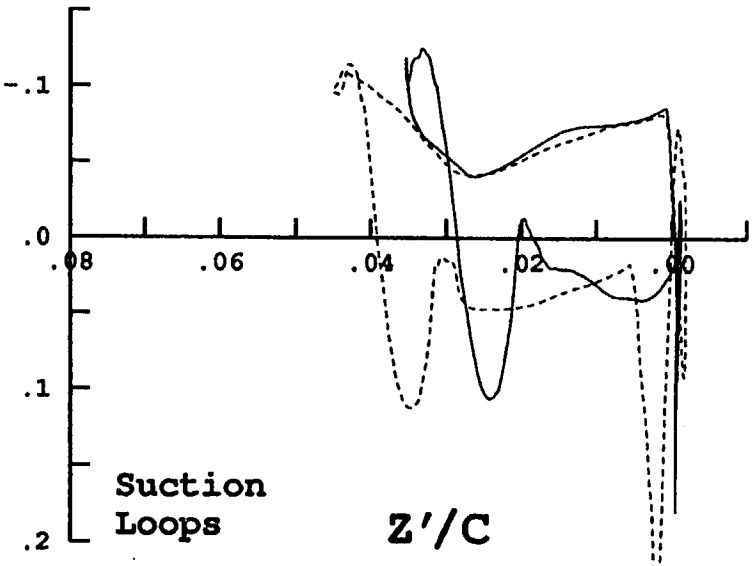

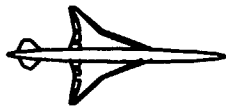

Effect of Optimization on Eta=0.609

This location, just inboard of the leading edge planform break, illustrates the dramatic local drag reduction due to optimization. The angle of attack of the optimized TCA airfoil indicates that the local upflow or upwash is significantly greater that of the TCA.

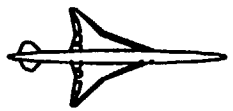

Effect of Optimization on Eta=0.609

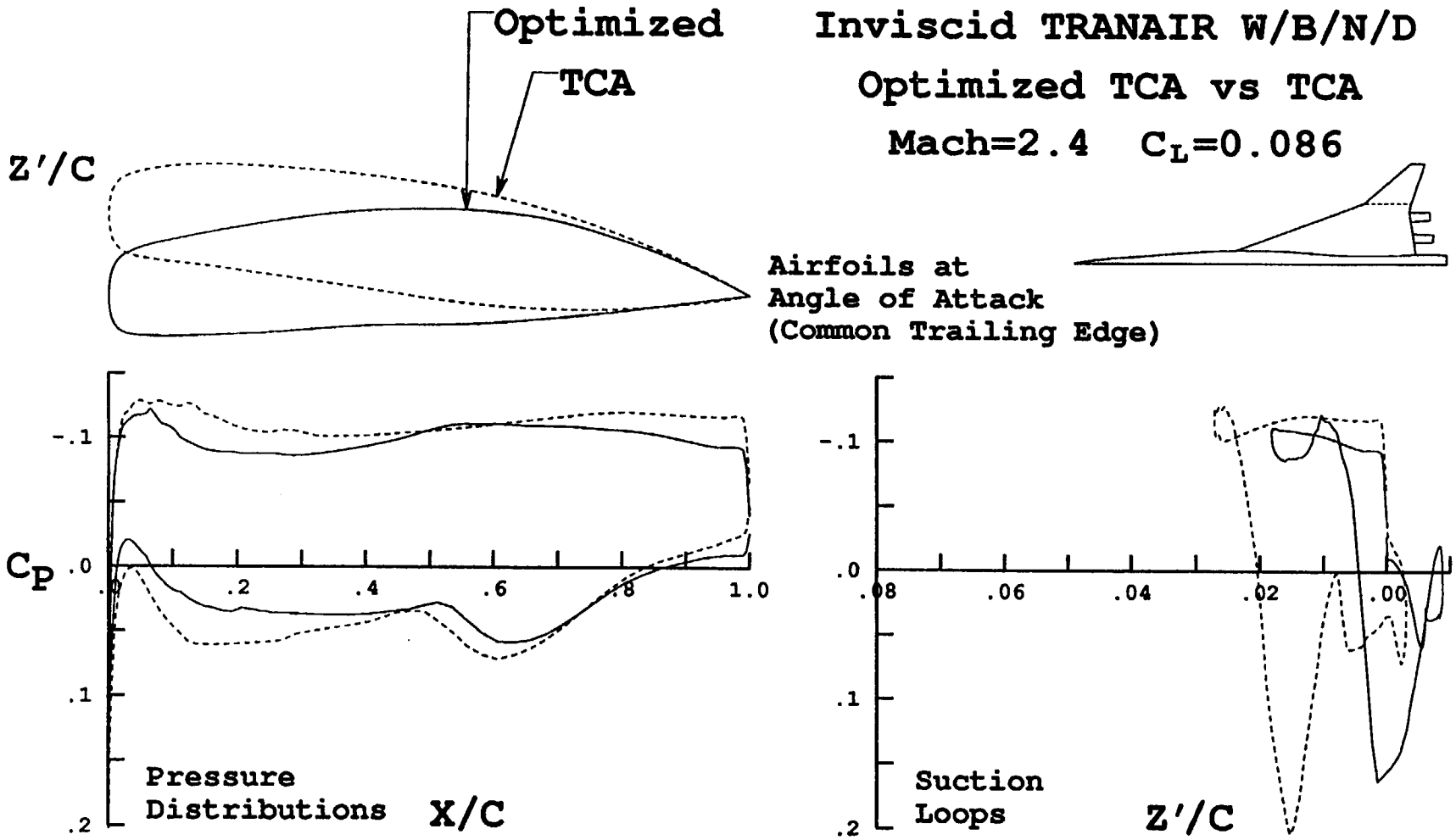

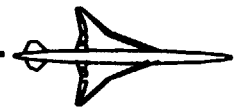

Effect of Optimization on Eta=0.618

This location, just outboard of the leading edge planform break, illustrates the additional dramatic local drag reduction due to optimization on the outboard wing. There is a region of upwash carryover on the supersonic leading edge portion of the wing. This is the location shown in the spanwise properties that is approaching zero inviscid local drag.

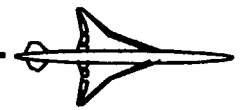

Effect of Optimization on Eta=0.618

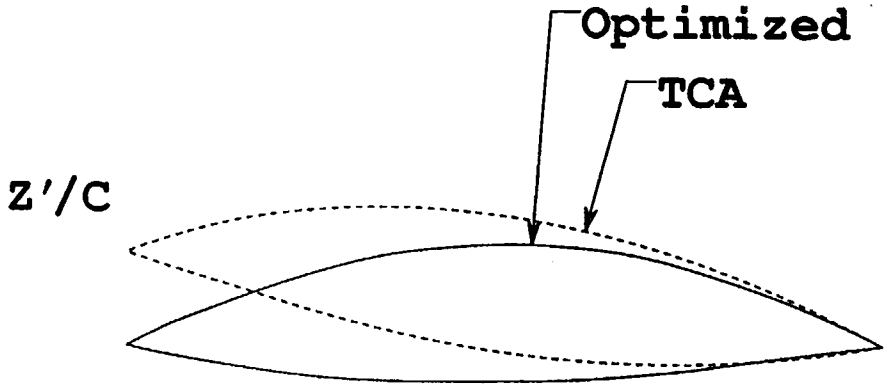

Inviscid TRANAIR W/B/N/D
Optimized TCA vs TCA
Mach=2.4 C_L=0.086

Airfoils at
Angle of Attack
(Common Trailing Edge)

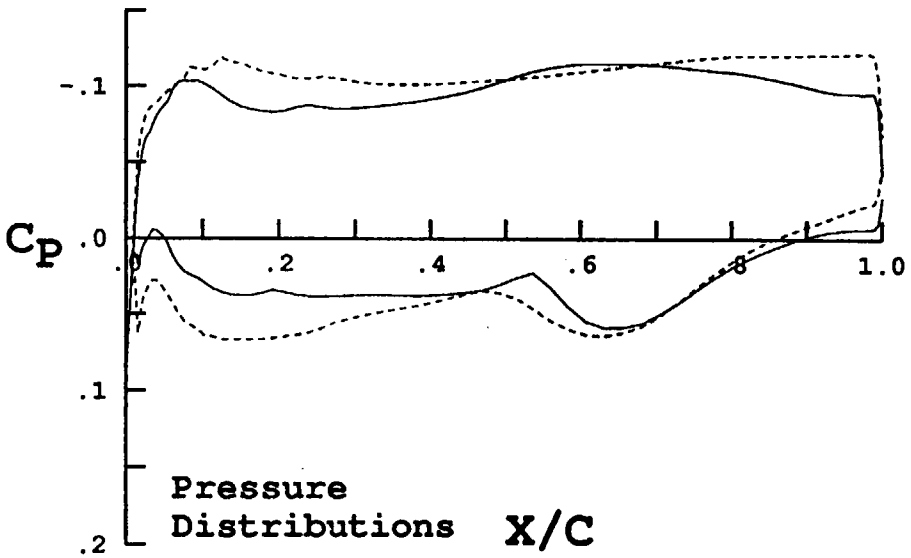

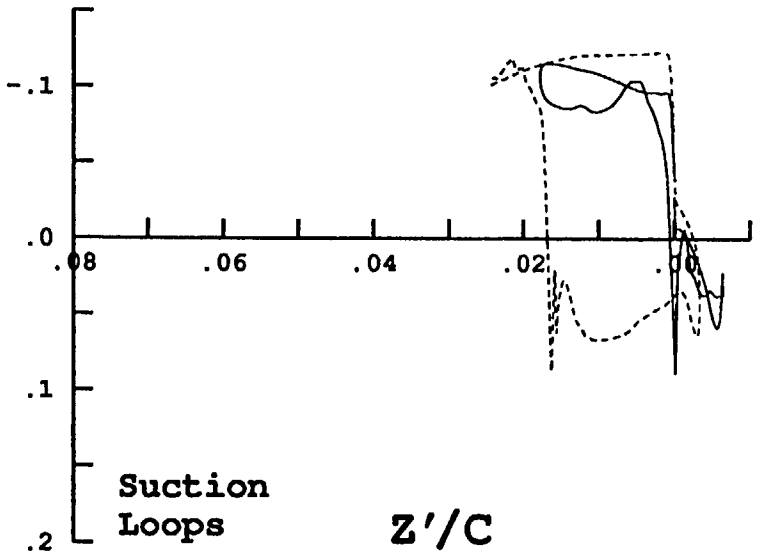

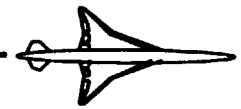

Effect of Optimization on Eta=0.771

This location illustrates that the optimization left this portion of the wing relatively unchanged.

Effect of Optimization on Eta=0.771

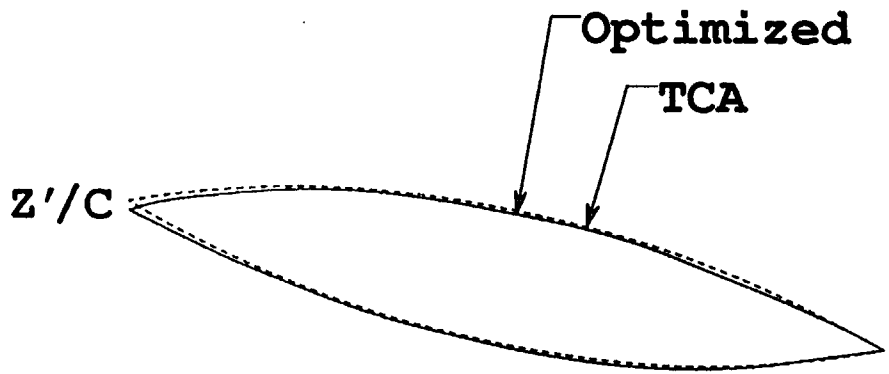

Inviscid TRANAIR W/B/N/D

Optimized TCA vs TCA

Mach=2.4 C_L=0.086

Airfoils at
Angle of Attack
(Common Trailing Edge)

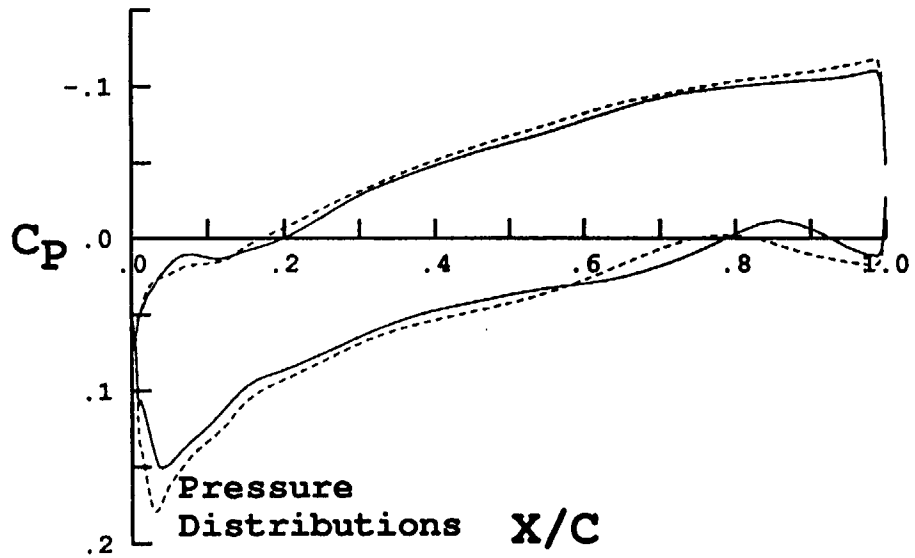

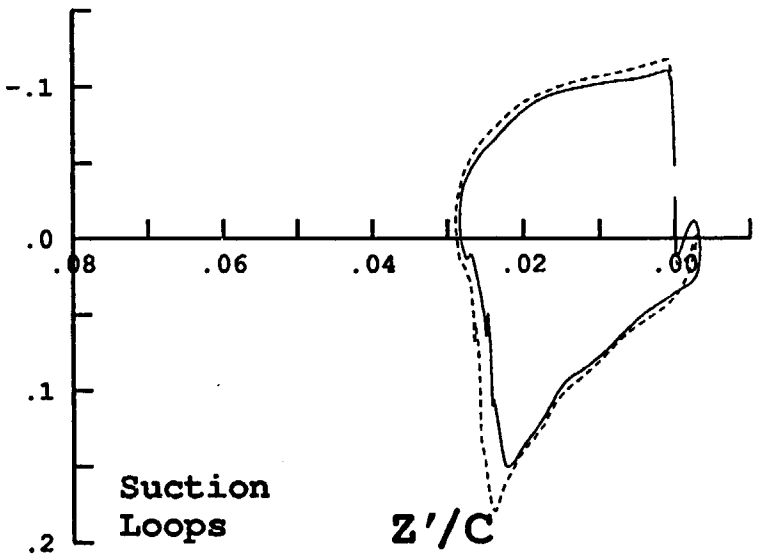

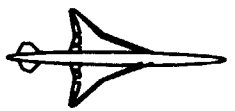

Effect of Optimization on Eta=0.961

This location illustrates the kind of change effected toward the tip of the wing. It may be an example of longitudinal lift redistribution.

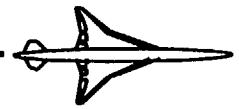

Effect of Optimization on Eta=0.961

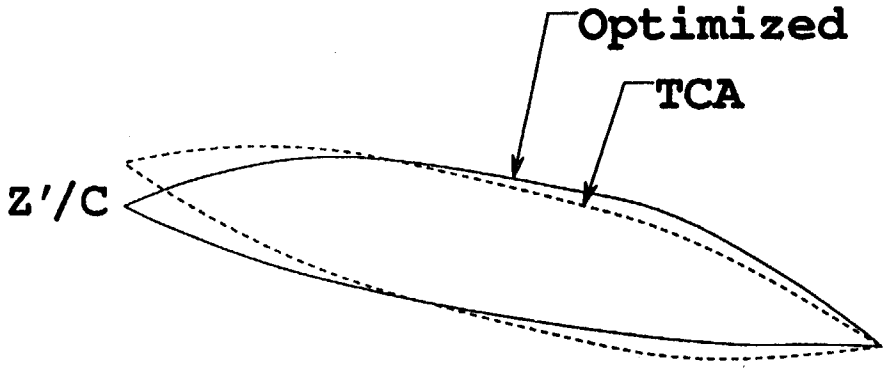

Inviscid TRANAIR W/B/N/D

Optimized TCA vs TCA

Mach=2.4 C_L=0.086

Airfoils at
Angle of Attack
(Common Trailing Edge)

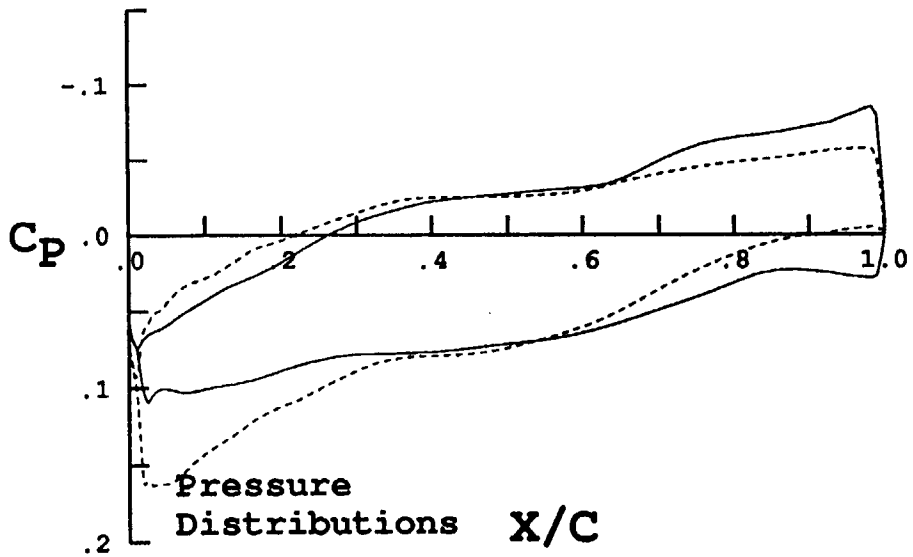

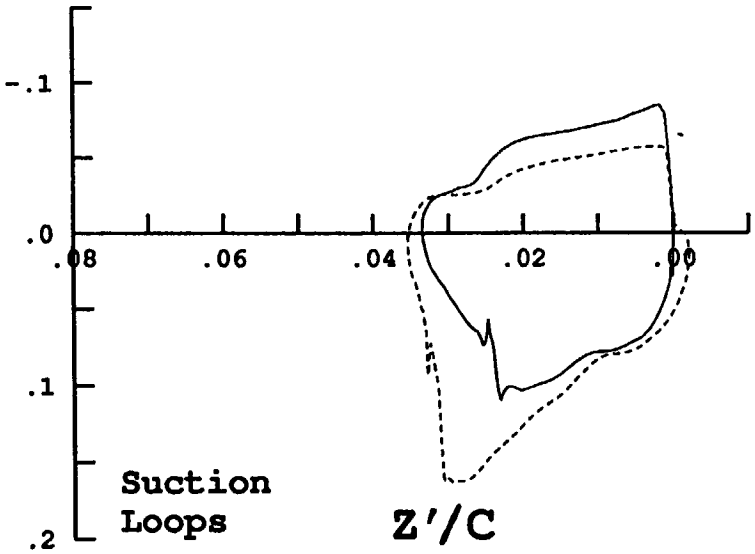

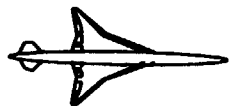

Upwash Plane Layout : Optimized TCA

The final section presents images of the upwash fields of the TCA and the optimized TCA. The images are a series of swept vertical planes. This slide shows four views of the optimized TCA configuration, with the two bounding upwash planes. These planes stretch from the side of body to the planform break, from below the nacelle keel line to above the wing surface. For clarity, the planes in this image are shown with a sparse grid, rather than the actual grid.

Upwash Plane Layout : Optimized TCA

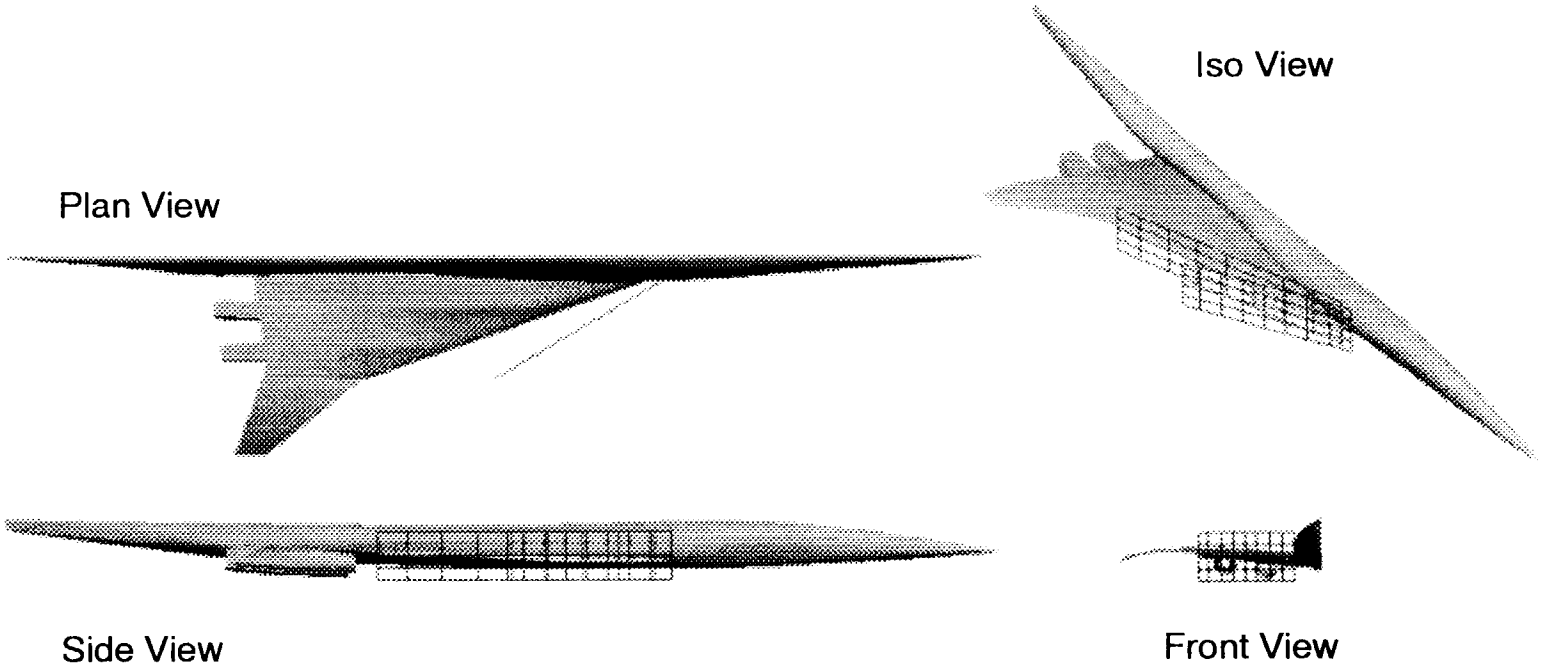

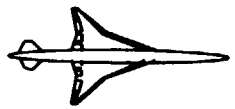

Upwash Plane Layout : Closeup of Plane Family

This image shows a closeup of the planview of the optimized TCA configuration, with the seven upwash planes. These planes stretch from the side of body to the planform break. The forward plane is ahead of the wing flow disturbances and is referred to as the forebody plane. The plane closest to the wing is parallel to the leading edge and is 10 inches, full scale, upstream of the leading edge. It is referred to as the leading edge plane.

Upwash Plane Layout : Closeup of Plane Family

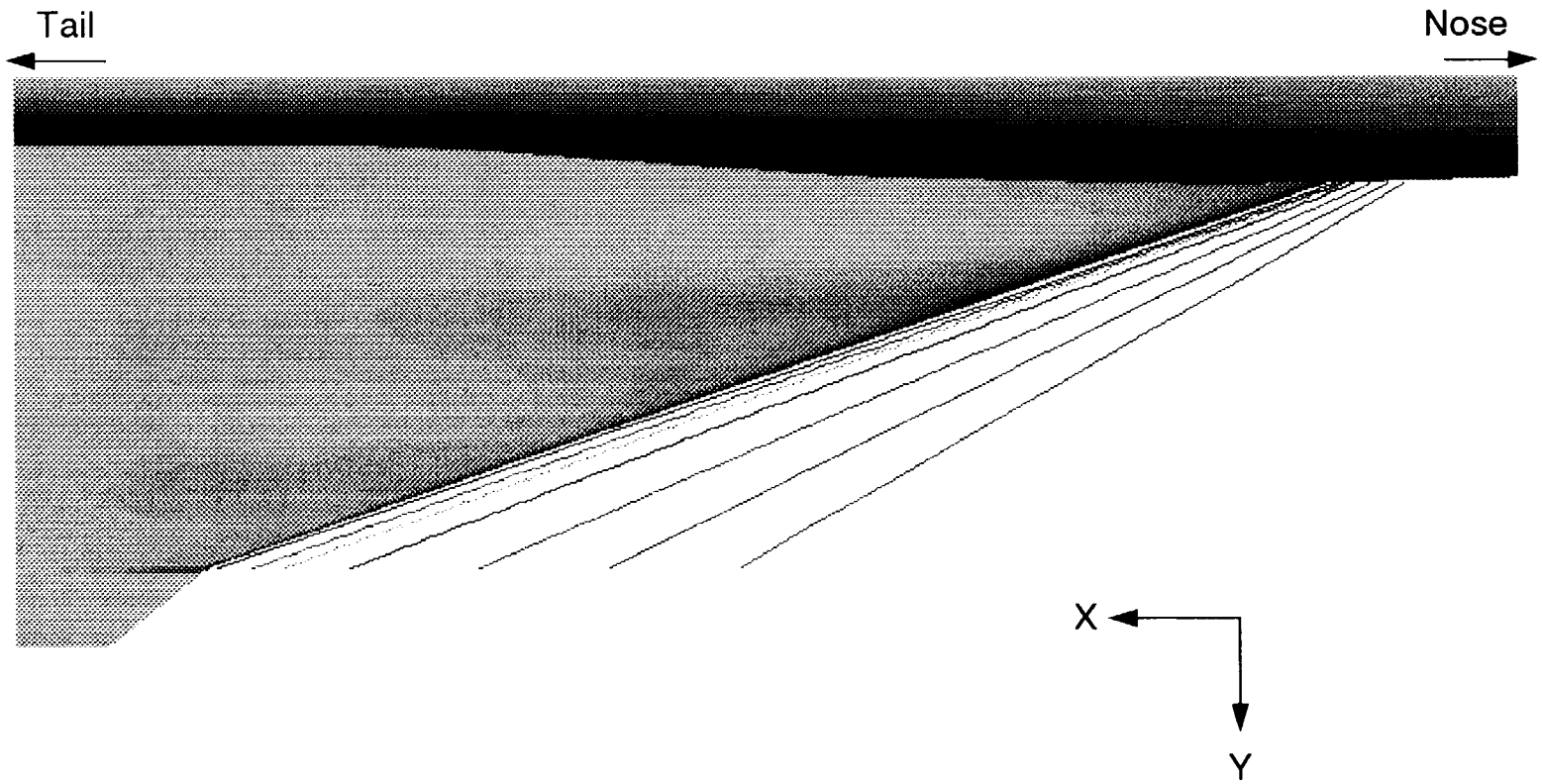

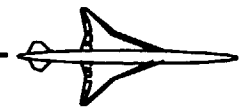

Upwash Plane Layout : Optimized TCA – Front View

This image is the front view of the optimized TCA configuration, with the upwash plane. The density of the interrogation plane grid is shown. Again, these planes stretch from the side of body to the planform break, from below the nacelle keel line to above the wing surface. All the plane images which follow are in this view. In this view, all the planes have the same height and width. This is the front view in the reference coordinate system. The cruise condition, from which the following images were made, is four degrees relative to this view. The upwash or upflow shown in the images is defined relative to the freestream vector. So, zero upwash corresponds to the freestream direction.

Upwash Plane Layout : Optimized TCA : Front View

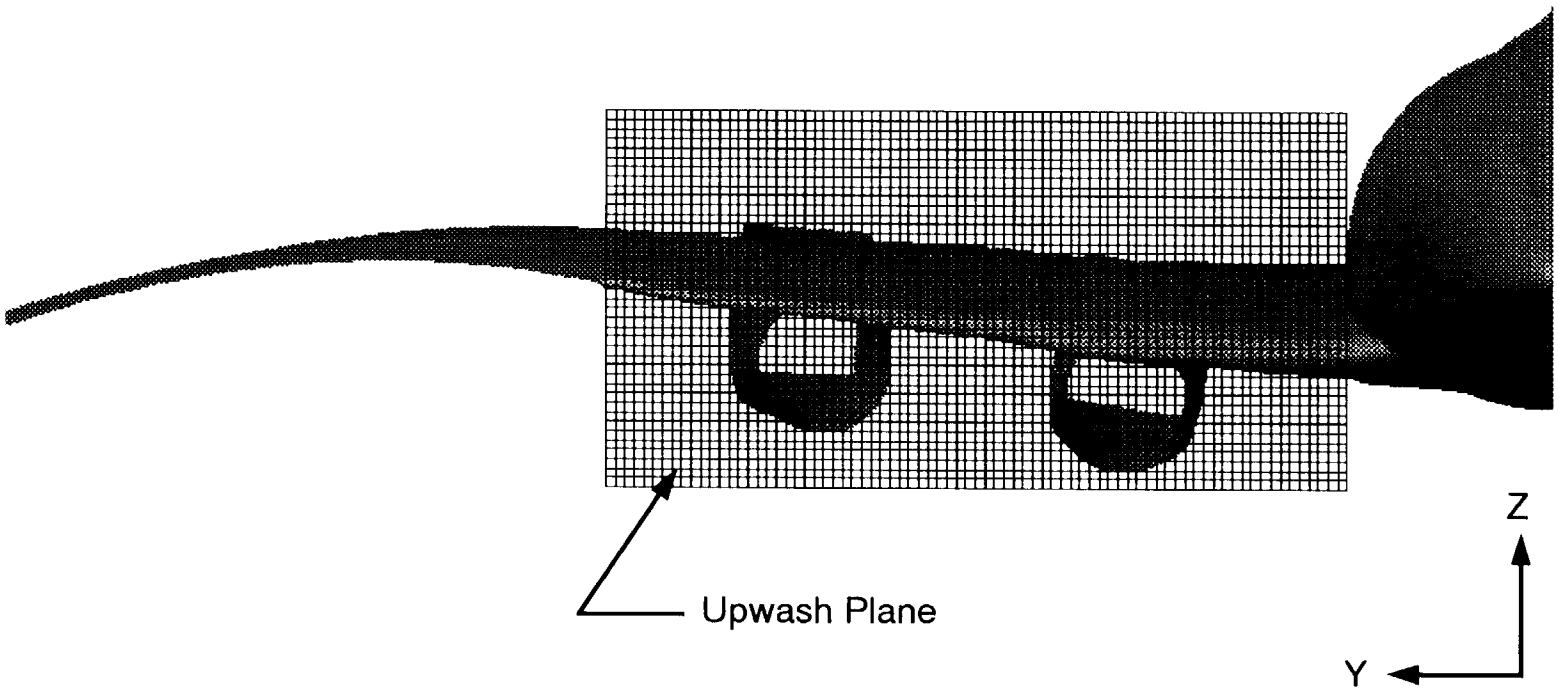

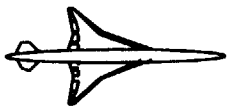

TCA Forebody Upwash Plane

This image shows the TCA forebody upwash plane. Note in this and all the following images that zero is denoted by the lower edge of the black isocontour.

TCA Forebody Upwash Plane

Inviscid TRANAIR Solution
Mach=2.4 CL=0.086

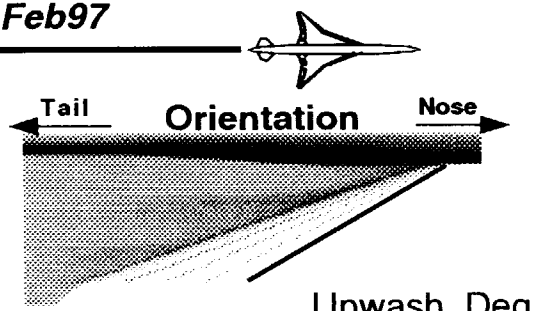

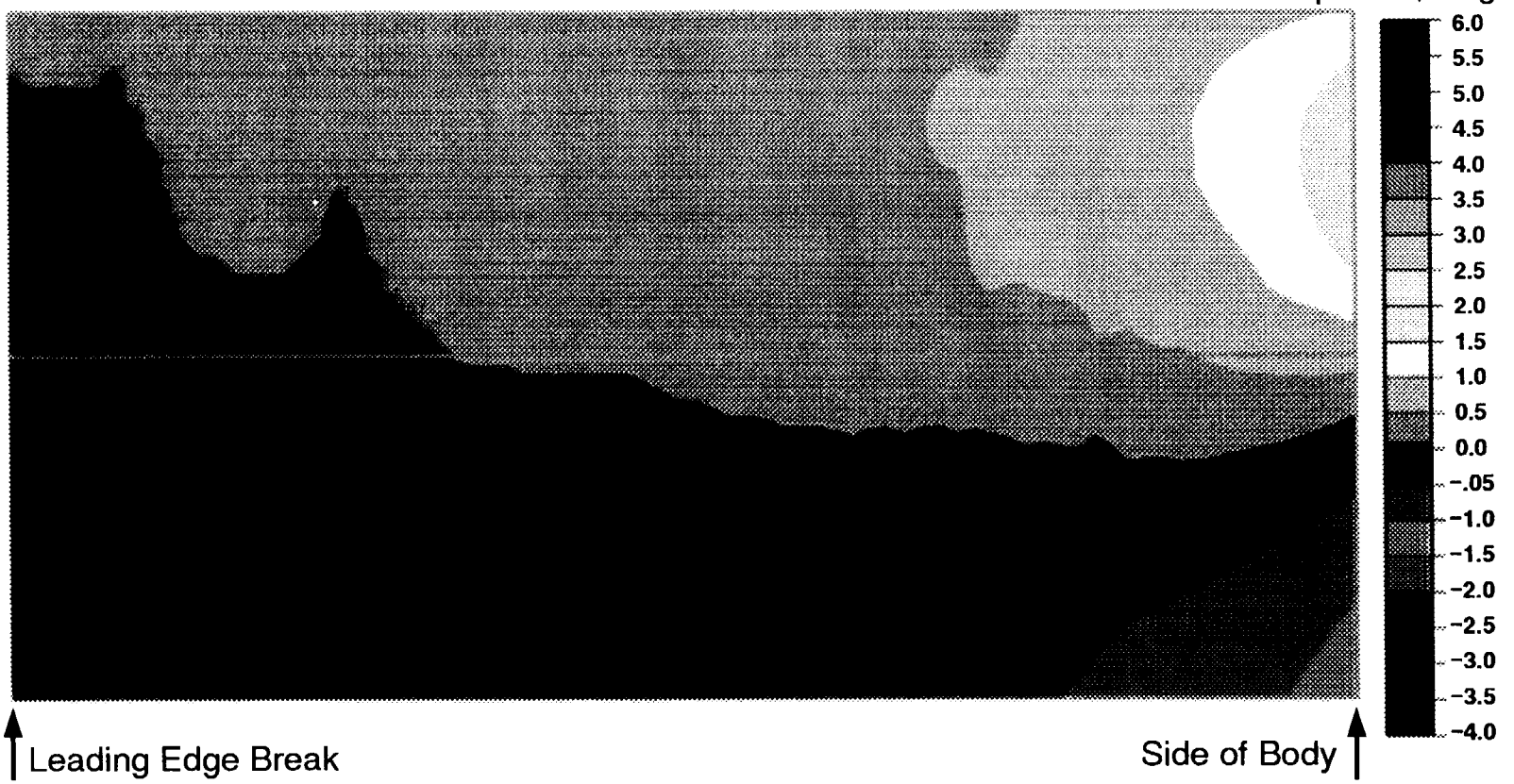

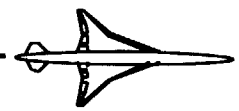

Optimized TCA Leading Edge Upwash Plane

This image shows the optimized TCA leading edge upwash plane. The field is clearly stronger that that of the TCA. It also appears to be the cumulative result of several different lobes. This can be seen more clearly by considering the progression through the set of planes, from forebody plane to leading edge plane, shown in the remainder of this presentation.

Optimized TCA Forebody Upwash Plane

Inviscid TRANAIR Solution
Mach=2.4 CL=0.086

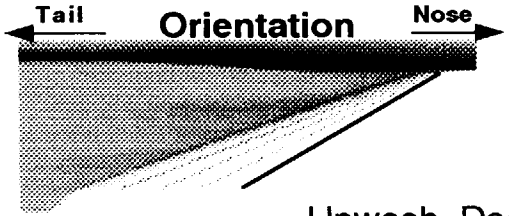

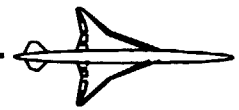

TCA Leading Edge Upwash Plane

This image shows the TCA leading edge upwash plane.

TCA Leading Edge Upwash Plane

Inviscid TRANAIR Solution
Mach=2.4 CL=0.086

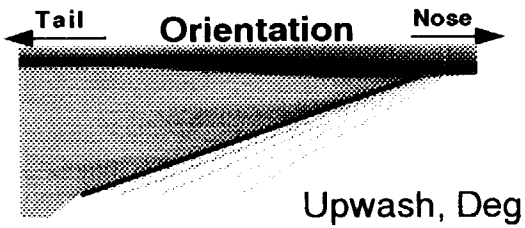

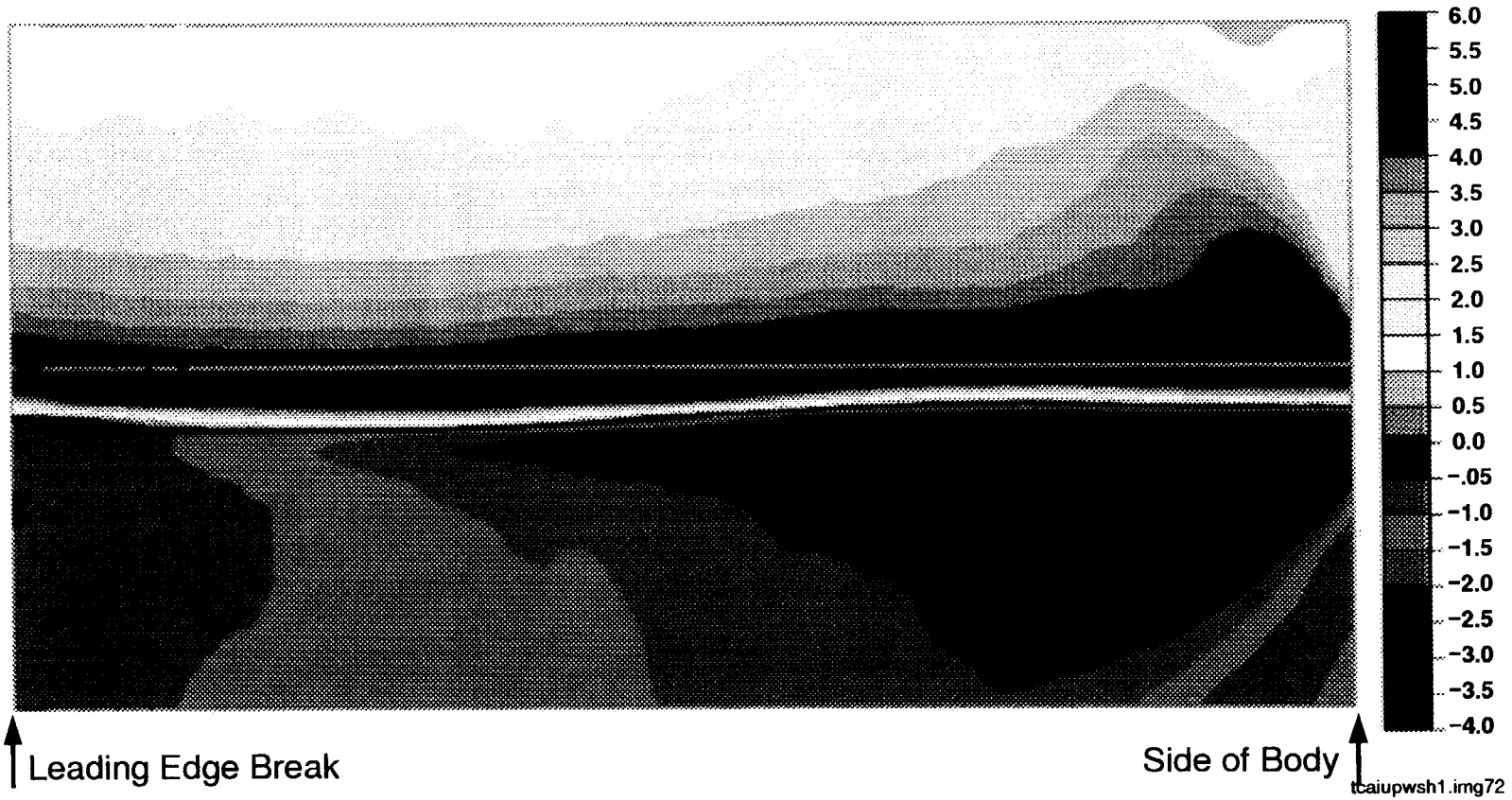

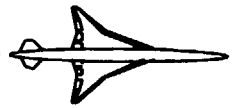

Optimized TCA Leading Edge Upwash Plane

Return to the optimized TCA leading edge upwash plane image. The four lobes are now all clearly defined. Again, there is increased intensity relative to the TCA and the tendency is for the field to rise with span. The fourth and final lobe appears to be due to the outboard portion of the inboard wing.

Optimized TCA Leading Edge Upwash Plane

Inviscid TRANAIR Solution
Mach=2.4 CL=0.086

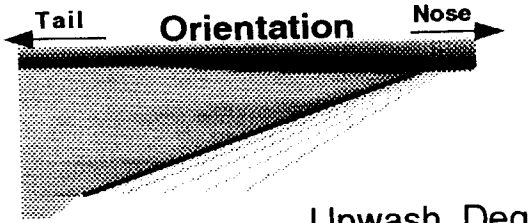

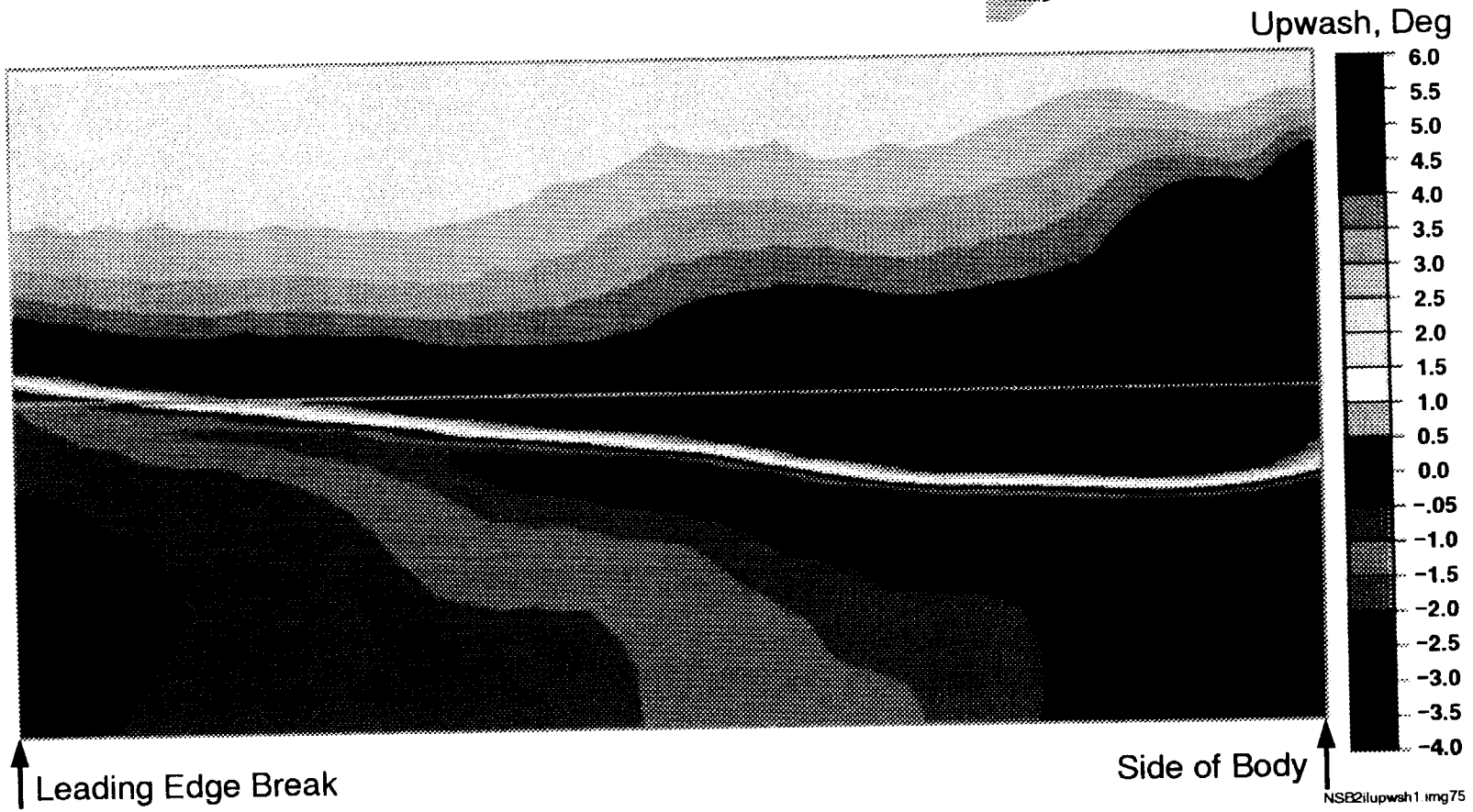

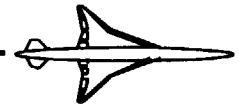

Optimized TCA Intermediate Upwash Plane 2

This image shows the optimized TCA intermediate upwash plane 2. Here, one can see the beginning appearance of another lobe in the field.

Optimized TCA Intermed. Upwash Plane 2

Inviscid TRANAIR Solution
Mach=2.4 CL=0.086

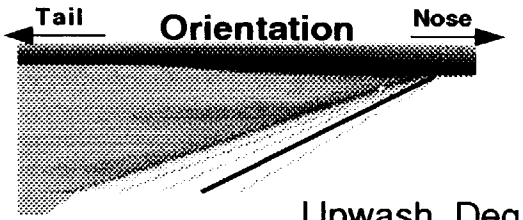

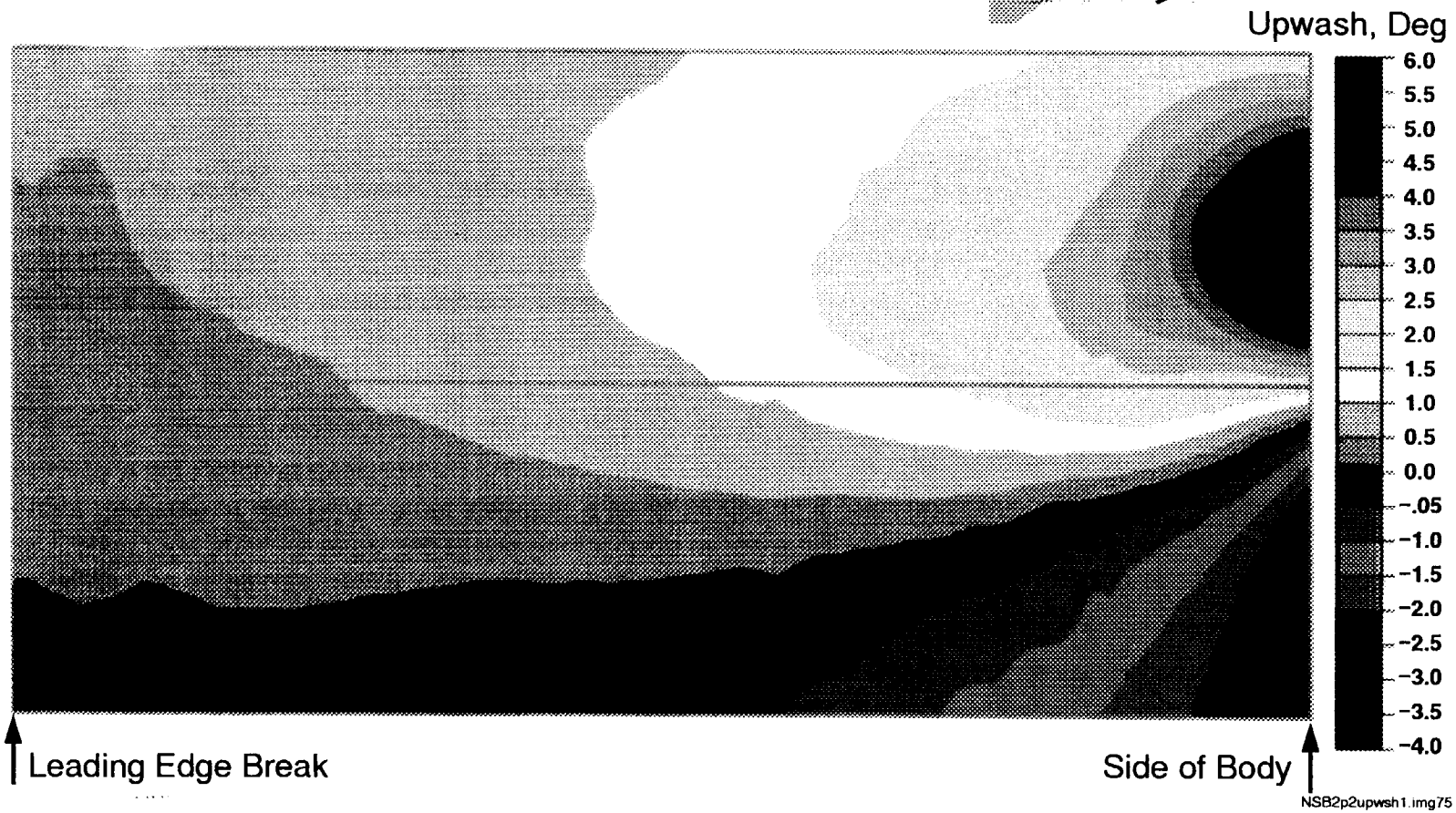

Optimized TCA Intermediate Upwash Plane 3

This image shows the optimized TCA intermediate upwash plane 3. The second lobe is now clearly defined. This second lobe appears to be due to the intersection of the wing leading edge and the body. It is clearly stronger than that of the TCA. Note also that it tends to rise as it goes outboard. This appears to be why the optimized wing takes on dyhedral.

Optimized TCA Intermed. Upwash Plane 3

Inviscid TRANAIR Solution
Mach=2.4 CL=0.086

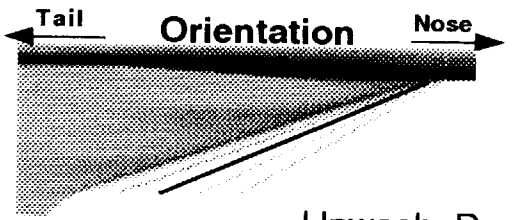

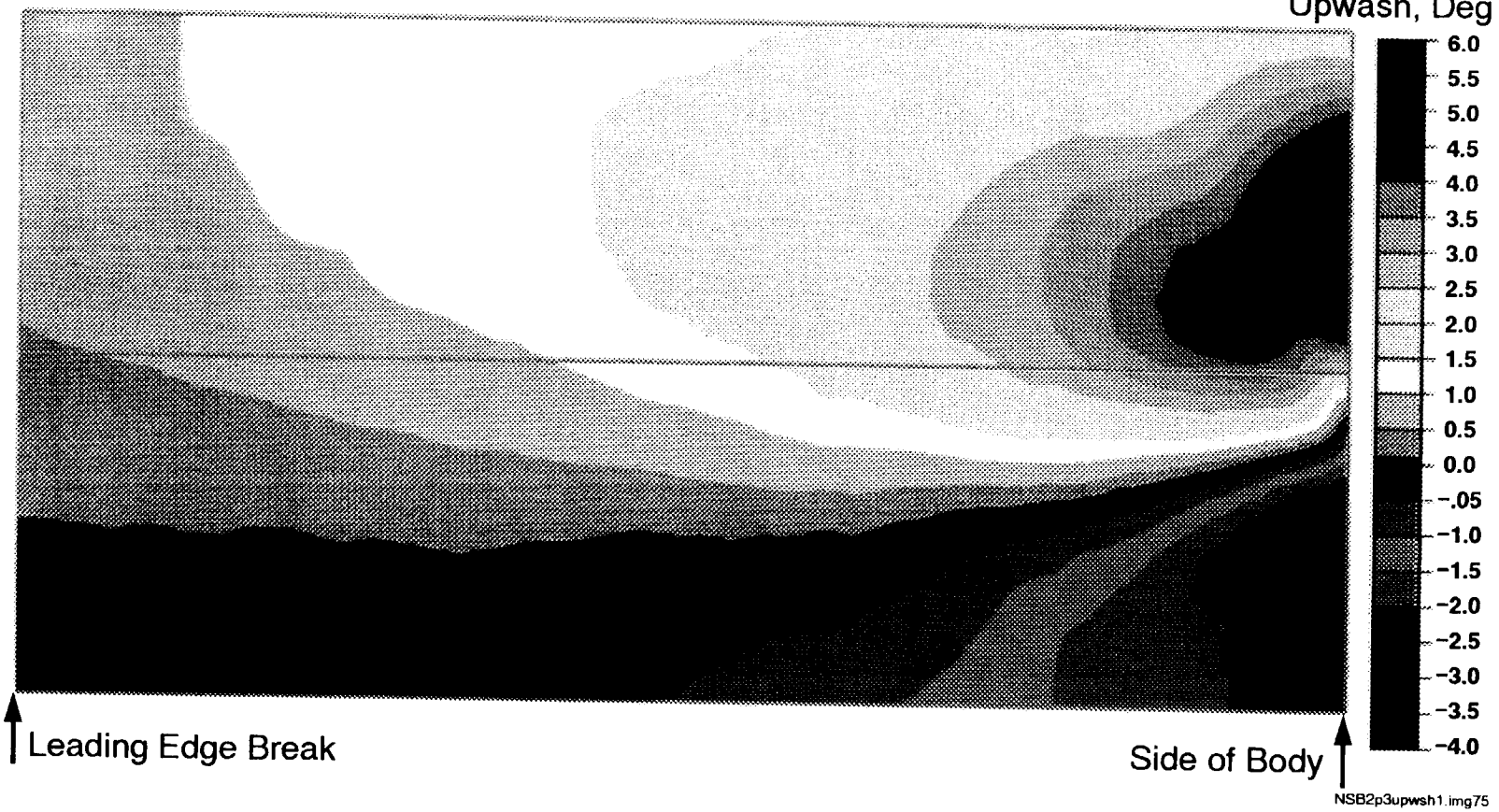

Optimized TCA Intermediate Upwash Plane 4

This image shows the optimized TCA intermediate upwash plane 4. A third lobe is now apparent in the field, also trending upward with span.

Optimized TCA Intermed. Upwash Plane 4

Inviscid TRANAIR Solution
Mach=2.4 CL=0.086

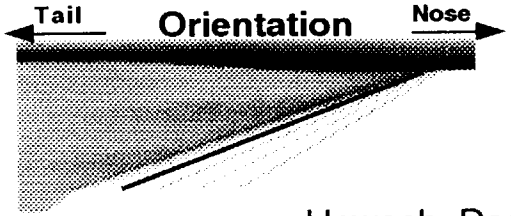

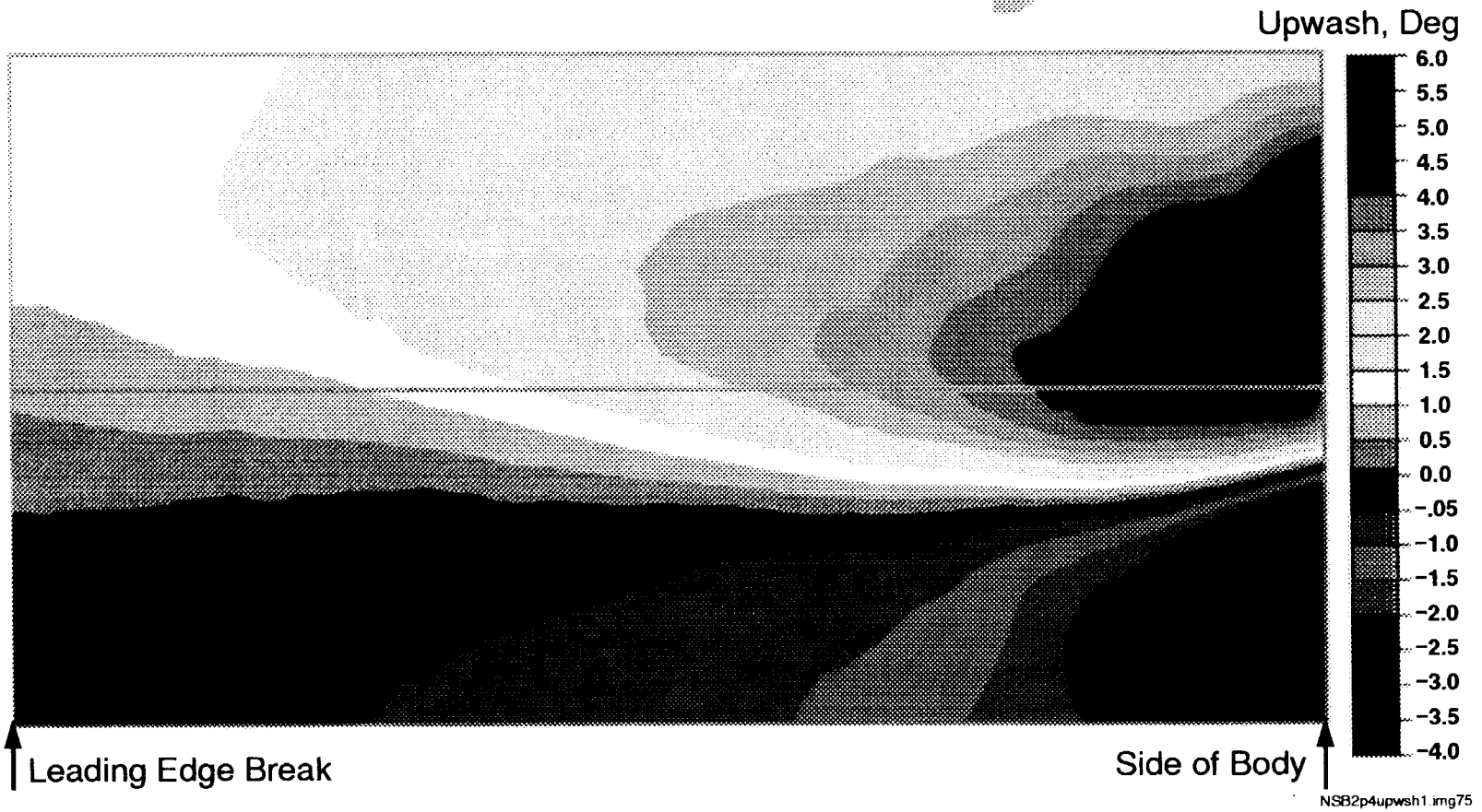

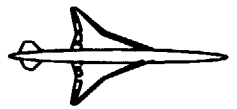

Optimized TCA Intermediate Upwash Plane 5

This image shows the optimized TCA intermediate upwash plane 5. A third lobe is now well defined and is of greater spanwise extent than the first two. This third lobe appears to be caused by the inboard wing leading edge.

Optimized TCA Intermed. Upwash Plane 5

Inviscid TRANAIR Solution
Mach=2.4 CL=0.086

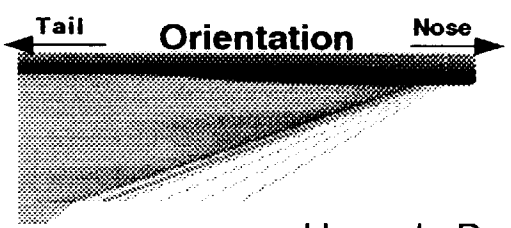

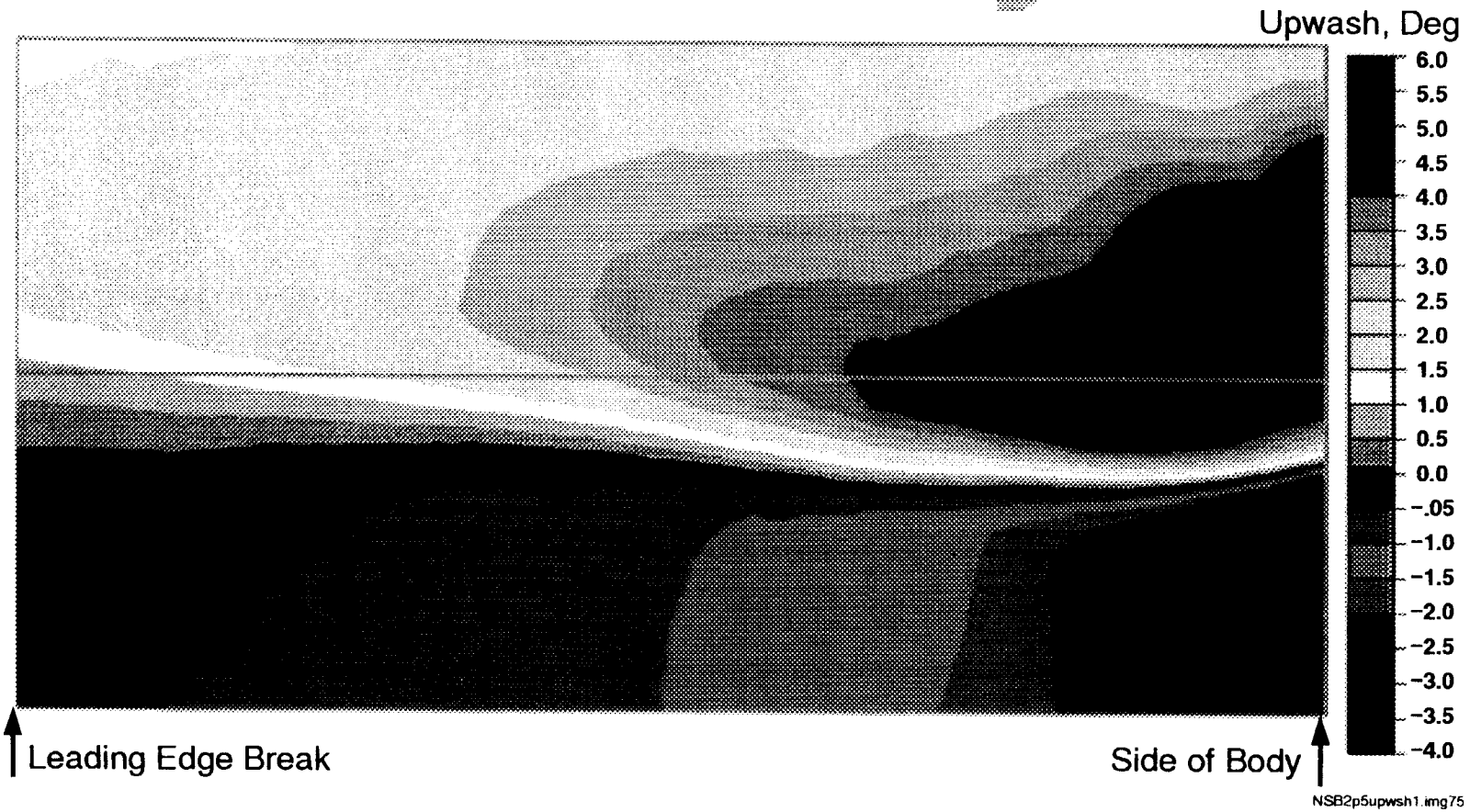

Optimized TCA Intermediate Upwash Plane 6

This image shows the optimized TCA intermediate upwash plane 6. This is the final intermediate plane. The well defined third lobe is now joined by what appears to be a fourth and final lobe, also tending up with span.

Optimized TCA Intermed. Upwash Plane 6

Inviscid TRANAIR Solution
Mach=2.4 CL=0.086

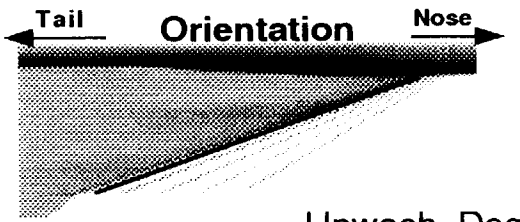

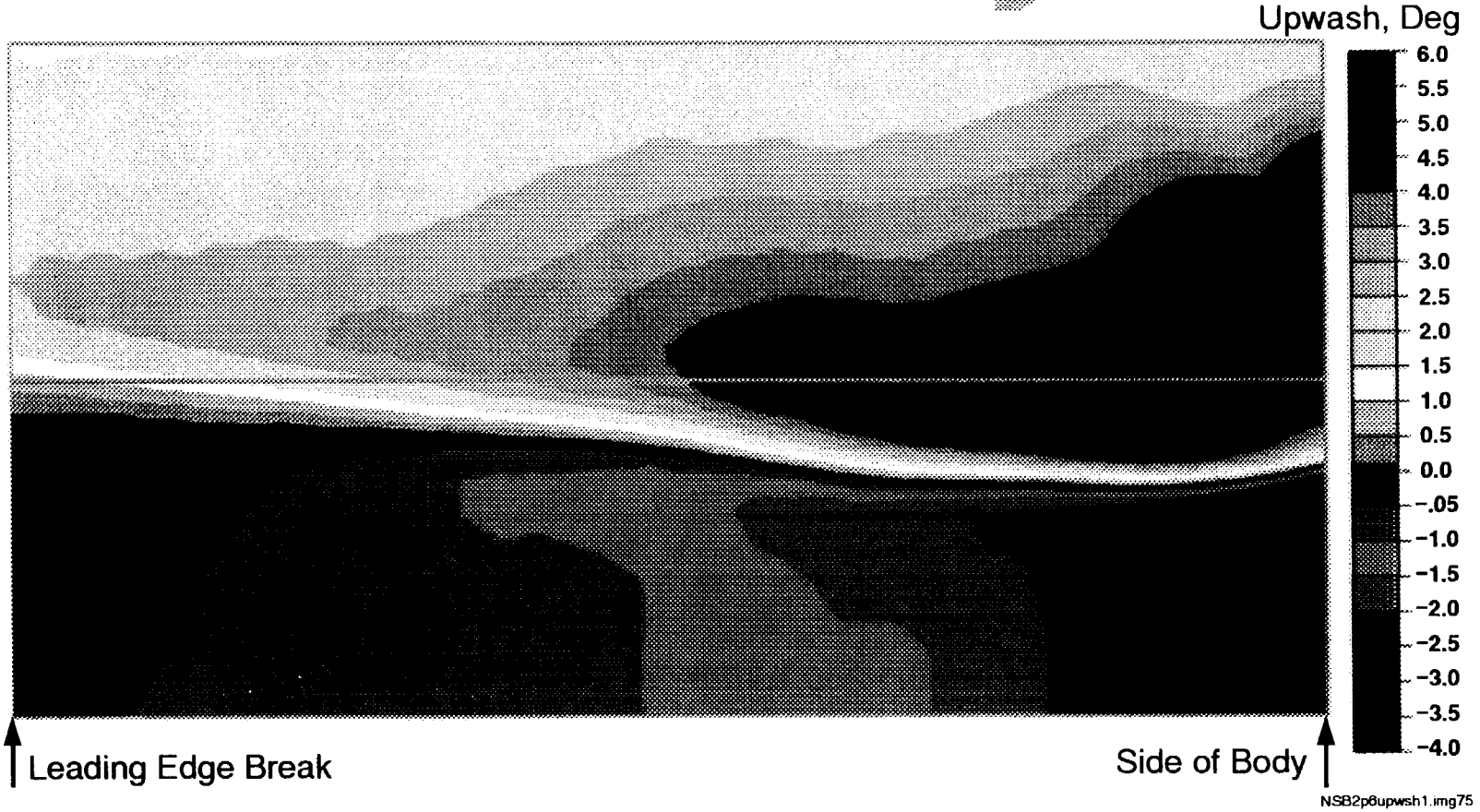

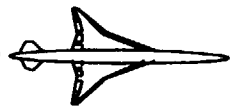

Optimized TCA Leading Edge Upwash Plane

Return to the optimized TCA leading edge upwash plane image. The four lobes are now all clearly defined. Again, there is increased intensity relative to the TCA and the tendency is for the field to rise with span.

Transonic Flap Optimization at Flight Reynolds Number

1997 HSR Aerodynamic Performance Workshop

NASA Langley Research Center
Hampton, VA
February 25-28, 1997

Max Kandula
Dynacs Engineering Co. Inc.
Renton, WA 98055

Dynacs ENGINEERING CO. INC.

---This page is intentionally left blank---

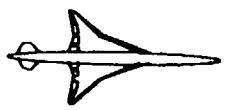

Acknowledgements

- Ross Sheckler (Dynacs)
  - AGPS Geometry for Ref. H outboard wing
- Steve Chaney (Boeing HSCT)
  - Surface grids for Ref. H & TCA
    - » body, inboard wing, collar, box, ellipsoid

Dynacs ENGINEERING CO. INC.

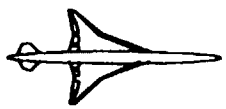

Objectives

The objective of this task is to conduct a parametric viscous Computational Fluid Dynamics Analysis (CFD) study of Ref. H and TCA wing/body confugurations at flight Reynolds number. Optimum outboard wing leading edge (LE) and trailing edge (TE) flap settings at transonic cruise (M=0.9) and acceleration (M=1.1) will be determined by independently varying the flap deflections. The flight Reynolds numbers Re (based on mean aerodynamic chord) for the Ref. H are 171E6 at M=0.9 and 190E6 at M=1.1, and those for the TCA are 164E6 at M=0.9 and 301E6 at M=1.1. Another objective of the work is to understand the transonic flowfield at flight Reynolds number, including leading edge vortex and flow separation about the hinge line and the trailing edge flap.

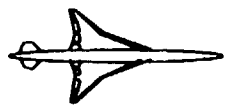

Objectives

- Optimize Transonic Flaps at Flight Reynolds Number for Ref. H & TCA Wing/Body Configuration with OVERFLOW CFD code
  - Ref. H: Re=171E6 (M=0.9), Re=190E6 (M=1.1)
  - TCA: Re=164E6 (M=0.9), Re=301E6 (M=1.1)
- Understand Flowfield at Flight Reynolds Number
  - leading edge vortex
  - Flow separation (hinge line, trailing edge)

Dynacs ENGINEERING CO. INC.

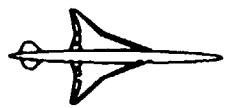

Approach

The approach is to build on the FY 95 work on Ref. H at wind tunnel Reynolds number. The OVERFLOW Navier-Stokes code based on chimera overlapping grid scheme is used to obtain CFD solutions. The optimum flap deflections for the leading edge and the trailing edge of the outboard wing will be parametrically determined at flight Reynolds number at transonic cruise (M=0.9) and acceleration (M=1.1).

Initially, the TE flap is optimized, with the leading edge set at an angle close to the optimum deflection. With the optimum TE flap deflection thus determined (first level), the LE flap optimization is performed. If the optimum LE deflection is significantly different from the originally assumed value, then the TE flap is once again optimized (second level).

Approach

- Build From FY 95 CFD Work on Ref. H
  - Re=10E6, 30E6, 80E6 (Wind Tunnel- NTF)
  - Re=5.8E6 (Wind Tunnel- LaRC 16 ft)
- Parametrically Determine Optimum Flaps
  - Vary TE flap angle, with LE flap angle fixed
  - Vary LE flap angle, with TE flap angle fixed

Dynacs ENGINEERING CO. INC.

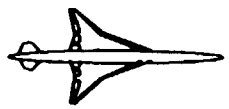

Details

Existing surface grids from Boeing are used for components other than the outboard wing (fuselage, collar, box, and ellipsoid grids). The surface geometry for the outboard wing with the delfected flaps was prepared using the AGPS code (Boeing proprietary). Surface grids are generated with the GRIDGEN elliptic code (version 9) in conjunction with the GRIDTOOL code for projection of the surface grid to the data base. The volume grids are constructed by means of the HYPGEN hyperbolic code. Volume grid communication is established by chimera overlapping scheme with the PEGSUS code. The flow solutions are obtained from the OVERFLOW Navier-Stokes code with the Baldwin-Barth one-equation turbulence model .

Optimization of flap deflections is based on the consideration of quadratic curve fits for the drag polar, and for the variation of L/D vs. flap angle. Only wing/body configurations are considered here in the optimization of transonic flaps.

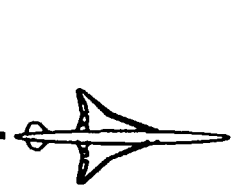

Details

- Geometry: *AGPS*
- Surface Grids: *GRIDGEN-2D & GRIDTOOL*
- Field Grids: *HYPGEN & PEGSUS*
- Flow Solutions: *OVERFLOW*
  - Baldwin-Barth 1-Eqn. Turbulence Model
- Optimization
  - Quadratic curve-fit for drag polar
  - Quadratic curve-fit for L/D vs. Flap Deflection

Dynacs ENGINEERING CO. INC.

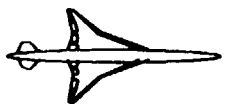

Ref. H Flap Optimization

Ref. H Surface Grid for the Outboard Wing

Shown in this figure is a typical surface grid (221x75) for the Ref. H outboard wing, indicating the grid distribution and areas of grid clustering. The inset includes typical LE and TE flap configurations analyzed in the optimization study. The total number of grid points in the entire grid system is 4.2E6, which includes body, inboard wing, collar, box and the outermost ellipsoid.

Ref. H Surface Grid for Outboard Wing

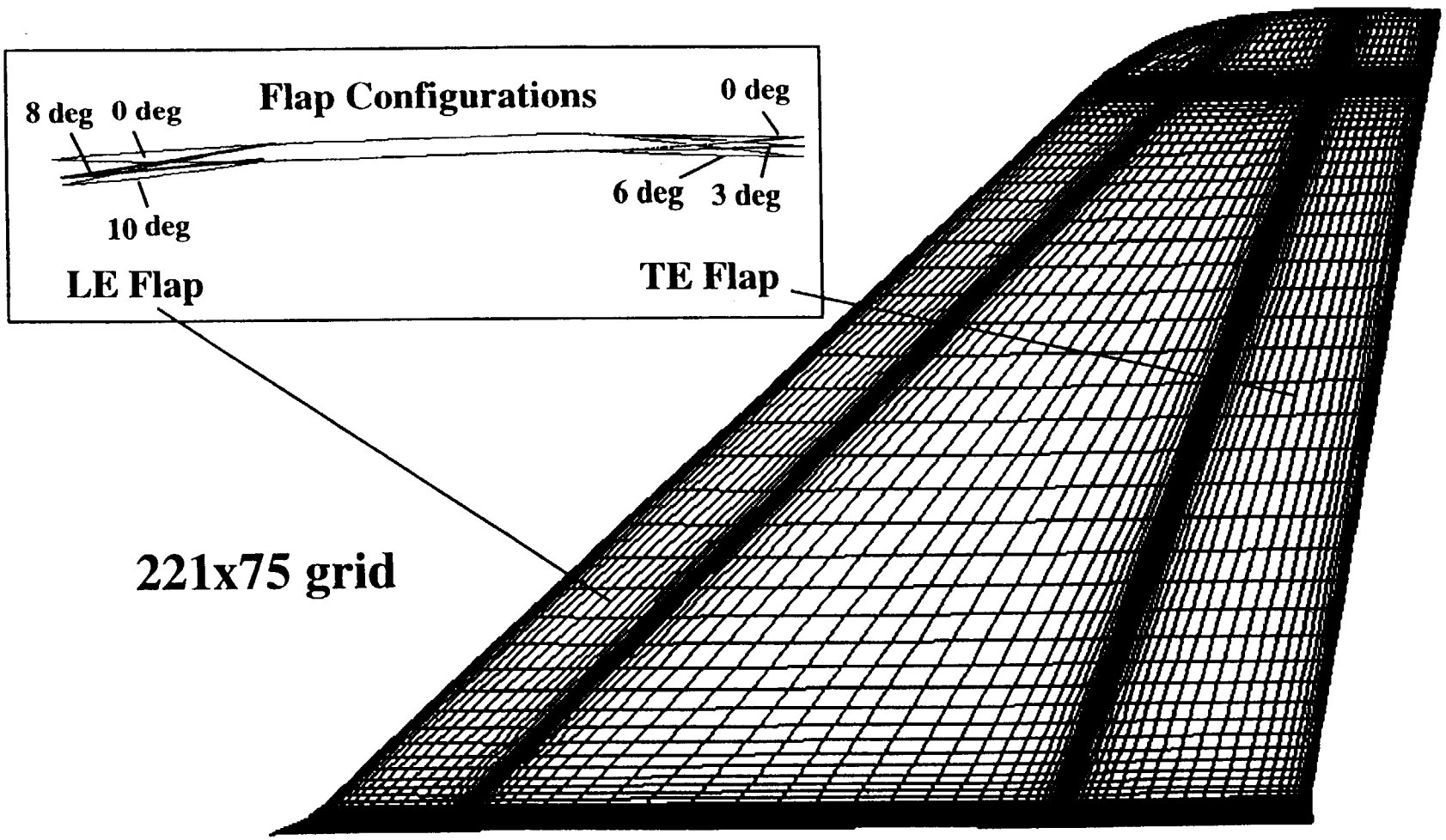

Dynacs Engineering Co. Inc.

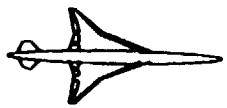

Flap Angle Matrix for Ref. H

This Table shows the flap angle matix considered for the Ref H flap optimization for M=0.9 and M=1.1, including the baseline case of 0/0 deg. Based on the available wind tunnel data and CFD solutions at wind tunnel Reynolds number for Ref. H, a relatively sparse matrix of flap deflections was constructed. At M=0.9, TE flap deflection of 0, 3, and 6 deg, and LE flap deflections of 0,8,10 and 12 deg are considered. At M=1.1, the TE flap is set at 0 deg, and the LE flap deflections of 6,8 and 10 deg are included. The drag polar for each LE/TE flap geometry was based on a quadratic curve fit through the solutions for alpha=2, 4 and 6 deg. A typical OVERFLOW solution (without multi-gridding) converges in about 3200 iterations, and requires about 20 CPU hours on C-90. The overall grid system has 4.2 million grid points. The y^+ value is in the range of 2.5 to 3.5.

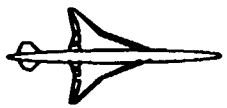

Ref. H Flap Angle Matrix

M=0.9

TE, deg \ LE, deg	0	8	10	12
0	X	X	X	
2.5		X		
3		X	X	X
6		X	X	

M=1.1

TE, deg \ LE, deg	0	6	8	10
0	X	X	X	X

Drag Polars for Ref. H LE flap of 10 deg at M=0.9

In this figure, typical drag polars for Ref. H at M=0.9 for a constant LE flap angle of 10 deg, and various TE flap deflections. The drag polar is constructed form a quadratic curve fit of solutions at alpha=2 deg, 4deg and 6 deg.

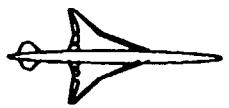

Drag Polar

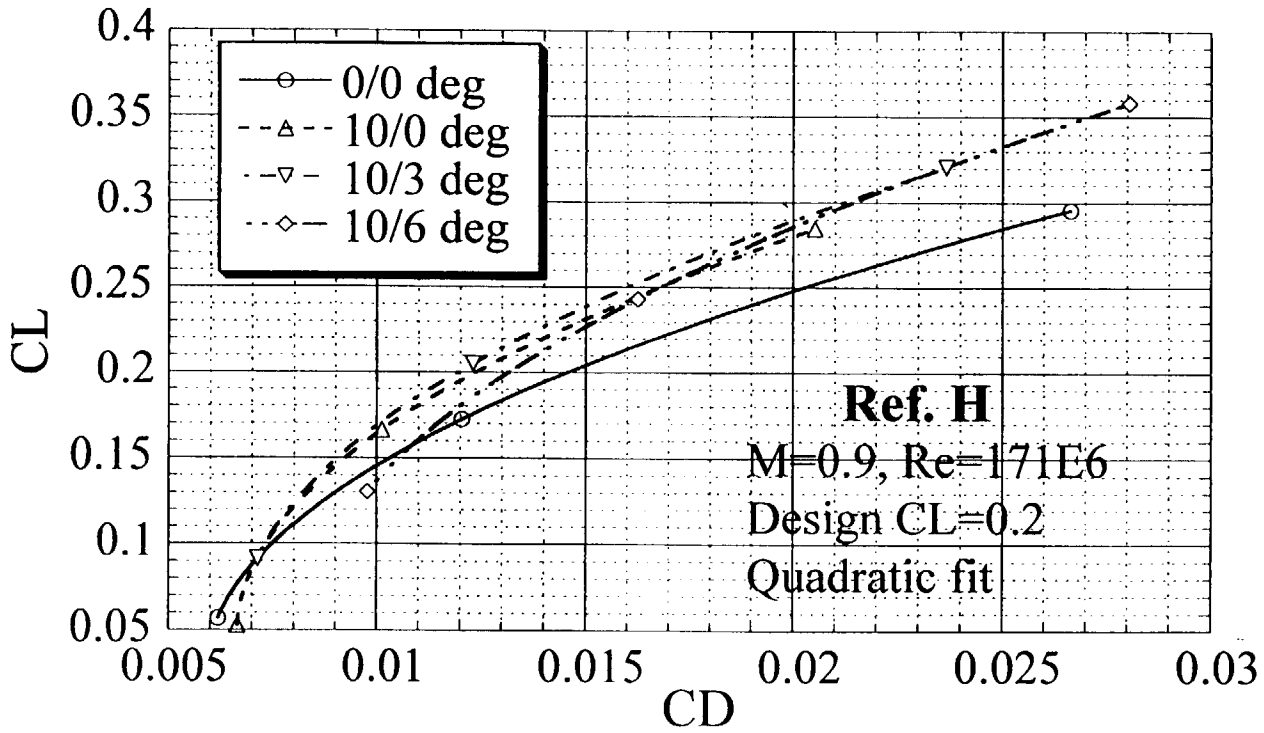
0/0 deg
10/0 deg
10/3 deg
10/6 deg
Ref. H
M=0.9, Re=171E6
Design CL=0.2
Quadratic fit
CL
CD
0.4
0.35
0.3
0.25
0.2
0.15
0.1
0.05
0.005
0.01
0.015
0.02
0.025
0.03

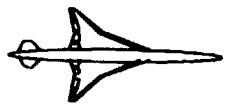

Drag Polars for Ref. H LE flap of 10 deg at M=0.9 (Expanded View)

An expanded view of the drag polar of the previous slide is indicated in this plot. For the LE flap of 10 deg, a computed drag benefit of about 26 counts is noted for the 10 deg LE flap relative to the base line case. This value in drag benefit is comparable to an observed drag reduction of 29 counts for Ref. H at M=0.9 (@ CL=0.2) with the 10/3 deg flap at a wind tunnel Re of 5.8E6 (LaRC 16-ft, 1.675 % scale model) (Ref: P. Vijgen, Final Report on Ref. H Outboard Wing Leading Edge Flap Transonic Performance Test in Langley 16-ft Tunnel (Test 469); Boeing HSCT Aerodynamics Rept. AERO-B-B143-C96-1995).

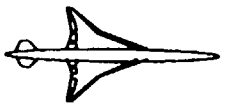

Drag Polar (Exp. View)

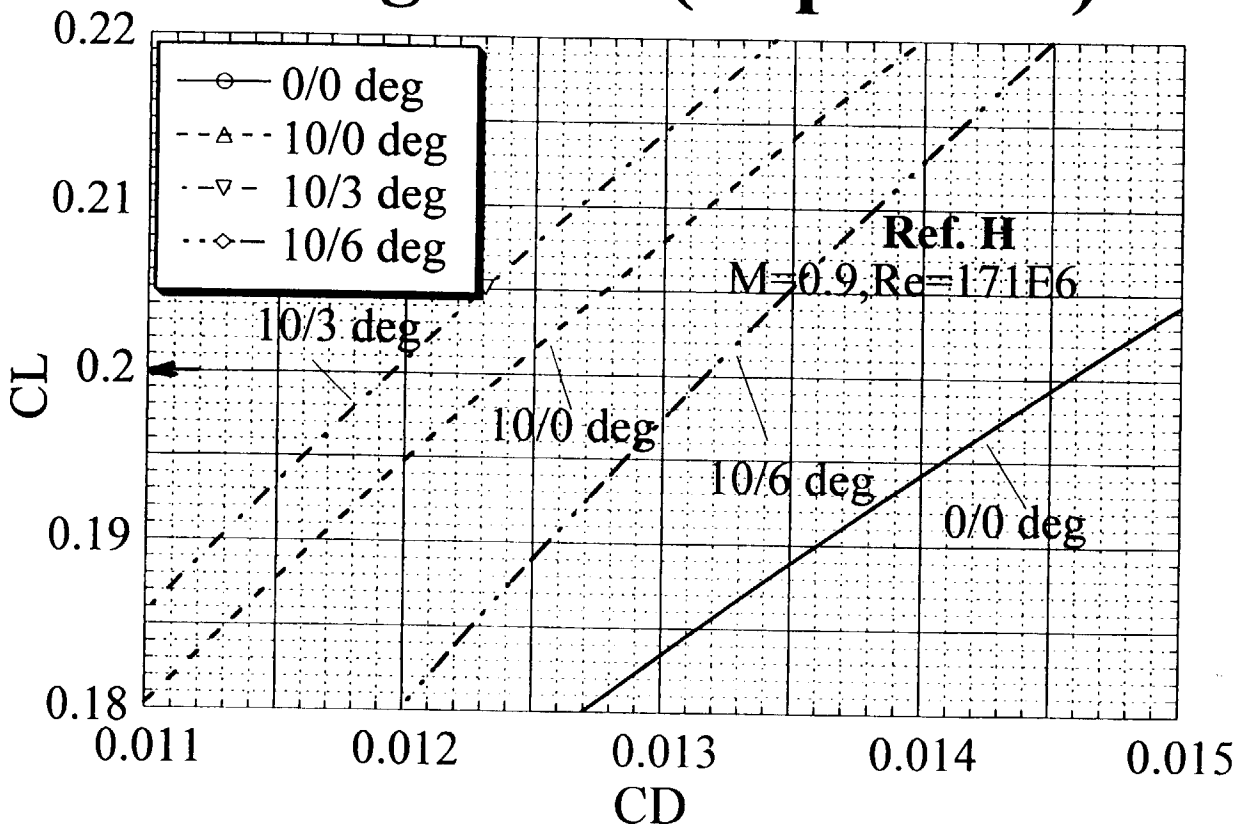

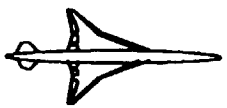

Trailing Edge Flap Optimization (First Level) for Ref. H at M=0.9

This plot shows the outcome of the first level of TE flap optimization, with the LE flap set at 10 deg. In this figure, the variation of L/D corresponding to design CL=0.2 is plotted as a function of TE flap angle. The solid line due to the quadratic curve fit suggests that the optimum TE deflection is about 2.5 deg, resulting in the maximum L/D of about 16.8. The L/D value for the baseline case (undeflected flaps; 0/0 deg) is 13.732. Thus an improvement in L/D of 22.3 percent is obtained. The wind tunnel data (1.675 % scale Ref. H model at Re=5.8E6) on the other hand suggests an improvement of 19 percent in L/D with the 10/3 deg flaps.

Trailing Edge Flap Optimization (First Level)

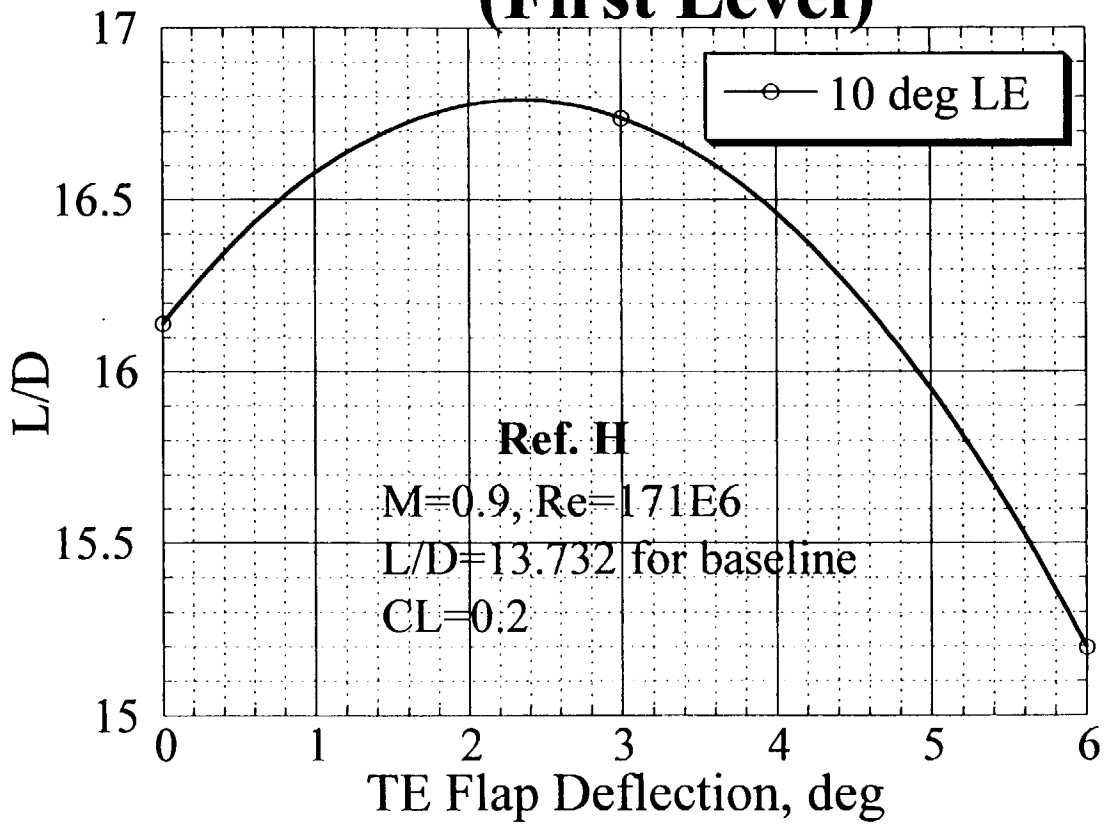

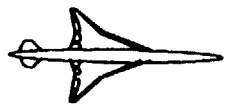

Drag Polars for Ref. H TE flap of 3 deg at M=0.9

An exapnded view of the drag polars for the Ref. H TE flap at M=0.9 with various leading edge flap orientations is dsplayed in this figure. The 8 deg LE flap is seen to be slightly bettter than the 10 deg LE flap in terms of the drag benefit.

Drag Polar (Exp. View)

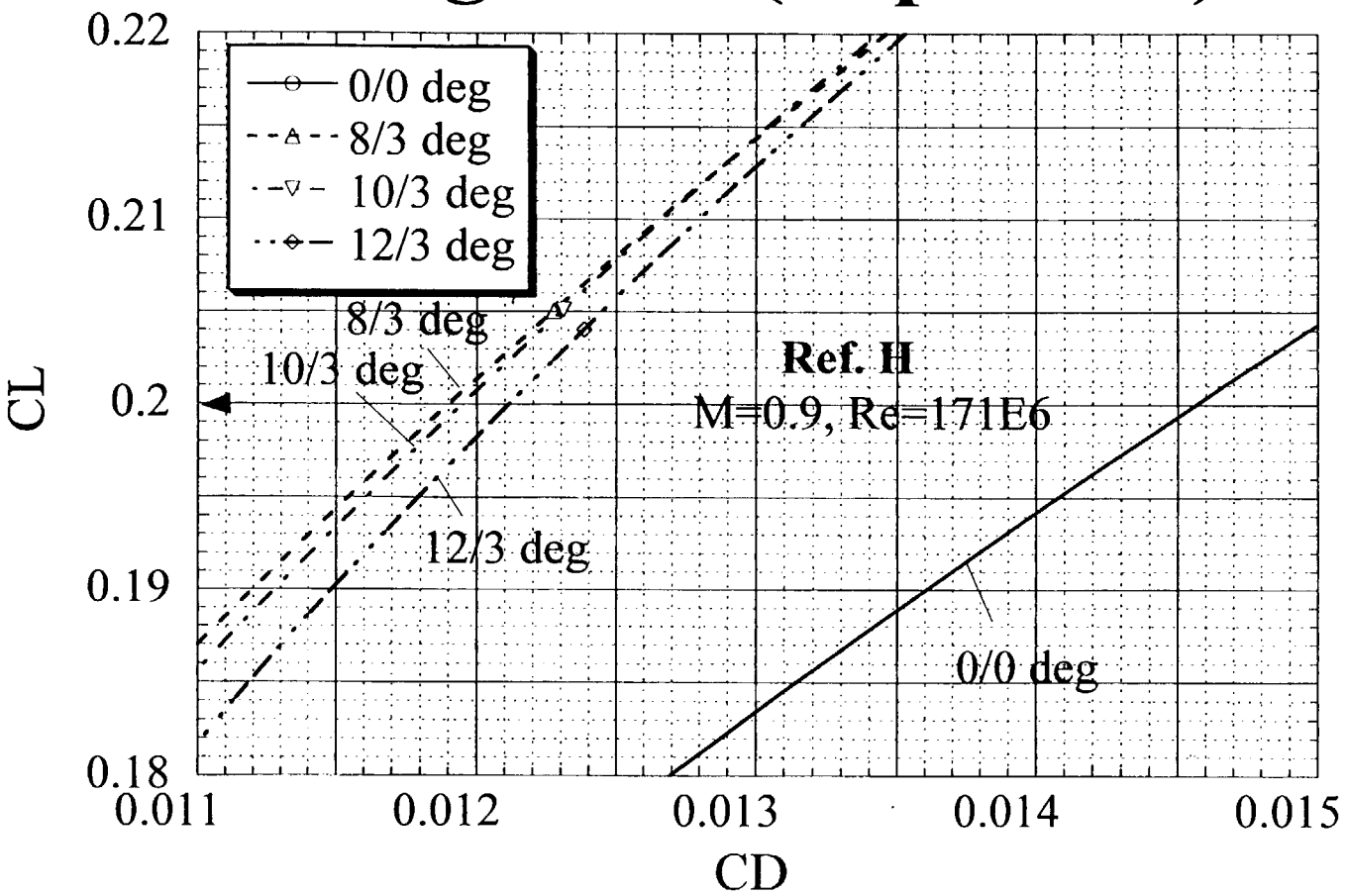

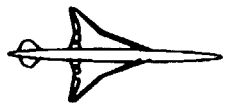

Leading Edge Flap Optimization (First Level) for Ref. at M=0.9

The variation of L/D with the LE flap deflection at a fixed TE flap angle of 3 deg is plotted in this figure. This result indicates that the optimum LE flap deflection is close to 8 deg. This result departs from the previoulsy estimated optimum value of 10 deg LE deflection.

Leading Edge Flap Optimization

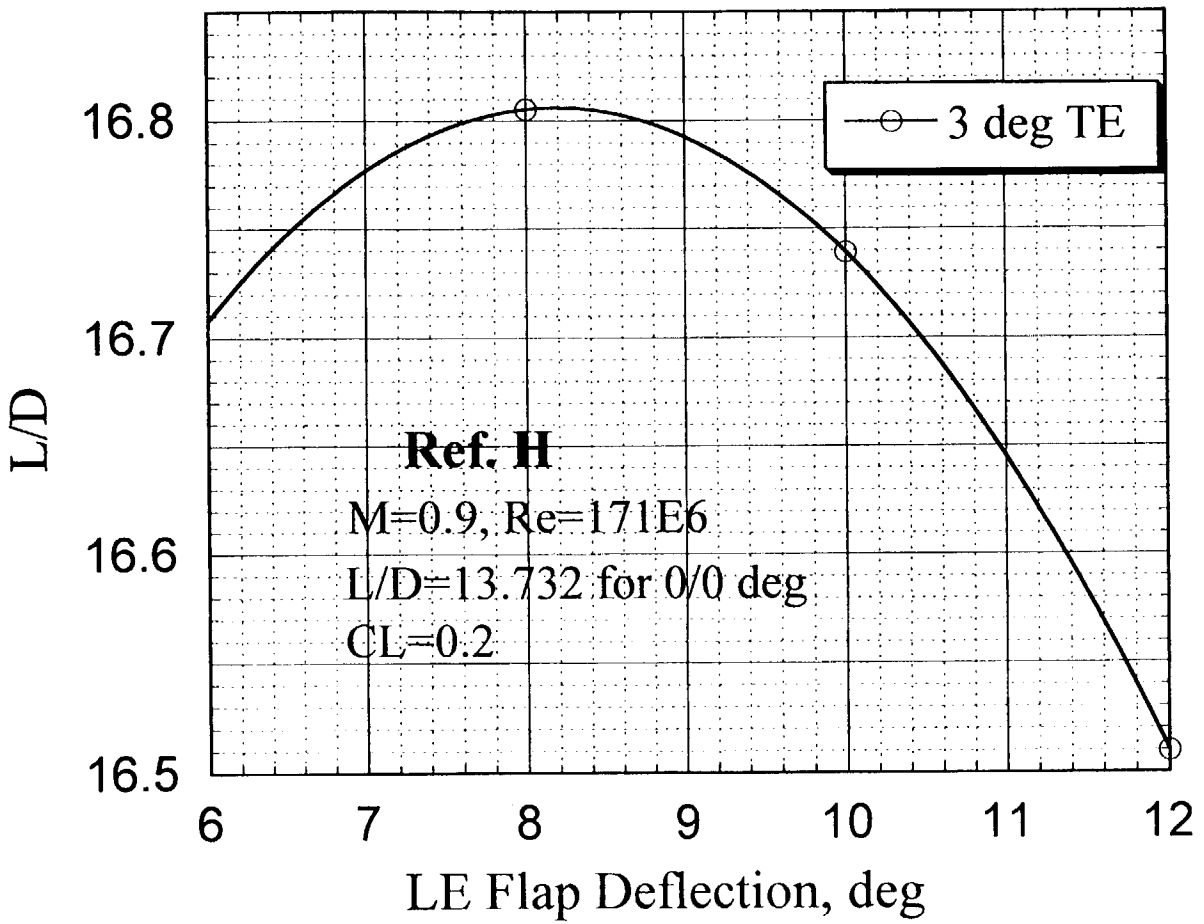

Drag Polars for Ref. H LE flap of 8 deg at M=0.9

For the Ref. H LE flap of 8 deg, a computed drag benefit of 27 counts is noted for the 2.5 or the 3 deg TE flap relative to the baseline case.

Drag Polar (Exp. View)

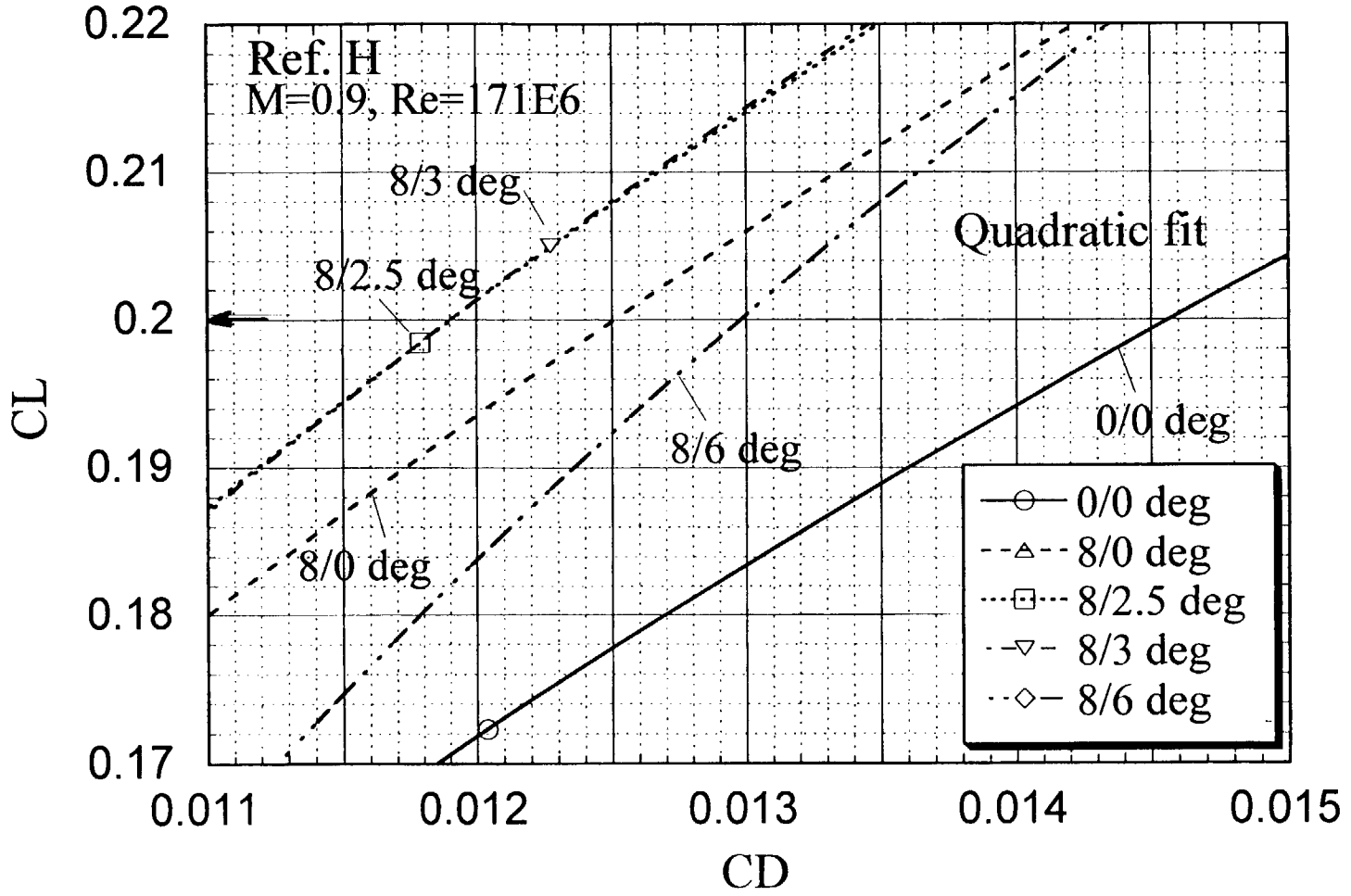

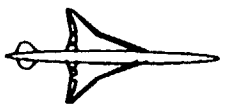

Trailing Edge Flap Optimization (Second Level) for Ref. at M=0.9

A second level of TE flap deflection is carried out with the LE flap set at 8 deg. A comparison of the variation of L/D vs. TE flap deflection for LE flap angles of 8 and 10 deg is demonstrated here. It is observed that the L/D curve is shifted to the right as the LE flap deflection is decreased from 10 deg to 8 deg. The shift in the optimum TE deflection as well as the maximum L/D are however not significant. At a given CL, the shift in optimum TE flap angle corresponding to a change in LE flap angle from 10 deg to 8 deg is of the order of 0.3 deg. Thus it may be supposed that the effects of interaction between the LE flap and the TE flap are finite, but not substantial.

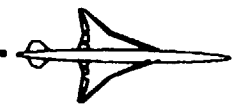

Trailing Edge Flap Optimization
(Second Level)

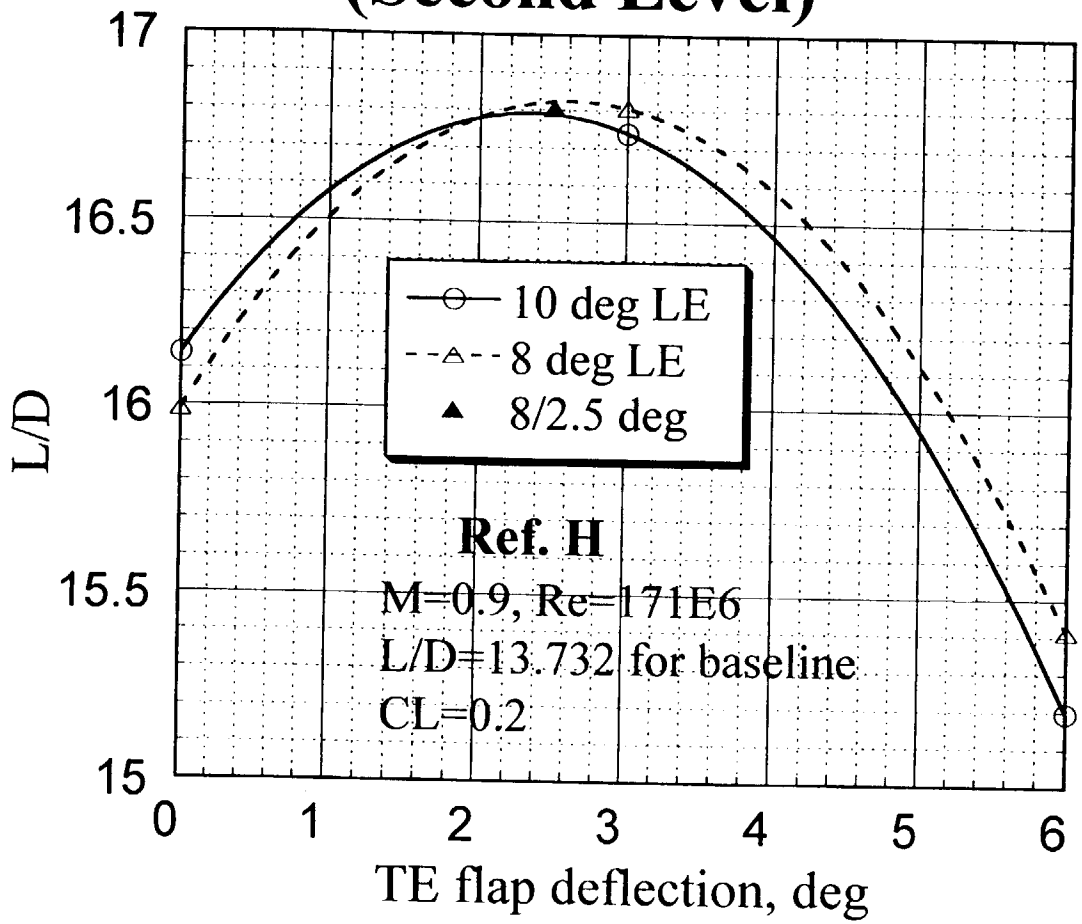

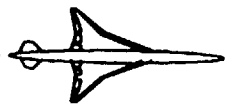

Comparison of Flap Performance for Ref. H at M=0.9

A comparison of the predicted flap performance for Ref. H at M=0.9 at flight Re with that at wind tunnel Re is shown here. The variation of $(L/D)/(L/D)_0$ vs. TE flap angle is plotted, where $(L/D)_0$ represents the baseline (0/0 deg flaps) value of L/D (13.732 at flight Re=171E6, and 11.111 at WT Re=5.8E6). The wind tunnel data is rather sparse. The best flap configuration of 10/3 deg at WT Re shows a 19 percent improvement in L/D, while the CFD at flight Re indicates that 8/2.5 deg flap performs the best and results in about 22.3 percent benefit in L/D.

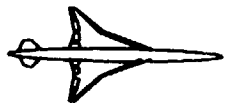

Comparison of Flap Performance
Ref. H, M=0.9

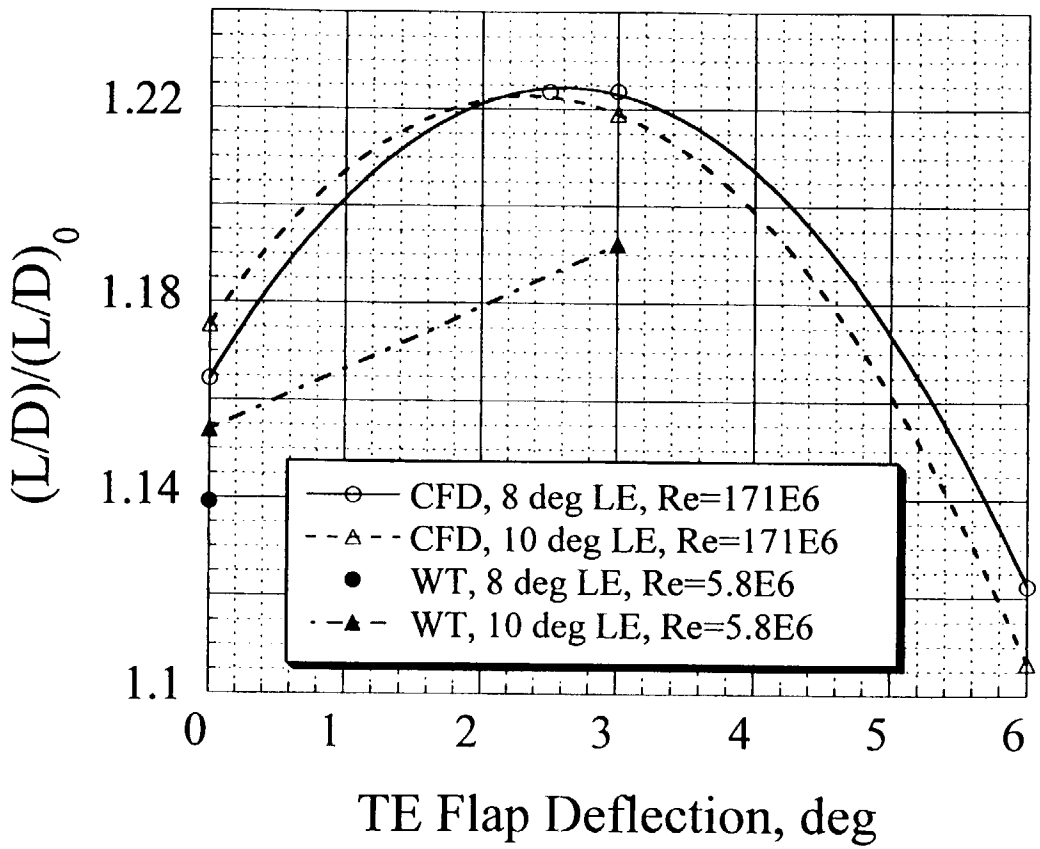

Surface Pressure Coefficient for Ref. H for 8/2.5 deg flaps at M=0.9 and alpha=4 deg

This figure presents the surface pressure coefficient distribution for the 8/2.5 deg flaps at M=0.9 and alpha=4 deg. The leading edge vortex on the inboard wing upper surface is noted. At this condition, the attachment line is on the lower surface of the outboard wing, and a vortex separation of small extent is noted on the upper surface leading edge. A discrete pocket of high pressure region is noted in the mid chord region near the wingtip.

Ref. H Transonic Flaps (8/2.5 deg); M=0.9, α=4 deg, Re=171E6

Surface Pressure Coefficient (OVERFLOW)

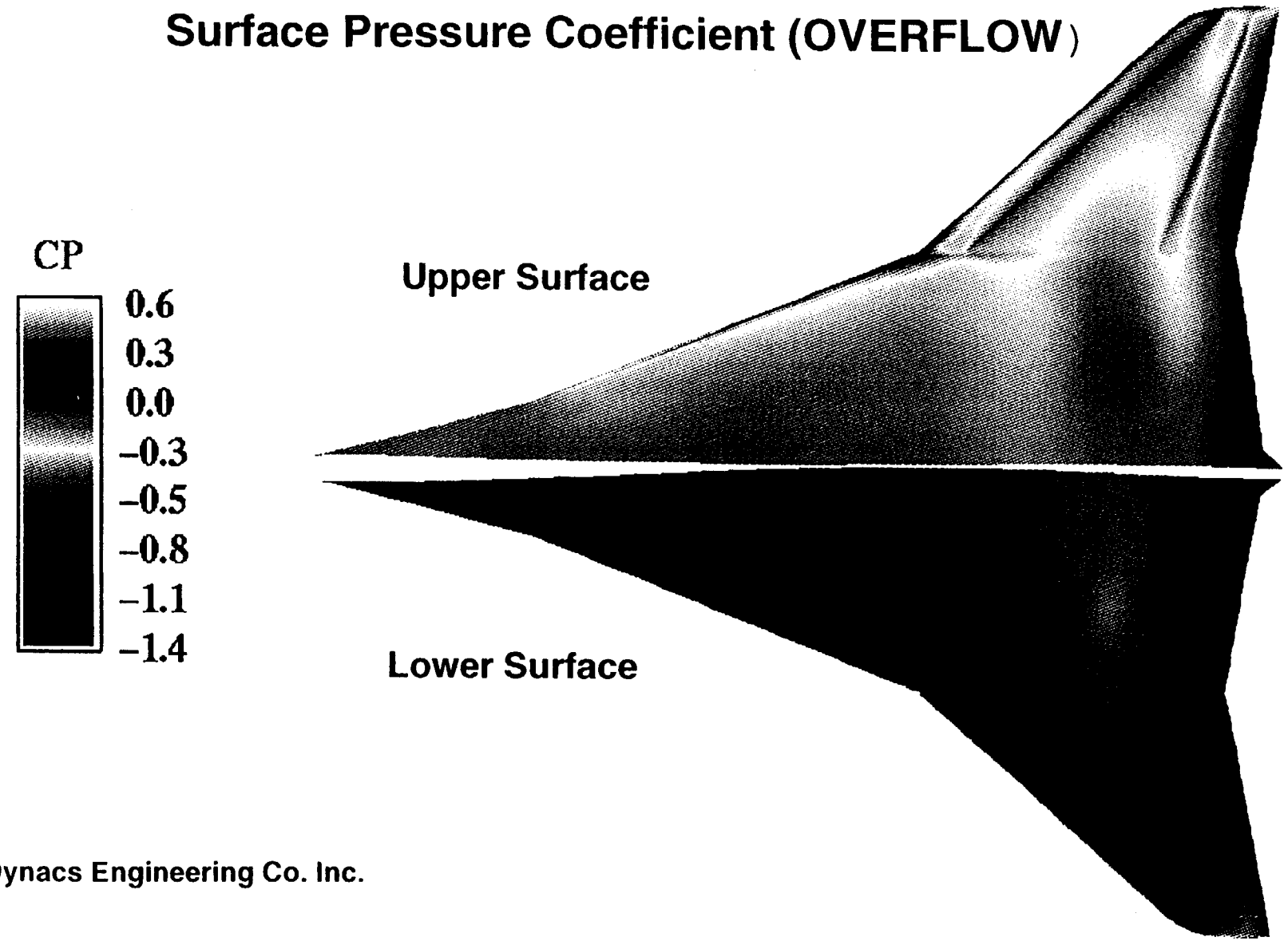

Dynacs Engineering Co. Inc.

Surface Streamlines for Ref. H for 8/2.5 deg flaps at M=0.9 and alpha=4 deg

The surface streamline pattern for the 8/2.5 deg flaps at alpha=4 deg suggests an absence of flow separation near the hingelines or the trailing edge flaps. The absence of flow separation of computed streamlines at flight Re is consistent with the previous observations that hinge line flow separation is noted only at the lowest Reynolds number tested (ie. Re=5.8E6), but absent at Re of 30E6 and higher. This result concurs with the theory of turbulent boundary layers that flow separation is delayed or prevented as the Reynolds number is increased.

Ref. H Transonic Flaps (8/2.5 deg); M=0.9, α=4 deg, Re=171E6

Surface Streamlines (OVERFLOW)

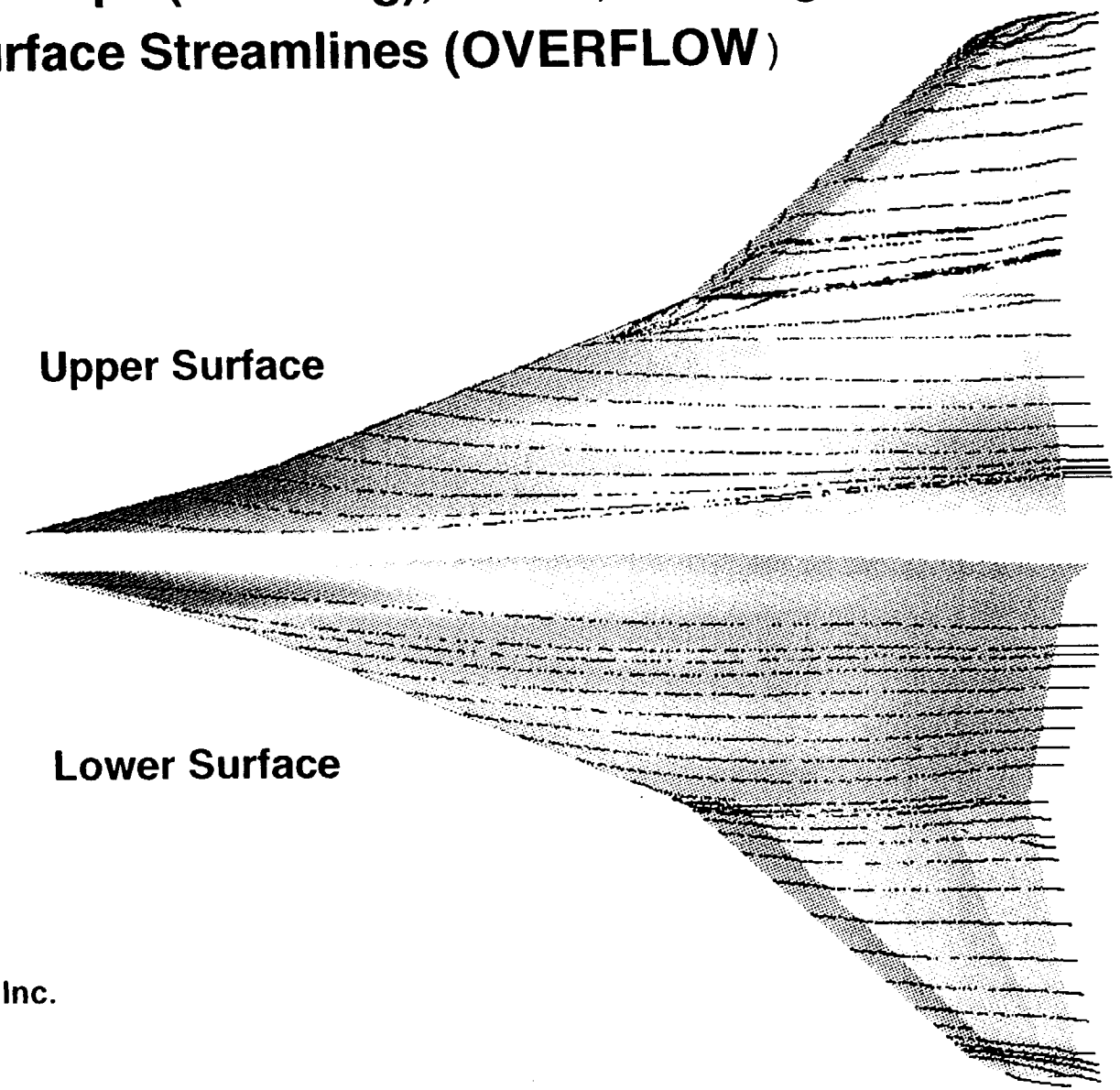

Dynacs Engineering Co. Inc.

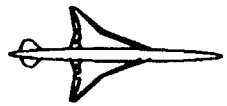

Surface Streamlines for Ref. H for 8/2.5 deg flaps at M=0.9 (expanded view)

An expanded view of the streamline pattern for the outboard wing is presented in this figure.

Ref. H Transonic Flaps (8/2.5 deg); M=0.9, α=4 deg, Re=171E6

Surface Streamlines (OVERFLOW)

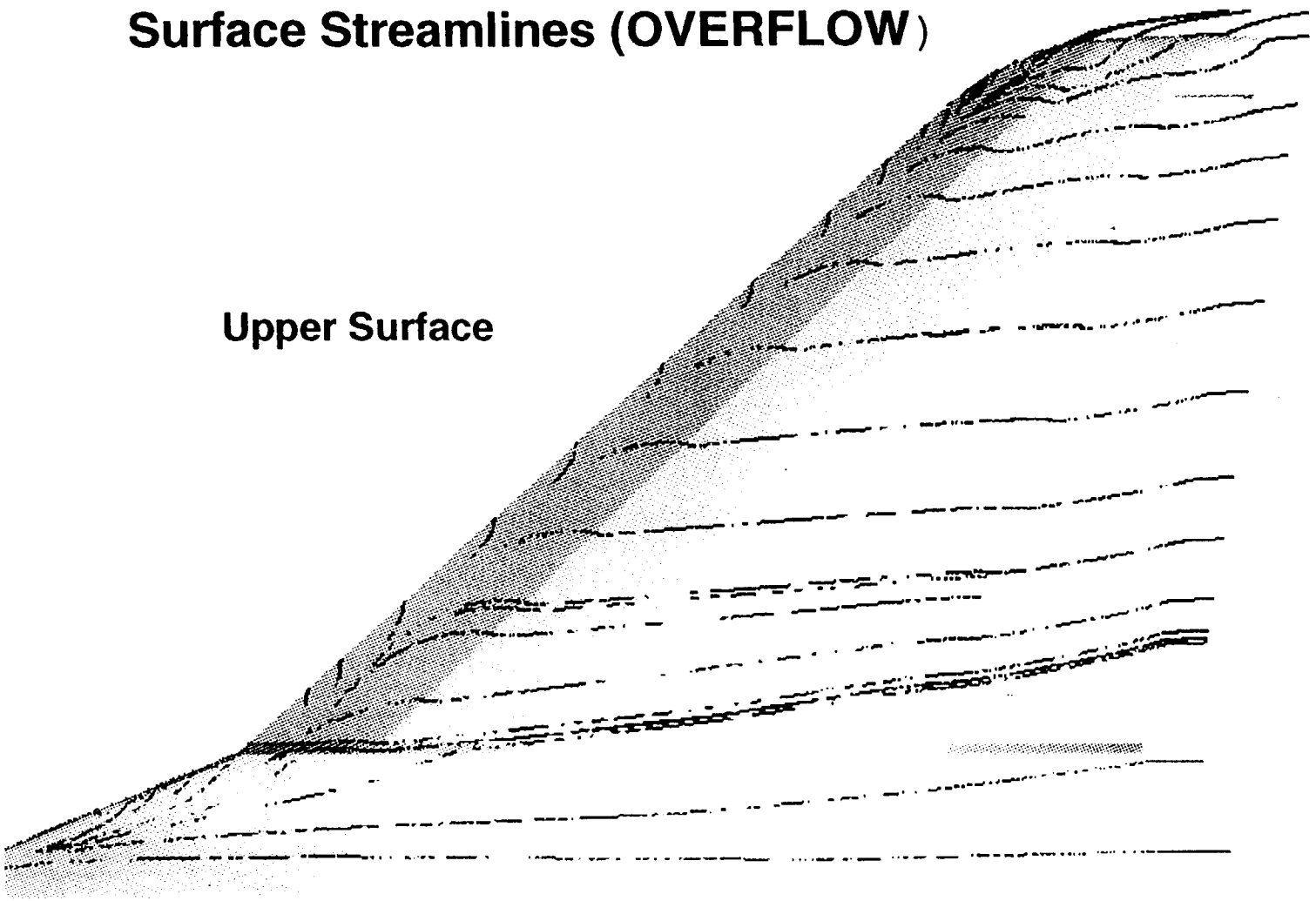

Dynacs Engineering Co. Inc.

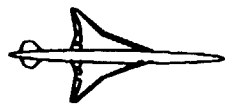

Surface Streamlines for Ref. H for 10/6 deg flaps at M=0.9 and alpha=2 deg

The streamline pattern for the 10/6 deg flaps at M=0.9 and alpha=2 deg shows trailing edge flap flow separation for roughly 50 percent of the span of the outboard wing. Such a flow separation is noted for the 10/6 deg flaps at alpha=4 deg also. This trailing edge flow separation explains a pronounced increase in pressure drag (CDP) at alpha=2 deg, as indicated by the drag polar (for LE flap of 10 deg) shown earlier. For the 10/6 deg flaps at alpha=2 deg, a pressure drag of 48 counts is predicted, as compared to 22 counts for the 10/3 deg flaps, 16 counts for the 10/0 deg flaps, and 12 counts for the baseline case of 0/0 deg flaps.

Ref. H Transonic Flaps (10/6 deg); M=0.9, α=2 deg, Re=171E6

Surface Streamlines (OVERFLOW)

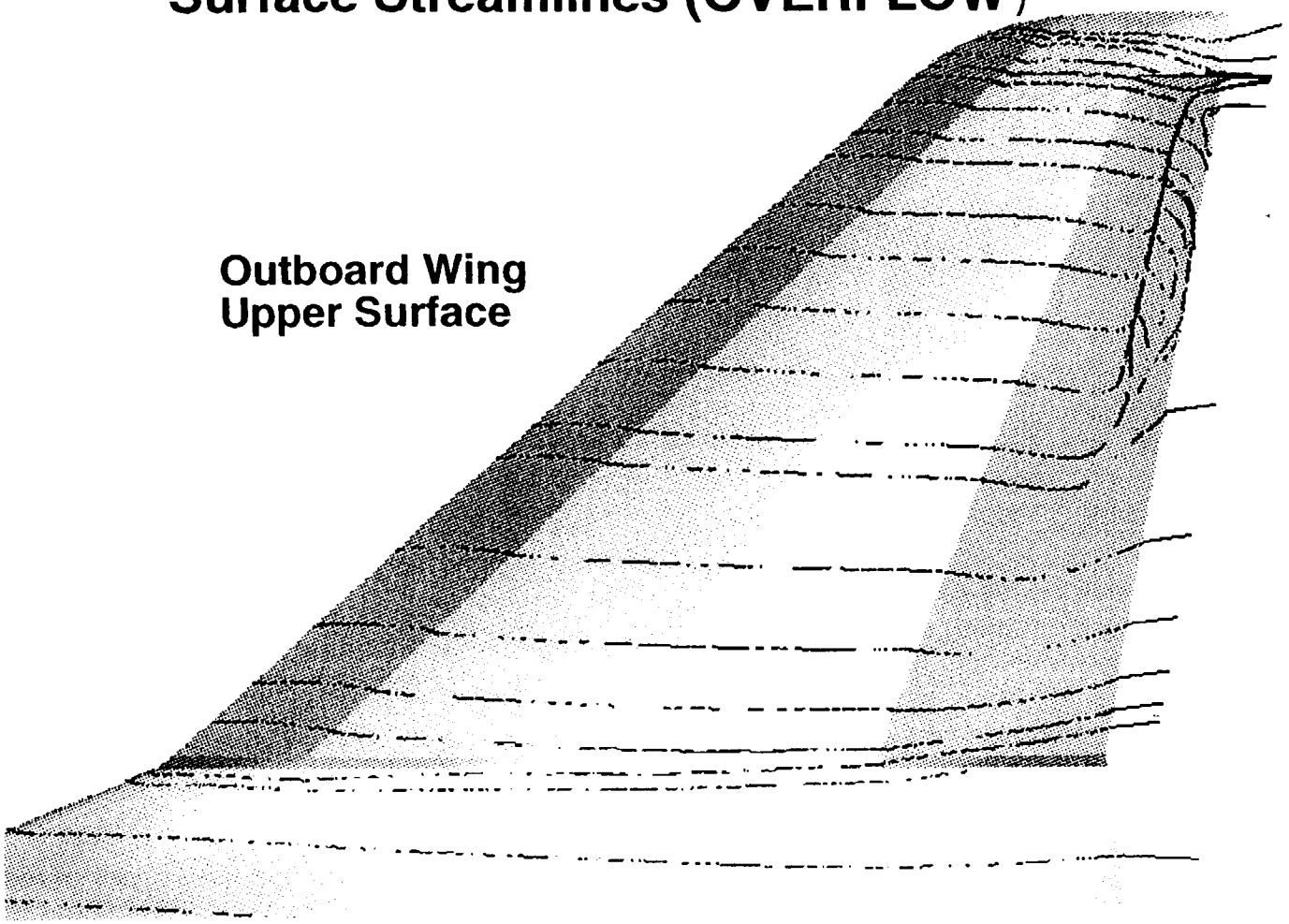

Dynacs Engineering Co. Inc.

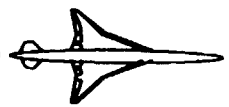

Reynolds Number Effect on Chordwise Surface CP for Ref. H 10/3 deg Flaps at M=0.9

Shown in this figure is the effect of Reynolds number (Re=6E6, 30E6 and 171E6) on the computed chordwise surface pressure distribution for the Ref. H 10/3 deg flaps at M=0.9 and alpha=4 deg, at a span station of y=550 in. It is evident that the displacement action of the boundary layer on the surface pressure distribution are confined primarily to the upper surface of the trailing edge flap.

Effect of Re on CP

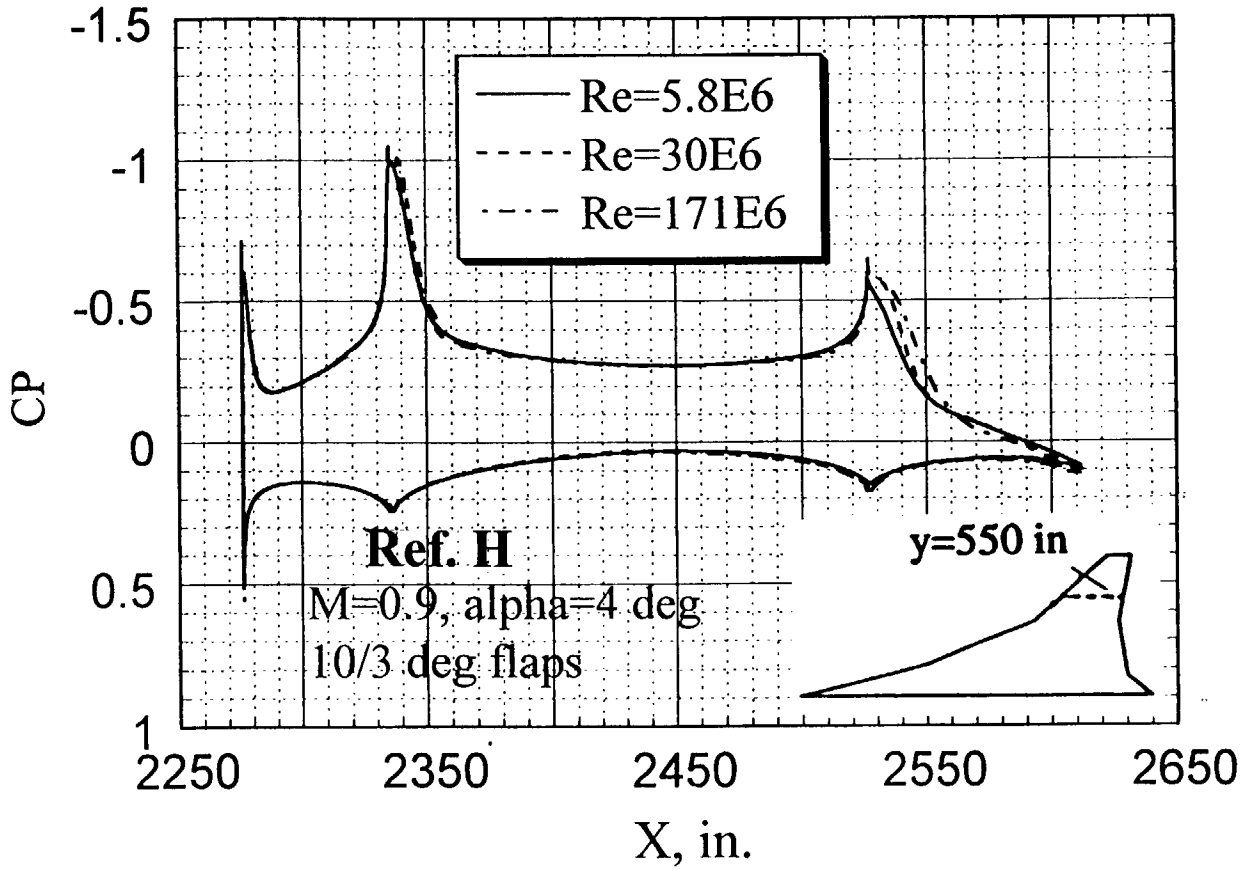

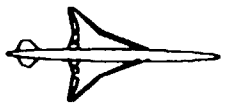

Drag Polars for Ref. H TE flap at M=1.1 (Expanded View)

For the low supersonic case (M=1.1), the leading edge flap is optimized with the trailing edge flap is set at 0 deg. Three leading edge flap deflections (4,6, and 8 deg) are considered for this purpose. In addition the baseline case of 0/0 deg (flaps up) was also analyzed. Drag polars for M=1.1 at various LE flap deflection are illustrated in this figure. The polars are generated from a quadratic fit of data at three values of alpha=2, 4 and 6 deg. The results show that at the design CL=0.2, the 6/0 deg flap performs the best, and offers a drag benefit of about 7 counts relative to the baseline, whereas the 8/0 deg flap provides a drag benefit of 6 counts. For purposes of comparison, at the wind tunnel Reynolds number of Re=5.8E6, the 8/0 deg flap shows a drag reduction of 9 counts relative to the baseline.

Drag Polar (Exp. View)

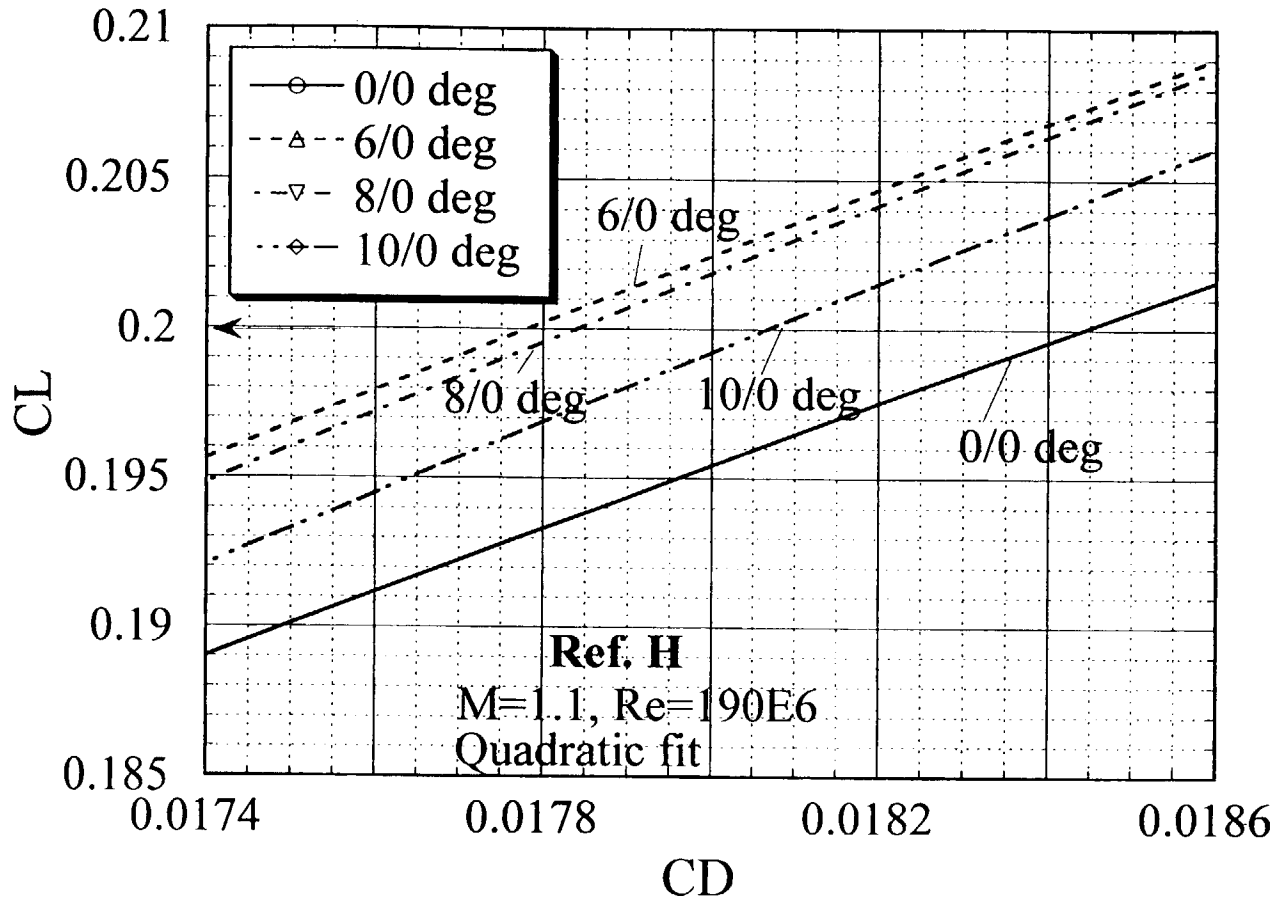

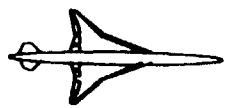

Leading Edge Flap Optimization for Ref. H at M=1.1

This plot depicts the variation of L/D with the leading edge flap deflection for Ref. H at M=1.1. The result suggests that a 6.4 deg LE flap is the optimum case, resulting in a maximum L/D of 11.25. The L/D for the base line case is 10.846. Thus an enhancement of 3.7 percent in L/D is noted at flight Re. This result compares with a 4.5 percent in L/D at M=1.2 for the 8/0 deg flaps at a wind tunnel Re of 5.8E6.

Leading Edge Flap Optimization

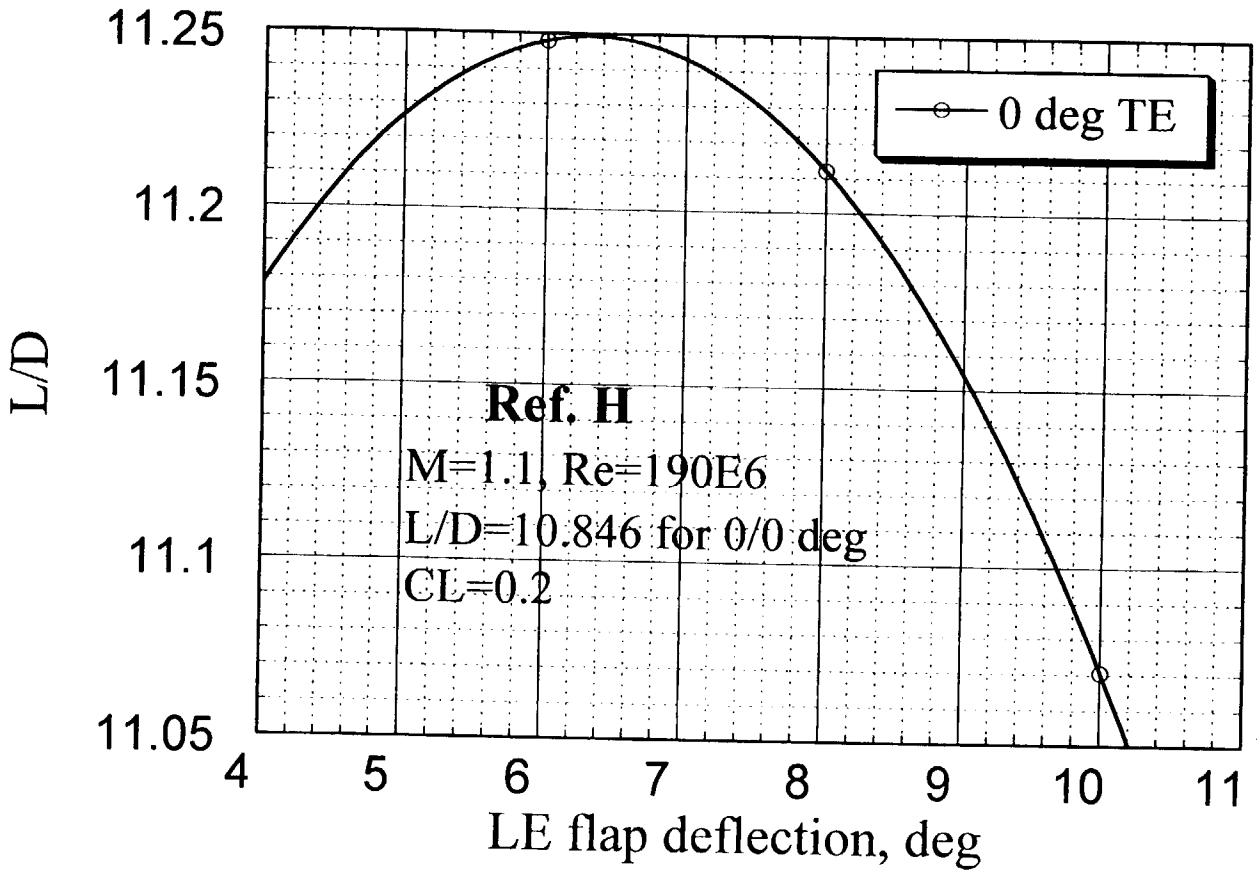

Comparison of LE Flap Performance for Ref. H at M=1.1

The comparson of the LE flap performance for Ref. H at M=1.1 is presented here. At flight Re the theory shows that 6/0 deg flap is optimum and results in L/D benefit of 3.7 percent (baseline value of L/D is 10.846 at Re=190E6), as compared to about 4.7 percent for the best configuration of 7/0 deg flap at wind tunnel Re of 6E6 (the data is curve fitted). Without the aid of the curve fit, the WT data shows that the 8/0 deg flap is the best and provides a 4.5 percent benefit.

The results show that the optimum LE flap deflection at flight CFD is about one deg less than that at the WT Re. Since the TE flap is set at 0 deg, it is believed that the Reynolds number effect on the LE flap performance is related to the leading edge vortex.

Comparison of LE Flap Performance

Ref. H, M=1.1

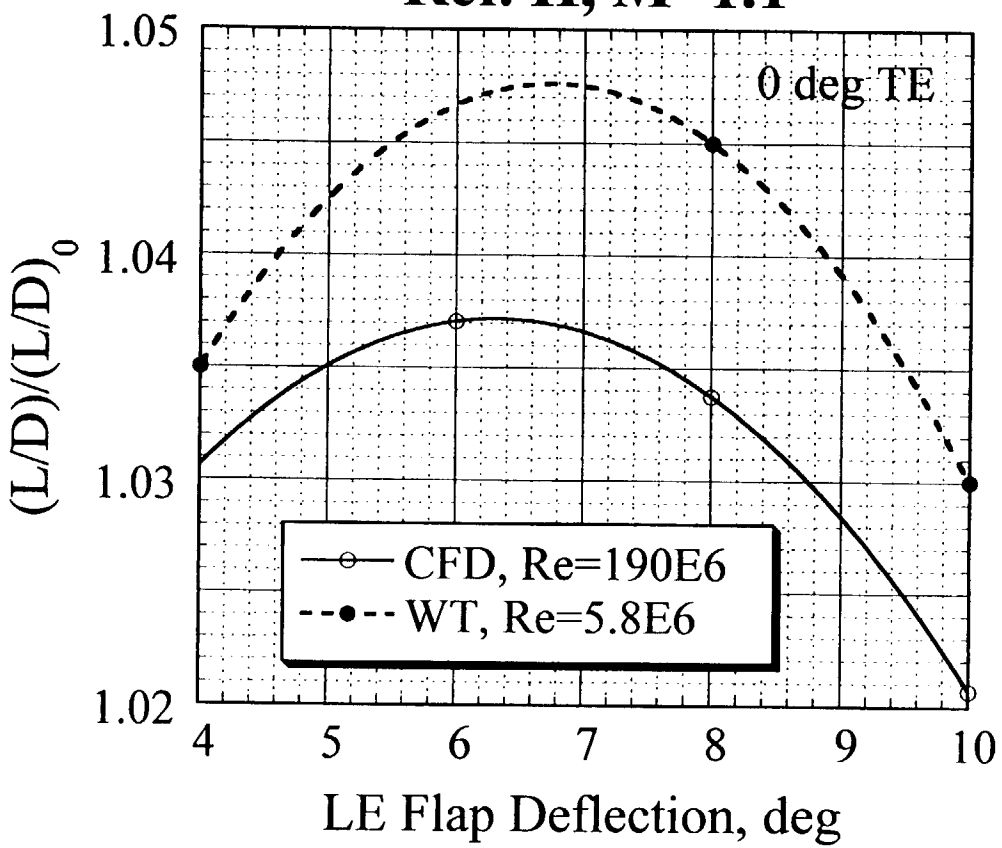

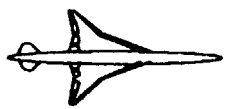

Surface Pressure Coefficient for Ref. H for 6/0 deg flaps at M=1.1

This figure presents the surface CP for the 6/0 deg flaps at alpha=4 deg. A conical region of compression downstream of the hingeline is noted on the upper surface of the outboard wing.

Ref. H Transonic Flaps (6/0 deg); M=1.1, α=4 deg, Re=171E6

Surface Pressure Coefficient (OVERFLOW)

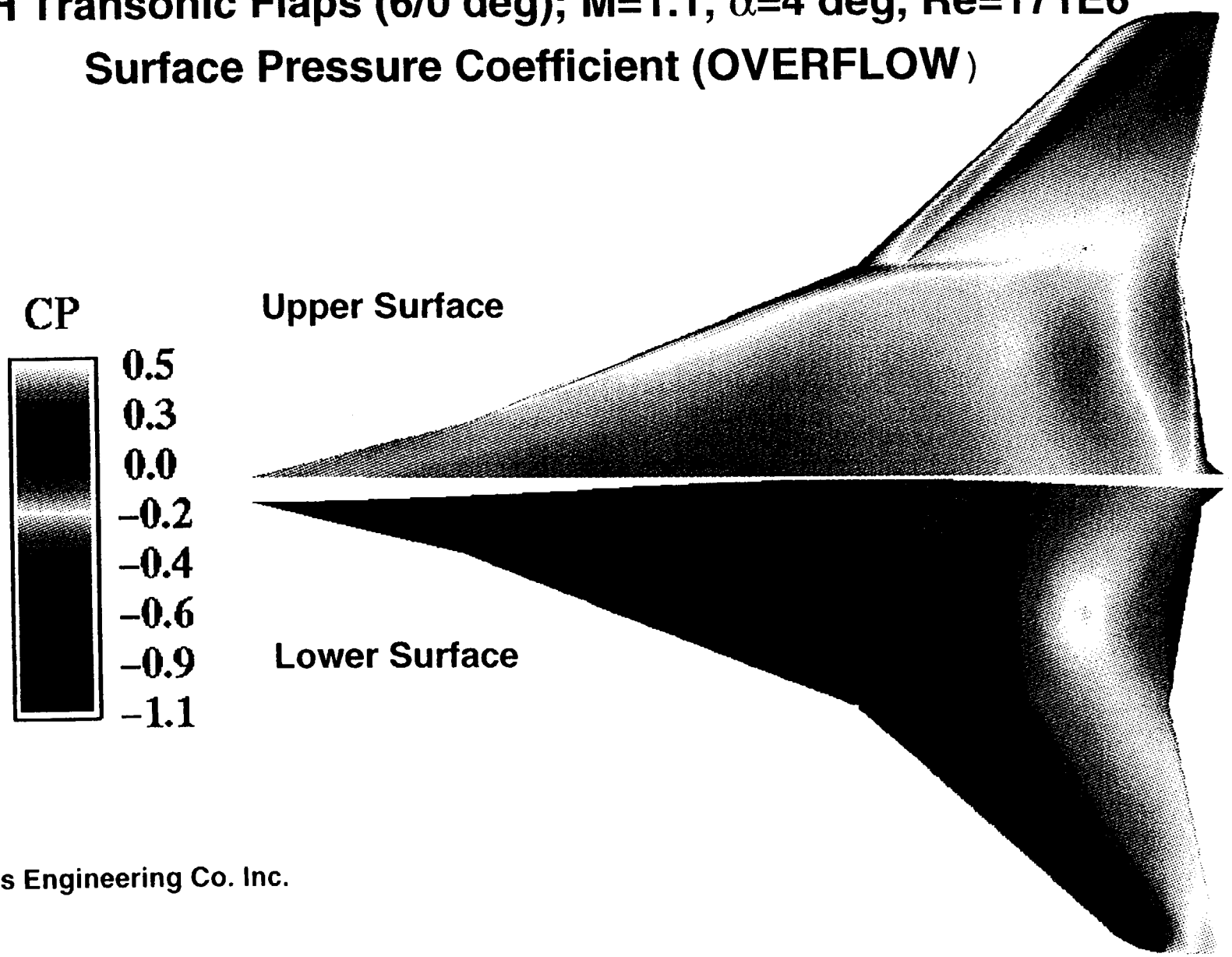

Dynacs Engineering Co. Inc.

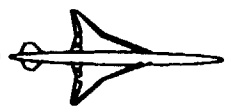

Surface Streamlines for Ref. H for 6/0 deg flaps at M=1.1 (expanded view)

The surface streamline plot for the 6/0 deg flaps at M=1.1 indicates a leading edge vortex separation. No hingeline flow separation is noted for this case.

Ref. H Transonic Flaps (6/0 deg); M=1.1, α=4 deg, Re=171E6

Surface Streamlines (OVERFLOW)

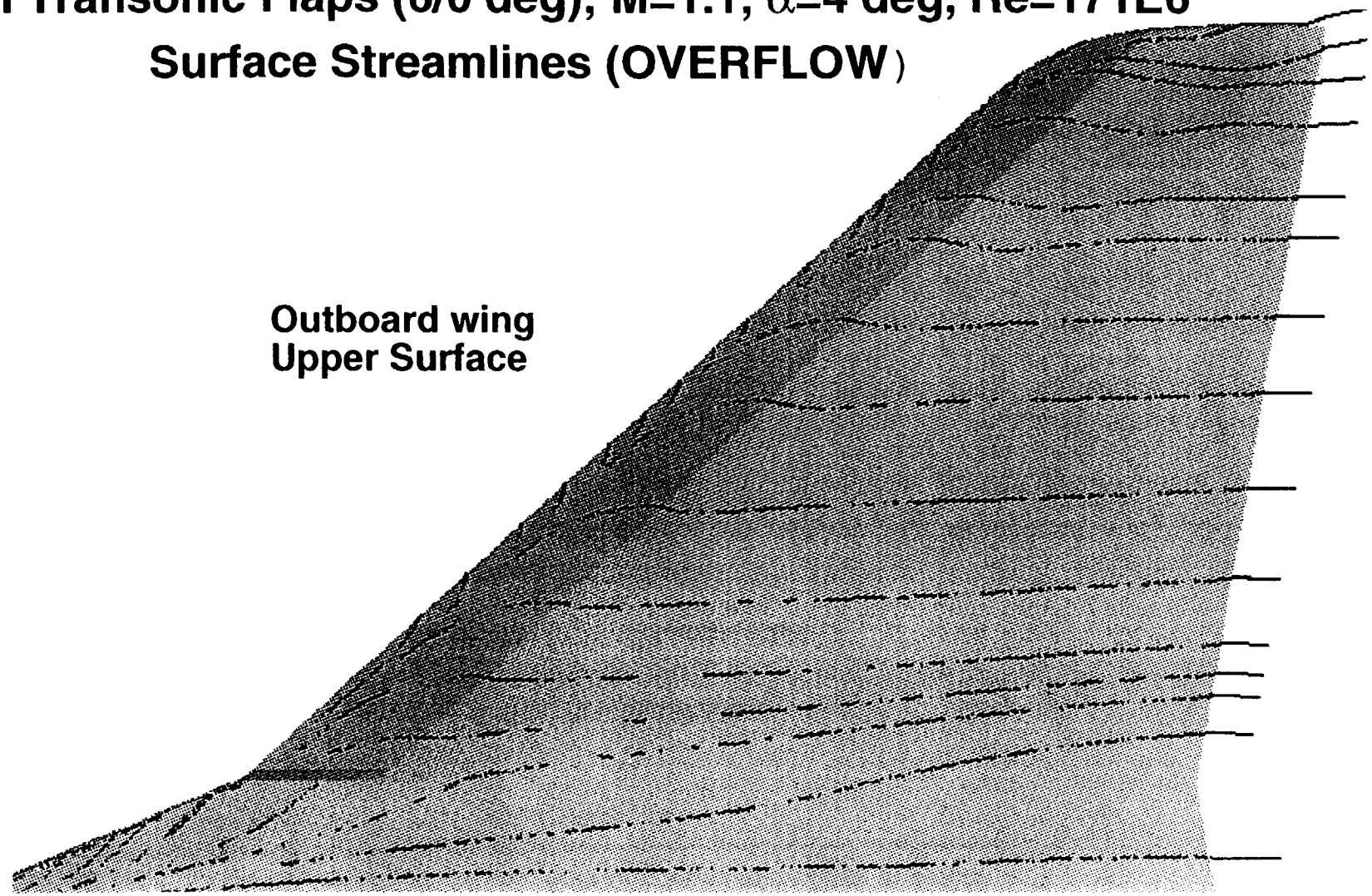

Dynacs Engineering Co. Inc.

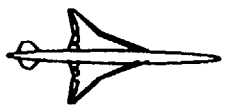

TCA Flap Optimization

TCA Surface Grid for the Outboard Wing

Shown in this figure is a typical surface grid (221x83) for the TCA outboard wing, indicating the grid distribution and areas of grid clustering. The total number of grid points in the entire grid system is 5E6, which includes body, inboard wing, collars, box and the outermost ellipsoid.

TCA Surface Grid for Outboard Wing

221x83 grid

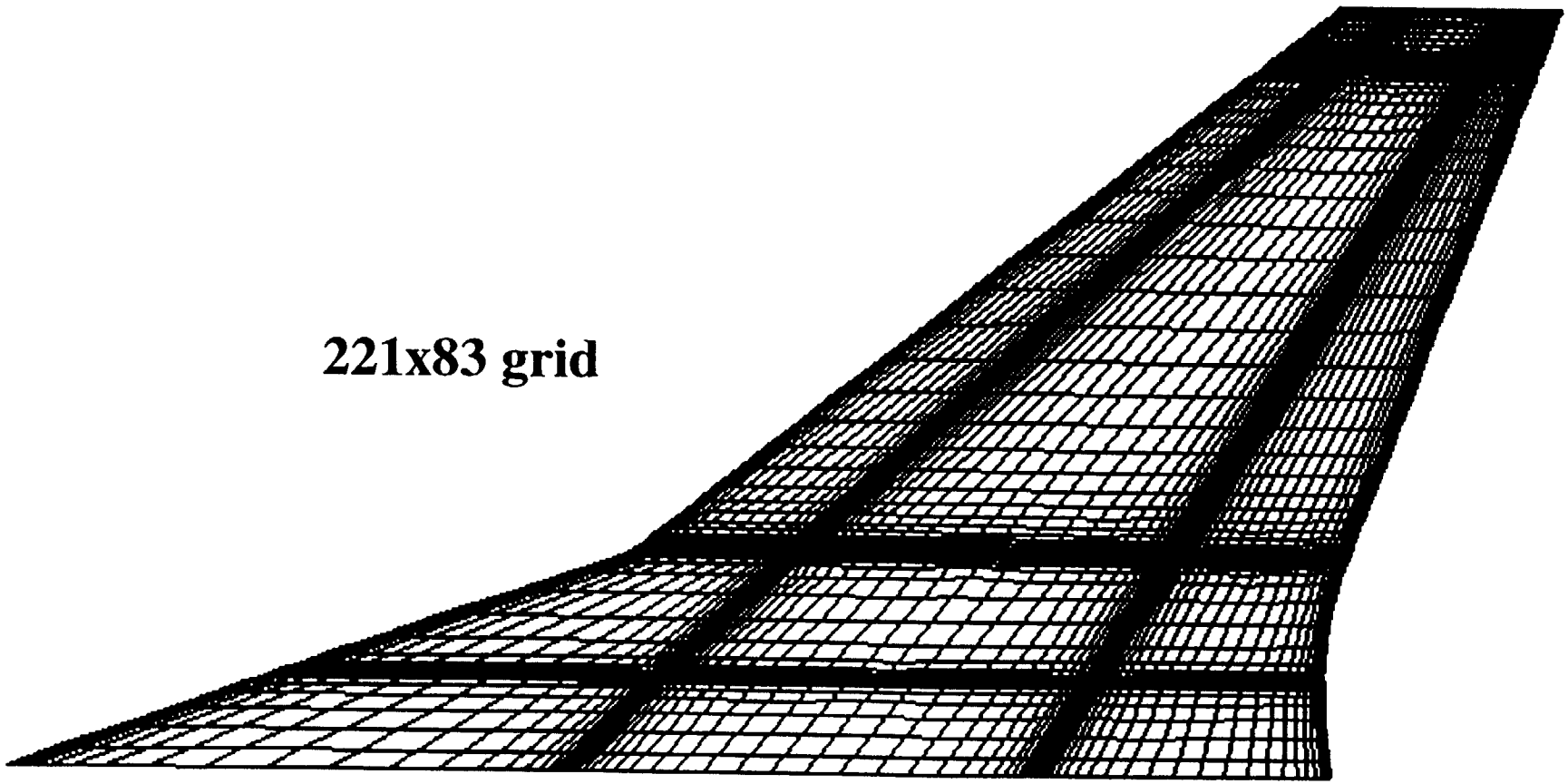

Dynacs Engineering Co. Inc.

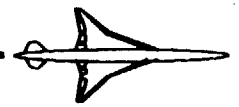

Flap Angle Matrix for TCA

This table shows the flap angle matrix considered for the TCA flap optimization. Based on the available wind tunnel data and CFD solutions for Ref. H, a relatively sparse matrix of flap deflections was constructed. At M=0.9, TE flap deflection of 1.5, 3, 4.5 and 8deg, and LE flap deflections of 6,8 and 10 deg are considered. At M=1.1, the TE flap is set at 0 deg, and the LE flap angles of 0, 4 and 6 deg are included. In addition, the baseline case of 0/0 deg is computed. The drag polar for each LE/TE flap geometry was again based on a quadratic curve fit through solutions for alpha=2, 4 and 6 deg. A typical OVERFLOW solution converges in about 3200 iterations, and requires about 23 CPU hours on C-90.

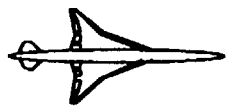

TCA Flap Angle Matrix

M = 0.9

TE, deg \ LE, deg	0	6	8	10
0	X			
1.5			X	
3			X	
4.5			X	
6		X	X	X
8			X	

M = 1.1

TE, deg \ LE, deg	0	4	6
0	X	X	X

Drag Polars for TCA LE flap of 8 deg at M=0.9

In this figure, an expanded drag polar for the TCA at M=0.9 for a constant LE flap angle of 8 deg. The drag for the 8 deg TE flap is considerably increased due to the TE flap flow separation.

Drag Polar (Exp. View)

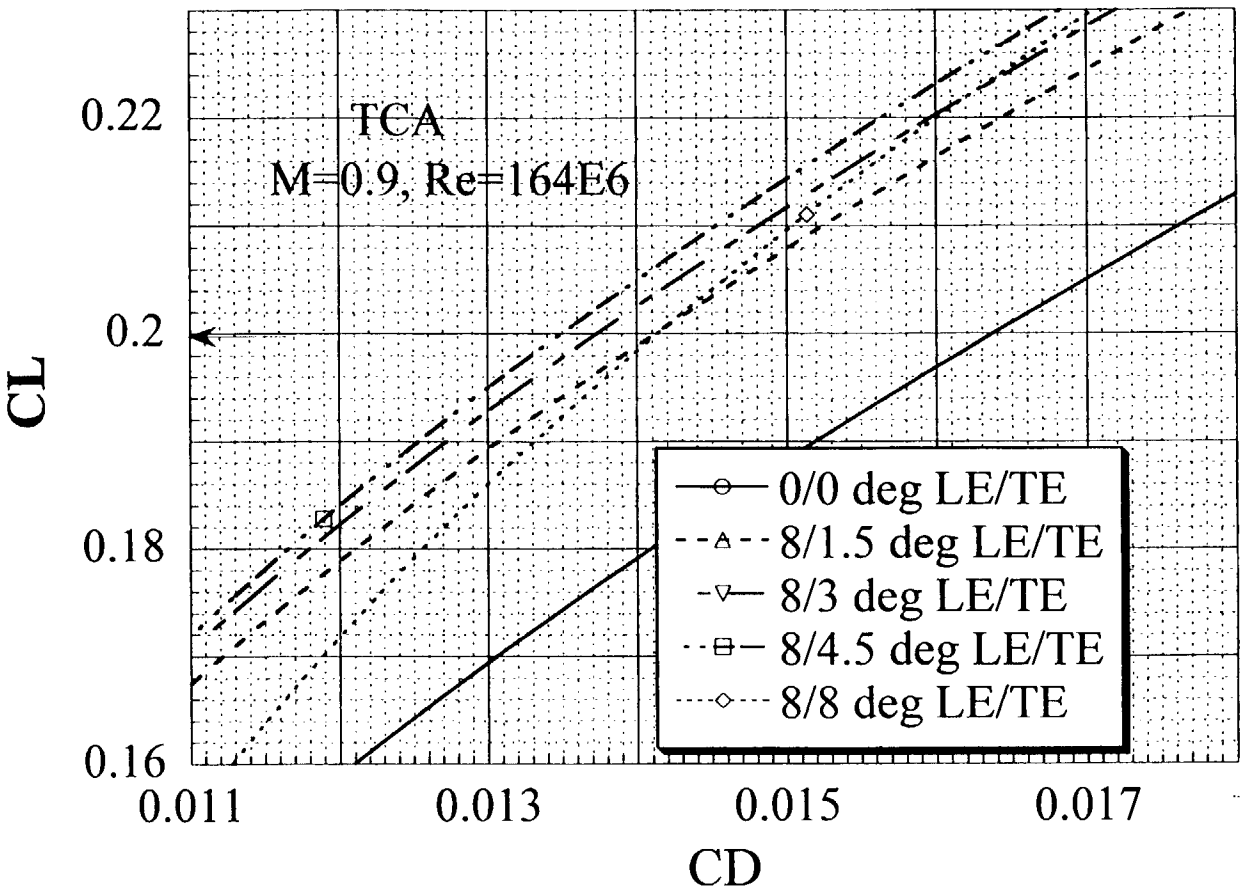

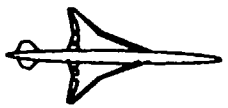

Trailing Edge Flap Optimization (First Level) for TCA at M=0.9

This plot shows the outcome of the TE flap optimization, with the LE flap set at 10 deg. In this figure, the variation of L/D corresponding to design CL=0.2 is plotted as a function of TE flap angle. The solid line due to the curve fit suggests that the optimum TE deflection is about 5.2 deg, resulting in the maximum L/D of about 14.85. The L/D value for the baseline case (undeflected flaps; 0/0 deg) is 12.216. This suggests an improvement in L/D of about 21.6 percent. This compares with the predicted benefit of 22.3 percent for Ref. H at M=0.9.

Trailing Edge Flap Optimization

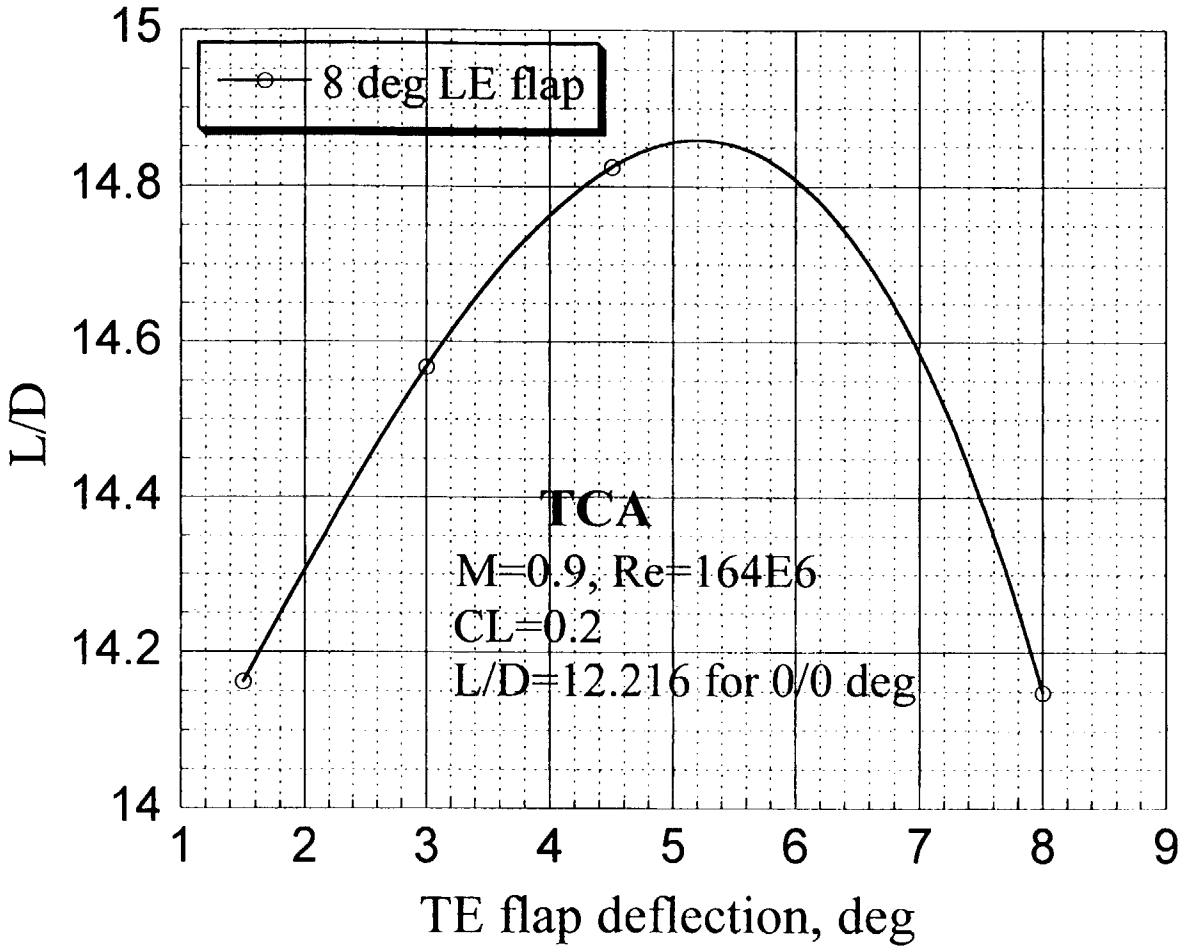

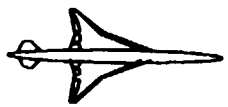

Comparison of TE Flap Performance for TCA at M=0.9

This plot presents a comparison of the TE flap performance for TCA with 8 deg LE flap at M=0.9 for flight Re and wind tunnel Re. The wind tunnel data for 1.675% TCA model are obtained from Kevin Mejia of Boeing HSCT (Ref. Kevein Mejia, Test summary- TCA model 2a at LaRC 16 ft Transonic Wind Tunnel (Test #484), Boeing HSCT Rept. AERO-BB155-C96-007, December 1996).

The baseline values of L/D are 12.216 at flight Re=164E6, and 10.695 at WT Re=6E6. The results suggest that at flight Re 5 deg TE flap is the best (providing about 21.5 percent benefit), while the WT data show that 6 deg TE is the best with a L/D benefit of 16 percent (although the WT data beyond 6 deg TE flap angle is unavailable, where TE flap flow separation may be present). Thus it appears that the optimum TE flap deflection at flight Re is about one deg less than that at WT Re. This result is attributable to the decambering effect of the boundary layer at the wind tunnel Re.

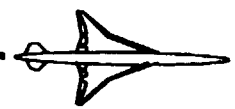

Comparison of TE Flap Performance

TCA, M=0.9

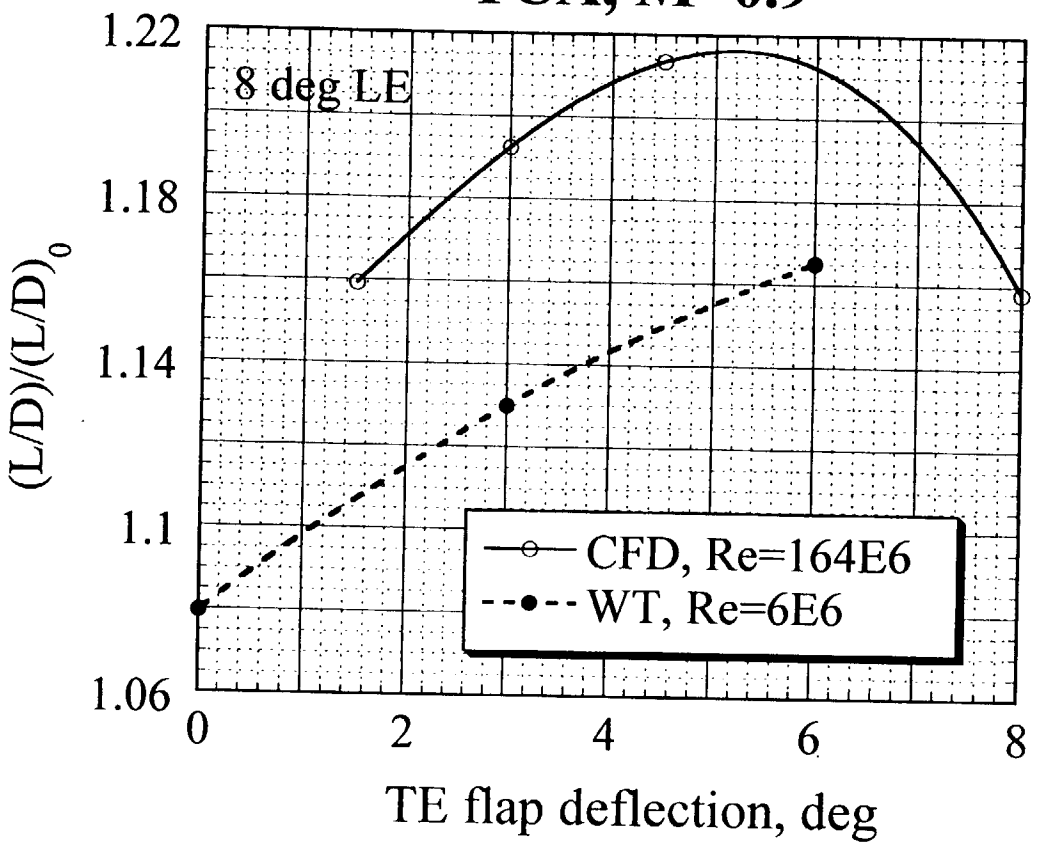

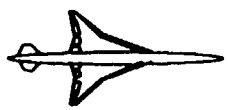

Drag Polars for TCA TE flap of 6 deg at M=0.9

An expanded drag polar for the TCA at M=0.9 for a constant TE flap angle of 6 deg. A drag benefit of about 28 counts is noted for the 8/6 deg flap relative to the base line case. The crossover of the polars for the 8/6 deg and the 10/6 deg flaps occurs at about CL=0.2. The TCA wind tunnel data at Re=6E6 indicate that at the best Wing/Body subsonic flap setting of 8/6 deg LE/TE flaps, a drag reduction of 26.5 counts was observed. The data uncertainity is believed to be within 1.5 counts.

Drag Polar (Exp. View)

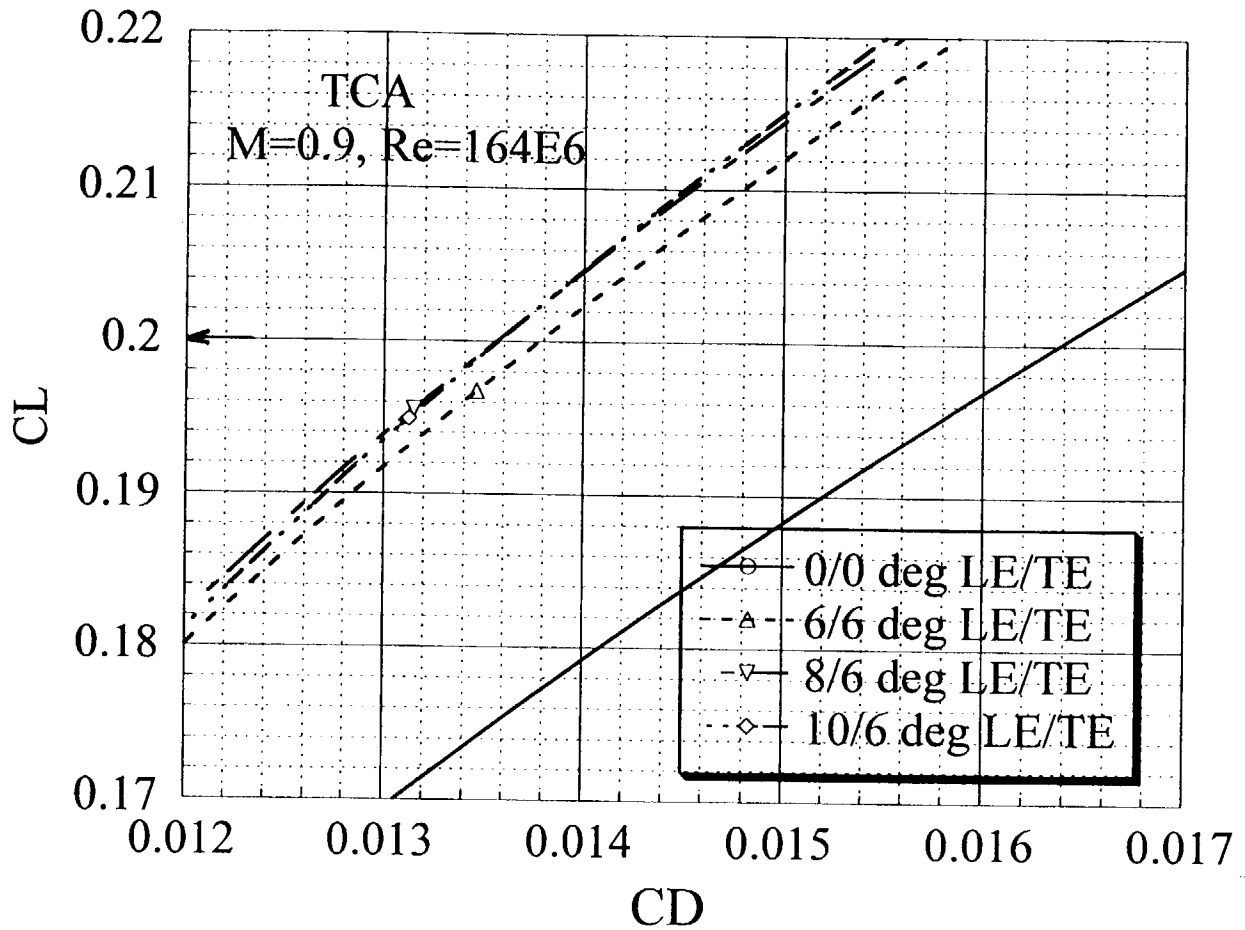

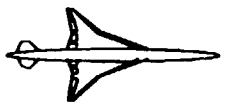

Leading Edge Flap Optimization for TCA at M=0.9

The variation of L/D with the LE flap deflection at a fixed TE flap angle of 6 deg is plotted in this figure. This result indicates that the optimum LE flap deflection is close to 9 deg, with a maximum L/D of 14.77. Thus it appears that the 9/5 .2 deg flap setting represents the optimum flap configuration at M=0.9. This optimum case corresponds to an angle of attack of 4 deg. As mentioned earlier, the wind tunnel data at Re=6E6 suggest that the 8/6 deg flap performs best at M=0.9 and CL=0.2, with a drag benefit of 26.5 counts.

Leading Edge Flap Optimization

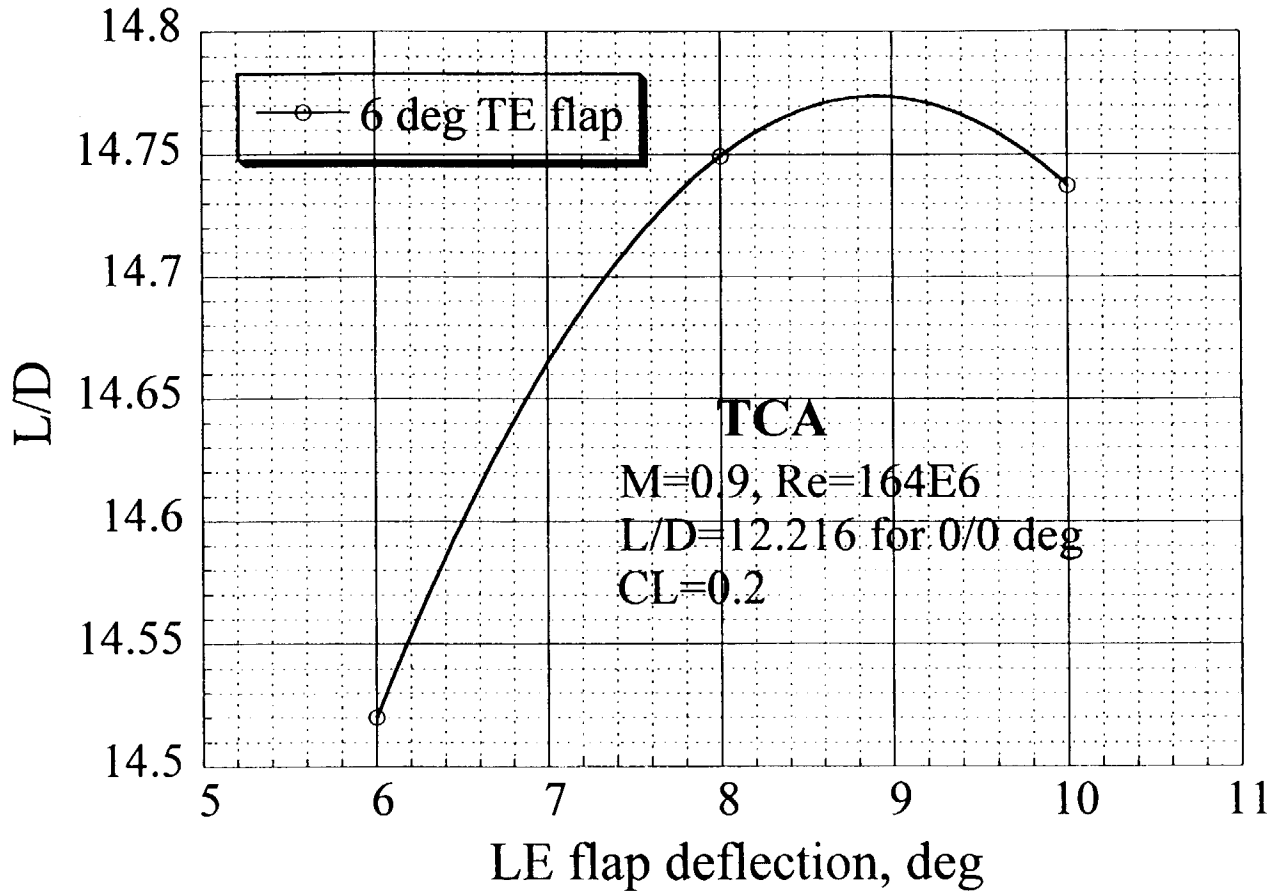

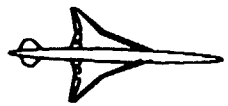

Comparison of LE Flap Performance for TCA at M=0.9

This plot displays a comparison of the LE flap performance for TCA at M=0.9 with the TE flap set 6 deg. The flight CFD shows that 9 deg LE flap performs the best (21 percent enhancement in L/D) , whereas the WT data (curve fit) suggest that 8.5 deg LE flap is optimum with a 16.5 percent improvement in L/D. Thus the optimum LE flap deflection at flight Re is about 0.5 deg larger than that at the wind tunnel Re.

Comparison of LE Flap Performance

TCA, M=0.9

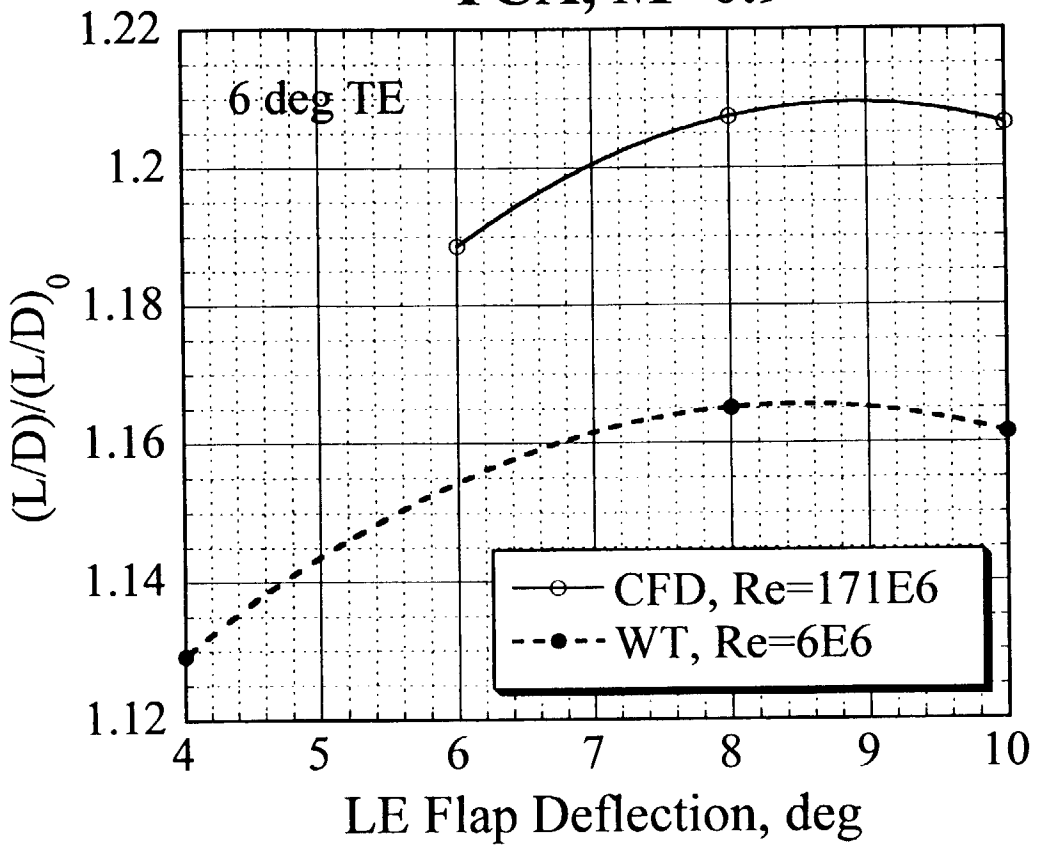

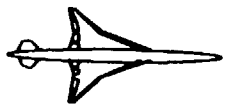

Surface Pressure Coefficient for TCA for 8/4.5 deg flaps at M=0.9 and alpha=4 deg

This figure presents the surface pressure coefficient distribution for the TCA **8/4.5 deg** flaps at M=0.9 and alpha=4 deg. At this condition, the attachment line is on the lower surface of the outboard wing, and a vortex separation of small extent is noted on the upper surface leading edge. The leading edge vortex on the inboard wing upper surface is also seen.

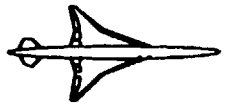

TCA Transonic Flaps (8/4.5 deg); M=0.9, α=4 deg, Re=164E6

Surface Pressure Coefficient (OVERFLOW)

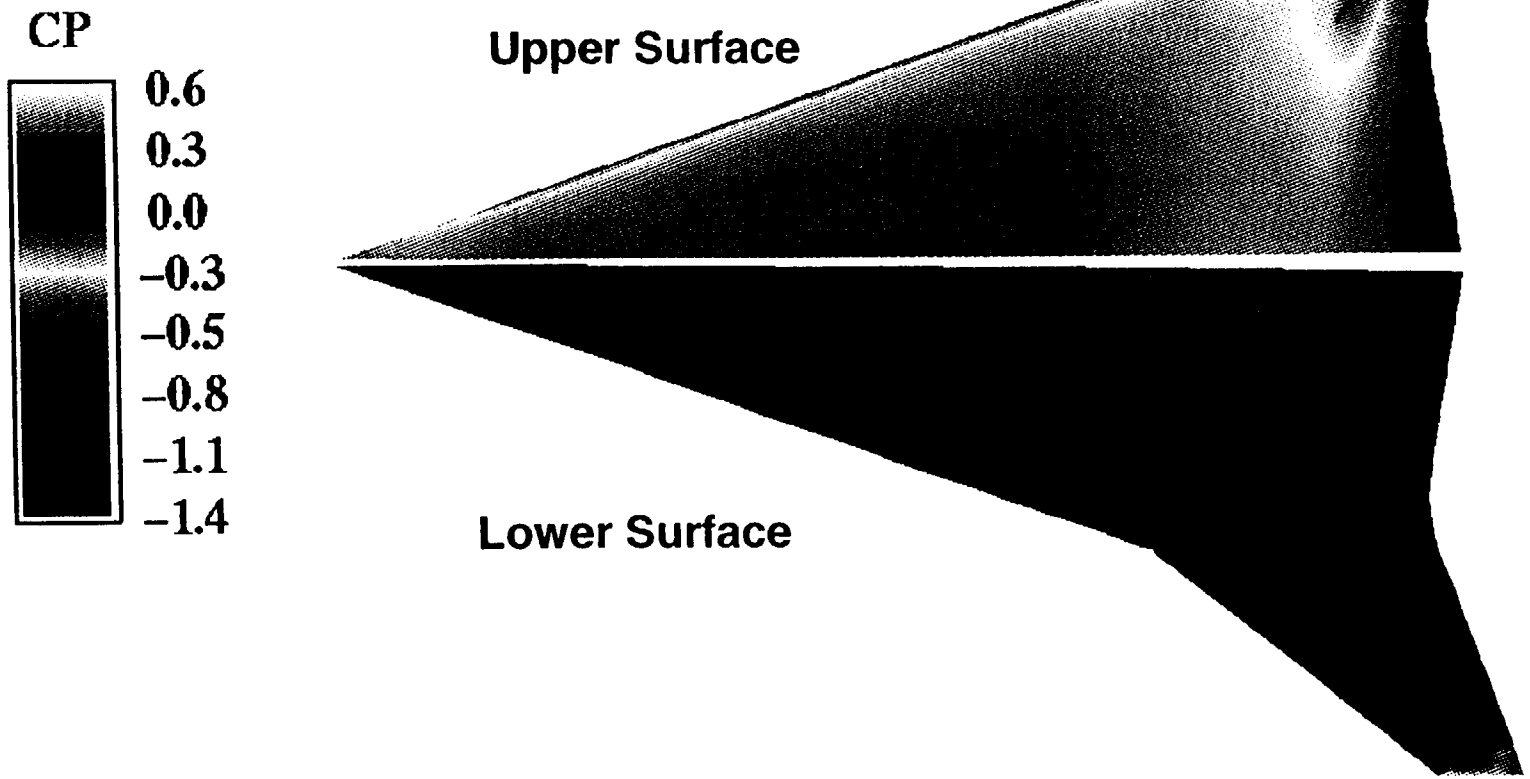

Dynacs Engineering Co. Inc.

Surface Streamlines for TCA for 8/4.5 deg flaps at M=0.9 and alpha=4 deg

The surface streamline pattern for the 8/4.5 deg flaps at alpha=4 deg suggests the absence of flow separation near the hingelines or the trailing edge flaps.

TCA Transonic Flaps (8/4.5 deg); M=0.9, α=4 deg, Re=164E6

Surface Streamlines (OVERFLOW)

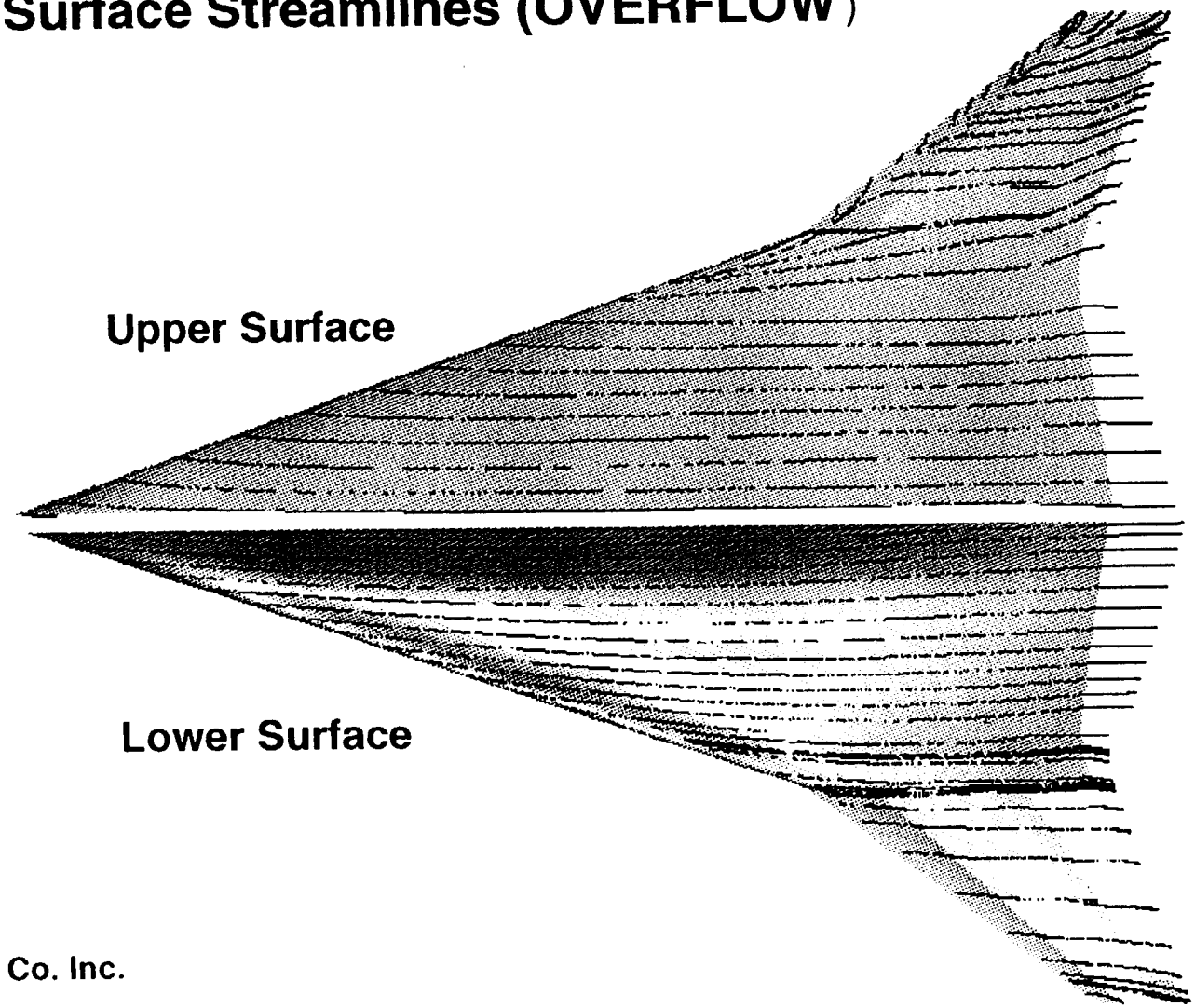

Dynacs Engineering Co. Inc.

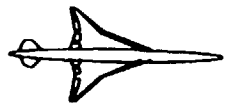

Surface Streamlines for TCA for 8/4.5 deg flaps at M=0.9 (expanded view)

An expanded view of the streamline pattern for the outboard wing is presented in this figure. The streamlines suggest that the flow on the TCA outboard wing is more spanwise than that for the Ref. H configuration.

TCA Transonic Flaps (8/4.5 deg); M=0.9, α=4 deg, Re=164E6
Surface Streamlines (OVERFLOW)

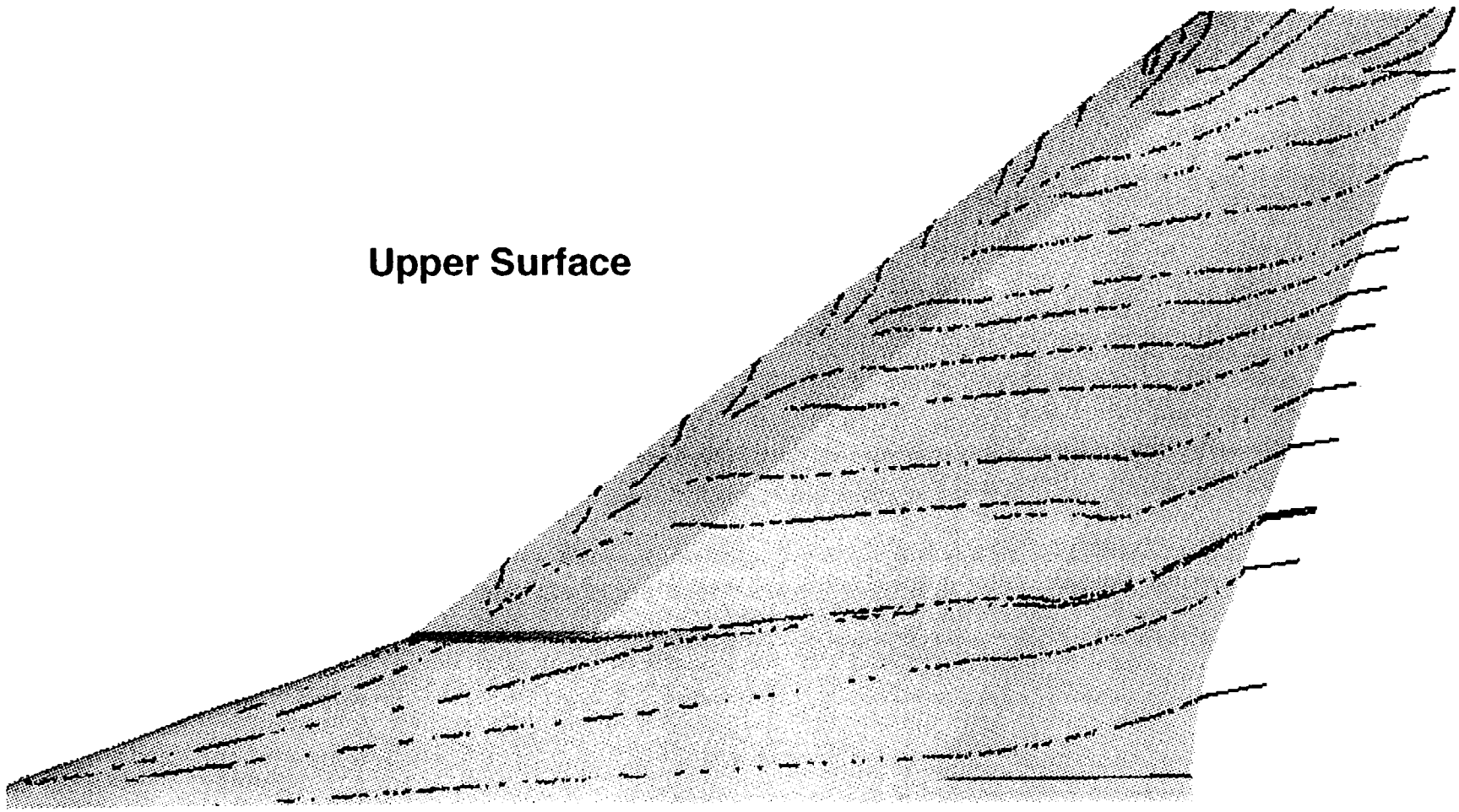

Dynacs Engineering Co. Inc.

Comparison of CL-alpha for the TCA 0/0 deg Flap at M=0.9

The next several figures illustrate a comparison of the TCA transonic flap predictions at flight Reynolds number with TCA wind tunnel data for CL-alpha and the drag polars. Comparisons are made here only for a few selected cases.

The CL-alpha comparison between the flight CFD (Re=164E6) and the wind tunnel data (Re=6E6) for the baseline case (0/0 deg flaps) at M=0.9 indicates close agreement, with the CL values slightly higher than those at wind tunnel Re. This result is to be generally expected for the case of undeflected flaps.

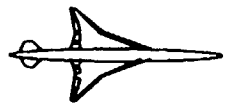

Comparison of CL-alpha

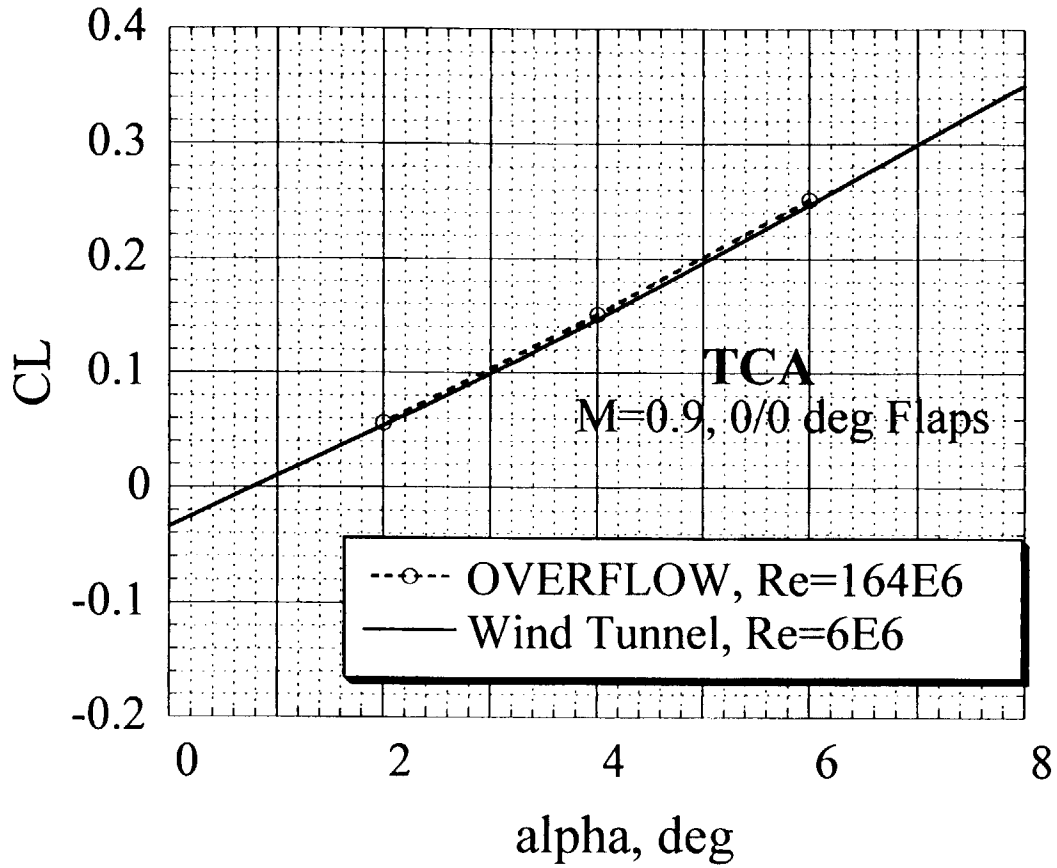

Comparison of CL-alpha for the TCA 8/3 deg Flap at M=0.9

A comparison of the CL-alpha for the 8/3 deg flap suggests that the CL values for the flight CFD are somewhat higher than that for the wind tunnel data. The incremental CL due to changes in Re are higher for the 8/3 deg flaps than those for the 0/0 deg flaps.

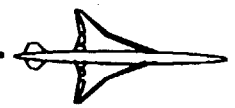

Comparison of CL-alpha

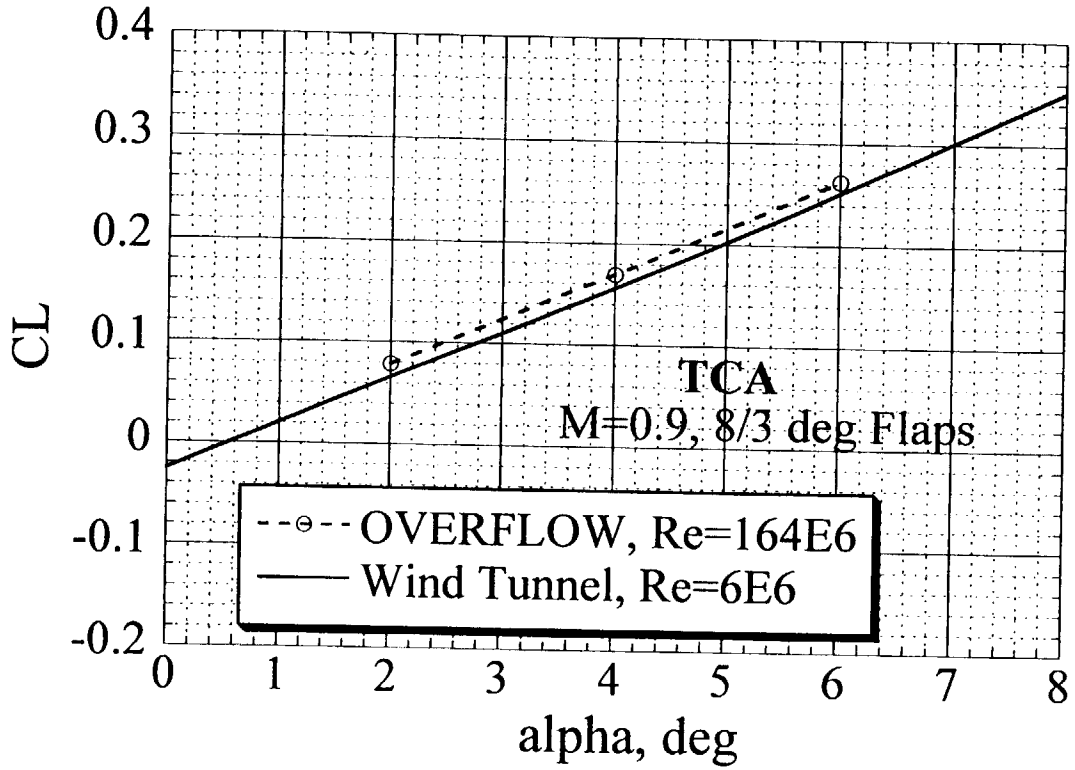

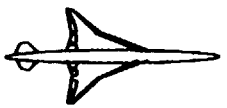

Comparison of CL-alpha for the TCA 8/6 deg Flap at M=0.9

A comparison of the CL-alpha for the 8/6 deg flap suggests that the CL values for the flight CFD are considerably higher than that for the wind tunnel data. Thus it is seen that with an increase in TE flap deflection, there is an increasing deviation between the CFD and the data. This discrepancy is believed to be a consequence of the dispalcement action of the boundary layer. At the flight Reynolds number, the boundary layer thickness at the trailing edge is considerably thinner (wing is less decambered), and is more resistant to separation as compared to that at the wind tunnel Reynolds number. The chordwise surface pressure distribution near the trailing edge is thereby altered as the Reynolds number increases from the wind tunnel value to the flight value (as demonstrated earlier by the computations for the Ref. H) so as to result in an increase in the flap benefit at the flight Re relative to that at the wind tunnel Re.

Comparison of CL-alpha

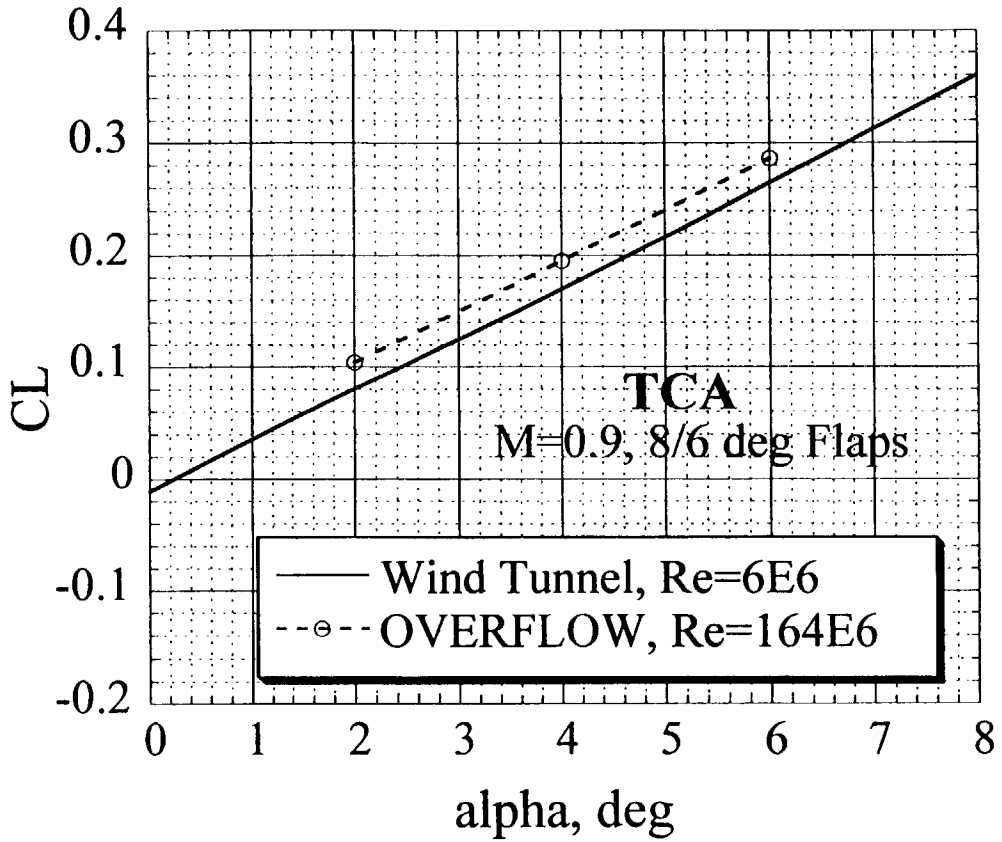

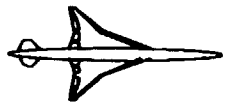

Comparison of Flap Effect on Incremental CL for the TCA at M=0.9

This figure illustrates a comparison of the incremental CL due to trailing edge flap deflection for the TCA at M=0.9. The comparison is made between the wind tunnel data at Re=6E6 and the OVERFLOW predictions at Re=164E6 for the 8/3 deg flaps and the 8/6 deg flaps. The wind tunnel measurements indicate a peak in incremental CL at about alpha=2 deg. Although the shapes of incremental CL vs. alpha for the wind tunnel data and the flight CFD, the computed flap increments in CL at flight Reynolds number considerably exceed those at wind tunnel Re (a factor of about two at alpha=2 deg) for both the 8/3 deg flaps and the 8/6 deg flaps. This discrepancy is perhaps due to the displacement effect of the boundary layer near the trailing edge flap, as discussed earlier. At a given Reynolds number (both wind tunnel and flight), the incremental CL is progressively higher as the TE flap deflection is increased in the range of alpha considered here.

Flap Effect on Incremental CL

(relative to baseline 0/0 deg flaps)

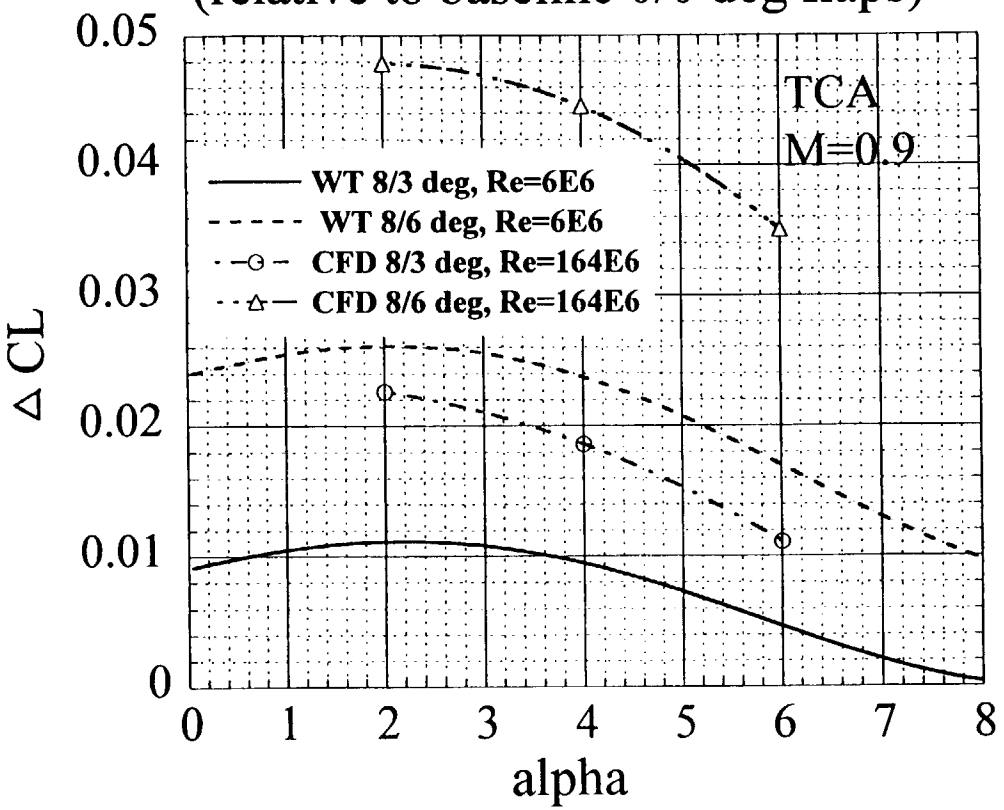

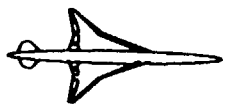

Comparison of Drag polar for the TCA 8/6 deg Flap at M=0.9

In this plot, a comparison of the drag polar for the TCA 8/6 deg flap at M=0.9 is made for the wind tunnel and the flight case. At a given CL, the lower total drag for the flight case is primarily due to reduced skin friction drag at the higher Reynolds number. A more direct comparison can be made if CFD computations are performed at the wind tunnel Re. However in the present case, simple flat plate theory (Sommer-Short) is used to predict the skin friction drag for the wind tunnel Reynolds number and flight Reynolds number (85.5 counts viscous drag at Re=6E6, and 52.5 counts viscous drag at Re=164E6). The OVERFLOW computations at Re=164E6 provide skin-friction drag of 50.6 counts, 49.8 counts and 50 counts at alpha=2.4, and 6 deg respectively, indicating good agreement with the flat plate theory. Previous computations for Ref. H 10/3 deg flaps at wind tunnel Reynolds number of 6E6 and 30E6 also show good agreement wih the flat plate theory.

The incremental CDV of 33 counts in skin friction drag as obtained from the flat plate theory due to a change of Re from 164E6 to 6E6 is now applied to the OVERFLOW result at Re=164E6 to obtain an estimate of the computed drag polar at Re=6E6, assuming that the pressure drag CDP is the same at the wind tunnel Re and the flight Re. The agreement in the polars (wind tunnel data polar and the estimated polar) at Re=6E6 is good only at alpha=6 deg, and progressively diminishes as alpha is decreased to 2 deg (10 counts deviation), thus causing a shift in the polar shape. This discrepancy in the drag polars at Re=6E6 is perhaps due to the fact that the assumption of equality of pressure drag at the wind tunnel and the flight Re is questionable, in view of the significant deviations in the incremental CL for the 8/6 deg flaps at the two Reynolds numbers. Uncertainty in the accuracy of the one-equation Baldwin-Barth turbulence model in the prediction of the pressure drag at low angles of attack. (where flow separation takes place near the lower surface of the outboard wing leading edge), as evidenced in the Ref. H study, also contribute to the deviations in the polars.

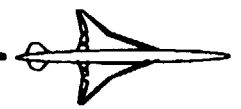

Comparison of Drag Polar

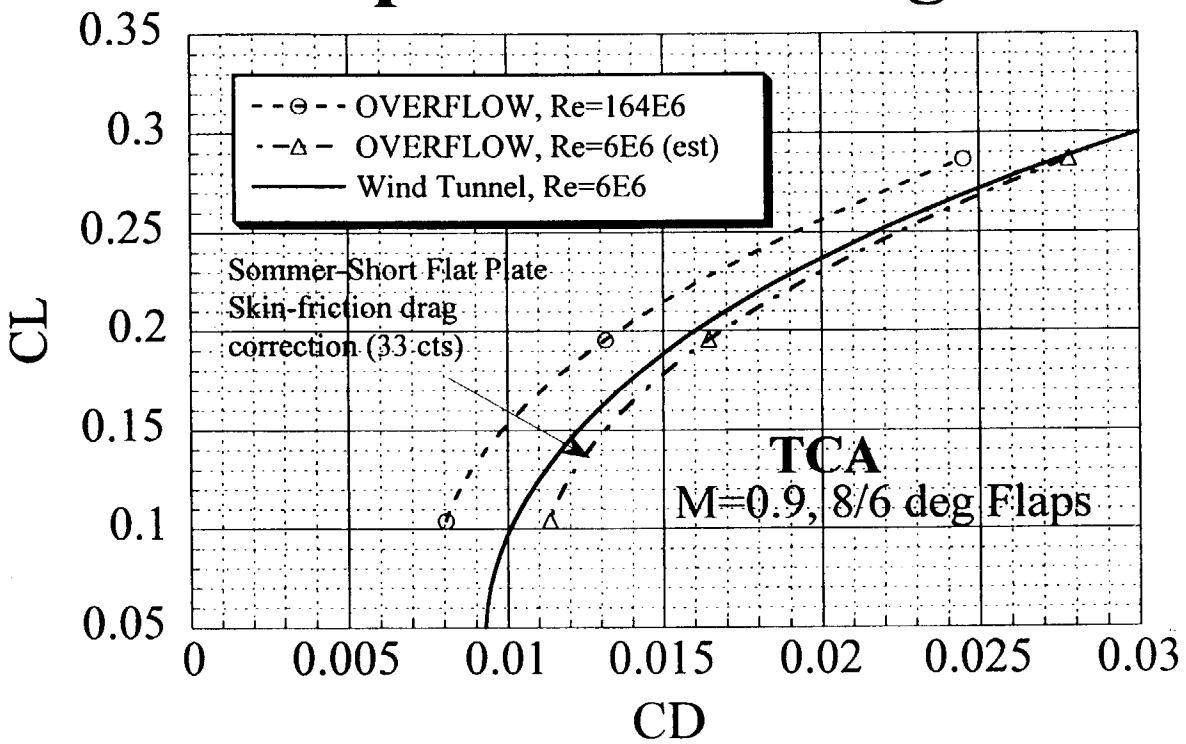

Drag Polars for TCA at M=1.1 (Expanded View)

For the low supersonic case (M=1.1), the leading edge flap is optimized with the trailing edge flap fixed at 0 deg. Three leading edge flap deflections (0,4 and 6 deg) are considered for this purpose. Typical drag polars for M=1.1 at various LE flap deflection are illustrated in this figure. The polars are generated from a quadratic fit of data at three values of alpha=2, 4 and 6 deg. At the design CL of 0.175, a drag benefit of about 6.5 counts is noted for the 6/0 deg flap relative to the baseline case.

Drag Polar (Exp. View)

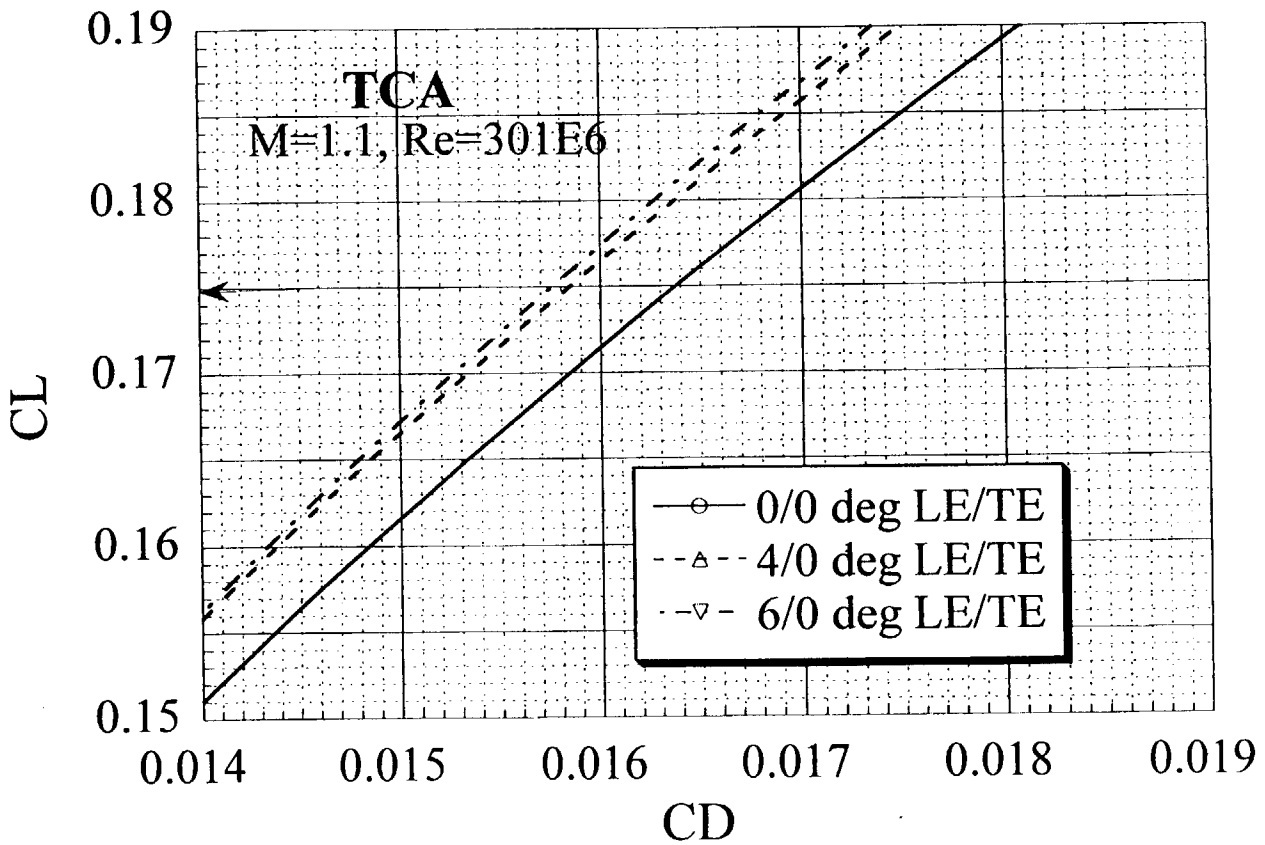

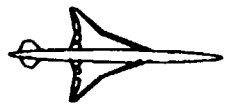

Leading Edge Flap Optimization for TCA at M=1.1 and Re=301E6

This plot depicts the variation of L/D with the leading edge flap deflection. The result suggests that a 6 deg LE flap is the optimum case, resulting in a maximum L/D of 11.1. The L/D for the baseline case is 10.686. Thus a benefit in L/D of 3.9 % is realized. For comparison, the wind tunnel data for the TCA at Re=6E6 demonstrate that at M=1.07 and CL=0.16, the 4/3 deg flap performs the best with a benefit of 4.3 counts relative to the baseline case.

Leading Edge Flap Optimization

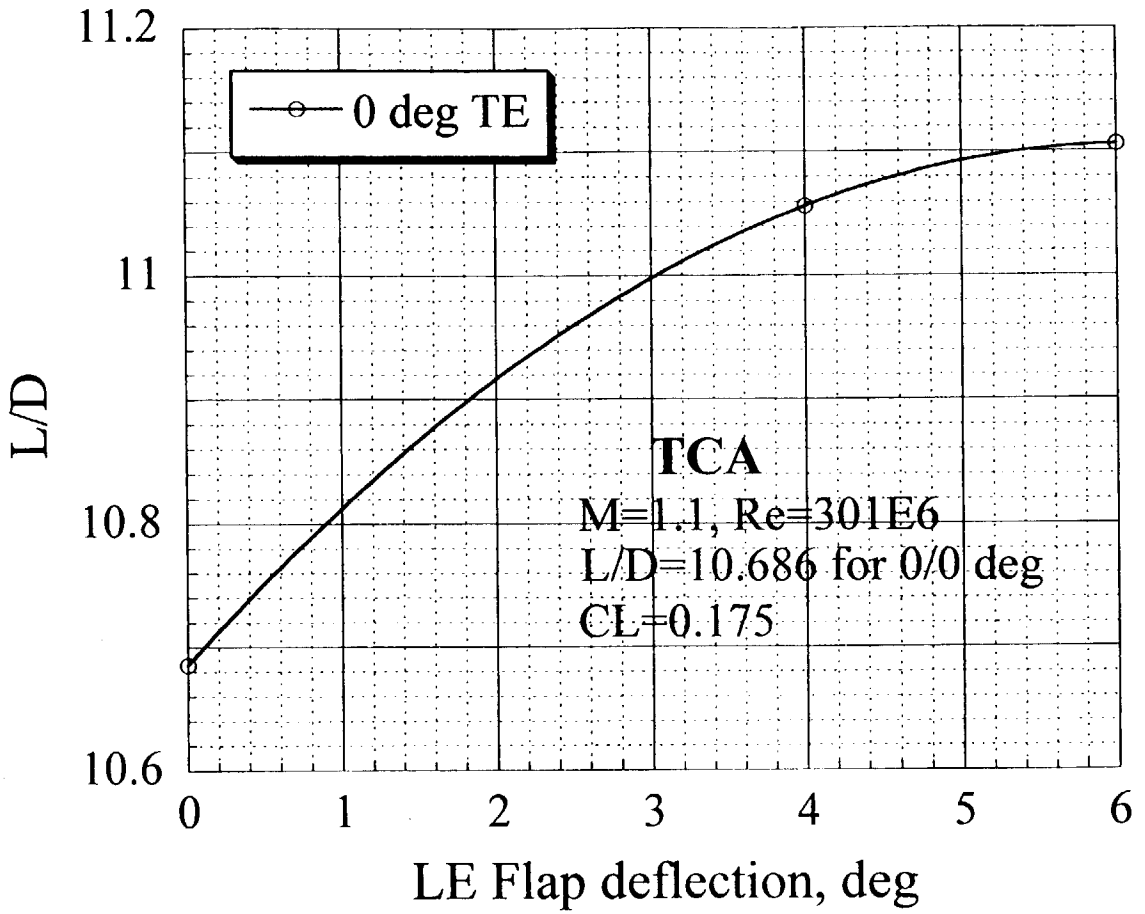

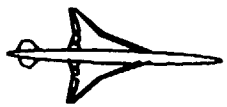

Comparison of LE Flap Performance for TCA at M=1.1

For the TCA at M=1.1 and a TE flap delfection of 0 deg, the optimum flight LE flap deflection is found to be 6 deg, which results in about four percent benefit in L/D relative to the baseline. The baseline L/D values are 10.686 at flight Re=301E6, and 9.09 at WT Re=6E6. Since the wind tunnel data with flap deflections are not avilable at M=1.1, data at M=1.07 are compared here. The wind tunnel data shows that the 7 deg LE flap performs the best at the wind tunnel Re with a 0 deg TE flap. With a 3 deg TE flap, the wind tunnel performance is seen to be better than that with 0 deg TE flap.

Comparison of LE Flap Performance

TCA, M=1.1

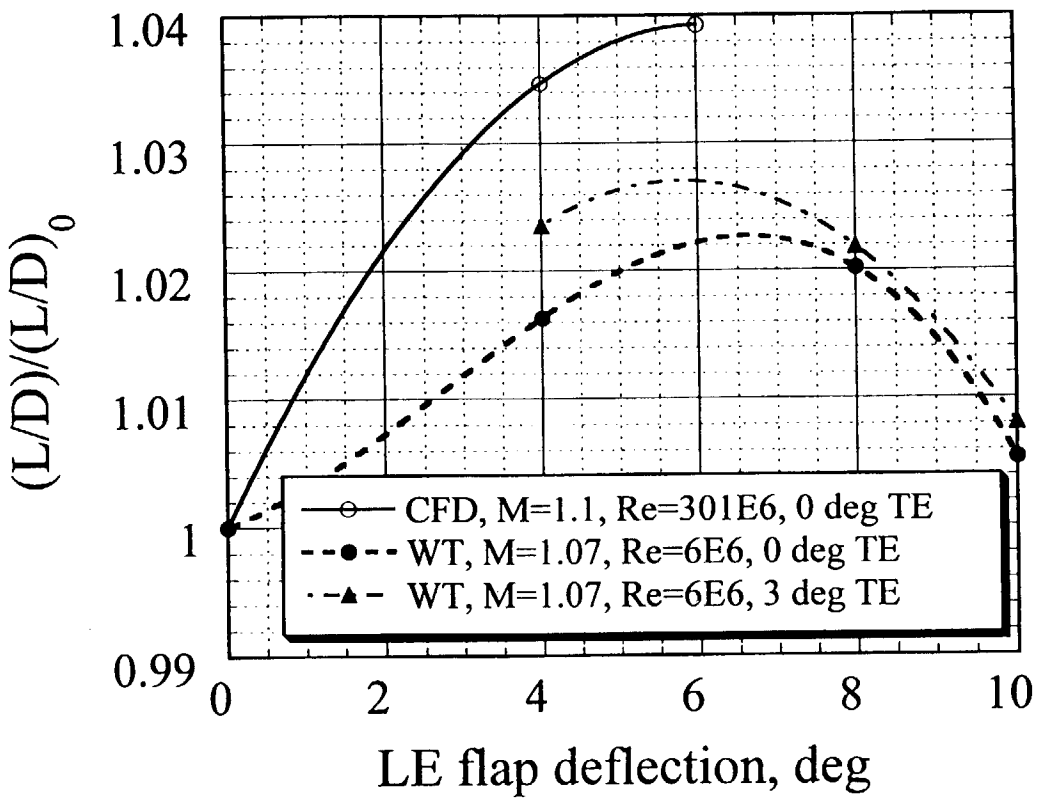

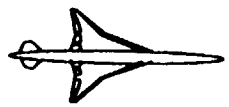

Surface Pressure Coefficient for TCA for 6/0 deg flaps at M=1.1

This figure presents the surface CP for the 4/0 deg flaps at M=1.1 and alpha=4 deg. A conical region of compression downstream of the hingeline is noted on the upper surface of the outboard wing.

TCA Transonic Flaps (6/0 deg); M=1.1, α=4 deg, Re=301E6

Surface Pressure Coefficient (OVERFLOW)

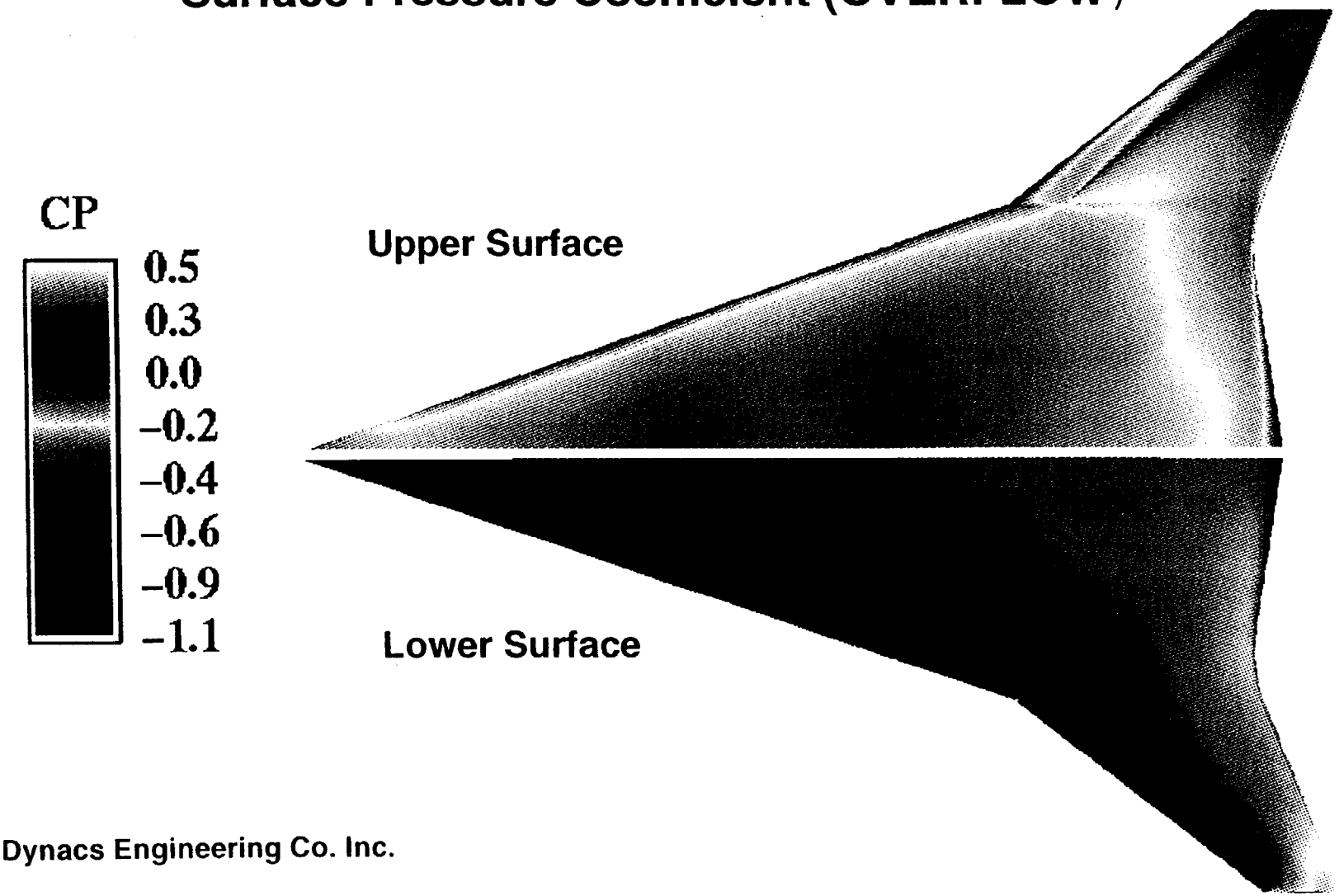

Dynacs Engineering Co. Inc.

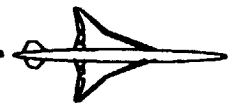

Surface Streamlines for TCA for 6/0 deg flaps at M=1.1 (expanded view)

The surface streamline plot for the 6/0 deg flaps at M=1.1 indicates a leading edge vortex separation on the outboard wing upper surface. No hingeline flow separation is noted for this case.

TCA Transonic Flaps (6/0 deg); M=1.1, α=4 deg, Re=301E6
Surface Streamlines (OVERFLOW)

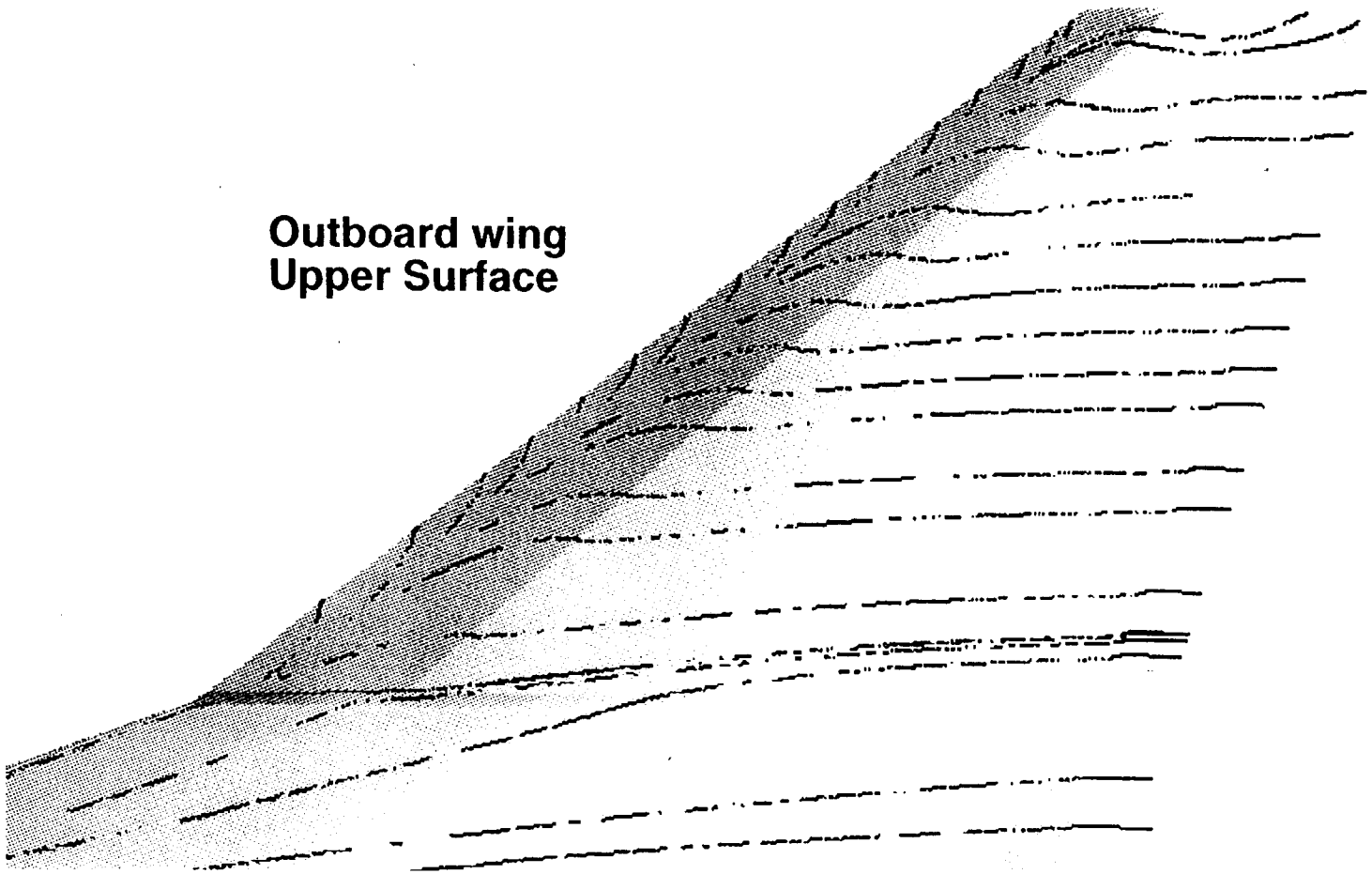

Dynacs Engineering Co. Inc.

Comparison of CL-alpha for the TCA 4/0 deg Flap at M=1.1

This plot dispalys a comparison of the CL-alpha curve for the 4/0 deg flaps at M=1.1. Satisfactory comparison is noted between the CFD and the wind tunnel data. This result suggests that the leading edge flap deflection does not introduce any appreciable Reynolds number effect on CL.

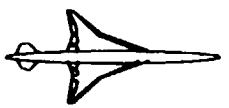

Comparison of CL-alpha

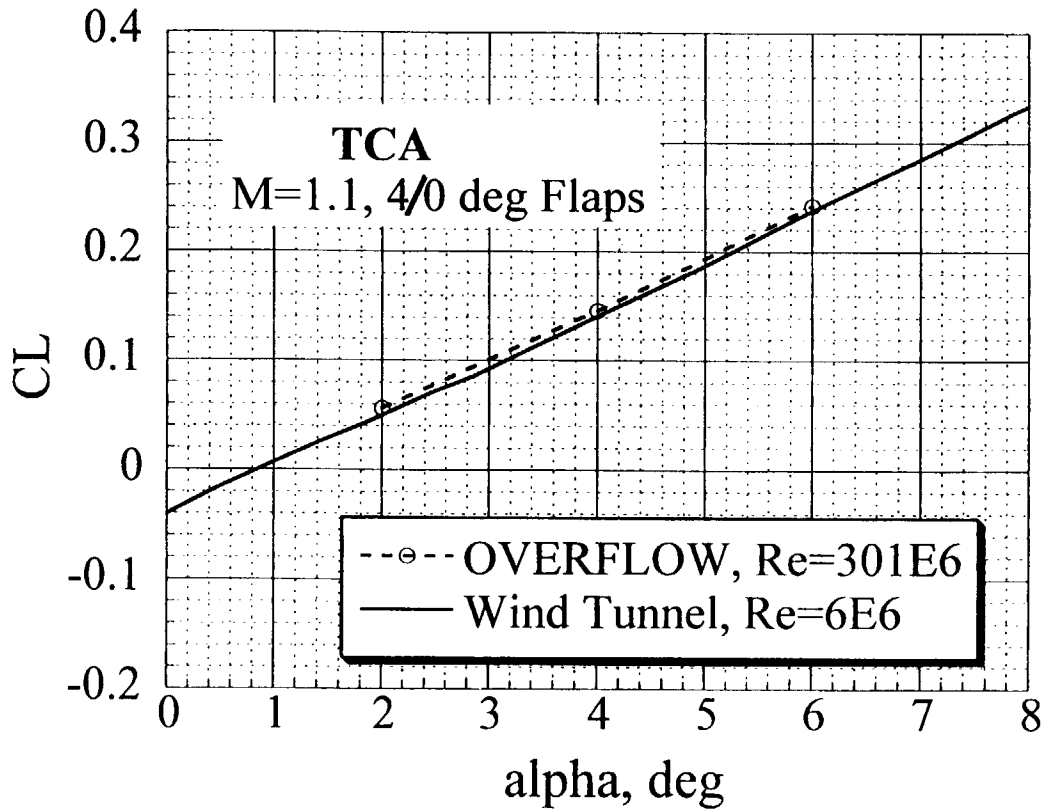

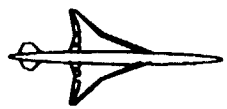

Comparison of Drag Polar for the TCA 4/0 deg Flap at M=1.1

In this plot, a comparison of the drag polar for the TCA 4/0 deg flap at M=1.1 is made for the wind tunnel and the flight case. The Sommer-Short flat plate theory predicts the skin friction drag of 83.1 counts at the wind tunnel Reynolds number of 6E6, and 46.7 counts at the flight Reynolds number of 301E6. The OVERFLOW computations at Re=301E6 produce skin-friction drag close to that of the flat plate theory (45.5 counts, 44.3 counts and 43.7 counts at alpha=2.4, and 6 deg respectively).

The incremental CDV of 36.4 counts in skin friction drag as obtained from the flat plate theroy due to a change of Re from 301E6 to 6E6 is now applied to the OVERFLOW result at Re=301E6 to obtain an estimate of the computed drag polar at Re=6E6. The estimated polar shows a drag increase of about 5 counts at alpha=2 deg, and about 10 counts at alpha=6 deg. This discrepancy is again attributable to Reynolds number effects and the accuracy of the turbulence model. Since the LE flap deflection does not introduce significant Re effect on CL-alpha curve, it appears that the Reynolds number effect on the pressure drag in the 4/0 deg flap may not be as significant as in the 8/6 deg flap at M=0.9.

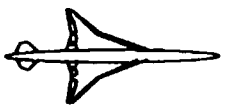

Comparison of Drag Polar

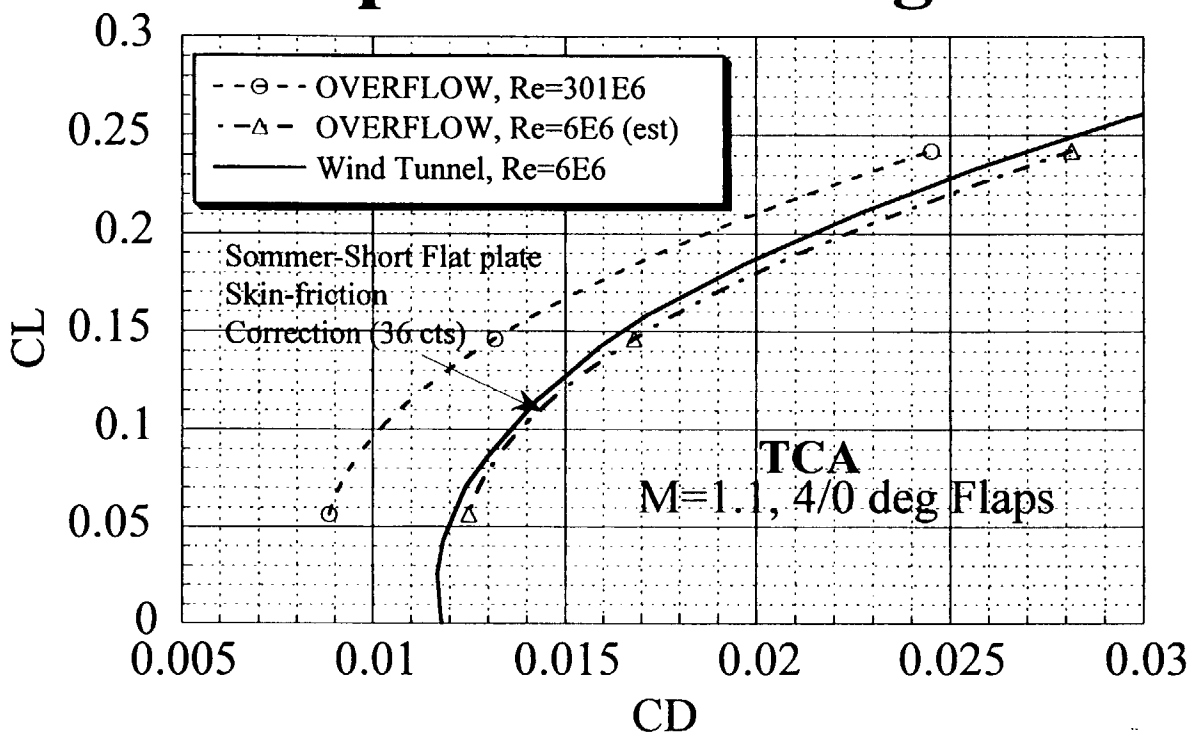

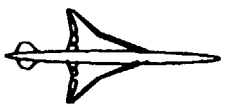

Conclusions - Ref. H

For the Ref. H configuration, the 8/2.6 deg flaps is found to be optimum at M=0.9 and Re=171E6. The 6/0 deg flap results in optimum performance at M=1.1 and Re=190. No hingeline flow separation is noted for the optimum flap conditions at flight Reynolds number. However at M=0.9, the flow separates at the trailing edge flap at a TE flap angle of 6 deg.

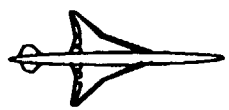

Conclusions- Ref. H

- At subsonic flight (M=0.9),
  - The optimum flap setting is 8/2.6 deg LE/TE
    - » No hinge line flow separation is predicted at this condition
  - Trailing edge flow separates for TE flap at 6 deg
- At supersonic flight (M=1.1),
  - The optimum flap setting is 6/0 deg LE/TE
    - » No hinge line flow separation is predicted at this condition

Conclusions - TCA

For the non-optimized TCA configuration, the 9/5 deg flaps is found to be optimum at M=0.9 and Re=164E6, and the 6/0 deg flap results in optimum performance at M=1.1 and Re=301E6. No hingeline flow separation is noted for the optimum flap conditions at flight Reynolds number. At M=0.9, the flow separates at the trailing edge flap at a TE flap angle of 8 deg.

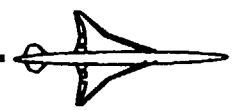

Conclusions- TCA

- At subsonic flight (M=0.9),
  - The optimum flap setting is 9/5 deg LE/TE
    - » No hinge line flow separation is predicted
  - Trailing edge flow separates for TE flap at 8 deg
- At supersonic flight (M=1.1),
  - The optimum flap setting is 6/0 deg LE/TE
    - » No hinge line flow separation is predicted

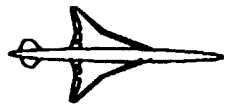

Conclusions - General

Comparisons of OVERFLOW predictions at flight Reynolds number with the wind tunnel data for CL-alpha suggest that Reynolds number effect on CL is pronounced at increased trailing edge flap deflections.

The optimum LE/TE flap settings predicted at flight Reynolds number are found to be within 0.5 to 1 deg of those at the wind tunnel Reynolds number for both Ref. H and TCA configurations.

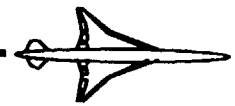

Conclusions- General

- Reynolds number effect on CL is pronounced at increased TE flap deflection (decambering effect of the boundary layer).
- The predicted optimum LE/TE flap deflections at flight Reynolds number are within 0.5 to 1 deg of those at the wind tunnel Reynolds number.

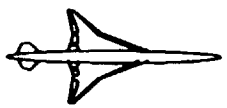

Work in Progress

The optimization of transonic flaps for non-optimized TCA wing-body configuration using TRANAIR is in progress, and the results will be compared with the foregoing OVERFLOW Navier-Stokes solutions. The flat plate theory for skin friction will be evaluated by a comparison with OVERFLOW for a symmetric wing-body configuration of the TCA. The transonic flap optimization for the optimized TCA configuration will be carried out with the OVERFLOW codes, hopefully with the multi-grid version of the code.

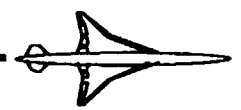

Work in Progress

- TCA Transonic Flap Optimization withTRANAIR
  - complete TRANAIR analysis
  - compare TRANAIR & OVERFLOW Results
- Flat Plate Theory Skin Friction vs. OVERFLOW
  - Symmetric TCA at alpha=0 deg
  - M=0.7 to 2.4 (WT Re); 0.9 & 2.4 (flight Re)
- Optimize transonic Flaps for optimized TCA W/B

Dynacs ENGINEERING CO. INC.

Second NASA/Industry High Speed Research Configuration Aerodynamic Workshop

Bryan W. Westra, Michael B. Malone, and Charles C. Peavey
Northrop Grumman Military Aircraft Systems Division
Pico Rivera, California 90660

The 1996 Nacelle/Diverter Design and Airframe Integration Study (WBS 4.3.1.3) was initiated to develop an understanding of how the nacelle and diverter integration affect the performance of the High Speed Civil Transport Technology Concept Airplane (TCA). Boeing subcontracted Northrop Grumman Corporation (NGC) to assist in the Assessment of Nacelle Integration (WBS 4.3.1.3.1) and the Nacelle/Diverter Integration (WBS 4.3.1.3.3). NGC's contribution to WBS 4.3.1.3.1 and WBS 4.3.1.3.3 consisted of two tasks: a Nacelle Orientation Study and a Diverter Shape Study. The computations for this study were performed on the NAS Cray C-90 at the cost of approximately 300 CPU hours.

Both tasks involved a parametric, viscous CFD analysis and were performed on the full scale TCA at Mach 2.4, altitude 56,500 feet. The objective of the Nacelle Orientation task was to provide guidance for determining the minimum aircraft drag and minimum inlet distortion configurations. For this task, the orientation of the nacelle was changed by varying the toe-in angle, pitch angle, and diverter height. For the Diverter Shape Study, the objective was to provide design criteria for the diverter shape and wing trailing edge to nacelle spacing to minimize the installed, 2D nozzle/nacelle drag.

The initial phase of the Diverter Shape Study was to reconcile a viscous drag discrepancy observed in the 1995 Ref. H Transonic Nozzle Boattail Drag Study. It was suspected that the discrepancy was due to flow solver difference between OVERFLOW and GCNSfv. It was determined that the solvers agree within 0.3% (0.4 drag counts) and that the discrepancy was due to different amounts of off-body grid stretching.

For the Nacelle Orientation task, eight variants were developed by repositioning the nacelle/diverters. Two variants were created for each geometric variable, i.e. nacelle pitch, inboard nacelle toe angle, outboard nacelle toe angle, and diverter height. Based on the variants, it was predicted that a 0.68 count reduction could be achieved by pitching both nacelles down and toeing-out the inboard nacelle. This optimum configuration was generated and resulted in a 0.66 count reduction. The minimum inlet distortion configuration was achieved by primarily two adjustments: an inboard nacelle pitch up and an outboard nacelle toe-in.

Another eight variants were created for the Diverter Shape task. In addition to the baseline diverter geometry, a thin diverter (similar to the Ref. H diverter) and a NGC developed hybrid diverter shape were examined at different wing trailing edge to nacelle spacings. It was concluded the best diverter shape for drag reduction was the hybrid diverter. The best trailing edge to nacelle spacing was when the aft end of the nacelle was pitched down until it no longer protruded through the upper surface of the wing, giving a 0.65 drag count reduction.

Finally, the results of both studies were used to define a configuration that reduced drag by a total of 1.10 counts.

Second NASA/Industry High Speed Research Configuration Aerodynamic Workshop

Objectives

Nacelle/Diverter Design and Airframe Integration Task (WBS 4.3.1.3)

Assessment of Nacelle Integration (WBS 4.3.1.3.1)

Nacelle Orientation

- Perform a Parametric, Viscous CFD Analysis
- Provide Guidance for Determining Minimum Drag and Minimum Inlet Distortion Configuration
- Use Nacelle Toe-in, Installation Pitch Angle and Diverter Height as Variable Parameters

Nacelle/Diverter Integration (WBS 4.3.1.3.3)

Diverter Shape

- Perform a Parametric, Viscous CFD Analysis
- Provide Guidance for Integration of Diverters, Nacelles and Wing for 2D Nozzle-Nacelles
- Use Diverter Shape and Wing T.E. to Nacelle Spacing (Pitch) as Variables
- Verify OVERFLOW/GCNSfv agreement and Determine Boundary Layer Grid Stretching Schemes to Obtain the Most Accurate Absolute Drag Levels

NORTHROP GRUMMAN

In 1996 Boeing subcontracted Northrop Grumman Corporation (NGC) to contribute to the Nacelle/Diverter Design and Airframe Integration Task (WBS 4.3.1.3). NGC assisted in the Assessment of Nacelle Integration (WBS 4.3.1.3.1) and Nacelle/Diverter Integration (WBS 4.3.1.3.3) tasks by performing two studies: a Nacelle Orientation and a Diverter Shape Study. Both studies were performed at the cruise condition.

The objective of the Nacelle Orientation study was to perform a parametric, viscous CFD analysis to provide guidance for determining the minimum aircraft drag and minimum inlet distortion configurations. For this task, the orientation of the nacelle was changed by varying the toe-in and pitch angles. Diverter height was also varied by a vertical displacement of the nacelles.

The objective of the Diverter Shape study was to provide design criteria for the diverter shape and wing trailing edge to nacelle spacing (varied by pitching the nacelle) to minimize the installed, 2D nozzle/nacelle drag.

The initial phase of the Diverter Shape Study was to reconcile a viscous drag discrepancy observed in the 1995 Ref. H Transonic Nozzle Boattail Drag Study. This was done to verify that the NGC flow solver (GCNSfv) agrees with OVERFLOW and to determine the drag effect of boundary layer grid stretching schemes.

Second NASA/Industry High Speed Research Configuration Aerodynamic Workshop

Generalized Compressible Navier–Stokes Code

- NASA Ames ARC Thin–Layer Navier–Stokes Algorithm
- Implicit, Node–Based Finite–Volume Scheme
- Multi–Block Structured Grids for Complex Geometries
- Class 1, 2 ,3, & 4 Patched Block Interface Mappings
- Chimera Overlapping Grid Block Option
- Grid Sequencing & Multigrid Convergence Acceleration
- 2–Equation Menter's SST, Girimaji ARSM, Spalart–Allmaras, & Baldwin–Barth Turbulence Models
- Extensive Boundary Condition Menu

NORTHROP GRUMMAN

The CFD code used was GCNS, developed by Northrop Grumman. It is based on the ARC3D thin–layer Navier–Stokes algorithm created at NASA Ames. The convergence method is an implicit, node–based finite–volume scheme. Complex geometries are analyzed by using multi–block structured grids. The boundary conditions between blocks can be specified as patched, class 1 through 4, where class 1 is point–to–point matching, class 2 is incremental point–to–point matching, class 3 is arbitrary face matching, and class 4 is arbitrary sub–face matching. A Chimera overlapping grid block option is also available. To speed steady–state convergence, grid sequencing and multigrid convergence schemes can be used. GCNS provides four turbulence models to the user: the Menter's k–ω SST 2–equation model (used in this study), the Girimaji Algebraic Reynolds Stress model, the Spalart–Allmaras model, and the Baldwin–Barth model. GCNSfv offers many boundary conditions, including propulsion specific conditions such as characteristic inflow (mass flow ratio, corrected mass flow, and inlet bleed) and outflow (total pressure and temperature) conditions. The code runs at approximately 12 μs/iteration/grid–point on the NAS Cray C–90, and parallelization allows the code to utilize six of the available sixteen processors, allowing effective use of the multi–task batch queue.

Solver Comparison & Viscous Grid Stretching

Results – Ref. H

- GCNS & OVERFLOW Agree within 0.3% / 0.4 cts. C_D
- Grid Stretching (Using GCNS)...

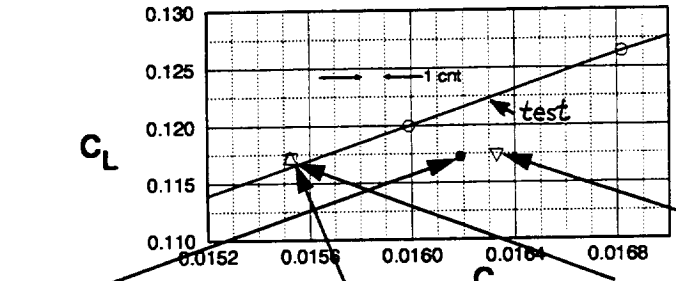

Notes:

M = 2.4, α = 4.4 deg.

Results do not include forces on body aft of station 2,904"

Turbulence models: Grid 1–Menter SSt, Grids 2,3,and 4–Baldwin Barth

Grid 1 data is corrected to Re=7,000,000

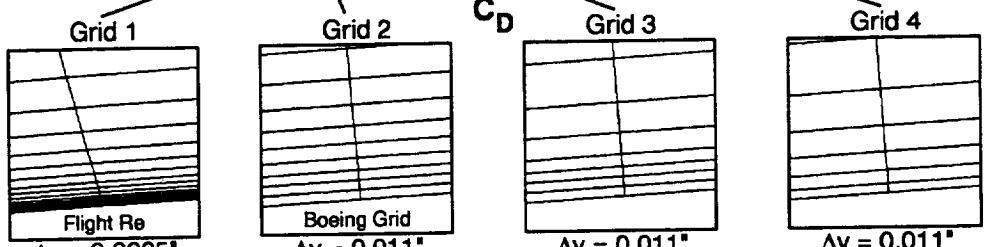

Grid 1: Δy = 0.0005" stretching at surface

Grid 2: Δy = 0.011" 4 cells const. then minimal stretching

Grid 3: Δy = 0.011" 4 cells const. then significant stretching

Grid 4: Δy = 0.011" stretching at surface

NORTHROP GRUMMAN

It was suspected that the viscous drag discrepancy observed in the 1995 Ref. H Study was due to flow solver difference between OVERFLOW and GCNS. After running the same grid in both solvers, the drag results were within 0.3% (0.4 drag counts). The boundary layer grid stretching schemes were then investigated.

Four grid schemes were used to determine the stretching effects. Grid 1 was taken from the 1995 Study at a flight Reynolds number of 40 million. The second, third, and fourth grids shown were generated for a wind tunnel Reynolds number of 7 million. Grid 2 was developed by Boeing.

Grid 4 stretched in a similar manner, and produced results similar to grid 1 after the grid 1 results were corrected for Reynolds number differences. The small drag discrepancy is likely due to the different turbulence model used. The grids with a region of constant off–body spacing, grids 2 and 3, agree well with the test results. This determined that the grid stretching near the wall should be minimal for the first several off–body cells. It is important to note that stretching after the region of constant cells could be increased without a significant change in drag results.

Nacelle Orientation Variant Matrix

Variation	INBOARD NACELLE			OUTBOARD NACELLE		
	PITCH	TOE-IN	HEIGHT	PITCH	TOE-IN	HEIGHT
Baseline	0	0	0	0	0	0
1	tangent (+0.58°)	0	0	tangent (+0.40°)	0	0
2	2xVar 1 (+1.16°)	0	0	2xVar 1 (+0.80°)	0	0
3	0	0	0	0	+1.0°	0
4	0	0	0	0	-1.0°	0
5	0	-1.0°	0	0	Min C_D	0
6	0	+1.0°	0	0	Min C_D	0
7	0	Min C_D	+0.25H	0	Min C_D	+0.25H
8	0	Min C_D	+0.50H	0	Min C_D	+0.50H

Notes: Increments are from the baseline geometry.
H is the inboard diverter height

NORTHROP GRUMMAN

Before the study began, a variant matrix was developed to isolate the effects of each reposition variable. This table shows the nacelle positions for the eight variants generated.

The first two variations have the aft end of the nacelles pitched down. Each nacelle on the first variation was pitched until the aft end of the nacelle no longer penetrated the upper surface of the wing. At this point the nacelle upper surface was tangent to the wing trailing edge. The second variant was pitched twice the amount used for variant 1. The outboard toe-in angle was varied for configurations 3 and 4. Variation 5 and 6 have the inboard nacelle toe-in angle varied and the outboard nacelle toe-in fixed at the minimum drag position determined by variant 3, 4, or baseline. Finally, the diverter height was increased by dropping the nacelles down while using the optimum toe-in angle for each nacelle.

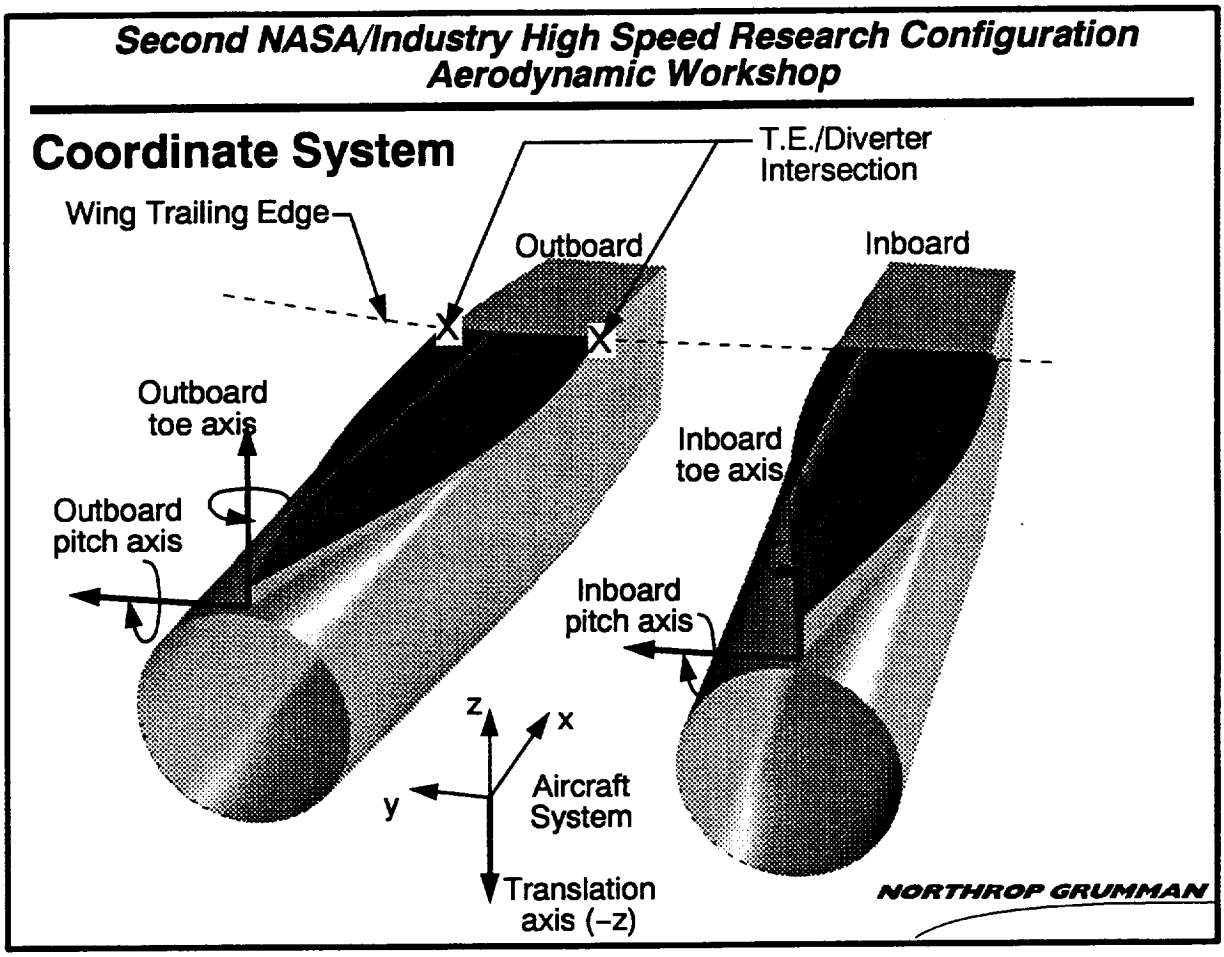

An axis system was developed for each nacelle. The origin of each nacelle axes system was located at the leading edge of the diverter where it intersects the nacelle. Two rotational axes, pitch and toe (yaw), were used to define the nacelle orientation.

The pitch axis direction was identical to the isolated nacelle "y" axis (the nacelle axis before it is repositioned or "rigged" onto the wing). A pitch up rotation was defined as pitching the front end of the nacelle up and aft end down. The toe axis was used to yaw the nacelle. It was defined as a vector normal to the plane created by three points: the coordinate system origin and the inboard and outboard trailing edge/diverter intersection points. This maintained the aft nacelle elevation at the trailing edge during changes in toe angle. The diverter was rotated with the nacelle for the toe cases to maintain the centerline relationship between the components. A positive toe rotation, toe-in, brings the aft end of the nacelle away from the fuselage. The diverter height (at diverter leading edge) was changed by translating the nacelle down in the z direction.

Pitch Variants

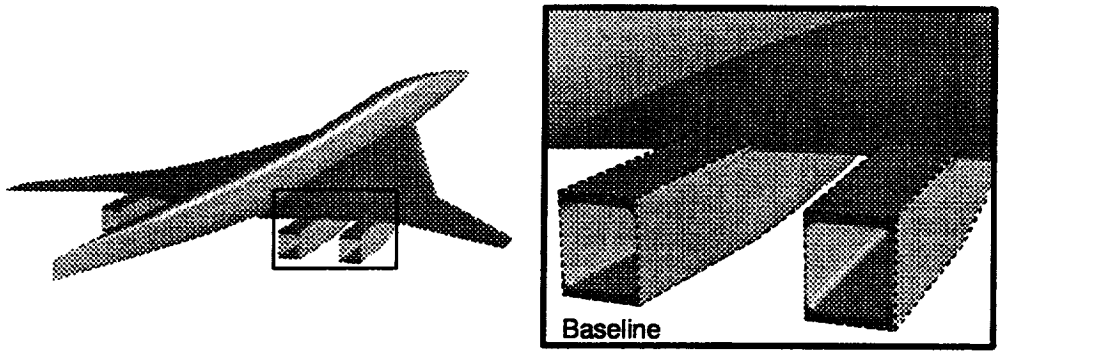

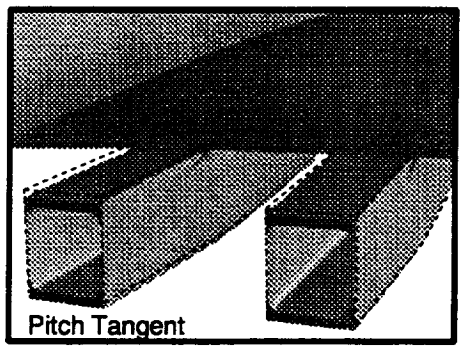

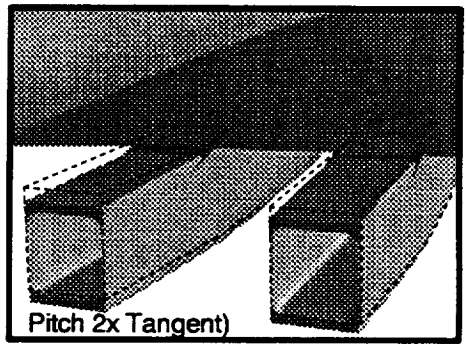

NORTHROP GRUMMAN

The nacelles for the baseline TCA protrude through the upper wing surface near the wing trailing edge. When the aft end of the nacelle was pitched down to the "tangent to wing trailing edge" position, the nacelles no longer intersected the upper wing surface. At twice this pitch amount, a fairing was required to close the gap between the trailing edge and the nacelle. A ramp was created which extended from the wing trailing edge to the nacelle upper surface.

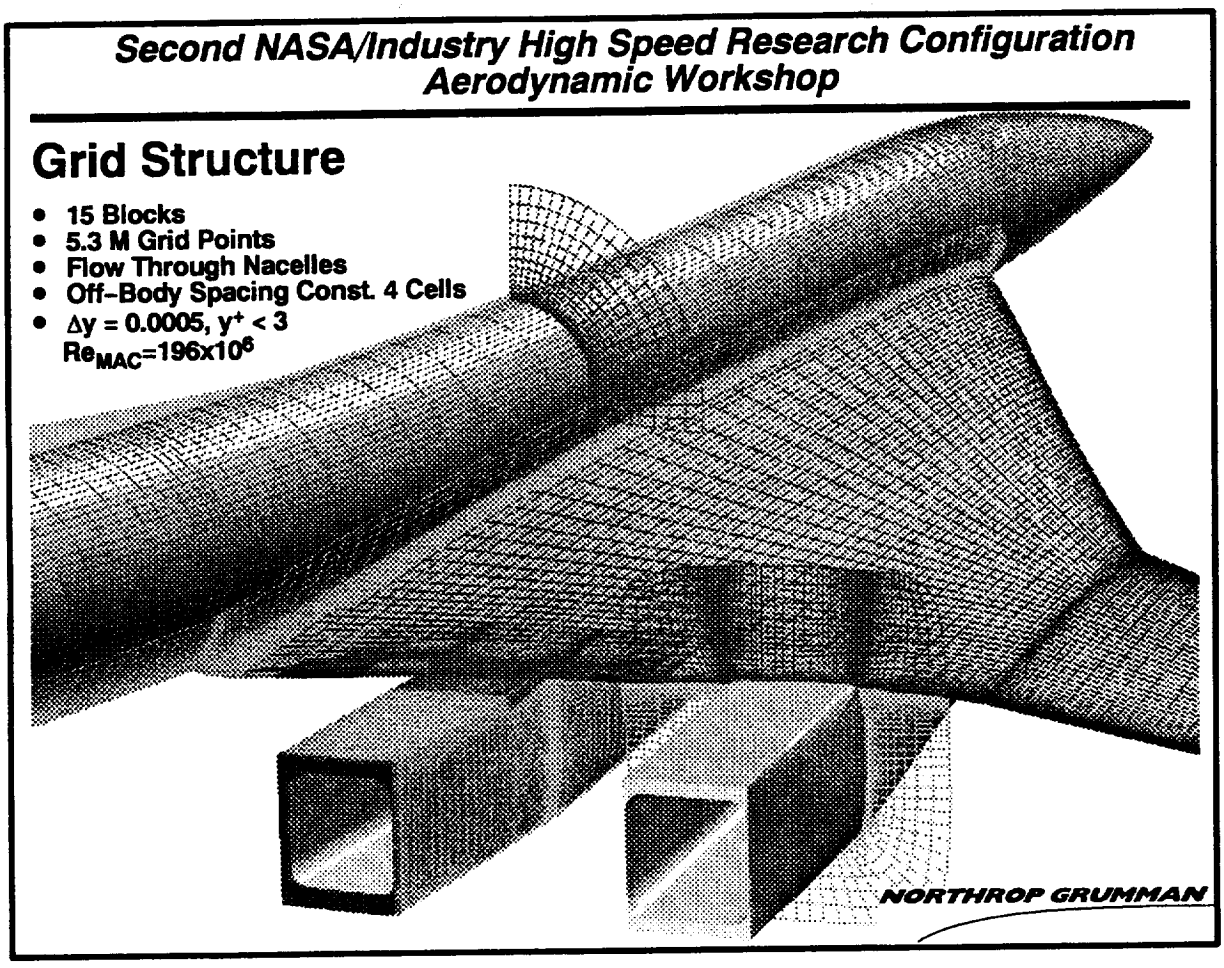

The grid consisted of 5.3 million grid points distributed over 15 blocks. Both patched and Chimera (overset) grid methods were applied. Flow through nacelles were modeled after the wind tunnel model.

At the body surface, an off-body spacing of 0.0005" was used. After post processing the baseline TCA results, it was observed that the values of y^+ were less than 3.0 everywhere on the wing surface. This should be adequate for the turbulence model (Menter's SST). As previously mentioned, the off-body stretching was near zero for the first 4 cells to ensure viscous force accuracy.

Each nacelle was defined by approximately 1.4 million points (2.8 million for both nacelles) and consisted of 5 blocks. The nacelles were modeled to simulate the wind tunnel model by incorporating a flow through duct, eliminating the nozzle ramp, and excluding the inlet spike. The remaining 2.5 million points were used to model the aircraft fuselage, collar, wing, wing tip and far field.

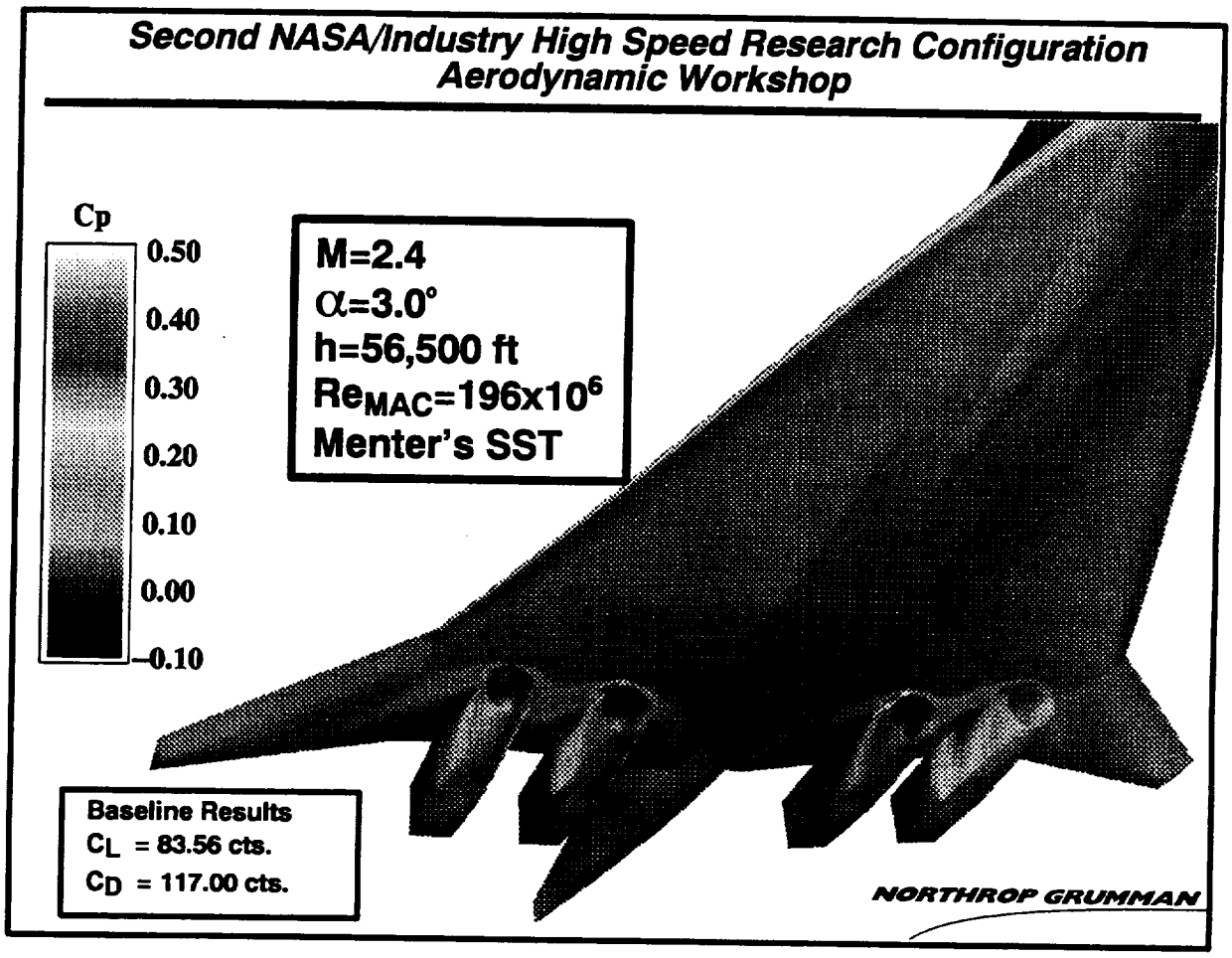

A freestream Mach number of 2.4, angle of attack of 3.0 degrees, and flight Reynolds number of 171.58 x 10^3 /in (Re_{MAC} = 195.50 x 10^6) were used for all runs. This Reynolds number was obtained from the full scale configuration at an altitude of approximately 56,500 ft and a free stream temperature of 390.0°R. The baseline TCA configuration was run at two additional angles of attack, 2.5 and 3.5 degrees. Forces obtained were referenced by the mean aerodynamic chord (MAC) of 94.952 ft and wing reference area of 8,500 ft^2.

A lift coefficent of 83.56 counts and a drag coefficent of 117.00 counts was calculated for the baseline configuration.

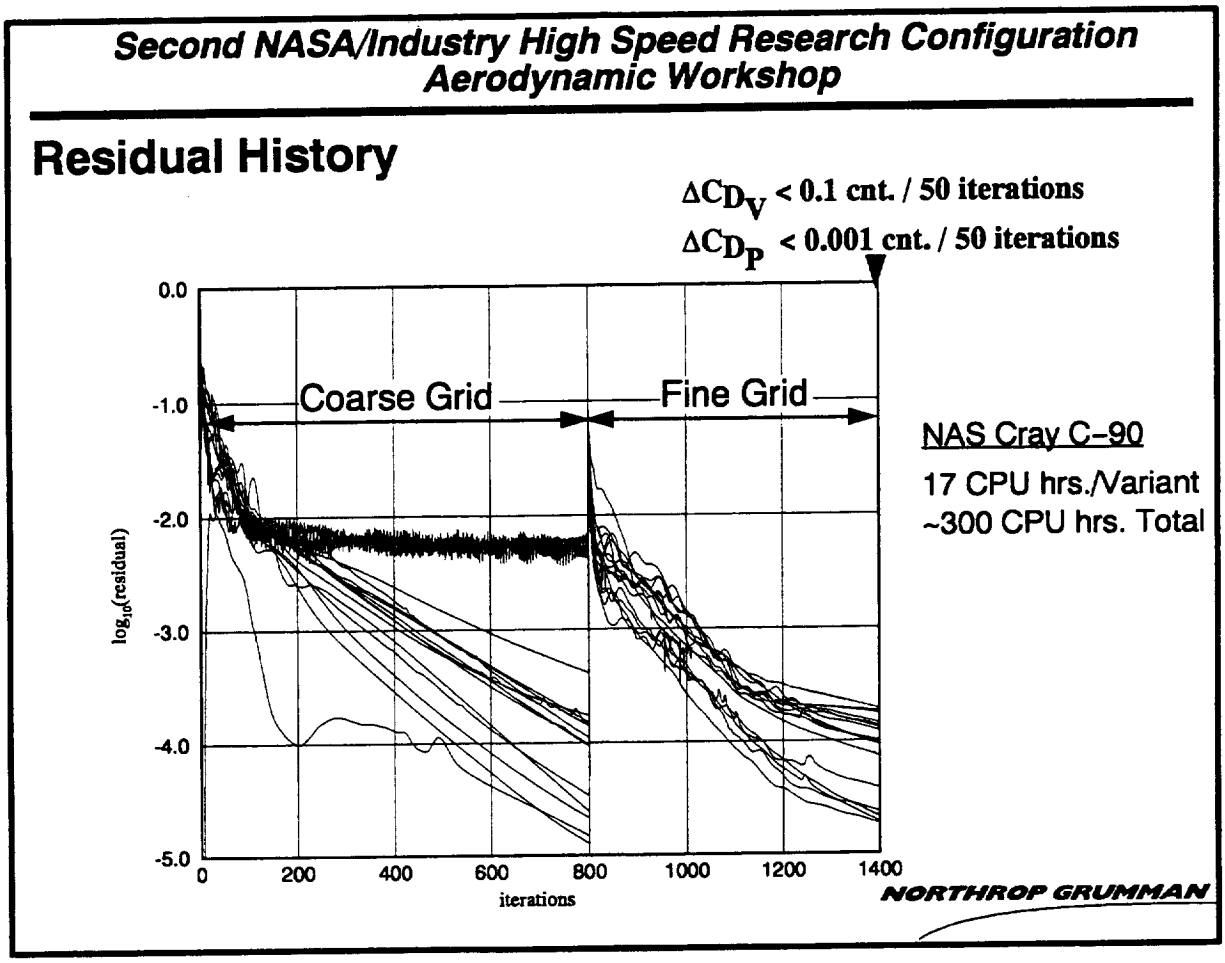

All grids for this study were run in GCNSfv v3.6 for an identical number of iterations. A sequenced grid method was used to reduce the computational time. Eight hundred coarse grid iterations were initially performed. During the coarse run, the exhaust blocks failed to converge due to the lack of points at this sequence level. All blocks were at an adequate level of convergence after running 600 fine grid iterations. After the fine grid iterations, the viscous drag changed less than 0.1 counts per 50 iterations, and the pressure drag changed less than 0.001 counts per 50 iterations. All variants in the nacelle orientation study were run the same number of iterations. The total CPU time required for convergence on the NAS Cray C-90 was approximately 17 CPU hours per configuration. Approximately 300 CPU hours were used for both studies.

Cross Flow vs. Nacelle Orientation

–Obtained from Baseline TCA Flow Field

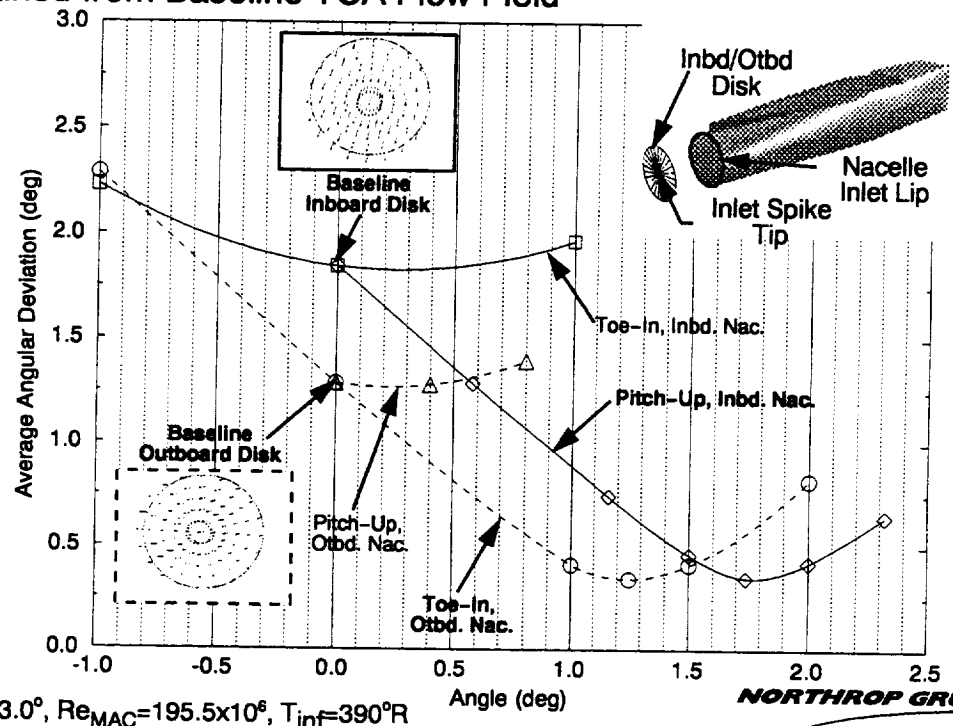

M=2.4, α=3.0°, Re_{MAC}=195.5x10^6, T_{inf}=390°R

NORTHROP GRUMMAN

The predicted optimum orientation to obtain minimum inlet crossflow for the inboard nacelle is 0.26 degrees toe–in and 1.76 degrees pitch–up. For the outboard nacelle, the predicted optimum orientation to minimize crossflow is 1.24 degrees toe–in and 0.23 degrees pitch–up.

The cross flow was determined by moving a disk positioned at the spike tip through the baseline TCA's flow field. It was not necessary to reposition the nacelle grid and run the flow solver because the supersonic flow field upstream of the nacelle is unaffected by the nacelle orientation. The cross flow (flow in the plane of the disk) for the inboard and outboard nacelles was reduced by 87% and 82%, respectively. Since the minimum cross flow configuration was not modeled, it is uncertain what amount of drag penalty must be paid for this minimum cross flow configuration. It is likely that the drag would increase by more than 0.6 counts, based on the drag increase observed for the variants of this study.

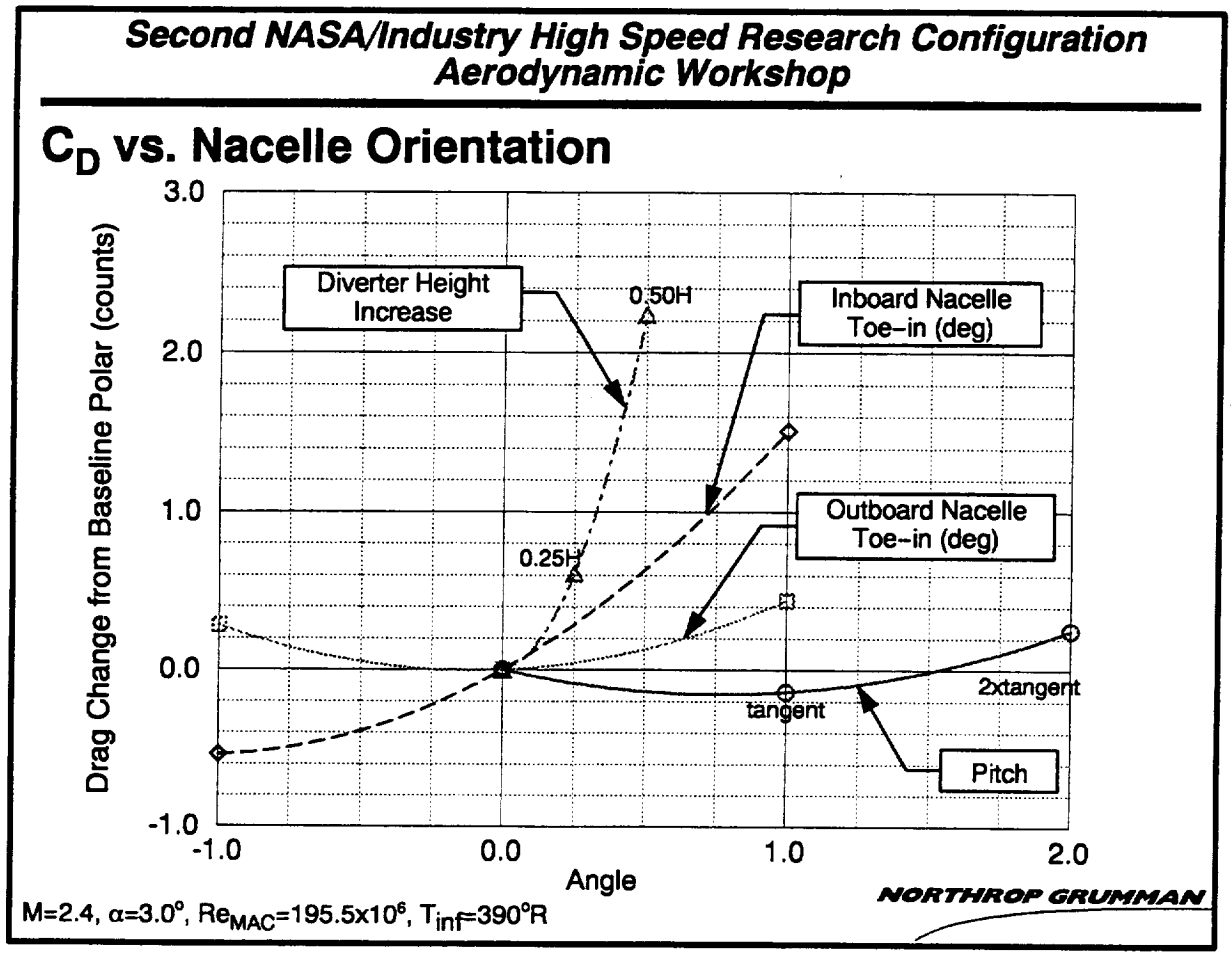

The effect of each parameter on drag is shown in the above cross plots. Pitch angles 76% of the variant 1 amount (i.e., 0.44 deg. inbd./0.31 deg. otbd.) are predicted to reduce the drag by 0.16 counts from the baseline drag polar. The outboard nacelle should be toed–out by 0.11 degrees to decrease drag an additional 0.04 count. When the inboard nacelle is toed–out by at least 1.0 degree, a further drag reduction of 0.54 counts is predicted. The diverter height phase of the study showed that any increase in diverter height increases the drag.

If we assume that the effects of pitch, toe, and diverter height are linear, then the principal of superposition would suggest that the independent effects are additive. Thus, a configuration that uses the minimum drag value of each variable would be the minimum drag configuration, and reduce drag by 0.74 counts.

Note that the minimum drag configuration is not the configuration with minimum cross flow.

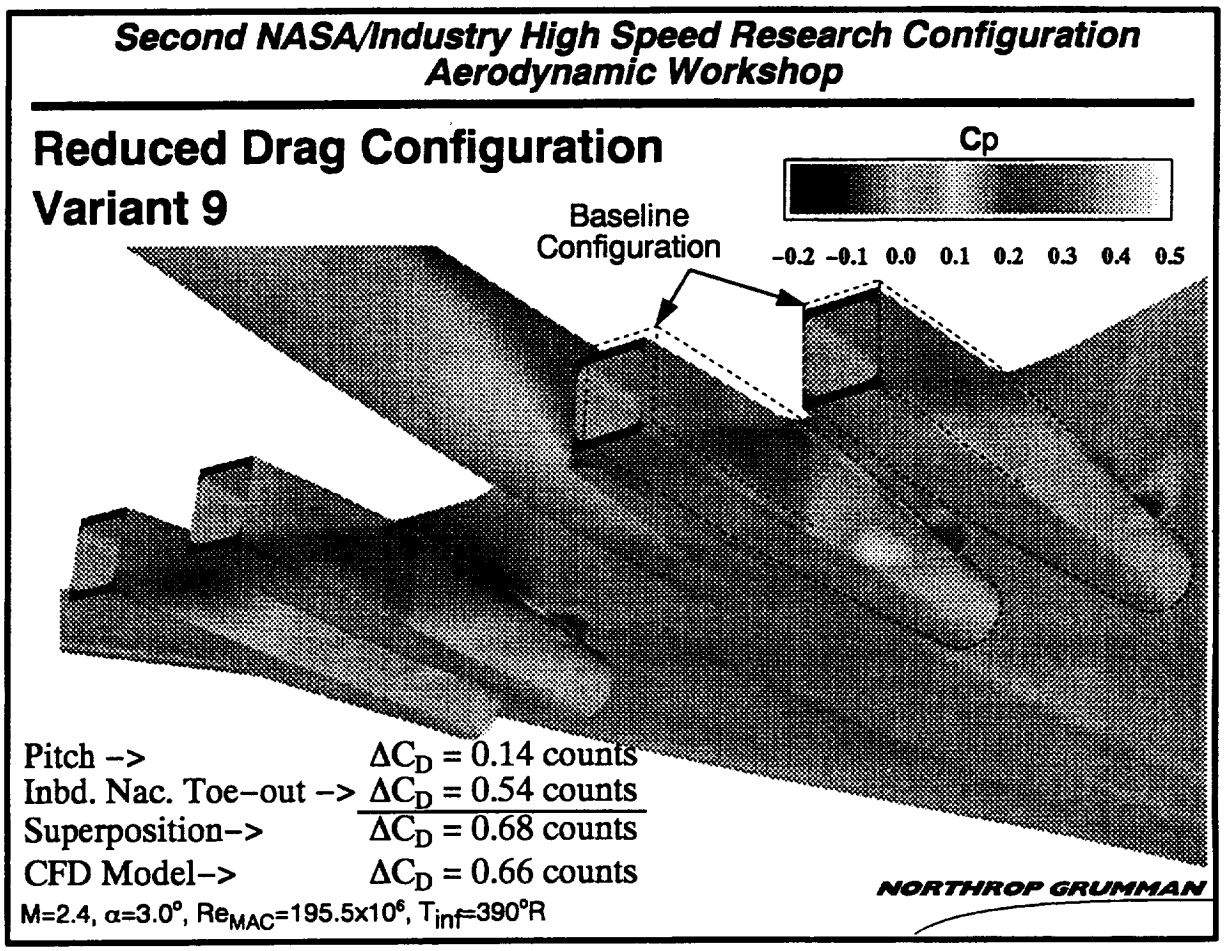

To investigate if the nacelle variables were orthogonal (no cross coupling) with additive effects, a variant 9 was modeled where both nacelles were pitched to the "tangent to wing trailing edge" (0.58 degree inboard / 0.40 degree outboard) position and the inboard nacelle was toed-out 1 degree. The diverter height for both nacelles was identical to baseline, as was the outboard nacelle toe angle.

From earlier configurations, the drag decreased by 0.14 counts due to pitch and 0.54 counts due to inboard nacelle toe-out. Based on superposition, a drag decrease of 0.68 counts was predicted for the new geometry. CFD results revealed that the variant 9 configuration decreased drag 0.66 counts. Thus, it can be concluded that the superposition/additive method is valid for the range of angle variations examined.

Second NASA/Industry High Speed Research Configuration Aerodynamic Workshop

Diverter Shape Variant Matrix

Variation	Diverter Shape	Nacelle Pitch
Baseline	Wide (TCA geometry)	0
1	Wide (TCA geometry)	tangent at T.E.
2	Wide (TCA geometry)	2.0 x variant 1
10	Thin (Ref. H. geometry)	0
11	Thin (Ref. H. geometry)	tangent at T.E.
12	Thin (Ref. H. geometry)	2.0 x variant 1
13	Hybrid	0
14	Hybrid	tangent at T.E.
15	Hybrid	2.0 x variant 1

Notes: Increments are from the baseline geometry.

NORTHROP GRUMMAN

For the Diverter Shape Study, 8 variants were generated. Note that the numbering sequence continues from the variants developed in the Nacelle Orientation section of this report. Three diverter shapes were used in this study.

The wide diverter is 70.6 inches wide and is the baseline TCA diverter. It has a leading edge angle of 22 degrees.

The thin diverter was based on the Ref. H diverter. At 32 inches wide with a 17 degree leading edge, it represents the minimum volume configuration, bounded by structural requirements.

The hybrid diverter begins with a 17 degree leading edge, but expands to the wide geometry at the trailing edge by following a parabolic curve .

The wing trailing edge to nacelle spacing was changed by pitching the nacelle as in the Nacelle Orientation study. As previously discussed, The "tangent at wing trailing edge" condition occurs when the nacelle is pitched until the aft end no longer penetrates the upper surface of the wing .

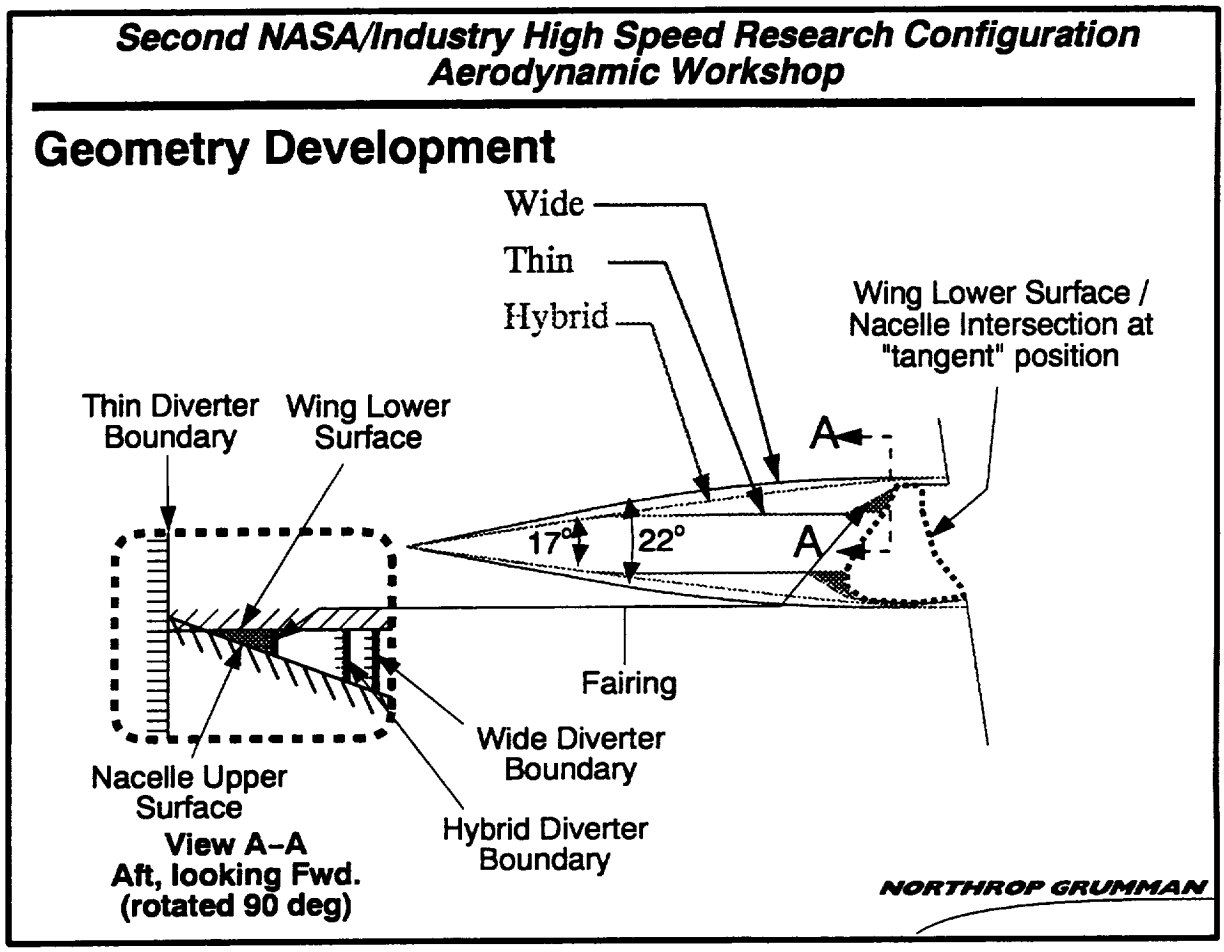

A plan view shows the diverter geometry for the condition where the nacelle is pitched tangent to the wing trailing edge. For the thin diverter geometry, the nacelles intersected the wing lower surface near the trailing edge outside the diverter bounds. In many cases, the resulting geometry had a thin "V"-channel created where the nacelle upper surface and wing lower surface met at sharp angles. This channel was removed by creating a small fairing, less than 1 inch tall, which spanned from the wing lower surface to the nacelle.

The hybrid diverter concept arose from observing the flow near the thin diverter fairing. Specifically, there were regions of high viscous stress where the fairing met the thin diverter. These regions were eliminated by constructing the hybrid diverter.

Diverter Shape Results

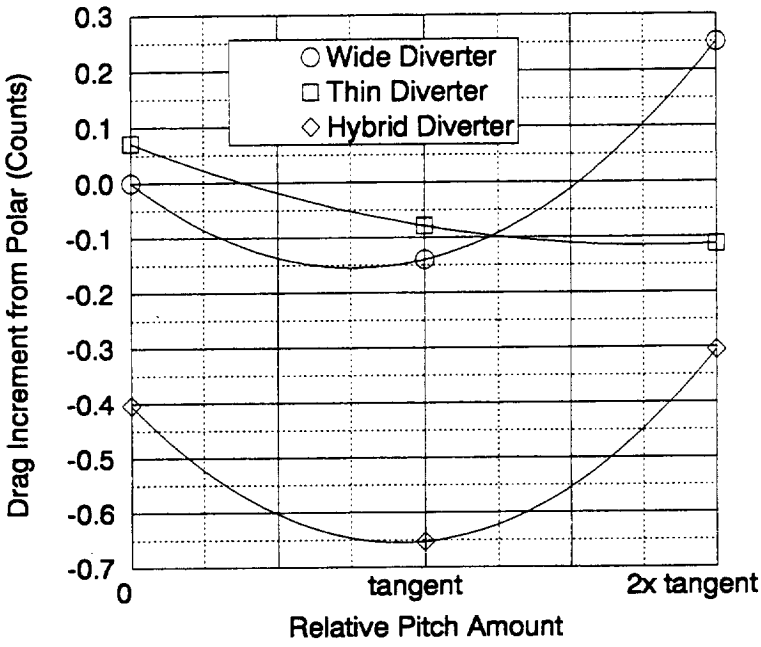

NORTHROP GRUMMAN

M=2.4, α=3.0°, Re_{MAC}=195.5x10^6, T_{inf}=390°R

The thin diverter did not improve from its wide diverter equivalent until the nacelle was pitched to the "2x tangent" position. At this pitch angle, the thin diverter was more beneficial than the wide diverter because the inboard diverter becomes a true pylon, supporting the nacelle completely off of the wing, and the flow does not "pinch-off" between the wing and nacelle. For this configuration, the drag decreased by 0.11 counts from the baseline wide diverter at the "0x tangent" position. Note that the drag is 0.36 counts lower than the "2x tangent" position wide diverter.

The hybrid diverter performed best at reducing drag. It decreased the drag by 0.40 counts from the baseline TCA configuration. At the "1x tangent" pitch, the drag was reduced by 0.65 counts. Recall from the nacelle orientation study that the wide diverter only decreased drag by 0.14 counts for the "1x tangent" pitch.

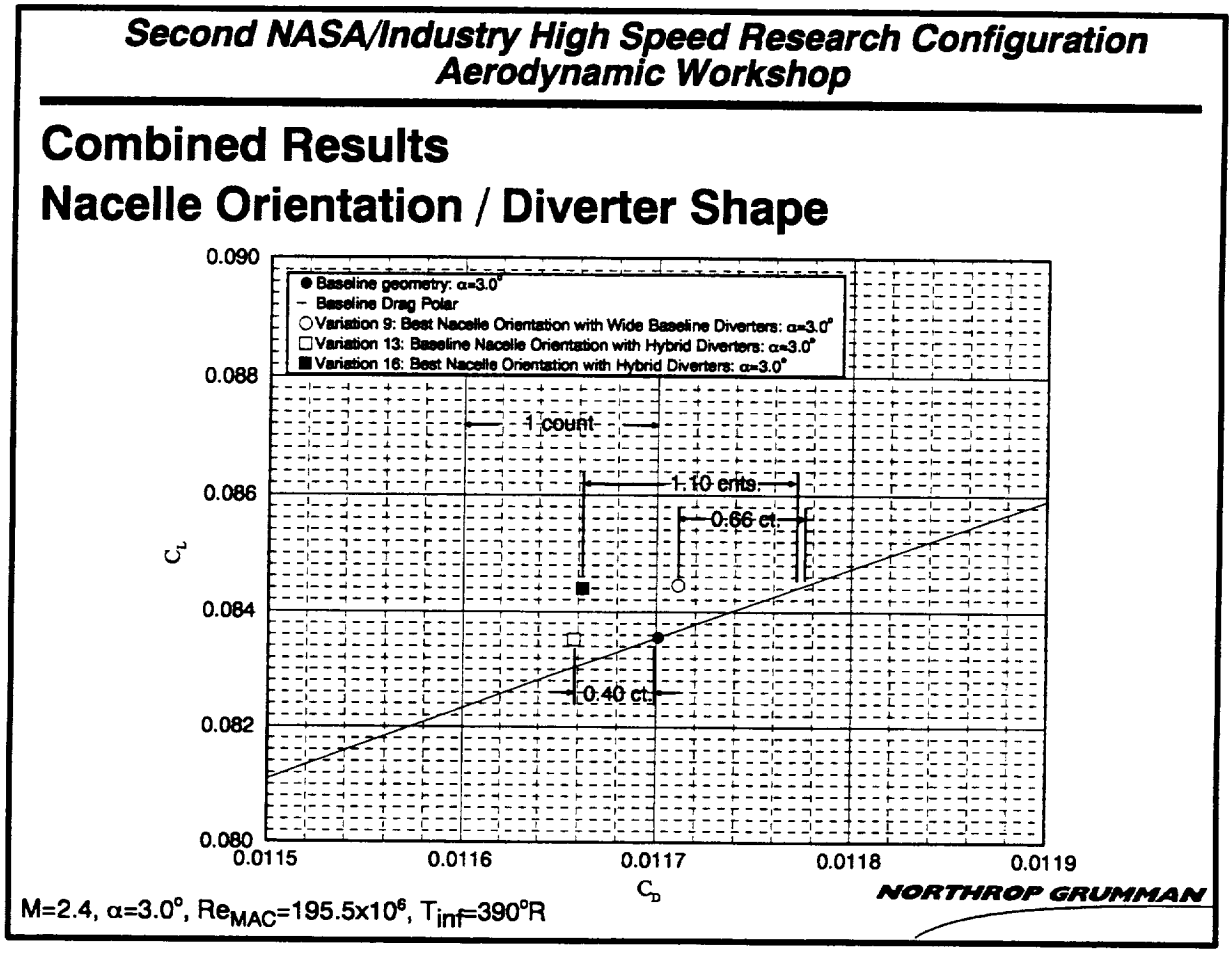

It was decided to use the best diverter shape found in the diverter shape study and combine it with the best nacelle orientation observed in the nacelle orientation study. It was predicted that the new geometry would combine the drag benefit of 0.66 counts from the nacelle orientation with the 0.40 counts from the hybrid diverter. This would provide a 1.06 count reduction in drag. When the combined geometry (variation 16) was run, the result was a drag reduction from the baseline drag polar of 1.10 counts.

Nacelle Orientation: Conclusions

- Minimum Cross Flow Configuration – Determined
  - **Inboard Nacelle: Primarily Pitch Up**
  - **Outboard Nacelle: Primarily Toe-in**
- Minimum Drag Configuration – Determined
  - **Pitch Change – decreased drag 0.14 counts**
  - **Outboard Nacelle Toe Change – no significant change**
  - **Inboard Nacelle Toe Change – dec. drag 0.54 counts**
  - **Diverter Height Increase – increased drag**
- Method of Isolated Variable Effects – Validated
  - ΔC_D(pitch) + ΔC_D(toe) $\cong$ ΔC_D(pitch & toe)

NORTHROP GRUMMAN

The nacelle shape study determined the minimum drag and minimum inlet distortion configurations for the TCA geometry. The minimum cross flow configuration was obtained by primarily two adjustments: an inboard nacelle pitch-up and an outboard nacelle toe-in.

The minimum drag configuration can be achieved by pitching both nacelles up and a toe out adjustment of the inboard nacelle. This will reduce the drag by approximately 0.7 counts.

Separate pitch and inboard toe variations both reduced drag. When a configuration was modeled that contained both the pitch and inboard toe change, the resulting drag decrease was nearly identical to the sum of the separate drag reductions. Thus, the isolated effects of each variable can be considered additive for small variable increments. Future studies could use this approach provided the magnitude of the changes were similar to those used in this study.

Diverter Shape: Conclusions

- **Effect of Diverter Shape on Drag**
  - -Thin With "Pinched" Flow (0x and 1x tangent): increased from baseline equivalents
  - -Thin Without "Pinched" Flow at Inbd. Nacelle (2x tangent): 0.36 cnt. reduction from wide equivalent
  - -Hybrid: 0.40 to 0.56 cnt. reduction from wide diverter equivalents
- **Effect of Nacelle to Wing Trailing Edge Spacing on Drag**
  - -Best Position for Wide and Hybrid Diverters: Tangent
    - 0.14 cnt. reduction for wide diverter from baseline polar
    - 0.65 cnt. reduction for hybrid diverter from baseline polar
  - -Best Position for Thin Diverter: 2x Tangent
    - 0.11 cnt. reduction from baseline polar

Combined Studies: Conclusion

Decreased Drag By 1.10 counts

NORTHROP GRUMMAN

This study showed that the thin diverter configuration had higher drag than the wide diverter configuration when the flow in the diverter channel was pinched off. When the aft end of the nacelle was pitched enough to eliminate the pinch–off, the thin diverter reduced the drag by 0.36 counts from a wide diverter at the same pitch angle. The hybrid diverter proved to be the diverter that resulted in the least drag, providing a reduction of 0.40 to 0.56 counts from the wide diverter cases.

The best pitch angle observed for the wide and hybrid diverters was the "1x tangent" value. At this position, the wide diverter reduced the drag by 0.14 counts and the hybrid by 0.65 counts. The best pitch angle observed for the thin diverter was at twice this pitch angle. The resulting drag reduction was 0.11 counts from the baseline drag polar.

When the hybrid diverter was modeled with the best observed nacelle pitch and toe angles from the Nacelle Orientation and Diverter Shape studies, the new configuration reduced the drag by 1.10 counts from the baseline TCA..

Recommendations for Future Work

- **Investigate the Drag Effects of Inlet Spike with Optimum Nacelle Orientation and Diverter Shape**
- **Evaluate the Drag Effects of Inlet Spillage and Inlet Bleed Flows.**

NORTHROP GRUMMAN

This study made use of a flow through nacelle without an inlet spike. The effect of the spike on drag after the nacelle orientation and diverter shape have been optimized should be investigated.

Likewise, the drag effects of inlet spillage and bleed extraction/exhaust should be evaluated for design and off-design conditions.

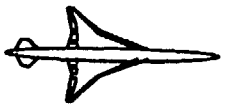

Nacelle / Diverter Design and Airframe Integration

4.3.1.3

Presenter: Steve Chaney

Team Members: Gordon Blom

Steve McMahon

Steve Ogg

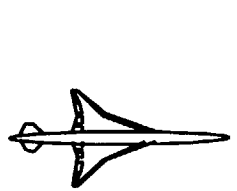

The primary objective for propulsion/airframe integration (PAI) work stated in the planning and control document (PCD) is to develop technology required to support the development of the High Speed Civil Transport (HSCT). The technology development includes:

1) Developing computational and empirical based tools for the aerodynamic design & analysis of complex geometry configurations. This development consists primarily of adapting current state-of-the-art computational fluid dynamics (CFD) codes to the HSCT PAI configurations and conditions. This is followed by validation with wind tunnel or flight aerodynamic data.

2) Identifying the key design variables for HSCT PAI installations with the tools described above. Exercising these variables in parametric or direct design optimization studies in order to develop design guidelines for efficient nacelle installations.

These overall three year objectives for sub-task 3 were reduced to specific objectives for 1996 as described below.

Objective (midterm 96)

- PCD: Develop PAI technology required to support HSCT development.
  - Develop, adapt, apply, validate, evaluate computational and empirical based aerodynamic design/analysis tools.
  - Identify key design variables and develop design guidelines for efficient nacelle installations.

- For 1996 the specific objectives were:
  - Continue investigation of bifurcated vs axi inlet drag differences.
  - Apply computational tools validated on Ref. H to assess the TCA baseline and optimized configurations.
  - Investigate and develop design guidelines for nacelle orientation, nacelle cambering, diverter shaping.
  - Continue to develop OVERFLOW gridding, solution, and post-processing tools and strategies for complex PAI geometry analysis and design.

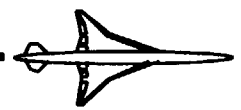

The approach taken in the 1996 PAI contract studies was to build on the experience and knowledge gained in the 1995 Reference H studies as much as possible. The analyses continued to focus on the supersonic cruise condition. The last design study on the Reference H was completed by moving the diverters aft on the bifurcated inlet installation. A complete assessment of the new TCA configuration was planned at wind tunnel and flight Reynolds number. Nacelle/Diverter shape variation studies were divided between Boeing and Northrop as shown below.

After the conclusion of the bifurcated inlet studies on the Reference H no more bifurcated work was planned. This situation changed just about the time that the TCA assessment analyses were being completed. The propulsion staff became much more interested in the bifurcated and requested a drag assessment of a bifurcated inlet nacelle on the TCA. Based on the experience gained on the Reference H it was agreed that it would be necessary to design a bifurcated nacelle installation specifically for the TCA and do a complete analysis of it. The decision was made to replace the Boeing nacelle cambering and alternate diverter studies with a bifurcated installation and analysis task on the TCA, including an accurate transonic comparison of the bifurcated and the axisymmetric inlets. At this time the supersonic solutions have just completed on the bifurcated and are being analyzed; the transonic analyses are in progress.

As the indicated below the plan included a brief assessment of the PAI installation on the TRANAIR optimized configurations. This plan was also changed in mid-task. The decision was made in the Boeing HSR optimization community to use OVERFLOW (instead of TLNS) for the viscous check and final viscous analysis of the optimized configurations. This work therefore fell under subtask 2.

The plan included assessment of the wind tunnel corrections (such as nacelle internal duct drag) and the effect of the wind tunnel model changes to the actual TCA configuration (such as wing upper surface nacelle bump).

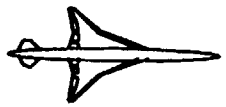

Approach (midterm 96)

SUPERCRUISE (M=2.4) STUDIES

- Viscous CFD analysis of translated diverter for Ref. H bifurcated nacelle configuration.
- Viscous CFD analysis of TCA W/B @ wind tunnel and flight Re#.
  - Inlet flow field assessment (Boeing & Northrop).
- Viscous CFD analysis of TCA W/B/N/D @ wind tunnel and flight Re#.
- Nacelle shaping and orientation:
  - Nacelle cambering study (Boeing).
  - Nacelle orientation study (Northrop).
- Diverter design:
  - Alternate diverters; asymmetric, flow–through (Boeing).
  - Diverter aft fairing, full vs. half width, wing/nacelle/diverter channel(Northrop).
- Analysis of optimized TCA configurations as required for PAI issues.
- Wind tunnel data corrections: nacelle internal duct calculations, upper surface bump on / off, nozzle flap extensions.

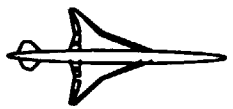

Based on the approach described in the previous chart the resulting analyses were broken down into the three main areas shown below. The TCA and TRANAIR optimized configuration assessments were from a PAI perspective primarily (the complete optimized configuration assessment is detailed in sub-task 2 report). The bifurcated inlet studies include a brief review of the Reference H results, followed by the TCA installation discussion. Each configuration analysis is described by surface pressures, integrated forces, and the state of the inlet flow field.

Outline

- TCA baseline PAI assessment.
  - Mach 2.4 OVERFLOW analyses / NASA LaRC Unitary Test Data.
  - Isolated nacelle analyses (Mach 0.9 to 2.4).
- Optimized TCA PAI assessment.
  - Mach 2.4 OVERFLOW analyses.
- Bifurcated inlet studies.
  - Bifurcated inlet nacelle (axi nozzle) on Ref H.
  - Bifurcated inlet / 2–D nozzle on TCA.
- Each configuration and condition assessed using surface pressures, integrated forces, inlet flow field chararacteristics.

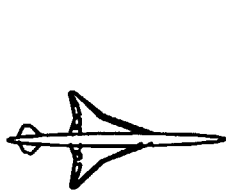

The OVERFLOW analysis results for the baseline TCA were compared to the LaRC Unitary test (#1671) of the 1.675%-scale TCA model (#2a). The data used in the comparisons shown here were the 4 million per foot runs (ReMAC = 6.4 million) with the baseline boundary layer trip.

OVERFLOW grids of the TCA wing/body and wing/body/nacelle/diverter were built for the above test condition (Mach 2.4). In addition, a flight Reynolds number grid for the wing/body has been built (wall spacing is 0.0006 inches for y+ of 1).

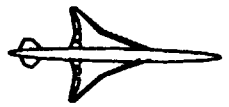

Baseline TCA Test Data

- LaRC UPWT 1671, 1.675%–scale model (2a).

Baseline TCA OVERFLOW Analyses

- W/B, W/B/N/D (Mach 2.4).
  - Wing upper surface nacelle bump on/off.
  - Outboard wing LE, nacelle lip infinitely sharp.
  - Wing LE planform break transition in 1 inch.
  - No nozzle flap extensions (flat base as on WT model).
- Isolated nacelle (Mach 0.9, 1.2, 1.4, 2.4).
- NASA LaRC Unitary WT Reynolds Number (4 million/ft).
  - $\Delta y \sim 0.013$ inches, $y^+ \sim 1$.
- Spalart–Allmaras turbulence model.
- No–slip walls are all turbulent.
- Central difference.
- Multi–gridding.

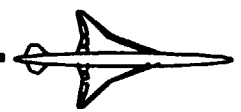

The OVERFLOW wing/body grid for the TCA configuration is shown here. The topology is atypical in that there are two collars connecting the wing and the body, instead of the usual one. This is due to the fact that the TCA wing/body intersection line is not continuous. The wing lower surface actually spans the symmetry plane below the body around the midchord point so that the intersection lines end on the symmetry plane. Collars were built to follow these intersection lines; the collars overlap aft of the wing TE instead of forming the usual C–grid wake boundary condition. The wing, body, and collar grids are surrounded by a single box grid and an outer boundary ellipsoid grid.

TCA Wing/Body OVERFLOW Grid

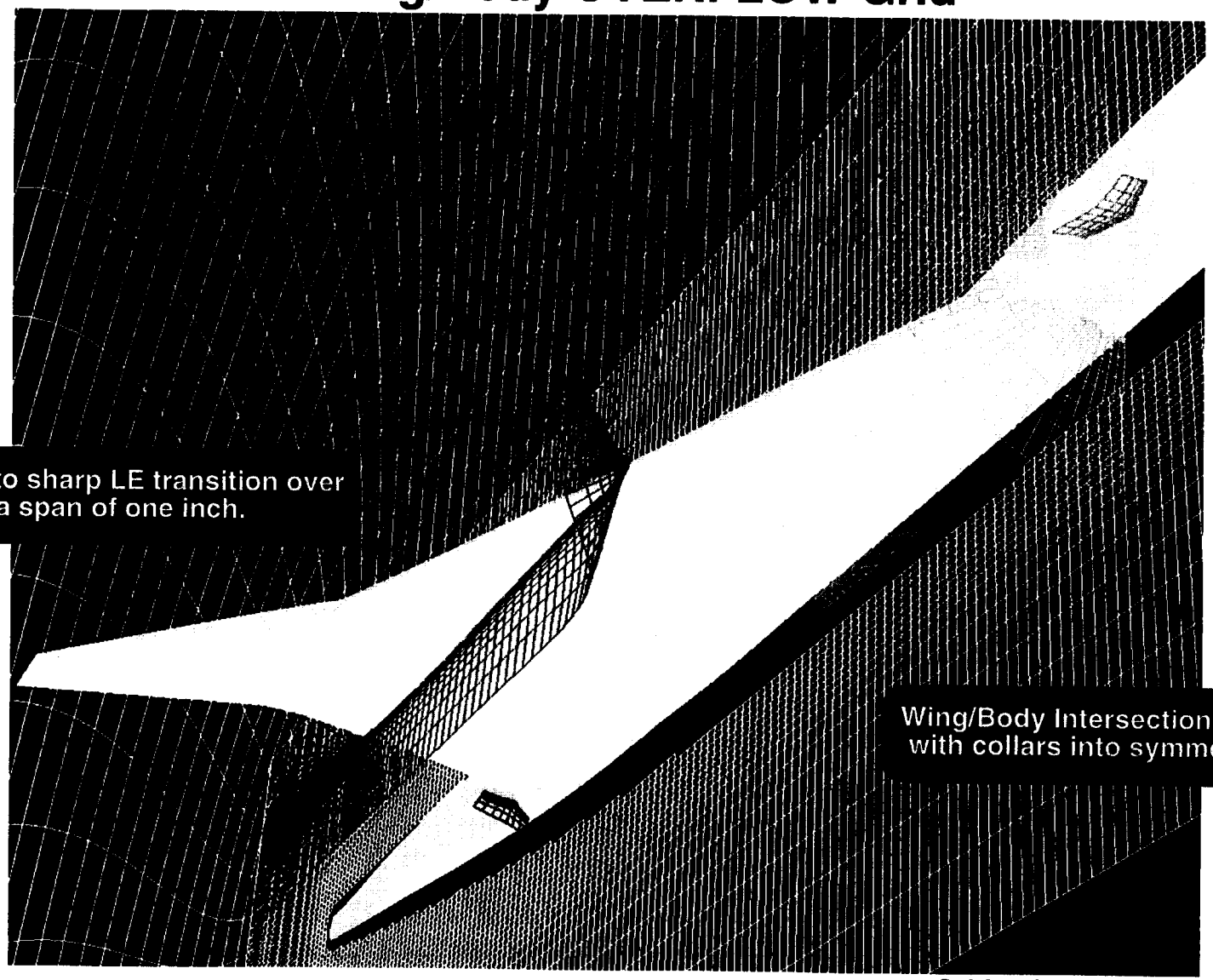

Grid points removed for clarity.

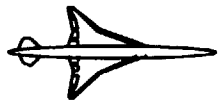

The OVERFLOW TCA wing/body grid had 3.5 million grid points for the LaRC unitary wing tunnel condition. The grid stretching strategy from the surface developed on Reference H OVERFLOW analyses of using 3 equally spaced cells was employed on the TCA configuration as well. The wing had 106 points chordwise on the upper and lower surfaces. A stretching ratio limit of 1.2 was adhered to strictly.

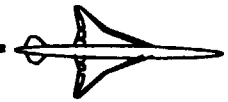

TCA Wing/Body OVERFLOW Grid Dimensions

Component	j_{max}	k_{max}	$l_{max,wt}$	$l_{max,flight}$	points,wt	points,flight
Body	208	93	49	61	947,856	1,179,984
Wing	271	117	45	69	1,426,815	2,187,783
Collar1	221	25	37	53	204,425	292,825
Collar2	53	25	37	53	49,025	70,225
Box	220	52	64	same	732,160	same
Ellipsoid	78	45	31	same	108,810	same
TOTAL					3,469,091	4,571,787

Wind Tunnel: NASA LaRC Unitary, 1.675%–scale, Re/ft = 4 million,
Re_{MAC} = 6.4 million, $y^+ = 1.0 \rightarrow dy_{surface} = 0.013$ in.

Flight: Mach 2.4, Mid–cruise, altitude = 56,500 ft,
Re_{MAC} = 195 million, $y^+ = 1.0 \rightarrow dy_{surface} = 0.0006$ in.

NOTES: Three equidistant points from surface.
Stretching ≤ 1.2
Wing surface has 106 points from LE to TE:
Δs_{LE} = .01% to .02% chord, Δs_{TE} = .4% to .5% chord.

The OVERFLOW gridding around the nacelles is shown. Each nacelle requires 7 additional grid blocks. Three blocks to do the nacelle external and internal geometry, two blocks on either side of the diverter, fairing grid spanning the wing TE and upper nozzle area, and a box grid (fitted to wing lower surface) to help tie all the blocks together. The nacelle leading edge lips are modeled by overlapping external and internal grid blocks that start forward of the lip by about 20 inches. A single grid block wraps around the nacelle base region. The grid blocks on either side of the diverter overlap ahead of the diverter LE and proceed forward ahead of the nacelle LE.

TCA W / B / N / D OVERFLOW Grid

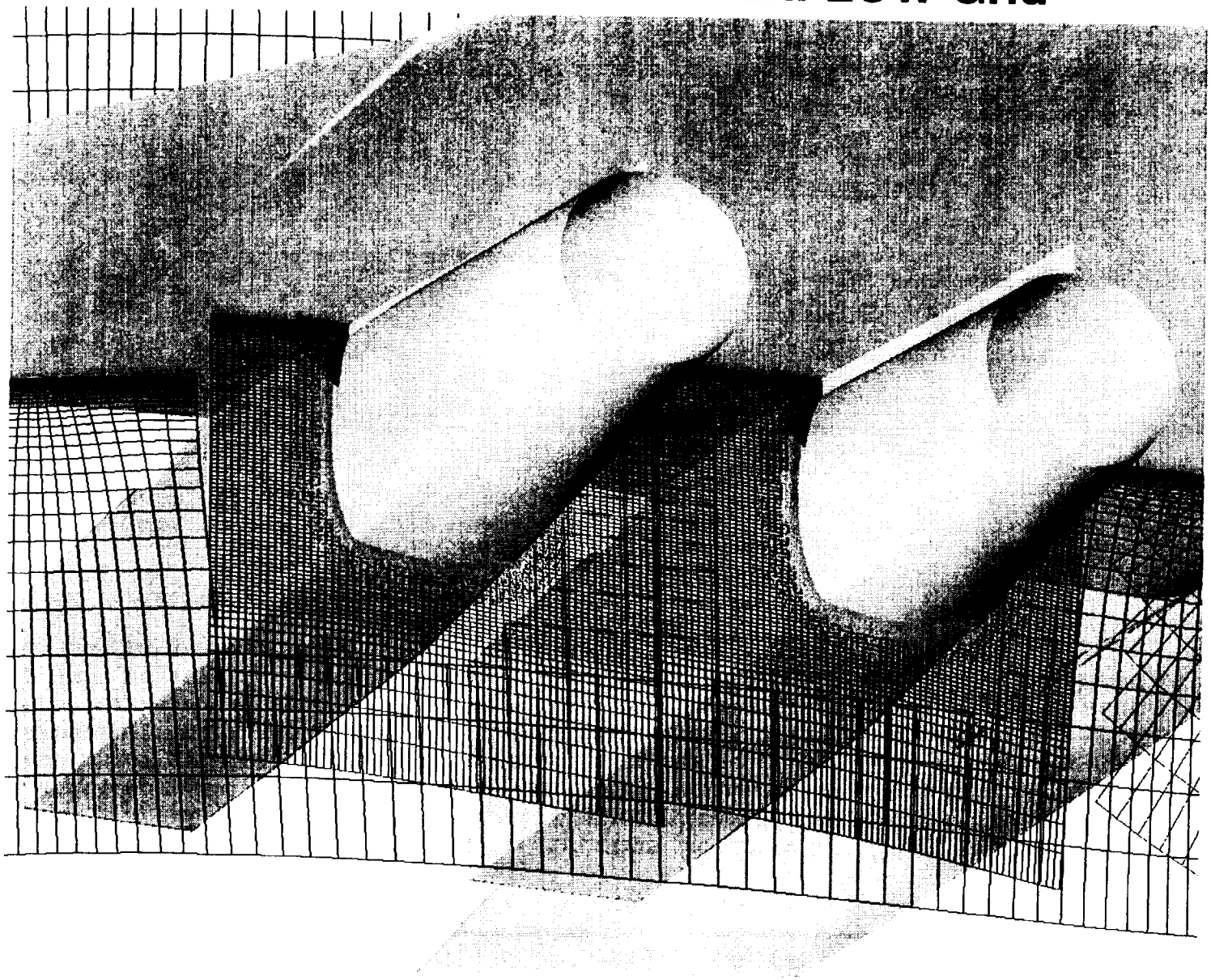

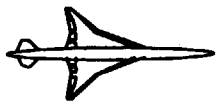

Each nacelle adds a total of 3.1 million grid points, yielding a total wing/body /nacelle/diverter grid size of 9.7 million.

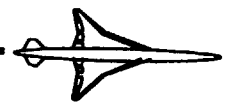

TCA Wing/Body/Nacelle/Diverter OVERFLOW Grid Dimensions

Component	j_{max}	k_{max}	$l_{max,wt}$	$l_{max,flight}$	points,wt	points,flight
Wing/Body INBOARD	–	–	–	–	3,469,091	4,571,787
Nacelle Box	131	67	107	–	939,139	–
Nac Cowl	80	161	37	–	476,560	–
Nac Nozzzle	71	161	37	–	422,947	–
Nac Internal	57	161	37	–	339.549	–
Diverter Left	176	37	57	–	371,184	–
Diverter Right	176	37	57	–	371,184	–
Div Fairing	113	59	37	–	246,679	–
OUTBOARD Nac / Div	–	–	–	–	3,037,964	–
TOTAL					9,751,419	–

Wind Tunnel: NASA LaRC Unitary, 1.675%–scale, Re/ft = 4 million,
Re_{MAC} = 6.4 million, $y^+ = 1.0 \rightarrow dy_{surface} = 0.013$ in.

Flight: Mach 2.4, Mid–cruise, altitude = 56,500 ft,
Re_{MAC} = 195 million, $y^+ = 1.0 \rightarrow dy_{surface} = 0.0006$ in.

NOTES:
- Three equidistant points from surface.
- Stretching ≤ 1.2
- Wing surface has 106 points from LE to TE:
  Δs_{LE} = .01% to .02% chord, Δs_{TE} = .4% to .5% chord.

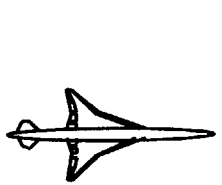

The OVERFLOW multi-gridding code enhancement was released in mid-1996. Boeing HSCT aerodynamics spent a large amount of time testing it and attempting to integrate it into the analysis process. The end results have been very successful as shown here. Wing/body case can now be run for 2-3 hours, and wing/body/nacelle/diverter cases in ~10 hours (charged on NAS vonneumann) for the Mach 2.4 condition at wind tunnel Reynolds Number. The gridding and solution strategies (DT and CFL values) required to achieve this convergence have proved to be fairly robust across several different wing/body and nacelle configurations.

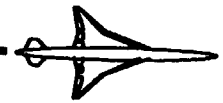

TCA Wing/Body OVERFLOW Convergence History
Multi-Grid Code Enhancement
Mach 2.4, α = 3.0 deg, Re_{MAC} = 6.4 million

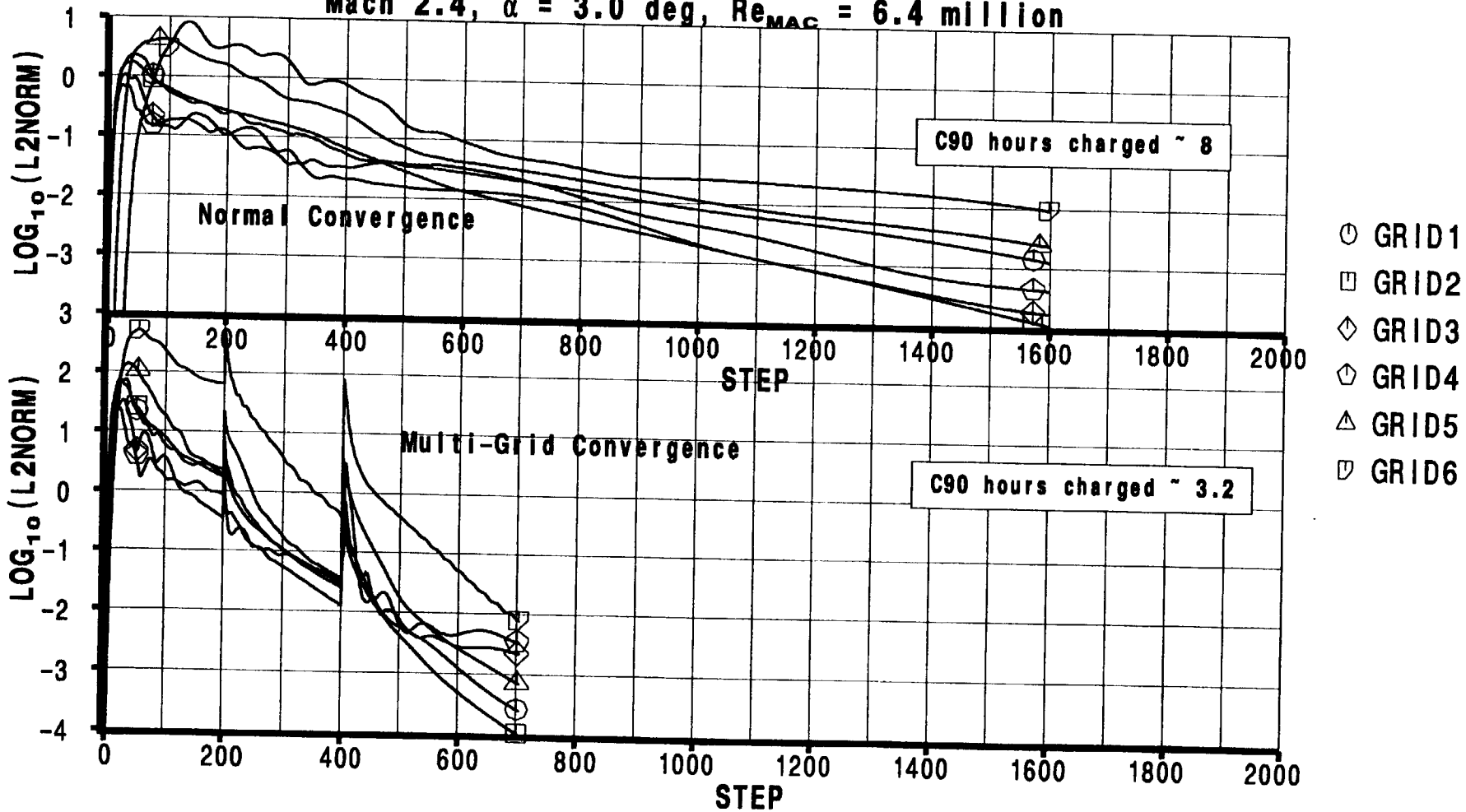

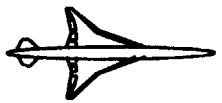

The TCA baseline configuration includes a bump on the wing upper surface where the nacelle protrudes above the wing OML. The 1.675%–scale TCA model was built with the bump as a separate fairing piece that could be removed. OVERFLOW grids were built to model both configurations. The shaded images below were made from the OVERFLOW surface grids in order to illustrate the level of detail in the grid.

Wing / Nozzle Transition Geometry

Baseline: Nozzle protrudes above wing upper surface.

Modified: Nozzle is clipped to remove wing upper surface bump.

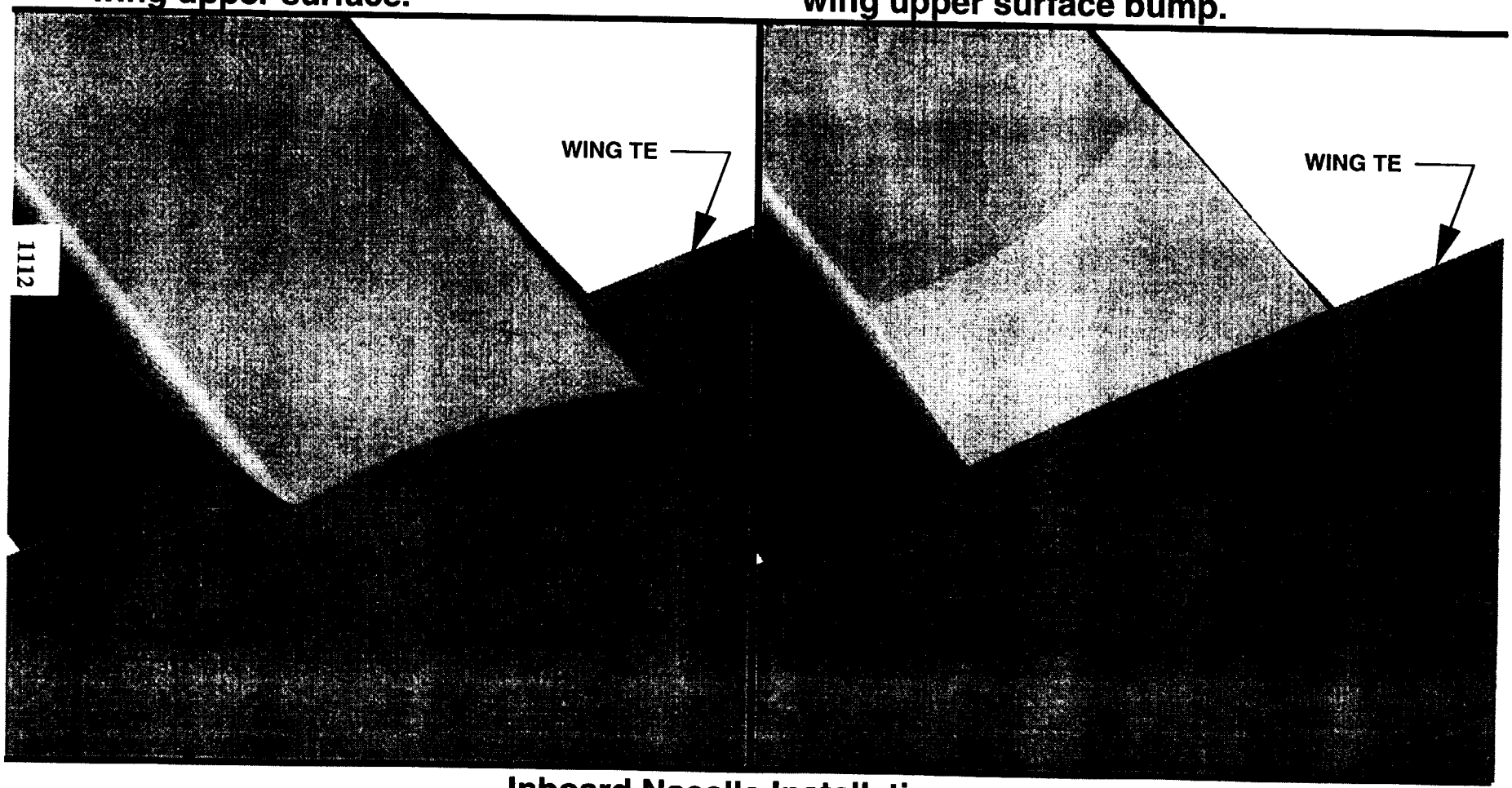

1112

Inboard Nacelle Installation

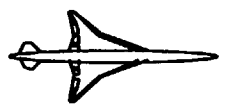

OVERFLOW solution surface pressures are shown for the wing/nozzle transition region. A polar was completed for the bump on configuration. A single angle of attack was run for the bump off case: alpha = 3.0 deg, CL = 0.83. A comparison of the two configurations showed that the bump on case had 0.3 counts less drag than the bump off case. Examination of the flow field indicated that this was primarily due to the bump reducing the aft facing area with negative Cp on the upper surface of the wing near the TE, i.e. the area covered up by the bump. NASA LaRC has reported a bump increment of - .1 to - .2 drag counts at minimum drag and an increment of - .4 counts at CL=0.1; this is very close to the OVERFLOW result.

Wing / Nozzle Transition Surface Pressure
Mach 2.4, Re_{MAC} = 6.4 million, α = 3.0 deg
OVERFLOW Solution

Baseline

Modified

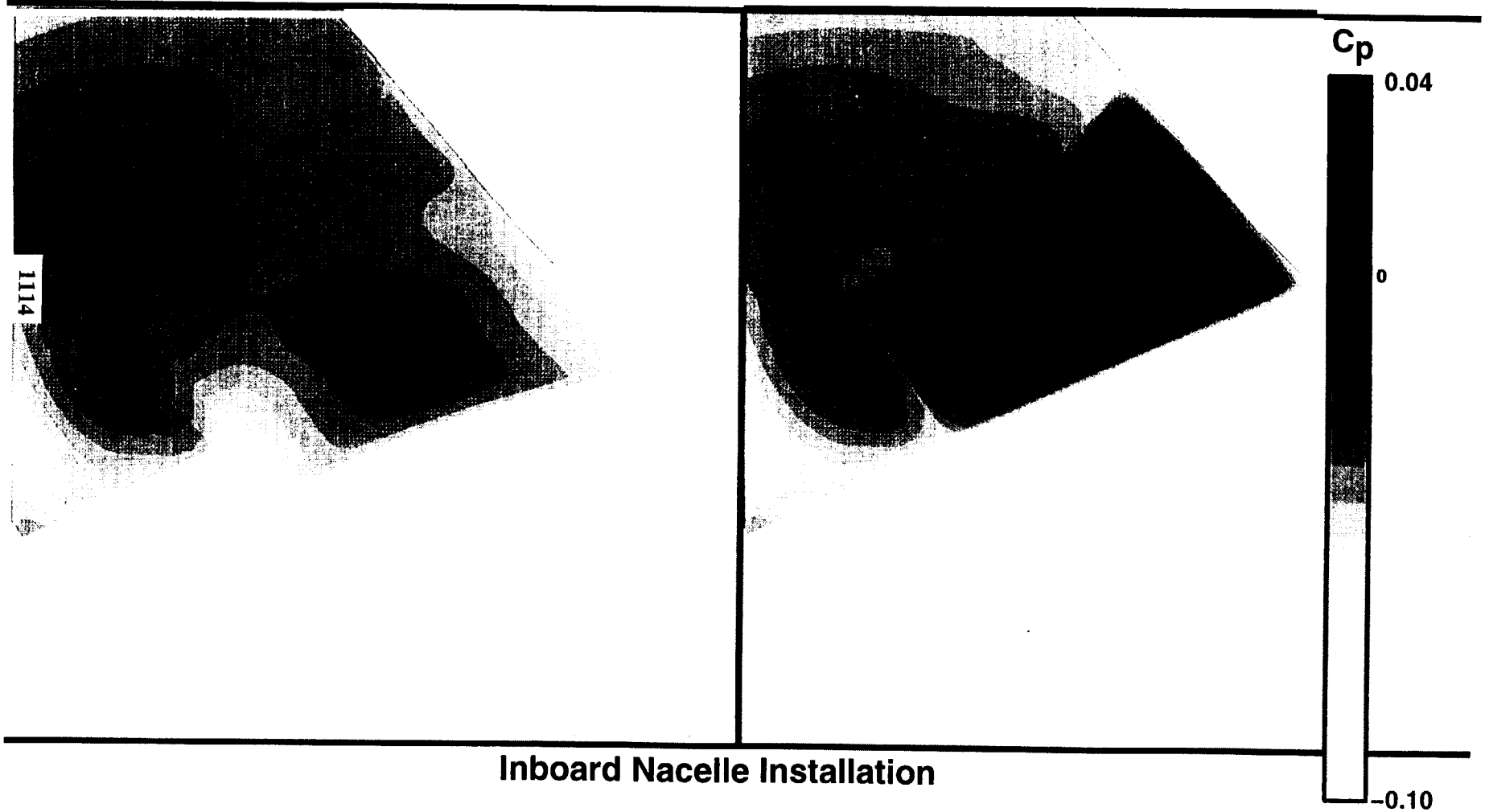

Inboard Nacelle Installation

The wing lower surface pressure distribution from the OVERFLOW analysis of the TCA at supersonic cruise is shown. The wide diverter planform can be clearly seen. The nacelle is also represented in black outline in order to see how the pressure field relates to the nacelle geometry. The surface characteristics are similar to Reference H. The primary difference being a slightly higher and larger high pressure region around the diverter LE due to the TCA diverter planform half-angle increase over the Reference H (11 vs 8.6 deg).

TCA Wing/Body/Nacelle/Diverter Lower Surface Pressure Coefficient

Mach 2.4, Re_{MAC} = 6.4 million, OVERFLOW Solution

α = 3.0 deg., C_L = 0.0840

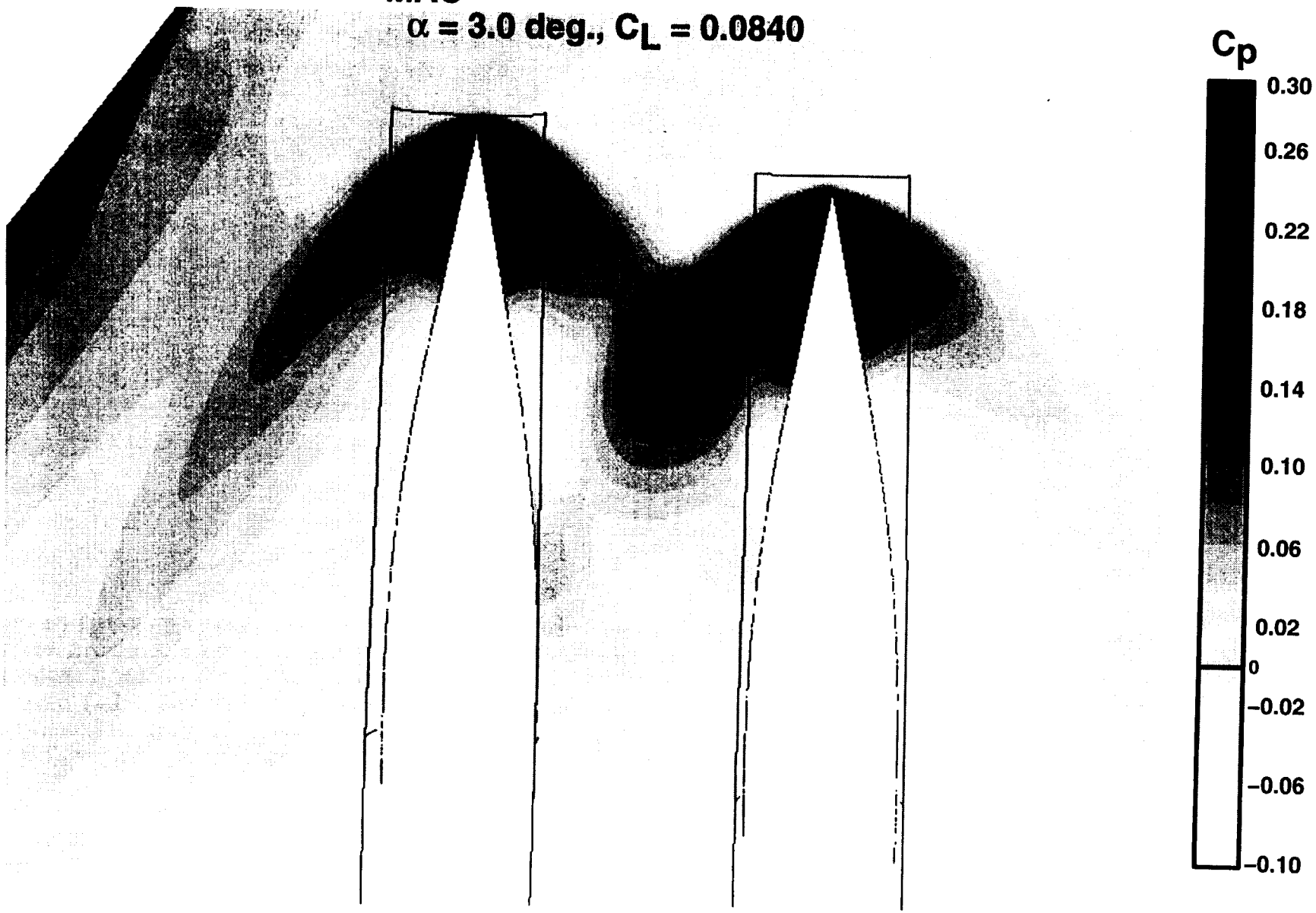

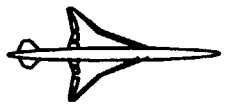

The TCA wing lower surface pressure distribution for the wing/body is shown here for reference to the wing/body/nacelle/diverter case shown in the previous figure.

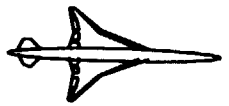

TCA Wing/Body Lower Surface Pressure Coefficient
Mach 2.4, Re_{MAC} = 6.4 million, OVERFLOW Solution
α = 3.0 deg.

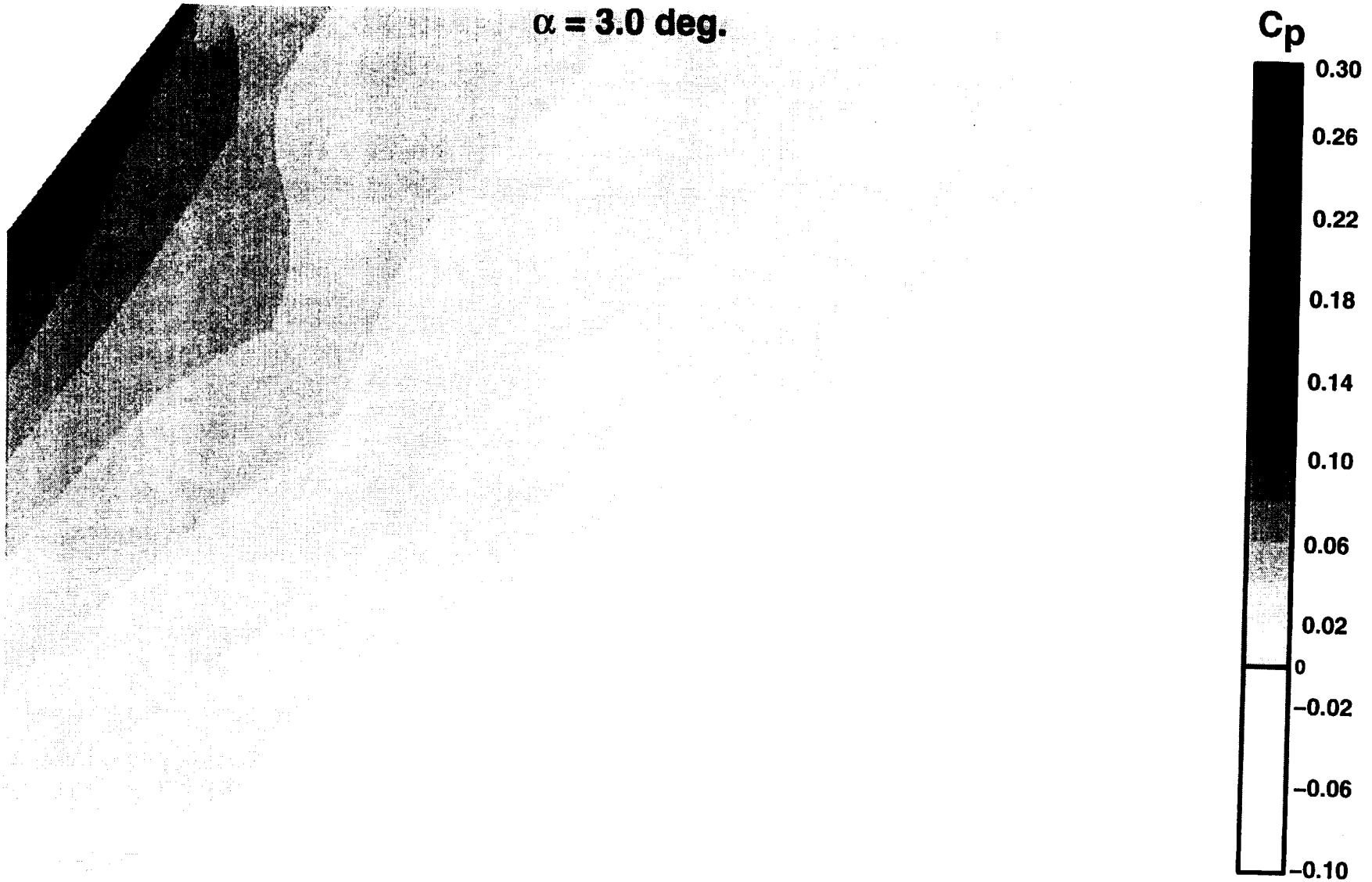

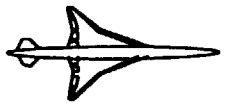

The nacelle/diverter surface pressure distribution from the OVERFLOW solution is shown here. These are also very similar to Reference H results except for the higher pressures around the diverter LE discussed previously. The diverter shock had remained attached in both inboard and outboard installations. However, the outboard is noticeably unswept in comparison to the inboard. This is due to the much smaller channel the diverter flow is being forced into in the case of the out board installation.

TCA Wing/Body/Nacelle/Diverter Nacelle Surface Pressure Coefficient
Mach 2.4, Re_{MAC} = 6.4 million, OVERFLOW Solution
α = 3.0 deg., C_L = 0.0840

Outboard

Inboard

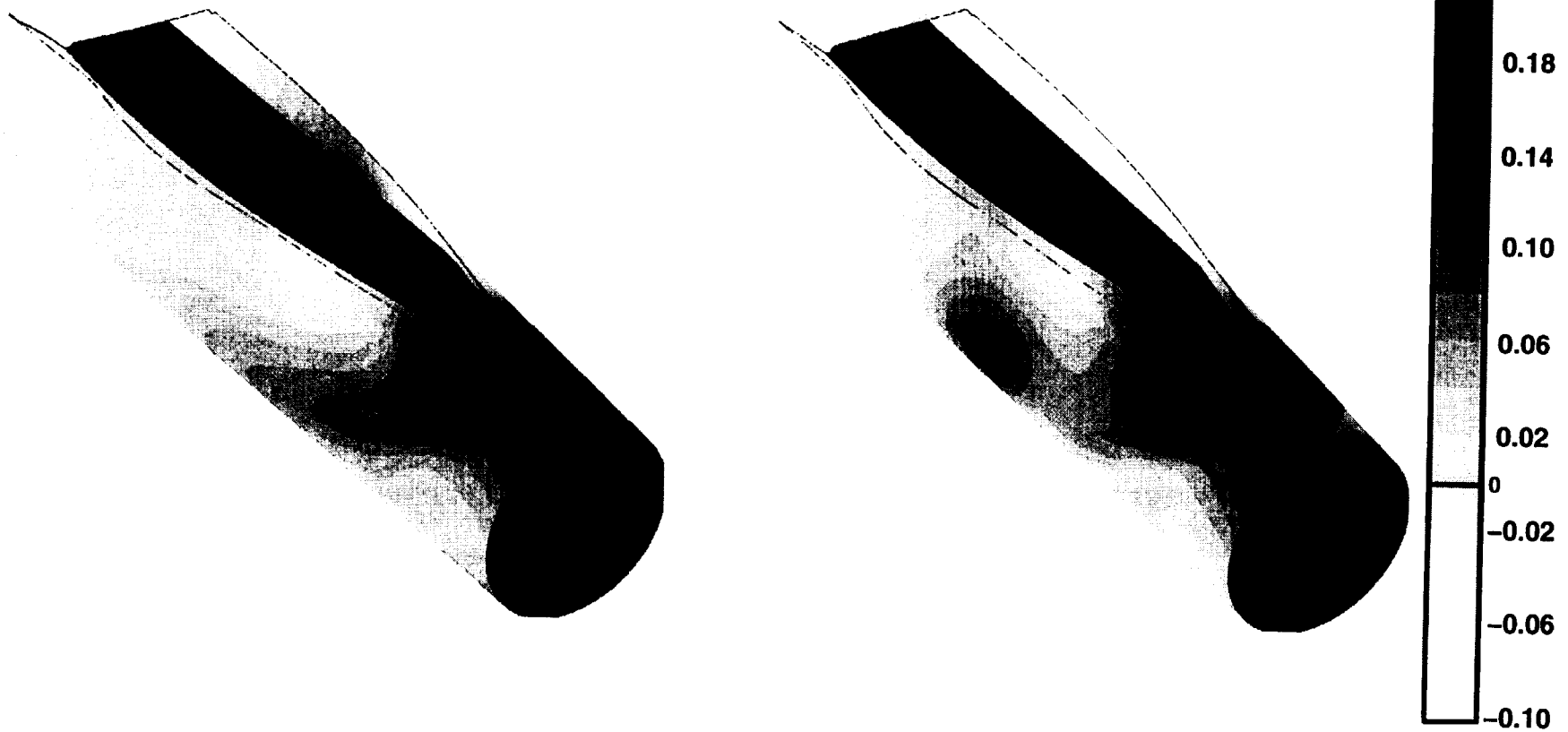

The next two figures show the wing pressure coefficient distribution at the cruise condition of Mach 2.4 and angle of attack of 3 degrees. The pressure signature of the nacelle/diverter combination is similar to the Reference H configuration analyzed previously, with one notable exception. The double shock feature between the nacelles is much stronger on the TCA configuration. The aft shock is just the result of the adjacent nacelle being farther away from the pressure tap row and the shock moving farther aft before crossing the span station. The increased strength is probably due to the longer diverter ramp on the TCA which brings the diverter out to the full width of the nacelle (unlike the Reference H which had diverter ramps that terminated at a 32 inch width).

Wind tunnel pressure data for the LaRC UPWT 1671 test of the TCA are also shown. The match between test and OVERFLOW results is very similar to the Reference H comparisons (ARC 9x7 test data). Of most intestest for PAI issues is the ability to match the nacelle diverter shock strength and location almost exactly in every case except one pressure tap on the 32.5% span row. The mismatch in this case is very large and not understood at this time. Some possible causes include:

1) inlet spillage (but the pressure data on other side of nacelle indicates no perturbation),
2) diverter channel choked (unlikely with a axisymmetric inlet),
3) pressure tap/ instrumentation problems (but the result for that tap was repeatable),
4) boundary layer separation.

TCA Wing/Body/Nacelle/Diverter Chordwise Pressure Distribution

Mach 2.4, α = 3 deg, Re_{MAC} = 6.4 million, OVERFLOW Solutions

Wing/Body (UPWT1671, solid=chine)

Wing/Body/Nacelle/Diverter (UPWT1671, solid=fairing)

B.L. 94.5, 12.0% (inbrd of inbrd nac.)

B.L. 256.2, 32.5% (outbrd of inbrd nac.)

B.L. 156.4, 19.9% (inbrd of inbrd nac.)

B.L. 324.7, 41.2% (inbrd of outbrd nac.)

CP

XoverC

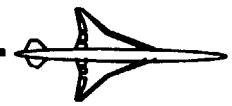

See previous facing text page.

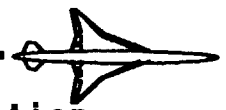

TCA Wing/Body/Nacelle/Diverter Chordwise Pressure Distribution

Mach 2.4, α = 3 deg, Re_{MAC} = 6.4 million, OVERFLOW Solutions

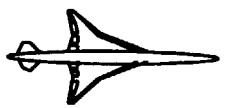

The lift and pitching moment results shown here confirm the lift delta between CFD and wind tunnel seen in previous HSR studies. A large fraction of the CFD lift delta above wind tunnel data is seen to be due to not including the nacelle internal duct negative lift. When this is included (as it is in the wind tunnel data) the delta CFD/test lift delta is reduced by about a third. The basic shape of the moment curves is very similar to the Reference H pitching moment data. However, the break in the moment slope appears to occur much closer to the cruise point than for Reference H. The OVERFLOW and wind tunnel pitching moment comparison indicates a moment reference center discrepancy that has not yet been resolved.

TCA Wing/Body/Nac/Div Lift & Pitching Moment

Baseline Axi/2D Nacelle, Mach 2.4, Re_{MAC} = 6.4 million

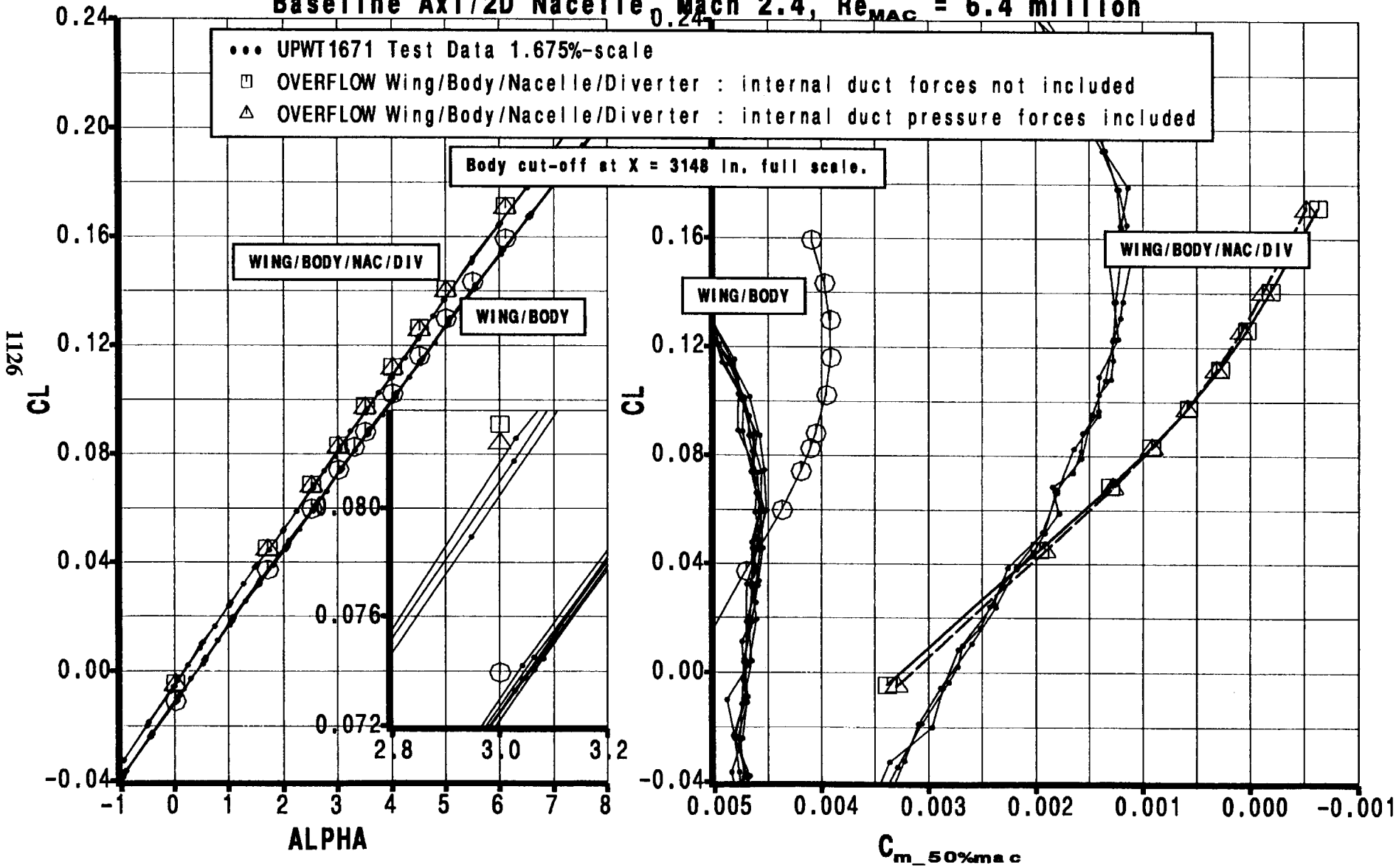

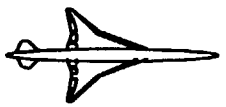

The Mach 2.4 drag polar is shown in this figure with the wing/body polar also shown for reference. The CFD drag values are typically less than the wind tunnel values; a discrepancy that has been attributed to trip drag in the past. A trip drag study was performed during this test with the results shown below, along with the OVERFLOW/test increments:

	Test–OVERFLOW	CDtrip
W/B	3.4	4.2
W/B/N/D	7.5	6.33

These values are using the OVERFLOW results with the nacelle internal duct lift included. The CFD/test deltas are close to the trip drag values but the values are skewed such that when the nacelle drag increment at constant lift is calculated the OVERFLOW results yield 9.4 counts and the test data 13.5 counts. A difference of 4 counts when the nacelle trip drag should only be 2.1 counts ! This discrepancy is discussed in the following figures.

HSCT High Speed Aerodynamics

TCA Wing/Body/Nacelle/Diverter Drag Polar

Baseline Axi/2D Nacelle, Mach 2.4, Re_{MAC} = 6.4 million

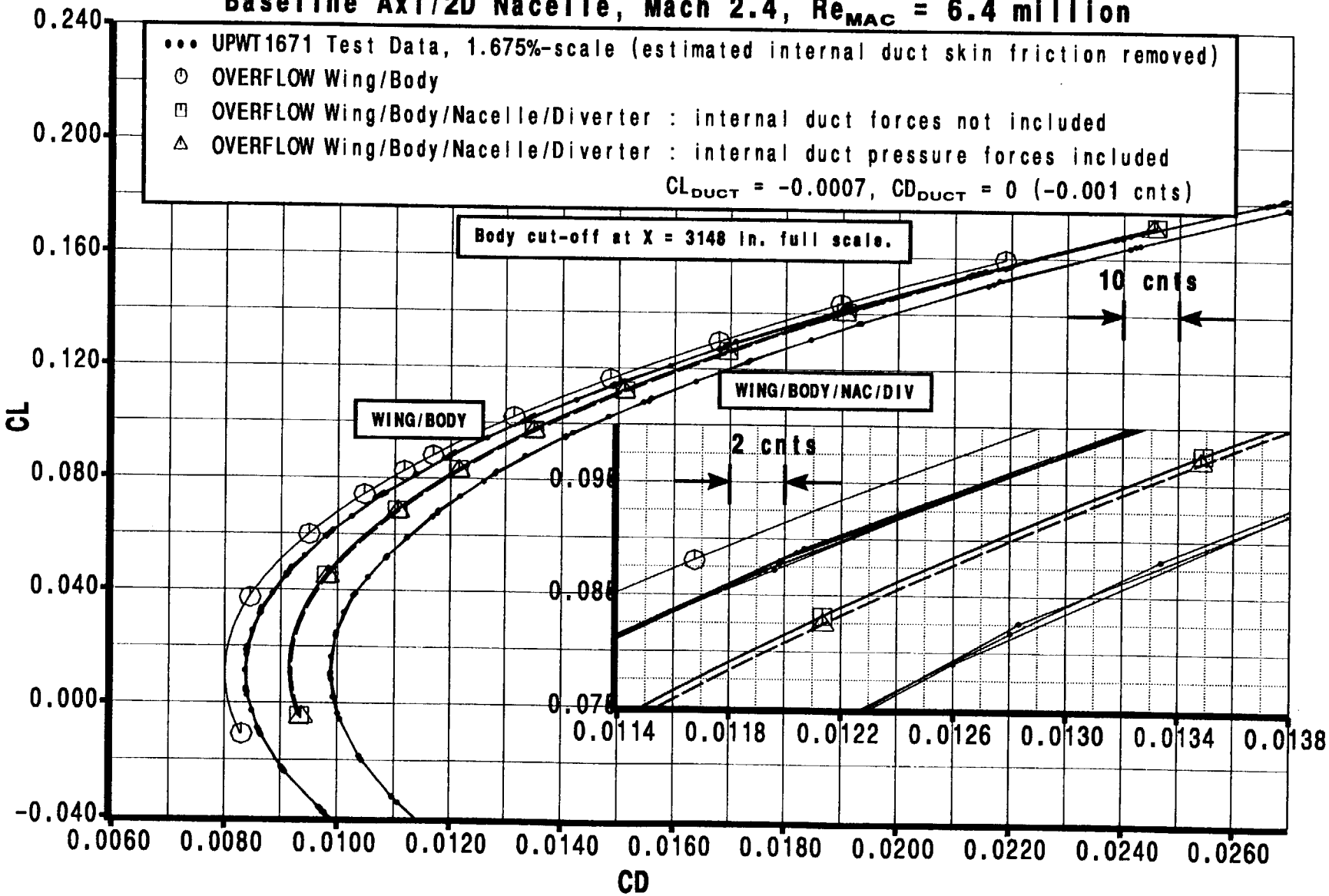

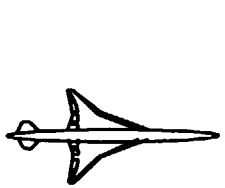

The nacelle/diverter force increments are shown in this figure. On the left, the drag and lift increments at constant angle of attack are shown. The plot on the right shows the final installed drag increment of the nacelle/diverter versus the lift of the wing/body/nacelle/diverter. The OVERFLOW data is shown with and without the internal duct lift included. The test data is shown both as a scatter band and as a curve fit to all data. The scatter data was obtained by simply calculating all deltas combinations possible from the 3 wing/body/nacelle/diverter runs and the 7 wing/body runs. This method gives a rudimentary feeling for the scatter in the data: +– 0.5 counts at cruise. The OVERFLOW nacelle force increment at the cruise lift coefficient is about 4 counts lower than the test data (9.5 counts compared to 13.5 counts). This can be partially explained by the trip drag of the trips on the nacelles themselves which amounts to 2.1 counts (6.3–4.2). This trip correction would still leave a 1.9 counts discrepancy between OVERFLOW and the test data. The next step in this investigation was to examine the internal duct skin friction correction made to the wind tunnel data.

TCA Wing/Body/Nacelle/Diverter PAI Force Increments

Baseline Axi/2D Nacelle, Mach 2.4, Re_{MAC} = 6.4 million

1130

ΔCDnac(@constant α)

0.0024
0.0022
0.0020
0.0018
0.0016
0.0014
0.0012
0.0010
0.0008
0.0006
0.0004

Isolated Nacelle Skin Friction Drag (Flat Plate)

Installed Nacelle/Diverter Skin Friction Drag (OVERFLOW)

ΔCLnac

0.010
0.008
0.006
0.004
0.002
0.000

≈ 0.93 cnt

0 1 2 ALPHA 3 4 5

Isolated Nacelle Pressure (4.43 cnts) + Viscous (10.62 cnts) (OVERFLOW)

1 cnt

ΔCDnac(@constant CL)

0.0024
0.0022
0.0020
0.0018
0.0016
0.0014
0.0012
0.0010
0.0008
0.0006
0.0004

0.00 0.04 0.08 CL 0.12 0.16

UPWT1671 Test Data, 1.675%-scale
Estimated nacelle internal duct axial force removed

Internal duct forces not included
OVERFLOW Wing/Body/Nacelle/Diverter

Internal duct pressure forces included
OVERFLOW Wing/Body/Nacelle/Diverter

Body cut-off at X = 3148 in. full scale.

This figure shows the wind tunnel estimated nacelle internal duct drag correction contained in the test data file compared to the OVERFLOW results. The comparison illustrates a significant difference in the variation with angle of attack between the wind tunnel estimated value and the OVERFLOW results. The wind tunnel estimate is relatively flat with angle of attack compared to the OVERFLOW results which increase with angle of attack. At 3 degrees angle of attack the difference between the estimate and the OVERFLOW values amount to 0.85 counts for the total of the inboard and outboard nacelles (estimate too low).

TCA Nacelle Internal Duct Friction Drag
Test Correction vs OVERFLOW, Mach 2.4, Re_{MAC} = 6.4 million

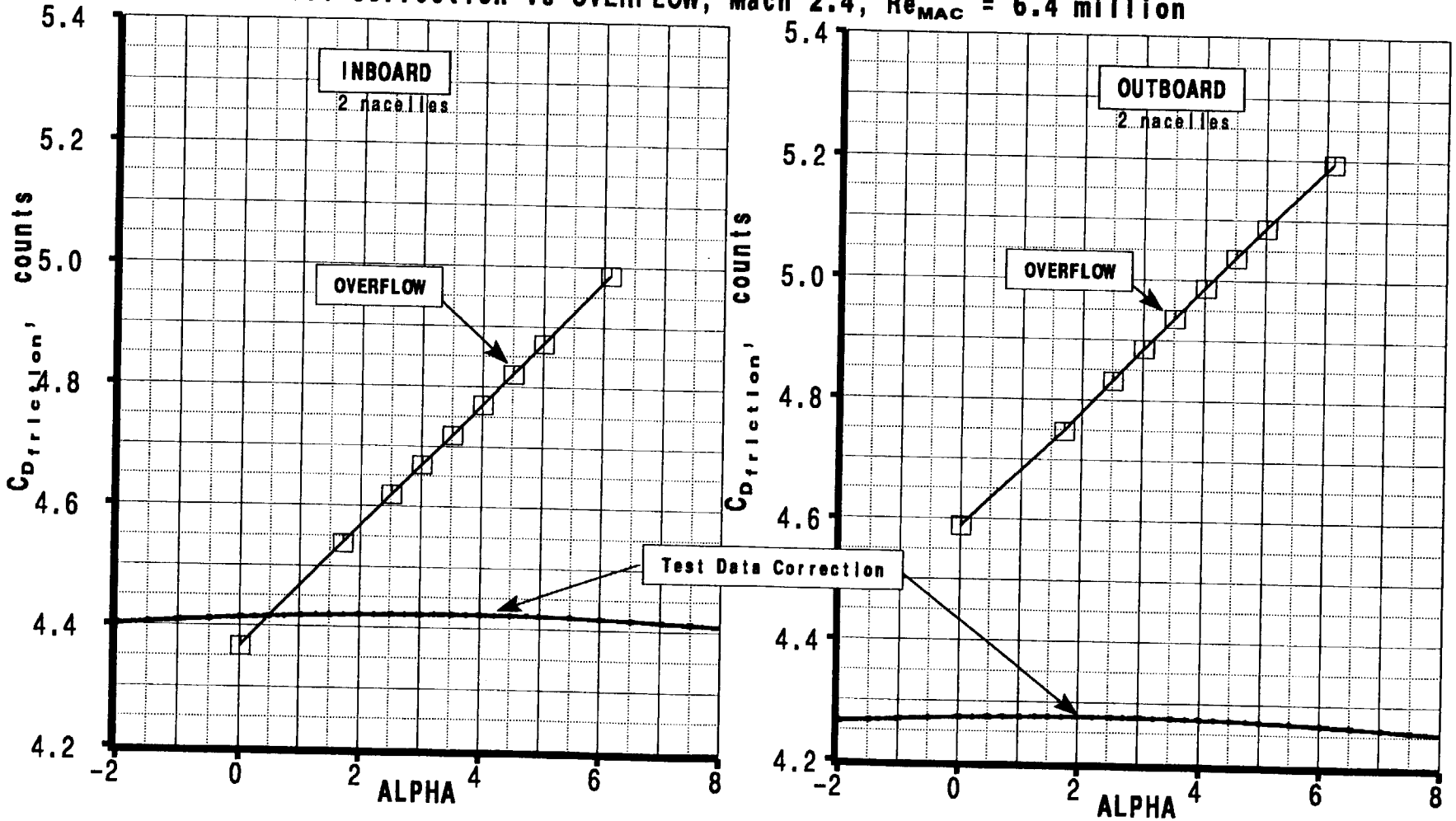

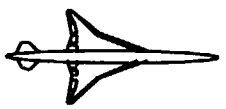

This figure shows the nacelle/diverter force increments recalculated with the nacelle internal duct forces uncorrected in the wind tunnel data, and all internal forces included in the OVERFLOW force integration. The OVERFLOW installed nacelle/diverter drag increment is now 3 counts less than the test data (21.8–18.8); taking into account the 2.1 nacelle trip drag this puts OVERFLOW within 0.9 counts of the test data nacelle force increment.

TCA Wing/Body/Nacelle/Diverter PAI Force Increments

Baseline Axi/2D Nacelle, Mach 2.4, Re_{MAC} = 6.4 million

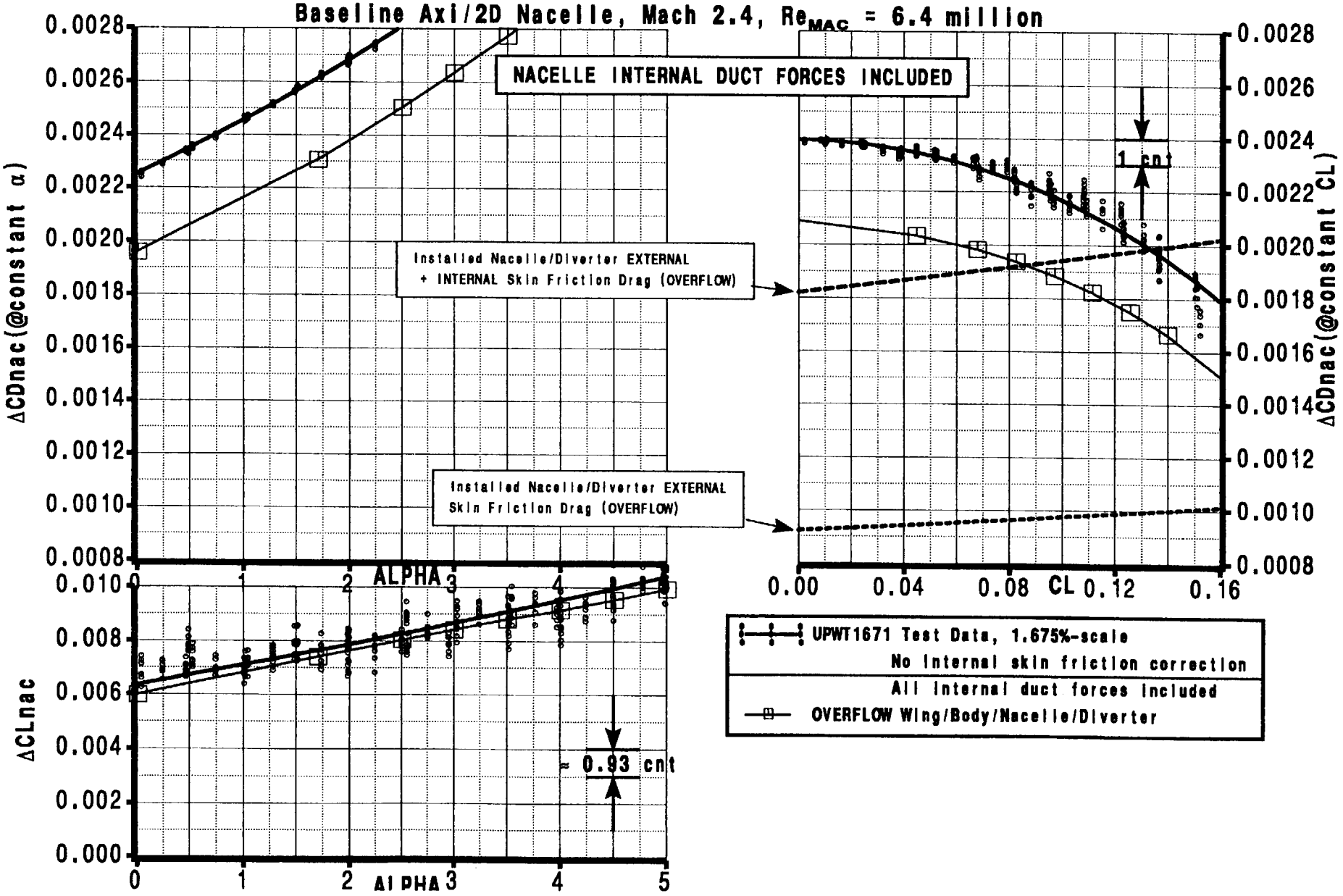

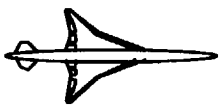

An assessment of the TCA inlet flowfield was made at the cruise flight condition of M=2.4, alpha=3.0 degrees, T_{inf}=390 deg. Rankine and Rn_c=195 million. The wing-body flowfield was calculated using the OVERFLOW Navier-Stokes code. The contours shown are cuts through the flowfield at the tip of the centerbody in a plane parallel to the respective inlet highlight.

The Mach contours at the outboard inlet show a reduction in variation relative to the Reference H configuration as a result of the movement of the leading edge planform break farther outboard. The outboard inlet shows a delta Mach of .027 while the inboard inlet has a delta Mach of .045. The current technology projection is .024 for Mach variation across each inlet. The inboard to outboard average Mach number delta is .046 with the inboard inlet seeing the higher value. This is significantly larger than the technology projection value of <.02. Of particular concern to inlet contro system designers are the high gradient regions near the crown of each inlet. If these gradients are not removed through optimization an increase in diverter height may be necessary.

The upflow and crossflow contours show that, in order to be aligned with the local flow, the inboard inlet would need to be tilted leading edge up 1.8 degrees and toed in 0.35 degrees while the outboard inlet would need to tilted leading edge up .2 deg and toed in 1.25 degrees. The crossflow variation is nearly 1 degree for both the inboard and outboard inlets. The technologyprojection for the total angular variation across an inlet is <.25 degrees.

TCA Inlet Flowfield Properties

Mach = 2.4, α = 3.0, β = 0.0, Re_{MAC} = 195 million

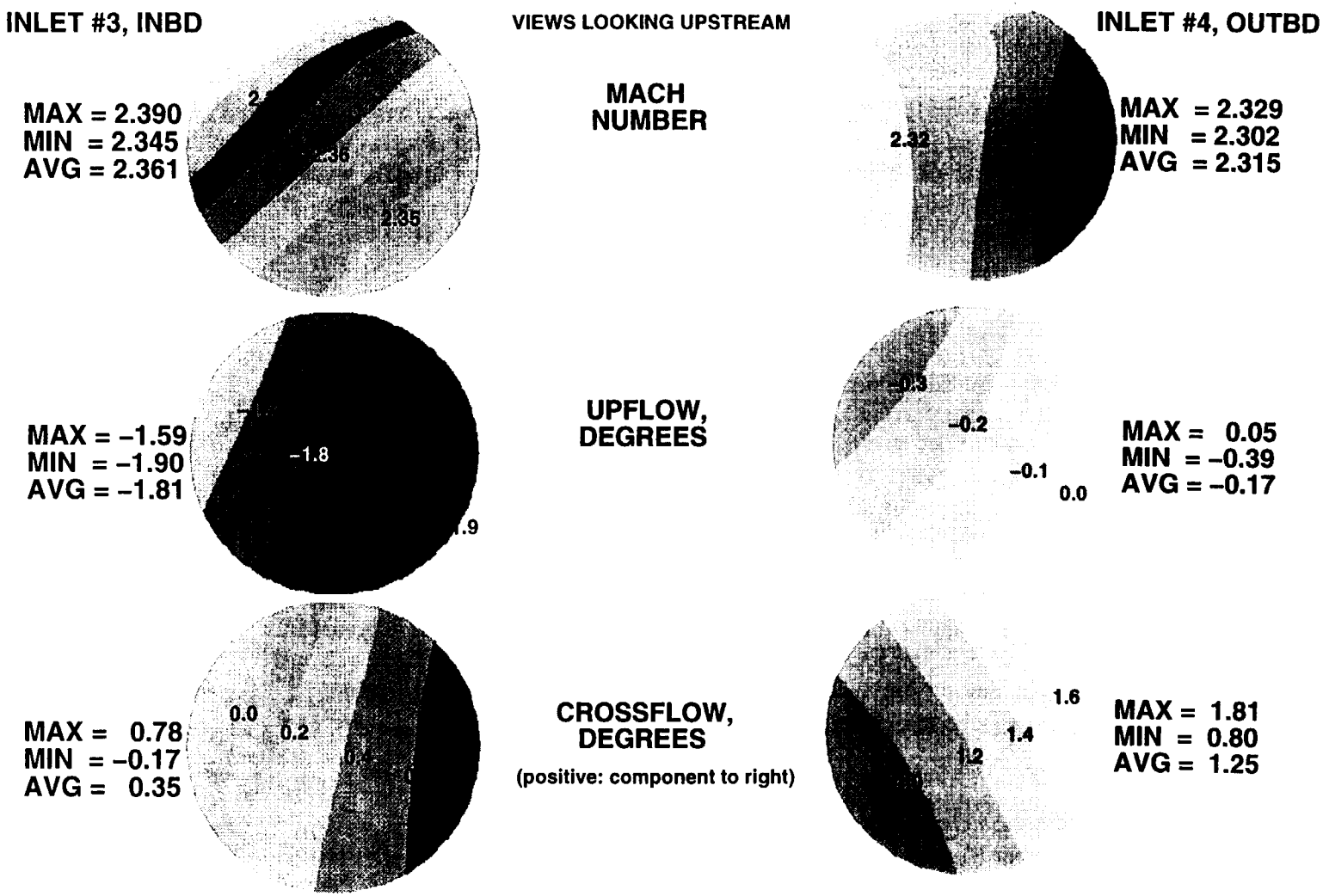

In order to accurately model transonic PAI effects the correct transonic inlet spillage must be modeled. In order to build up this capability an isolated nacelle analysis was initiated, starting with the wind tunnel flow through ducts. In order to establish a baseline the standard flow through duct geometry was run across the Mach range.

Mach number contours for the isolated nacelle at Mach 2.4 and 1.4 are shown in this figure. The Mach 1.4 case was run to determine whether OVERFLOW would confirm the assumption that the wind tunnel flow-through ducts would not unstart above Mach 1.3. As the figure shows, the internal flow decelerates to Mach 1.01 near the end of the duct but it does not normal shock.

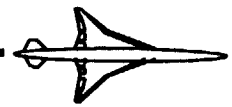

HSCT High Speed Aerodynamics

TCA Isolated Nacelle Symmetry Plane Mach Contours Supersonic OVERFLOW Solutions

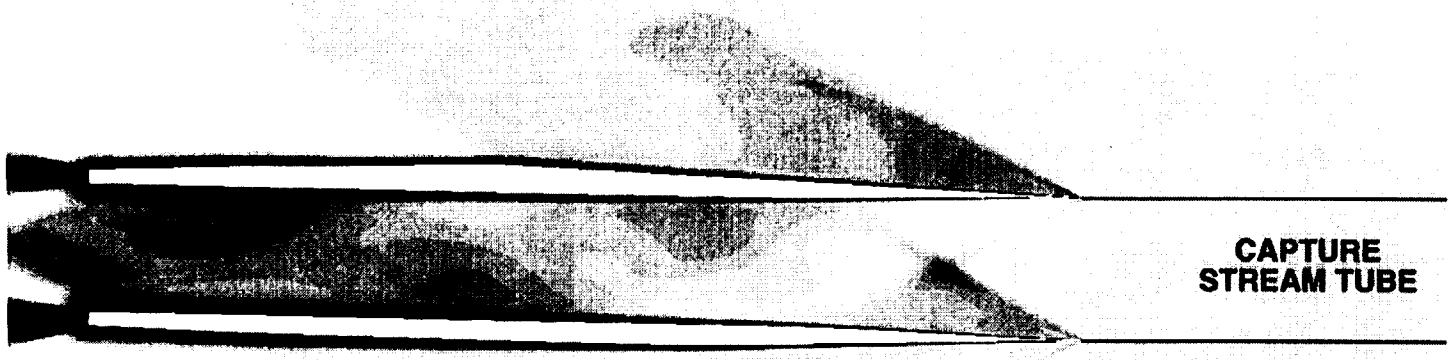

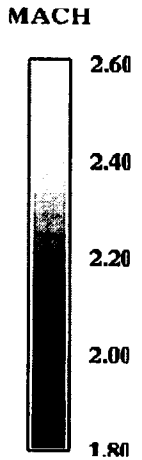

Mach 2.4, Re_{MAC} = 6.4 million

- Wind tunnel model flow–thru duct.
- Flow aligned with actual inlet centerline (not flow–thru duct).

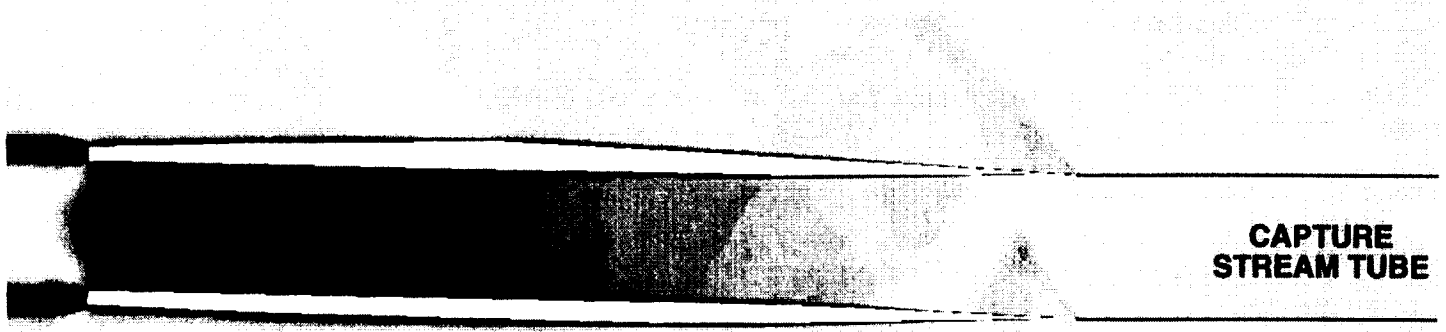

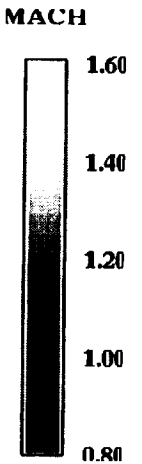

Mach 1.4, Re_{MAC} = 6.4 million

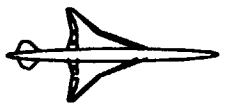

The isolated nacelle grid was modified for a transonic analysis at the PIE wind tunnel test condition (5.7%–scale model in ARC 11ft). The Mach contours for Mach 0.90 and 1.2 are shown in this figure. At Mach 1.2 the internal flow decelerated to a low enough Mach number that a normal shock was developed that than popped out in front of the inlet. Close examination of the capture stream tube indicates that both cases are spilling 10% or less. These conditions correspond to the flow field state of the typical high speed model tested with flow through ducts at transonici conditions. The actual inlet spills 35 – 40 % in flight at these Mach numbers and the flow is also altered by the presence of the centerbody.

TCA Isolated Nacelle Symmetry Plane Mach Contours Transonic OVERFLOW Solutions

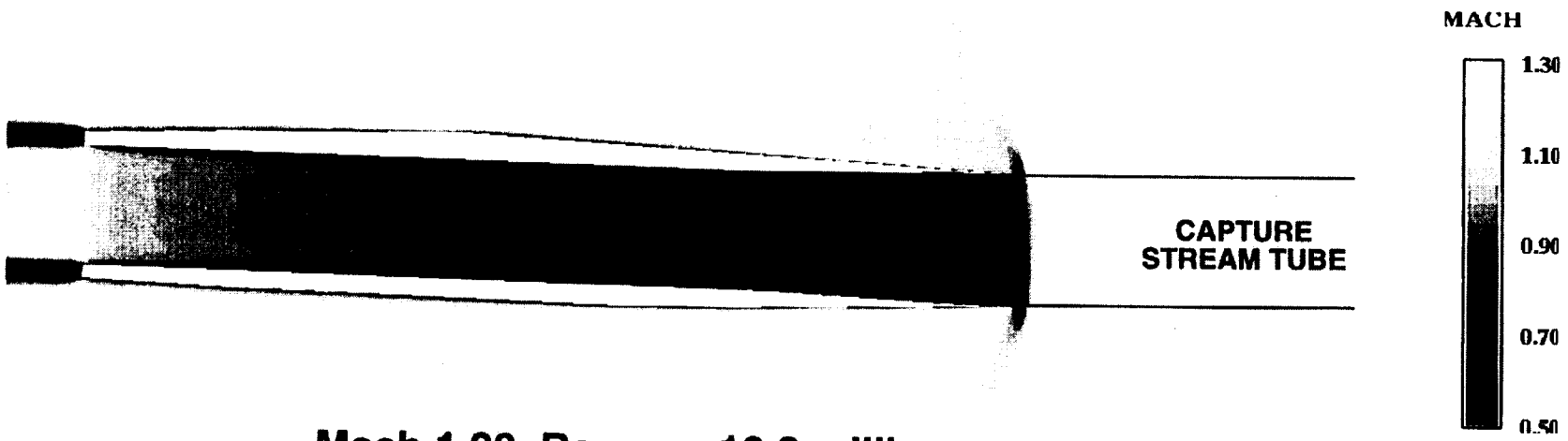

Mach 1.20, Re_{MAC} = 10.8 million

- Wind tunnel model flow–thru duct.
- Flow aligned with actual inlet centerline (not flow–thru duct).

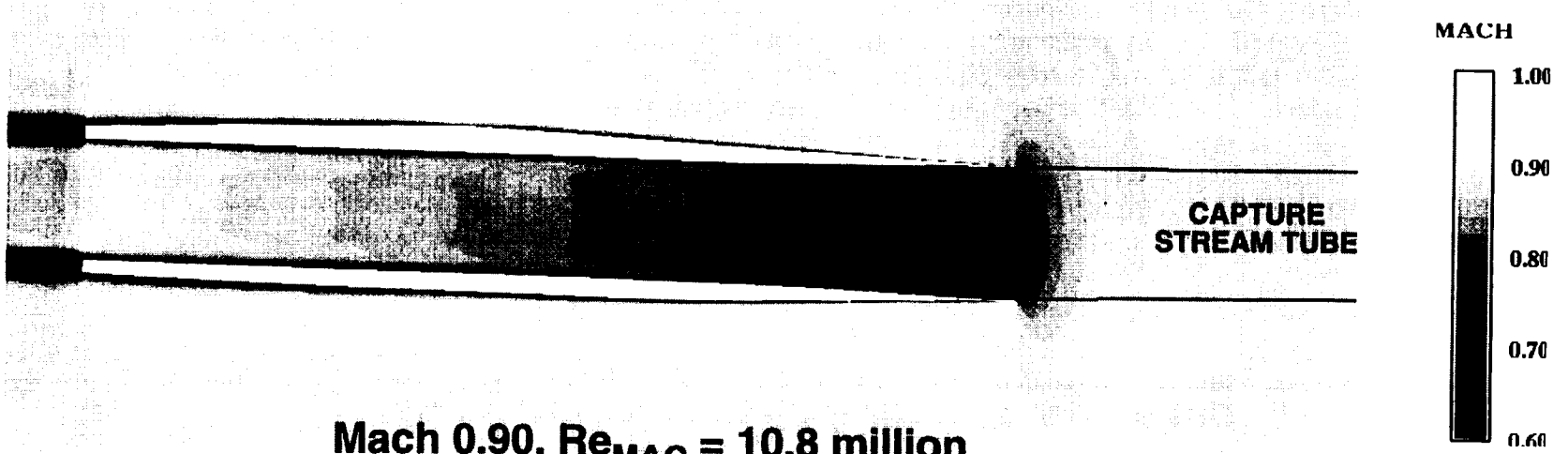

Mach 0.90, Re_{MAC} = 10.8 million

This figure shows the Mach contours for Mach 0.90 and 1.20 with the centerbody in the transonic position. The Mach 1.2 case has a normal shock near the lip and then the flow accelerates past the aft end of the centerbody to Mach number as high as 2.0. The flow separates off the end of the centerbody. The Mach 0.90 case was very similar but there was no normal shock at the lip and the separation on the centerbody occurred farther forward. As the capture streamtube lines indicate just putting the centerbody in the flow through duct increases the spillage considerably. In this case the Mach 0.90 solution is spilling 34.2 %. The actual inlet spills 40% in subsonic cruise flight.

TCA Isolated Nacelle Symmetry Plane Mach Contours Transonic OVERFLOW Solutions With Centerbody

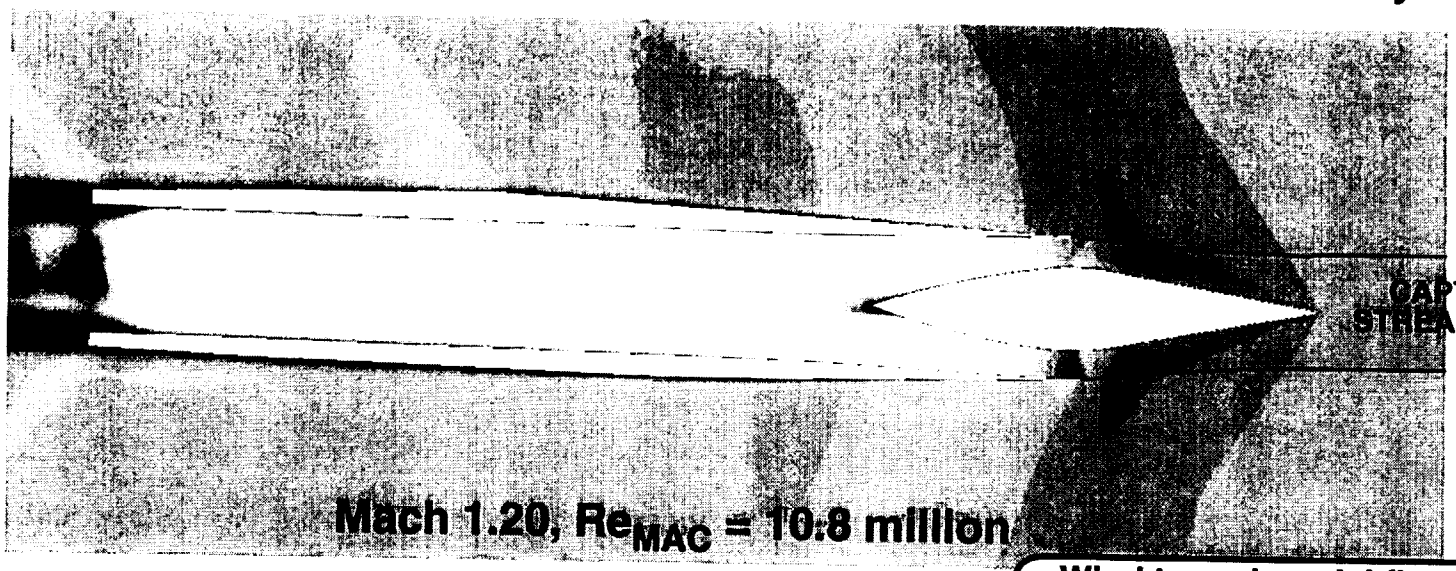

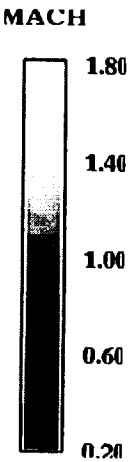

- Wind tunnel model flow–thru duct.
- Flow aligned with actual inlet centerline (not flow–thru duct).

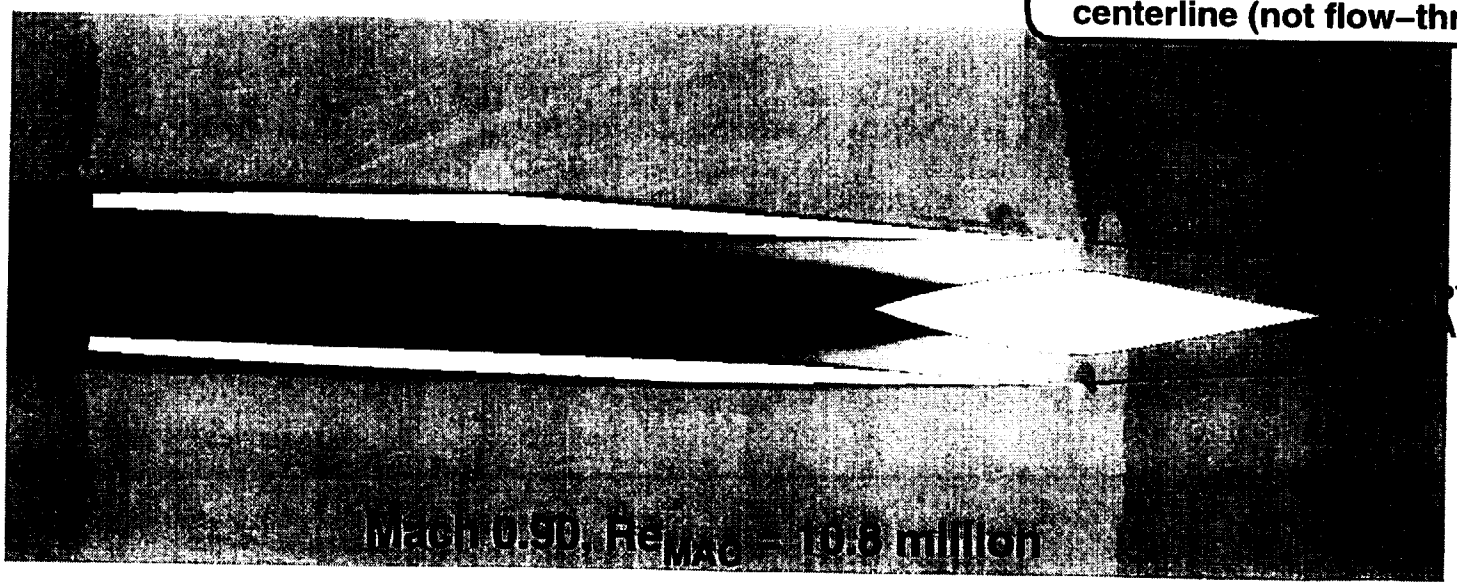

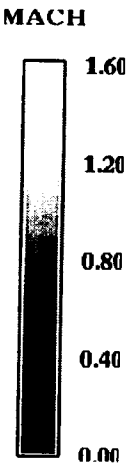

This figure show two Mach 0.90 cases with spillage control employed in the internal duct. The spillage was controlled by varying a pressure outflow boundary condition in the duct while measuring the duct flow rate. The pressure was adjusted during solution convergence to arrive at the correct flow rate. The convergence time was increased by a factor of 3. In the first case the mass flow rate was set to the same value as measured for the flow through duct discussed in the previous figure. The resulting capture stream tube is identical to the flow through case. Another case has also been run with 50% spillage to test a much smaller duct flow rate. The contraction of the capture stream tube is evident. The spilled flow accelerates around the cowl lip to supersonic speeds and then appears to shock back down to subsonic causing the boundary layer on the nacelle forecowl to thicken considerably or separate.

This study will continue with other Mach numbers, and implementation on a wing/body/nacelle/diverter model.

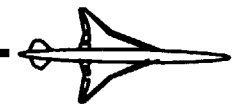

HSCT High Speed Aerodynamics

TCA Isolated Nacelle Symmetry Plane Mach Contours
Mach 0.90 OVERFLOW Solution with Centerbody and Spillage Control

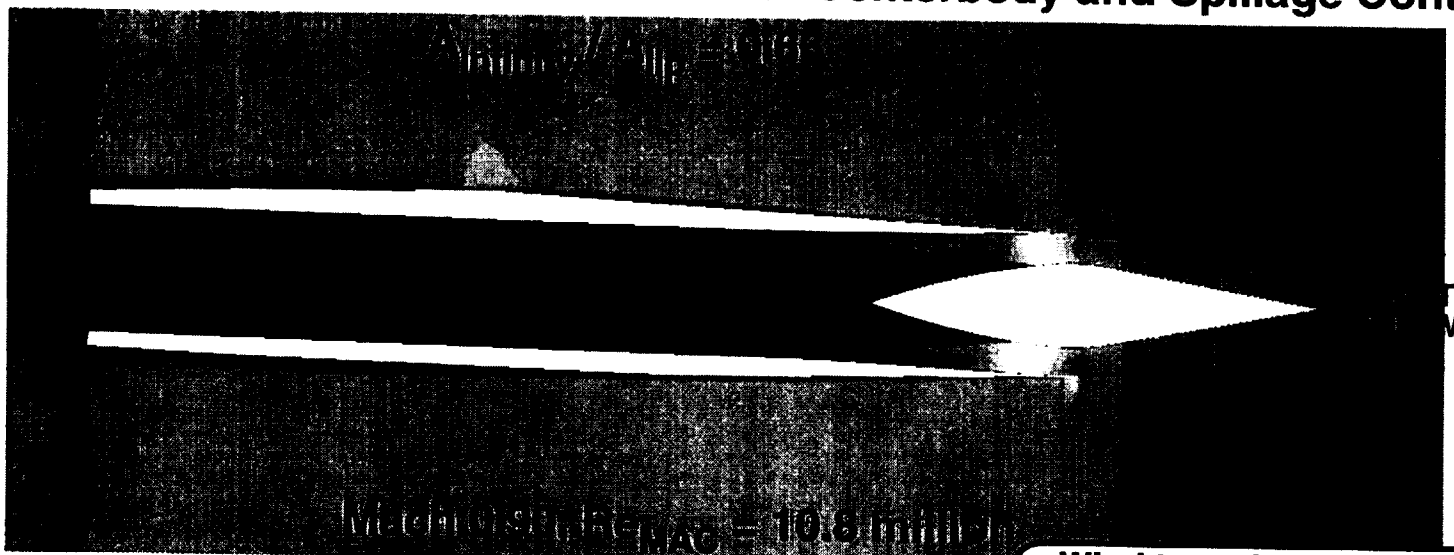

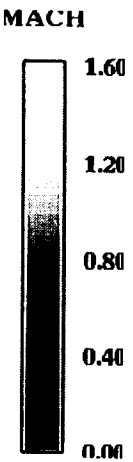

- Wind tunnel model flow–thru duct.
- Flow aligned with actual inlet centerline (not flow–thru duct).

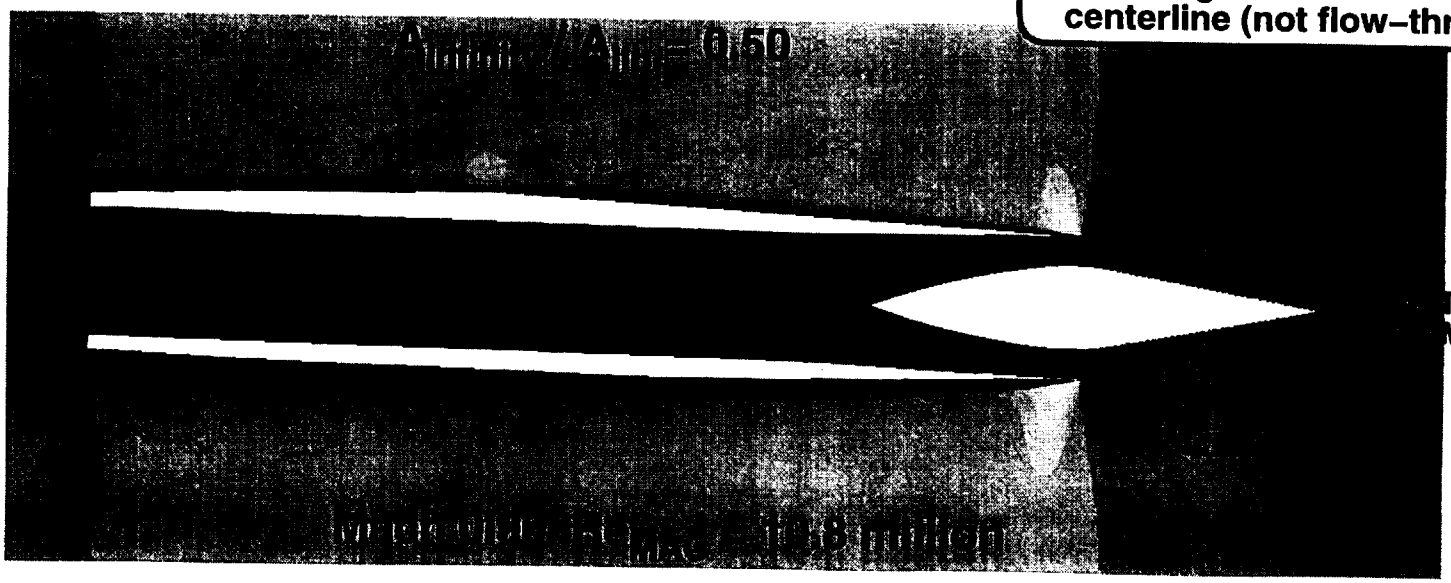

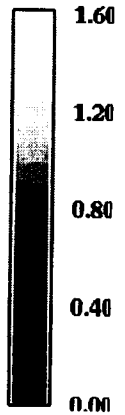

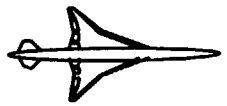

The wide diverter installation on the TCA (full nacelle width at wing TE) was based on TRANAIR analyses at the end of 1995. Viscous analysis (OVERFLOW) has indicated no surprises in the PAI characteristics. The TCA nacelle/diverters went on the airplane for less than the isolated nacelle analytic skin friction value, which is the usual figure of merit.

Comparison of the OVERFLOW CFD results with test data was similar to the Reference H analyses. Uncertainties continue to cloud the capability of CFD to simulate absolute drag values (trip drag, aeroelastics,nacelle internal duct forces).

TCA OVERFLOW analysis will continue with a flight Reynolds number grid for the W/B/N/D. The spillage modeling will continue to be developed, culminating in the ability to do accurate flight simulations of transonic flight conditions.

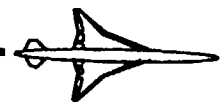

TCA Baseline PAI Assessment Summary

Conclusions

- TCA nacelle installation successful.
  - Installed nacelle drag increment less than skin friction.
  - Selection of wide diverter based on inviscid analyses (TRANAIR) was found to be acceptable.
- TCA OVERFLOW analysis comparison with test was typical.
  - Drag levels less than test values by trip drag increment.
  - Somewhat clouded by nacelle internal skin friction corrections.

Plans

- Mach 2.4 flight Reynolds number OVERFLOW analysis of W/B/N/D.
- Continue development of spillage modelling on isolated nacelle.
- Transonic wind tunnel and flight analysis of W/B/N/D with and without spillage.

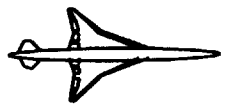

A complete description of the OVERFLOW analysis of the TRANAIR optimized configuration may be found in the sub–task 2 report. This section analyzes the results of that study with a very tight PAI focus.

One of the key processes that was developed in this study was the ability to take nacelle/diverter grids already built for one configuration and fit them onto a new wing /body. This shortens the time to get a viscous solution of an optimized configuration to 4–5 days. The current limitations in this process are that planfom and/or nacelle toe angles can not change.

Optimized TCA PAI Assessment

- Tranair drag optimized configuration analysed in OVERFLOW.
- Mach 2.4, NASA LaRC Unitary Reynolds Number.
- Baseline TCA nacelle/diverter grids re–rigged to new optimized wing/body grid.
  - Wing upper surface nacelle bump on.

This figures shows the optimized wing lower surface pressure distribution. Comparison of this plot to the baseline TCA plot shown previously clearly shows that the optimized has reduced the size of the negative Cp regions and decreased the pressure in the high pressure regions. In general the optimization has smoothed out both the low and the high Cp values across this portion of the wing.

TRANAIR–Optimized W/B/N/D Lower Surface Pressure Coefficient

Mach 2.4, Re_{MAC} = 6.4 million, OVERFLOW Solution

α = 3.98 deg., C_L = 0.0844

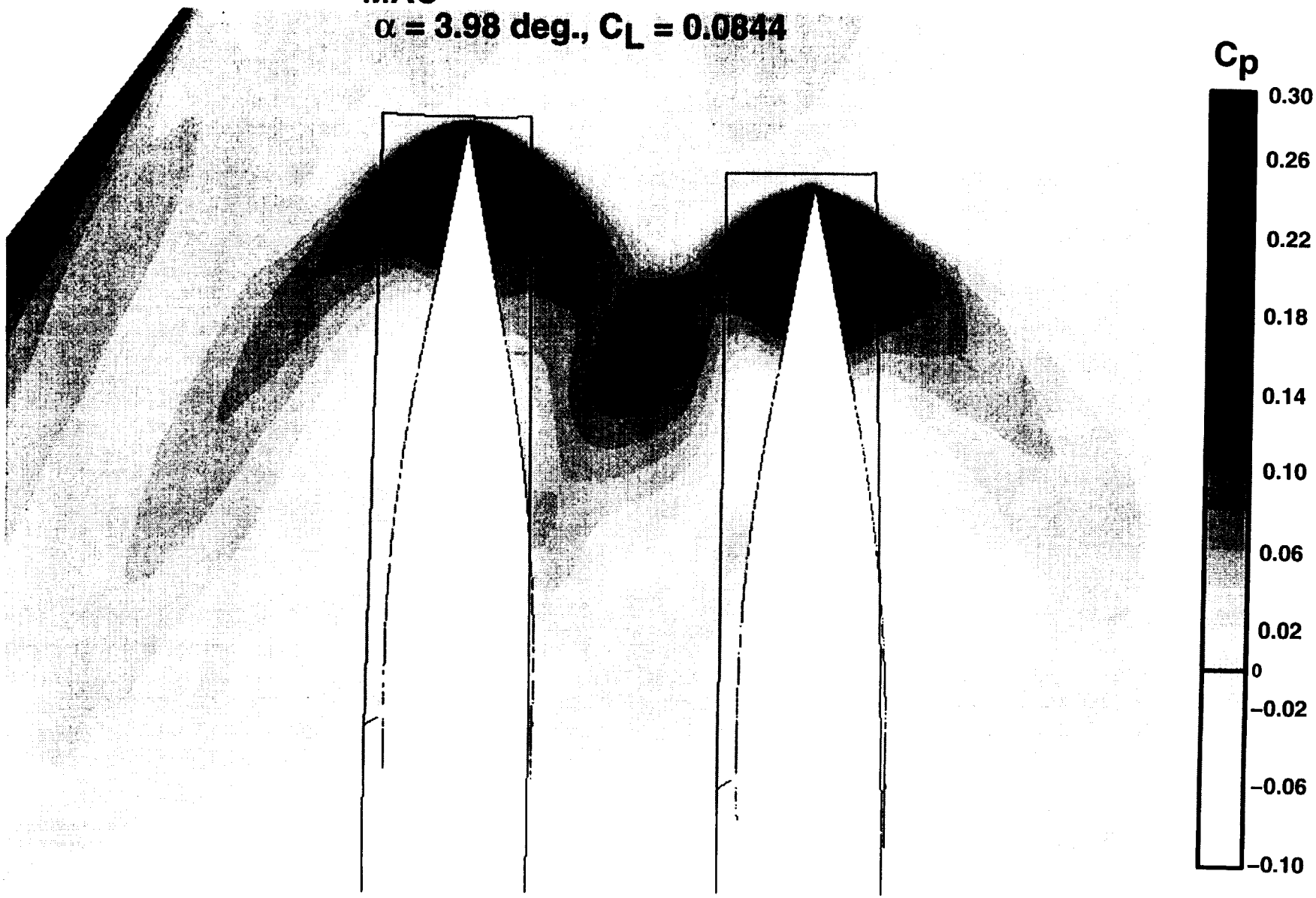

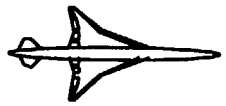

This figure of the TRANAIR optimized wing lower surface presure distribution for the wing/body is shown for comparison to the previous figure.

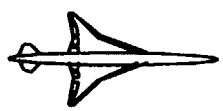

TRANAIR–Optimized W/B Lower Surface Pressure Coefficient
Mach 2.4, Re_{MAC} = 6.4 million, OVERFLOW Solution

α = 3.98 deg.

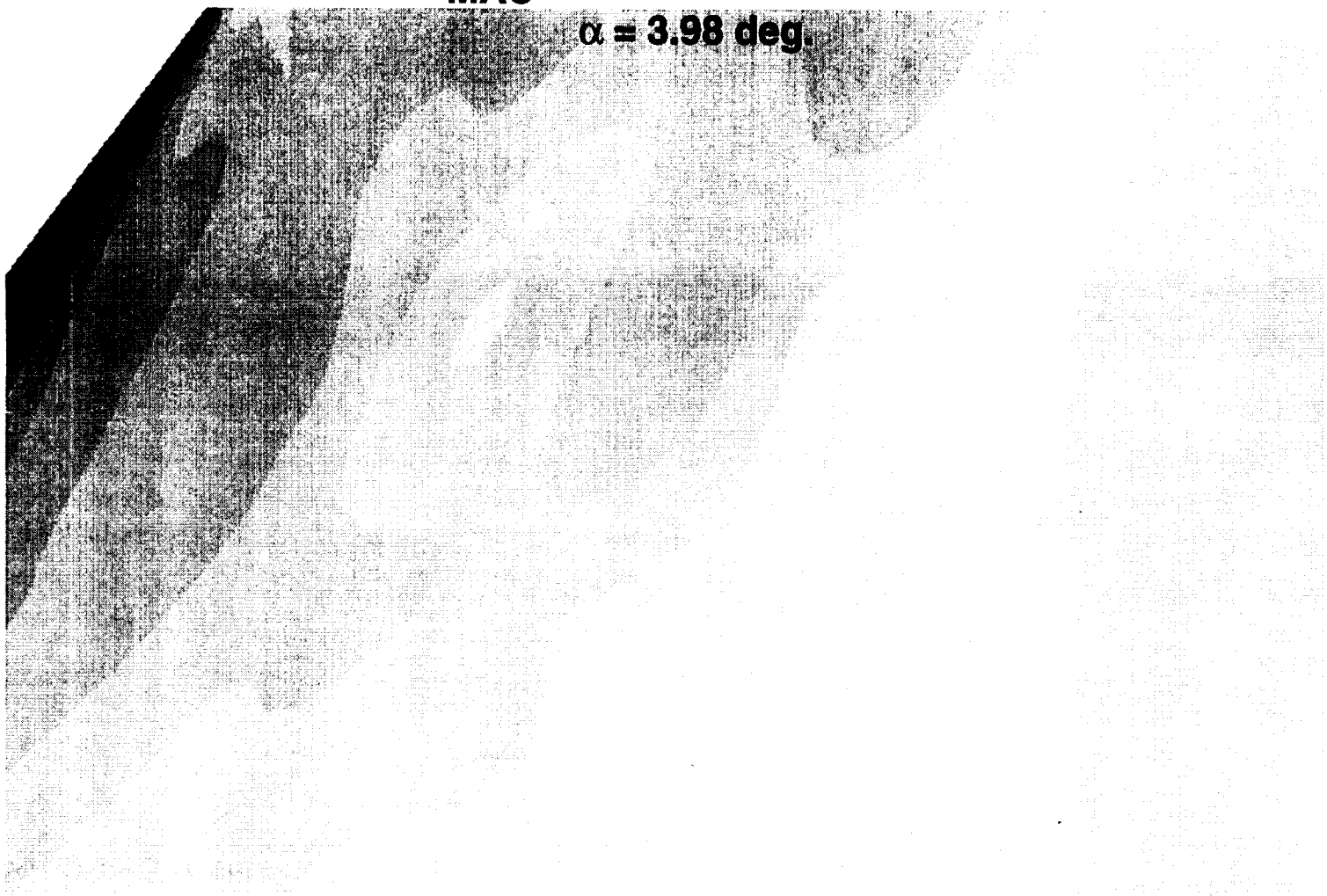

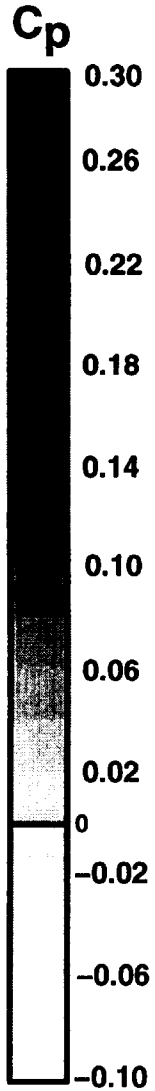

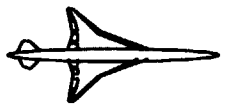

The nacelle surface pressure distributions for the nacelle/diverters on the TRANAIR optimized configuration are shown. The relationship between the inboard and outboard installation characteristics are very similar to that discussed previously for the baseline TCA: the outboard diverter channel is not unstarting but the diverter shock is definitely unswept compared to the inboard.

TRANAIR–Optimized W/B/N/D Nacelle Surface Pressure Coefficient
Mach 2.4, Re_{MAC} = 6.4 million, OVERFLOW Solution
α = 3.98 deg., C_L = 0.0844

Outboard

Inboard

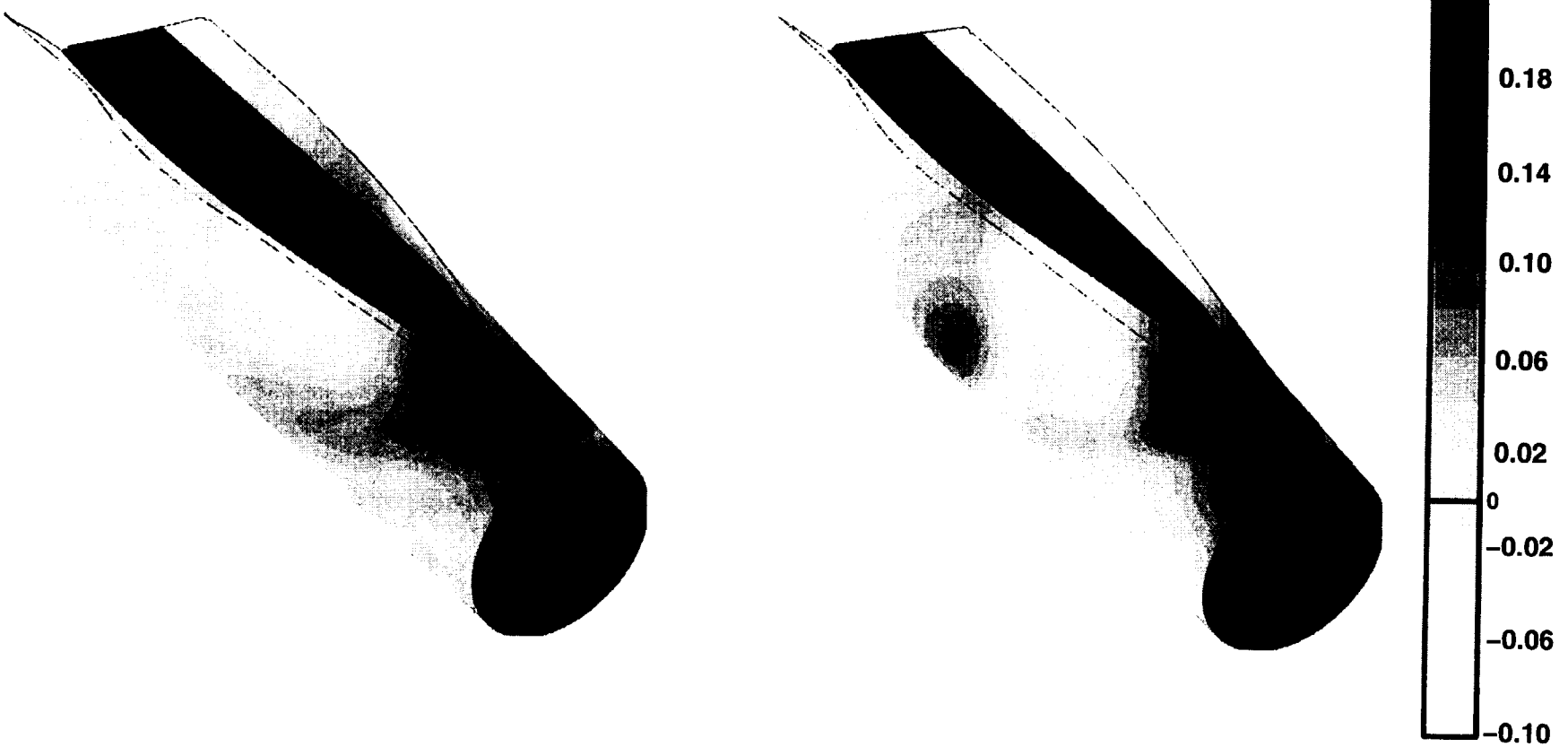

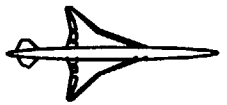

The next two plots show the nacelle pressure distributions from OVERFLOW solutions of the baseline TCA and TRANAIR optimized configurations side-by-side. This page is the inboard installation, the next page is the outboard installation. The comparisons show that there is a small but definite reduction in pressure over most of the nacelle/diverter surface. This effect resulted in the integrated drag felt by the nacelle/diverter surfaces being 1.3 counts less for the optimized configuration relative to the baseline.

Baseline TCA vs. TRANAIR–Optimized W/B/N/D Nacelle Surface Pressure
Mach 2.4, Re_{MAC} = 6.4 million, OVERFLOW Solution, C_L ~ 0.084
Inboard Nacelle

TCA

Optimized

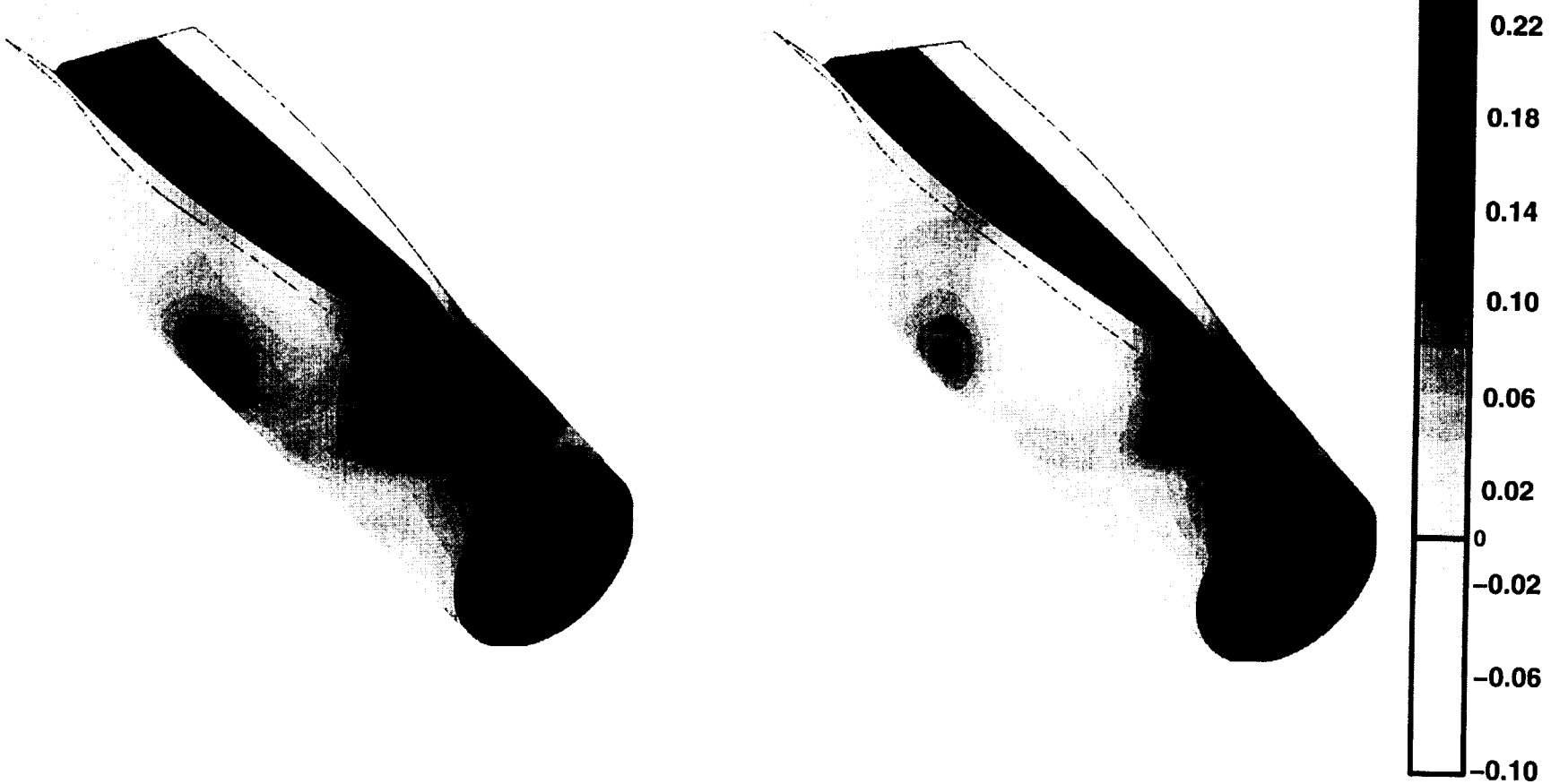

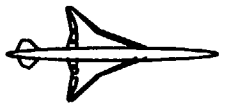

See previous facing text page.

Baseline TCA vs. TRANAIR–Optimized W/B/N/D Nacelle Surface Pressure
Mach 2.4, Re_{MAC} = 6.4 million, OVERFLOW Solution, C_L ~ 0.084
Outboard Nacelle

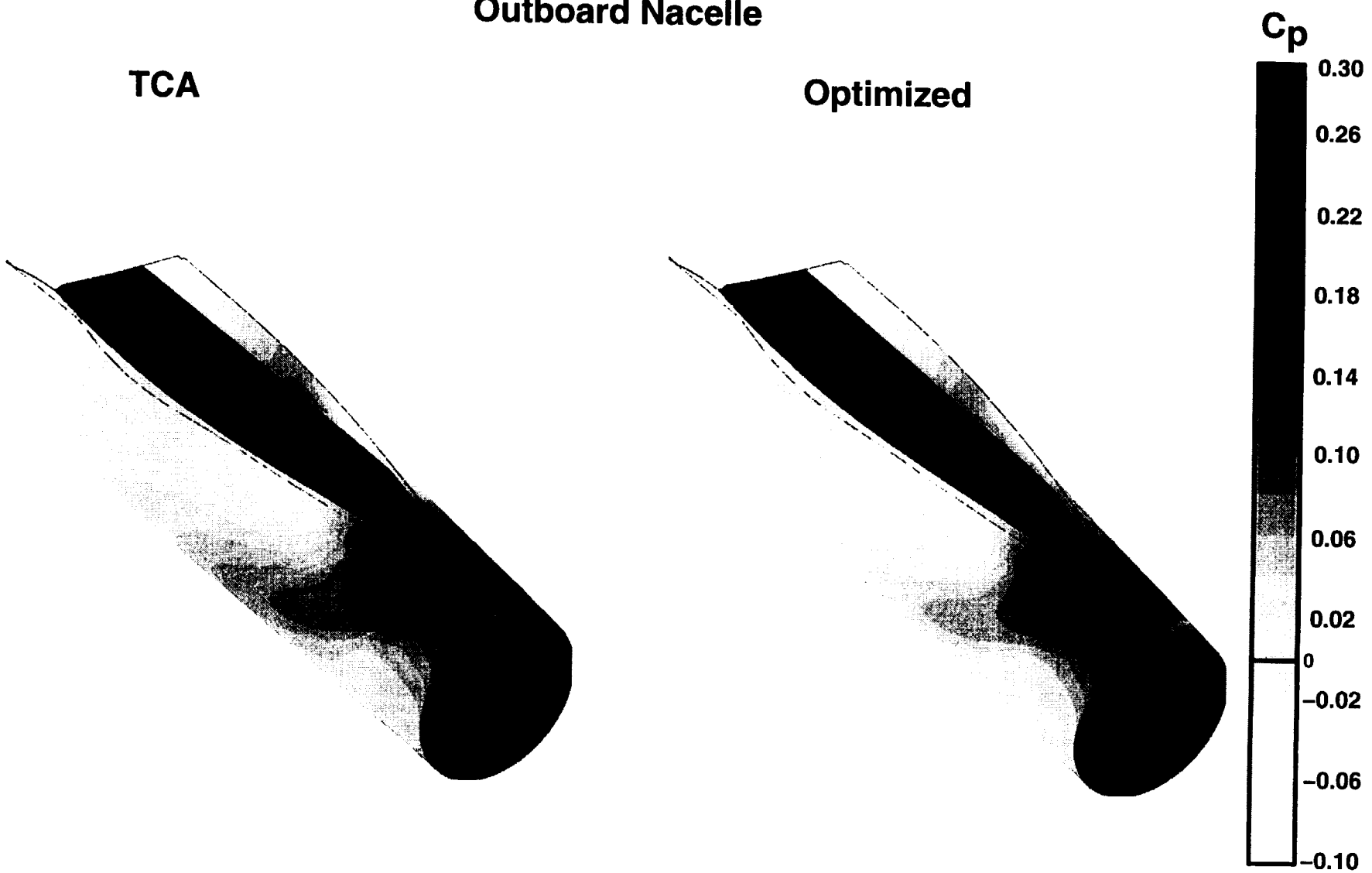

The nacelle installation force increments for the smoothed optimized configuration analyzed under subtask 2 are shown in this figure. The configuration analyzed in OVERFLOW was near to being the final configuration submitted for the wind tunnel model loft. The effect of the smoothing (changes from the preliminary configuration) on the PAI increments were very slightly unfavorable. The smoothed configuration had ~ 0.1 counts higher nacelle installation drag than the preliminary unsmoothed configuration. The nacelles are installed on the optimized configuration for about 2 counts less than on the baseline TCA. As discussed, on the previous page, 1.3 of this 2 count difference is due to reduced drag on the nacelle/diverter surfaces.

An additional reference value was added to this plot to allow comparison of the installed force increments to the isolated nacelle forces calculated by OVERFLOW. An isolated nacelle was run at zero angle of attack (the inlet centerline aligned with the flow) in OVERFLOW at Mach 2.4 and the same wind tunnel Reynolds Number as the wing/body/nacelle/diverter configuration. The total of the pressure and viscous forces for four nacelles was 15.05 counts. The viscous drag was very close to the flat plate skin friction value.

HSCT High Speed Aerodynamics

TCA vs Optimized W/B/N/D PAI Force Increments

Mach 2.4, Re_{MAC} = 6.4 million, OVERFLOW Analysis

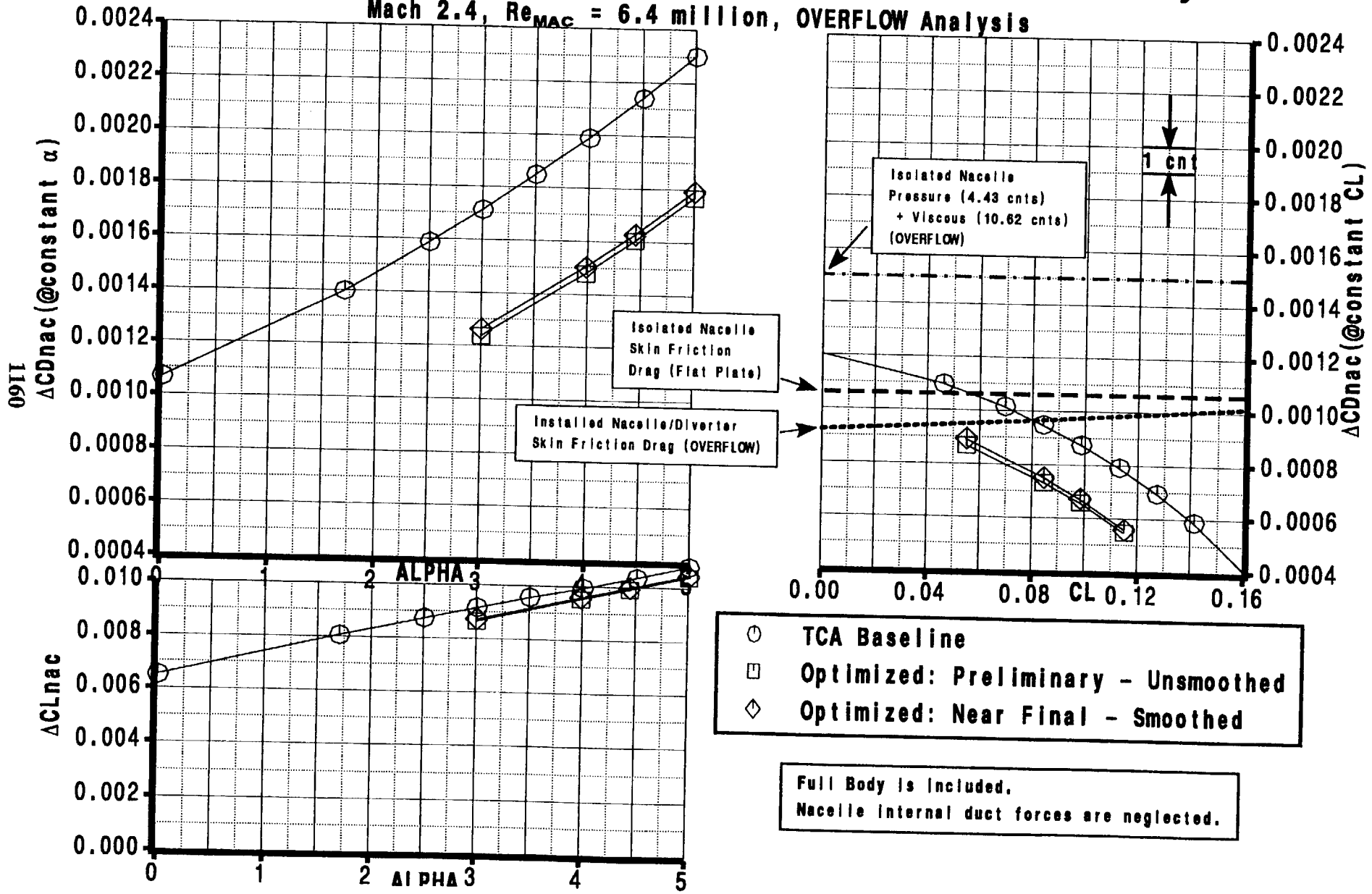

A comparison of the inlet flow Mach contours between the TCA and the drag optimized TCA at the cruise Mach number and angle of attack (Langley Unitary Rn) are presented. Of significance is the reduction in Mach variation across the inboard inlet from .05 on the TCA to .03 on the drag optimized TCA. There is also a reduction in the average inboard Mach number which results in a reduction in the inboard to outboard average Mach increment and provides a measure of additional precompression relative to the TCA.

Inlet Mach Number for TCA and Optimized TCA

WING–BODY OVERFLOW ANALYSIS
MACH=2.4, ZERO SIDESLIP, RNmac = 6.4 MILLION

TCA

ALPHA = 3.0

INBD

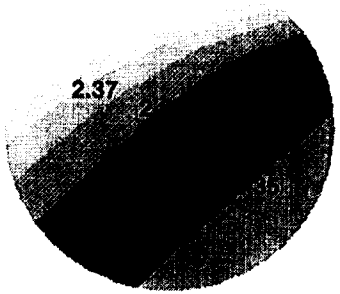

Mmax = 2.395
Mmin = 2.345
Mavg = 2.362
Mmax–Mmin = .050

OUTBD

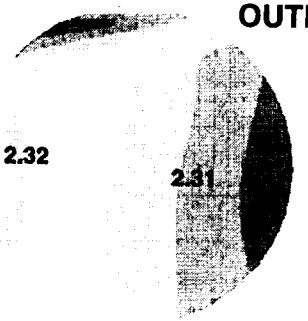

Mmax = 2.334
Mmin = 2.301
Mavg = 2.314
Mmax–Mmin = .033

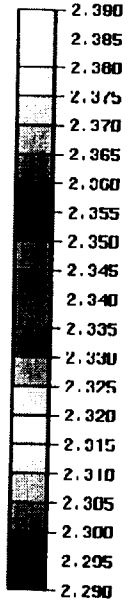

OPTIMIZED TCA

ALPHA = 3.98

INBD

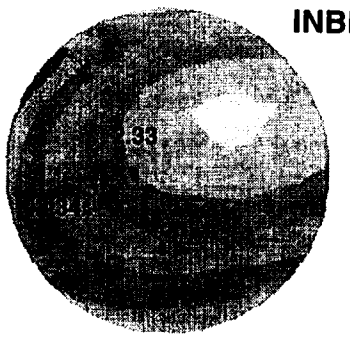

Mmax = 2.354
Mmin = 2.324
Mavg = 2.336
Mmax–Mmin = .030

OUTBD

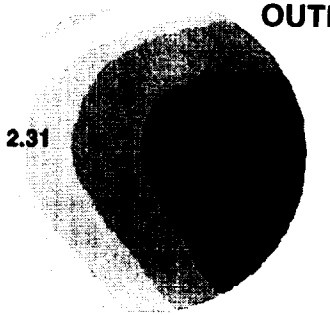

Mmax = 2.327
Mmin = 2.293
Mavg = 2.304
Mmax–Mmin = .034

outbd →

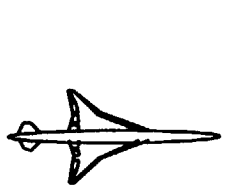

A comparison of the upflow contours between the TCA and the drag optimized TCA at the cruise Mach number and angle of attack (Langley Unitary Rn) are presented. The misalignment between the inlet centerline and the local flow is increased by .24 degrees at the inboard inlet and by .6 degrees at the ouboard inlet. These results are consistent with the increase in negative lift carried by the flow through ducts on the drag optimzed TCA relative to the TCA. The drag optimized TCA shows an increase in upflow variation at the inboard inlet of 0.7 degrees relative to the TCA. This is interesting in the fact that the Mach variation for this inlet was reduced for the drag optimized TCA. This may suggest that optimizing for minimum drag, minimum mach variation, and minimum flow angularity may be challenging.

Inlet Upflow Angle for TCA and Optimized TCA

WING–BODY OVERFLOW ANALYSIS
MACH=2.4, ZERO SIDESLIP, RNmac = 6.4 MILLION

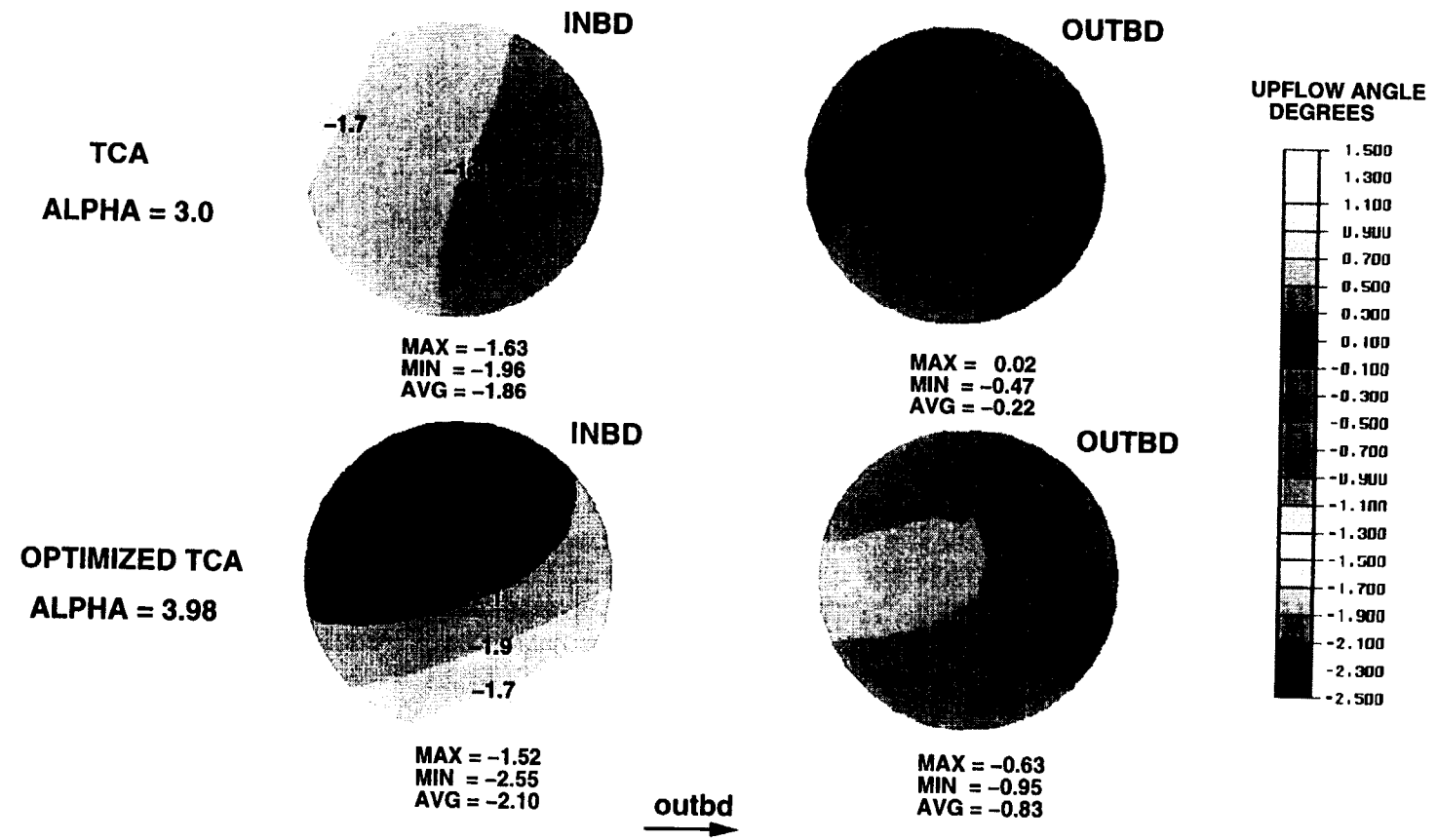

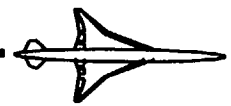

A comparison of the crossflow contours between the TCA and the drag optimized TCA at the cruise Mach number and angle of attack (Langley Unitary Rn) are presented. The drag optimized TCA continues to show the large (about 1 degree) crossflow variation exhibited by the TCA. This large amount of crossflow variation relative to the technology projection of <.25 degrees highlights this as a area of focus for future optimization efforts. The one significant change is the 1.4 degree increase in average crossflow at the inboard inlet. The average upflow and crossflow increased for both inboard and outboard inlets for the drag optimized TCA relative to the TCA. The impact of the installing of the nacelles with the inlets aligned with the local average flow should be considered to develop a trade between drag, inlet performance, and inlet control system complexity.

Inlet Crossflow Angle for TCA and Optimized TCA

WING-BODY OVERFLOW ANALYSIS
MACH=2.4, ZERO SIDESLIP, RNmac = 6.4 MILLION

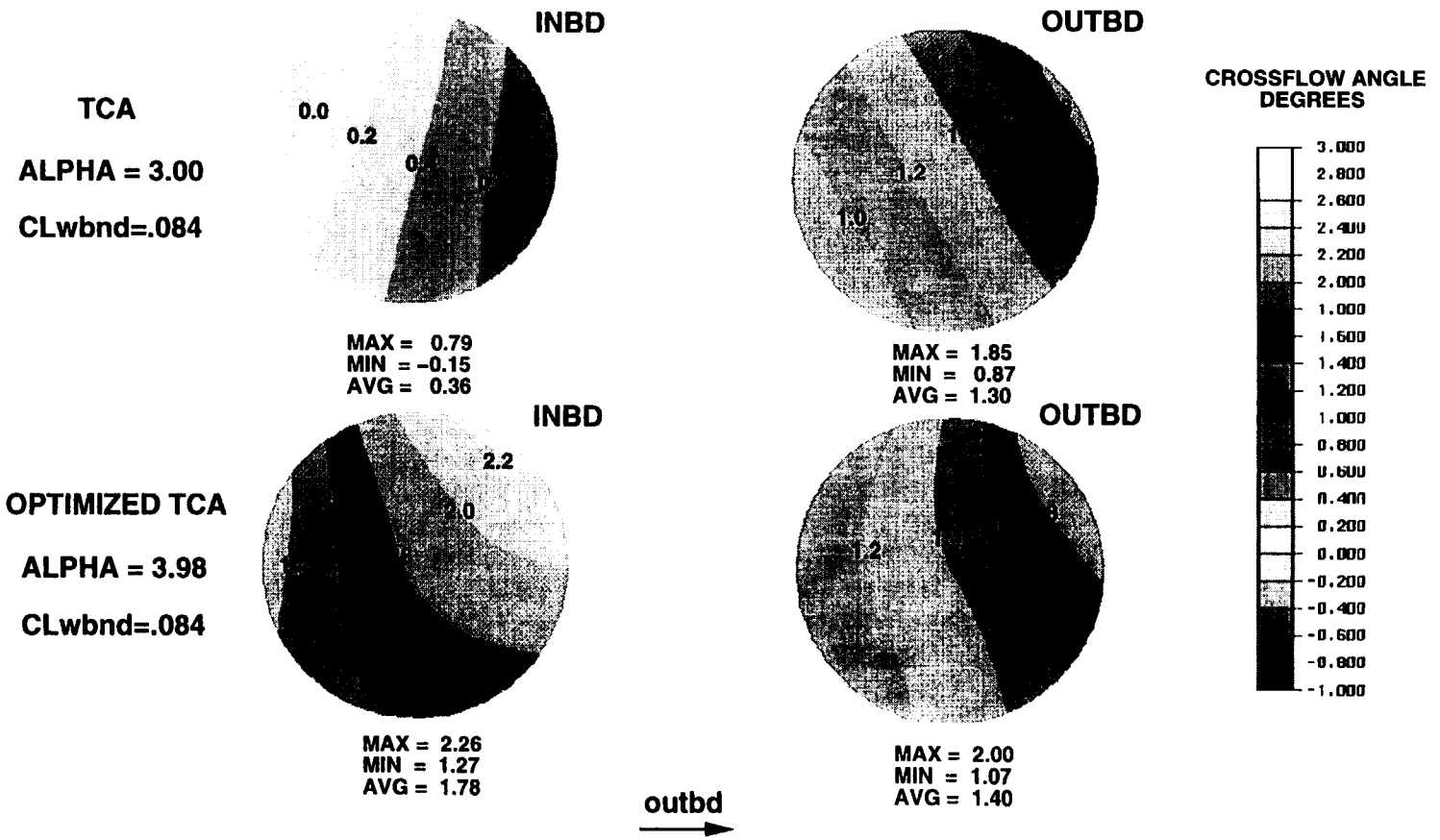

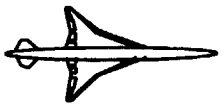

This figure summarize the results of a Boeing IR& D task to optimize the inlet flow field using wing lower surface re-contouring. The work will be continued as a inlet flow field optimization task under contract in 1997.

HSCT INLET FLOWFIELD IMPROVEMENT

The quality of the airflow approaching the engine inlets is of importance to the inlet performance in terms of recovery and distortion as well as margins to inlet unstart. This research was an attempt to recontour the wing lower surface of the TCA configuration unstream of the inlets with the objective to improve the flow quality of the streamtube approaching the inlets.

The complexity of the aerodynamic problem led to an attempt to use numerical optimization techniques coupled to a CFD method for the redesign. Evaluation grids were centered at the location of the inlet center-body apex and had the same diameter as the inlet hilite. Flow properties including local mach number, upflow and crossflow angles were computed at these grids.

The NASA OVERFLOW CFD solver was driven by a hybrid genetic optimizer to find wing lower surface contours that provided an improvement in inlet flow quality. Wing lower surface geometry changes were done using a free-form deformation technique where control points locations were controlled by the optimizer driver to minimize mach number variation.

The figure below shows how a measure of the flow quality, the variation in local mach number across the evaluation stations, were changed by the redesign process. Note that the variation across the inboard was substantially reduced while across the outboard the variation was slightly degraded. Figure 2 shows the wing lower surface geometry changes that were found by the optimization process. The geometry changes are less than 0.60 inches, full scale. These changes are remarkably small and as seen in the previous figure provide a substantial improvement to the inboard inlet flow quality.

Effect of Wing Lower Surface Recontouring on Inlet Mach Number

TCA CONFIGURATION
MACH=2.4 ALPHA=3.0

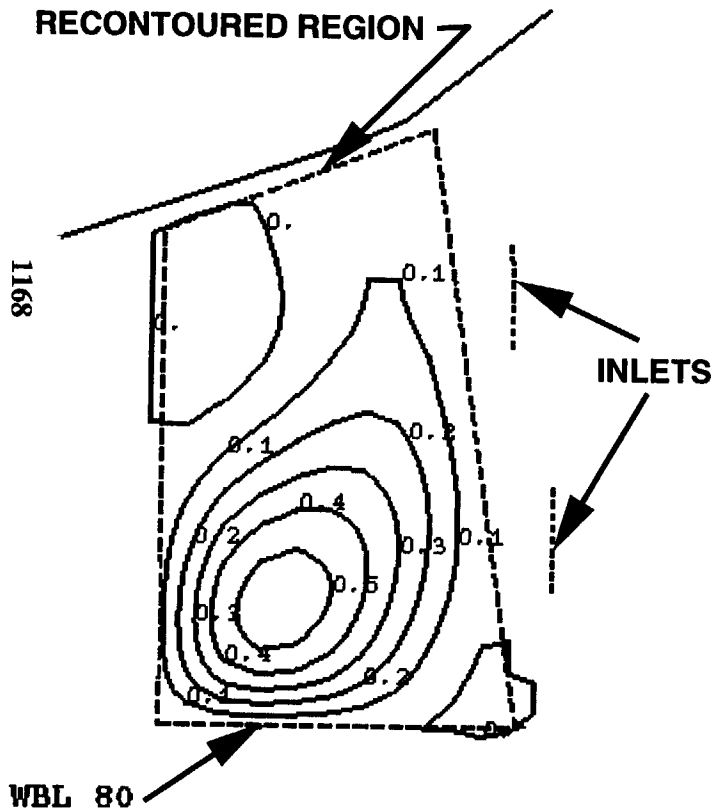

1168

CONTOURS OF DELTA-Z, INCHES

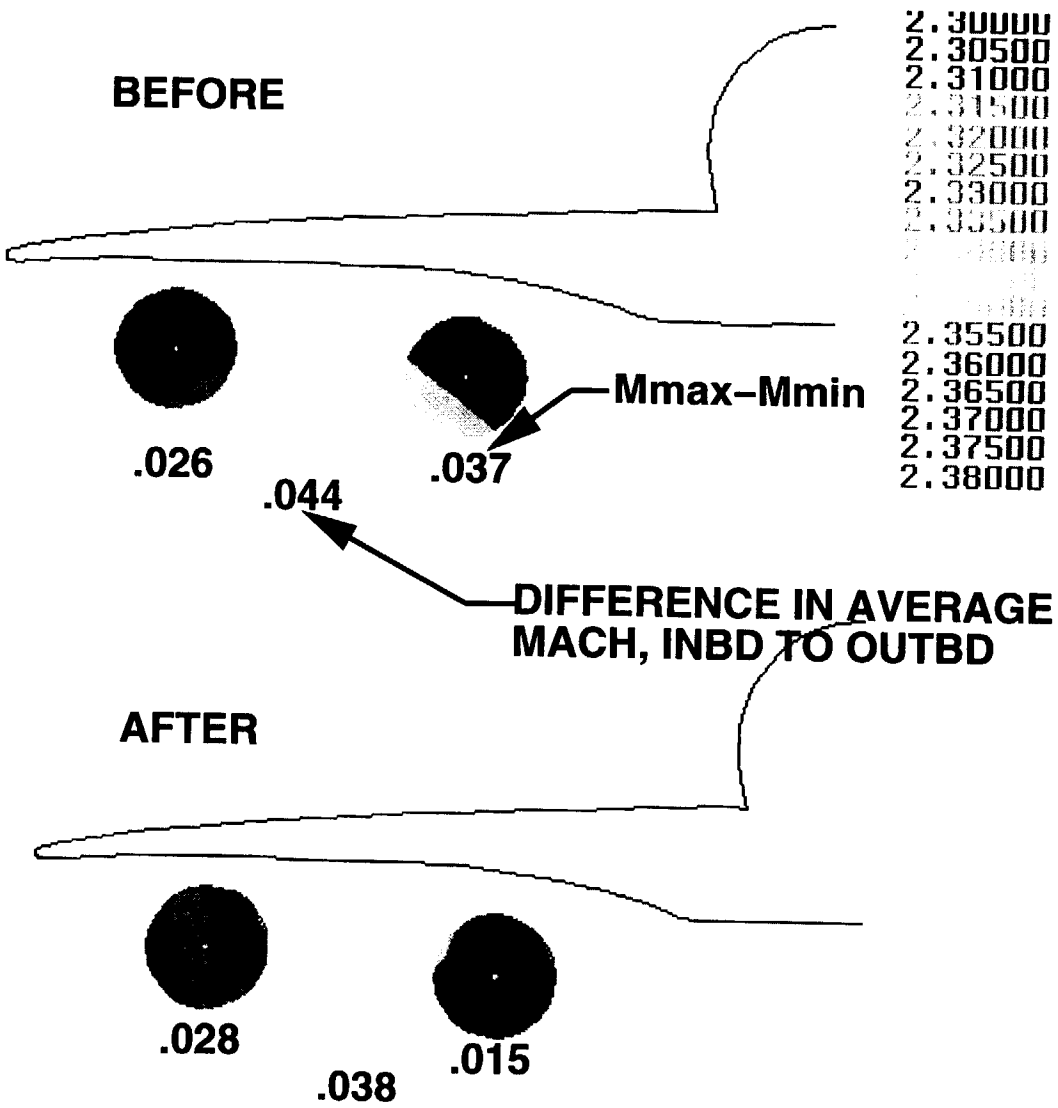

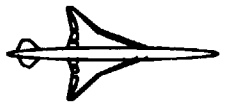

The OVERFLOW analysis of the TRANAIR optimized configuration indicated a 2 count improvement in nacelle/diverter installation drag, a large portion of which was due to reduced pressure on the nacelle/diverter surfaces.

While no attempt was made to effect inlet flow quality in this study (drag optimization only) the inlet flow characteristics were assessed. The Mach number characteristics improved, but the inlet flow angularity got worse.

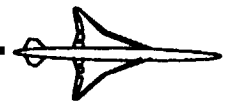

Optimized TCA PAI Assessment Summary

Conclusions

- TRANAIR optimization reduced the pressure in high pressure areas around the nacelle/diverter, and increased the pressures in low pressure areas.
- The nacelle installation drag increment was reduced by 2 counts.
  - The drag on the nacelle/diverter surfaces was reduced by 1.3 counts.
- Inlet flowfield Mach number characteristics improved.
  - Inlet crossflow and upflow characteristics were degraded.

Plans

- Incorporate inlet flowfield optimization started in 1996 on Boeing IR&D into 1997 contract flowfield optimization studies.

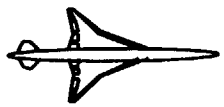

The bifurcated inlet study replaced the nacelle cambering and diverter variation study that was planned for this past year. After the analysis of the aft diverter on the Reference H bifurcated installation, there had been no plans to do any more bifurcated work. However, the bifurcated inlet started to get a lot more attention (again) and the need arose to do a real bifurcated installation on the TCA and run both a supersonic and transonic analysis comparing the baseline axisymmetric to the 2D bifurcated inlets.

This section will review briefly the Reference H bifurcated study conclusions, then discuss the lofting of new bifurcated inlet nacelle for the TCA, and then review the results of the OVERFLOW supersonic analysis of the bifurcated on the TCA.

Bifurcated Inlet Studies

- Review analyses of bifurcated inlet on Reference H.
- Installation of bifurcated inlet on TCA.
- OVERFLOW analysis of bifurcated inlet on TCA.

The Reference H bifurcated analysis started out with a Mach 2.4 bifurcated penalty relative to the axisymmetric inlet of 4 – 5 counts. After a complete analysis of the test and OVERFLOW results several discrepancies and inconsistencies in the inlet comparisons were found that led to this drag penalty being reduced to an estimated 1.5 – 2.5 counts (see last year's final report). In addition, several problems with the bifurcated inlet installation on the Reference H were brought to light. One of which was the diverter LE location leading to the diverter shock being ingested by the inlet. Gridding of the Reference H configuration with bifurcated inlet nacelle was completed with the diverter leading edge moved aft to a station adjacent to the sidewall inlet lip. An OVERFLOW solution was ran at Mach 2.4 and angle of attack of 4.4 degrees to compare to the baseline bifurcated installation analyzed last year. It had been anticipated that this configuration change would decrease the airplane drag by 0.5 counts (see final contract report for 1995) due to the reduced pressures on forward facing ramps of diverter surface. As the table below shows this reduction in drag on the diverter surface was achieved but the total airplane drag remained essentially unchanged:

	DCD		DCDCL		
wing(lower surface)	+ 0.5 cnts		−1.4 cnts		
nacelles	+ 0.4 cnts		+1.3 cnts		
diverters	– 0.7 cnts		0		
TOTAL =	+ 0.2	+	−0.1	=	+ 0.1

This result was surprising at first, but upon closer inspection it becomes clear that non–optimal installation of the nacelles on this configuration are skewing the answer again (also discussed in the 1995 final contract report). The inlet faces are tilted into the underwing flowfield such that negative lift forces are generated on the nacelle internal surface. When the diverter was moved aft a large portion of the upper surface of the nacelle was now exposed to this misaligned flow. The resulting positive pressures acting on a forward facing surface result in substantial amounts of positive drag and negative lift (which translates into positive drag as shown in table). In addition, these positive

Continued on next page

Bifurcated Inlet Reference H W/B/N/D Nacelle Surface Pressure Coefficient Mach 2.4, Re_{MAC} = 7 million, OVERFLOW Solution, α = 4.4 deg Inboard Nacelle

Diverter Translated Aft

Baseline

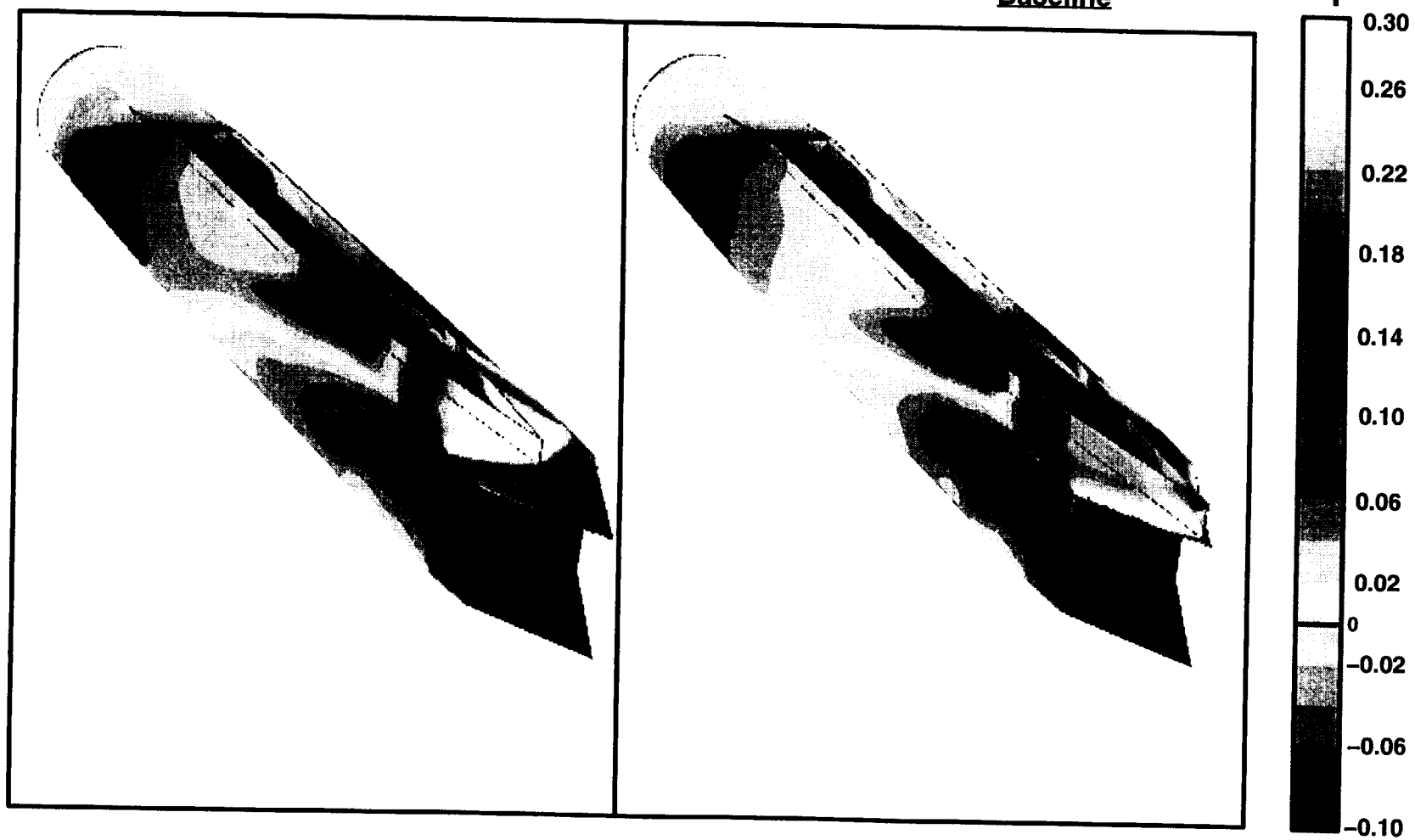

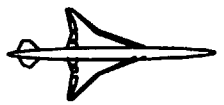

Continued from previous page

pressures are reflected up onto the now exposed wing lower surface which results in a large positive lift increment (negative drag). Since these reflected pressures are less than the nacelle surface pressures the magnitude of the lift delta on the wing lower surface was expected to be less than magnitude on nacelle, but as the table shows the magnitude of the drag due to lift delta was actually greater on wing than nacelle. This is due to two factors:
1)the pressures acting on the wing lower surface have a larger area to act upon (the nacelle top surface falls off toward the sides), and,
2)the movement of the diverter aft moves a substantial amount of negative expansion pressures from the diverter shoulder off the trailing edge of the wing reducing the negative lift.

The next step in this analysis would have been to reduce the diverter height to the value actually required for this installation, which would tend to rotate inlet up and lessen the misalignment. Both changes should reduce drag.

The previous figure shows that the moved aft diverter on the inboard installation worked as expected; diverter shock is now missing the inlet. However, as the figure on this page shows the diverter channel on the outboard installation unstarted. This did not effect the integrated forces very much but the inlet flow field would be severely degraded.

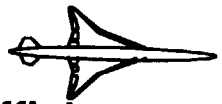

HSCT High Speed Aerodynamics

Bifurcated Inlet Reference H W/B/N/D Nacelle Surface Pressure Coefficient Mach 2.4, Re_{MAC} = 7 million, OVERFLOW Solution, α = 4.4 deg Outboard Nacelle

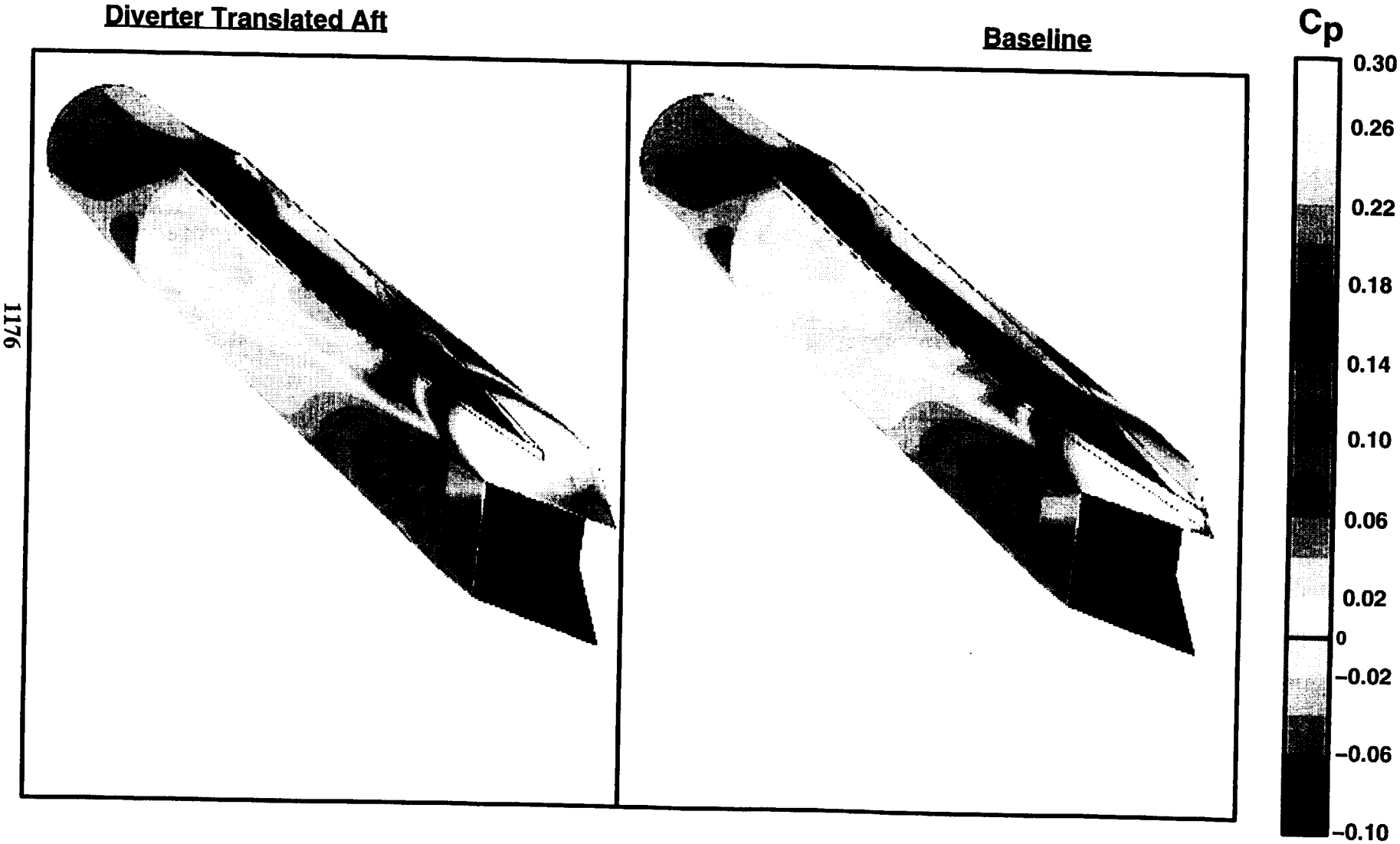

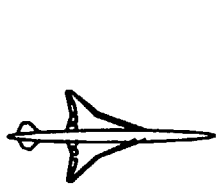

A bifurcated inlet nacelle has been configured and installed on the TCA for support of the inlet downselect milestone. This configuration was the result of a joint effort of high speed aerodynamics and propulsion design staffs. The normal nacelle installation guideline for diverter height was adhered to while also matching the end of the nacelle forecowl to the current TCA baseline nacelle nozzle. For the outboard nacelle this was possible without moving the current nozzle position. On the inboard installation it was necessary to rotate the nozzle slightly (nose up 0.3 deg). This inlet has a much larger lip bevel than the baseline TCA axisymmetric, but the bevel is smaller than previous bifurcated inlets as the result of some structural analyses and material studies allowing a redesign. The baseline TCA axisymmetric inlet has a 12 deg lip bevel that extends aft until the wall thickness is ~ 0.04 inches. The bifurcated inlet lip bevel extends aft along a 12 deg angle until the wall thickness is 0.2 – 0.3 inches.

The diverter LE was slid forward slightly ahead of the cowl lip station. This was done in order to try to start pushing the diverter channel flow out before it could choke as it did on the Ref H installation. In addition the nacelle top shoulders were rounded as quickly as possible aft of the lip bevel in order to provide some relief to the diverter channel area. The diverter planform half-angle at the diverter LE was the same as the baseline TCA (11 deg). However, on the bifurcated installation this half-angle went immediately into a large radius to fair into the maximum diverter width at the rear. This was in contrast to the baseline diverter planform which held the 11 deg half-angle on a straight line before starting a smaller radius and fairing into max width.

Bifurcated Inlet Design for the TCA

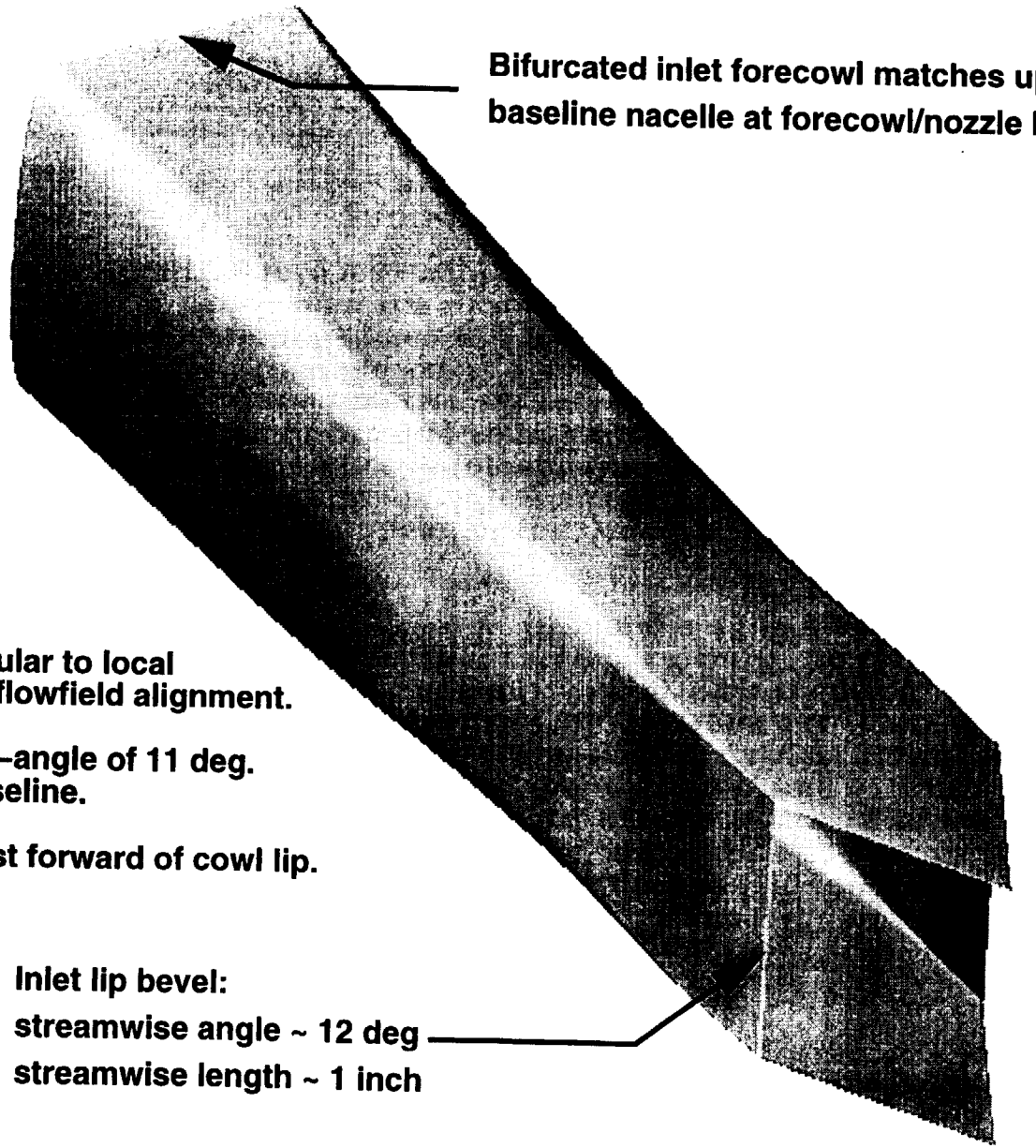

- Inlet nearly perpendicular to local wing surface for inlet flowfield alignment.
- Diverter planform half-angle of 11 deg. retained from TCA baseline.
- Diverter LE located just forward of cowl lip.

The difference in the diverter planform shape is evident if this figure is compared to the similar figure for the baseline TCA. The OVERFLOW wing lower surface pressure distribution for the bifurcated installation on the TCA is shown. The high pressure regions around the nacelle/diverter LE are much smaller than on the baseline TCA installation. This is due to the quickly reducing diverter planform angle starting at the diverter LE and the low forecowl angle of the forward part of the nacelle. As the nacelle area growth picks up further aft a second positive pressure signature is generated (clearly evident outboard of outboard nacelle).

Bifurcated Inlet TCA W/B/N/D Lower Surface Pressure Coefficient
Mach 2.4, Re$_{MAC}$ = 5.4 million, OVERFLOW Solution, α = 3.0 deg.

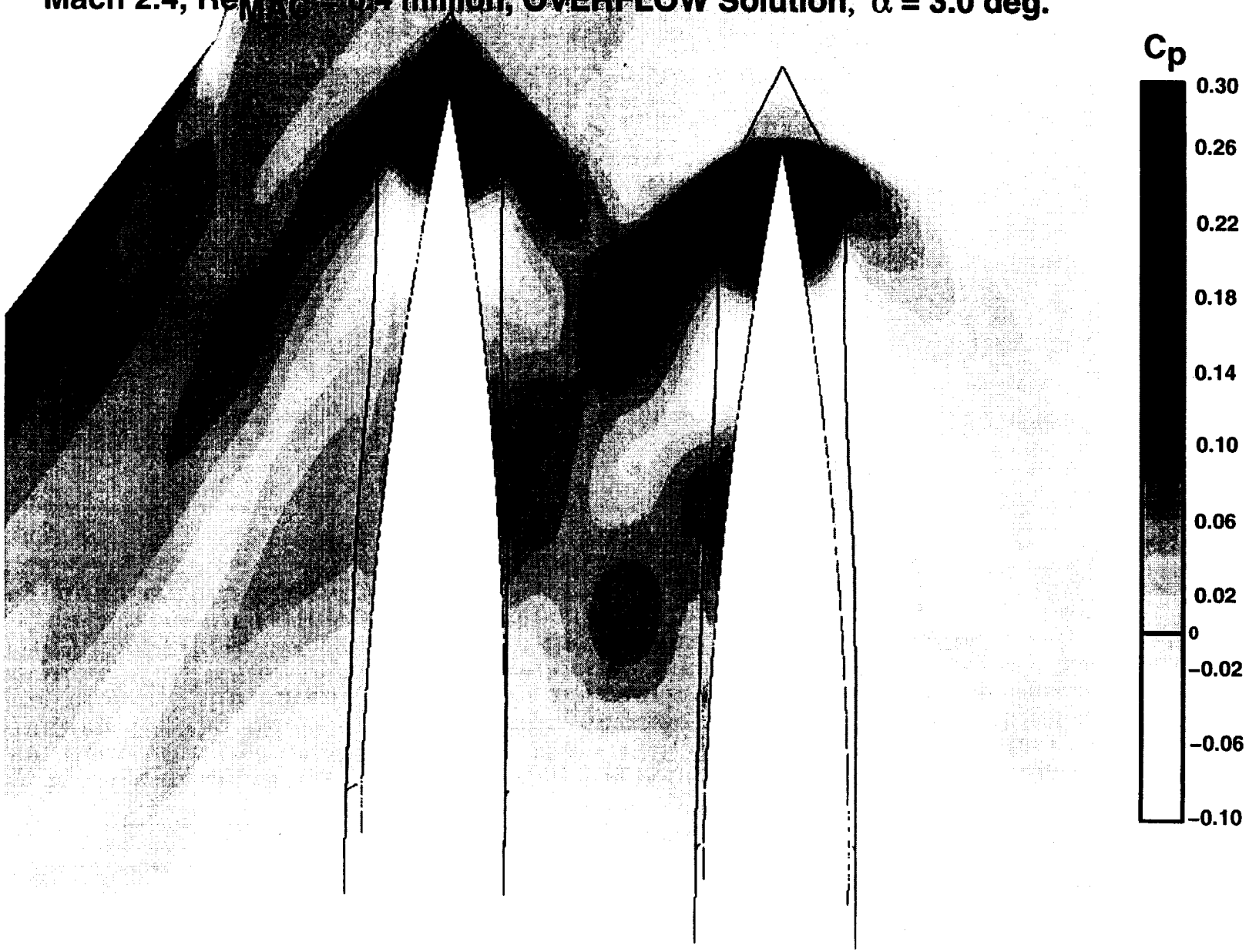

The OVERFLOW pressure distribution on the nacelle/diverters is shown for the bifurcated inlet installation on the TCA. Despite all the design effort the outboard diverter channel still unstarted. The inboard diverter shock remained attached but is probably too close to the inlet lip. The inboard diverter should be slid aft, and the outboard diverter slid aft and increased in height in order to relieve the unstart. This design change would have to be worked in concert with a flight Reynolds analysis as the outboard diverter channel choking may be strongly Reynolds number dependent.

Bifurcated Inlet TCA W/B/N/D Nacelle Surface Pressure Coefficient Mach 2.4, Re_{MAC} = 6.4 million, OVERFLOW Solution, α = 3.0 deg.

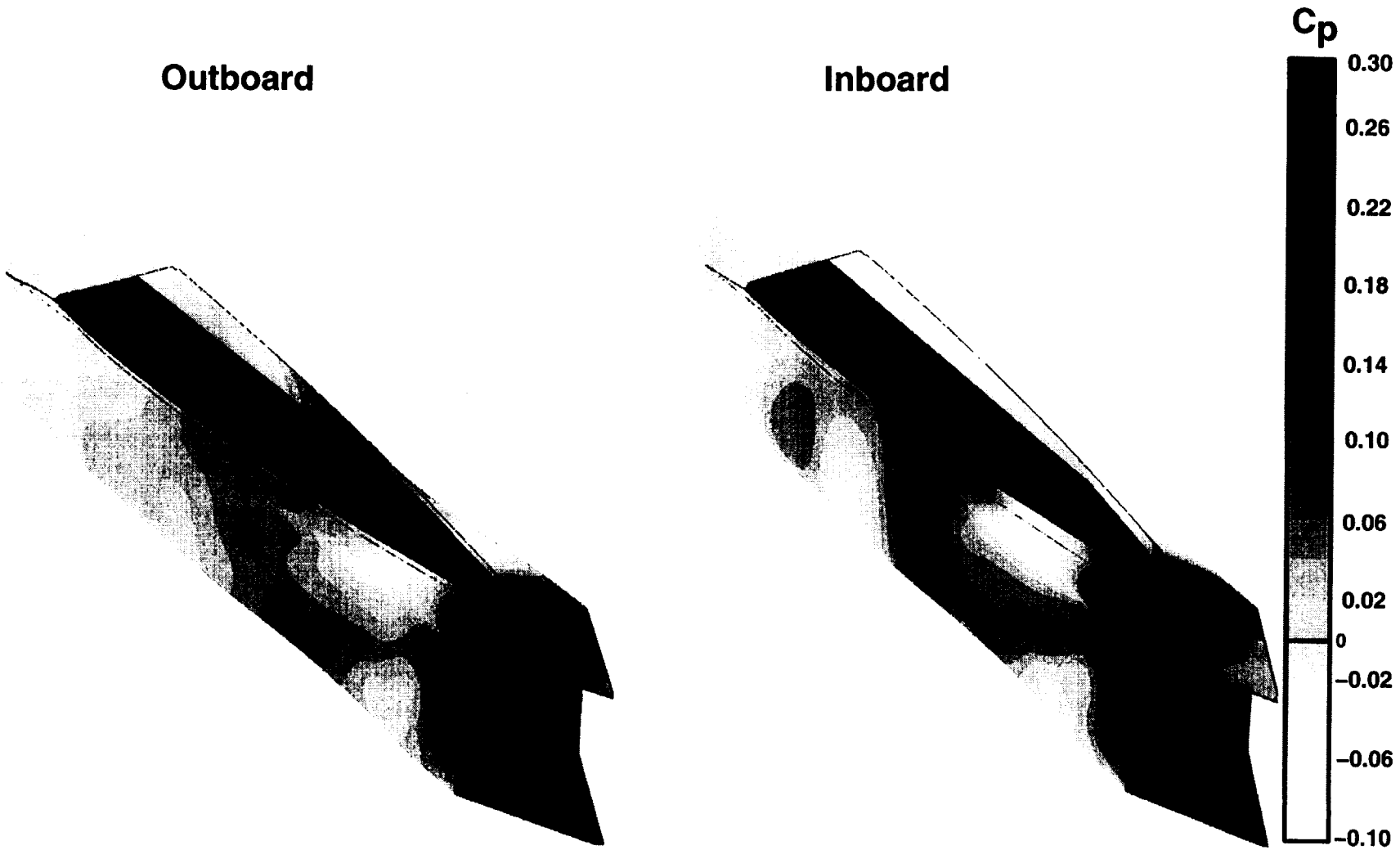

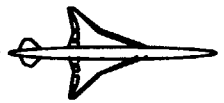

The next two figures show side-by-side comparisons of the nacelle/diverter pressure distributions on the baseline TCA and bifurcated inlet nacelles from OVERFLOW solutions. In general, the bifurcated installations tend to have a smaller region of high pressure around the nacelle/diverter LE regions (as seen previously on the wing lower surface) but a larger region of positive pressure spread out along the mid part of the nacelle. The integration of these pressure distributions resulted in a higher nacelle surface drag for the bifurcated (delta=1.3 counts, 0.6 of which is due to the lip bevel) and a slightly lower diverter surface drag compared to the baseline (-0.7 counts). Although the bifurcated diverter is longer than the baseline, this is compensated for by not being as tall (the diverter height was sized for the smaller wing boundary layer height at the forward location of bifurcated inlet on the wing).

Baseline TCA vs Bifurcated W/B/N/D Nacelle Surface Pressure Coefficient Mach 2.4, Re_{MAC} = 6.4 million, OVERFLOW Solution, α = 3.0 deg.

Inboard Nacelle

TCA (Axisymmetric)

Bifurcated

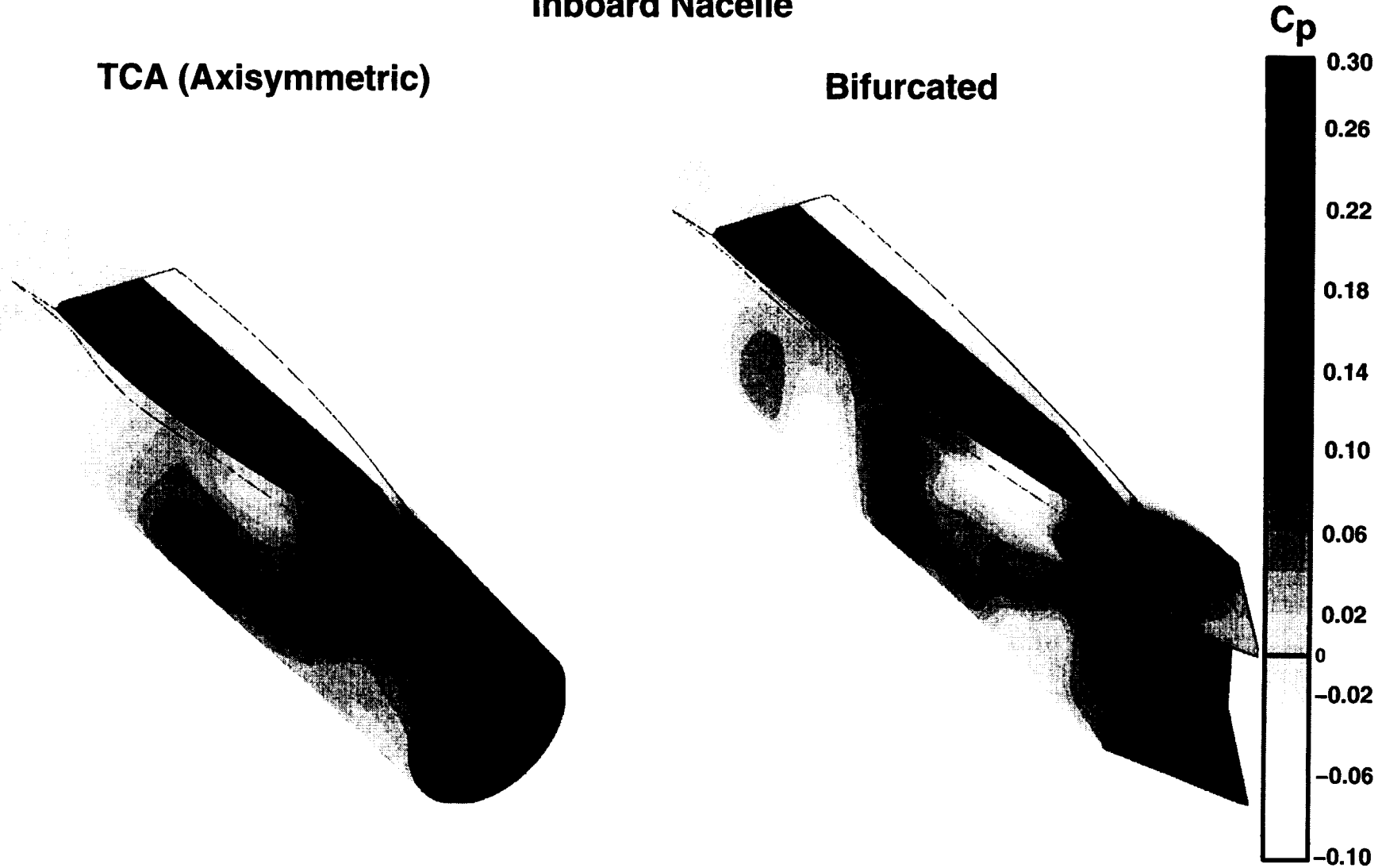

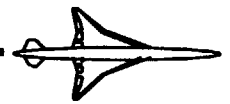

See previous facing text page.

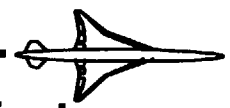

Baseline TCA vs Bifurcated W/B/N/D Nacelle Surface Pressure Coefficient

Mach 2.4, Re_{MAC} = 6.4 million, OVERFLOW Solution, α = 3.0 deg.

Outboard Nacelle

TCA (Axisymmetric)

Bifurcated

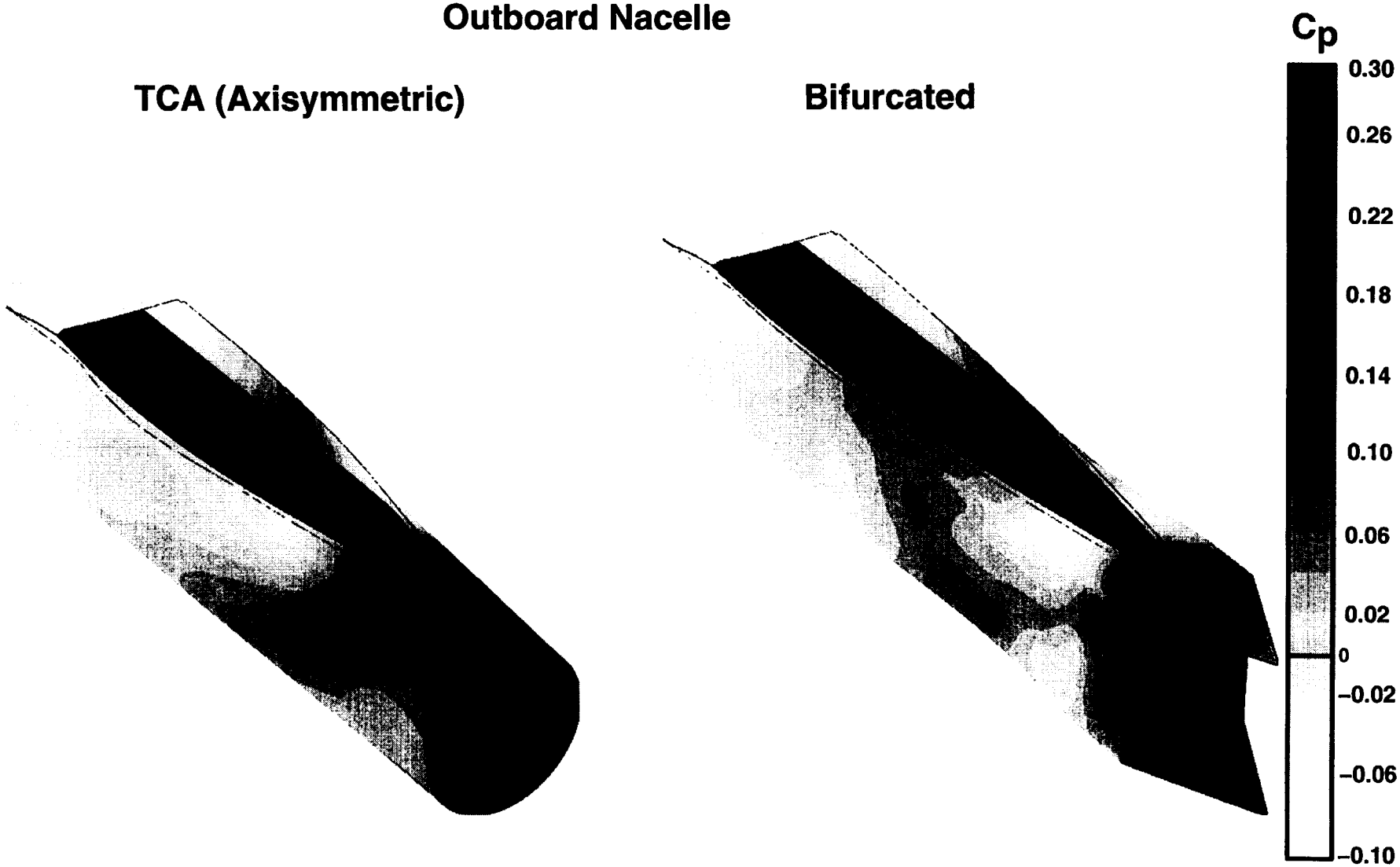

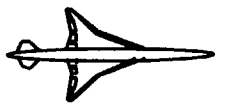

The installed nacelle force increments of the bifurcated are compared to the baesline TCA in this plot. The bifurcated installation drag is nearly identical to the axisymmetric across the supersonic cruise lift range (bifurcated about 0.2 counts higher drag). There is very little lift or drag delta at constant angle of attack. This particular bifurcated installation is nearly identical to the axisymmetric baseline TCA from a drag perspective. However, there will be a penalty for fixing the outboard diverter channel choking that will have to be incurred.

HSCT High Speed Aerodynamics

Baseline TCA vs Bifurcated W/B/N/D PAI Force Increments

Mach 2.4, Re_{MAC} = 6.4 million, OVERFLOW Analysis

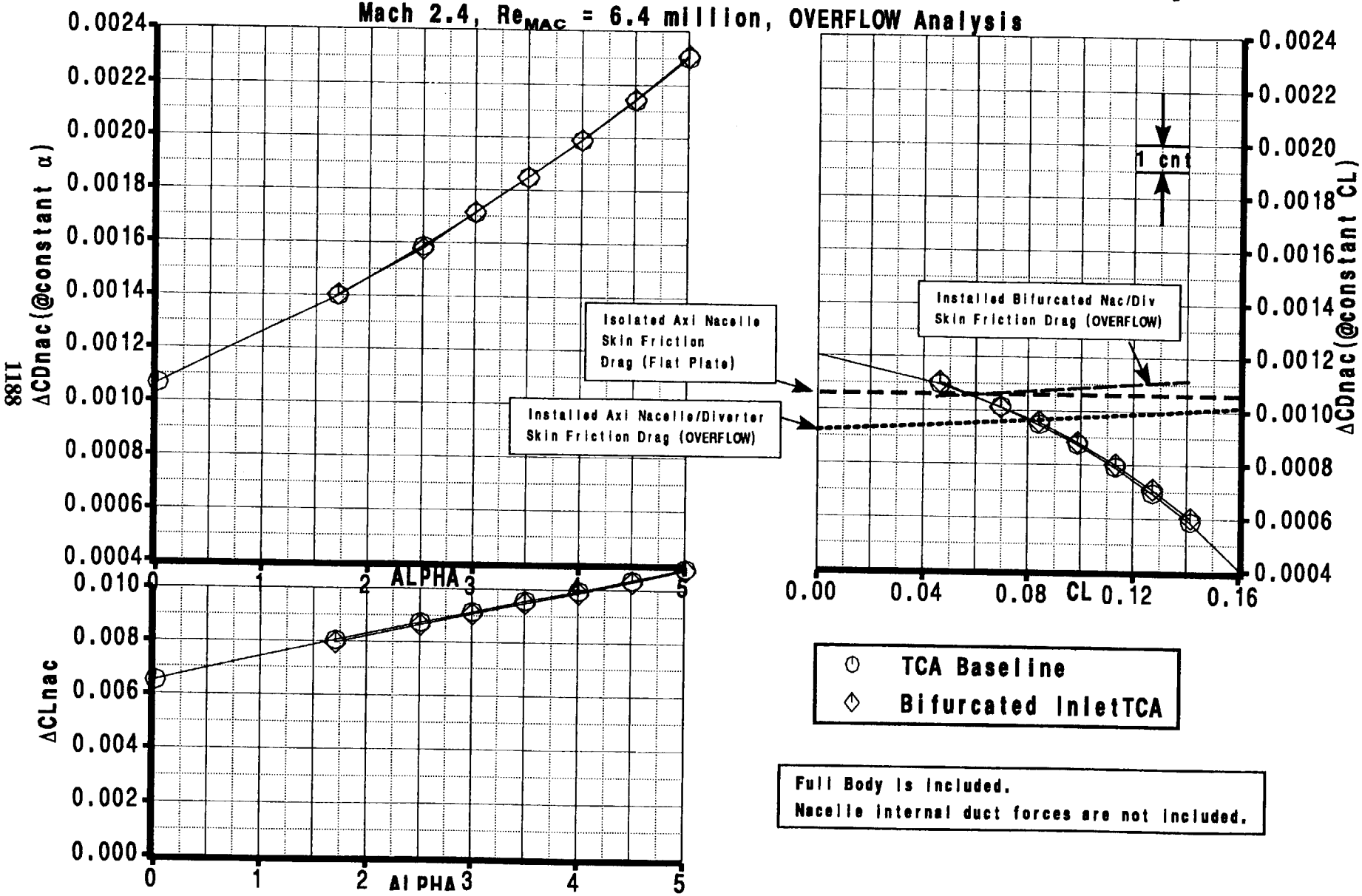

Full Body is included.
Nacelle internal duct forces are not included.

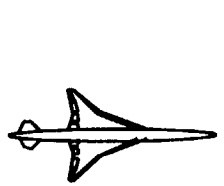

The drag penalty for dropping the outboard inlet is estimated to be ~1 count. Before doing this redesign however, several other analyses must be performed. A flight Reynolds number evaluation of the bifurcated and baseline configurations should be completed and determine if outboard bifurcated installation still unstarts. An isolated nacelle analysis of the bifurcated to aid the buildup of the component forces should be run.

The crucial difference between the two inlets may turn out to be the transonic Mach range so the transonic modeling capability started on the baseline axisymmetric should also be applied to the bifurcated.

Bifurcated Inlet Study Summary

Conclusions

- Supersonic drag penalty of bifurcated inlet on TCA as designed is zero.
- Drag penalty for fixing outboard diverter channel choking is ~ 1count.

Plans

- Isolated analysis of bifurcated inlet nacelle.
- Flight Reynolds Number analysis.
- Increase diverter height of outboard nacelle.
- Transonic comparison of bifurcated and axisymmetric inlets.

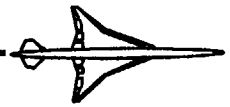

Configuration Aerodynamics End-of-Year Report

February 26, 1997

WBS 4.3.1.4.2 TCA STABILITY AND CONTROL ASSESSMENT

--highlighting--

Computation of Aeroelastic S&C Characteristics using AEOLAS

Douglas L. Wilson
The Boeing Co.

Participants:
Mike Elzey
Brian Nishida
Christine Titzer
Ross Sheckler (Dynacs Engineering)

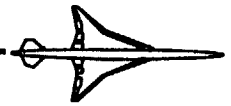

WBS 4.3.1.4.2 TCA STABILITY AND CONTROL ASSESSMENT

Objectives:

- Assess the high speed stability and control characteristics of the Technology Concept and design variations through computational analysis and experimental wind tunnel testing.
- Generate a CFD and wind tunnel data base of stability and control characteristics for the baseline and design variations at transonic and supersonic speeds.
- Make inputs to help guide Technology Configuration development.
- Develop design variations to improve stability and control characteristics.

1996 - 1997 (ytd) Tasks:

- Develop TCA S&C CFD Database
- Compute Aeroelastic S&C Characteristics
- Develop TCA S&C Experimental Database
- Develop methodology for S&C Aero Requirements (no activity to date)

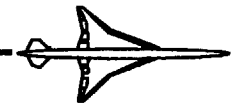

Develop TCA S&C Experimental Database

- Participated in requirements and planning for supersonic (UPWT) and transonic (16') tests.
- Participated in requirements and model definition for TCA controls model (Model 20).
- Prime Industry responsibility for transonic testing support and documentation; test currently in progress.
- Participating in requirements and planning for aft-body closure test (WBS 4.3.1.1) and propulsion-induced effects test (WBS 4.3.1.3).

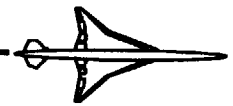

Develop TCA S&C CFD Database / Compute Aeroelastic S&C Characteristics

Strategy:

- Use CFD to correct experimental data and estimate rigid aerodynamic characteristics where experimental results are inadequate.
- Calculate elastic-to-rigid increments using linear methods; combine with rigid data to estimate elastic characteristics.
- Use aero model in simulation as structure for S&C database.

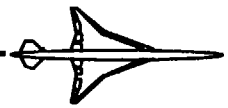

Approach:

- Calculate corrections to wind tunnel data using A502 panel method (e.g., aft body geometry, support interference).

- Compute rigid S&C characteristics for conditions not covered by experimental results (e.g., near M=1.0) using Euler code.

- Calculate elastic-to-rigid increments using AEOLAS:
  - Free-free boundary conditions
  - "Linear" methods
  - Aerodynamic influence coefficients based on A502 model
  - Structural stiffness and mass model based on ELFINI FEM, with order reduced to surface nodes using Guyan reduction (TBV).

- Add linear elastic corrections to rigid non-linear data; "non-linearize" elastic corrections where required using global methods.

- Tabulate data in n-dimensional FDHS format used in simulation (funded by GFC).

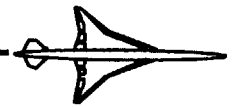

A502 Model of TCA

- Model comprises Wing/Body/Nacelle/Diverter/Empennage/Controls
- Same model used for subsonic and supersonic conditions except for nacelle inlet/outlet boundary conditions and other minor mods.
- Full model for asymmetric conditions (sideslip, control deflections); half model for symmetric conditions.
- Computational efficiency is critical for elastic computations because of number of conditions to be analyzed.
- S&C database covers full flight and loading envelope.
- Variables in database (not all variables for each term):
  Mach, alpha, beta, control surface deflections (~11), dynamic pressure, mass case

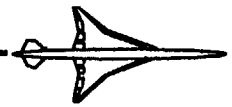

Upper surface pressure contours from A502 model: Mach=2.4, Alpha = 4.0

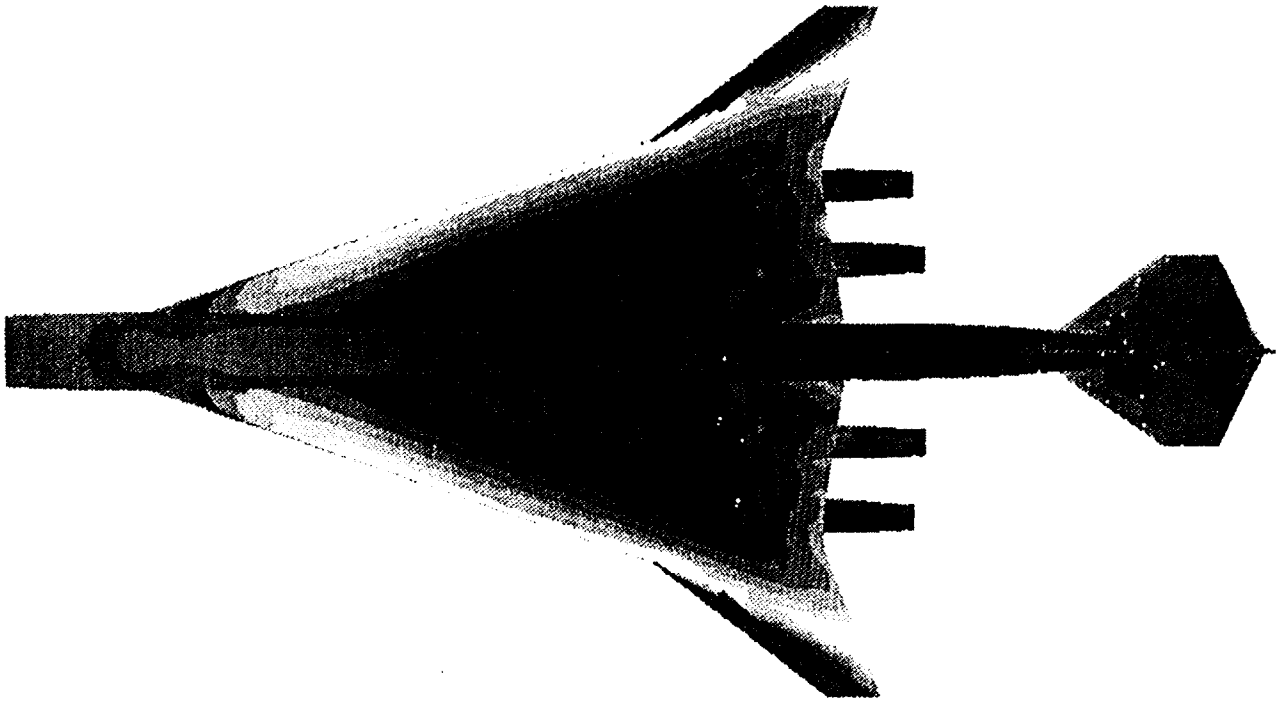

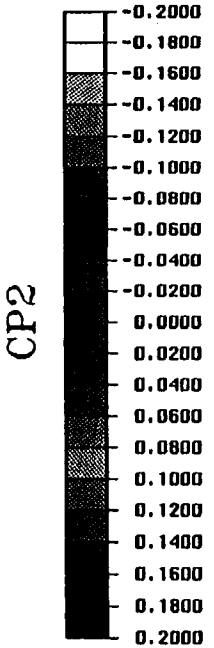

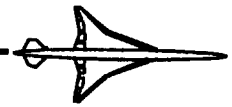

Lower surface pressure contours from A502 model: Mach=2.4, Alpha = 4.0

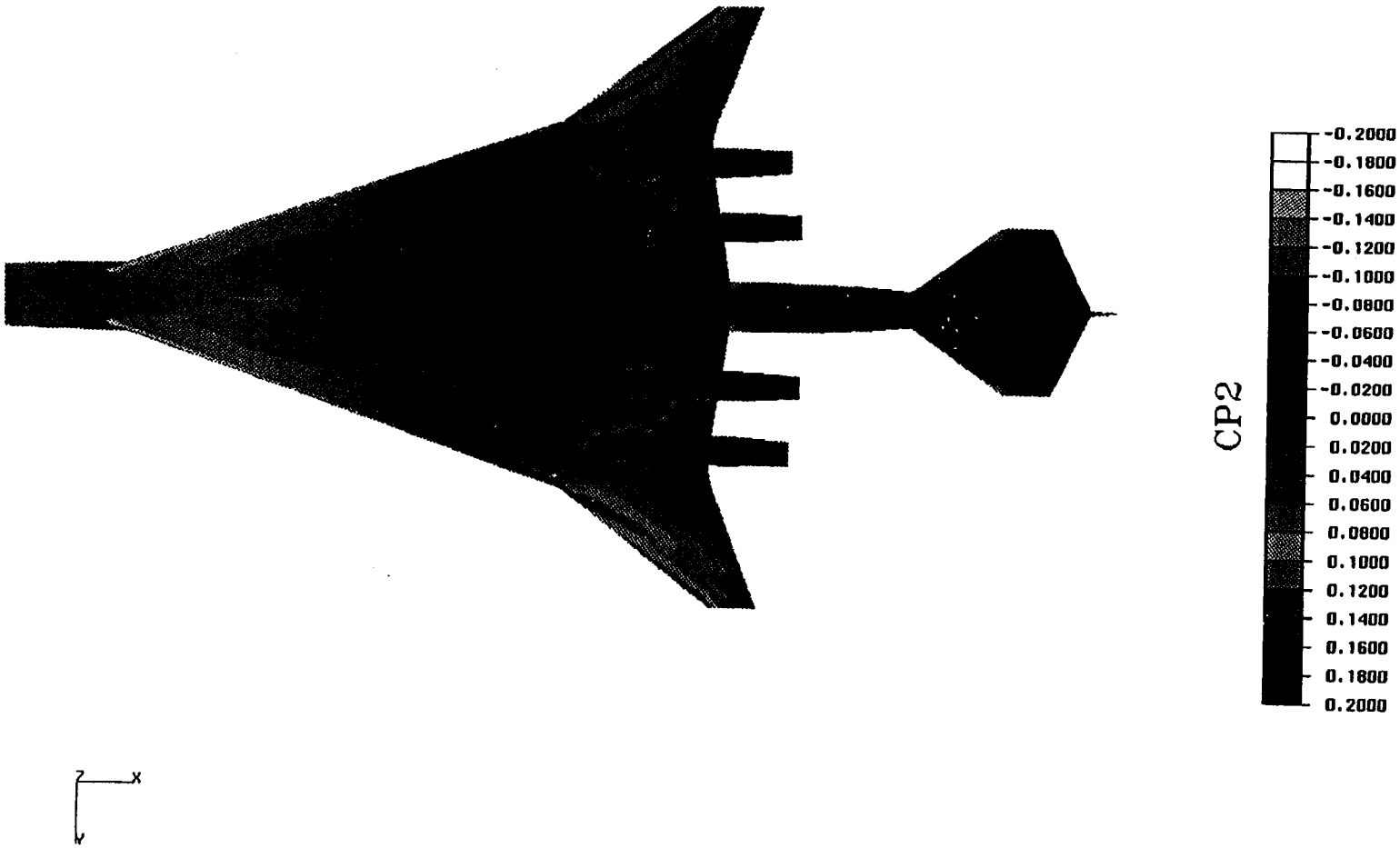

IMPROVEMENTS TO THE SINGLE-BLOCK ADJOINT-BASED AERODYNAMIC SHAPE DESIGN METHOD, SYN87-SB

James Reuther RIACS/AAH
David Saunders Sterling Software
Raymond Hicks MCAT

February 25-27, 1997

IMPROVEMENTS TO THE SINGLE-BLOCK ADJOINT-BASED AERODYNAMIC SHAPE DESIGN METHOD

James Reuther, RIACS/High Speed Research Branch, NASA Ames
David Saunders, Sterling Software/High Speed Research Branch, NASA Ames
Raymond Hicks, MCAT/High Speed Research Branch, NASA Ames

February 1997

This presentation focuses on the enhancements made since July 1996 to the single-block Euler- and adjoint-based wing/body design code, SYN87-SB. For completeness, an introduction to CFD-based design methods in general is given, along with an outline of adjoint-based methods in particular. Comparisons of the adjoint-based gradients with finite differencing are presented, reflecting recent corrections. In conclusion, some future enhancements to the single-block code are listed as desirable—substantial progress with the multiblock SYN87-MB notwithstanding: SYN87-SB's relative ease of use, particularly with its automated grid generation, its proven constraint handling, and its validated ability to approximate the effects of wing-mounted engines for supersonic applications, should ensure its enduring value as an aerodynamic design tool.

The recent improvements have been implemented by James Reuther (RIACS) and David Saunders (Sterling Software), with important contributions from Steven Edwards (U.C. Davis) in the form of elliptic grid smoothing and transfinite interpolation utilities. The wing/body optimization of TCA-6 at Ames was performed by Susan Cliff (High Speed Research Branch), Ray Hicks (MCAT), and James Reuther, with some contributions earlier from Robert Kennelly (High Speed Research Branch). The fundamental Euler and adjoint solvers are the work of Professor Antony Jameson (Princeton/Stanford) and James Reuther. The optimization packages used (QNMDIF and NPSOL) are due originally to a team from the Systems Optimization Laboratory at Stanford (Gill, Murray, Wright, and Saunders).

Outline

- **Motivation for Current Research**
- **Related Works**
- **Rationale for Adjoint Methods**
- **Symbolic Development of the Adjoint Method**
- **Single-Block Design Approach (SYN87-SB)**
- **Improvements in Design Methodology since 7/96**
- **Comparisons of Gradient Calculations**
- **Future Developments**

Motivation for Current Work

Computational Fluid Dynamics (CFD) algorithms for analyzing the flow about complete aircraft configurations have advanced, along with the speed of computer hardware, to the point where predicted flight performance can generally match experimental results well. The far greater cost of fabricating and testing wind tunnel models can therefore be replaced to a considerable extent by computation to help eliminate inadequate designs. But mere analysis is just a beginning. If the computational cost of the analysis can be lowered to the point where *many* analyses with sufficient fidelity are feasible during a typical batch job, then some form of automated design improvement becomes practical.

In the mid-1990s, the state of the art for rapid flow analyses of meaningful configurations is basically limited, for single processors, to Euler calculations (inviscid) for wing/body geometries (with possible inclusion of engine nacelle effects, but with treatment of the empennage unlikely). Massively parallel implementations are now capable of handling all components—multiple grid blocks lend themselves well to distributing among multiple processors—and Navier-Stokes analyses rather than mere Euler are becoming a viable option. This presentation describes progress with an approach that is practical for single (very fast) processors; the related multiblock/parallel approach is treated in a separate presentation.

Automated design implies optimizing some measure of aerodynamic performance, such as the match to a desirable target pressure distribution, or the drag at a specified lift. Trial-and-error is not easily automated, though genetic-type algorithms appear to be making some progress along that line. The early class of methods know as inverse methods (determining the shape that produces given surface pressures as opposed to determining the surface pressures for a given shape) have the advantage of being very efficient if they work, but their limitations are many (among them being the need to guess at what represents a good target pressure distribution, and the inability to impose desirable geometric constraints).

Given the sophisticated general purpose nonlinear optimization packages widely available nowadays, applying them to the (admittedly relatively expensive) objective functions of the type requiring solution of partial differential equations on large computational grids is a natural approach to take if those functions can be made to behave as smoothly as the optimization package normally requires. Gradient-based packages remain the most efficient under the same proviso—that the objective function is well-behaved enough for usable gradients to be estimated (analytic gradients being virtually out of the question, although automating the differentiation of this type of function is being pursued by some researchers). The present work involves gradient-based optimization packages, both unconstrained and constrained.

Motivation for Current Work

- **Extend the Maturing Computational Fluid Dynamics Capability to Treat Aerodynamic Design with a View Towards Rapid Design Cycles and Efficient Use of Expensive Wind Tunnel Testing**
- **Aerodynamic Design Strategies**
  - Cut and try
  - Inverse Methods
  - Numerical Optimization
- **Optimization Algorithms**
  - **Gradient-Based** (Steepest Descent, Quasi-Newton)
    - Smooth Design Spaces
    - Local Minimums
  - **Non-Gradient-Based** (Genetic Algorithm)
    - Arbitrary Design Space
    - Global Minimum

Motivation for Current Work (Continued)

The need for gradients of even a moderately expensive objective function can become prohibitive if the standard approach of finite differencing is taken. For instance, if a flow calculation takes just 5 minutes but there are 100 design variables, one gradient will take more than 500 minutes by forward differencing. Moreover, the flow calculations must be highly converged to give 6-7 digits of precision in the objective function, because the leading several digits are lost by the differencing. Thus 5 minutes may not be enough on a mesh with the required resolution, although after the first flow calculation the perturbed flow solutions have a nearby starting guess which perhaps halves the cost of subsequent function evaluations. Thus, the finite differencing approach is limited both by the number of design variables that can be afforded and by the high degree of flow field convergence that is necessary for accuracy.

SYN87-SB provides for finite differencing as an option—always desirable for checking an alternative gradient method. The high degree of convergence necessary is indeed provided by the embedded FLO87 Euler solver, with its multigrid strategy and proven techniques such as residual smoothing and artificial dissipation for accelerating convergence. However, it also offers a vastly more efficient method of calculating gradients—the adjoint-based method.

- **Gradient Calculation Methods**
  - **Finite Difference**
    - Expensive
    - Easy Implementation
    - Accurate (Subject to Flow Solution Convergence)
  - **Adjoint Variable (Continuous or Discrete Sensitivities)**
    - Very Efficient
    - Difficult Implementation
    - Accurate (Subject to Implementation)
  - **Automatic Differentiation**
    - Moderately Efficient
    - Moderate Implementation
    - No Adjoint Yet
    - Very Accurate
- **Even with Adjoint Gradients, Shape Design for Complex Configurations is Computationally Expensive.**
- **There is a Need for Parallelization to Enhance Speed.**

Related Works

- **R. Hicks, et al.** (1974-present)
  - Introduced Aerodynamic Design via Numerical Optimization
  - Current Work: Aerodynamic Design of Supersonic Transports
- **A. Jameson and J. Reuther** (1988-present)
  - Introduced Aerodynamic Design via Control Theory
- **O. Baysal, M.E. Eleshaky and G.W. Burgreen** (1991-present)
  - Introduced the Use of Discrete Sensitivity Methods
- **V.M. Korivi, A.C. Taylor P.A. Newman, et al.** (1991-present)
  - Introduced Incremental Strategy Discrete Sensitivities
- **S. Ta'asan, G. Kuruvila and M.D. Salas** (1992-present)
  - Introduced One Shot Methods
- **V. Modi and J. Huan — J. Lewis and R. Agarwal — D. Young**

Rationale for Adjoint Methods Instead of Finite Difference Methods

The alternative method of determining gradients that is a major key to SYN87-SB's effectiveness as a design tool is the adjoint-based method. The calculus of variations (or control theory) points to this far more efficient (though more complex) approach to computing sensitivities. As outlined mathematically below, the variation of the objective function with respect to *any number of design variables* can be determined cheaply at the cost of solving a second set of differential equations—the adjoint equations—comparable to the flow equations. The same multigrid and convergence-speeding techniques developed for the Euler equations are directly applicable to the adjoint equations once the appropriate boundary conditions (the hardest part) have been determined.

The cost of a gradient vector is thus reduced to little more than one flow solution and one adjoint solution. Given that the adjoint system is related to the flow system and solved by similar techniques, the cost of a gradient is thus reduced to the equivalent of 2 flow solutions. In contrast, the finite difference method requires $n+1$ flow solutions for n variables. Error analysis for the adjoint approach shows that the error in the sensitivities obtained is comparable to the error in the cost function. Thus not only are just 2 solutions required per gradient—those solutions need not be as thoroughly converged as the traditional approach demands.

Thus the adjoint mode of SYN87-SB allows for large numbers of design variables and can behave well with flow and adjoint solutions converged 5 and 3 orders respectively, compared with the 6 - 7 orders recommended for reliable finite differencing. Some gradient comparisons are shown below. Part of the progress made in recent months has been to improve these comparisons for the case where supersonic nacelle/diverter effects are included in what is inherently a wing-alone or wing+body code because of the single grid block topology. This pseudo nacelle approximation is discussed further below as well.

In principle, the adjoint approach could provide full second derivative (Hessian) information for about the same cost ($n+2$ flow solutions) as the finite difference approach requires for first derivatives alone. Finite difference Hessians require $n^2/2$ flow solutions which are normally prohibitive. For the present, removing the traditional limit on the number of design variables is so computationally attractive that any attempt to go beyond first derivative methods makes little sense. Quasi-Newton rather than full Newton methods serve adequately for hundreds of variables; and limited-memory variations of the quasi-Newton methods, which avoid storing even some approximate Hessian or its factors in favor of retaining the last few low-rank updates only in vector form, appear to be the direction in which adjoint-based optimization is likely to move as the number of design variables grows. Of course, no more variables should be used than is strictly necessary even if the gradients are cheap, and good choice of design variables is a topic unto itself (more on which below).

Rationale for Adjoint Instead of Finite Difference Methods

- **Reduce Computational Costs**
  - Gradient Evaluations
    - Finite Difference Method: $n + 1$ Flow Calculations
    - Adjoint Method: 2 Flow Calculations
  - Full Hessian Information
    - Finite Difference Method: $\approx \frac{n^2}{2}$ Flow Calculations
    - Adjoint Method: $n + 2$ Flow Calculations

Rationale for Adjoint Methods Instead of Finite Difference Methods (Continued)

The above equivalent flow solution counts applied to a single objective function with no aerodynamic constraints, or to composite objectives (linearly combined) at the same flight condition. They also apply to cases where lift is constrained by means of an inner iteration on Alpha. But in general, the gradient cost increases by one adjoint solution for each additional objective or aerodynamic constraint, because these affect the right-hand side of the adjoint system. (Purely geometric constraints do not require further adjoint solutions.) Thus for an objective function or an aerodynamic constraint at second flight condition, a second flow solution and a second adjoint solution must be recomputed.

In comparison, the finite difference gradient picture is no worse for additional objectives or aerodynamic constraints at the same flight condition, but for multi-point design it is even more bleak, requiring another $n+1$ flow solutions for each additional flight condition. Thus the adjoint strategy is especially desirable for multi-point design.

Presently, SYN87 is strictly a single-point design code, with one of the available objective functions switched on at run time, and no aerodynamic constraints other than the fixed-lift option. (Numerous geometric constraints are supported—more on these below.)

- **Increase Number of Objective Functions and Aero. Constraints**
  - Gradient Cost for Each Additional Objective or Aero. Constraint
    - At Same Flight Conditions
      - Finite Difference: 0 Flow Solutions
      - Adjoint: 1 Flow Solution
    - At Different Flight Conditions
      - Finite Difference: $n + 1$ Flow Solutions per Condition
      - Adjoint: 2 Flow Solutions per Condition
- **Provide Sensitivity Derivatives for any Desired Change Without Additional Calculations**

Symbolic Development of the Adjoint Method

The next two slides show the basic analysis behind the adjoint approach as outlined under the ***Rationale*** section above. The following references provide a more complete treatment and cover the actual application to the governing Euler equations:

1) J. Reuther and A. Jameson. Aerodynamic shape optimization of wing and wing-body configurations using control theory. *AIAA paper 95-0123*, Reno, January, 1995.

2) J. Reuther and A. Jameson. Supersonic wing and wing-body shape optimization using an adjoint formulation. *Technical report, The Forum on CFD for Design and Optimization (IMECE 95)*, San Francisco, November 1995.

Symbolic Development of the Adjoint Method

Let I be the **cost** (or **objective**) function

$$I = I(w, \mathcal{F})$$

where

$$\begin{aligned} w &= \text{flow field variables} \\ \mathcal{F} &= \text{grid variables} \end{aligned}$$

The **first variation** of the cost function is

$$\delta I = \frac{\partial I}{\partial w}^T \delta w + \frac{\partial I}{\partial \mathcal{F}}^T \delta \mathcal{F}$$

The **flow field equation** and its **first variation** are

$$R(w, \mathcal{F}) = 0$$

$$\delta R = 0 = \left[\frac{\partial R}{\partial w}\right] \delta w + \left[\frac{\partial R}{\partial \mathcal{F}}\right] \delta \mathcal{F}$$

Introducing a **Lagrange Multiplier**, ψ, and using the **flow field equation** as a **constraint**

$$\begin{aligned}\delta I &= \frac{\partial I}{\partial w}^T \delta w + \frac{\partial I}{\partial \mathcal{F}}^T \delta \mathcal{F} - \psi^T \left\{ \left[\frac{\partial R}{\partial w}\right] \delta w + \left[\frac{\partial R}{\partial \mathcal{F}}\right] \delta \mathcal{F} \right\} \\ &= \left\{ \frac{\partial I}{\partial w}^T - \psi^T \left[\frac{\partial R}{\partial w}\right] \right\} \delta w + \left\{ \frac{\partial I}{\partial \mathcal{F}}^T - \psi^T \left[\frac{\partial R}{\partial \mathcal{F}}\right] \right\} \delta \mathcal{F}\end{aligned}$$

By choosing ψ such that it satisfies the **adjoint equation**

$$\left[\frac{\partial R}{\partial w}\right]^T \psi = \frac{\partial I}{\partial w},$$

we have

$$\delta I = \left\{ \frac{\partial I}{\partial \mathcal{F}}^T - \psi^T \left[\frac{\partial R}{\partial \mathcal{F}}\right] \right\} \delta \mathcal{F}$$

This reduces the **gradient** calculation for an arbitrarily large number of design variables at a **single design point** to

One Flow Solution

\+ **One Adjoint Solution**

Single-Block Design Approach (SYN87-SB)

The capabilities of the current production version of the inviscid wing/body design code SYN87-SB are now described in further detail. The Euler flow solver and adjoint technology is well explained in other references, so only highlights and performance details are included here.

Euler Solution (FLO87)

Each flow solution is calculated by a subroutine form of the FLO87 Euler solver by Antony Jameson as modified by James Reuther for wing/body applications rather than wing-alone. FLO87 computes cell-centered Euler solutions using a multistage Runge-Kutta-like time-stepping scheme. Its mature combination of multigridding, residual averaging, enthalpy damping, and 2nd- and 4th-order blended artificial dissipation provide the rapid, reliable convergence needed for design applications. Some tuning of the suggested convergence parameters may be required for each new configuration or grid dimensions, but the following performance is typical:

For the 5 orders of convergence recommended for use with the adjoint solver, FLO87 takes about 200 multigrid cycles (4-level W cycles) and about 970 CRAY C90 CPU seconds from a free-stream start on a 193 x 49 x 65 grid (at Mach 2.4 and $C_L = 0.1$ for an HSCT configuration). Line search solutions from a nearby solution normally require significantly less time. (SYN87 updates the stored flow solution whenever the objective function decreases, even during a line search.)

Adjoint Solution (ADJ87)

SYN87's adjoint method is based on the continuous sensitivity approach (applied to the underlying PDE) as opposed to the discrete sensitivity approach (applied to the discretized governing equations). As a result, the ADJ87 subroutine can employ the same cell-centered multistage Runge-Kutta-like time-stepping algorithm already perfected for FLO87, including the 2nd- and 4th-order artificial dissipation and the multigridding and residual-averaging convergence acceleration schemes. Several variations of the co-state flux formulations have been tried, with only minor differences apparent in the resulting gradients. Each multigrid cycle presently takes a little longer than a flow cycle, but experience shows that only 3 orders of convergence are needed in the adjoint solution, combined with 5 orders for the flow solution, in order to produce accurate gradients (to be illustrated below).

For the above Mach 2.4 case, ADJ87 typically takes about 135 cycles and 670 CPU seconds to achieve 3 orders of convergence. Then each gradient element takes about 4.4 CPU seconds includng the grid perturbation and pseudo nacelle effects (more on which momentarily).

Single-Block Design Approach (SYN87-SB)

- **Euler Flow Solver (FLO87) + Adjoint Solver (ADJ87)**
  - Robust, Efficient Inviscid Analysis + Cheap Gradient Calculation
- **Numerical Optimization Algorithms**
  - **QNMDIF** — Unconstrained Quasi-Newton Algorithm
  - **NPSOL** — Constrained Sequential Quadratic Programming (SQP) Method
- **Single-Block Wing/Body C-H Mesh Generation**
  - Arbitrary Wing/Body Geometry Handled
  - Single-Block C-H Topology (193 x 49 x 65 for TCA Design)
  - Very Efficient Grid Perturbation (WARP3D & WARPQ3D)
  - **Algebraic** Mesh Generation + **Elliptic Smoothing** with Blended Thomas-Middlecoff Spacing and Sorenson-type Orthogonality
  - **Automatic Wing/Body Intersection** (Even for High or Low-Mounted Wings)

Single-Block Design Approach (SYN87-SB), continued

Numerical Optimization Packages

Unconstrained Quasi-Newton Algorithm (QNMDIF2)

Given that judicious choice of design variables can impose equality constraints implicitly (e.g., on wing section thickness), an unconstrained optimization package served SYN87-SB well for several years, and has been retained in spite of the introduction of a constrained package. QNMDIF2 has been adapted moderately from the QNMDIF of Gill, Murray, *et al.* (National Physical Laboratory, U.K., later Systems Optimization Laboratory, Stanford) to handle expensive iteratively-calculated functions better by trapping function failure and allowing retries where appropriate. QNMDIF2 is also fully argument driven (no local storage vectors of length n). Note that the availability of adjoint-based gradients is transparent to QNMDIF2 with one exception: QNMDIF's automatic switching from forward to central differencing under certain conditions makes no sense if the gradients are derived from adjoint-based variations. This is therefore handled appropriately in QNMDIF2.

Constrained Sequential Quadratic Programming Method (NPSOL)

Optimization of TCA-6 demanded explicit treatment of numerous constraints, linear and nonlinear. Therefore, the widely used NPSOL package from the authors of QNMDIF has been installed in SYN87-SB as an option. (If there are no constraints, NPSOL and QNMDIF performance will be similar though not identical.) NPSOL uses a sequential quadratic programming (SQP) algorithm in which the search direction is the solution of a quadratic programming (QP) subproblem. Variable bounds, linear constraints, and nonlinear constraints are treated separately. The variable bounds and linear constraints are always satisfied during the optimization; the nonlinear constraints on the other hand are not necessarily strictly satisfied except at a minimum. During each line search, NPSOL ensures a sufficient decrease in an "augmented Lagrangian" merit function. Such a merit function balances the (usually conflicting) aims of reducing the objective and satisfying the nonlinear constraints.

NPSOL treats all matrices as dense, so it is suited to a few hundred variables and constraints (but not thousands). Typical SYN87-SB design runs use 100-200 variables (in adjoint mode) and 100 linear constraints and a few nonlinear geometric constraints (more on which below). In applications such as these, any CPU time spent in the optimization package is negligible compared with the CPU time spent computing the objective function and its gradient.

Switching Between Optimization Packages

A single input variable switches between QNMDIF2 and NPSOL. Any constraint inputs do not need to be removed if QNMDIF mode is specified. Indeed, the constraints are still monitored (if not enforced) when QNMDIF mode is selected. One reason for choosing the unconstrained mode is to avoid the initial *feasible point search* performed by NPSOL prior to any objective function calculation. NPSOL requests that first objective calculation, whereas in QNMDIF mode it is performed before entering QNMDIF2. Occasionally, the initial geometry is such that some linear constraints (e.g., on wing section T/C at specified X/C) are not quite satisfied. In this case, NPSOL is obliged to adjust the initial design variables in a minimal way if possible to satisfy the linear constraints, meaning the first flow analysis no longer corresponds to the specified design variables (probably all zeros)—sometimes to the consternation of the user.

Single-Block Design Approach (SYN87-SB), continued

Single-Block Wing/Body C-H Mesh Generation

SYN87's present automated C-H grid generation for wing and wing/body configurations has its origins in Lockheed's WBGRID software, but it has largely been rewritten to improve the grid quality, which is marginal at best on the nose and aft-body because of the single-block topology. The most recent improvements are discussed on a later slide.

Meshes dimensioned 193 x 49 x 65 were employed for most of the TCA-6 optimization, with the 65 spanwise grid stations highly desirable to resolve the pseudo nacelle effects adequately. This leads to a 55 Mword memory requirement on the CRAY C90.

Normally, SYN87-SB performs an initial full grid generation, although reading a previously-stored grid is now an option. About 93 CPU seconds are required on the C90. Subsequent grids take ~4.4 seconds via perturbation techniques.

Full Grid Generation

Full grid generation starts with regularizing the wing sections (and body sections if necessary), and determining the wing/body intersection as a sequence of parametric surface/line intersection subproblems. This intersection line overwrites the regularized center-line section used to compute it, then the wing surface grid is established via bilinear interpolation. Cranks in the leading edge may be captured automatically by smoothly-varying adjustments of the nominal spanwise distribution.

The body surface grid is (usually) done parametrically, working with an *un*normalized form of the regular body geometry arc lengths in order to deal with the singularity at the nose. These arc-lengths are equilibrated in the streamwise direction to avoid a ragged boundary at $v = v_{max}$ corresponding to the last body station, and they are recentered about $u = 0.$ in the circumferential direction to moderate the stretching of u at the nose. Boundary (u,v) distributions are then established (an awkward 2D inverse problem along the wing/body intersection), then transfinite interpolation (TFI) and 2D elliptic smoothing are applied in four regions, followed by parametric bicubic interpolation at the resulting interior (u,v) points. Redistribution along the resulting radial lines then provides precise control of the arc-length spacing at the wing root and at the crown line.

Once the outer boundary grids have been established, the volume grid is initialized via 3D transfinite interpolation then smoothed elliptically with control of both spacing and orthogonality at most boundaries. More details are given below.

Grid Perturbation

Even with its adjoint-based gradient capability, SYN87-SB still needs to do a grid calculation for every gradient element because this portion of the technique remains in finite difference form. A cheap perturbation method of regenerating the grid is clearly needed to take full advantage of the adjoint approach. If the wing/body intersection changes, as it may well do, simply perturbing the initial grid along lines off the surfaces may not be viable. Thus a generalized scheme is required which allows for any or all of the grid faces to move. Such a utility has been implemented as subroutine WARP3D. Given perturbed block face grids (or sub-block face grids), WARP3D determines corresponding perturbed interior grid points efficiently.

Single-Block Design Approach (SYN87-SB), continued

Single-Block Wing/Body C-H Mesh Generation, continued

Grid Perturbation, continued

WARP3D is best understood by considering its 2D analogue, WARP2D. Here, a 2-stage algorithm solves the problem—one stage to deal with possible corner point motion, and a second stage to adjust for any further edge motion. Consider perturbing a rectangular grid. If any of the corners has moved and the desired edges remain straight lines, then the first stage alone achieves the desired result because the moved edges are the final edges. Conversely, if the corners remain fixed and only the edges have moved (no longer straight lines), the second stage does all the work. In general, with both corner and (dissimilar) edge motion, each stage does part of the work.

Stage 1 effectively perturbs all points (including edge points) based only on the motion of the 4 corner points. In practice, the edge points are treated first. Stage 1 initially establishes intermediate edge perturbations from the corner perturbations by the obvious 1D method of imposing the same relative locations between the new corners as between the original corners. Corresponding interior point perturbations are then derived from the perturbations of the two pairs of opposite edge points defined by the relevant indices. Since both directions affect these interior perturbations, the contributions from each index direction must be combined as a weighted average.

Stage 2 first determines edge point perturbations from the intermediate edges to the desired edges, then updates each interior point based on the motions of the relevant end points in each index direction. The contributions from each direction can be simply added: they are now independent because the corners haven't moved.

Analogously, WARP3D performs a 3-stage algorithm to handle motion of corners, edges, and faces. That is, the interior point perturbations for stage 1 account for any corner point motion; for stage 2 they account for any additional edge point motion; and for stage 3 they account for any additional face point motion. Perturbations determined from each index direction need to be combined as (different) weighted averages in Stages 1 and 2, while in the final stage where they are independent.

Rather than making three passes through the interior volume points, WARP3D stores the face perturbations for each stage then accumulates corresponding interior perturbations in a single pass through the volume, which fully vectorizes.

WARPQ3D is also applied to sub-block faces where possible. This helps significantly because these boundary grids otherwise require 2D elliptic smoothing.

The bulk of the time required for SYN87-SB's grid regeneration is now spent on the wing/body intersection calculation followed by the wing and body surface grid generation, with little hope for improvement. Typical regridding CPU times are 2.42 seconds for a gradient element evaluation (single design variable perturbation), and 2.65 seconds for a line search evaluation (all design variables perturbed, with greater impact on the starting guesses for each point of the wing/body intersection calculation).

Single-Block Design Approach (SYN87-SB), continued

Pseudo Nacelle Effects (Supersonic Applications Only)

The most obvious drawback of the basic SYN87-SB wing/body design procedure is its single-block structured grid, for which the Euler solutions (particularly for body wave drag) are only marginally trustworthy. At best, it may be expected just to predict increments in aerodynamic performance. At worst, an inability to incorporate additional components such as nacelles can make wing/body-alone design optimizations worthless.

The importance of including the nacelles and diverters as part of the HSCT design problem was appreciated from the start. Thus SYN87-SB (like its precursors OPT3D and OPT67) provides an option to simulate their effects using the nacelles-off and nacelles-on flow fields from a more capable solver such as AIRPLANE (as originally suggested by Bob Kulfan at Boeing). These are termed Pseudo or Ghost Nacelle effects. In SYN87-SB, they have been incorporated into the adjoint method for the first time. The original scheme has also been made more thorough in the past 6 months (as will be described below).

The pseudo-nacelle option consists of three distinct parts. The first part uses the surface delta Cps (differences between nacelles-on and nacelles-off, interpolated from the input AIRPLANE results onto the SYN87-SB grid) to estimate the changes caused by the nacelle/diverters in the forces on the wing and the body (Nacelle on Wing effects).

The second part estimates the changes in the forces that might occur on the nacelles as the local flow field in which they reside changes as a function of design changes (Wing on Nacelle or delta buoyancy effects).

The third part (most recently incorporated) makes use of the Cps read with the nacelle/diverter coordinates from AIRPLANE. These surface Cps had been ignored originally, but they allow lift and drag forces on these components to be estimated, and these estimates change slightly as the nacelle orientations and diverter areas change to follow lower wing perturbations. (These corrections to the total force coefficients are termed the delta nacelle Cp effects.)

The following details are retained from the February 1996 presentation because of the importance of the pseudo nacelle capability to the HSR program:

Consider for example the case where C_D is the cost function to be minimized. For the nacelle simulation, SYN87-SB evaluates the objective function as the sum of three components. C_D-wing-body refers to the drag that is actually calculated on the wing-body configuration which results strictly from the flow analysis (i.e., the portion without the nacelle effects). C_D-nacelle-on-wing refers to the contribution to drag developed by the nacelle on wing effects (i.e., by correcting the wing lower surface Cps with delta Cps derived from another solver's results before performing the force integration). This is equivalent to performing two force integrations (one for the uncorrected Cps, and one for just the delta Cps) and then summing them after the fact. The third term, C_D-wing-on-nacelle, refers to the integrated delta forces on the ghost nacelle geometry. (The delta nacelle Cp effects required only a minor change to the adjoint-based gradients.) In order to understand how the adjoint method develops the gradient for this problem, each of these terms must be examined in turn.

Single-Block Design Approach (Continued)

- **Pseudo Nacelle Effects**
  - Simulate Nacelle on Wing Effects (Lower Surface Δ Cps)
  - Simulate Wing on Nacelle Effects (Δ Nacelle Buoyancy)
  - Simulate Nacelle Motion Effects (Δ Nacelle Cps)
  - Diverter Areas May Change (Leading/Trailing Edge Heights Fixed)
- **Objective Functions**
  - Target Wing Pressure Distribution
  - Drag at Fixed Alpha
  - Drag at Fixed Lift
  - L/D at Fixed Alpha
- **Linear Constraints**
  - Wing Section T/C (or Y) at Specified X/C
  - Cabin Section Radius at Specified Polar Angle (Body Camber Fixed)

Single-Block Design Approach (SYN87-SB), continued

Pseudo Nacelle Effects, ccontinued

Since the first term does not involve the pseudo nacelles in any way, how it is treated in adjoint mode is independent of the presence of pseudo nacelles. The integrated C_D on a configuration without pseudo nacelles is dependent on the flow field variables at the surface and the mesh metrics at the surface. Thus if we want to know the gradient of this drag with respect to changes in a design variable, we must know the gradient of the values of these two vector quantities with respect to the same change in the design variable, as shown by the chain rule of calculus. The gradient of the flow field variables with respect to the design variable is determined by specifying an adjoint boundary condition, solving the adjoint system, and performing a volume integral involving products of the adjoint variable over the entire domain. The derivatives of the surface mesh metric terms can be obtained from a simple surface integral that is a product of these changes in the metrics. No adjoint variable is necessary. Although this, so far, is simply a repeat of what has been presented in the existing references on the use of adjoint methods, it is discussed here to emphasize the point that the variation involving flow field quantities requires an adjoint boundary condition and solution, while variations of the mesh terms require only surface integrals with these variations explicitly calculated.

The second term in the cost function summation, C_D-nacelle-on-wing, is defined as an integral over the geometry surface of constant pre-calculated values of delta Cp. Thus the gradient of this term contains no variation of the flow field quantities and hence there is no contribution to an adjoint boundary condition. The only gradient term that results from this term is a surface integral arising from changes in the metrics.

The last term, C_D-wing-on-nacelle, is unfortunately not so simple. It is represented by a surface integral over the ghost nacelles and diverters which involves both changes in the location of these entities (i.e., mesh metrics) and changes in the flow field variables acting on them. This implies that the gradient of this term not only will have a contribution from a surface integral over the nacelle/diverters (mesh metric variation term) but will also have a forcing function that affects the adjoint solution. Now, since the actual position of the ghost nacelles is out in the volume domain of the adjoint system, the contribution to the adjoint forcing function occurs not at the surface as a boundary condition but out in the domain as a source term. It is noteworthy that this HSR-specific adaptation of the adjoint method is the first time that a non-boundary term has been incorporated into the technology by our group. It represents a fundamental advance in the science.

The initial set-up for the ghost nacelle option can and should be saved for reuse. It consists of bilinear and trilinear interpolation pointers and blanking information to account for the portions of the lower wing surface covered by the diverters. In the case of the TCA-6 geometry, the set-up takes several thousand CPU seconds to generate, largely because several dozen AIRPLANE surface data points on the upper aft nozzles project into the *upper* half of the C-H mesh, whereas the scheme must pick the nearest grid cell from the *lower* half only. Any such search must check every cell of the lower half grid before concluding that the target point is not contained in any of them, and this is expensive. Updating the buoyancy corrections for each line-search solution takes about 1.8 CPU seconds, but basically after setting it up the pseudo nacelle simulation has negligible further cost.

Single-Block Design Approach (SYN87-SB), continued

Objective Functions

SYN87-SB provides a choice of likely objective functions which are activated by entering non-zero multipliers in the standard input. The initial non-HSR objective functions provided are matching of target wing pressures at grid points and (more properly, to avoid grid density effects) pressures integrated over the wing area. The target and calculated pressure distributions are parameterized for the least-squares comparison, meaning the wrap-around wing surfaces are transformed to normalized (u,v)-space on [0,1] x [0,1]. A full, structured target distribution is thus expected, but portions of it may be suppressed via the input i and k range (indices referring to the current surface mesh). With each new flow solution, the target distribution is bilinearly interpolated to the current wing surface cell centers in order to perform the objective function evaluation. A typical case requires 0.32 C90 seconds for the first set of interpolations, and 0.2 seconds after that thanks to the better starting guesses.

It was recently realized that the parameterization of pressure distributions must be done in real space (as opposed to reading an already-normalized target distribution). To put it another way: if a surface pressure solution is saved in normalized form then read back for use as a target distribution, there is no way for wing thickness, sweep, and taper information to appear in that target distribution, particularly if the comparison is weighted by area as it should be. Thus SYN87-SB now expects target pressure distribution inputs to include denormalization quantities which are applied before the arc-length-based parameterization is performed.

Other objective function options developed in conjunction with the HSR program include C_D at fixed Alpha, C_D at fixed C_L, and L/D at fixed Alpha (i.e., minimization of C_D/C_L). Pressure coefficients less than a specified limit may also be penalized as part of any objective, and penalty functions may also be activated in conjunction with a target C_L or a target C_M.

Minimizing drag at fixed lift requires an inner iteration on angle of attack, which is adjusted every 10 or so multigrid cycles. The adjustment in and of itself tends not to slow the convergence rate significantly. Rather, somewhat greater convergence should be specified to be sure of achieving the specified C_L, since no explicit test is made for terminating once the C_L is within some small tolerance. Experience shows that one extra order of magnitude (6 and 7 for adjoint and finite difference modes respectively) easily achieve the target C_L to more digits than is typically acceptable for any objective function. For instance, 6 orders with a target C_L = 0.11 produced C_L = 0.10999996 in one example. Thus in finite difference mode, fixing the lift costs about half as much again as fixing Alpha (using 7 orders rather than the normal 6 orders).

The adjoint situation is different because some additional sensitivities must be estimated with respect to Alpha. SYN87-SB actually perturbs the target C_L by -0.005 and performs an additional flow solution prior to the normal flow solution. Combined with the extra order of convergence recommended (6 rather than 5) this represents roughly a doubling of computational cost (including the associated adjoint solution) unless, as is optional, the necessary derivatives are estimated only once at the beginning of the run or (also an option) read as input.

In practice, adjusting CDo so that the desired C_L is close to the L/D_{max} location allows D/L to be minimized effectively at fixed Alpha, and this is significantly cheaper.

Single-Block Design Approach (SYN87-SB), continued

Linear Constraints

With the incorporation of NPSOL, SYN87-SB provides for constraining various geometric quantities, and this is best done in *linear* form if possible, since nonlinear constraints (such as on fuel volume) require finite difference derivatives which can become expensive in the presence of many variables. (Geometric operations normally do not vectorize.) It turns out that both wing section thickness and body section radius can be constrained linearly, since the design variables are typically the linear (multiplier) coefficients associated with the shape functions. Since it is *perturbations* to the initial geometry that are being optimized, it is actually the *change* in T/C (say) that is constrained.

During its preliminary set-up of the linear constraint matrix, SYN87-SB determines the initial, unperturbed T/C (say, at the specified X/C), compares it with the specified bound (probably a lower bound only, with no upper bound necessary), and subtracts to give the linear constraint bound seen by NPSOL. It then evaluates all the relevant shape functions at the specified location (many probably 0.), and stores the results in AMAT(m,n) for each constraint m and each variable n, to use NPSOL notation.

A user-friendly option enables specification of the existing T/C as the lower bound without knowing what that T/C is. This is indicated by naming the constraint 'THK0' rather than 'THK'.

The upper or lower section ordinate (Y/C in Jameson flow solver notation) may be constrained similarly, using the linear constraint names 'YUP', 'YLO', or 'YUP0', 'YLO0' if the initial relative locations are to be preserved (as an indirect means of constraining curvature, perhaps).

Cabin radius constraints may be treated linearly if the fuselage camber is held fixed. For TCA-6, the cabin section constraint polygons are defined in terms of polar coordinates with origin at the cabin floor, which is different from the streamwise mean-line. However, essentially equivalent constraints can be derived by transforming the polar coordinates to have origin at the mean-line. This origin provides the natural radial direction for the peaks of a class of body section shape functions applied circumferentially:

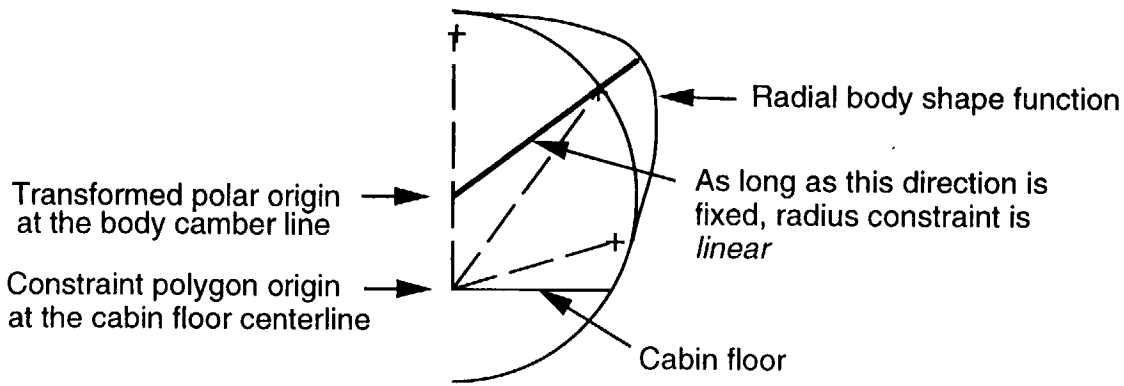

Single-Block Design Approach (SYN87-SB), continued

Nonlinear Constraints

SYN87-SB supports all of the geometric constraints specified for the TCA-6 optimization, although in practice not all of them needed to be invoked because they tended to be easily satisfied. While linear constraints actually help the optimization process, unnecessary use of nonlinear constraints is best avoided. They have the effect of making the objective function more nonlinear than it already is, and the finite difference derivatives required can add significantly to the computational cost. For instance, the TCA-6 fuel volume constraint derivative Jacobian elements take 180+ CPU seconds on the C90 in the presence of 103 wing design variables. Imposing the cabin radius constraints nonlinearly at many stations in the presence of 100+ body design variables, while an option, would have been much more costly than the option used in practice (described above, where the body camber line needs to be held fixed).

For the record, the nonlinear constraints implemented in SYN87-SB are:

- Wing fuel volume, defined by subvolumes between wing sections with specified X/C ranges
- Cabin section radius at specified polar angle with origin at cabin floor centerline, if body camber line is varying
- Cabin floor angles and changes in floor angles between cabin classes
- Wing section T/C (max)
- Wing section trailing edge angle
- Cabin floor/wing section clearance at specified X and section number *k*

The fuel volume calculation proved to be too crude with the trapezoidal rule applied to wing section areas. (It depended too much on the number of defining wing sections—anywhere from 14 to 40 in the Ames effort, with 40 eventually being settled on.) The numerical integration now used involves (in a sum over subvolumes) spline quadrature for the inboard and outboard wing subsection areas, linear lofting of a wing subsection halfway between, spline quadrature of the lofted subsection, and Simpson's rule applied spanwise to these areas:

$$\text{Volume} = \Sigma\, \delta V = \Sigma\, (A_{left} + 4\, A_{middle} + A_{right})\, \delta Z / 6$$

With 20 such subvolumes defined in the standard input, one fuel volume calculation takes 0.09 seconds on the C90, including the regularization of the defining wing sections needed to assist the lofting. (Derivatives of fuel volume necessarily include perturbing the geometry which also requires handling the possibility that the wing has dropped below the body. Hence the 180+ CPU seconds quoted above for 100+ variables is much more than ~100 * 0.09 seconds.)

A cabin section radius calculation involves linear interpolation of a (regularized) cabin section at the specified X and solution of a 2-space curve/curve intersection problem using parametric techniques with a Newton iteration.

Cabin floor angle constraints require cabin class constraint polygons as inputs (for 4 floor segments in the case of TCA-6). SYN87-SB expects this information at the end of the wing/body geometry input file. It is transmitted to the saved optimized geometry file.

Computing cabin floor/wing section clearance at the side-of-body is unnecessarily awkward—at a specified wing section suffices.

- **Nonlinear Constraints**
  - Finite Differencing for all Geometric Nonlinear Constraints
  - Wing Fuel Volume
  - Cabin Section Radius at Specified Polar Angle (Body Camber Varying)
  - Cabin Floor Angles & Δ Cabin Floor Angles
  - Wing Section T/C (max)
  - Wing Section Trailing Edge Included Angle
  - Wing Section/Cabin Floor Clearance
- **Design Variables**
  - Wing Planform (Span, Sweep, Taper, Dihedral, Twist)
  - Wing Section Hicks-Henne Shape Functions (Sine, Exp, LE, TE)
  - Wing Section Wagner Functions
  - Fuselage Camber
  - Fuselage Area Ruling (Fixed Section Shape)
  - Fuselage Section Shape
  - Cabin Floor Kink Point Locations

Single-Block Design Approach (SYN87-SB), continued

SYN87 Design Variables

SYN87-SB design variables are specified by name via a table in the standard input. The present scheme was generalized for bidirectional control of the body shape functions, and the lofting of the wing design variables has since been generalized similarly. This requires a primary variable name (for the streamwise direction) and a secondary variable name (for the transverse direction), with 4 further inputs for each direction. Application of the Hicks-Henne-type shape functions has been modularized in a form suited to evaluations at multiple X/Cs per call (which vectorize, as for perturbing wing sections) and to a single evaluation per call (as for constraints imposed at specific X/Cs).

Wing Design Variables

Planform-related choices include span, sweep, dihedral, taper ratio, and twist. **Wing section** perturbing variables include the Hicks-Henne "sine bump" functions in standard, reflected, and symmetric forms, and leading and trailing edge droops (either smoothly varying or as slats or flaps). The Wagner functions (an oscillatory family well-suited to airfoils) are provided as well. The thickness distribution may be preserved implicitly by applying any of these Y/C perturbations to both surfaces, thus varying camber only. Otherwise, the thickness may be allowed to vary (probably with explicit T/C constraints) by perturbing just one surface, or both surfaces independently.

The **spanwise** extent of the section perturbations may be constant over the specified geometry range ("width" exponent = 0., as appropriate for slats and flaps), but typically they are tapered off to 0. at one side of "center" or the other side or on both sides. The decay may be linear or nonlinear, with some overlap of the different variable influences possible. The original linear or polynomial lofting is indicated with LIN for the secondary variable name along with 3 *integer* inputs referring to left, "center", and right wing sections. SYN87-SB now automatically distinguishes between integer and reals in these 3 columns; decimal imputs are now assumed to refer to spanwise coordinates rather than wing section numbers, so the lofting need not start or end at a defining section

The option of Hicks-Henne-type functions for the spanwise lofting is too new to have been used during the TCA-6 optimization, but it is doubtful that they will help overcome the fundamental tendency towards spanwise waviness in optimized designs.

Body Design Variables

There are now 4 kinds of primary design variable for the body, plus X and Y locations of the cabin floor kink points. Any of the standard Hicks-Henne shape functions may be applied in the streamwise direction to the body **camber**, body **span**, body **radius**, or body **area**. For the first 3 of these, circumferential variation is applied parametrically (u = 0. and 1. at the keel and crown respectively) using the Hicks-Henne shape functions, including some new ones with preferred curvature at the crown or keel: COSL and COSR, or LCOS and RCOS (~ 1. - COSL, etc.).

The body section **area** variables preserve section shape, using an iterative procedure to achieve the specified streamwise area ruling. The fuselage volume may be conserved implicitly by a choice of 2 streamwise perturbations which add zero net cross-sectional area.

Single-Block Design Approach (SYN87-SB), continued

Automated PostScript Plotting of Surface Data

A small collection of PostScript utilities allows straightforward programming of surface data plots as routine outputs from SYN87-SB runs. Plotting at specified streamwise or chordwise stations—either at precise cuts or along grid lines—is provided. The cross-stream cuts show any cabin constraint polygons and the cabin floor if these are defined. Plots at constant X or Z are implemented as *contours* of Y and of Cp with respect to the parametric body and wing surfaces formed by the computational surface grid. Any target Cps are overlaid, and initial surface geometry and Cps may optionally be displayed with results from each design step. A carpet plot of the wing (grid) sections and the surface Cps is also generated (the most recent design iteration only).

- **Automated PostScript Plotting of Surface Data**
  - Sectional Cuts (Spanwise and/or Chordwise Geometry + Cps)
  - Plots Along Grid Lines (Spanwise and/or Chordwise)
  - Overlays (Initial Geometry & Cps and/or Target Cps)
  - Constraints (Cabin Radius Polygons and Cabin Floor)
  - Carpet Plots (Final Wing Surface Grid Sections + Cps)

Improvements to SYN87-SB since 7/96

Pseudo Nacelle Effects

Three main refinements have been made to the ghost nacelle approximation in SYN87-SB:

- Diverter area changes are accounted for during the optimization
- Force coefficients for the nacelle/diverters using the full-configuration surface Cps are updated during the optimization
- These forces are further broken down by component: exterior, interior, base, and diverter for each nacelle

By holding the input values of the original Cps constant on the nacelles and diverters (any changes to these Cps are accounted for by the Δ buoyancy terms), but allowing these geometries to change in area and orientation, it is possible to calculate the influence these changes have on the lift and drag estimated for these components. The original scheme did not make use of these full-configuration input surface Cps, although it did (and still does) account for buoyancy changes using the initial and current FLO87 flow fields.

The diverter leading edge and trailing edge heights are preserved by shifting the trailing edge and rotating about the new upper-edge trailing edge points (a line/surface intersection problem solved as for one point along the wing/body intersection line). The diverters are held *vertical* in the present scheme (no rolling). The diverter areas are adjusted by reinterpolating the upper edge coordinates bilinearly within the perturbed lower wing surface mesh.

The diverter edges are now defined in file `syn87.dvr` via *pointers* into the (unstructured) (x,y,z,Cp) data read from `syn87.pts`. The connectivity file `syn87.cnt` now contains a 4th column indicating component number 1 through 4 to enable the above-mentioned force breakdown.

An option has been provided, at the request of McDonnell Douglas, to invoke just the lower-surface ΔCps portion of the ghost nacelle approximation, but this has not been made use of at Ames.

Improvements to SYN87-SB Since 7/96

- **Pseudo Nacelle Effects (Old Method)**
  - Impose Δ Cps from Nacelles-On/Off Calculations (e.g., AIRPLANE) onto Wing/Body Lower Surface (Nacelle on Wing Effects)
  - Pitch/Translate Nacelle/Diverter Geometry To Preserve Diverter LE and TE Heights
  - Integrate Cps from FLO87 Solutions on the Initial & Shifted Nacelle Geometries to give Δ Nacelle Buoyancies (Wing on Nacelle Effects)

Improvements to SYN87-SB Since 7/96 (Continued)

- **Pseudo Nacelle Effects (New Method)**
  - Impose Δ Cps from Nacelles-On/Off Calculations (e.g., AIRPLANE) onto Wing/Body Lower Surface (Nacelle on Wing Effects)
  - Pitch/Translate Nacelle/Diverter Geometry To Preserve Diverter LE and TE Heights
  - Adjust Upper Edges of Diverters to Match Lower Wing
  - Integrate Cps from Original W/B/N/D Solution on the Modified Nacelle/Diverter Geometry (Nacelle Pitch & Diverter Growth Effects)
  - Integrate Cps from FLO87 Solutions on the Initial & Shifted Nacelle Geometries to give Δ Nacelle Buoyancies (Wing on Nacelle Effects)

Improvements to SYN87-SB since 7/96, continued

Fortified Body Design Capability

The body design enhancements implemented for the TCA-6 optimization are:

- Parametric circumferential blending of the streamwise perturbations
- Provision for constraining cabin floor angles and angle changes (and for treating the floor kink points as design variables)
- Treatment of cabin radius constraints in two forms, particularly the *linear* form if the body camber line is held fixed

An illustration of how body section radial perturbations permit the linear radius constraint option appears above under the **Linear Constraints** subheading of ***Single-Block Design Approach***.

Proper circumferential perturbation of body sections at the crown and keel prompted introduction of the COSL & COSR shape functions and the related pair LCOS & RCOS, which have the proper curvature at their end-points on [0, 1].

Radial and vertical body section perturbations (washed out to zero) have been added to the earlier body camber and body span design variables.

Generalized Lofting of Wing Section Perturbations

The bidirectional parametric scheme introduced for the body section perturbations has been applied to the lofting of wing section perturbations, although it has been realized that the spanwise variations should *not* be specified in normalized form (but rather in terms of defining section numbers, as originally supported, or in terms of arbitrary spanwise locations—not necessarily restricted to the defining stations). Generalization of the spanwise lofting from linear (or polynomial) to use of the Hicks-Henne functions is the most recent change to SYN87-SB; it came too late for the TCA optimization performed so far.

Improvements to SYN87-SB Since 7/96 (Continued)

- **Fortified Body Design Capability**
  - Area Ruling Design Variables (Fixed Section Shapes)
  - Section Shape Design Variables (Lofted Streamwise)
    - Vertical, Spanwise, & Radial Perturbations
    - Each Perturbation is Attenuated Circumferentially via Hicks-Henne Shape Functions, Including A Few New Ones
  - Cabin Floor Kink Point Locations may be Design Variables
  - Cabin Radius Constraints are **Linear** if Body Camber is Fixed
  - Nonlinear Constraints
    - Cabin Section Polygons (Body Camber Varying)
    - Cabin Floor Angles & Δ Cabin Floor Angles
    - Cabin Floor/Wing Spar Clearance
- **Generalized Lofting of Wing Section Perturbations**
  - Hicks-Henne Shape Function Lofting + Original Polynomial Lofting

Improvements to SYN87-SB Since 7/96 (Continued)

- **Grid Generation**
  - 3D Transfinite Interpolation for Initial Algebraic Volume Mesh
  - Addition of Sorenson Orthogonality to Thomas-Middlecoff Spacing in Elliptic Smoothing
  - Greater Spacing Control via 6 Sub-Blocks Rather Than 4
  - Automated Handling of Wing Above or Below the Crown/Keel Line to Protect the Wing/Body Intersection Calculation
  - Two-panel Wing Surface Grid Option Prevents Nacelle Shifts During Grid Perturbation if Wing Root Shifts Spanwise
- **Improved Input/Output**
  - Option to Read Grid + Flow Field Speeds Drag Polar Calculations
  - Nacelle/Diverter Lift/Drag Breakdown + Linear Constraint Details
  - PostScript Plots May Include Spanwise and Chordwise Surface Cuts + Overlays + Cabin Constraint Polygons

Improvements to SYN87-SB since 7/96, continued

Grid Generation

The most significant of the recent single-block grid enhancements is the introduction of orthogonality control at the boundaries, as this should improve the Euler and adjoint solutions and hence the adjoint-based gradients. Greater control over the off-surface spacing has also been provided with a switch from 4 sub-blocks to 6. The added artificial interior boundary is above and below the wing trailing edge. The other artificial boundaries are the ~vertical plane of the wing tip and the ~horizontal plane forward of the leading edge.

In the order of the steps in the (full) grid generation process, the recent changes are outlined as follows:

- The wing/body intersection calculation is protected through automated handling of a wing above or below the body. For instance, in case the inboard wing lower surface has dropped below the body, each point of each fuselage section inboard of some fraction (such as 0.6) of the maximum section width is checked against the interpolated lower wing surface. If the wing point Y is lower, then the fuselage point Y is replaced by the wing Y minus a margin such as 1" for the TCA. In this way, a "shelf" is constructed on the body geometry, without actually altering the external wing/body lines, apart from the slight safety margin added to assist the wing/body intersection calculation.

- The intersection calculation is also made somewhat more robust by an option to choose bilinear rather than bicubic interpolation for the body surface, and by proceeding from the leading edge aft for both upper and lower intersection lines rather than from trailing edge to trailing edge in the more convenient wrap-around order.

- Significant spanwise perturbations at the wing root can affect the pseudo nacelle scheme adversely, because the (costly) set-up phase is heavily grid-dependent. The work-around is to generate the wing surface grid in two panels, with an artificial boundary at a span location of, say, 125" for the TCA optimization. Outboard of this boundary, the wing surface grid lines are strictly planar and at fixed locations, so there is no effective spanwise shifting of the pseudo nacelle effects. This option has the added benefit of capturing the planform crank for the full chord rather than just at the leading edge.

- Grid spacing control has been improved with 3 pairs of leading edge & trailing edge inputs, for $K = K_{root}$, K_{tip}, and K_{max}. The new trailing edge control anticipates a Navier-Stokes option, and forced the move from 4 sub-blocks to 6 sub-blocks.

- New routine ELLIP2D provides both Thomas-Middlecoff spacing control and Sorenson-type orthogonality control for appropriate sub-block boundaries. (ELLIPQ3D has been implemented but is not quite as it should be yet.)

- New routines TFI2D, TFI3D, and TFIQ3D initialize the sub-block interiors, using transfinite interpolation with Soni-type optimal blending functions.

- New routine ELLIP3D smooths the sub-block interiors with full spacing and orthogonality control as for ELLIP2D.

For subsequent perturbed grids, WARPQ3D and WARP3D are applied to the various sub-block faces and interiors (very efficient).

Improvements to SYN87-SB Since 7/96 (Continued)

- **Fortified Body Design Capability**
  - Area Ruling Design Variables (Fixed Section Shapes)
  - Section Shape Design Variables (Lofted Streamwise)
    - Vertical, Spanwise, & Radial Perturbations
    - Each Perturbation is Attenuated Circumferentially via Hicks-Henne Shape Functions, Including A Few New Ones
  - Cabin Floor Kink Point Locations may be Design Variables
  - Cabin Radius Constraints are **Linear** if Body Camber is Fixed
  - Nonlinear Constraints
    - Cabin Section Polygons (Body Camber Varying)
    - Cabin Floor Angles & Δ Cabin Floor Angles
    - Cabin Floor/Wing Spar Clearance
- **Generalized Lofting of Wing Section Perturbations**
  - Hicks-Henne Shape Function Lofting + Original Polynomial Lofting

Improvements to SYN87-SB since 7/96, continued

Improved Input/Output

Various tabulations have been improved, particularly for the linear constraints (with any violations flagged in a more readable form than that provided by NPSOL, which constrains, for instance, wing section T/C *changes* rather than constraining T/C directly).

Other useful input/output changes:

- Reading a previously-saved grid is now an option. This facilitates drag polar calculations.
- Force coefficient contributions for the 4 components of each nacelle/diverter are now tabulated, both for the buoyancy corrections (from the FLO87 pressure fields) and for the input surface Cps read with the nacelle/diverter coordinates. The breakdown distinguishes the nacelle interiors, exteriors, bases, and diverters.
- Plotting of surface data at specified cuts is fully implemented for both constant X and constant Z (span station). Included are the nacelle interference pressure effects and (in the cross-stream plots) the locations of the diverters and of the cabin floor and the cabin radius constraint polygon. The geometry may also be scaled up to make perturbations from the overlaid results more visible.

Improvements to SYN87-SB since 7/96, continued

More Frequent Updates of Pseudo Nacelle Input Data

Updating of the pseudo nacelle data inputs to SYN87-SB has become a more routine procedure thanks to the 3-stage scheme developed specifically for perturbing AIRPLANE surface definitions. For previous design efforts, the surface line strings had to be prepared laboriously on the CAD system, but the perturbation scheme takes advantage of the initial definition for the baseline geometry by deriving a parametrically equivalent surface definition for a similar geometry. The CAD system must still supply a regular surface mesh for each new design, and for the baseline (e.g., 30 + 100 + 100 cuts of 200 points per upper/lower surface for the near-body, mid-wing, and supersonic panel of the TCA configurations), but these cuts are not labor-intensive for the CAD operator.

An outline of the 3-stage perturbation process follows:

- **Stage 1** – Parameterize the **baseline** surface definition (once only, for use by all perturbations):
  - * Obtain regular surface meshes from the CAD system (e.g. for 3 wing panels).
  - * Parameterize each sub-panel (e.g., upper and lower surface sub-panels for each of the 3 wing panels).
  - * Process the baseline AIRPLANE surface line strings one point at a time to determine parametric coordinates (u,v) for each (x,y,z). This requires minimizing a squared-distance function with respect to 2 variables u and v for each of the sub-panels involved, and choosing the solution corresponding to the smallest such squared distance. Results are saved in a form similar to the input line strings, but with an indication of which parametric sub-surface each (u,v) applies to. QNMDIF performs thousands of such 2-D minimizations in a very moderate time.
- **Stage 2** – For each application to a **perturbed design**:
  - * Obtain new regular surface meshes from the CAD system, and parameterize them.
  - * Interpolate a new (x,y,z) for each of the baseline (u,v)s via bilinear interpolation within the appropriate sub-panels.
- **Stage 3** – Ensure **exact matching** of the (x,y,z) coordinates at all boundaries where line strings may meet:
  - * For each AIRPLANE panel processed, copies of line strings along boundaries are concatenated as a list of target (x,y,z)s, then all points of all line strings are (potentially) compared for closeness to all points in the target list. Any point found to be within a small distance of a target edge point is replaced with that edge point. Once such a substitution is made, the searching can be terminated for that point. The process goes very quickly even if though it sounds slow.

The perturbation scheme required a refinement for the same reason as indicated above for the single-block wing surface grid—to overcome unintended spanwise shifts in the nacelle/diverter locations caused by changes at the wing root, particularly if the fuselage diameter has been modified. Hence an artificial boundary was introduced (at span station 125" for the TCA designs), and the perturbation procedure now absorbs all wing-root changes in the resulting near-body panel.

Improvements to SYN87-SB Since 7/96 (Continued)

- **More Frequent Updates of Pseudo Nacelle Input Data via Routine Application of AIRPLANE Wing Surface Perturbation Procedures**
  - AIRPLANE Surface Definition Time Reduced from 3 Weeks to 3 Days
  - Stage 1: Done Once for Baseline AIRPLANE Surface Definition
    * Obtain Regular Surface Mesh Cuts from CAD
    * Parameterize Baseline Geometry
    * For Each AIRPLANE Surface (x,y,z) Calculate Parametric Coordinates (u,v) via 2-D Minimization
  - Stage 2: For Each New Optimized Design
    * Obtain New Regular Surface Mesh from CAD & Parameterize
    * Interpolate New (x,y,z)s at Baseline (u,v)s from Stage 1
  - Stage 3: Ensure Exact (x,y,z) Matching at All Boundaries
  - TCA Optimization Made Use of 5 Sets of Nacelle Data (4 Updates)

SYN87-SB Gradient Comparisons (Adjoint vs. Finite Differences)

Figure 1 shows a **no-nacelles** comparison of gradients calculated by forward differencing and by the adjoint method. The geometry is the **baseline TCA-6**, the objective function is C_D/C_L **at fixed Alpha**, and the variables are two rows of 10 SIN bumps focused at the wing sections 10 and 18 (of 40) nearest to the diverters. Linear lofting to zero perturbation occurs at section numbers 5 & 15 and 14 & 24. The variables perturb both upper and lower surfaces in unison (**camber** changes). All shape functions have 3.5 exponents.

The flow and adjoint solvers were converged 6 & 3 orders for the adjoint method, while 7 orders for the flow solver were specified for the finite difference calculations, with two choices of differencing step confirming accuracy in Figure 1. In practice, these convergence criteria might be safely relaxed to 5 & 2-2.5 orders (adjoint) and 6 orders (finite difference), although for the case of minimizing drag at fixed *lift* the tighter tolerances are recommended because the iteration on Alpha terminates with the specified reduction in average residual (only) rather than guaranteeing that the target lift has indeed been achieved as well.

Figures 2 and **3** show gradient comparisons **before** and **after** the most recent corrections involving proper blanking of the diverter areas. The details are as for Figure 1 except that the pseudo nacelle effects are included.

Figures 4 through **6** are representative of extensive **re**testing of the adjoint-based gradients at supersonic speeds following the recent corrections to the pseudo nacelle case. The bulk of the 3-dozen-plus comparisons made involved the Ames 12-31 configuration which is close to the final Ames 01-03 design and therefore considerably closer to a design optimum than the baseline, meaning the gradient elements are expected to be smaller and therefore harder to compute accurately. *Note that all plots have the same vertical scale so that small discrepancies in the gradients are not exaggerated when the gradients themselves are small.*

The perturbing functions are 17 of the SIN2 bumps (symmetric about X/C = 0.5) with exponents 7, at X/C = 0.05 - 0.95 by 0.05, centered on wing section 9 and lofted linearly to zero at sections 5 and 13. They are near the inboard nacelle.

Figure 4 applies to perturbing **camber**, while **Figure 5** differs only in that the shape functions are applied to the **lower surface**.

Figure 6 shows the case of minimizing **drag at fixed lift** for three geometries: the **baseline**, an intermediate **Ames 11-04** stage, and the near-final **Ames 12-31** stage. The perturbing functions are as for Figure 4 (applied to **camber**).

Conclusions:

- The no-nacelle case gradient comparison is extremely good (Figure 1).
- The comparable pseudo nacelle case is now almost as good for the *baseline* geometry (Figure 3).
- The *fixed-lift* situation is now comparable to the fixed Alpha situation (Figure 6).
- As the design approaches an optimum, the adjoint gradients near the nacelles may show moderate discrepancies for some shape functions applied near the nacelles (Figures 4 and 6, showing camber cases) but may agree very well for other cases (Figure 5, showing lower surface, and other cases not shown involving other shape functions).
- Improving the adjoint-based/pseudo-nacelle-case gradients further will be difficult but may still be warranted.

Gradient Comparisons

- **Adjoint-Based Gradients in the Presence of Pseudo Nacelles Generally Agree Well With Finite Differencing**
  - Problems With Blanking of Lower Wing Diverter Areas Have Been Corrected
  - W/B/N/D Comparisons Are Still Not Quite as Clean as Wing/Body
  - Near a Design Optimum, Gradient Discrepancies may be Relatively Larger or Differ in Sign, but Are No More Significant Because the Magnitudes are Small (Not Much Room for the Optimizer to Move Either Way)

SYN87-SB Gradient Comparisons (Adjoint vs. Finite Differences, continued)

Figure 1 shows a **no-nacelles/fixed Alpha** comparison of gradients calculated by forward differencing and by the adjoint method. The geometry is the **baseline TCA-6**, and the variables perturb **camber**. Further details appear above. Clearly, the comparison is excellent.

SYN87-SB Gradient Comparison

L/D Objective for fixed Alpha = 3.6 deg.; 2 x 10 sine bumps modifying camber

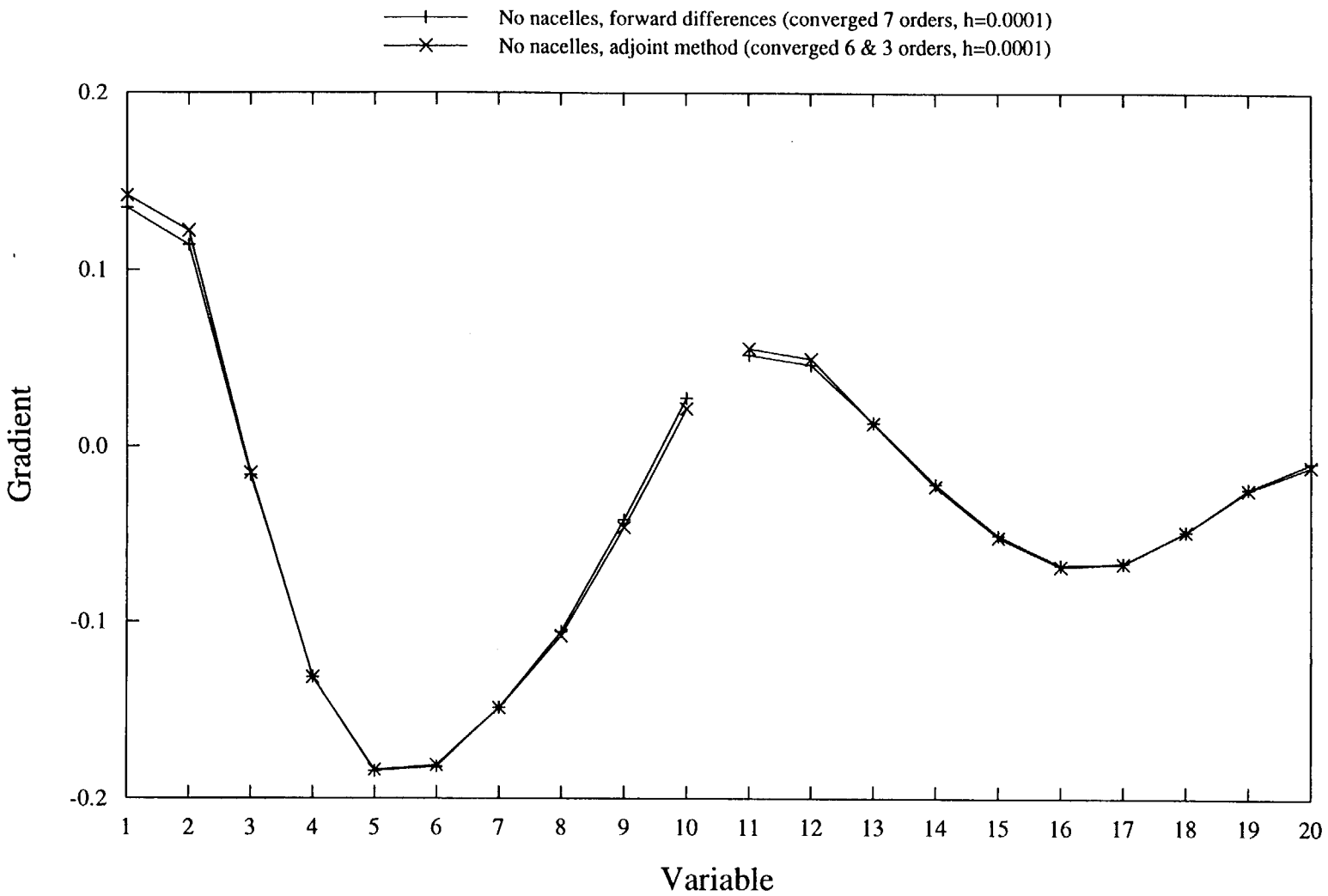

TCA-6 HSCT, Wing/Body, Mach = 2.4

11/21/96

SYN87-SB Gradient Comparisons (Adjoint vs. Finite Differences, continued)

Figures 2 and 3 show pseudo-nacelle-case gradient comparisons **before** and **after** the most recent corrections involving proper blanking of the diverter areas. Figure 2 includes *two* cases of forward differencing with different intervals, promoting confidence in those estimates. (Earlier testing has included central differencing as well, with similar agreement, but the cost becomes prohibitive.)

Figure 3 shows how the earlier gradient discrepancies in the nacelle regions (aft portions of the chord for each group of 10 variables) have largely been eliminated for this test case.

Note that even though the same design variables were employed in Figure 1 as in Figures 2 and 3, there are dramatic differences in the character of the gradients due to the pseudo nacelle effects. This is in direct contrast to the results observed during the Reference H optimization. The current level of differences for TCA-6 is attributed to the significantly larger nacelles compared with Ref-H. This large difference exposed errors in the gradient calculations for the pseudo nacelle case which had gone undetected earlier.

SYN87-SB Gradient Comparison

L/D Objective for fixed Alpha = 3.6 deg.; 2 x 10 sine bumps modifying camber

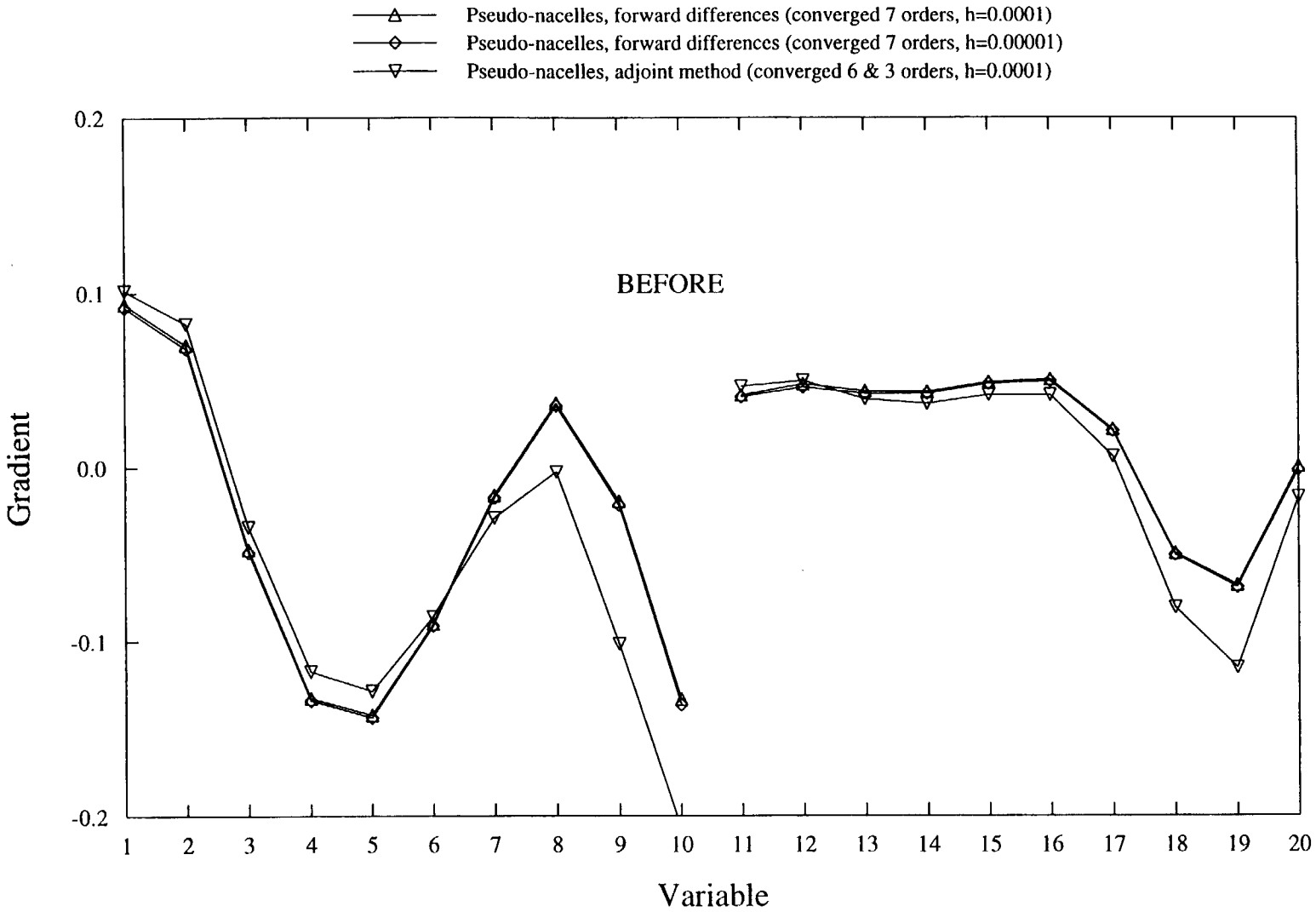

TCA-6 HSCT, W/B/N/D, Mach = 2.4

10/24/96

SYN87-SB Gradient Comparison

L/D Objective for fixed Alpha = 3.6 deg.; 2 x 10 sine bumps modifying camber

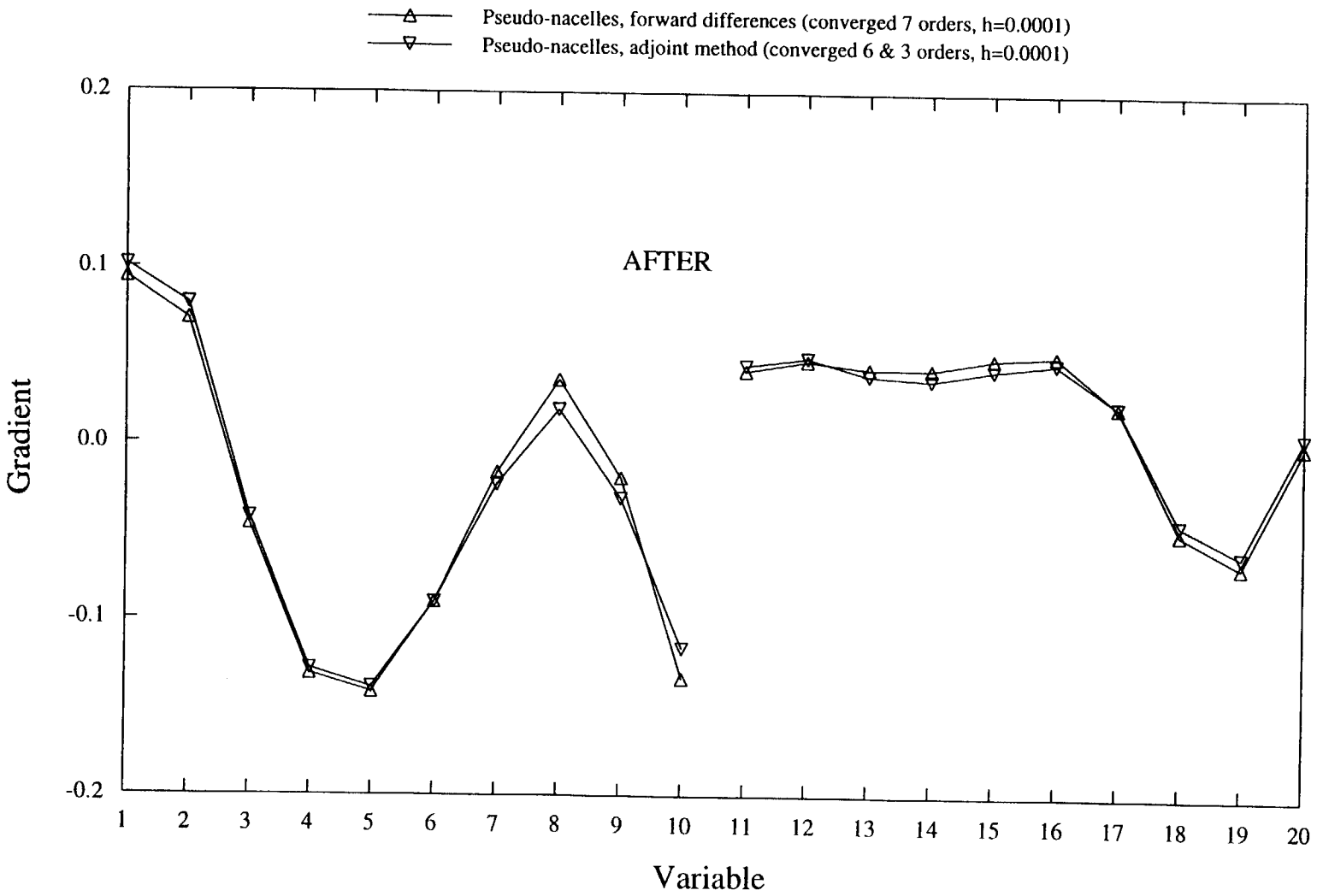

TCA-6 HSCT, W/B/N/D, Mach = 2.4

11/21/96

SYN87-SB Gradient Comparisons (Adjoint vs. Finite Differences, continued)

Figure 4 shows how, for **a design nearer to an optimum**, some discrepancies in the nacelle region may still appear when the gradients are close to zero. This is for the **camber** case. The fact that the two methods are on opposite sides of zero in this case (and in other comparisons) means that optimizer search directions will be quite different. However, it should be kept in mind that there is apparently not much room to move (with these design variables) in either direction.

Figure 5 (**lower surface**, but otherwise the same as for Figure 4) shows better agreement in the nacelle region, possibly because these gradient elements are not as small.

SYN87-SB Gradient Comparison

D/L Minimization at Fixed Alpha; 17 SIN2 bumps at K = 9 modifying camber; exponents 7

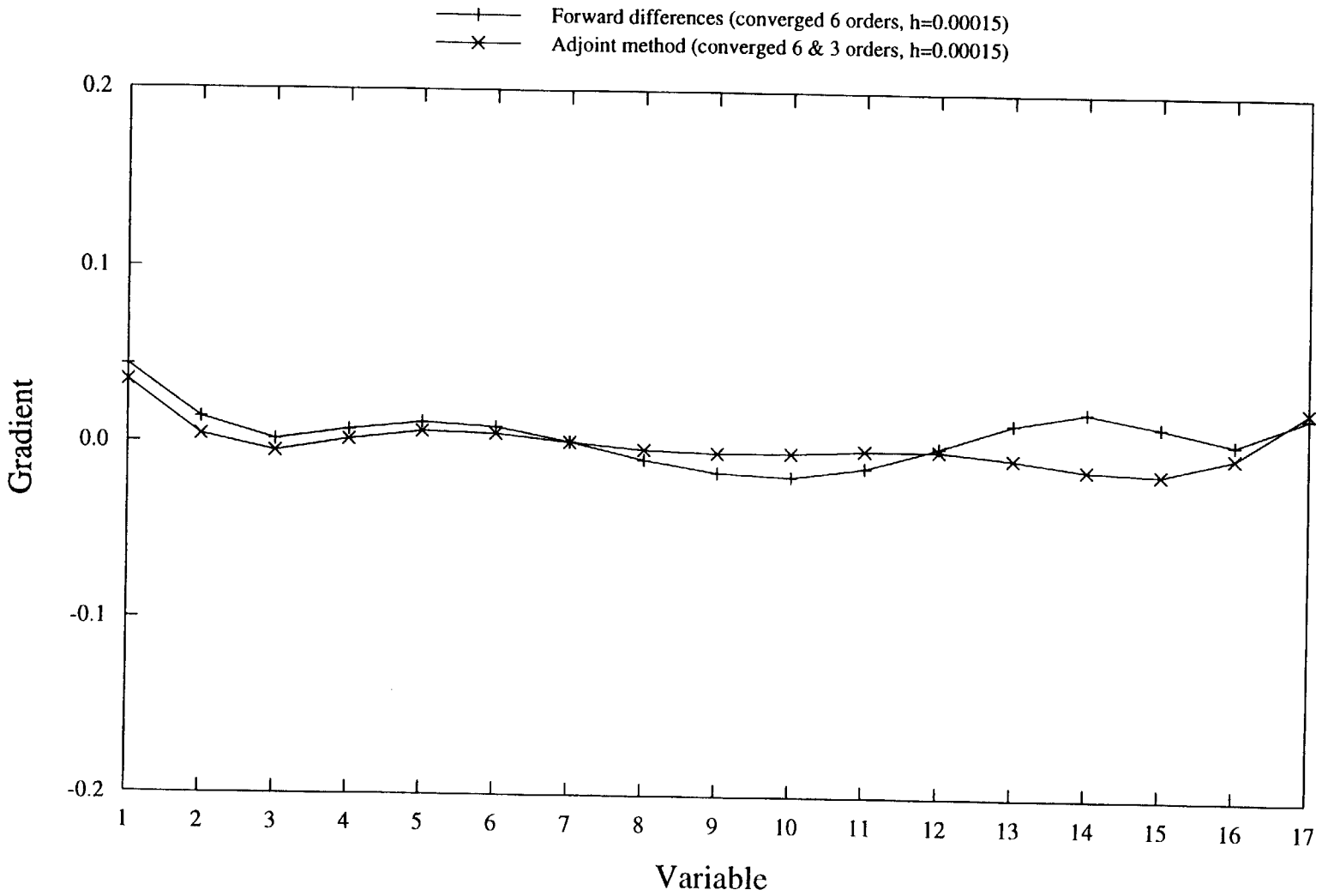

Ames 12-31, W/B/N/D, Mach = 2.4

01/31/97

SYN87-SB Gradient Comparisons (Adjoint vs. Finite Differences, continued)

Figure 5 (**lower surface**, but otherwise the same as for Figure 4) shows better agreement in the nacelle region, possibly because these gradient elements are not as small.

SYN87-SB Gradient Comparison

D/L Minimization at Fixed Alpha; 17 SIN2 bumps at K = 9 modifying Lower Surface; exponents 7

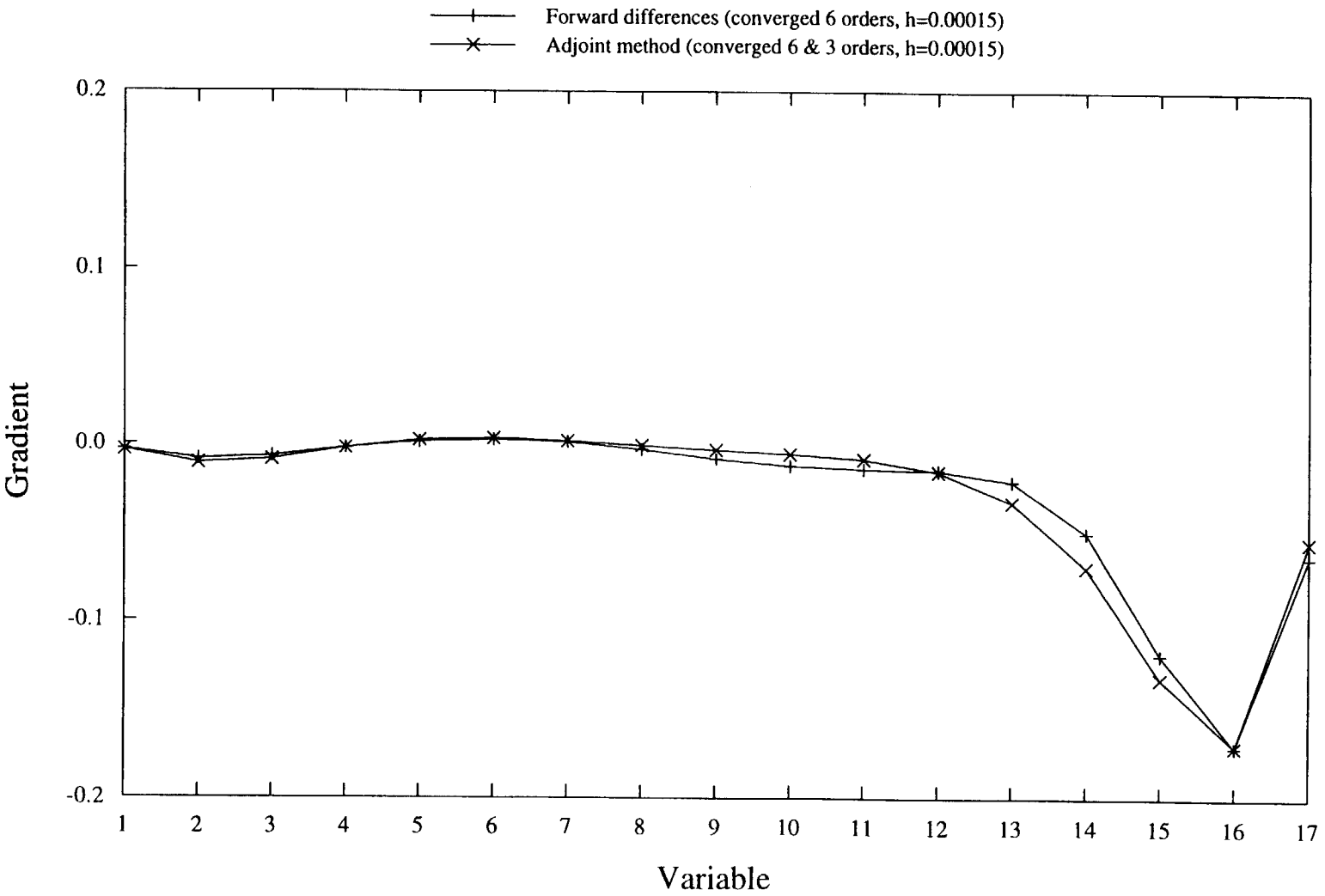

Ames 12-31, W/B/N/D, Mach = 2.4

01/31/97

SYN87-SB Gradient Comparisons (Adjoint vs. Finite Differences, continued)

Figure 6 is for the **fixed lift** case, showing three configurations far from, part-way-towards, and near to the final Ames design. As for the fixed Alpha situation, the moderate discrepancies are in the nacelle region and they increase somewhat as those gradient elements decrease in magnitude with the geometry.

SYN87-SB Gradient Comparison

Drag Minimization at Fixed Lift; 17 SIN2 Bumps Modifying Camber

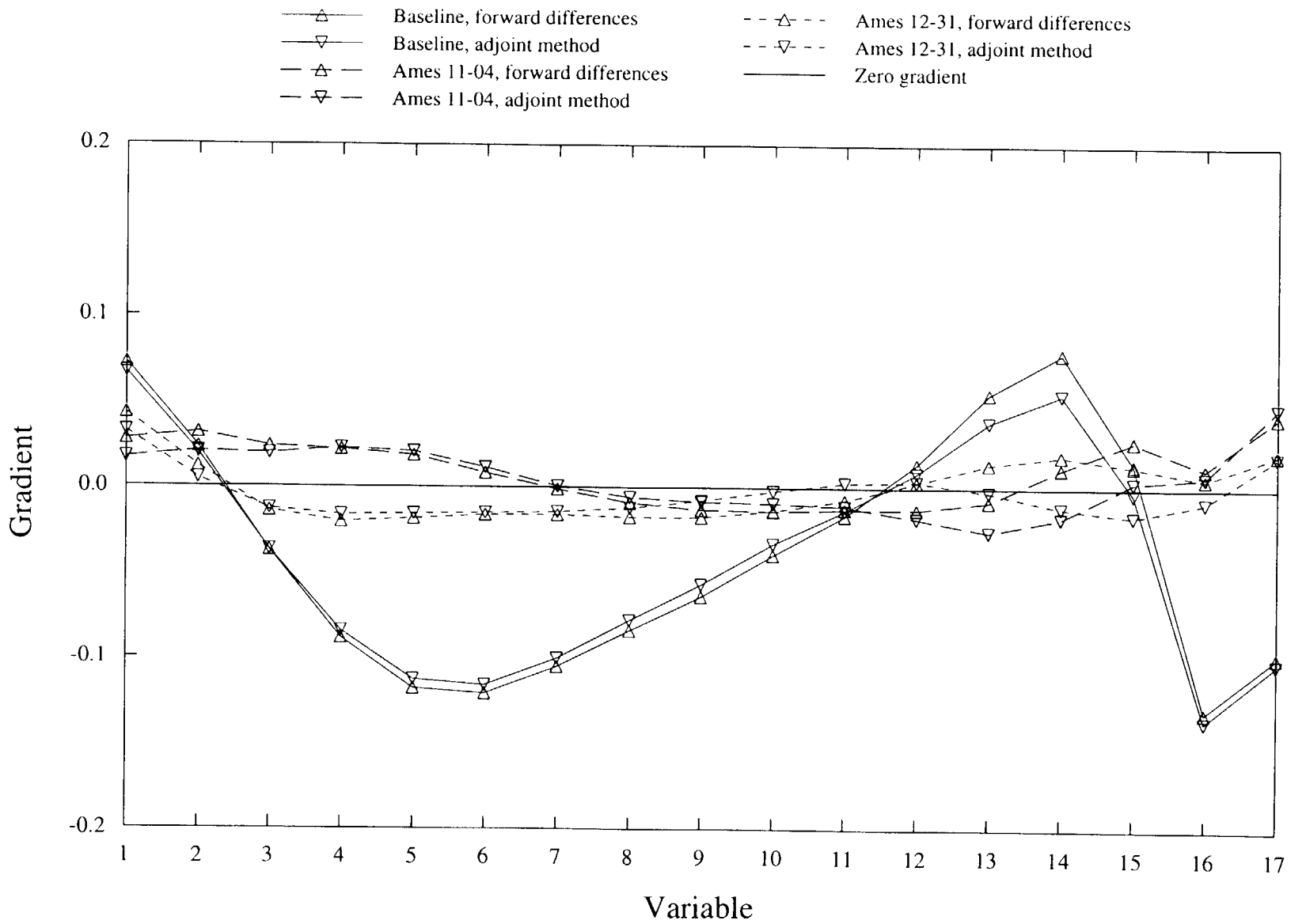

W/B/N/D Cases, 6 & 3 Orders Convergence, 0.00015 Differencing Intervals, Mach = 2.4 02/22/97

Further SYN87-SB Developments

Better Design Variables?

The TCA optimization was hampered by the fact that the lofting of the wing section design variables inherently follows the wing sweep, whereas in order to take full advantage of the nacelle/diverter shocks, the design perturbations should follow the different sweep of those shocks.

Grouping more defining sections near the nacelles could have helped to some extent, but only if the computational grid included comparable bunching, which it does not at present. A larger spanwise grid dimension would almost certainly be necessary to achieve the bunching that is desirable in the nacelle region.

More fundamentally, some different type of design variable and/or lofting not tied to wing sweep should be introduced. The subject of alternative design variables is discussed further below under the CAD Integration subheading.

Multipoint Design Capability?

Multipoint design has already been demonstrated with the multiblock code SYN87-MB. Incorporating it in SYN87-SB for HSCT applications would be less trivial because of the pseudo nacelle approximation, which is presently tied to a single Mach and Alpha and would be cumbersome to replicate for a second flight condition. Moreover, the approximation is valid only at supersonic speeds. Thus, including a transonic condition may lead to settling for wing/body-only solutions. A decision needs to be made on whether multipoint capability for SYN87-SB is worth its limited applicability.

C-O Grid Version

A mid-1996 version of SYN87-SB was adapted to improve the grid resolution of the fuselage—inherently the worst feature of the standard C-H topology. This C-O version should be brought up to date with the current C-H version. Reworking the pseudo nacelle effects (not attempted at all yet for the new topology) would be the most time-consuming aspect of this work, because the implementation is heavily grid-specific.

Further Adjoint-Based Gradient Studies

Refining the adjoint-based gradient calculations will continue to be a desirable background activity. Given the occasional anomalies revealed by the above comparisons, efforts should be made to retest the two alternative sets of more elaborate flux discretization routines in the adjoint solver which are currently present but not active in the production code.

Multitasking

In view of the preference given to jobs in the "mtask" queue on the C90s at Ames, an effort was made in October/November 1996 to make use of Cray's autotasking capability to allow multiple CPUs to work in parallel on the same job without performing major surgery on the code. However, results at that time were extremely disappointing.

Initial indications were promising: of the two dozen routines using more than 0.1% of the test run time, only one was found not to parallelize with the autotask compiler switch. Introduction of ten 2-D arrays in place of ten vectors soon achieved the desired parallelization in subroutine EFLUX.

Unfortunately, this was only the beginning of a tedious chore isolating some routines which were evidently being parallelized incorrectly, since the flow solver diverged quickly and (once that was apparently overcome) the adjoint solver crashed immediately. Eventually, subroutine STEP and all of the multigrid-related routines were eliminated as culprits, but the measure of parallelism was a dismal 2.15 equivalent CPUs when 8 were requested. Reworking STEP somewhat (10.7% of the reference single-CPU time) achieved apparent correctness and raised the measure to 2.51 out of 8, while 4 CPUs gave a measure of 2.23.

More unfortunately still, a longer run showed that this parallelized version would not converge beyond 4.86 orders in average residual. The effort was abandoned at this point, but it leaves a disturbing mystery which ought to be explained some day.

Related Aside: Inlining Low-Level Routines

The autotasking results above include the outcome of another related and similarly unrewarding effort prompted by the same flowtrace reports: that of inlining selected routines to eliminate the overhead of many calls. (A finite difference gradient comparison run, for instance, showed more than 30 million calls to several small utilities used by the 1-D and 2-D local spline routines.)

Applying the inline option to a compile of the `numutil.f` collection of general-purpose numerical utilities produced an object file 3 times larger, with a great deal of inlining performed, yet the resulting execution time (single CPU) actually *in*creased somewhat.

Ultimately, a very modest improvement was accomplished by *explicit* inlining of a 2x2 LUSOLVE call in the BILINT portion of the RIPPLE2D search utility. Even this change was time-consuming and error-prone. There are many instances of the 3-point derivative utilities responsible for the above 30+ million calls—so many that explicitly inlining them would be onerous. Thus this approach to improving efficiency is not likely to be pursued. But the present poor performance of the compiler at automating the inlining may improve some day.

Further SYN87-SB Developments, continued

Improved Geometry Integration With CAD Systems

This subject touches on the alternative design variable issue. It has long seemed clear that, since CAD is standardizing on NURBS curves and surfaces, these should constitute the natural entities to be treated by the design-by-optimization tools. Past efforts at Ames have demonstrated that the control point coordinates of B-spline curve representations of wing sections can serve as design variables.The minimal integration of B-spline curves with the flow solvers still involved discretizing the B-spline curves for compatibility with the built-in grid generation, and development of a number of airfoil-related B-spline utilities (such as one for locating the parametric variable associated with the precise leading edge—a 1-D minimization problem).

Other 2-D studies have indicated that B-spline control points are not necessarily ideal as design variables. Specifically, whereas the Hicks-Henne or Wagner shape function perturbations tend to preserve smooth airfoil-like shapes throughout the optimization, this can very easily not be true in the B-spline case. Indeed, with the substantial number of control points needed to match typical discrete airfoil definitions adequately, high frequency irregularities in the intermediate geometries are evidently inevitable, just as they are in the extreme case of working with all the discretized points as variables.

While some form of implicit smoothing may counter this phenomenon, such smoothing remains an inexact science, and the (still unfamiliar) move from B-spline curves to NURBS surfaces appears destined to be plagued by even greater waviness problems than present techniques encounter. Perhaps *constrained* optimization provides the answer, although if the constraints are many, and nonlinear (as in the case of local curvature) they become prohibitive—they must be linear or linearizable.

Nonetheless, the attraction of employing the same geometric entities as the CAD systems remains, so this aspect of aerodynamic design by optimization represents an important topic for further creative research.

Future SYN87-SB Developments

- Wing Sweep-wise Lofting of Perturbations is Inconsistent with Diverter Shock Sweep — Better Design Variables are Needed
- Multipoint Design Capability
- C-O Grid Version Needs to be Brought up to Date with C-H Version
- Further Studies of Adjoint-Based Gradients vs. Finite Differencing are Needed
- Autotasking Efforts Should be Pursued (Inadequate Parallelization Achieved so far on C90, and Convergence Stalls Out)
- Geometry I/O Should be Better Integrated with CAD (NURBS Curves)

Ames Optimized TCA Configuration

Susan E. Cliff, NASA Ames Research Center

James J. Reuther, RIACS

Raymond M. Hicks, MCAT

February 25-27, 1997

Team Effort

The design of the Ames 1-03 was a difficult task. The numerous constraints imposed on the design required tremendous efforts by many individuals at Ames. This figure acknowledges the individuals and the tasks that they performed. Although the three authors were responsible for the design effort it was the team effort of all individuals that made the overall activity a success.

Team Effort

Wing Design:	**Susan Cliff** **Ray Hicks** **Rob Kennelly**
Fuselage Design:	**James Reuther** **Mark Rimlinger**
Software Support:	**James Reuther** **David Saunders** **Scott Thomas**
AIRPLANE Computations:	**Susan Cliff** **Alex Te** **David Saunders** **Tim Baker**
SYN87-MB Computations:	**James Reuther** **Mark Rimlinger**
UPS Computations:	**Scott Lawrence**
OVERFLOW Computations:	**Goetz Klopfer** **David Baker**

Design Approach

Configuration design at Ames was carried out with the SYN87-SB (single block) Euler code using a 193 x 49 x 65 C-H grid. The Euler solver is coupled to the constrained (NPSOL) and the unconstrained (QNMDIF) optimization packages. Since the single block grid is able to model only wing-body configurations, the nacelle/diverter effects were included in the optimization process by SYN87's option to superimpose the nacelle/diverter interference pressures on the wing. These interference pressures were calculated using the AIRPLANE code. AIRPLANE is an Euler solver that uses a unstructured tetrahedral mesh and is capable of computations about arbitrary complete configurations. In addition, the buoyancy effects of the nacelle/diverters were also included in the design process by imposing the pressure field obtained during the design process onto the triangulated surfaces of the nacelle/diverter mesh generated by AIRPLANE. The interference pressures and nacelle buoyancy effects are added to the final forces after each flow field calculation. Full details of the (recently enhanced) ghost nacelle capability are given in a related talk.

The pseudo nacelle corrections were greatly improved during this design cycle. During the Ref H and Cycle 1 design activities, the nacelles were only translated and pitched. In the cycle 2 design effort the nacelles can translate vertically, and pitch to accommodate the changes in the lower surface geometry. The diverter heights (between their leading and trailing edges) were modified during design as the shape of the lower wing changed, with the drag of the diverter changing accordingly.

Both adjoint and finite difference gradients were used during optimization. The adjoint-based gradients were found to give good direction in the design space for configurations near the starting point, but as the design approached a minimum, the finite difference gradients were found to be more accurate. Use of finite difference gradients was limited by the CPU time limit available on the Cray machines. A typical optimization run using finite difference gradients can use only 30 to 40 design variables and one optimization iteration within the 8 hour queue limit for the chosen grid size and convergence level. The efficiency afforded by the adjoint method allowed for 50-120 design variables and 5-10 optimization iterations in the 8 hour queue.

Geometric perturbations to the wing and fuselage were made using the Hicks/Henne (HH) shape functions. The HH functions were distributed uniformly along the chords of the wing defining sections and lofted linearly. During single-surface design, constraints on thickness and volume at selected wing stations were imposed. Both fuselage camber and cross-sectional area distributions were permitted to change during design. The major disadvantage to the use of these function is the inherent surface waviness produced by repeated use of such functions. Many smoothing operations were required following optimization runs to produce a configuration with reasonable smoothness. Wagner functions were also used on the wing sections but were never used on the fuselage. The Wagner functions are a family of increasingly oscillatory functions that have also been used extensively in airfoil design . The leading and trailing edge regions of the wing were designed by use of polynomial and monomial functions respectively. Twist was attempted but was abandoned because of little performance improvement available from changing the baseline twist.

Design Approach

Optimization:

- SYN87-SB (Euler, single block) + NPSOL/QNMDIF
- Wing/body + AIRPLANE nacelle/diverter effects
- Improved pseudo nacelle corrections
- Adjoint and finite difference gradients

Wing Design:

- Apply Hicks-Henne and Wagner shape functions to wing defining sections
- Camber and thickness modifications only
- Periodic implicit / explicit spanwise smoothing

Fuselage Design:

- Includes convex pressure vessel created by analytic reconstruction to meet constraints
- Camber and area distribution modifications using Hicks-Henne shape functions
- Periodic explicit smoothing in circumferencial direction

Analysis Methods

Intermediate and final analyses were carried out by use of both Euler and Navier-Stokes codes. The Euler codes used were AIRPLANE and SYN87-MB (multi-block). AIRPLANE uses an unstructured tetrahedral mesh while SYN87-MB uses structured grid blocks. The two codes were found to give similar results but AIRPLANE has an extensive history of giving good prediction of design increments and therefore was the main validation code used to check new configurations.

AIRPLANE and SYN87-MB can be run on parallel platforms, and both utilize MPI (Message Passing Interface) which makes them very portable. AIRPLANE has been shown to have linear speed up as the number of processors is increased. The SYN87-MB has nearly linear speed up, and its multi-grid option further increases the computational efficiency of the code.

The Navier-Stokes analyses were performed by OVERFLOW and UPS. OVERFLOW was used to analyze the wing/body/nacelle/diverter configurations while UPS was restricted to wing/body configurations. The UPS code was used last year to validate the Ames 704 design and was found to be fairly accurate. OVERFLOW has little HSR history, but has been compared with experimental data for the baseline TCA. Navier-Stokes solutions are sensitive to grid topology and density and to turbulence model, giving some concern for the accuracy of the predicted aerodynamic performance for arbitrary configurations. The time required to obtain Navier-Stokes solutions (especially for the grid generation) is considerably longer than that for Euler solutions. Therefore, Euler solutions were relied upon to validate intermediate configurations more often than Navier-Stokes solutions.

Analysis Methods

AIRPLANE:

- Euler - unstructured tetrahedral mesh - MPI on IBM SP2
- Extensive validations on HSR configurations
- 4-5 day lead time for similar configurations
- Provides pressures for psuedo nacelle effects + validation of intermediate TCA designs with nacelles/diverters

SYN87-MB:

- Euler - structured mesh - multigrid - MPI on IBM SP2
- Validated by comparison with AIRPLANE on TCA designs
- 1-2 day lead time for similar configurations
- Provides validation of intermediate TCA designs with nacelles/diverters

UPS:

- Navier-Stokes - marching scheme
- Validated on HSR configurations
- 1-2 day lead time for similar configurations
- Provides wing-body viscous validation

OVERFLOW:

- Navier-Stokes - overset grids - Cray multitasking
- Validated for TCA Baseline
- 2-3 week lead time for similar configurations
- Provides validation of final design with nacelles/diverters

Optimization Summary

The shape functions used during the TCA optimization are listed below in descending order of frequency. The range and typical values of chordwise placement and width exponent are shown when appropriate.

Function	Chordwise location	Width exponent range	typical Width value
SIN	.10 to .90	2 to 8	5
SIN1	.10 to .90	5 to 7	5
SIN2	.10 to .90	2 to 8	5
EXP	.04 to .08	4 to 6	6
TRL	----------	4 to 5	5
LED	----------	4 to 7	5
WAG	----------	--------	1 - 5
SINF	.10 to .90	6	6

Forty wing defining stations were used throughout the optimization process. These stations did not change during the design process. The shape functions were lofted linearly over 6 to 10 stations or approximately 20% of the span.

The flow solutions were converged 6 orders and the adjoint solutions were converged 3.5 orders. These levels of convergence were thought to improve the gradient calculations.

Inboard wing panel optimization was performed more frequently than complete wing or outboard panel. Very little performance improvements could be attained from the supersonic outboard panel.

The number of design variables ranged from 40 to 130 for adjoint mode and 30 to 40 for finite difference mode.

Optimization Summary

- 40 wing defining sections, shape functions lofted over 6 to 10 stations (~20% span).
- Shape functions used and exponent range: SIN (2-8), SIN1(5-7), SIN2(1-5), SINF(6), EXP(4-6), TRL (4-5), LED (4-7), WAG(1-5).
- Chordwise bumps maximum t/c location varied from 0.04 to 0.9 chord, spaced 0.05 chord apart.
- Convergence levels: flow solver 6 orders, adjoint solver 3.5 orders.
- Number of design variables: adjoint (40-130), finite difference (30-40).

Shape functions

This figure shows all of the shape functions that were used to modify the wing camber and thickness during optimization of the Ames 1-03 configuration, with the exception of simple monomials used to camber the leading and trailing edges. The sine function is what has recently been referred to as a Hicks-Henne function. The sin1 and sin2 are forms of the sine function that are symmetric about the mid chord. The sin1 function is identical to the first half of the sine function, while the sin2 function is identical to the aft portion of the sine function. The sinf function is a "flipped" sine function, where the original sine function is flipped about the mid chord. The most common exponent applied during design are shown in the figure. The exponent determines the width of the shape function.

The exponential function is used solely to modify the leading edge radius of wing defining sections. The Wagner function are generalized sine functions. The Wagner functions with values of 1 to 5 shown in the figure were used during optimization. Larger values were not used because they tend to introduce curvature problems at the leading and trailing edges. These functions offer a very different design variable to the design space which is what is often needed to continue making performance improvements.

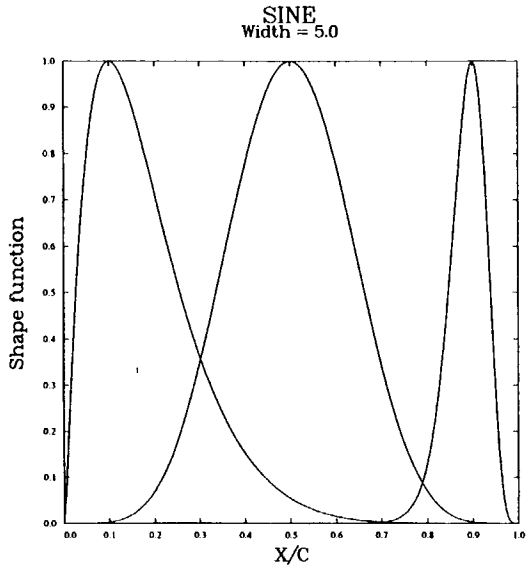
SINE
Width = 5.0
Shape function
X/C

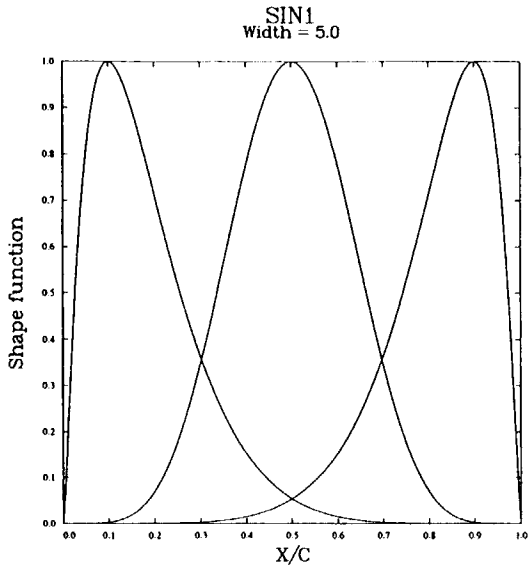
SIN1
Width = 5.0
Shape function
X/C

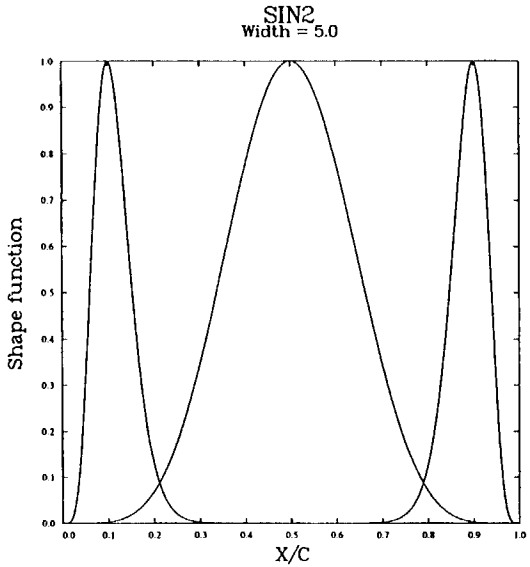
SIN2
Width = 5.0
Shape function
X/C

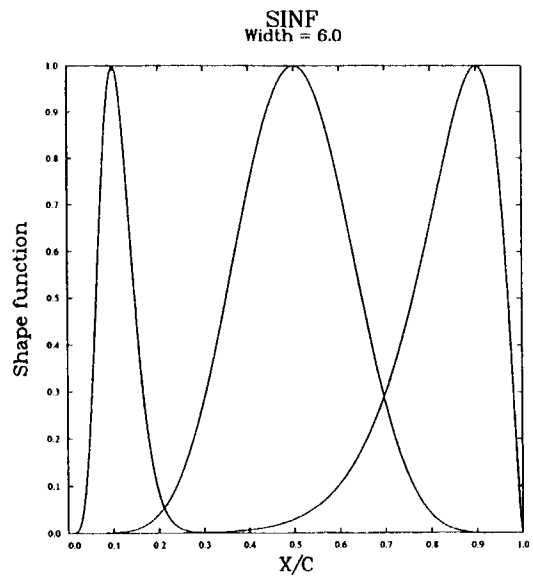
SINF
Width = 6.0
Shape function
X/C

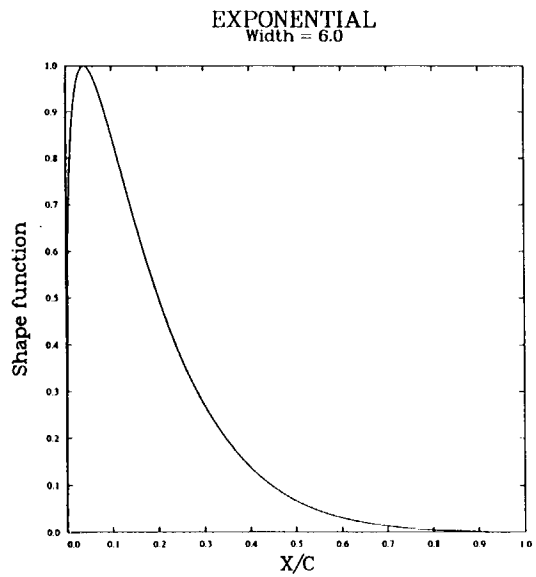
EXPONENTIAL
Width = 6.0
Shape function
X/C

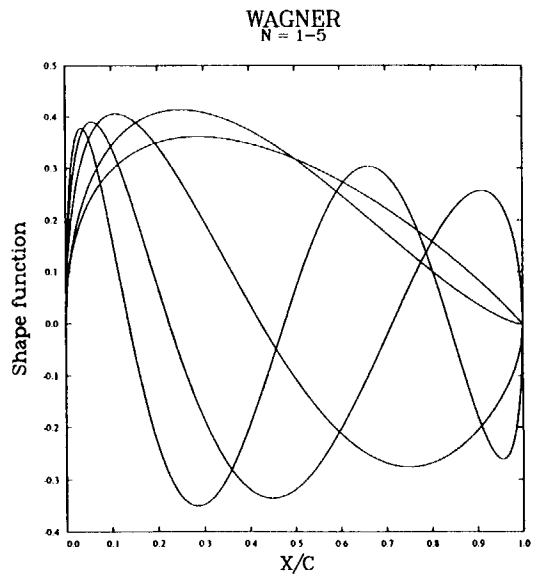
WAGNER
N = 1-5
Shape function
X/C

Wing Defining Stations in SYN87-SB

The 40 wing defining stations are shown in this figure. It should be noted that these stations do not correspond to the computational grid. The airfoil sections are not uniformly distributed from root to tip. Some additional clustering of defining stations near the nacelle/diverters might improve the integration of those components into the wing lower surface provided the number of stations do not exceed the number in the computational grid. Note the attempt to capture the planform break by including an additional defining station just outboard from the break. It was not possible to place the wing defining stations at the computational stations since the grid lines were not at constant span and varied significantly spanwise because the wing/body intersection is highly non-planar.

Wing Defining Stations in SYN87-SB

AIRPLANE Cp's for AMES 1-03

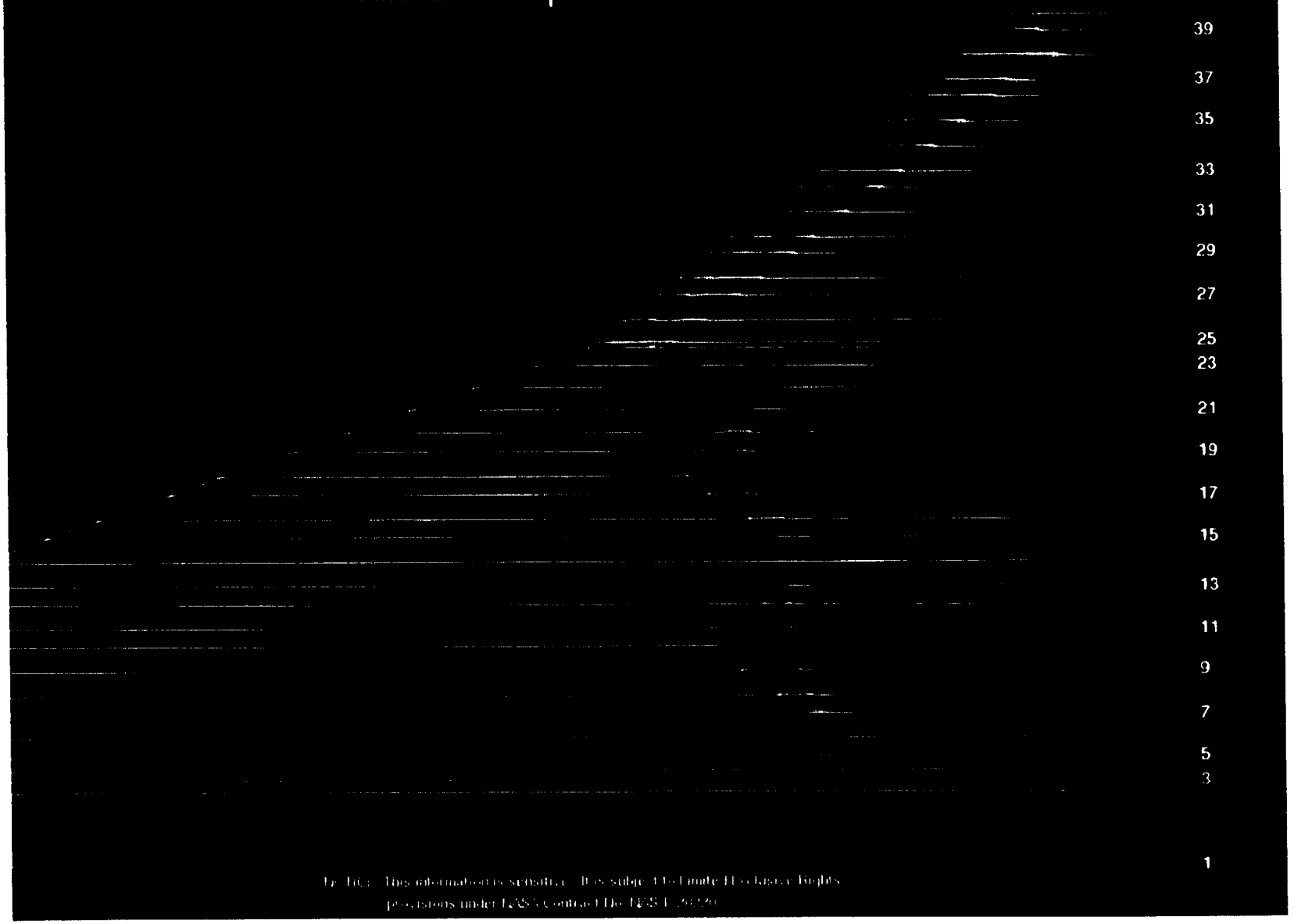

Optimization Procedure

The following tasks must be accomplished before numerical optimization can begin for configuration design:

1) An analysis of the wing/body/nacelle/diverter configuration at several angles of attack near the cruise condition must be accomplished to determine the angle of attack for the cruise lift coefficient. An Euler code should be used for this task if the design code uses an Euler equation solver.

2) Analyze the wing/body configuration with the same Euler code at the design angle of attack determined from task 1.

3) Prepare surface geometry and Cp files for SYN87's pseudo nacelle effects, and perform a set up run to calculate the interference pressures due to the nacelles and diverters to be superimposed on the lower surface of the wing during optimization.

4) Make several runs with the design code including the interference pressures to obtain a Cdmin such that (L/D)max occurs at the design angle of attack. These runs should be at angles of attack slightly above and below the design value to avoid extrapolation and provide more accurate results. This step is not essential unless angle of attack or some form of twist is used as a design variable. The lift coefficient may still shift during optimization, but not significantly.

5) Optimize at the design angle of attack using the adjusted Cdmin to maintain the design lift coefficient.

6) Continue to optimize until it is deemed necessary to update the nacelle effects on intermediate designs. The required frequency of updating the nacelle effects needs further study. However in general, depending on the time requirements for complete solutions, the interference pressures should be updated frequently, although this may not be crucial if the pressures are not changing significantly during design. The time required to prepare an AIRPLANE surface definition for a perturbed design has been reduced substantially, enabling four updates of the pseudo-nacelle data during the TCA optimization.

Note: tasks 1 - 4 must be repeated when the nacelle/diverter interference pressures are updated.

Optimization Procedure

- Step 1: Obtain AIRPLANE W/B/N/D mini-polar to obtain α_d for design CL.
- Step 2: Obtain AIRPLANE W/B solution at α_d.
- Step 3: Postprocess AIRPLANE solutions for Δ Cps on wing, and nacelle buoyancy effects.
- Step 4: Obtain mini-polar using SYN87-SB + pseudo nacelle effects to adjust CD_{min} so that L/D_{max} occurs at α_d.
- Step 5: Optimize at α_d with adjusted CD_{min} (L/D_{max}).
- Step 6: repeat step 5, and periodically update pseudo nacelle effects on intermediate designs (steps 1-4).

705 Comparison of Lower Surface Cp

The lower half of this figure shows the AIRPLANE lower surface grid and Cp contour lines of the intermediate 7-05 design. The nacelles and diverters are removed so that the lower surface could be more easily viewed. The upper half of the wing shows the SYN87-SB surface grid with the SYN87 wing/body Cps plus the difference in the AIRPLANE Cps caused by the influence of the nacelles and diverters.

The extremely fine mesh for the AIRPLANE solution yields refined shocks from the nacelles and diverters. The SYN87 grid captures a significant portion of these effects but the level of grid refinement in the nacelle region determines the extent that the nacelle effects can be captured. The SYN87-SB grid size used was as large as could be afforded with the available memory on the Cray C90 machine. The SYN87-SB design code with the grid size shown here required 58 MW of memory. This large memory requirement significantly reduced the turn-around time on the Cray, but it was believed that at least this level of accuracy was necessary to adequately integrate the nacelle effects into the design.

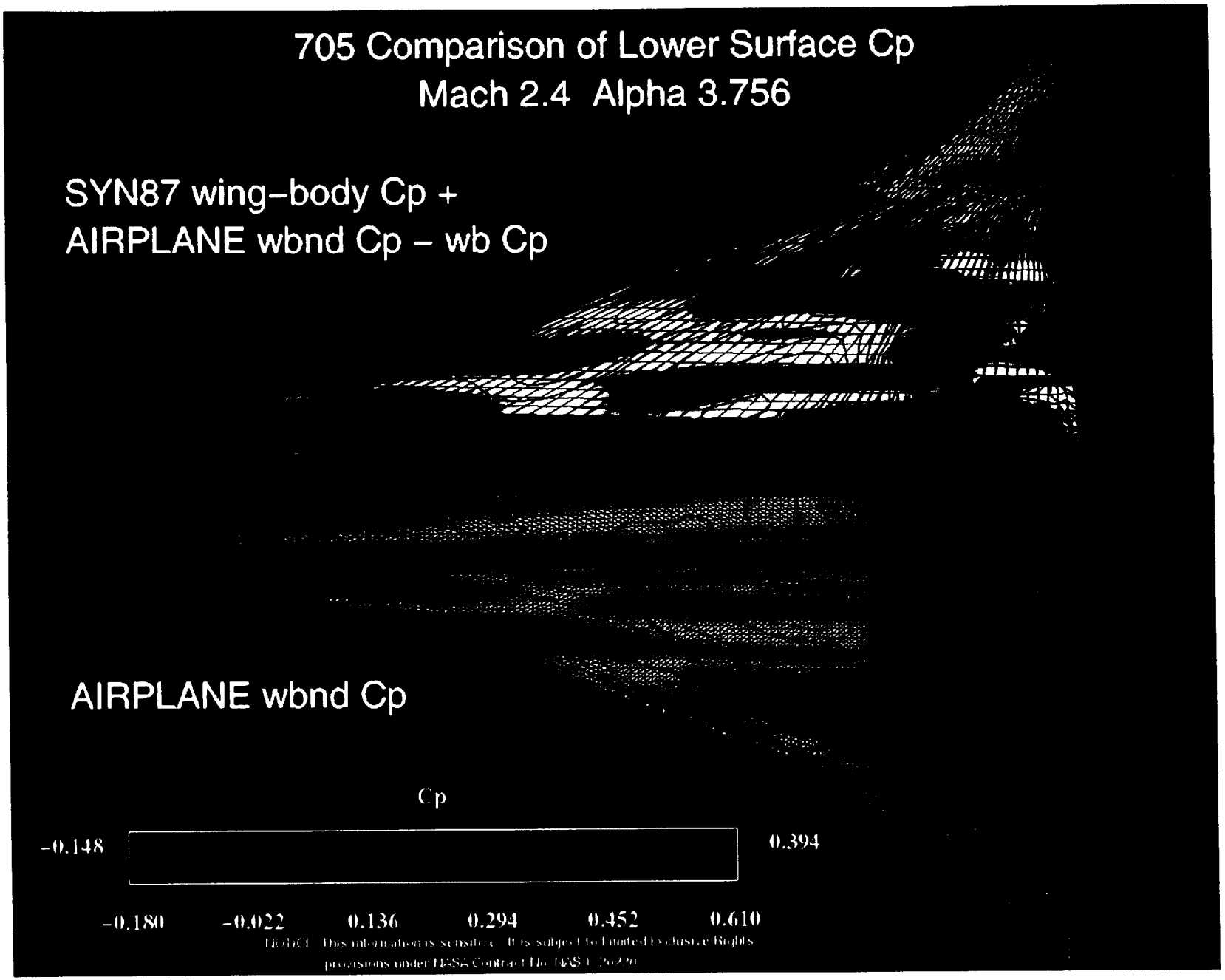
705 Comparison of Lower Surface Cp
Mach 2.4 Alpha 3.756
SYN87 wing-body Cp +
AIRPLANE wbnd Cp - wb Cp
AIRPLANE wbnd Cp
Cp
-0.148
0.394
-0.180
-0.022
0.136
0.294
0.452
0.610

Design Statistics

The design presented here consisted of approximately 220 optimization runs. Nearly forty percent of the runs were determined to be unsuccessful. This success rate is poorer than typical design by optimization methods primarily because of the large number of constraints that had to satisfied, and the difficulty of maintaining spanwise and chordwise smoothness. The performance improvements were slow to be realized from the inception of the design. This design could not have been completed in the 2-3 month time period that was first allotted to this design effort.

The adjoint method was used for a majority of the design work. An optimization run utilized 40 to 130 design variables and 8 to 15 optimization iterations when using adjoint gradients and 30 to 40 design variables and 1 or 2 optimization iterations when using finite difference gradients. The adjoint mode permitted the entire wing to be perturbed while the finite difference mode allowed only a limited number of design variables to be used which typically limited the regions of the wing to be reshaped during any given run. Finite difference gradients proved to be a little more accurate when the configuration is near a minimum in the design space.

The design effort was focused on the wing since it was thought to be the most fruitful place to obtain performance gains, and the fuselage camber/area gains were found to be somewhat independent of wing camber and thought to be more a function of planform. The wing design continued unabated for the 7-8 month duration of the design effort, and little gain is thought to be left. The fuselage received significantly fewer design iterations than the wing, due to a late start on this part of the design. However, the gains were achieved more quickly than for the wing, which may suggest that more improvements could be realized with more attention to fuselage design.

The nacelle/diverter pressures were updated as often as time permitted but questions still remained as to the required frequency of the updates and whether the updates should have been underrelaxed to produce a convergent process. The updates did increase the performance increments on the wing, but presumably made them more accurate.

Usually a single wing surface was designed subject to 177 linear constraints and 1 nonlinear constraint, in order to keep the number of design variables around 100 in adjoint mode. The lower surface was more extensively reshaped than the upper surface due to the presence of the nacelle/diverter flow field. The gains achieved were limited by a still-unresolved, sporadic phenomenon which permitted violated linear constraints under some conditions. When violated constraints were encountered, manual intervention was required to return the design to feasible space.

Design Statistics

- 220 Design changes, 40% were determined unsuccessful
- Nearly constant performance improvements from inception of design
- Adjoint method was used for 72 % of runs - Finite difference runs yielded the same or greater performance improvements
- Design effort was focused on the wing, little additional improvement available
- Significant improvement from fuselage design, but additional improvements may be available
- Updating nacelle-diverter effects did not accelerate design improvements
- Lower surface thickness design yielded greater improvements than upper surface thickness design
- Pure camber perturbations were found to cause excessive waviness and not used in later designs

Euler-Based Optimization of TCA-6 (Delta L/D Improvements Between Design Runs)

This figure displays the relative performance gains or losses of each successive design change from the beginning of the design to the final Ames 1-03 configuration. These geometric changes were achieved either by use of the SYN87-SB optimization code or by implicit smoothing off-line or by hand manipulation of the geometry. The nacelle/diverter interference pressure updates are shown along the run axis. Note that five different sets of interference pressures were used beginning with the baseline TCA configuration. The total period of time allowed for design of this configuration was approximately 7 months with the pressure updates occurring at approximately 2 month intervals. The date of creation of intermediate wing designs from which the interference pressures are obtained is contained in the file name. E.g., 07-05 indicates that the interference pressure files are for the wing created on July 5, 1996.

Most of the successful perturbations occurred on the lower surface of the wing. Camber improvements were fairly successful but resulted in more spanwise waviness than either upper or lower surface design so camber was abandoned a little past the mid-point of the design cycle. Fuselage design produced substantial improvements in the lift/drag ratio in a fairly short time period. Additional improvement might have been achieved by fuselage camber and cross-sectional area changes if more time were available for design or if the optimization code had achieved production status earlier in the design cycle. Manual design changes were necessary to correct violated constraints, to achieve design improvements not found by the optimization code, and to smooth the geometry using an implicit/explicit smoothing procedure. Only hand design changes could produce performance losses. In this figure the open circular symbol represents the unsuccessful design changes. Nearly 40% were unsuccessful, and most were eliminated due to excessive waviness, while others were rejected as unrealistic designs that may be apt to fail in a viscous flow-field.

Euler-Based Optimization of TCA-6

Delta L/D Improvements Between Design Runs

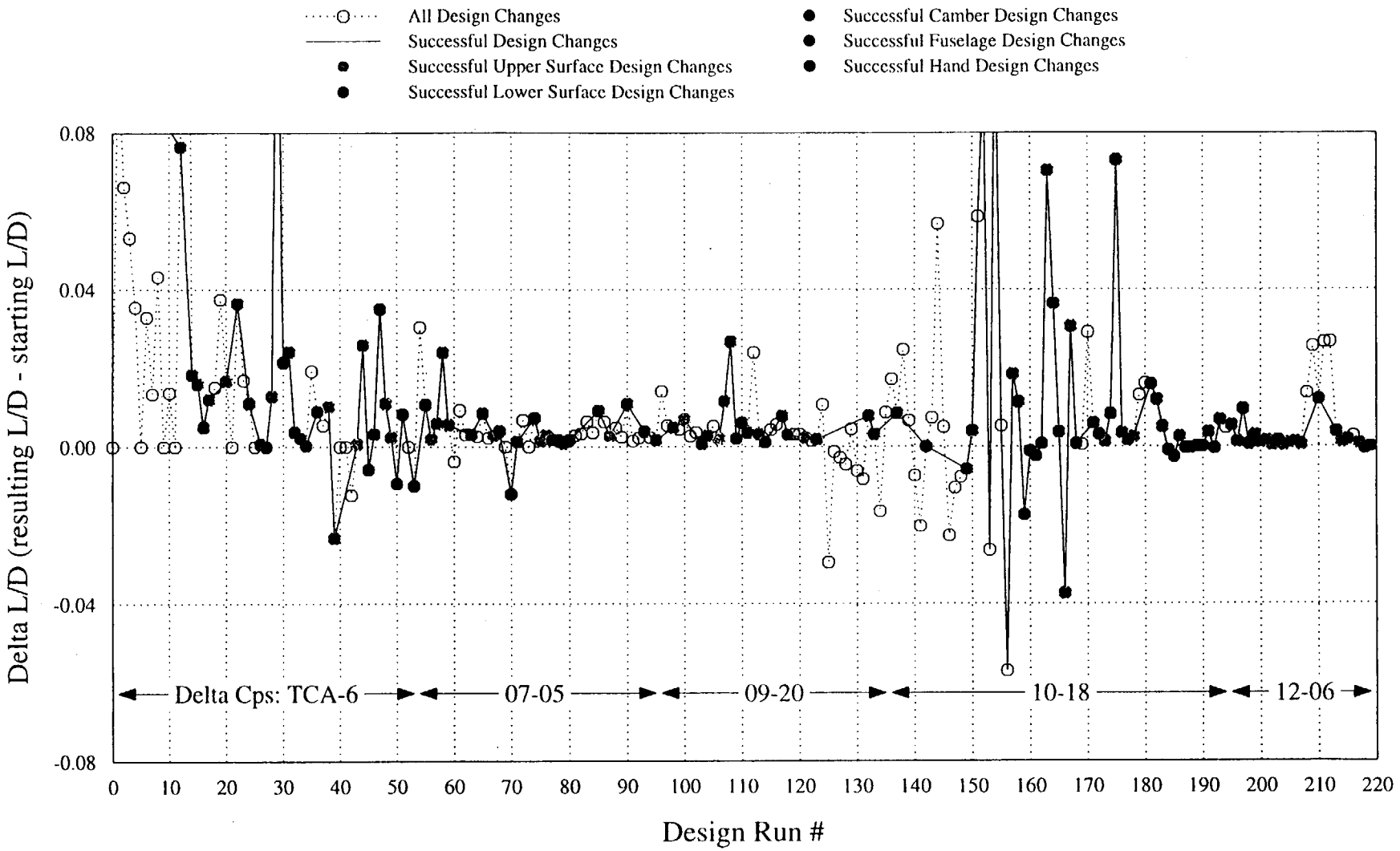

SYN87 Calculations (193 x 49 x 65 Mesh), Mach 2.4
Pseudo-Nacelle Pressures from AIRPLANE

01/24/97

Euler-Based Optimization of TCA-6 (Cumulative L/D Improvements Between Runs)

This figure displays a running sum of the performance improvements shown in the previous figure. Several points of interest are better made by this presentation than the previous figure. In particular, note that the nacelle/diverter interference pressure updates are not associated with any major step-improvements in the objective function. In fact the curve seems to approach zero slope following the change from the 09-20 pressures to the 10-18 pressures. However, fuselage design clearly shows abrupt and substantial improvement in the lift/drag ratio. Again it is clear that wing lower surface design yields greater improvement in the objective function than upper surface optimization. The slope of the improvement history curve tends to zero before each fuselage redesign. This is followed by additional improvement in the lift/drag ratio when the wing is redesigned in the presence of the new fuselage. The most powerful message to be derived from this and the preceding figure is the large number of design iterations and the long calendar and CPU time needed to complete the design. This may be somewhat surprising to the uninitiated in numerical optimization design since it is sometimes assumed that numerical optimization provides the designer with a "black box" requiring little manual intervention to complete a design. In fact, the designer is required to have good aerodynamic and fluid dynamic intuition to use existing optimization design codes.

Euler-Based Optimization of TCA-6

Cumulative L/D Improvements Between Design Runs

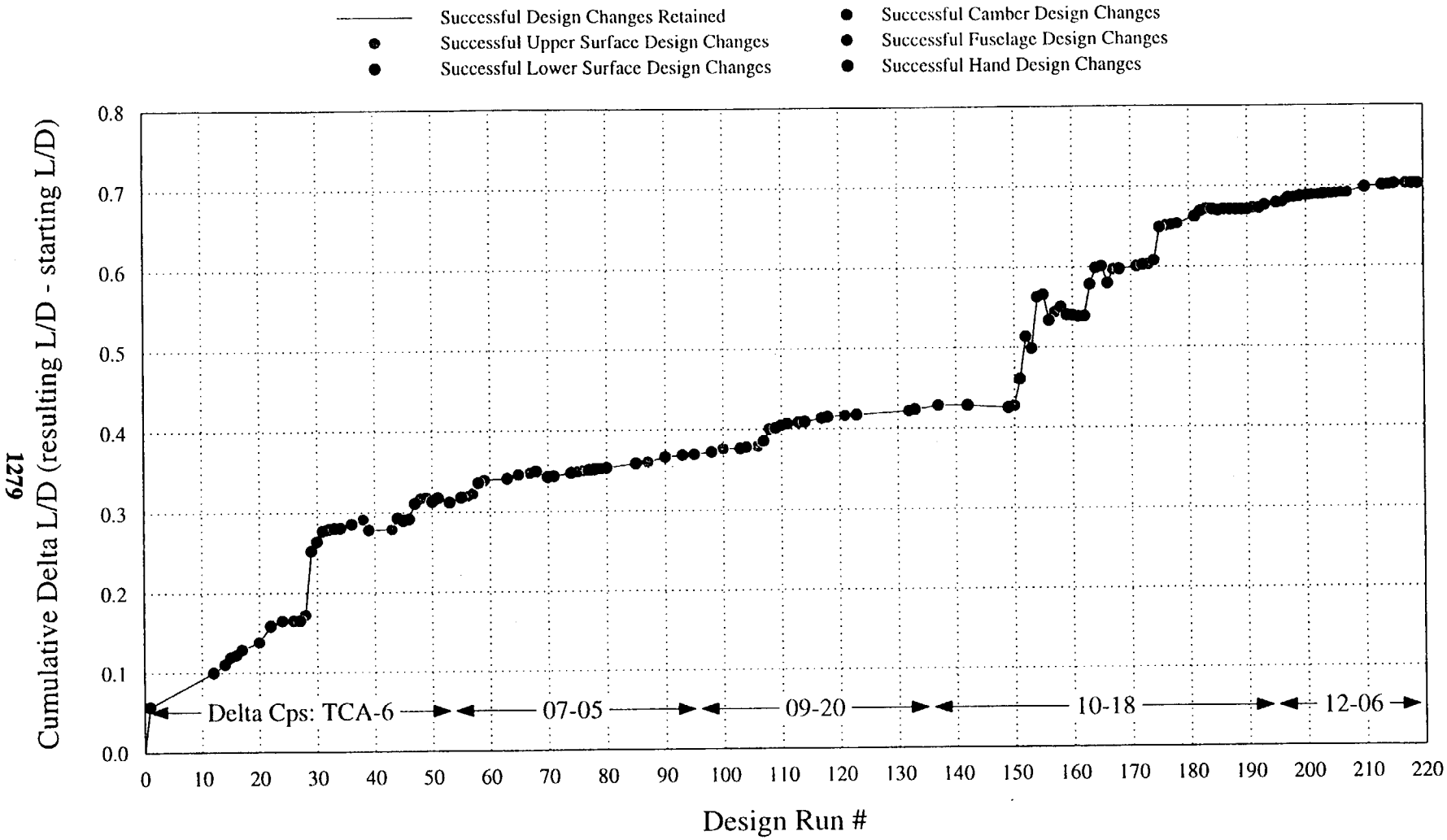

SYN87 Calculations (193 x 49 x 65 Mesh)
Pseudo-Nacelle Pressures from AIRPLANE

01/24/97

SYN87 Optimization of TCA-6: Adjoint-Based Gradients vs. Finite Differencing

The running sum of performance improvements for successful optimization runs are colored by the type of method used to calculate the gradient. The adjoint-based gradient method was used for the majority of the optimization runs. The adjoint method is much more efficient than finite difference methods. It only requires one solution of the flow equations and one solution of the adjoint equation for any number of design variables. However, it was found that the adjoint method failed to find a gradient direction during the design process. This was due to a number of errors in the SYN87 design method that have been fixed to some extent in the current version of the code. The finite difference method continued to find improvements at approximately the same rate as the adjoint method during approximately a two month time period while the problems with the adjoint method were resolved.

The finite difference method is generally believed to more accurately predict gradient information than the adjoint method, particularly when nearing the valley in the design space. However, the computational expense of using such a method makes it infusible to use with any greater than 30-40 design variables.

SYN87 Optimization of TCA-6: Adjoint-Based Gradients vs. Finite Differencing

Cumulative L/D Improvements from Design Runs

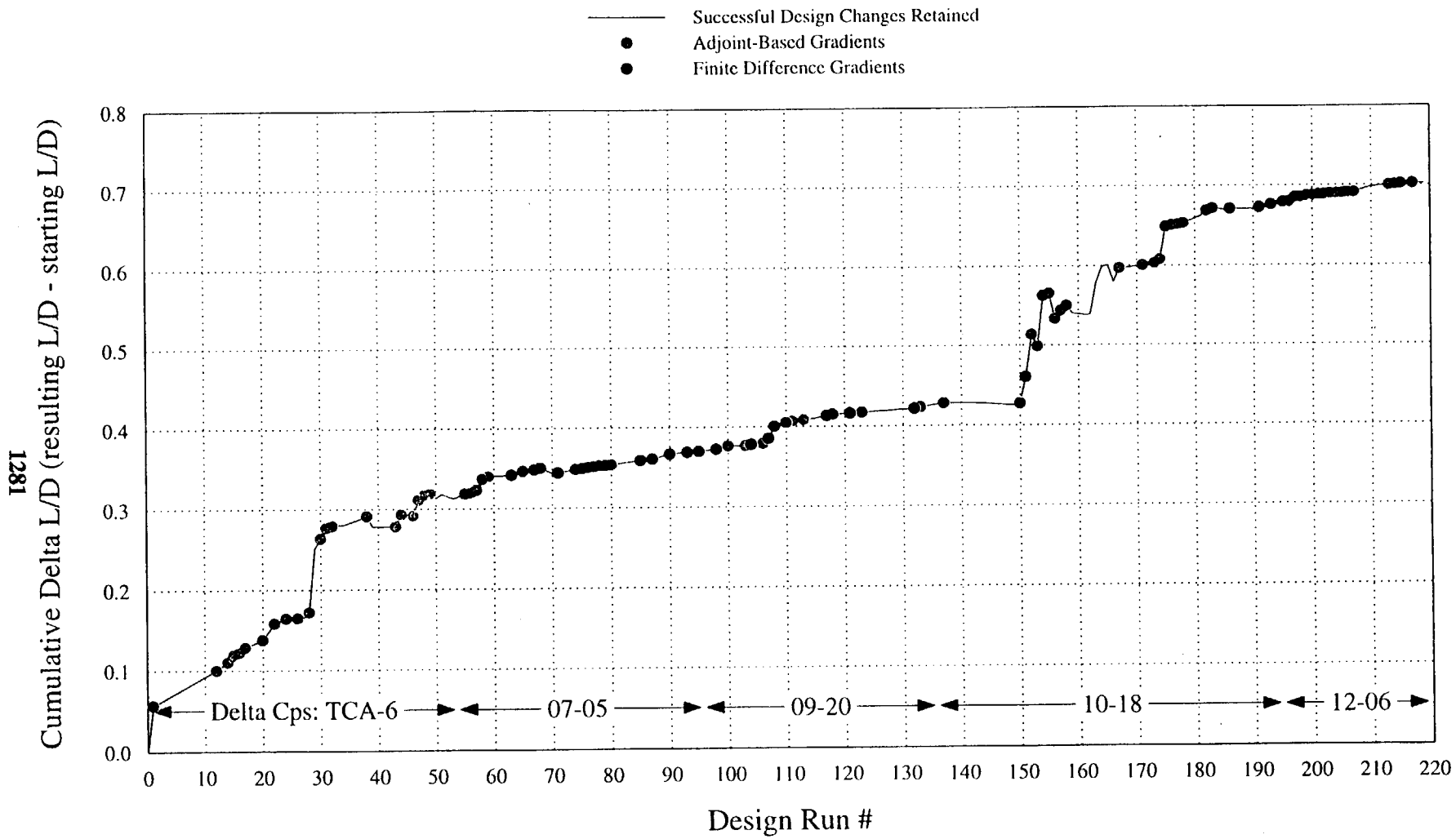

SYN87 Calculations (193 x 49 x 65 Mesh)
Pseudo-Nacelle Pressures from AIRPLANE

02/10/97

Performance Differences: Adjoint vs. Finite Difference Gradients

This chart shows the change in the L/D (L/D final - L/D initial) for seven different optimization cases. Cases 1-6 are for fixed angle of attack applied to a configuration that is mid-way between the baseline and the final Ames 1-03 optimized configuration. Case 7 is for a fixed CL case applied to the baseline TCA configuration.

These results are for "sub optimization" problems, consisting of a single row of shape functions at various span stations for the individual cases. The shape functions represented are for a sine2, exponential, and twist design variables. Each case is for only 1 optimization iteration. It must be pointed out that the individual changes in the figure are small but would be cumulative when additional design variables and optimization iterations are run.

When the two gradient types do not correlate well, it has been observed that the finite difference method appears to give better improvements (Cases 1-5). Whereas when the gradient types correlate well (cases 6 and 7), the adjoint method can give better improvement. This is only a status report of the much more extensive gradient study that is currently underway.

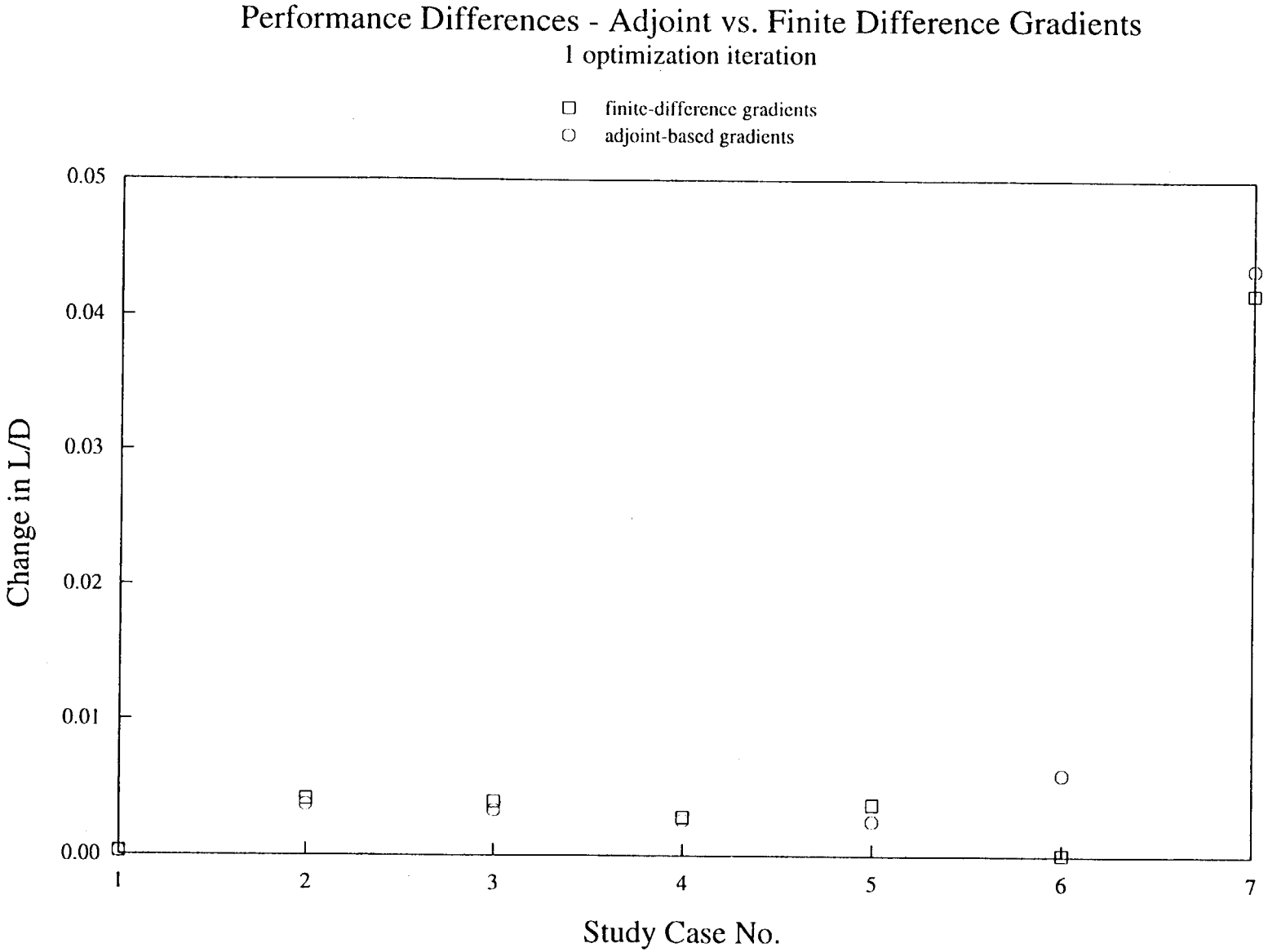
Performance Differences - Adjoint vs. Finite Difference Gradients
1 optimization iteration
finite-difference gradients
adjoint-based gradients
Change in L/D
0.05
0.04
0.03
0.02
0.01
0.00
1
2
3
4
5
6
7
Study Case No.

Intermediate Design Cps: AIRPLANE

The sequence of designs shown in this figure clearly show good nacelle/diverter integration, at least from an inviscid analysis. The baseline configuration shows strong shock waves emanating from the leading edge of the nacelles and diverters. The region of high pressures from the combined shocks of the inboard and outboard nacelles located between the nacelles nearly disappears by the 7-05 configuration. The strength of the nacelle/diverter shocks decreases rapidly also. Note the asymmetry that appears for the outboard nacelle/diverter for the 7-05 and 9-20 configurations. Symmetry returns to the shocks for the 10-18 wing with the shock pressure field remaining nearly constant to the final design. The reduction in shock strength is accomplished by developing an expansion field immediately upstream of the nacelle/diverter leading edge. The localized increase in the thickness and curvature of the wing lower surface also produces an aft facing slope for the remaining high pressure field associated with the shocks to act on giving a thrust component with an associated drag reduction and a lift/drag ratio improvement. At this time it will not be claimed that the localized reshaping of the lower surface is optimum because the expansion field strength and location are based on inviscid design methods and an expansion field on the lower surface causes a reduction in both lift and thrust. A large expansion region inboard of the inboard nacelle has been continuously reduced throughout the design process, and is nearly eliminated on the Ames 1-03 design. Also the reflective shock originating from the outboard nacelle, striking the inboard nacelle, and reflecting back to the outboard nacelle was reduced in the final design.

The design presented here represents the most extensive integration of the nacelle/diverters into the wing geometry of any of the HSR designs.

Intermediate Design Cps: AIRPLANE

Mach 2.4, alpha 3.756

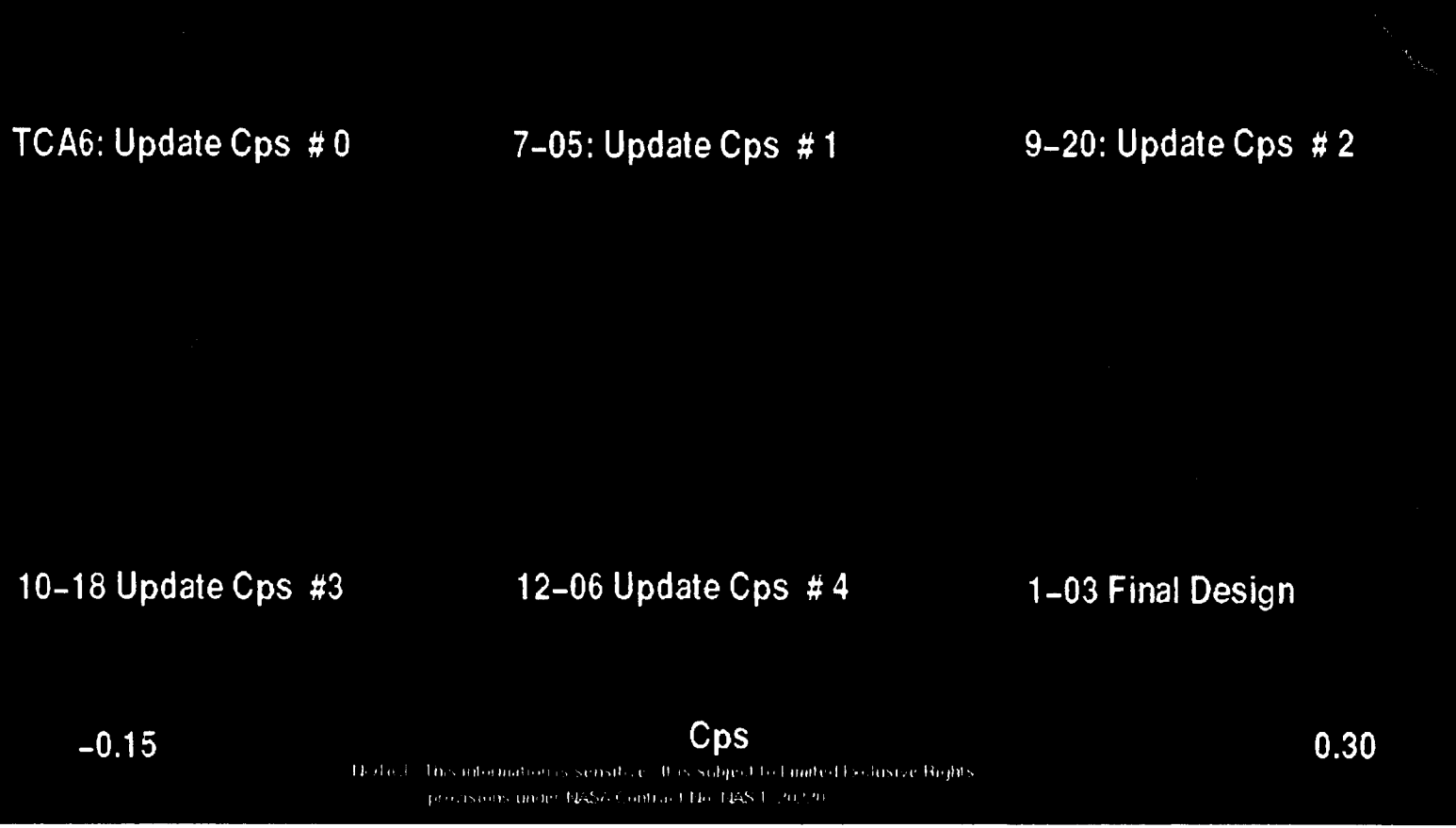

NASA Ames 1-03 Wing/Body (front view)

The final Ames 1-03 wing/body configuration is shown in front view here. The camber of the leading edge of the inboard wing panel is clearly visible in the figure. Note the fairly abrupt contour of the landing gear box adjacent to the body on the lower surface of the wing. The asymmetric coloring left to right is due to the placement of the light source and does not indicate an asymmetric configuration. Due to the view angle of the figure, the upswept fuselage aft-body appears as a bump on the top of the fuselage.

NASA Ames 1-03 Wing/Body

Baseline Wing/Body (front view)

The baseline TCA wing/body shown here appears to be slightly smoother, having less leading edge camber and a more gradual fairing of the landing gear box into the wing lower surface than the Ames wing/body configuration shown in the previous figure.

Baseline Wing/Body

NASA Ames 1-03 Wing/body (isometric view)

The isometric view of the Ames 1-03 wing/body shown in this figure has exhibits a small amount of spanwise waviness on the lower surface of the wing. These waves have been reduced considerably since the first design review. They are unavoidable using the lofting techniques employed by the optimization method. The wing exhibits localized "bumps" upstream of the nacelle/diverters which generate carefully placed expansion fields to counteract the strong shocks emanating from the leading edge of the nacelles and diverters. These carefully placed contours give a thrust component for drag reduction and lift/drag ratio increase. Also evident is a small bump placed in between the nacelles to greatly weaken the strength of the combined inboard and outboard nacelle shocks and provide the aft facing slope necessary to obtain localize thrust. The abrupt lower surface contour at the side of the landing gear box is also visible in the figure. The landing gear box constraint was difficult to maintain. Clearly a mid-mounted wing has less drag due to the reduction of the wetted area of the wing than a wing that is mounted below the fuselage. This rapid change in lower surface curvature at the side of the gear box was necessary to obtain the performance level of this configuration and meet the landing gear box constraint. A more gradual blend with the gear box has more wetted area, and therefore more drag.

NASA Ames 1–03 Wing/Body

Baseline Wing/body (isometric view)

Comparing this figure with the last shows that the baseline configuration has greater spanwise smoothness than the Ames configuration. The greater smoothness is partly responsible for the lower lift/drag ratio of the baseline configuration. This level of smoothness precludes localized tailoring of the surfaces around the nacelle to reduce the drag in this region of the wing. A slight increase in forebody camber of the Ames configuration can be seen by comparing this figure with the last figure. Changes to the cross-sectional area of the fuselage are not visible in this figure.

Baseline Wing/Body

Wing Leading Edge Spar Depth Constraint

This figure shows that the Ames 1-03 configuration has met the leading edge spar depth constraint on the wing. Note that the thickness constraints for the leading edge spar depth shown in this figure were active from approximately 350 inches from the centerline of the fuselage to the tip. The aerodynamic requirement for thin sections in the supersonic outboard wing panel will be apparent when this and the next two figures are examined. The inboard wing panel exhibits some transonic characteristics so minimum section thickness is not a hard requirement there. In fact, there is considerably more thickness than required by the constraints immediately outboard of the side of the body primarily because of a large leading edge radius constraint. This constraint was sometimes slightly violated after optimization due to numerical round-off errors from repeated writing of the output wing geometries, and because the optimization code sometimes permitted violation of these constraints during design—a puzzle yet to be explained.

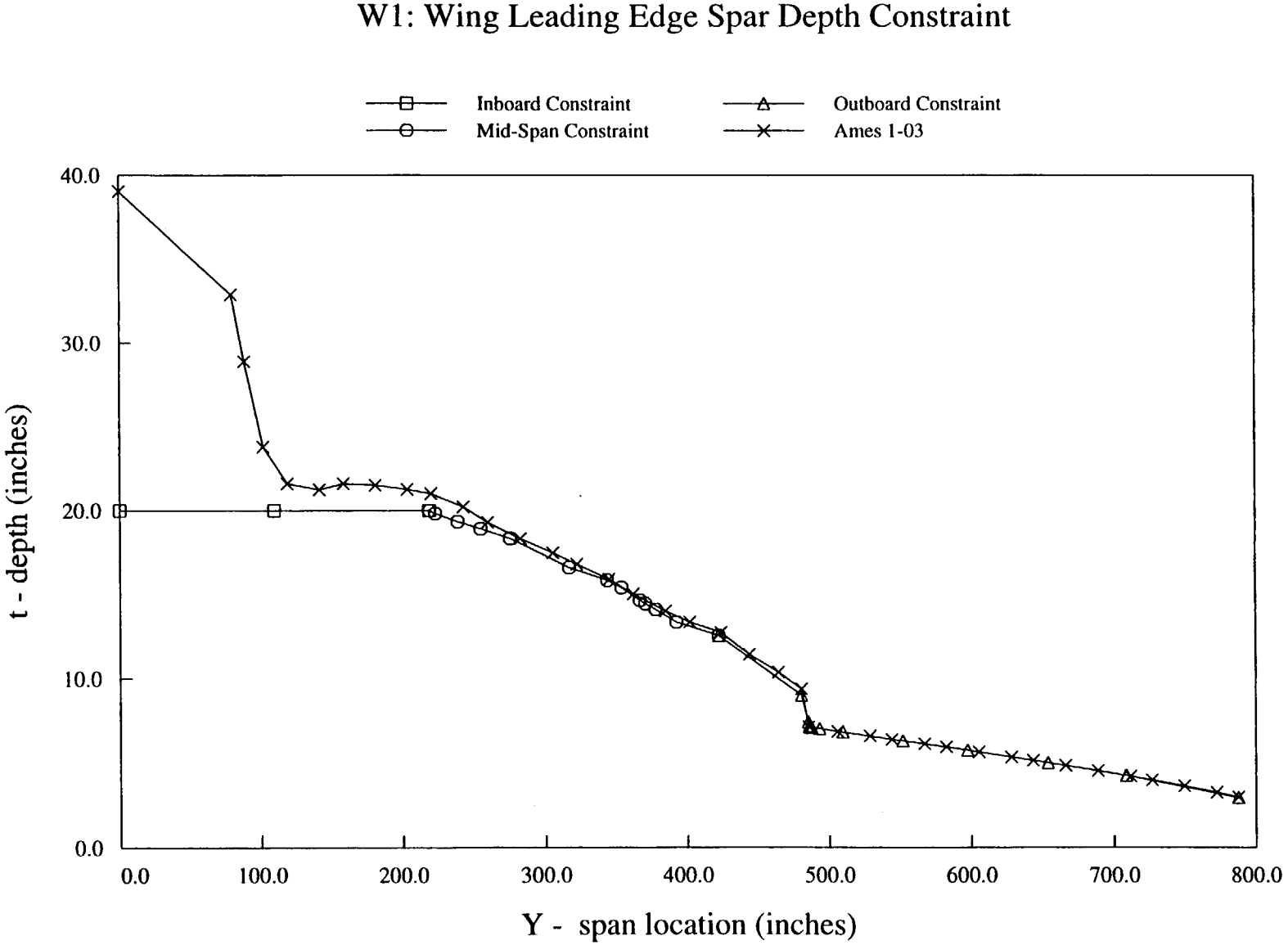
W1: Wing Leading Edge Spar Depth Constraint
Inboard Constraint
Outboard Constraint
Mid-Span Constraint
Ames 1-03
40.0
30.0
20.0
10.0
0.0
t - depth (inches)
0.0
100.0
200.0
300.0
400.0
500.0
600.0
700.0
800.0
Y - span location (inches)

Wing Trailing Edge Spar Depth Constraint

The wing trailing edge spar depth constraint was active over more of the wing than the leading edge spar depth constraint for the final Ames 1-03 configuration. Again manual intervention was occasionally required to correct slight violations of the aft spar constraints.

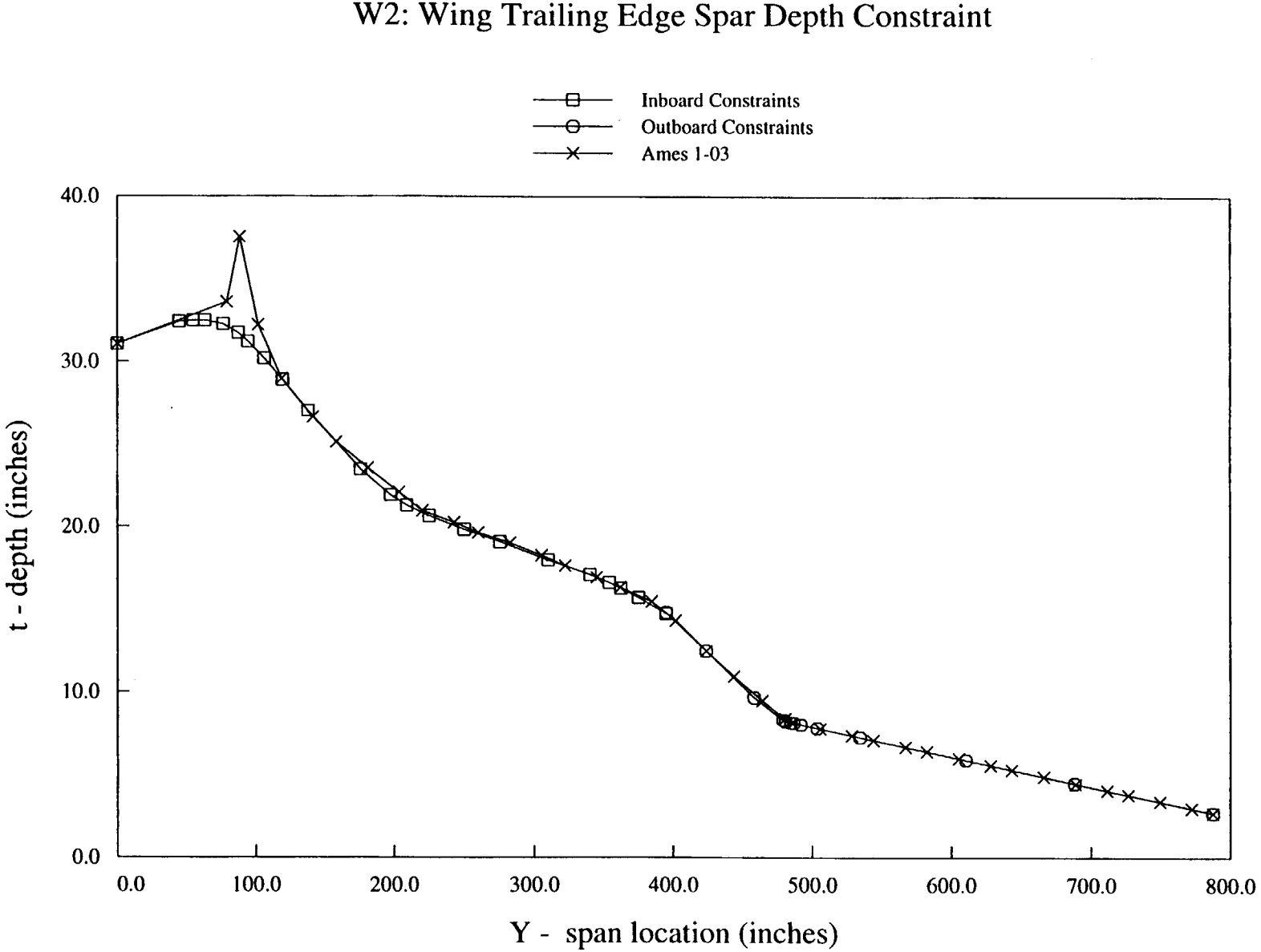
W2: Wing Trailing Edge Spar Depth Constraint
Inboard Constraints
Outboard Constraints
Ames 1-03
40.0
30.0
20.0
10.0
0.0
t - depth (inches)
0.0
100.0
200.0
300.0
400.0
500.0
600.0
700.0
800.0
Y - span location (inches)

Maximum Thickness/Chord Ratio Constraint

A minimum value of maximum thickness/chord ratio of 2.4-percent was imposed on the wing design at all defining stations. The thickness/chord ratio values shown in this figure verify the point made earlier that thin sections are desirable where the flow is entirely supersonic to minimize wave drag. Linear theory states that wave drag is proportional to thickness squared. Note that the transonic cross-flow over the upper surface of the inboard wing panel and the careful integration of the nacelles and diverters into the lower surface of the wing dictates that careful local shaping of the wing sections is more important here in reducing drag than the value of maximum thickness. As discussed previously, thickness was added to the lower surface of the wing upstream of the nacelles to create expansion fields to reduce the strength of the shocks emanating from the leading edge of the diverters and nacelles. Such local thickening of the wing surface affects the value of maximum thickness of those sections. The design code's option to constrain maximum t/c explicitly was not needed.

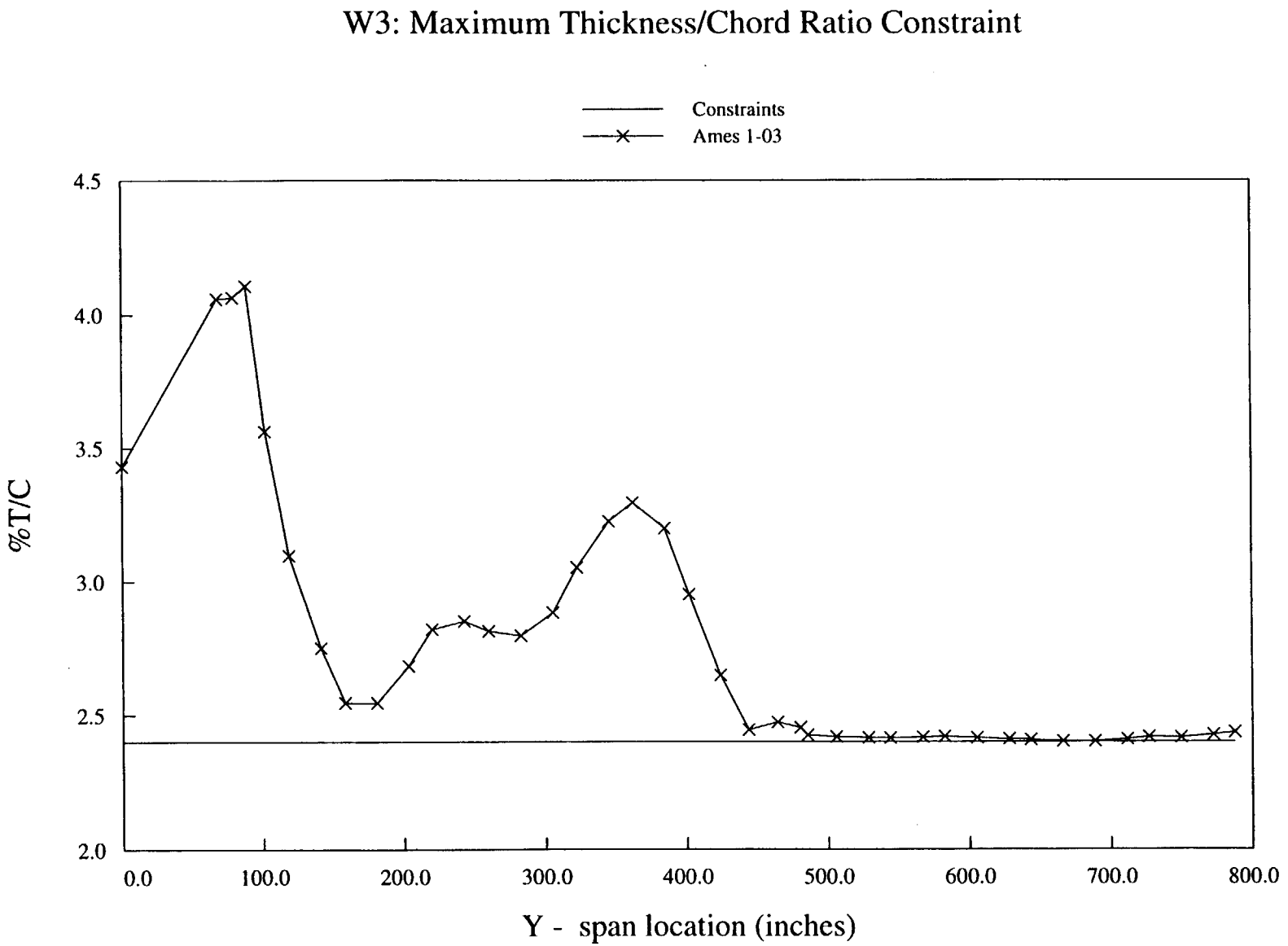
W3: Maximum Thickness/Chord Ratio Constraint
Constraints
Ames 1-03
%T/C
4.5
4.0
3.5
3.0
2.5
2.0
0.0
100.0
200.0
300.0
400.0
500.0
600.0
700.0
800.0
Y - span location (inches)

Landing Gear Box Constraint

The spanwise cross-sectional cuts shown in this figure were taken at fuselage stations of 2191 and 2339. These cuts represent the location of the fore and aft edges of the gear box. This figure shows that the box containing the landing gear meets the constraint of wing containment. Also shown in the figure is the aerodynamic fairing developed by optimization of the fuselage cross-sectional area distribution. Note that a pressure vessel is contained within the outer mold line of the fuselage which meets all the curvature constraints imposed on the fuselage design. The polygon shown inside the outer mold line is the constraint surface for the fuselage cross-section at this station. The outer mold line clearly contains this constraint surface. The abrupt decrease in vertical wing position near the side of the body was caused by a floor to upper wing surface distance constraint.

W4 WHEEL GEAR BOX CONSTRAINT

1301

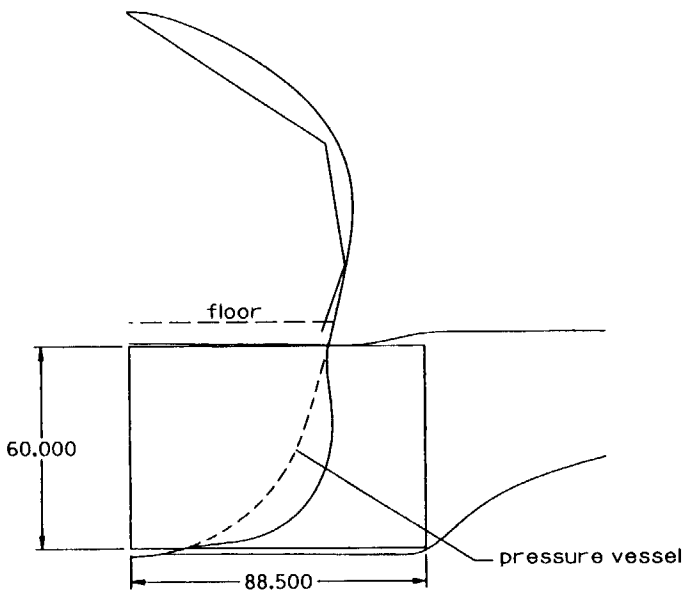

X STATION 2265

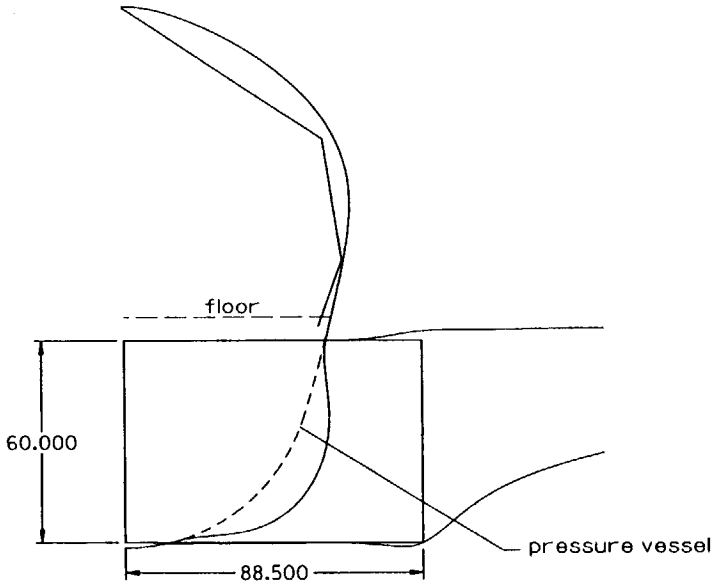

X STATION 2339

Cockpit Cross-Sectional Area Constraint

The only constraint violation of significance on the Ames optimized configuration is the cross-sectional area of the cockpit. The cross-sectional area of the Ames 1-03 configuration is 7.3% below that of the baseline. Cross-sectional cuts at x = 400 inches are shown in the figure. This violation occurred because the designers were not aware of the constraint during optimization. It is felt that the area could be increased to the constraint value without incurring a drag penalty. Note that the position of the area decrease is well above the plane of the wing and considerably forward of the apex of the wing/body juncture implying that the area reduction was generated primarily for body drag reduction rather than to provide favorable interference for the wing.

B2 COCKPIT AREA CONSTRAINT

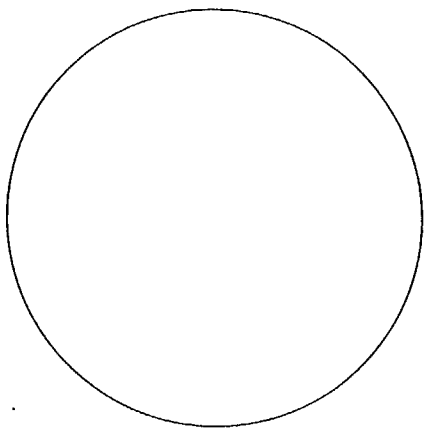

baseline area = 50.38 sq. ft.

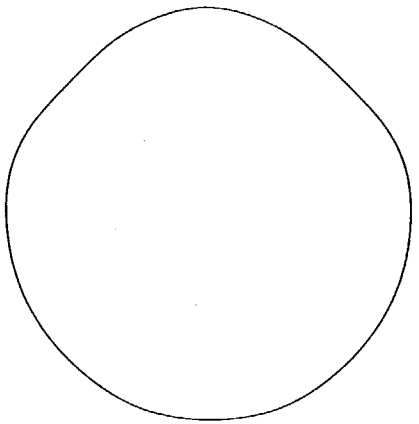

optimized area = 46.70 sq. ft.

X STATION 400

Fuselage Curvature Constraints

The final Ames configuration has been analyzed with two different fuselage configurations. The first fuselage represents the preferred outer mold lines of the Ames 1-03 configuration. It represents a configuration where an aerodynamic fairing has been added to a "pressure vessel" fuselage geometry. This fairing emerged from the optimization because it gave a drag reduction despite the fact that it adds volume and violates external mold line surface curvature constraints, which were not being imposed explicitly.

To address the problem of surface curvature constraints being violated a "pressure vessel" fuselage geometry was subsequently defined. The pressure vessel geometry has the following properties: 1) It fits inside the fuselage with fairing geometry everywhere and corresponds with it in most places. 2) It satisfies all surface curvature constraints and all internal body cabin constraints.

The figure colors the fuselage using a scaled absolute value of curvature. Everything that is black satisfies the curvature constraints, all other colors indicate a violation. The fuselage curvature constraints were imposed for fuselage stations 500 through 3600. Note that the baseline TCA configuration exhibits constraint violations both in regions between x=3300 (second vertical line) and x=3600 (third vertical line), and in a narrow band running over a large portion of the fuselage. The white curves drawn on the lower half of the TCA baseline and Ames 1-03 with fairing configurations represent the wing-body intersection. Thus any violations within the area encompassed by the curves should be ignored. The baseline TCA violations unfortunately occur outside this area. The Ames 1-03 design with the added fairing similarly violates constraints, while the pressure vessel alone is shown to satisfy all constraints between x=500 and 3300. Constraints were not forced to be satisfied between x=3300 and 3600 since the baseline so obviously violates this constraint in this region.

Since most practical aircraft have some form of aerodynamic fairing at the wing/body juncture it is felt that the more reasonable configuration to be considered for manufacture here is the model with pressure vessel plus fairing. AIRPLANE analysis of the Ames 1-03 configuration with and without the fairing has shown that the fairing gives a drag reduction of 0.25 counts and therefore must be chosen as the final design.

Fuselage Curvature Violations

TCA6

Ames 01-03: Pressure Vessel + Fairing

Ames 01-03: Pressure Vessel

Euler Computations - Wing/Body/Nacelle/Diverter - Lift Curves

Lift curves for the baseline and Ames 1-03 optimized configuration (with the fuselage fairing) using AIRPLANE, SYN87-MB and SYN87-SB are shown in this figure. AIRPLANE is considered to be the most reliable analysis code of the three codes shown in the figure. AIRPLANE has an extensive history of analyzing numerous supersonic configurations over the past several years. Note that AIRPLANE and SYN87-MB give the same lift curve slope for both configurations while SYN87-SB gives a slightly different slope. This is not surprising since both AIRPLANE and SYN87-MB model the complete configurations while SYN87-SB models the wing/body with pseudo nacelle/diverter effects which are not included in the flow equation solution. The baseline SYN87-SB solution has the baseline TCA pressures whereas the Ames 1-03 has the pressures from the intermediate design preceding the final configuration, both of which were calculated by AIRPLANE. The approximation of the nacelles and diverters in the SYN87-SB code has been discussed previously and hence will not be repeated here. The reduction in camber for the Ames 1-03 configuration is evident from the lower value of lift coefficient for a given angle of attack. A similar result was observed during the design of the Reference H configurations. The Ames 704 Ref H configuration had this characteristic to a small extent, but it was most pronounced in the Boeing W27 design (2.0 degree increase in angle of attack was required to obtain the lift of the baseline Ref H model). The current design would have a much greater reduction in camber if the cabin floor angle constraints had not been active.

Euler Computations, Wing/Body/Nacelle/Diverter

M=2.4, no internal or base nacelle forces, entire fuselage

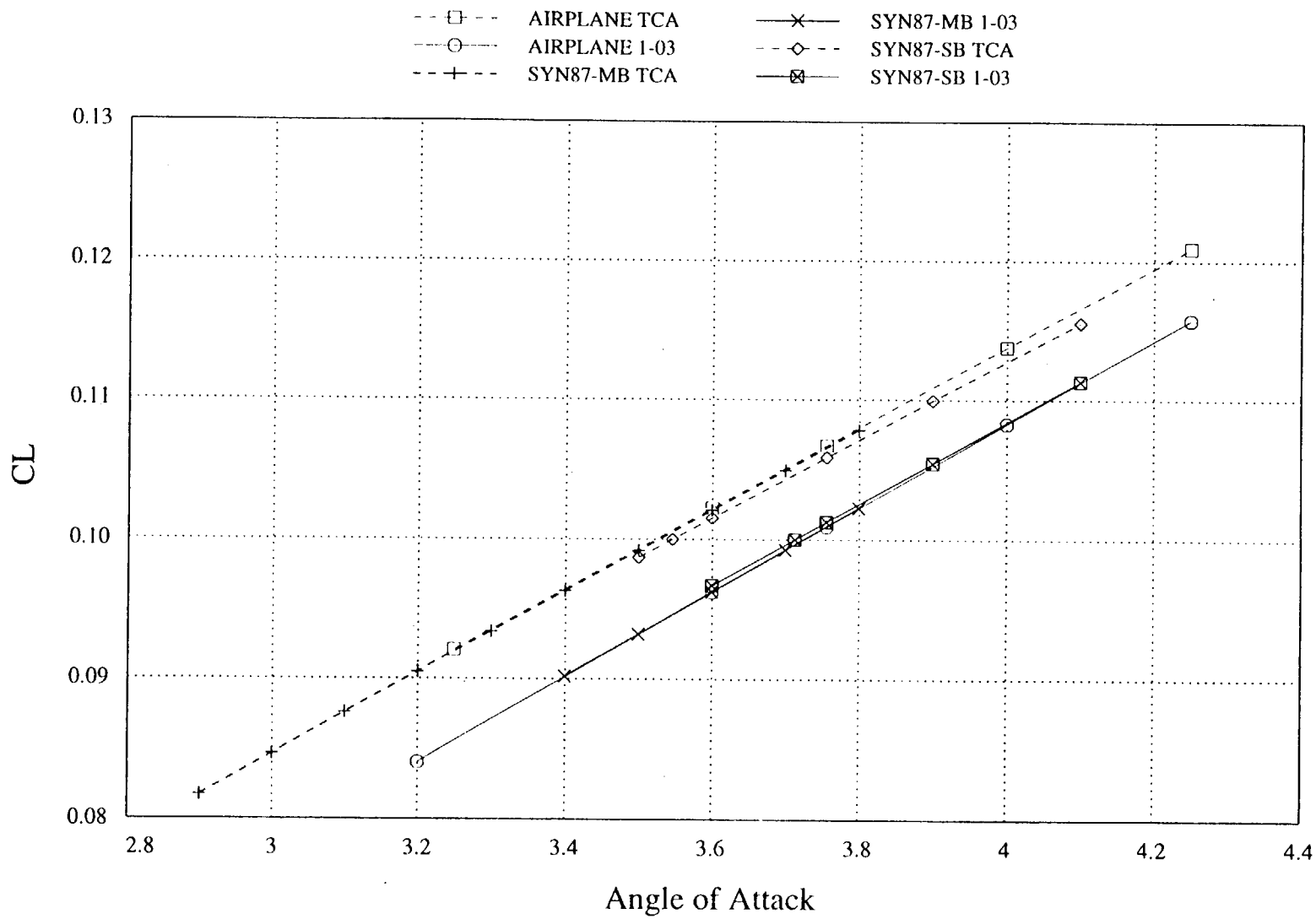

Euler Computations - Wing/Body/Nacelle/Diverter - Drag Polars

The good correlation for the three Euler code solutions for the baseline and optimized configuration lift curves shown in the previous figure is not observed for the drag polars shown in this figure. Note that the drag level computed by AIRPLANE is approximately 1.5 drag count higher than that of SYN87-SB and SYN87-MB for both configurations. Since the drag increments are the most important values for design, the absolute drag level has not been considered to be critical. The drag increment between the baseline and optimized configurations predicted by AIRPLANE is 6.95 counts whereas SYN87-SB and SYN87MB predict drag increments of 7.9 and 7.0 counts respectively. Note that the polars predicted by SYN87-SB and SYN87-MB exhibit slightly different slopes near the cruise lift coefficient indicating that the drag due to lift is not exactly the same for the two codes. This is presumably because the pseudo nacelle data used for the single block calculations apply to a single angle of attack, apart from the lagging of these corrections in the Ames 1-03 case.

Euler Computations, Wing/Body/Nacelle/Diverter

M=2.4, no internal or base nacelle forces, entire fuselage

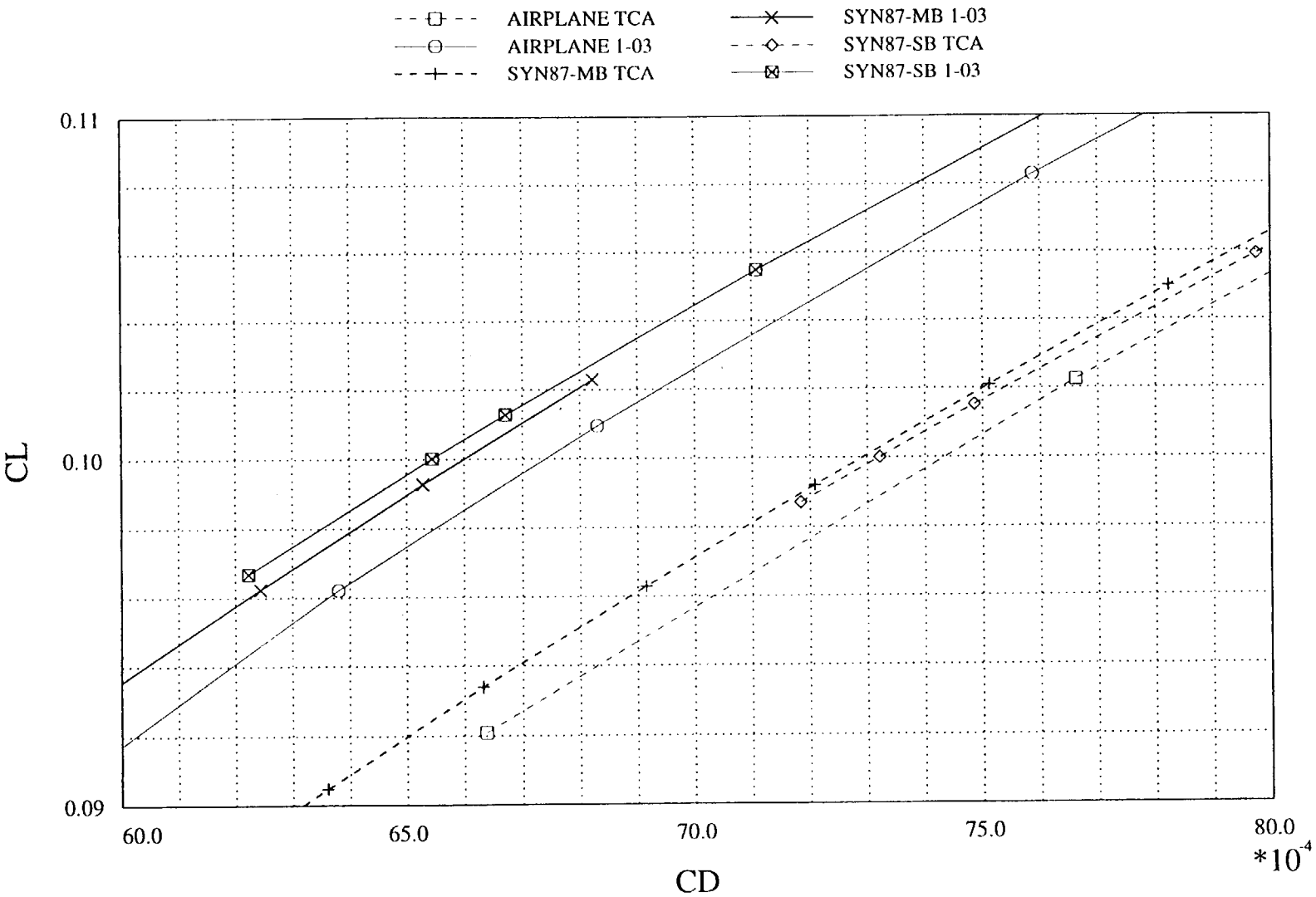

Effect of Fuselage Fairing - Wing/Body/Nacelle/Diverter

The drag increment due to the aerodynamic fairing on the side of the fuselage near the trailing edge of the wing root has been discussed previously so a full discussion will not be repeated here. This figure shows that the 0.25 drag count improvement due to the fairing is fairly constant over the small range of lift coefficients shown in the figure.

Effect of Fuselage Fairing, Wing/Body/Nacelle/Diverter

M=2.4, no internal or base nacelle forces, entire fuselage

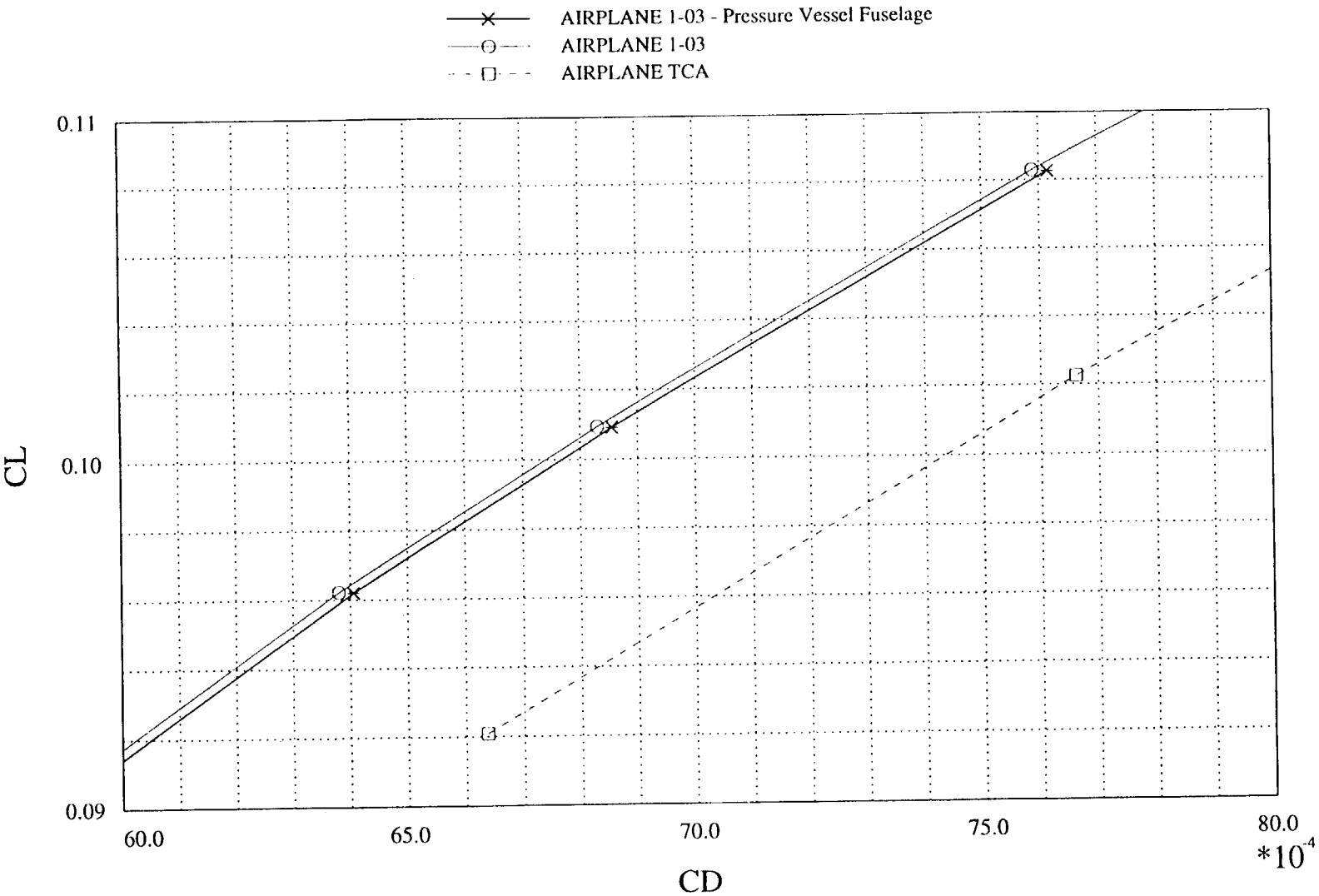

Full Length vs Truncated fuselage - Wing/Body/Nacelle/Diverter

All calculations shown in the previous figures have been for a full length fuselage since it was decided among the organizations to compare new configurations from the different HSR design teams with a full fuselage. However, the fuselage must be truncated fairly close to the wing for the wind tunnel model since a sting mount will be used with an internal strain gauge balance. It is interesting that the drag increment between the TCA baseline and Ames 1-03 configurations is greater for the truncated body. This indicates that a wave drag penalty is associated with the aft section of the fuselage. The fuselage design optimization was carried out with the full length fuselage, however, the forward fuselage was more heavily optimized since it affects the downwash over the entire wing, whereas the aft portion has a more limited effect.

Whole vs Truncated Fuselage Computations, Wing/Body/Nacelle/Diverter

M=2.4, no internal or base nacelle forces

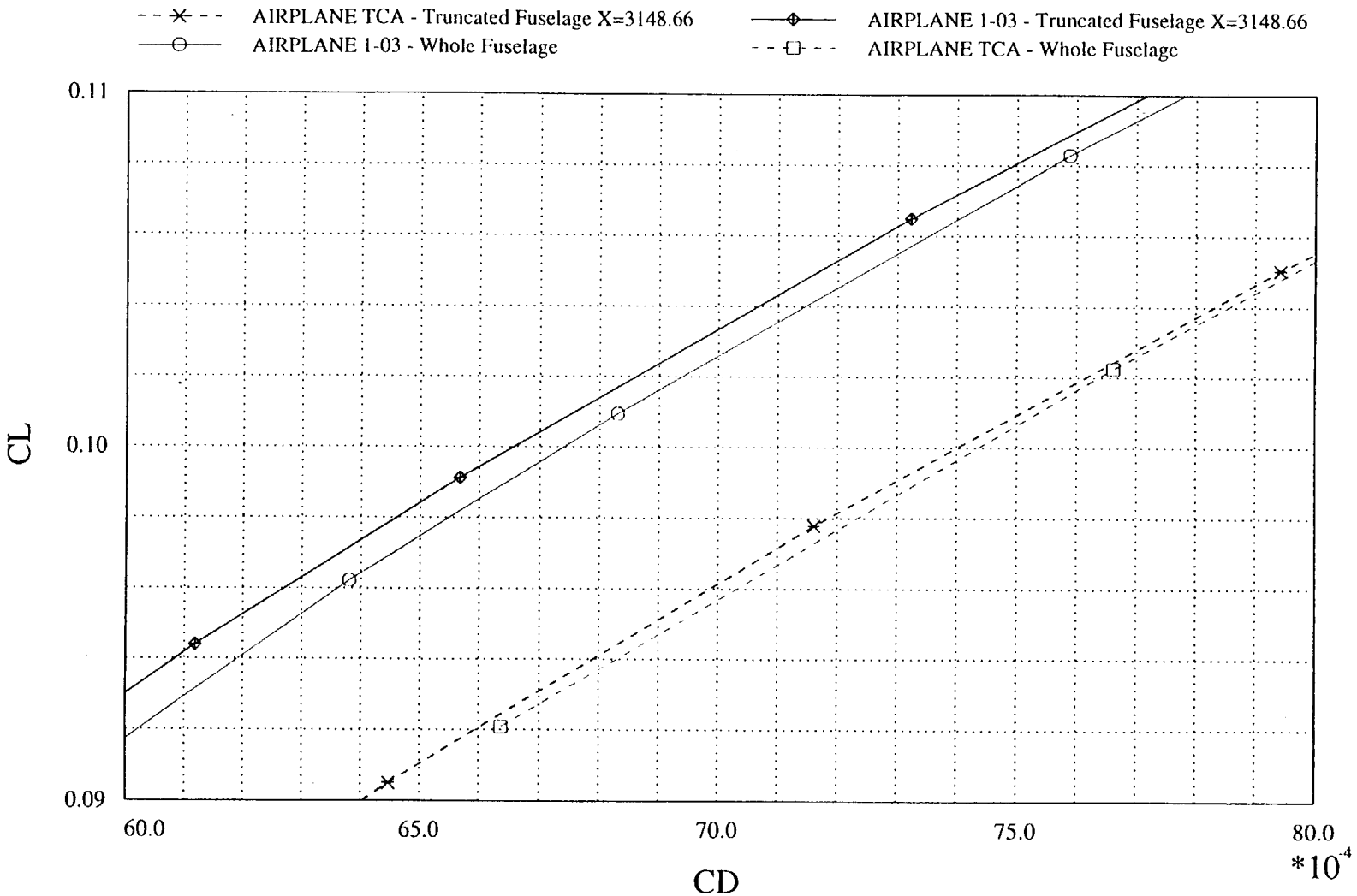

Euler vs. Navier-Stokes - Wing/Body/Nacelle/Diverter - Lift Curves

The lift curves for the baseline and Ames optimized TCA configurations calculated by the Euler solver, AIRPLANE, and the Navier-Stokes code OVERFLOW are compared in this figure. The SYN87-MB results are not shown since they were shown to be nearly identical to the AIRPLANE computations. The lift curve slopes from the two codes appear identical at this scale but OVERFLOW predicts a slightly lower lift coefficient for a given angle of attack consistent with the effects of viscosity. A boundary layer displacement thickness usually causes a reduction in camber for positive lift coefficients on conventional airfoil sections since the boundary layer is usually thicker on the upper surface where the pressure gradients are more severe. The thicker upper surface boundary layer gives the camber reduction. This trend might not be true for supercritical airfoils where a large portion of the lift is carried on the lower surface near the trailing edge. Reliable Navier-Stokes calculations are always more difficult to achieve than Euler calculations because more factors must be considered when setting up the problem. For example, the choice of turbulence model can significantly affect the final result. Grid stretching and aspect ratio near the surface must be carefully controlled or the viscous effects will be erroneous. Volume grid density and local model component definition are also important in obtaining good flow field values. Despite these difficulties the lift curves correlate fairly well. However, lift is usually one of the easiest aerodynamic quantity to calculate.

Lift Curve Comparisons, Wing/Body/Nacelle/Diverter

M=2.4, no internal or base nacelle forces, entire fuselage

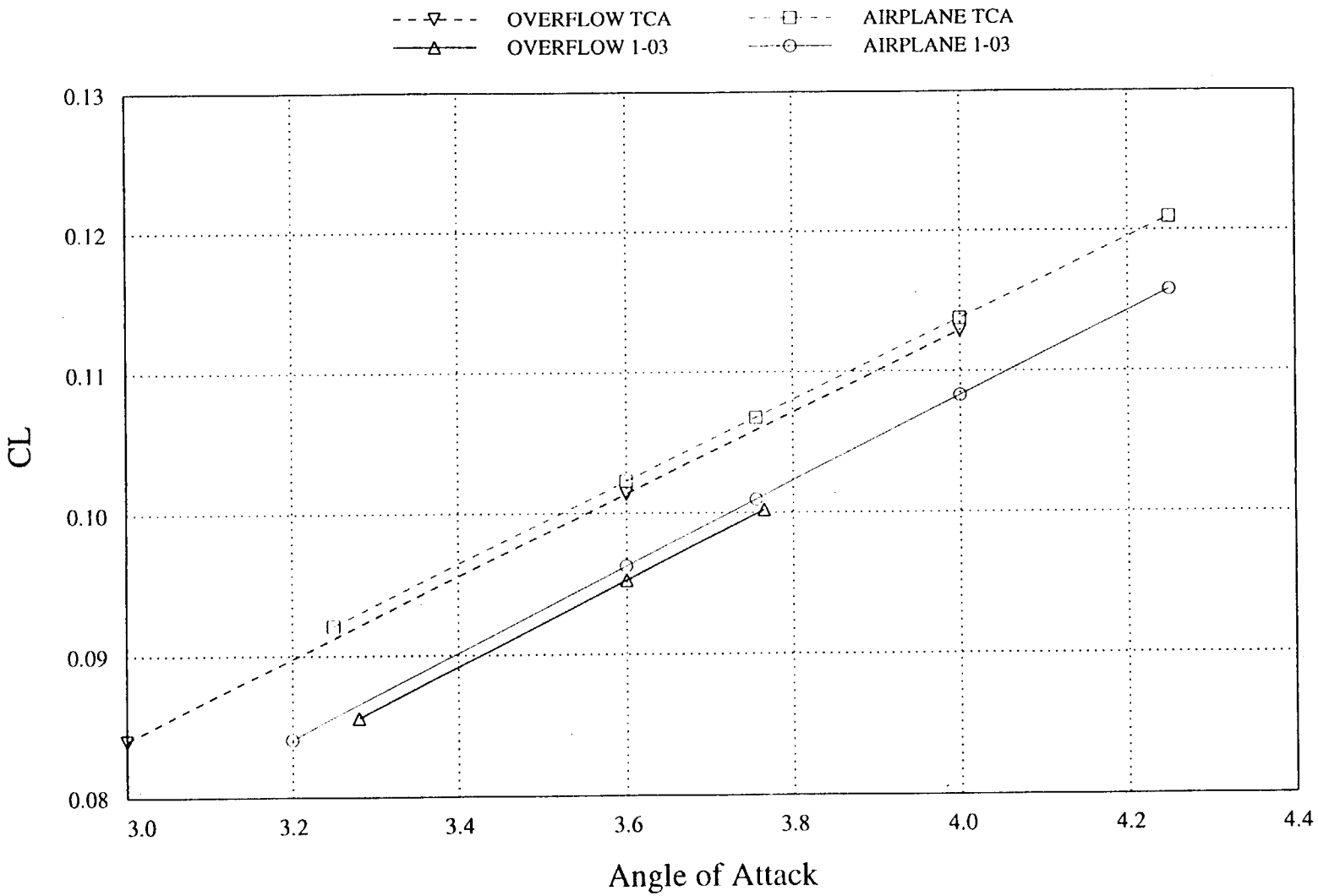

Navier-Stokes Drag Polars - Wing/Body/Nacelle/Diverter

Drag polars for the baseline and Ames optimized TCA configurations are shown in this figure. The results shown here should be considered somewhat preliminary since there are known surface deviations on the entire fuselage grid in the region of the wing. The maximum deviations are 1.6 inches (full scale) from the true surface. These surface problems originated in the grid generation process, and will be corrected within the next few months.

The drag increment shown in the figure between the baseline and Ames configuration is approximately 6.0 counts. This value seems a little low since AIRPLANE plus flat plate skin friction gives a 7.0 count improvement. The reason for the 1.0 count loss in improvement has not been identified.

OVERFLOW Computations, Wing/Body/Nacelle/Diverter

M=2.4, no internal or base nacelle forces, entire fuselage

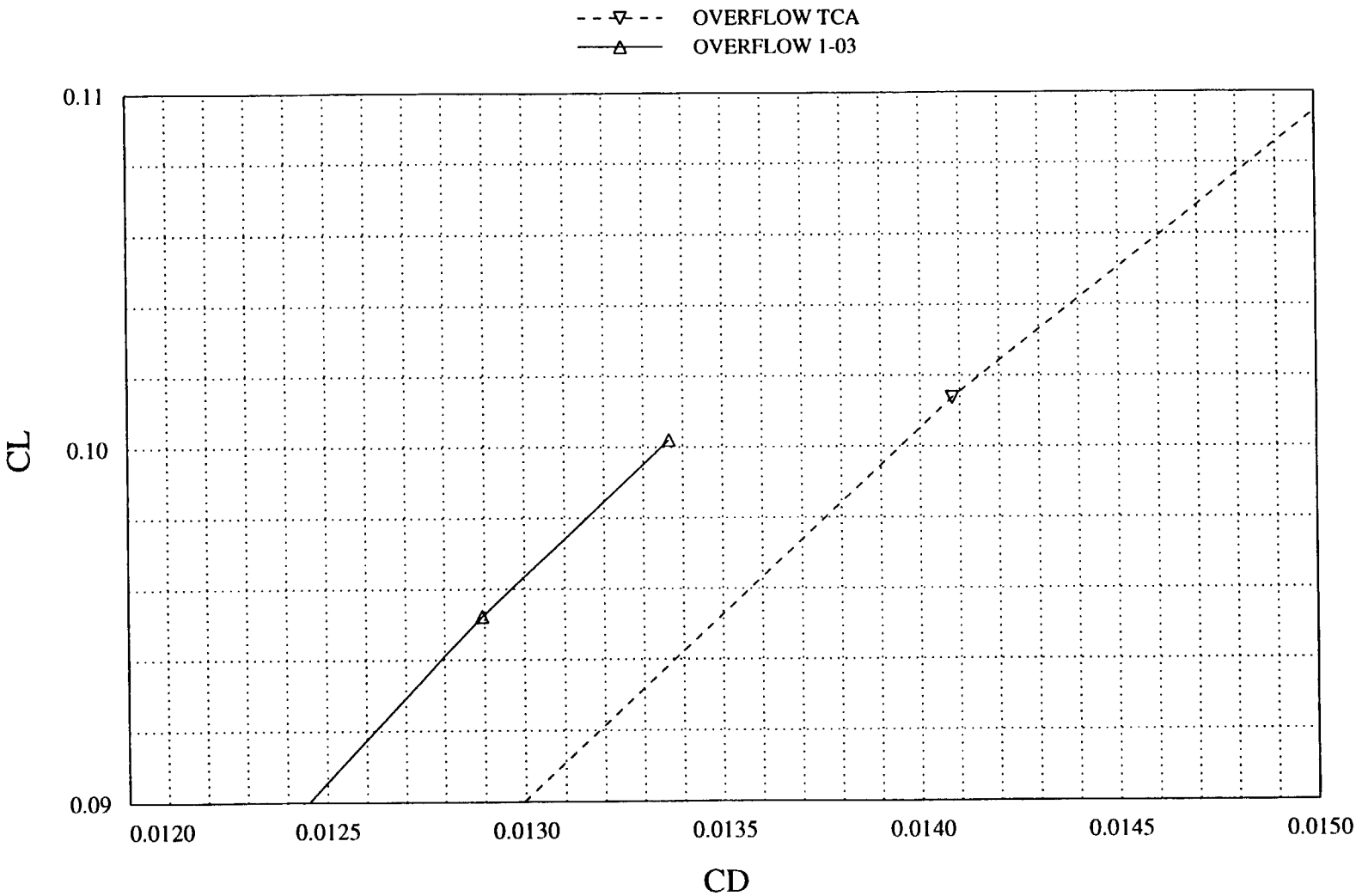

Pressure Drag Comparison - Wing/Body/Nacelle/Diverter

The pressure drag comparisons shown here indicate similar trends to those shown previously for the total drag for some of the codes used. The AIRPLANE pressure drag is approximately 1.5 counts higher than the value from SYN87-MB for both the TCA baseline and the Ames optimized configurations. The OVERFLOW pressure drag for the Ames 1-03 configuration lies midway between the SYN87-MB and AIRPLANE values. It is interesting that SYN87-MB and OVERFLOW give nearly the same value of pressure drag for the baseline but differ by approximately 0.7 counts for the optimized configuration. The pressure drag increase predicted by OVERFLOW for the 1-03 configuration may change after the fuselage surface grid is corrected. In spite of the differences in absolute value of pressure drag for the various codes the drag increments between the baseline and optimized configurations is the important parameter for design. The drag increment given by AIRPLANE and SYN87-MB is approximately 7.0 counts while the increment from OVERFLOW and SYN87-MB is 6.3.

Pressure Drag Comparisons, Wing/Body/Nacelle/Diverter

M=2.4, no internal or base nacelle forces, entire fuselage

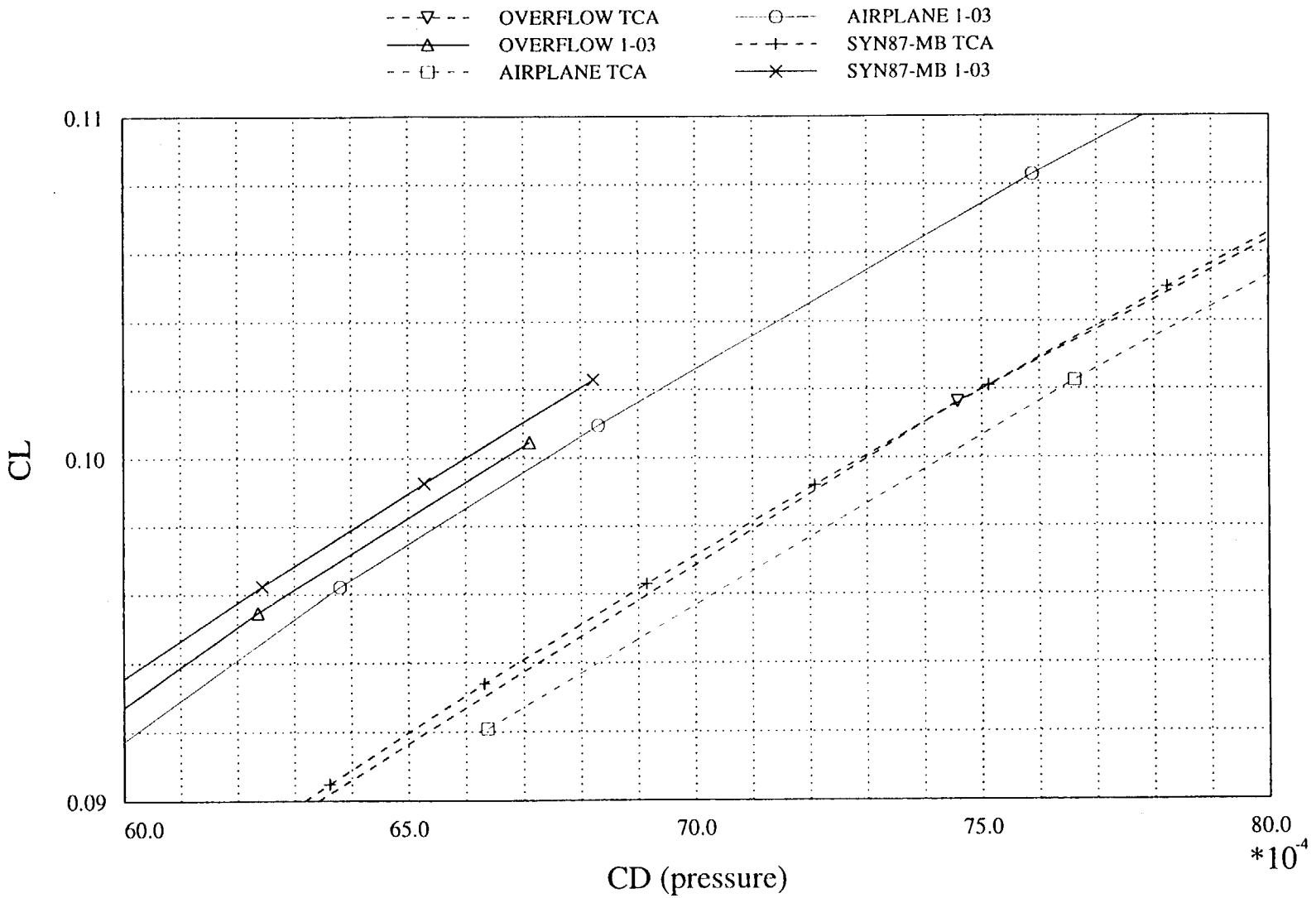

Viscous Drag Comparison - Wing/Body/Nacelle/Diverter

The viscous drag computed by Navier-Stokes codes is considered to be less reliable than the pressure drag because surface shear is sensitive to turbulence modeling and grid density and topology. This figure tends to support that hypothesis. The difference between flat plate and OVERFLOW skin friction drag is approximately 4.0 counts. Historically, flat plate skin friction has been considered to be correct to within 1.0 count for well-behaved attached flow. Note that the Navier-Stokes friction drag is less than the flat plate value indicating that regions of low energy boundary layer must exist on both configurations. Also note that the friction drag of the Ames configuration is 0.2 counts less than that of the baseline due to a smaller fuselage wetted area whereas the OVERFLOW friction drag for the Ames configuration is 0.3 counts higher than the baseline value.

Viscous Drag Comparisons, Wing/Body/Nacelle/Diverter

M=2.4, no internal or base nacelle forces, entire fuselage

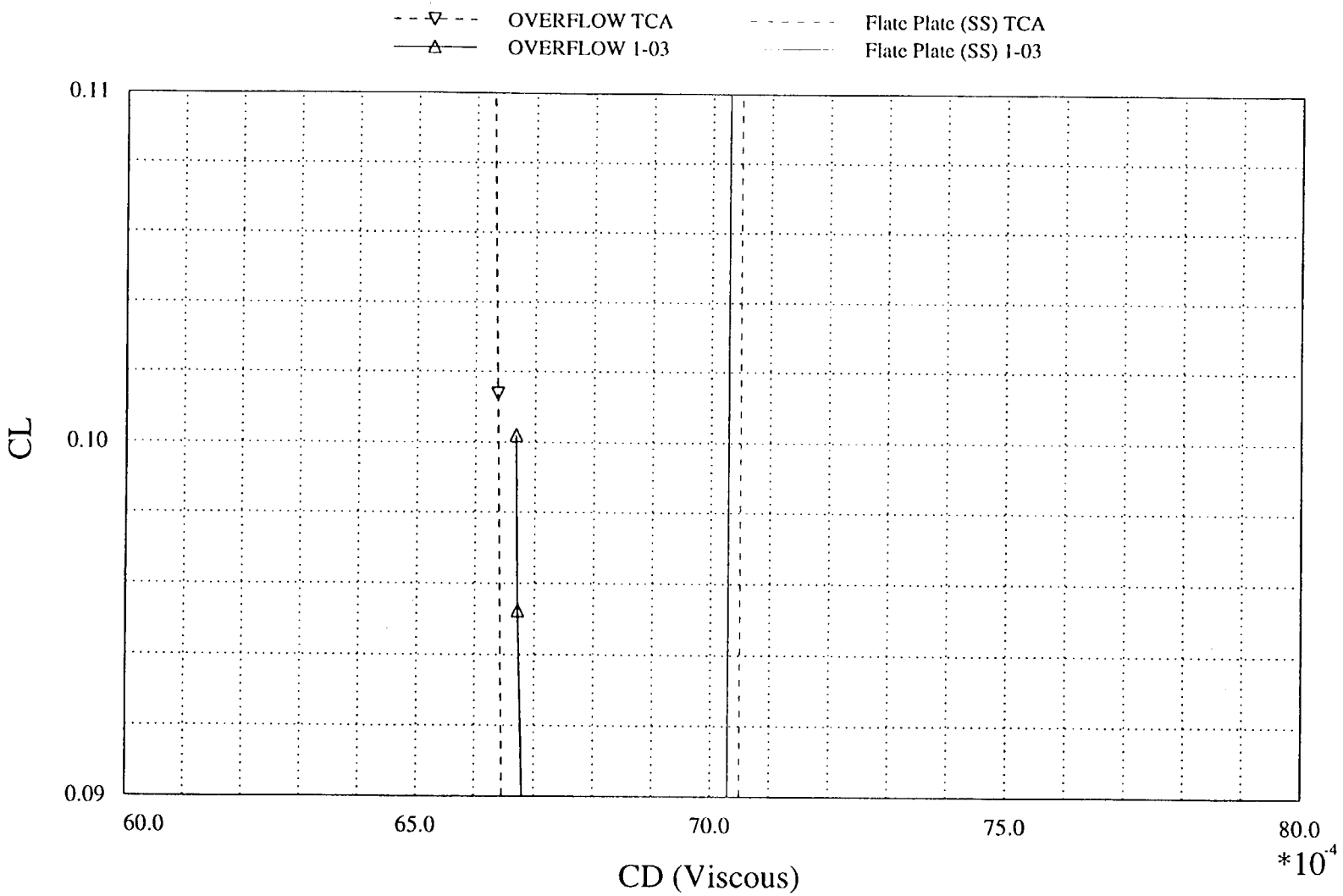

Surface Pressures - Baseline - AIRPLANE

The AIRPLANE lower surface grid and pressure contours in the region of the nacelles and diverters for the TCA baseline configuration are shown in this figure for the cruise condition. This represents one of the most refined tetrahedral surface grid ever used by AIRPLANE. The grid has a total of 824,229 grid points with 86,026 points on the surface. The grid about the nacelles is extremely dense, much denser than typically found on an Euler grid. This fine grid should accurately capture the abrupt changes in pressures caused by the presence of nacelles. The wing grid increases in density in this region also. The small portion of the wing leading edge shows the increased density of points in this region to accurately capture the low pressures generated by the blunt leading edge. Also note that the leading edge break accurately models the step from the rounded inboard sections to the sharp supersonic outboard panel. This very refined Euler solution and subsequent intermediate solutions using the same surface grid densities were used to provide the pseudo nacelle data used during optimization.

A strong shock wave impingement on the side of the inboard nacelle emanating from the outboard nacelle/diverter is seen in the figure. Strong shock pressures from both nacelles and diverters can also be seen on the lower surface of the wing. These are the pressures that the optimization code seeks to reduce and use to improve the performance of the configuration.

Baseline TCA: AIRPLANE Solution
Mach 2.4 $\alpha = 3.6$

Surface Pressures - Ames 1-03 - AIRPLANE

This figure shows a similar view of the surface pressures on the lower surface of the wing and on the nacelles and diverters for the Ames 1-03 optimized configuration as shown in the previous figure for the baseline configuration. This grid was obtained by use of a re-gridding scheme that projects the points from a previous mesh onto the new surface. This method preserves the surface grid which is necessary for accurate performance increments. It also greatly reduces the time required to generate new AIRPLANE meshes.

The strong shock pressures observed in the last figure are nearly absent from this figure showing that the optimization code has been very successful in integrating the nacelles and diverters into the wing lower surface. The integration of the nacelles and diverters into the wing takes two forms. First the high pressures are partially canceled by expansion zones created by recontouring the lower surface of the wing immediately upstream of the nacelles and diverters; and second the optimization code creates aft-facing slopes on the wing lower surface for the remaining high pressures to act on thereby producing a component of thrust to reduce the drag and increase the lift/drag ratio.

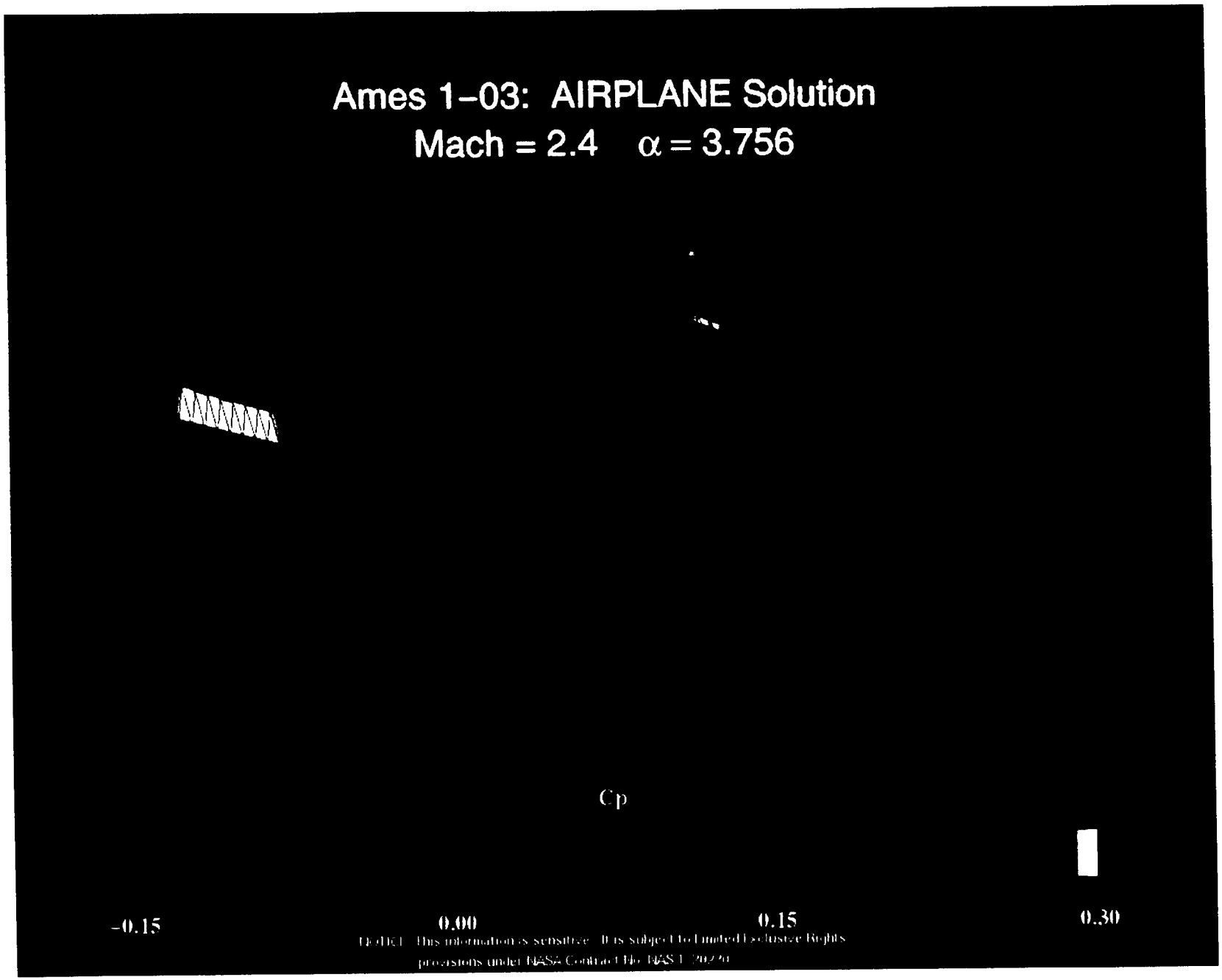

Surface Pressures - Baseline TCA - AIRPLANE

AIRPLANE surface pressures for the entire baseline lower surface of the wing are shown in this figure. The high pressure regions on the wing surface associated with the nacelles and diverters are clearly displayed here. The high pressures along the leading edge of the outboard wing are also visible in the figure. These leading edge pressures are associated with an oblique shock lying along this supersonic edge that is produced by the oblique turning angle of the flow with the sharp leading edge. The angle of attack is therefore greater than the negative half angle of the leading edge causing the flow to turn into itself and produce an oblique shock.

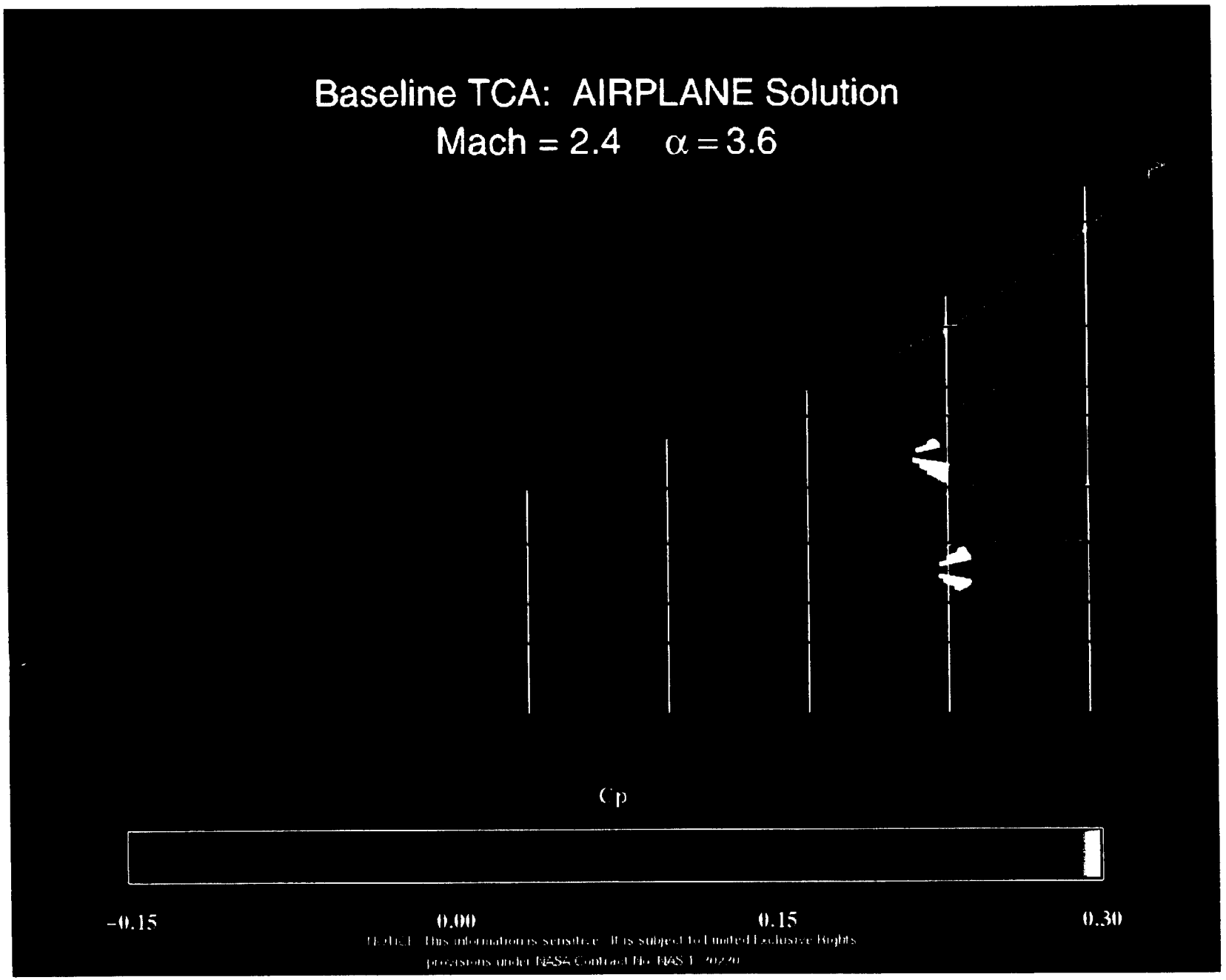

Surface Pressures - Ames 1-03 - AIRPLANE

The AIRPLANE lower surface pressures for the Ames 1-03 are shown using the same color bar range as the baseline in the previous figure for ease of comparison. These computations were obtained very near the design lift coefficient of 0.1 for a valid comparison with the previous figure. The high pressures seen on the baseline wing lower surface are considerably weaker on the Ames optimized configuration. The reasons for the lower pressures have been discussed extensively previously and will not be repeated here. The primarily purpose for this figure is for reference during detailed examination of the pressure distributions in subsequent figures.

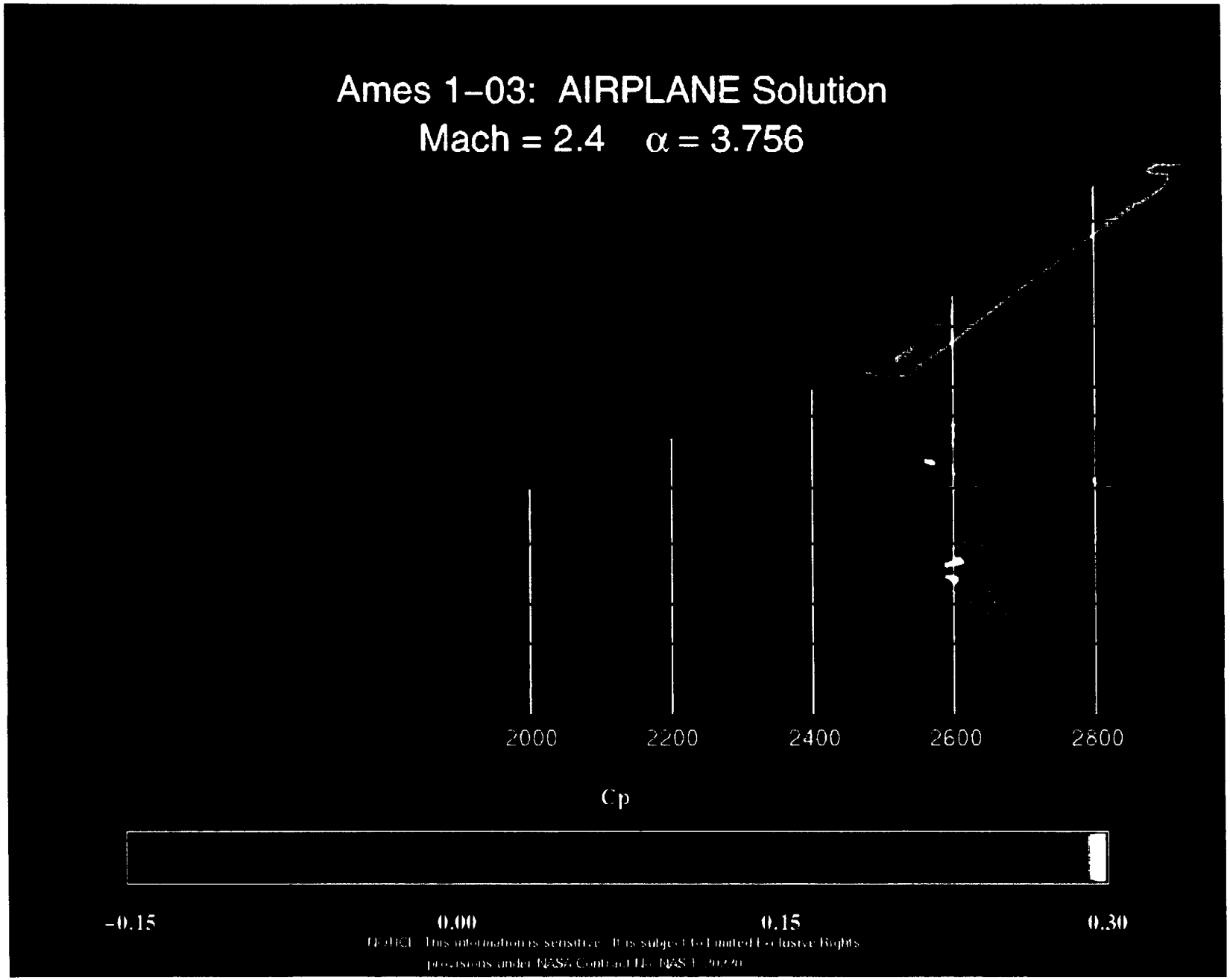

Surface Pressures - Ames 1-03 - OVERFLOW

The pressures for the wing lower surface predicted by OVERFLOW for the Ames optimized configuration are again shown using the same color bar range as the previous figures. The pressures resulting from solutions of the viscous and inviscid equations are similar, in particular, the region of high pressures associated with the nacelles and diverters are alike from the two solutions but the pressures calculated by OVERFLOW are slightly lower with greater shock angle because of the effects of viscosity. Viscosity tends to smear shock waves and cause the edges of regions with strong pressure gradients to appear less well defined. The reflective shock pattern between the nacelles is less pronounced for the OVERFLOW computation. The grid used 5.2 million grid points, with approximately 85,000 surface points. The number of surface grid points is slightly less than the number used for the AIRPLANE solutions. The pressure distributions will next be compared in detail for several of the chordwise and spanwise positions shown in the figure.

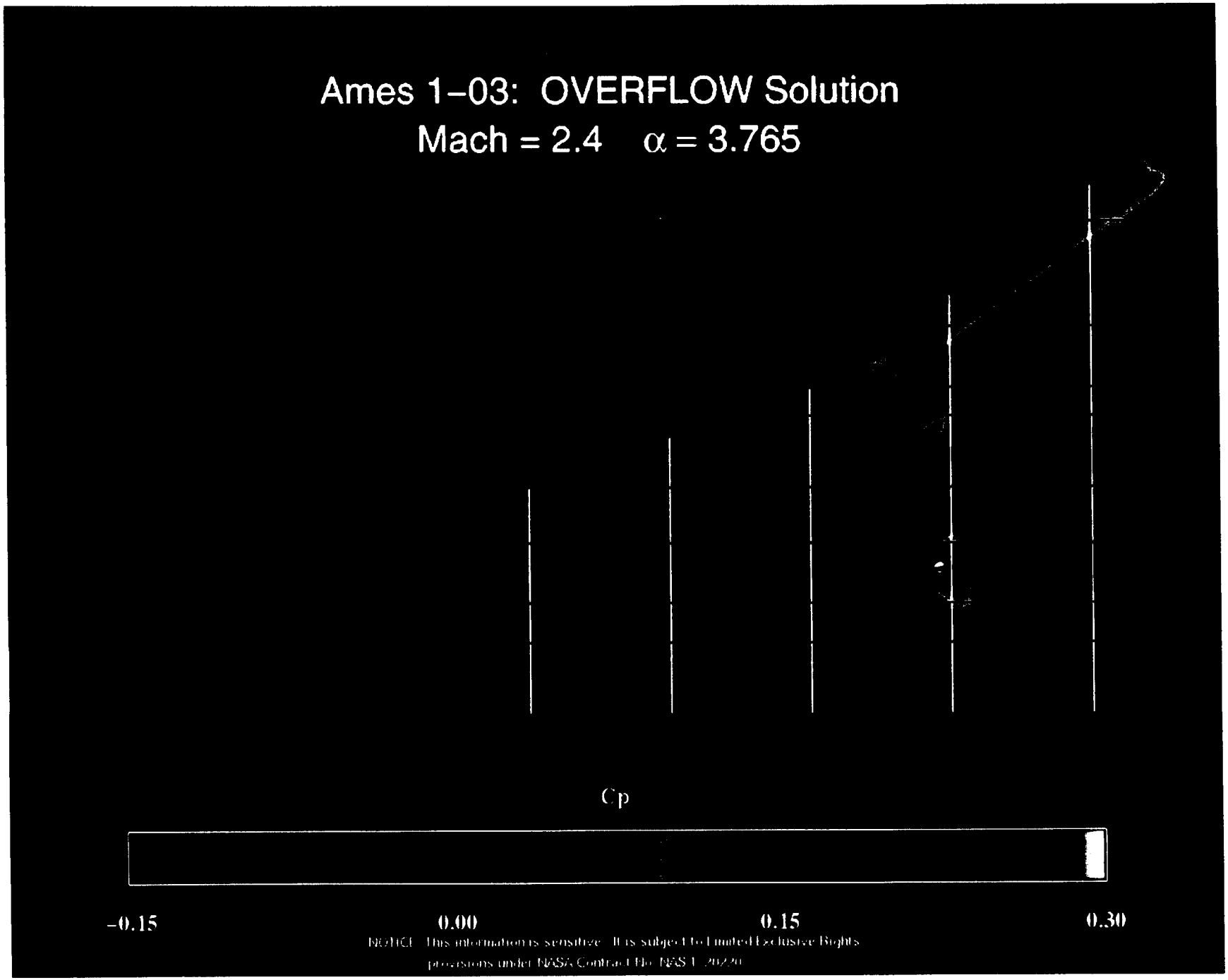
Ames 1-03: OVERFLOW Solution
Mach = 2.4 α = 3.765
Cp
-0.15
0.00
0.15
0.30
NOTICE This information is sensitive. It is subject to Limited Exclusive Rights
provisions under NASA Contract No. NAS1-20220

Pressure Distributions - Ames 1-03 - Wing/Body/Nacelle/Diverter (Z=158.256)

Chordwise pressure distributions for the Ames 1-03 configuration at a span station of 158.256 calculated by the three analysis codes used during the design cycle are shown in this figure. The wing section at this span station is shown without scaling and with the vertical dimension magnified 5 times at the bottom of the figure. AIRPLANE and SYN87-MB give similar upper surface pressures while OVERFLOW predicts a stronger pressure gradient near the leading edge. AIRPLANE and OVERFLOW predict similar lower surface waviness upstream from the nacelle/diverter pressures whereas SYN87-MB predicts less waviness. This waviness in not captured well with SYN87-MB because the grid is coarse in a region aft of the leading edge and upstream of the nacelles. The waviness is attributed to the leading edge radius and leading edge spar depth constraints. The optimization code has found that reducing the thickness between these constraints is beneficial.

Stronger nacelle/diverter shock pressures are predicted by the two Euler codes than by the Navier-Stokes code. The weaker inboard nacelle/diverter shock strength from OVERFLOW is a result of the diverter being buried in the boundary layer on the lower surface of the wing and hence subjected to lower Mach numbers. These differences indicate that it might be desirable to perform the SYN87-SB design with Navier-Stokes pressures superimposed on the wing lower surface rather than Euler pressures. It seems safe to say that the resulting lower surface expansion "bump" upstream of the nacelle/diverter would have a somewhat different shape due to the weaker Navier-Stokes pressures. The lower surface contour near the nacelle/diverter including the aft-facing slope is visible in the expanded wing section view. It appears that the aft-facing surface would be slightly farther forward with a smaller slope if the Navier-Stokes pressures had been used in the design.

Ames 1-03 Wing/Body/Nacelle/Diverter Solutions

M = 2.4, CL = 0.1

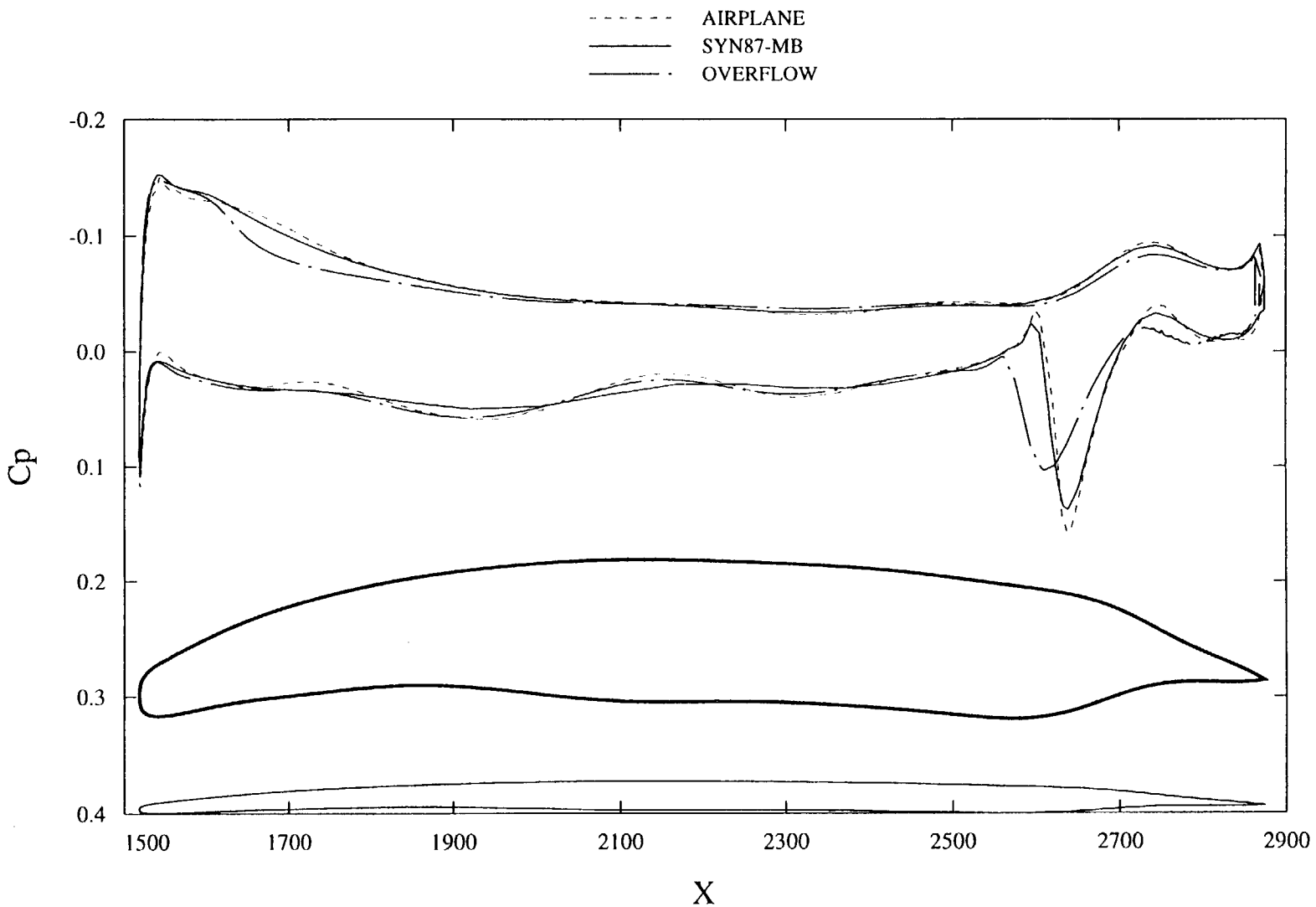

Z = 158.256

Pressure Distributions - Ames 1-03 - Wing/Body/Nacelle/Diverter (Z=322.369)

Surface pressure distributions at a span station of 322.369 inches are shown in this figure. Results from the three analysis codes are again compared. Differences in upper surface pressures from the three codes are somewhat greater at this station than at the previous station but the correlation is still considered good. Again the two Euler codes give similar nacelle/diverter shock positions and strengths while the Navier-Stokes code predicts a more forward position with lower strength for the reasons discussed with the last figure. This station is between the nacelles in closer proximity to the outboard nacelle (the span stations are marked with their associated spanwise positions in the previously shown figure titled "AIRPLANE lower surface Cp contours"). The inviscid solution shows two lower surface shocks are present. The forward shock emanates from the outboard nacelle, whereas the aft shock results from the inboard nacelle shock combined with the reflection shock off the outboard and inboard nacelle. The AIRPLANE solution shows a slight distinction between the two shocks, whereas the SYN87-MB solution shows a coalescence of the two into one shock.

Note that the aft-facing surface on the lower surface associated with the nacelle/diverter pressures is farther upstream and has a more gradual slope consistent with the position and strength of the nacelle/diverter shocks. The surface waviness can again be correlated with pressure waviness. The constraint positions are fairly obvious in the expanded view of the wing section. In particular, the effects of the leading edge thickness/radius constraints and the spar depth constraints are apparent.

Ames 1-03 Wing/Body/Nacelle/Diverter Solutions

M = 2.4, CL = 0.1

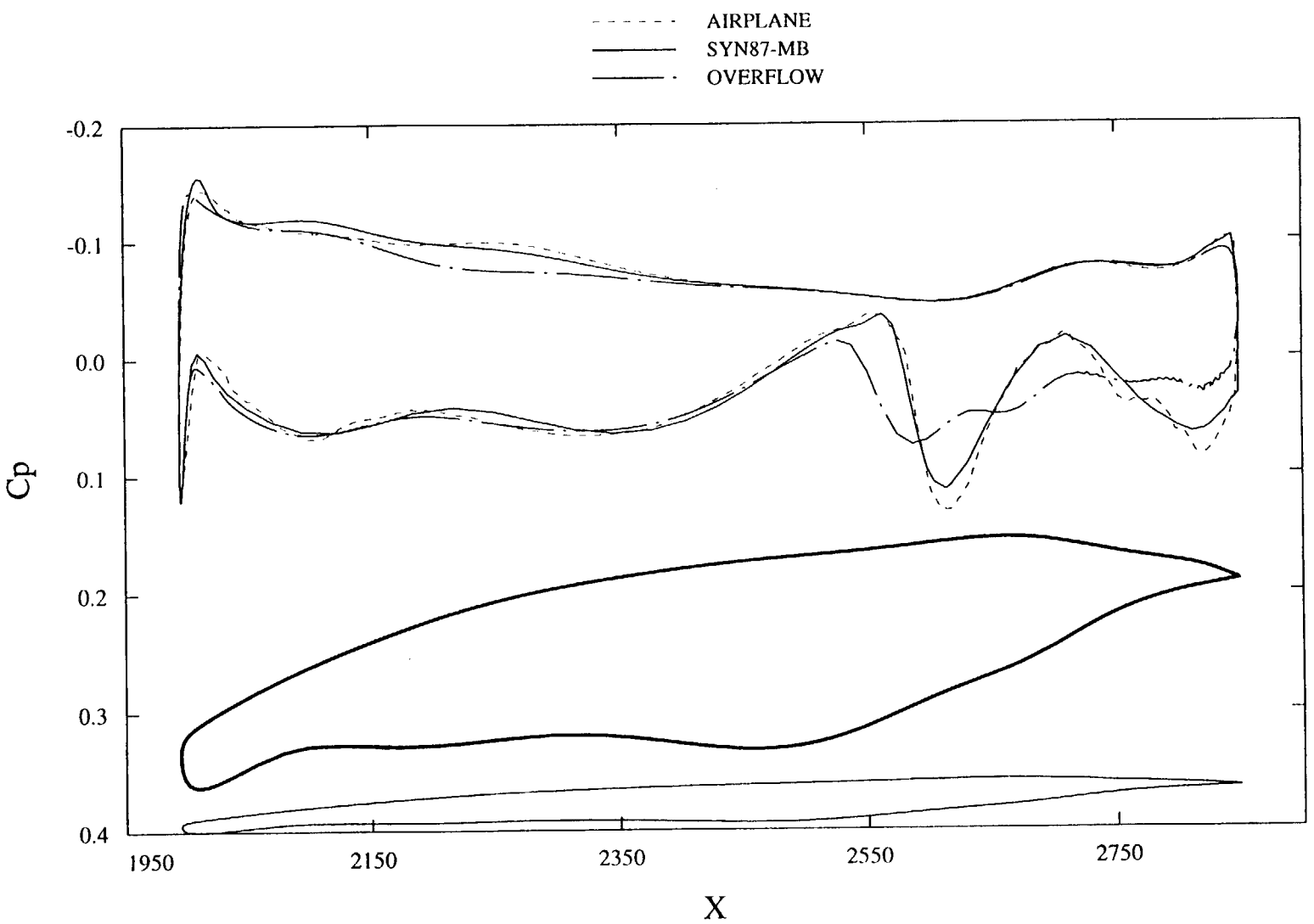

Z = 322.369

Pressure Distributions - Ames 1-03 - Wing/Body/Nacelle/Diverter (Z=464)

Surface pressure distributions at a span station outboard of most of the influence of the outboard nacelle/diverter and fairly near the planform break are shown here (Z=464). There appears to be a hint of the nacelle/diverter effect in the lower surface pressures just past mid-chord. The difference in the position of the nacelle effect between the Euler and Navier-Stokes solutions is greater at this station than at the two previous stations, because of the larger distance from the origin of the shock. The wing section at this station appears to be a little smoother than at the previous stations but the pressure distributions exhibit some waviness. The correlation between the three codes is quite good at this station. In particular, the two Euler codes give very similar results.

Ames 1-03 Wing/Body/Nacelle/Diverter Solutions

M = 2.4, CL = 0.1

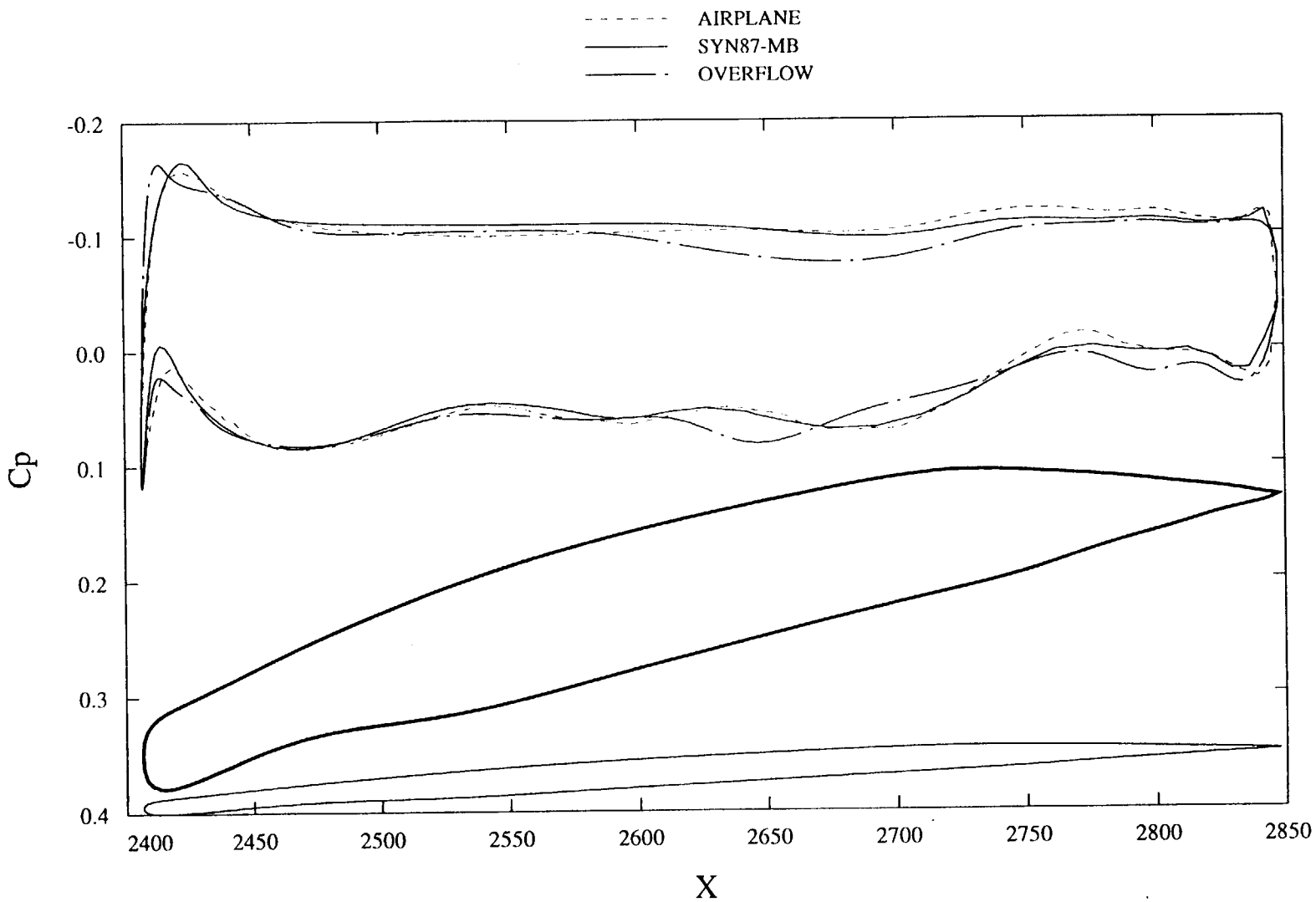

Z = 464.170

Pressure Distributions - Ames 1-03 - Wing/Body/Nacelle/Diverter (Z=700)

Surface pressures on the outboard wing panel approximately 87 inches inboard from the tip (Z=700) are shown in this figure. Again the correlation is good among the three codes with two interesting differences. OVERFLOW predicts a much higher pressure coefficient at the leading edge than the two Euler codes and AIRPLANE gives trailing edge pressures that are more divergent than SYN87-MB and OVERFLOW. Note that some waviness still exists for this sharp-edged section indicating that the optimization code attempted to reduce the thickness as much as possible without violating constraints. Thickness reduction for this supersonic section is particularly important. Spar thickness constraints can be seen in the expanded view of the wing section at this station.

Ames 1-03 Wing/Body/Nacelle/Diverter Solutions

M = 2.4, CL = 0.1

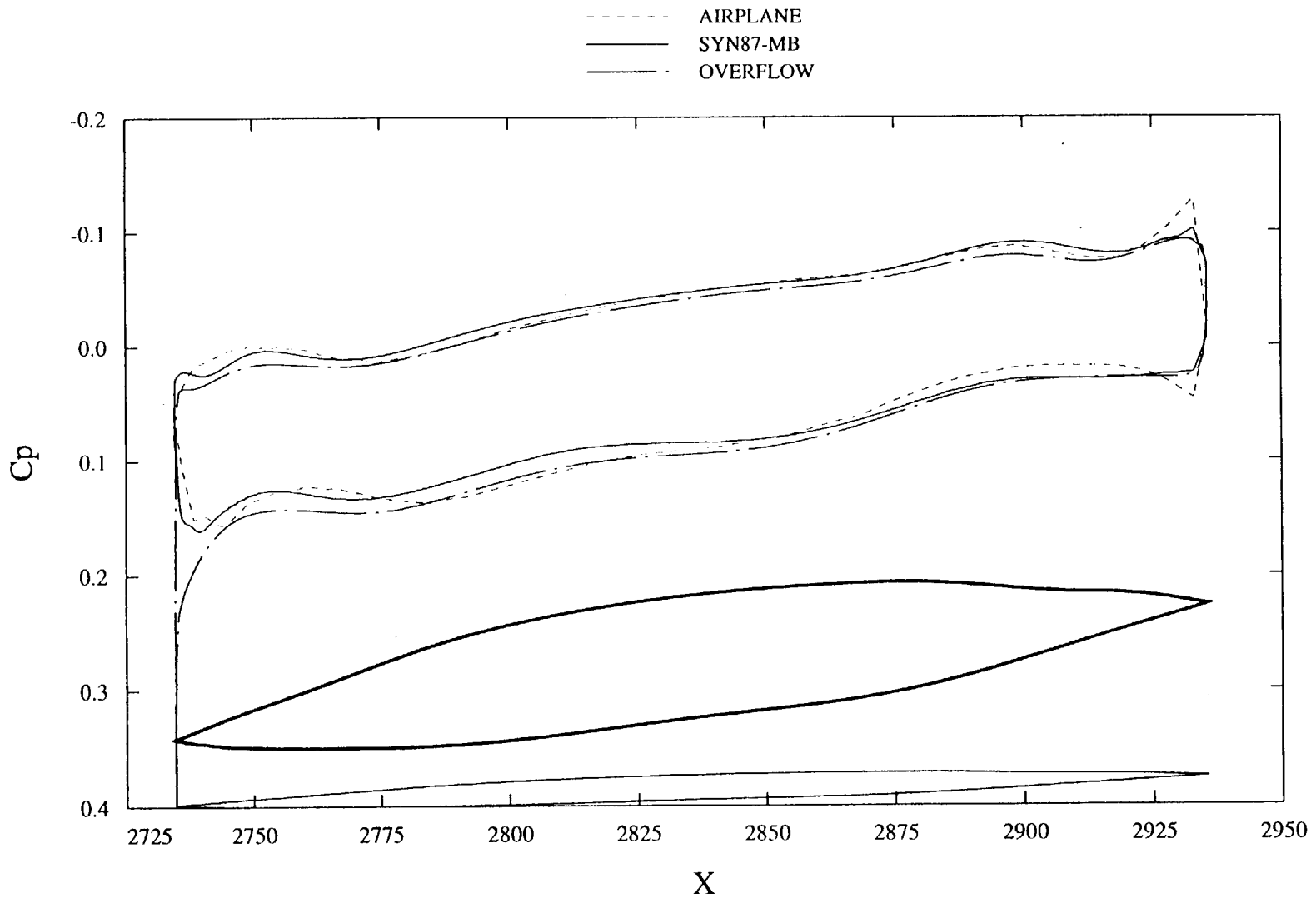

Z = 700.000

Pressure Distributions - Ames 1-03 - Wing/Body/Nacelle/Diverter (X=2200)

The spanwise pressure distribution for a fuselage station of 2200 inches is shown along with a non-scaled cross-sectional cut through the Ames 1-03 configuration in this figure. This station is upstream from the influence of the nacelles and diverters so the code correlation is quite good. SYN87-MB again indicates waves of slightly lower amplitude on the lower surface than either AIRPLANE or OVERFLOW owing to a coarse grid in this region. The leading edge pressure peaks on both the upper and lower surface are predicted to be a little lower by OVERFLOW than the two Euler codes. The lower pressure peak is related to the presence of a turbulent boundary layer on the wing surface which reduces the curvature and hence the flow acceleration near the leading edge. The geometry appears fairly smooth at the station except near the leading edge where the thickness between the leading edge bluntness and leading edge spar has been reduced to improve performance.

Ames 1-03 Wing/Body/Nacelle/Diverter Solutions

M = 2.4, CL = 0.1

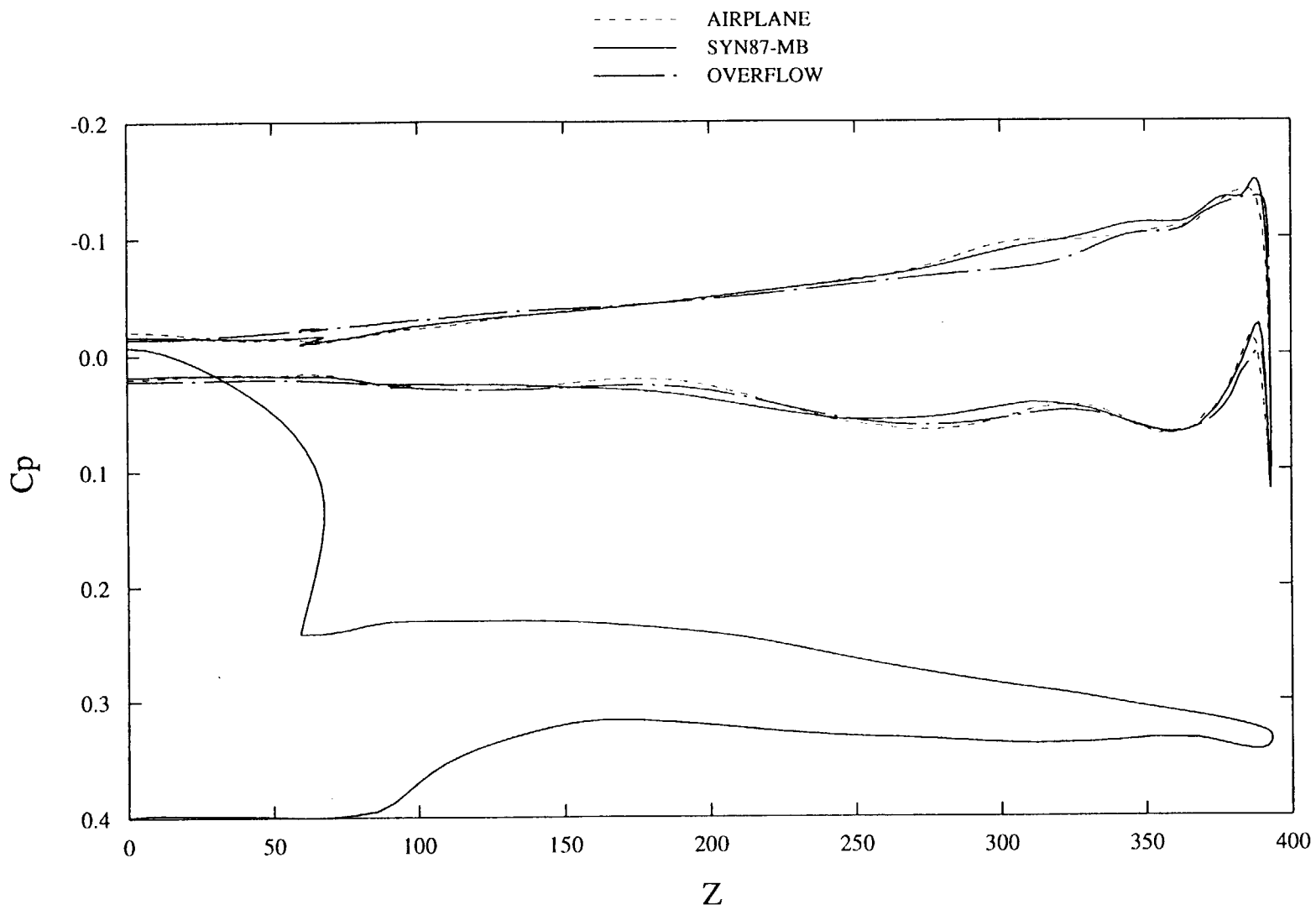

X = 2200.0

Pressure Distributions - Ames 1-03 - Wing/Body/Nacelle/Diverter (X=2600)

The spanwise pressure distributions calculated by the Euler and Navier-Stokes codes show fairly large differences along the lower surface of the Ames 1-03 configuration at fuselage station 2600 as observed in this figure. The effect of viscosity observed in the chordwise cuts is again seen here. The shock waves have lower strength and a larger shock angle that, in this view, are seen to be spread further from the spanwise position of the nacelles in the Navier-Stokes solution than in the Euler. The outboard nacelle/diverter shock is nearly absent from the Navier-Stokes solution since the outboard nacelle is further forward on the wing than the inboard nacelle. The upper surface pressure distributions from the three codes correlate well over the entire geometric cut showing that where the pressure gradients are weak Euler and Navier-Stokes codes give similar solutions. The geometry appears a little more wavy at this station than in the previous figure due to the local contouring of the lower surface of the wing to accommodate the high pressures emanating from the nacelles and diverters.

Ames 1-03 Wing/Body/Nacelle/Diverter Solutions

M = 2.4, CL = 0.1

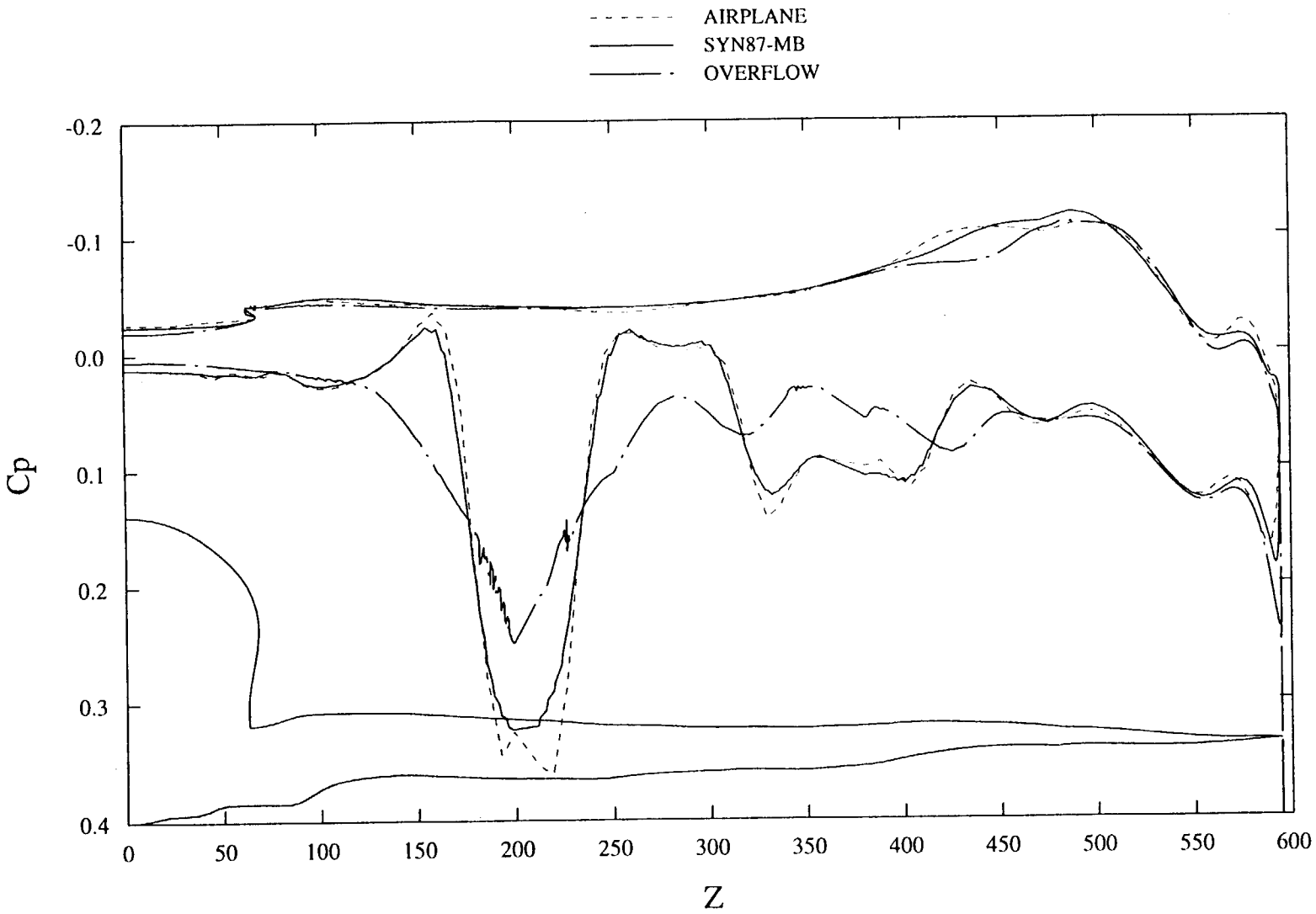

X = 2600.0

Predicted Drag Reduction - Wing/Body/Nacelle/Diverter

The final predicted drag reduction for the Ames 1-03 configuration relative to the TCA baseline configuration is summarized in this figure for the four CFD codes used during design. The largest drag reduction was calculated by SYN87-SB, the design code, for the configuration with the full length fuselage. This is considered to be the least reliable result because of the pseudo-nacelle/diverter effects used with this code. The Navier-Stokes code result may change slightly when the surfaces of the aft portion of the fuselage are more accurately modeled, but this effect should be small. The most trusted drag increment numbers shown in the figure were generated by the AIRPLANE solution. The AIRPLANE solutions for the truncated fuselage (TF) would have been of greatest interest if the configuration were to have been tested in the wind tunnel. It is interesting that the aft fuselage causes a 0.45 count increase in the configuration drag for the cruise condition. A possible explanation for this drag increase is the expansion field causing a suction force acting on an aft facing surface where the fuselage closes. Having identified this portion of the fuselage to have more drag than the baseline, it may be advantageous to optimize in this region further. The AIRPLANE solution for the configuration without the aerodynamic fairing at the side of the body near the wing root (the "pressure vessel" or P.V.) has 0.25 drag counts more than the configuration with the fairing.

W/B/N/D Performance Improvement
CL = 0.10

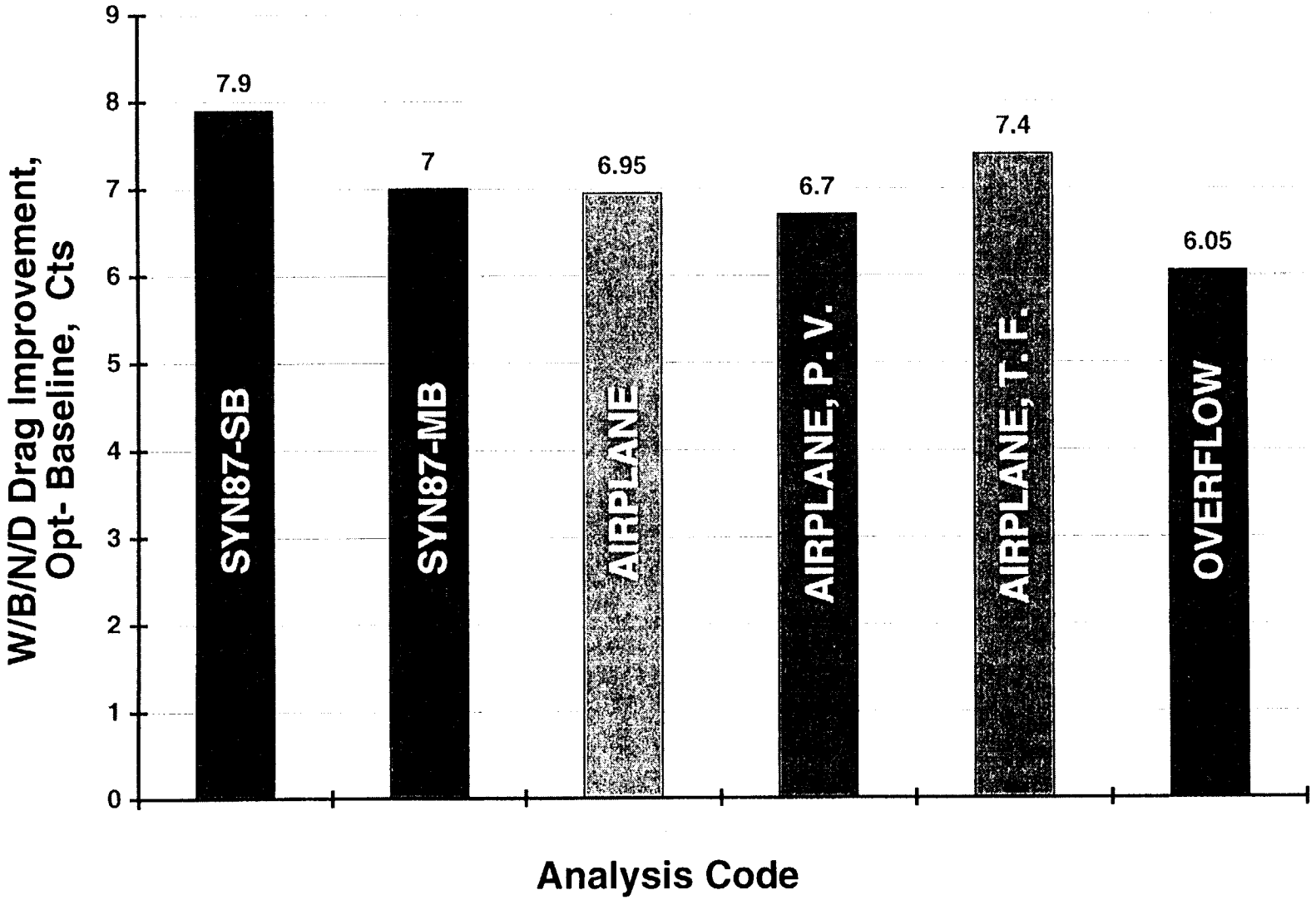

Predicted Drag Reduction - Wing/Body

The drag reductions calculated by the four CFD codes used for the Ames 1-03 and baseline wing/body configurations are approximately 50% less than for the configurations with the nacelles and diverters. This is a somewhat surprising result since the drag reductions predicted by CFD and measured in the wind tunnel for the Ames 704 and baseline Ref-H configurations were nearly the same with or without nacelles and diverters. The increased importance of including the nacelles and diverters in the optimization of the TCA configuration may be due to the larger size of the TCA nacelles and diverters compared with the Ref-H configuration. Note that the UPS Navier-Stokes code predicts the largest drag reduction when run in Euler mode of any code used. This may be due to a much finer grid for the UPS code. Chordwise pressure distributions calculated by the UPS code showed some fairly significant differences from those calculated by the other codes. These pressure distributions will not be shown here due to space and time limitations. The smallest drag reduction is calculated by the UPS code run in Navier-Stokes mode indicating some differences between flat plate skin friction drag and Navier-Stokes friction drag. As stated earlier, at this time more credence is placed on the flat plate skin friction drag for the reasons discussed. Note that SYN87-MB and AIRPLANE again correlate well.

W/B Performance Improvements @ CL = 0.10

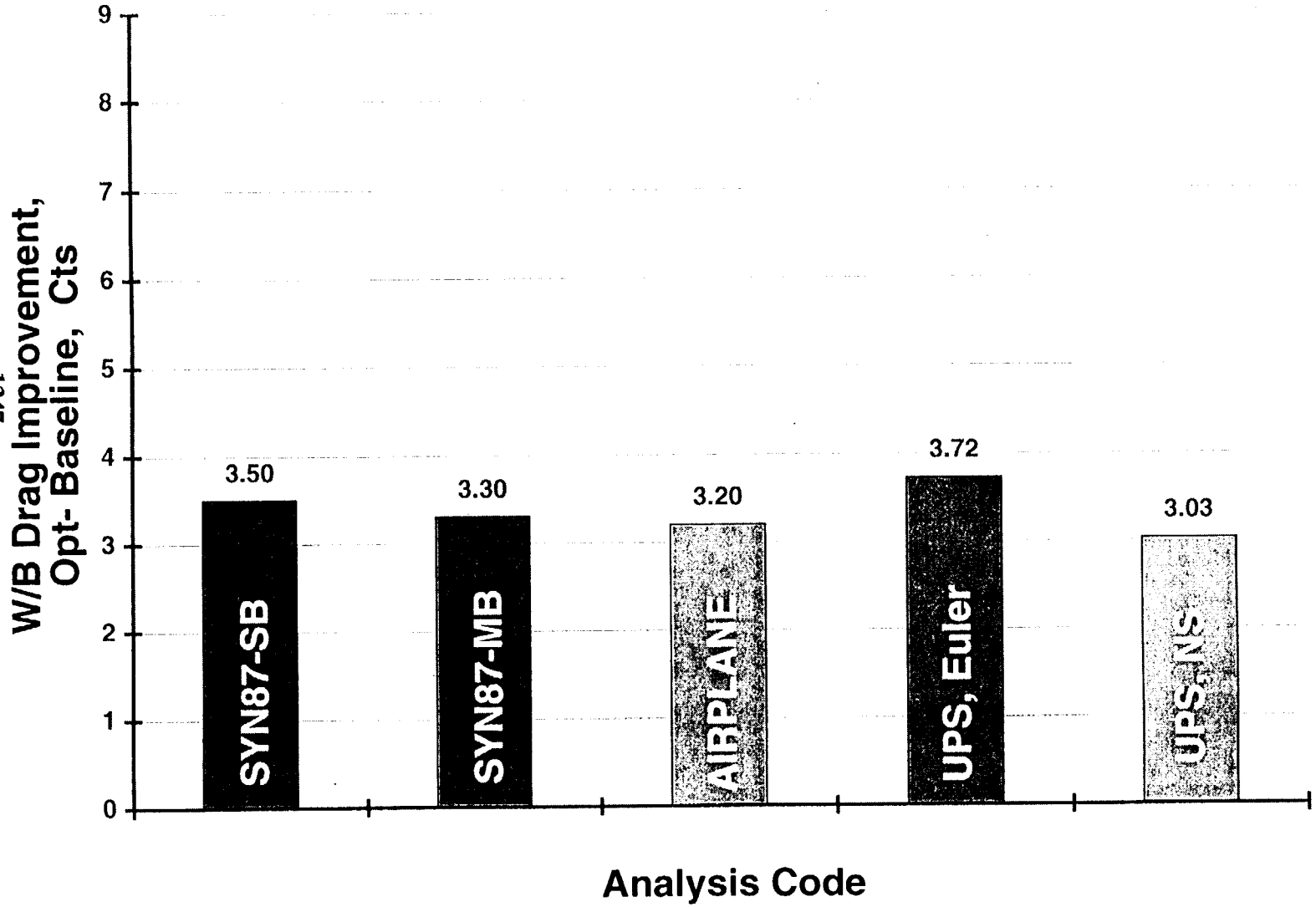

DEVELOPMENT AND VALIDATION OF A MULTI-BLOCK ADJOINT BASED DESIGN METHOD

James Reuther
RIACS/NASA Ames
Mark Rimlinger
Sterling Software/NASA Ames

February 25-27, 1997

DEVELOPMENT AND VALIDATION OF A MULTIBLOCK ADJOINT-BASED DESIGN METHOD

James Reuther, RIACS/High Speed Research Branch, NASA Ames
Mark Rimlinger, Sterling Software/High Speed Research Branch, NASA Ames

February 1997

This presentation describes the improvements made in the past year to the multiblock adjoint-based design tool, SYN87-MB, including extensions to handle multiple design points and to perform constrained optimization. Applications of SYN87-MB to a variety of complex configurations are also presented.

Outline

- Adjoint Based Aerodynamic Shape Design Overview
- Approach for Complex Geometries
- Multiblock Euler Analysis
- Analysis Results
- Multiblock Adjoint Based Design
- Geometry Specification and Constrained Optimization
- Multiblock Mesh Perturbations
- Parallel Implementation
- Design Results
- Conclusions and Future Work

Adjoint Based Optimization Overview

The development of a multiblock adjoint-based optimization method has been spurred by the desire for efficient treatment of increasingly complex geometries with an enhanced number of design variables and constraints.

Prior to the TCA design, efforts at employing aerodynamic shape optimization at NASA Ames have primarily been carried out using a single-block flow solver and a numerical optimization procedure utilizing the finite difference method to obtain gradients of the objective function. However it has become clear that the limitations inherent in this design method prevent its efficient use in the design of complex geometries. These limitations arise from two sources.

First, the reliance of the flow solver upon a single-block topology preclude design in the presence of all geometrical features, thus necessitating the development of approximations. In the context of the current HSR design, the inability to model the nacelle-diverter components required the creation of the pseudo-nacelle technique to impose nacelle pressures on the wing surface. Such approximations negatively impact the design effort by requiring a periodic re-analysis of the configuration outside of the design code in order to update surface pressures. Such re-analyses carry with them delays in the design cycle since the meshes for intermediate designs must be regenerated. While it is possible to build a level of automation in the grid generation procedure for geometries of similar planform, such re-analysis efforts may take from 3-5 days. Additionally, and perhaps much more detrimental, benefits obtained through optimization in the presence of approximations fail to capture fully the complexity of component interactions. Hence gains obtained in the design code fail to become realized when analyzed on the full configuration. Moreover, design improvements that arise from complex nacelle-diverter-wing interactions may be impossible to find with the current optimization technique.

A second limitation of the traditional design method concerns the use of finite difference methods to obtain gradient information. In a previous presentation, an adjoint method for the Ames single-block design tool (SYN87-SB) has been demonstrated to cut the cost of gradient calculations. The steady march toward increasing the complexity of the design geometry is allied with an increase in the required number of grid cells and a desire to augment the number of design variables. Thus traditional finite difference techniques, which require an additional flow solution for each design variable, begin to require a prohibitive amount of computational resources.

In order to surmount these barriers, a multiblock adjoint-based optimization procedure has been developed. In utilizing a flow solver capable of handling a multiblock topology, a degree of flexibility is introduced which permits increasingly complex geometries to be modeled directly in the design code, hence removing the need for approximations. Additionally, the use of an adjoint formulation whereby the design sensitivities for an arbitrary number of design variables are obtained with the equivalent of two flow calculations brings the cost of obtaining gradient information to an acceptable level. The computational costs in comparison with finite difference methods are further reduced since the adjoint solutions need not be highly converged to be useful.

Adjoint Based Optimization Overview

- Single-Block Design with Constraints is Slowed Primarily By the Use of Pseudo Nacelle Effects and Required Re-Analysis with Complete Configuration Methods
- By Using a Multiblock Method, Accurate Treatment of Nacelles/Diverters During Design Should Improve Nacelle Integration Performance and Remove Re-Analysis Overhead
- Traditional Finite Difference Gradient Methods, Computationally Expensive Even for Single Block Methods, become Unacceptable for Multiblock Meshes
- By Combining a Multiblock Methodology with an Adjoint Gradient Approach, Complete Configuration Design will Become Feasible Alternative to Current Single Block Approaches
- A Multiblock Adjoint Based Approach Naturally Extends to Design Methods that are Navier-Stokes Based

Approach For Complex Geometries

The benefits inherent to a multiblock adjoint-based design method arise from the development of four key areas: a multiblock flow solver, the use of an adjoint formulation, an efficient mesh perturbation scheme, and advantages associated with parallel computation.

First, the development of an accurate, efficent and robust multiblock flow solver to obtain solutions to the Euler equations was required. The previous flow solver used in the single-block design method (SYN87-SB) was enhanced to treat the modified mesh topology without losing any of the aforementioned attributes.

Secondly, the multiblock adjoint solver permits the inexpensive calculation of gradient information. Since the flow and adjoint solvers utilize the same routines to calculate solutions, the robustness of the adjoint solver was not negatively impacted by the switch to a multiblock strategy.

The third key to the multiblock implementation involves developing a mesh perturbation scheme capable of treating general moving meshes across block boundaries. The WARP3D procedure developed in the single-block method was reworked to update the multiblock meshes efficiently and automatically.

In spite of the large decrease in computational cost provided by an adjoint formulation, the aerodynamic optimization of a complete configuration still remains a formidable computational task. The advent of reliable and efficient parallel computers using distributed memory enables the design calculation of complete aircraft configurations to be treated with an acceptable turnaround time. Since the three components described above operate on a block-by-block basis, the full multiblock procedure readily lends itself to parallel implementation by using the natural domain decomposition along block boundaries.

The conversion from a single- to multiblock structure necessitates a change in the manner in which design variables and constraints are implemented. The current method utilizes a set of geometry entities representing the individual components in the geometry. Thus separate entities based upon the CAD definitions are created to represent the wing, fuselage, nacelles, and diverters. The design variables and constraints are applied to these underlying geometry entities in place of the mesh surface as was done in the single-block method.

Approach for Complex Geometries

- Use a **Multiblock Flow Solver** to Treat Complex Geometries
- Use a Complementary **Multiblock Adjoint Solver** to Obtain Inexpensive Gradients
- Use a **Multiblock Mesh Perturbation Scheme** to Treat General Moving Meshes
- Use the Natural **Domain Decomposition Along Block Boundaries** to Realize Parallel Speed-Ups
- Use a Set of **Geometry Entities** to Specify Design Variables and Impose Constraints

Multiblock Euler Flow Solver

The current optimization efforts employ the Euler equations to represent the flow-field. The following is a standard presentation of the Euler equations. The AIAA paper 97-0103 (Constrained Multipoint Aerodynamic Shape Optimization Using an Adjoint Formulation and Parallel Computers) and associated references give a complete treatment of the solution algorithm.

Multiblock Euler Flow Solver (FLO87-MB)

Define the **Euler equations** as

$$\frac{\partial w}{\partial t} + \frac{\partial f_i}{\partial x_i} = 0$$

where

$$w = \begin{Bmatrix} \rho \\ \rho u_1 \\ \rho u_2 \\ \rho u_3 \\ \rho E \end{Bmatrix} \quad f_i = \begin{Bmatrix} \rho u_i \\ \rho u_i u_1 + p\delta_{i1} \\ \rho u_i u_2 + p\delta_{i2} \\ \rho u_i u_3 + p\delta_{i3} \\ \rho u_i H \end{Bmatrix}.$$

Making a transformation to **general coordinates**, they become

$$\frac{\partial W}{\partial t} + \frac{\partial F_i}{\partial \xi_i} = 0 \qquad W = J \begin{Bmatrix} \rho \\ \rho u_1 \\ \rho u_2 \\ \rho u_3 \\ \rho E \end{Bmatrix} \quad F_i = J \begin{Bmatrix} \rho U_i \\ \rho U_i u_1 + p\frac{\partial \xi_i}{\partial x_1} \\ \rho U_i u_2 + p\frac{\partial \xi_i}{\partial x_2} \\ \rho U_i u_3 + p\frac{\partial \xi_i}{\partial x_3} \\ \rho U_i H \end{Bmatrix}.$$

Multiblock Euler Flow Solver, Continued

As mentioned above, the flow solver employed in the design code must satisfy the requirements of being accurate, efficient, and robust. The current flow solver is a multiblock extension of the single-block version of FLO87.

The general strategy in developing the multiblock flow solver is to construct and update a halo of cells around each block such that the flow solution inside each block is transparent to the block boundaries. This task requires establishing the size and location of halo cells adjacent to block boundaries, and loading the halo cell values with appropriate flow field data at the appropriate times. To accomplish this task, a two-level halo is constructed around each block. The requirement of this double halo results from the necessity of keeping a complete stencil of calculated fluxes entering and leaving each cell in the entire domain without regard to block boundaries. Since both the convective and the dissipative fluxes are calculated at the cell faces (boundaries of the control volumes), all six neighboring cells are necessary, thus requiring the existence of a single level halo for each block in the multiblock calculation. The dissipative fluxes are composed of a blend of first and third order differences corresponding to terms that mimic second and fourth derivatives of the flow quantities. This requires a second layer of halo cells at each block interface. Halo cells on the external boundary of the entire computational domain are constructed and updated by extrapolation and reflection. Coarse grids are computed in the usual fashion, by aggregating groups of eight cells and then repeating the above halo cell process. Once the halo configuration is set up for each block, standard methods for spatial discretization and time integration (including artificial dissipation, residual averaging, and multigridding) are employed to compute the flow solution within each individual block.

- Discretization and Time Stepping
  - Cell centered **finite volume** discretization
  - **Multi-stage Runge-Kutta**-like time marching
  - Blended **2nd** and **4th** order artificial viscosity
- Convergence Acceleration
  - Enthalpy damping
  - Implicit residual smoothing
  - **Multigridding**
- Block-to-Block Communication
  - **Double halo** (Allows complete convection and diffusion stencil)
  - Point-to-point match
  - Halo cells updated every stage (**No lagging at block boundaries**)
  - **Coarser meshes** in the **multigrid cycle** have the **same double halo** structure (Permits **proper multigrid convergence acceleration**)
- Multiblock Scheme is Well Suited to Parallelization

Supersonic Analysis of Three Optimized Designs

Throughout the recently concluded optimization efforts by NASA Ames on the TCA-6 geometry, the multiblock Euler flow solver (FLO87-MB) was successfully applied to the baseline and intermediate designs. The full configuration consisting of the wing, fuselage, nacelles, and diverters was modeled using a mesh with 180 blocks and 1.5 million cells. The drag increments predicted with FLO87-MB were consistent with the results from the AIRPLANE code.

Prior to the Cycle 2 Performance review, a cross-check of the designs provided by McDonnell Douglas and Boeing was performed.

Supersonic Analysis of Three Optimized Designs

- **Mesh**
  - Wing-Body-Nacelle-Diverter Geometry
  - 180 Blocks
  - 1.5 Million Cells
- **Quick Cross-Check Comparison of Three Designs**
  - TCA-6 Baseline Geometry
  - McDonnell Douglas Cycle 2
  - Boeing WB8wt
  - NASA Ames 1-03

Supersonic Analysis of Optimized Designs, Continued

The ability to provide such a rapid cross-check was made possible by both the advances in grid regeneration techniques for similar planforms and the efficiency of the FLO87-MB code in generating results rapidly on parallel machines.

The bulk of the cost in generating solutions with FLO87-MB continues to lie in the arena of grid generation. During the process of generating a design internal to Ames, flow solutions at design benchmarks were required to update surface pressures in the single-block code. Thus a method was developed in which an initial volume mesh, having been developed for the baseline geometry, was perturbed to reflect changes in surface geometry. The surface meshes for the modified design are generated by hand from the IGES definition using the Gridgen package developed by Pointwise, Inc. Then the mesh perturbation techniques developed for the design code are applied to the baseline volume mesh in the presence of the new surface meshes.

For a given design, a six hour investment of surface grid generation is required followed by the volume mesh perturbation which requires less than one minute of CPU time of an SGI. Work is currently under way to automate the surface mesh regeneration procedure in order to accelerate the reanalysis procedure further.

Having obtained a volume mesh for the modified design, flow solutions were obtained utilizing FLO87-MB on the IBM SP2 (babbage). For each configuration, five analysis points were calculated, each requireing 100 multigrid cycles. Utilizing 16 processors, 16 minutes of wall clock time was required for each analysis point which corresponded to a 95% linear speed up compared with the wall clock time on a single processor. Since the five design points were run concurrently on babbage, the complete drag polar could be obtained in less than half an hour.

- **Human Costs**
  - IGES Files Obtained Friday Jan 24
  - Solutions Completed Monday Jan 27
  - 6 Hours of Interactive Mesh Generation Time Per Configuration
  - Remeshing Will Be Completely Automatic in Six Months
- **Computational Costs**
  - Five Analysis Points Were Calculated for Each Configuration Using the IBM SP2 (Babbage)
  - Each Analysis was Run for 100 Multigrid Cycles
  - Using 16 Processors Each Analysis Used 16 Minutes of Wall Clock Time
  - Better Than 95% Linear Speed Up Was Demonstrated
  - Five Solutions Were Run Concurrently

Supersonic Analysis of Optimized Designs, Continued

MDC Upper Surface Iso-Cps

The following six figures represent iso-Cp contours of the upper and lower surfaces for the MDC, Boeing, and NASA Ames HSR Cycle 2 designs. Comparisons between designs are best seen when viewed all at once.

The McDonnell Douglas design represents the most conservative of the three designs obtained through repeated applications of surface smoothings at intermediate designs. The upper surface iso-Cp contours illustrate the smooth variation of surface pressure and does not deviate appreciably from the baseline. However, the upper surface shock has been moved toward the leading edge and is more clearly defined.

MDC Cycle2: SYN87-MB

Mach = 2.4 C_L = 0.1

Pressure Coefficient

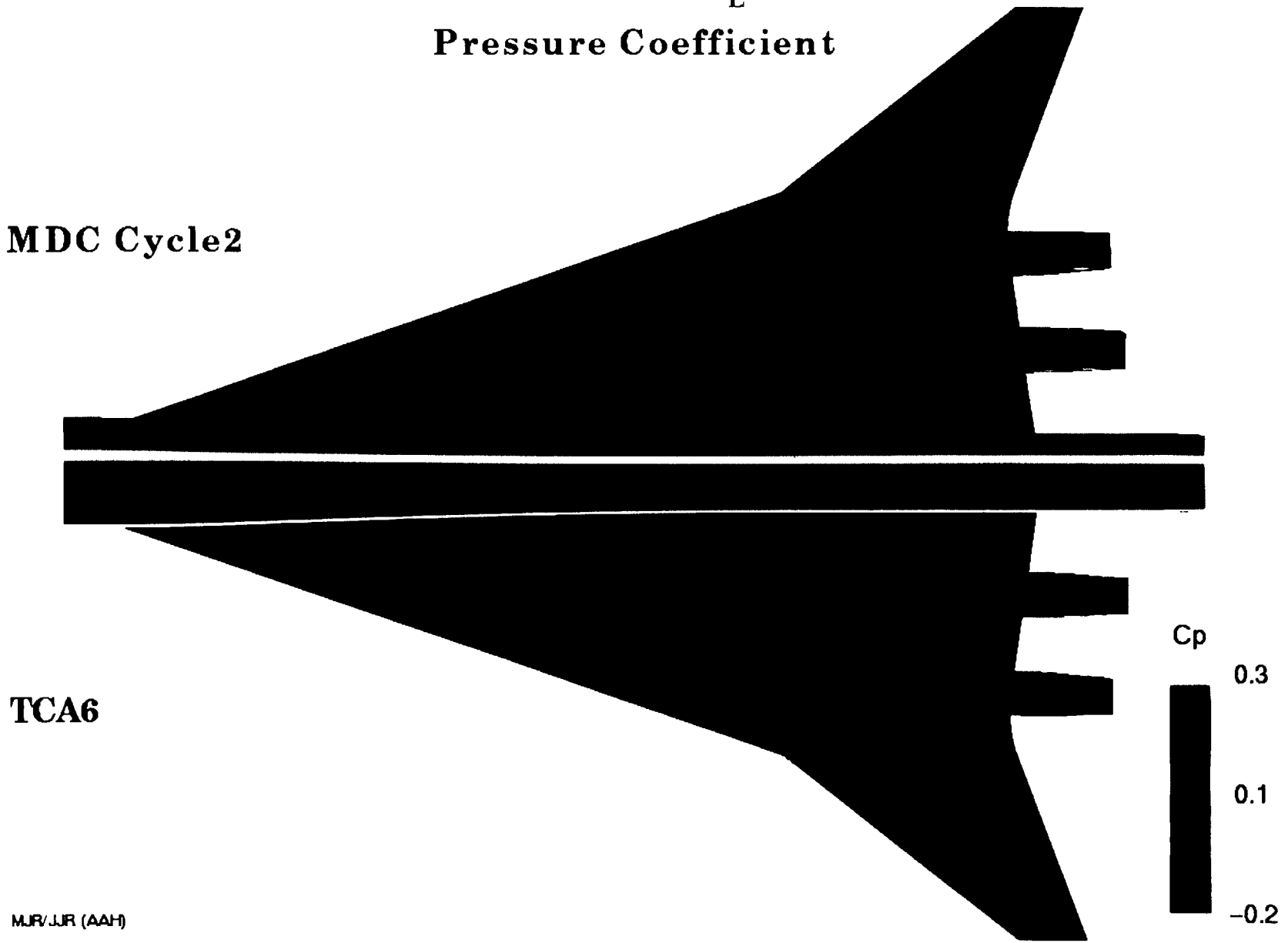

MJR/JJR (AAH)

Supersonic Analysis of Optimized Designs, Continued

MDC Lower Surface Iso-Cps

The lower surface iso-Cp contour plots for the MDC design continue to display the smoothness of their pressure contours. The severity of the shock interactions in the nacelle regions have been ameliorated slightly.

MDC Cycle2: SYN87-MB

Mach = 2.4 C_L = 0.1

Pressure Coefficient

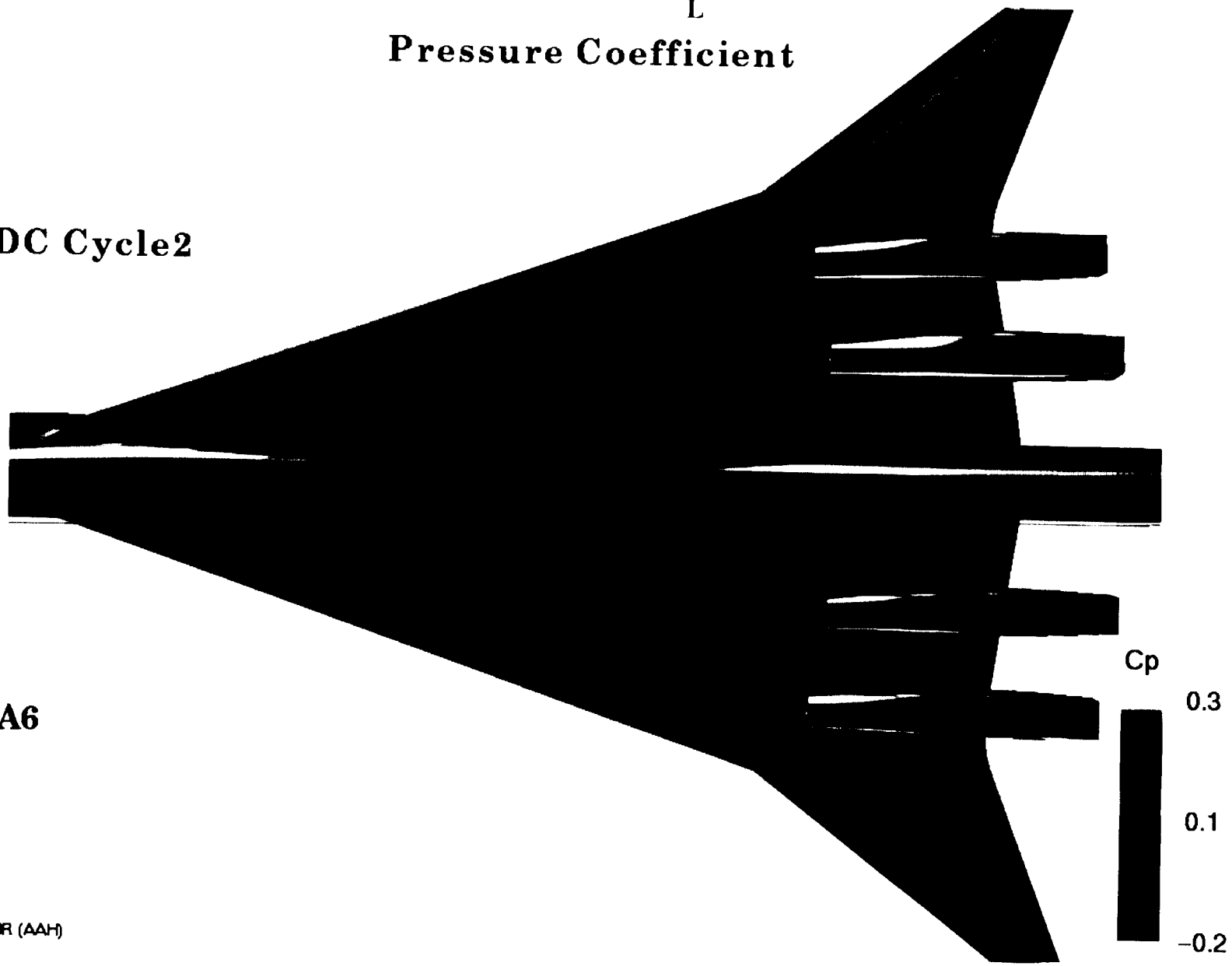

MJR/JJR (AAH)

Supersonic Analysis of Optimized Designs, Continued

Boeing Upper Surface Iso-Cps

The Boeing design represents one of the more radical optimization efforts, having as its trademark a "gull wing" character to the trailing edge. From the upper surface iso-Cp contours one can see that the general character of the pressure distribution has not been extensively modified from the baseline. The upper surface shock strength appears to have been increased significantly. Close attention to the fuselage reveals that the Boeing design has employed a significant amount of area ruling. The increased area fore and aft of the wing are taking advantage of the expansions in these regions for an additional contribution to the lift.

Boeing WB8WT: SYN87-MB

Mach = 2.4 C_L = 0.1

Pressure Coefficient

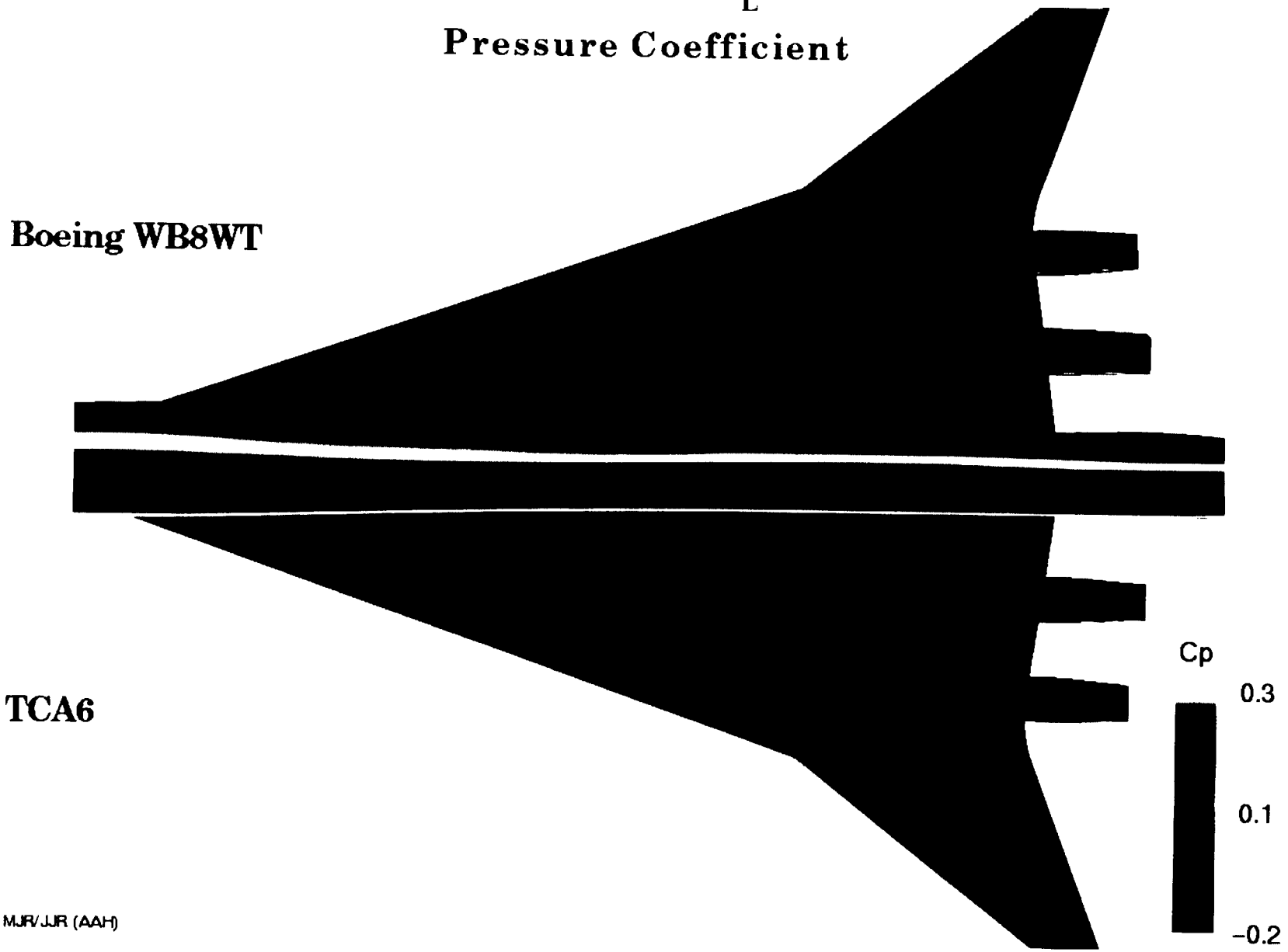

MJR/JJR (AAH)

Supersonic Analysis of Optimized Designs, Continued

Boeing Lower Surface Iso-Cps

The lower surface of the Boeing design begins to reveal some radical design features. Surface bumps running in the chordwise direction forward of the nacelles are in evidence which take advantage of the local increase in lower surface pressure for lift and thrust force components. As with the other three designs, the shock interaction region around the nacelles has decreased in strength though to a somewhat greater extent than the MDC design but not as much as the Ames design.

Boeing WB8WT: SYN87-MB

Mach = 2.4 C_L = 0.1

Pressure Coefficient

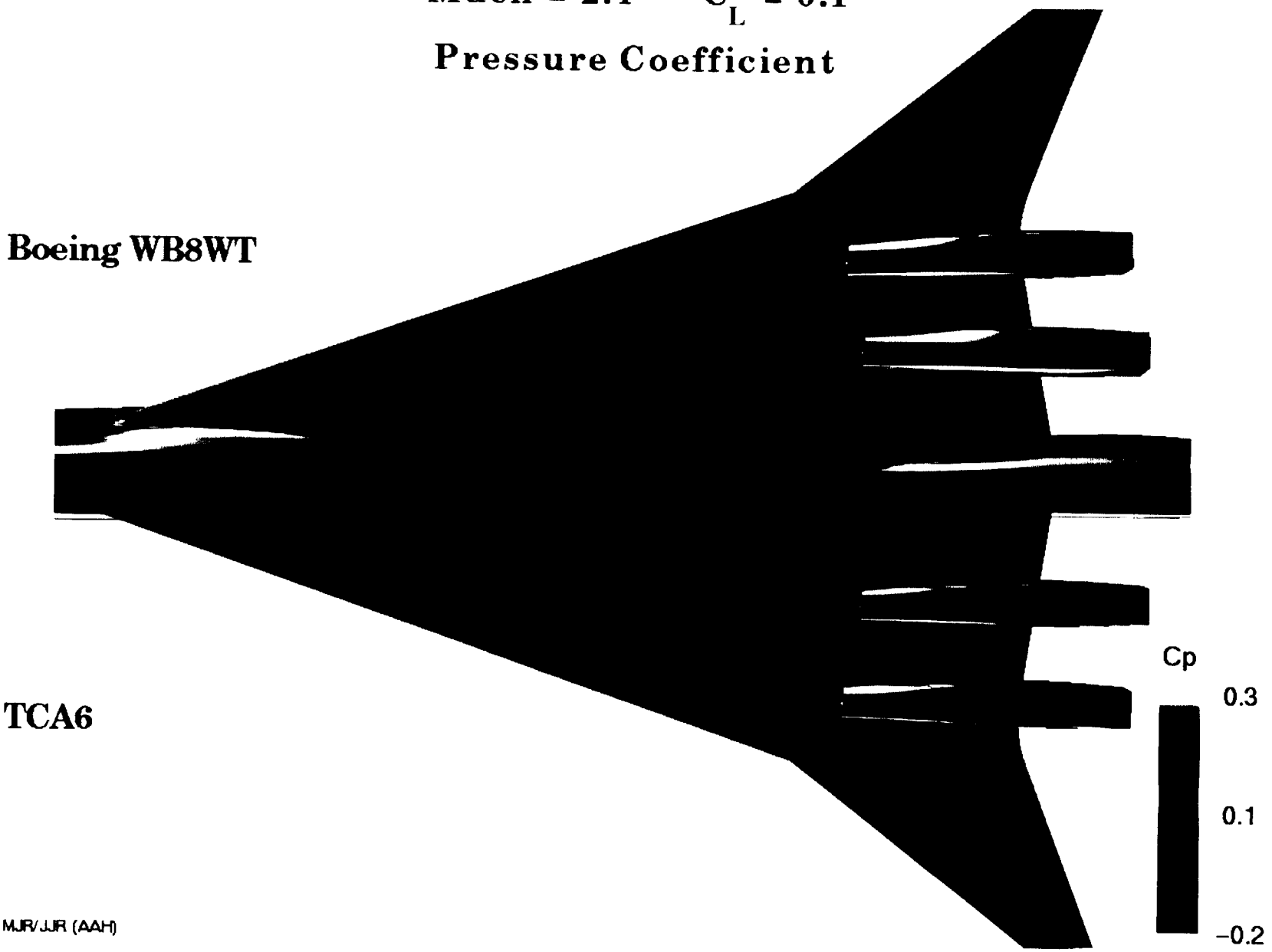

MJR/JJR (AAH)

Supersonic Analysis of Optimized Designs, Continued

Ames Upper Surface Iso-Cps

The Ames design also represents a more radical design effort. From the upper surface iso-Cp contours, one can see that the upper surface oblique shock has been greatly reduced in shock strength while a leading edge suction region has become more clearly delineated than in the baseline. Striations in the pressure field above the nacelles is a result of constant thickness wing optimization. As the lower surface shifted in the nacelle region to take advantage of the local pressure field the upper surface was correspondingly shifted to maintain thickness. An examination of the fuselage indicates the use of area ruling though to a lesser extent than that present in the Boeing design.

Ames 1-03: SYN87-MB

Mach = 2.4 C_L = 0.1

Pressure Coefficient

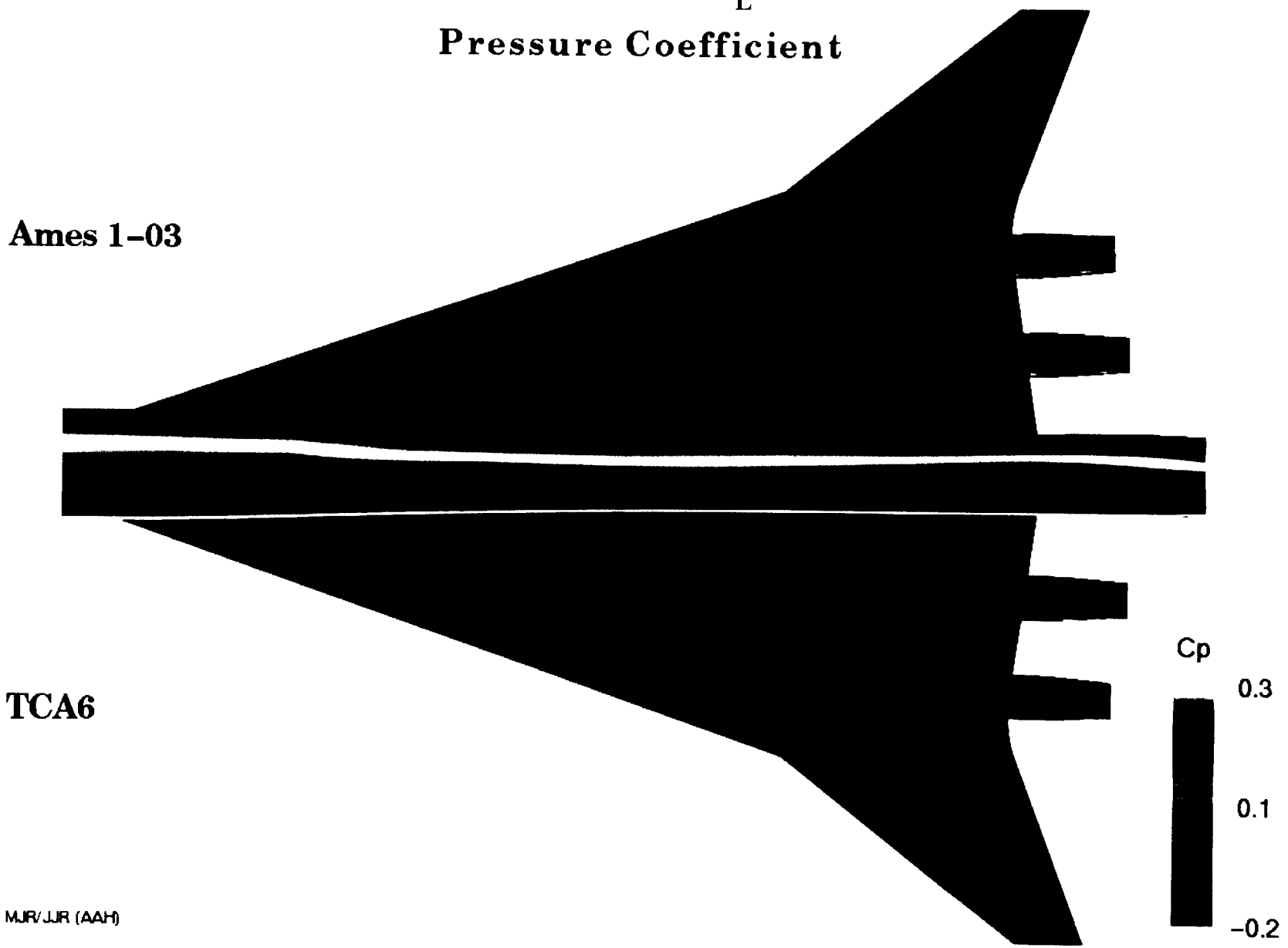

MJR/JJR (AAH)

Supersonic Analysis of Optimized Designs, Continued

Ames Lower Surface Iso-Cps

Some of the more noticeable features of the Ames design become apparent when examining the lower surface iso-Cp contours. A spanwise trough and peak can be ascertained near the leading edge where the design code encountered both the leading edge spar thickness and leading edge bluntness constraints. The thickness of the outboard leading edge has been decreased relative to the baseline to help minimize wave drag. An examination of the shock interaction in the nacelle region again indicates a decrease in overall strength. Comparing the nacelle regions of the three designs, one notes that the Ames design had the most dramatic effect upon nacelle integration in terms of reducing shock strength and limiting the extent of the supersonic expansion.

Ames 1-03: SYN87-MB

Mach = 2.4 C_L = 0.1

Pressure Coefficient

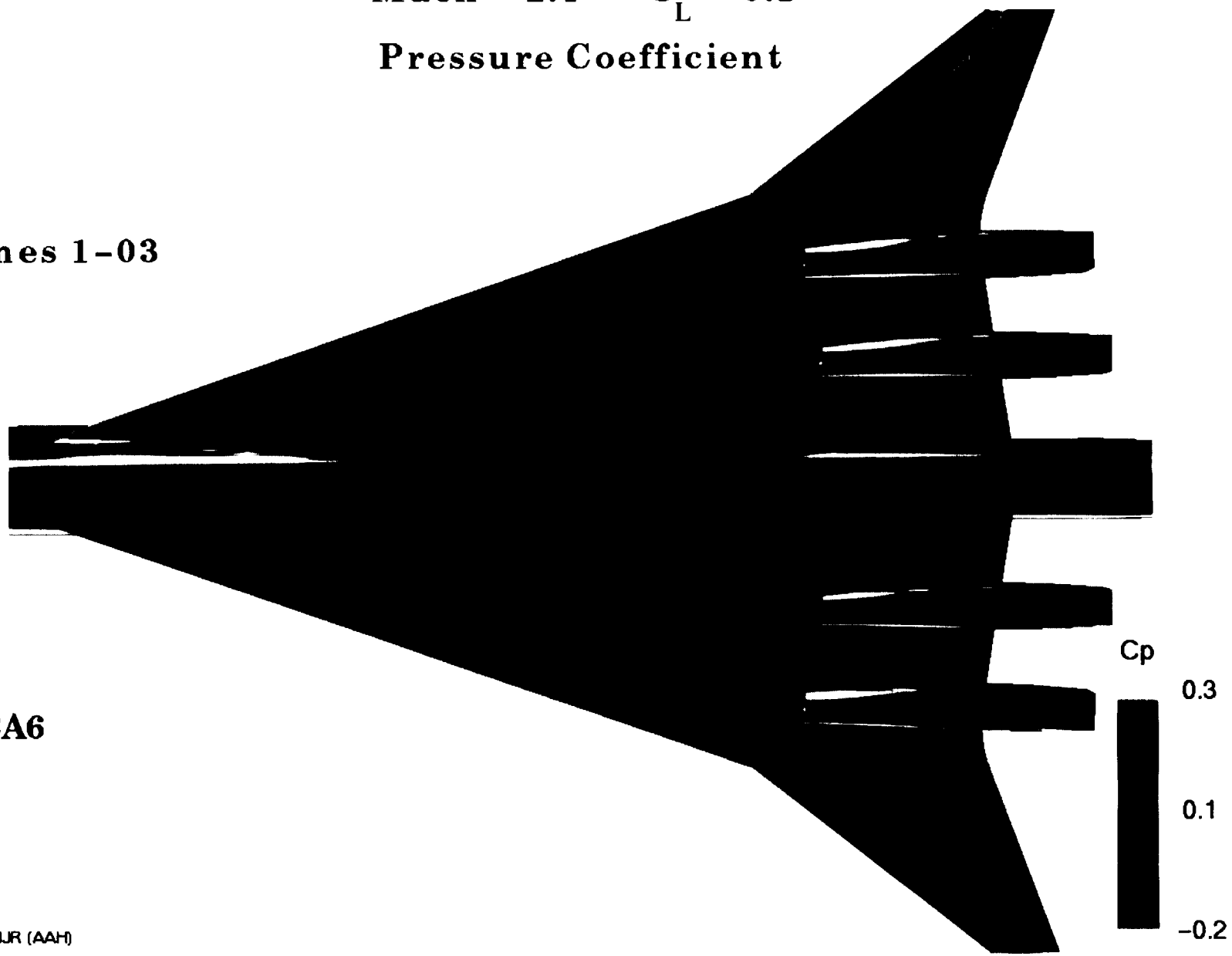

MJR/JJR (AAH)

Supersonic Analysis of Optimized Designs, Continued

Lift-Drag Polar Comparison

A comparison of the Lift-Drag polars as calculated by FLO87-MB for the MDC, Boeing, and Ames designs is shown in this figure. As can be determined from the curves, the drag reduction for the MDC design is 3.7 drag counts, the Boeing design has an improvement of 6.3 counts, while the Ames design attained a 7.0 drag count improvement.

Lift-Drag Polar Comparison

Wing-Body-Nacelle-Diverter (No Interior Forces) SYN87-MB

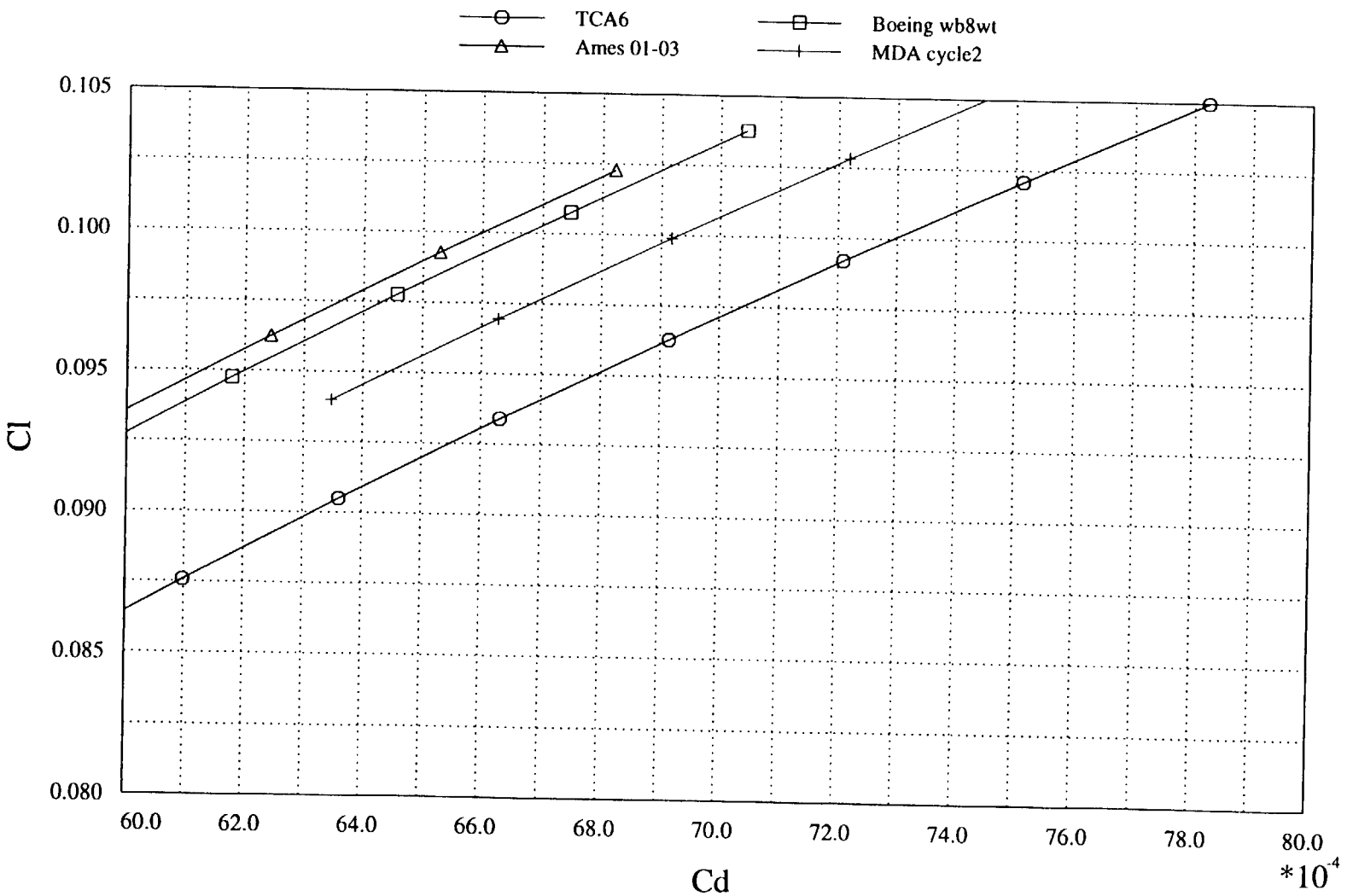

Multipoint Adjoint Method for the Euler Equations

The development of the adjoint method for the Euler equations is presented in the next three slides. An elaboration of the equations and method may be found in AIAA paper 97-0103 (Constrained Multipoint Aerodynamic Shape Optimization Using an Adjoint Formulation and Parallel Computers).

Multiblock Adjoint Method for the Euler Equations (ADJ87)

The **cost function** for the **inverse problem** can be defined as

$$I = \frac{1}{2} \iint_{B_W} (p - p_d)^2 \, d\xi_1 d\xi_2.$$

Taking the **first variation** of the **cost function**

$$\delta I = \iint_{B_W} (p - p_d) \, \delta p \;\; d\xi_1 d\xi_2.$$

Taking the **first variation** of the **governing equations**

$$\frac{\partial}{\partial \xi_i} (\delta F_i) = 0,$$

where

$$\delta F_i = Q_{ij} \left[\frac{\partial f_j}{\partial w} \right] \delta w + \delta \left(Q_{ij} \right) f_j$$

and

$$Q_{ij} = J \frac{\partial \xi_i}{\partial x_j}.$$

Multiplying by a **Lagrange Multiplier** ψ and integrating by parts gives

$$\int_D \left(\frac{\partial \psi^T}{\partial \xi_i} Q_{ij} \left[\frac{\partial f_j}{\partial w} \right] \delta w \right) \, d\xi_i + \int_D \left(\frac{\partial \psi^T}{\partial \xi_i} \delta Q_{ij} f_j \right) \, d\xi_i + \int_B \left(\bar{n}_i \psi^T \delta F_i \right) d\xi_j = 0$$

On the boundary

$$\delta F_\eta = \left\{ \begin{array}{c} 0 \\ Q_{\eta 1} \delta p \\ Q_{\eta 2} \delta p \\ Q_{\eta 3} \delta p \\ 0 \end{array} \right\} + p \left\{ \begin{array}{c} 0 \\ \delta \left(Q_{\eta 1} \right) \\ \delta \left(Q_{\eta 2} \right) \\ \delta \left(Q_{\eta 3} \right) \\ 0 \end{array} \right\} \quad \text{on} \quad B_W .$$

Choose ψ to satisfy the **adjoint equation**

$$\frac{\partial \psi}{\partial t} - \left(Q_{ij} \frac{\partial f_j}{\partial w} \right)^T \frac{\partial \psi}{\partial \xi_i} = 0 \quad \text{in } D,$$

with the **boundary condition**

$$\left(\psi_2 Q_{\eta 1} + \psi_3 Q_{\eta 2} + \psi_4 Q_{\eta 3} \right) = (p - p_d) \quad \text{on } B_W .$$

The **cost function** thus becomes

$$\delta I = -\int_D \frac{\partial \psi^T}{\partial \xi_i} \delta\left(Q_{ij}\right) f_j d\xi_k$$
$$-\iint_{B_W} \left\{\psi_2 \delta\left(Q_{\eta 1}\right) + \psi_3 \delta\left(Q_{\eta 2}\right) + \psi_4 \delta\left(Q_{\eta 3}\right)\right\} p \, d\xi_1 d\xi_2$$

Multipoint Adjoint Method, Continued

Solutions to the adjoint equations are obtained using the same multiblock strategy as the flow solver. Thus the efficiencies and robustness associated with FLO87-MB carry over to the adjoint solver.

The **Adjoint Solver** Uses the Same **Multiblock Strategy** as the **Flow Solver**

- Discretization and Time Stepping
  - Cell centered **finite volume** discretization
  - **Multi-stage Runge-Kutta**-like time marching
  - Blended **2nd** and **4th** order artificial viscosity
- Convergence Acceleration
  - Implicit residual smoothing
  - **Multigridding**
- Block-to-Block Communication
  - **Double halo** (Allows complete convection and diffusion stencil)
  - Point-to-point match
  - Halo cells updated every stage (**No lagging at block boundaries**)
  - **Coarser meshes** in the **multigrid cycle** have the **same double halo** structure (Permits **proper multigrid convergence acceleration**)

Geometry Modification and Constrained Optimization

The primary control upon which the entire design process revolves is the variation in the aerodynamic surfaces. Since aircraft configurations are composed of separate entites such as wings, fuselages, and nacelles upon which constraints are imposed, an underlying set of geometry entities acts as a starting input to the design process. These entities are independent of the multiblock boundaries as defined in the mesh topology. The user-specified design variables are allowed to act independently upon any of these geometry entities. In addition, the linear and nonlinear geometric constraints are also evaluated directly on these primary geometry entities.

At any particular point in the design process, changes to the mesh surfaces are obtained by first intersecting all of the geometry entities to construct a set of parametric surfaces representing the complete configuration. The location of each surface mesh point on this parametric representaion is determined for the initial configuration in a preprocessing step and subsequent perturbed surface mesh point locations are determined by evaluating the parametric geometry surfaces at these predetermined locations. Once the surface mesh points have been updated, the initial volume mesh may be perturbed and either the gradient or the solution calculated.

In the current implementation the input geometry entities are restricted to those defined by sets of points. However, in the the future, CAD entities such as NURBS surfaces will also serve in this role, thereby allowing both the input to and the output from the aerodynamic surface optimization to interface directly with a CAD database.

Geometry Modification and Constrained Optimization

- **Geometry Specification**
  - A set of **Geometry Entities** is input in addition to an **Initial Mesh** (e.g., Wing, Body, Nacelle)
  - **Design Variables** and **Constraints** are applied to these simple **Geometry Entities** to Create **Perturbed Geometry Entities**
  - During Optimization, **Perturbed Geometry Entities** are **Intersected** to obtain **Parametric Surface Representations**
  - **Mesh Motion** is Driven by **Projection onto these Parametric Surfaces**
  - Eventually, **CAD Entities** will be Used as the Underlying Geometry Entities

Geometry Modification and Constrained Optimization, Continued

The imposition of linear and nonlinear constraints in the optimization procedure has been handled by coupling the multiblock approach to the NPSOL algorithm of Gill, Murray, Saunders, and Wright. NPSOL is a sequential quadratic programming (SQP) method in which the search direction is calculated by solving the quadratic subproblem where the Hessian is defined by a quasi-Newton approximation of an augmented Lagrangian merit function. The Langrange multipliers in this merit function serve to scale the effect of any nonlinear constraints that thedesign may contain. Linear constraints are treated by solving the quadratic subproblem such that the projected search direction remains in feasible space. A complete treatment of the method and other optimization strategies is given by Gill, Murray, and Wright in the book Practical Optimization.

- **Constrained Optimization**
  - Flow Solver Coupled to the **NPSOL Sequential Quadratic Programming** Method (Gill, et al.)
  - Treats both **Linear** and **Nonlinear** Constraints

Multiblock Mesh Perturbation Algorithm (WARP3D-MB)

In order to obtain the change in the objective function, the variation in the metric terms must be obtained in each block. An analytic mesh perturbation algorithm has been developed for the single-block case and extended to the multiblock implementation. In this approach, a high quality mesh appropriate for the flow solver is first generated for the geometry prior to the start of the design. This initial mesh becomes the basis for all subsequent meshes which are obtained by analytical perturbations automatically during the design process.

Since the current flow solver and design algorithm assume a point-to-point match between blocks, each block may be independently perturbed by the WARP3D algorithm provided that the perturbed surfaces are treated continuously across block boundaries. Thus the perturbation algorithm naturally facilitates parallelization.

Since the mesh perturbation technique is analytical, it is theoretically possible to develop the analytical variations in the metric terms required to calculate the variation in the objective function. However, due to the complexity of the perturbation algorithm, the variation of the metrics is instead calculated by repeatedly applying the block perturbation algorithm to construct a finite difference approximation to the metrics. Therefore, care was taken to implement the algorithm such that the computational costs were kept to a minumum.

The multiblock mesh perturbation algorithm proceeds by first explicitly perturbing all faces that are directly affected by the design variables (active faces). Subsequently, all block edges which touch an active face, either in the same block or in an adjacent block, are implicitly perturbed utilizing a 1D arc length method. Inactive faces which include edges perturbed in the previous step are then implicitly perturbed using a quasi-3D form of WARP3D. Finally, the interior points of each block containing one or more explicitly or implicitly perturbed faces are adjusted using WARP3D.

Multiblock Mesh Perturbation Algorithm (WARP3D-MB)

- **Key Ideas**
  - Initial Multiblock Mesh is Used as an Input
  - All Subsequent Meshes are Automatically Generated During Design
  - Each Block is Independently Perturbed to Facilitate Parallelization
  - Perturbation Scheme Must be Very Fast and Robust
- **Multiblock Steps**
  - Perturb Active Faces According to Chosen Design Variables
  - Perturb All Edges that Touch an Active Face, Either in the Same Block or an Adjacent Block, Using a 1-D Arc Length Method
  - Perturb All Faces that Contain One or More Implicit Edges Using a Quasi-3D Form of WARP3D
  - Perturb Internal Points in Blocks Independently Using WARP3D

WARP3D-MB

For a more detailed explanation of the 3-stage WARP3D grid perturbation scheme, see AIAA paper 96-0094 (Aerodynamic Shape Optimization of Complex Aircraft Configurations via an Adjoint Formulation), 1996.

- **WARP3D**
  - Perturb Interior Mesh Points Within a Block, Based on Updated Faces
  - An Arc Length Based TFI Like Algorithm is Used to Determine Perturbations
  - Each Internal Mesh Point Perturbation is Dependent Upon the Motion of:
    * 8 Corners
    * 12 Edges
    * 6 Faces
  - Scheme is Explicit, Resulting in an Efficient and Robust Algorithm

Parallel Implementation

The main strategies used to accomplish the parallelization of the design code are: a domain decomposition model, a Single Program Multiple Data (SPMD) strategy, and the Message Passing Interface (MPI) standard for message passing. The choice of MPI was determined by the requirement that the resulting code be portable to different computing platforms as well as to homogeneous and heterogeneous networks of workstations.

The decomposition of the domain at multiblock block boundaries achieves natural parallelization for four of the six modules of the design algorithm. Specifically, the solution of the flow equations, the solution of the adjoint equations, the calculation of mesh perturbations, and the application of design variables to the geometry entities. Parallel implementation of the flow and adjoint solvers requires the use of MPI to update the double halo quantities at every stage of the time stepping while the mesh perturbation and imposition of design variables can proceed on each processor independently without requiring message passing.

No attempt has been made to parallelize the constrained SQP optimization algorithm of the calculation of the changes to the underlying geomtry entities. It is assumed that in the context of the design algorithm, the computational cost of determining the step sizes and search directions provided through the application of the optimization algorithm is insignificant when compared with the other elements necessary during the design. This is true for cases where the number of design variables is less than a thousand.

Parallel Implementation

- **SPMD (Single Program Multiple Data) Strategy**
- **MPI (Message Passing Interface) Library for Message Passing**
- **The Design Algorithm has Six Distinct Modules:**
  - Flow Solver
  - Adjoint Solver
  - Application of Design Variables to Surfaces
  - Mesh Perturbation Algorithm
  - Geometry and Constraint Algorithm
  - Optimization Algorithm
- **By Using Block Boundaries in the Multiblock Domain, Natural Parallelization is Achieved for the First Four Modules**
- **For the Flow and Adjoint Solvers, MPI is Used to Update the Double Halo Quantities at Every Stage of the Time-Stepping**

- For the Application of Design Variables and Mesh Perturbation No Message Passing is Needed
- It is Assumed that the Optimization Algorithm is Insignificant in Computational Cost (for Cases where the Number of Design Variables < 1000)

Multipoint Constrained Transonic Design

Numerical results will now be presented for two classes of problems to demonstrate the versatility of the multiblock adjoint-based design method.

The first test case explores constrained multiblock adjoint-based multipoint design for a typical business jet configuration under transonic flight conditions. The design method is applied in order to improve wing performance at three design points in the presence of the body and nacelles. The three design points are Mach = 0.81 with CL = 0.35, Mach = 0.82 with CL = 0.3, and Mach = 0.83 with CL = 0.25.

The initial multiblock mesh about the business jet wing, body, and nacelle has 72 blocks and 750K cells. The underlying geometry entities that are eligible for design changes include a wing with six defining stations and a fuselage. The initial configuration was designed for Mach = 0.8 and CL = 0.3.

Multipoint Constrained Transonic Design

- **Mesh**
  - Wing-Body-Nacelle Geometry
  - 72 blocks
  - 750K Mesh Cells
- **Wing Redesign** in the Presence of Body and Nacelles
  - Improve Performance at **Three Design Points**
- **Starting Conditions**
  - Generic Business Jet Configuration
  - Design Point 1: M = 0.81, CL = 0.35
  - Design Point 2: M = 0.82, CL = 0.30
  - Design Point 3: M = 0.83, CL = 0.25

Multipoint Constrained Transonic Design, Continued

The objective used is to minimize configuration drag at all three design points keeping Mach number and lift fixed by modifying the wing shape. Eighteen Hicks-Henne design variables are chosen for five of the six defining sections for a total of 90 design variables. Spar thickness constraints were also enforced at each defining station at x/c = 0.2 and x/c =0.8. Maximum thickness was forced to be preserved at x/c=0.4 for all six defining stations. Each section was also constrained to have the thickness preserved at x/c=0.95 to ensure an adequate included angle at the trailing edge. A total of 30 linear geometric constraints were imposed on the configuration. The results indicate a drag reduction of more than 15% for all three design points after 5 NPSOL design iterations.

- **Cost Function**
  - Minimize Configuration Drag at all Three Design Points Keeping Mach Number and Lift Fixed
- **Design Variables**
  - 90 Hicks-Henne Functions at 5 Wing Defining Stations
  - 30 Geometric Wing Constraints
- **Results**
  - 15+% Drag Reduction at all Three Design Points in 5 Design Cycles

Multipoint Constrained Transonic Design, Continued

The iso-Cp surface contours for the optimized and baseline transonic business jet configurations after 5 NPSOL design iterations are depicted in this slide. Note that the strong shocks present on the upper surface have been eliminated.

Transonic Business Jet Configuration
Iso-Cp Contours
M = 0.82, C_L = 0.30

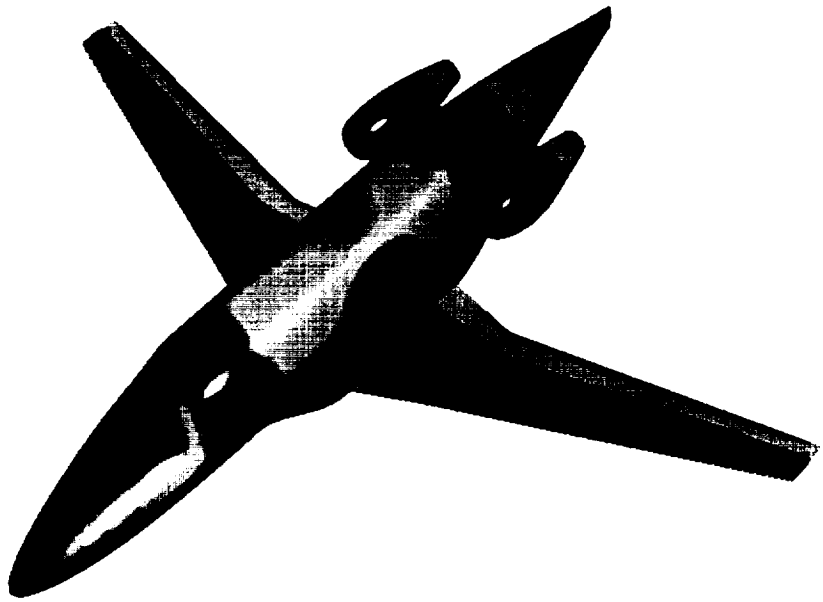

Baseline

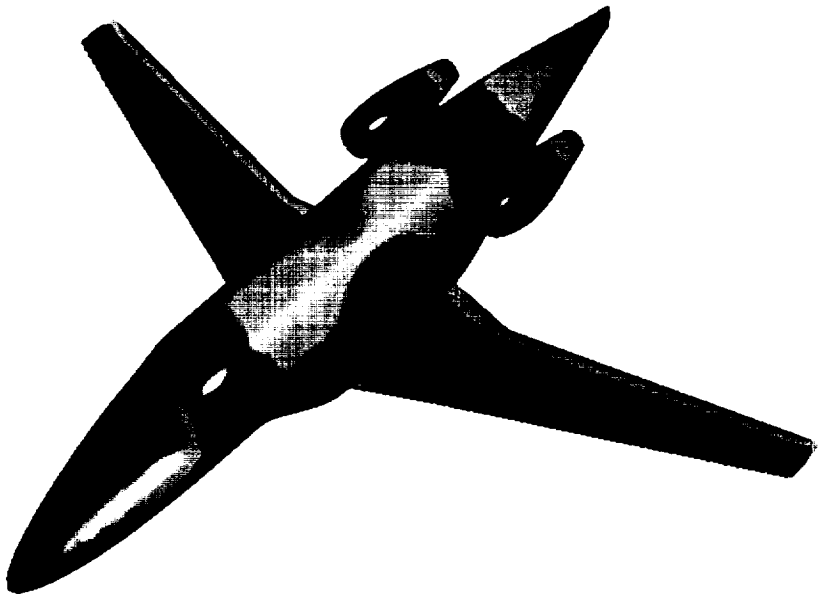

Optimized

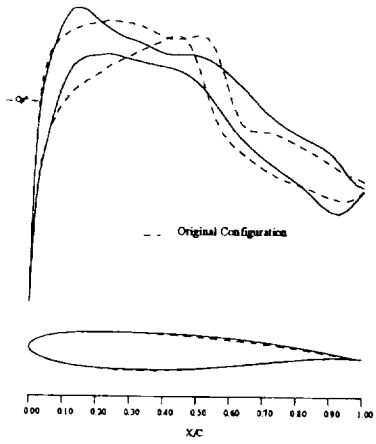

a: span station $z = 0.190$

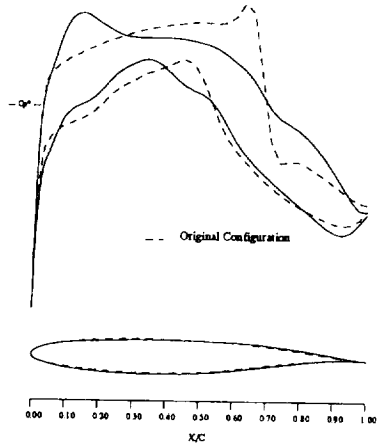

1b: span station $z = 0.475$

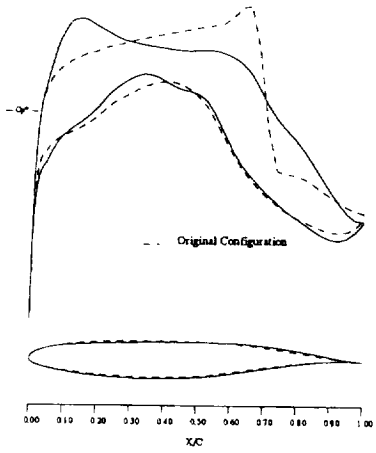

c: span station $z = 0.665$

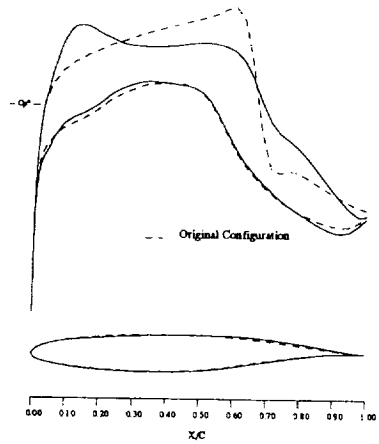

d: span station $z = 0.856$

Business Jet Configuration Configuration. Drag Minimization at Fixed Lift.
$M = 0.82, C_L = 0.3$
90 Hicks-Henne variables. Spar Constraints Active.
- - -, Initial Pressures
—, Pressures After 5 Design Cycles.

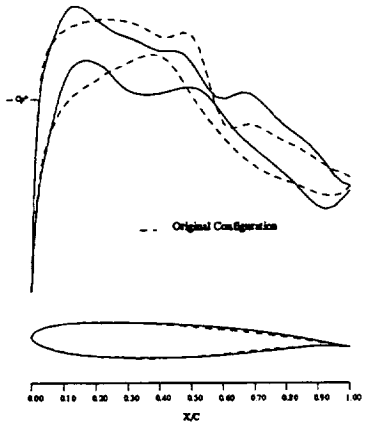

a: span station $z = 0.190$

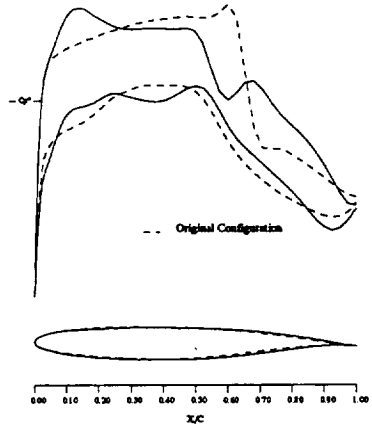

b: span station $z = 0.475$

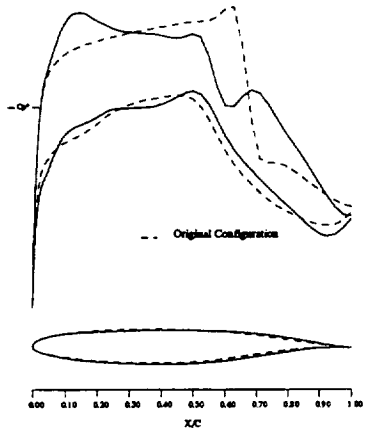

c: span station $z = 0.665$

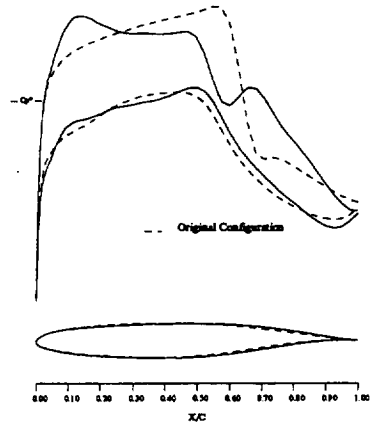

d: span station $z = 0.856$

Business Jet Configuration. Multipoint Drag Minimization at Fixed Lift.
Design Point 1, $M = 0.81$, $C_L = 0.35$
90 Hicks-Henne variables. Spar Constraints Active.
- - -, Initial Pressures
—, Pressures After 5 Design Cycles.

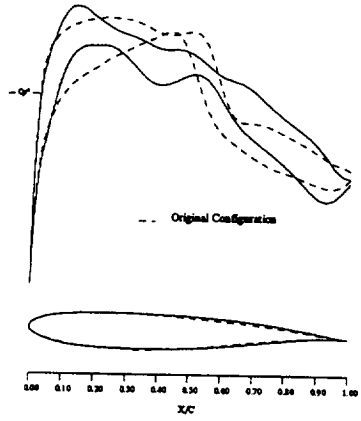

a: span station $z = 0.190$

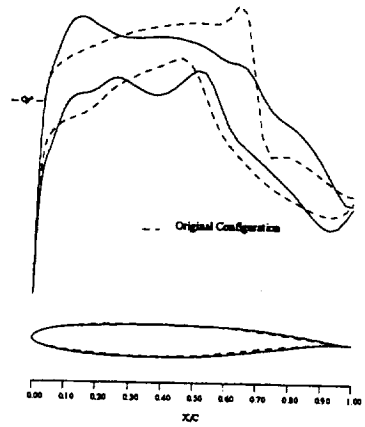

b: span station $z = 0.475$

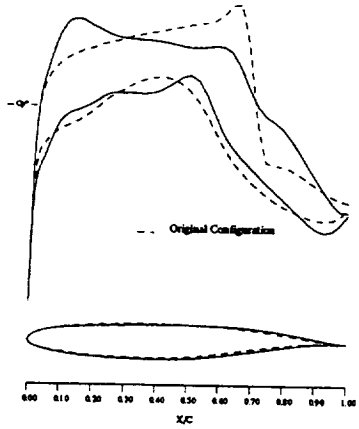

c: span station $z = 0.665$

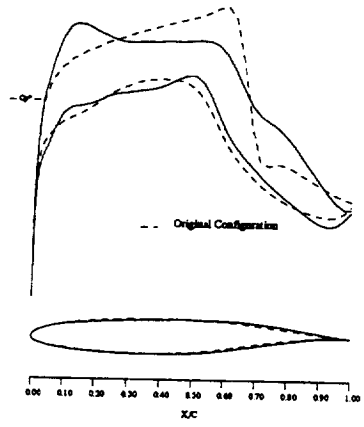

d: span station $z = 0.856$

Business Jet Configuration. Multipoint Drag Minimization at Fixed Lift.
Design Point 2, $M = 0.82$, $C_L = 0.30$
90 Hicks-Henne variables. Spar Constraints Active.
- - -, Initial Pressures
—, Pressures After 5 Design Cycles.

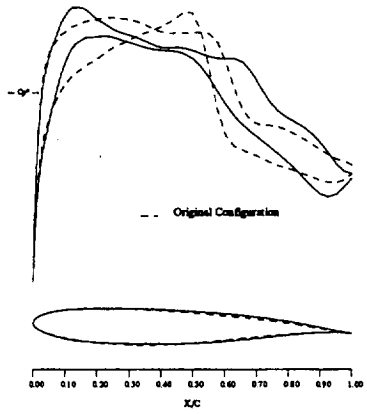

a: span station $z = 0.190$

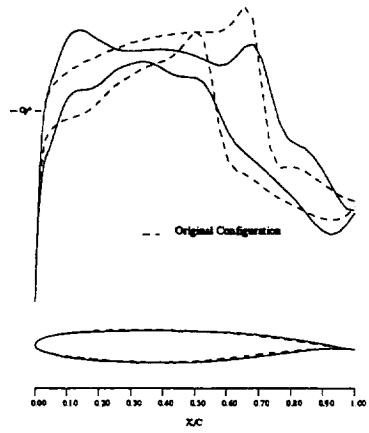

b: span station $z = 0.475$

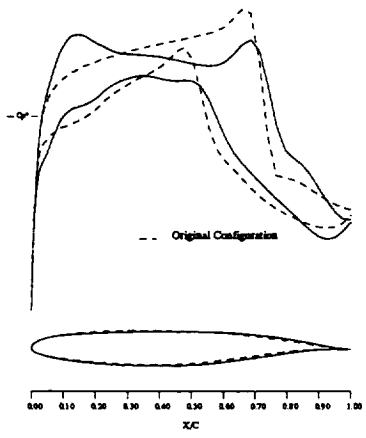

c: span station $z = 0.665$

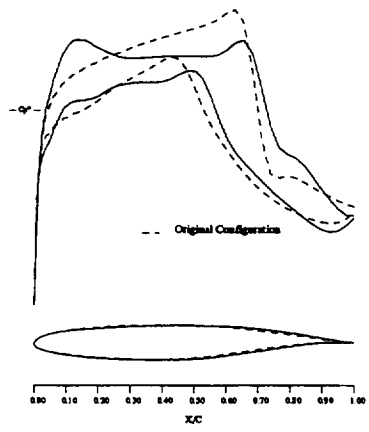

d: span station $z = 0.856$

Business Jet Configuration. Multipoint Drag Minimization at Fixed Lift.
Design Point 3, $M = 0.83$, $C_L = 0.25$
90 Hicks-Henne variables. Spar Constraints Active.
- - -, Initial Pressures
—, Pressures After 5 Design Cycles.

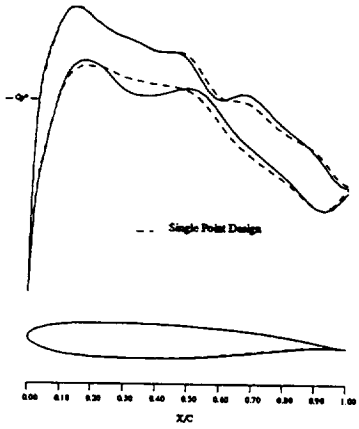

a: span station $z = 0.190$

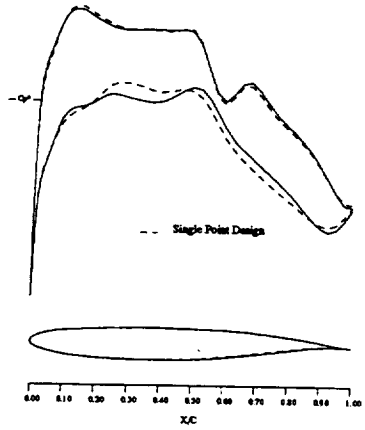

b: span station $z = 0.475$

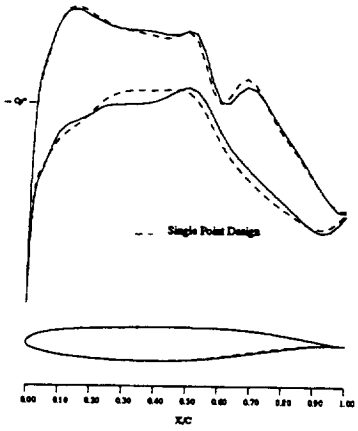

c: span station $z = 0.665$

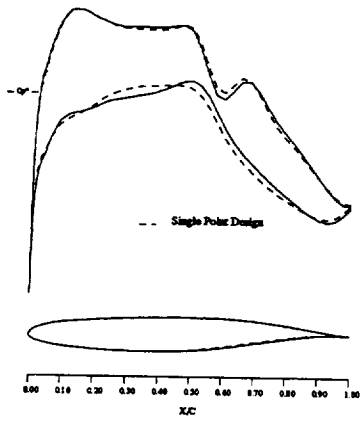

d: span station $z = 0.856$

Business Jet Configuration. Multipoint Drag Minimization at Fixed Lift.
Design Point 1, $M = 0.81$, $C_L = 0.35$
90 Hicks-Henne variables. Spar Constraints Active.
- - -, Pressures for Design Test Case 1.
—, Pressures After 5 Design Cycles.

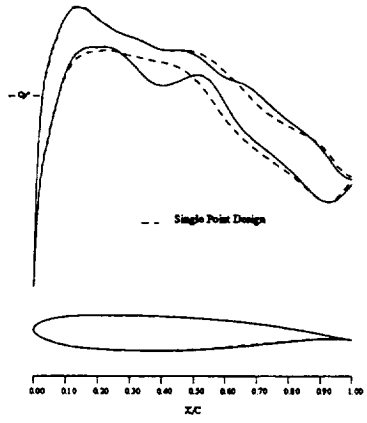

a: span station $z = 0.190$

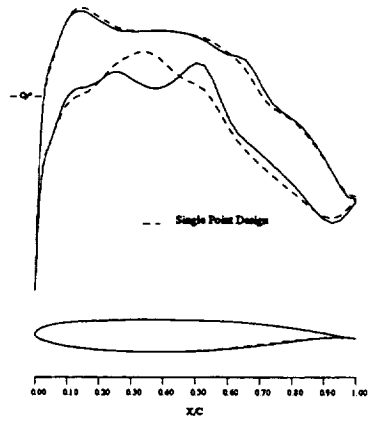

b: span station $z = 0.475$

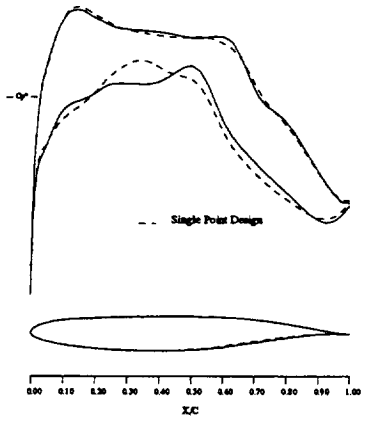

c: span station $z = 0.665$

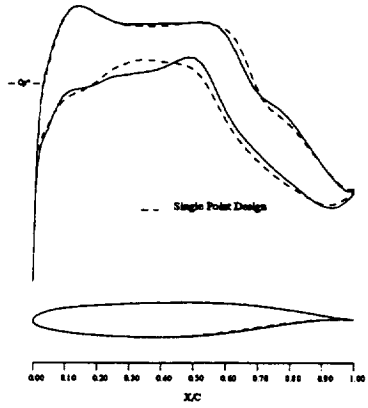

d: span station $z = 0.856$

Business Jet Configuration. Multipoint Drag Minimization at Fixed Lift.
Design Point 2, $M = 0.82$, $C_L = 0.30$
90 Hicks-Henne variables. Spar Constraints Active.
- - -, Pressures for Design Test Case 1.
—, Pressures After 5 Design Cycles.

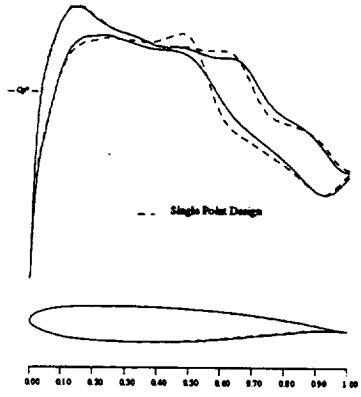

a: span station $z = 0.190$

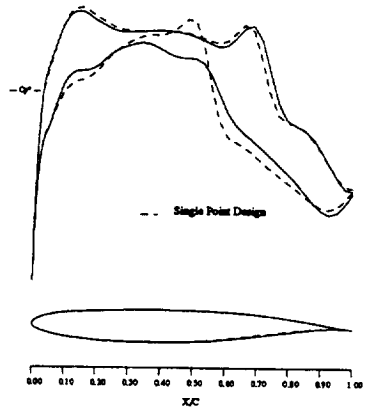

b: span station $z = 0.475$

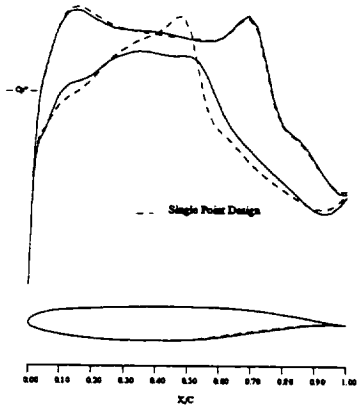

c: span station $z = 0.665$

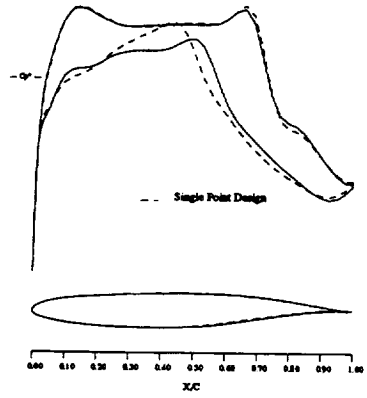

d: span station $z = 0.856$

Business Jet Configuration. Multipoint Drag Minimization at Fixed Lift.
Design Point 3, $M = 0.83$, $C_L = 0.25$
90 Hicks-Henne variables. Spar Constraints Active.
- - -, Pressures for Design Test Case 1.
—, Pressures After 5 Design Cycles.

Constrained Supersonic Design

The second test case treats a generic supersonic transport configuration in which the complexity of inboard and outboard nacelles and diverters has been included. The design objective is to redesign the wing such that the supersonic cruise point performance is improved. Specifically, the cost function employed is a minimization of configuration drag at fixed lift and Mach number.

The baseline supersonic transport configuration was sized to accommodate 300 passengers with a gross take-off weight of 750,000 lbs with a supersonic cruise point of Mach 2.2 and a CL of 0.105. The planform has a break in the leading edge. The inboard leading edge sweep is 68.5°, and the outboard sweep is 49.5°. Symmetric initial airfoils were chosen with the purpose of accommodating thick spars at roughly 10% and 80% chord over the span up to the leading edge break. Outboard of the leading edge break where the wing sweep is ahead of the Mach cone, a sharp leading edge was used to avoid undue wave drag. The airfoils were chosen to be symmetric, biconvex shapes modified to have a region of constant thickness over the mid-chord. The four-engine configuration features axisymmetric nacelles tucked close to the wing lower surface.The leading edge heights of the diverters are determined by the boundary layer local displacement thickness such that entrainment of boundary layer flow into the engines is avoided. Since the distances from the wing leading edge to the diverter leading edge are different for the two nacelles, this causes a corresponding diverter height difference.

The computational mesh on which the design is run has 180 blocks and 1,500K mesh cells, while the underlying geometry entities define the wing with 16 sectional cuts and the body with 200 sectional cuts. In this case, where we hope to optimize the shape of the wing, care must be taken to ensure that the nacelles remain properly attached with the diverter heights maintained. To accomplish this without the inclusion of additional geometry entities, the portions of the nacelles and diverters that are actually below the wing planform outline take their associated surface mesh point motion from their projected locations on the lower parametric wing surfaces.

Constrained Supersonic Design

- **Mesh**
  - Wing-Body-Nacelle-Diverter Geometry
  - 180 Blocks
  - 1500K Mesh Points
- **Wing Redesign in Presence of Complex Body and Nacelle/Diverter Geometry**
  - Improve Supersonic Cruise Point Performance
- **Starting Condition**
  - Generic Supersonic Transport
  - Mach = 2.2
  - CL = 0.105
- **Cost Function**
  - Minimize Configuration Drag at Fixed Lift and Mach Number

Constrained Supersonic Design, Continued

Just as in the transonic cases, 18 design variables of the Hicks-Henne type are chosen for a given wing defining section. However, instead of applying them to all 16 sections, they are applied to 8 of the sections and then lofted linearly to the neighboring sections. Spar constraints are imposed for all wing defining sections at x/c = 0.05 and x/c = 0.8. An additional maximum thickness constraint is specified along the span at x/c = 0.5. A final thickness constraint is enforced at x/c = 0.95 to ensure a reasonable trailing edge included angle. Thus a total of 64 geometric wing contraints are being applied.

- **Design Variables**
  - 144 Hicks-Henne Functions at 8 of 16 Wing Defining Stations
  - 64 Geometric Wing Constraints
  - Nacelles Follow Wing Lower Surface to Maintain Diverter Heights
- **Results**
  - Configuration Drag was Reduced by 8% in 5 Design Cycles

Constrained Supersonic Design, Continued

An iso-Cp representation of the initial and final designs of the generic surpersonic transport for both upper and lower surfaces is shown. It is noted that the strong oblique shock evident near the leading edge of the upper surface on the initial configuration is largely eliminated in the final design after 5 NPSOL design iterations. It is also seen that the upper surface pressure distribution in the vicinity of the nacelles has formed an unexpected pattern. However, it is recalled that thickness constraints abound in this design, and these upper surface pressure patterns are conjectured to be the result of sculpting of the lower surface near the nacelles which affects the upper surface shape through the thickness constraints. For the lower surface, the leading edge has developed a suction region while the shocks and expansions around the nacelles have been somewhat reduced. The final overall pressure drag was reduced by 8%, from CD = 0.0088 to CD = 0.0081.

Supersonic Transport Configuration
Iso–Cp Contours
$M = 2.2, C_L = 0.105$

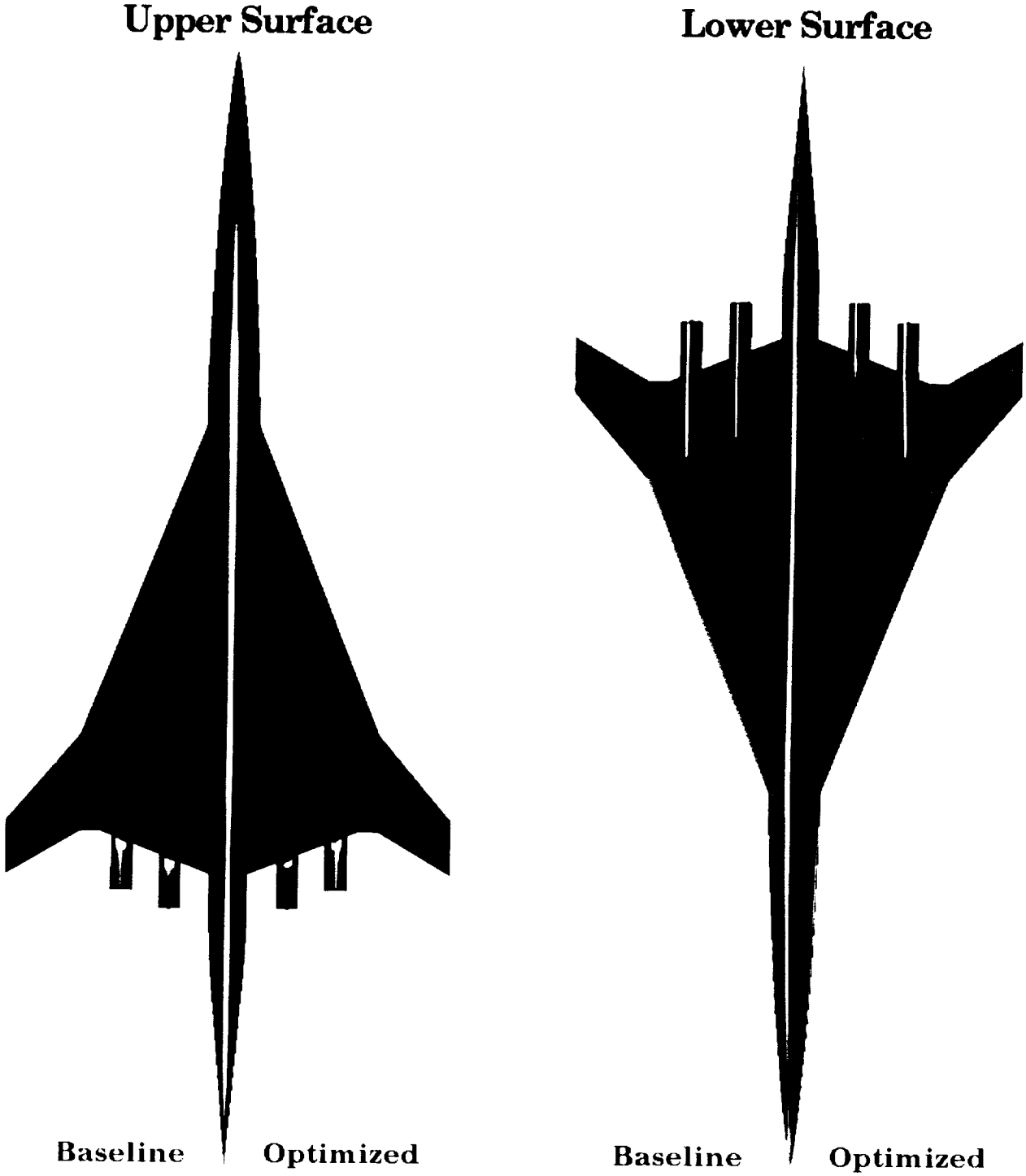

Conclusions

This presentation has shown how the complicated design of both transonic and supersonic aircraft configurations including airframe/nacelle integration effects can be accomplished in a routine fashion for multiple design points with the inclusion of constraints utilizing a multiblock adjoint-based design method.

This methodology is advantageous in two respects. First, the utilization of a multiblock scheme allows the treatment of complex geometries which were previously out of reach of single-block methods. Approximations, such as the pseudo-nacelle technique, are rendered unnecessary, permitting performance gains based upon component interactions to be fully exploited. Additionally, the need to reanalyze a complete configuration outside of the design code has been eliminated, reducing the cycle time in the design process.

Secondly, the use of the adjoint formulation allows a very large gain in computational efficiency over traditional finite difference methods of calculating gradient information. Thus an increased number of mesh cells and design variables are permitted when designing without the computational expense becoming prohibitive.

Furthermore, capitalizing on the natural domain decomposition at block boundaries has allowed the use of parallel computational techniques. The application of the current method on the IBM SP2 has realized a near-linear decrease in wall clock time as a function of the number of processors. Thus further increases in the number of design variables and computational cells associated with the design of complete aircraft configurations are attainable without prohibitive increases in the wall clock time per design cycle.

While the results presented in this paper have been restricted to the inviscid Euler equations, this limitation is not inherent and will soon be overcome in our future work. The focus here was instead to demonstrate the feasibility of realistic designs governed by simple geometry entities that are assembled and treated during the design process. Furthermore, with the proven coupling to NPSOL and the addition of multiple design point capability, the door is truly open for the method to act as a crucial element of a high fidelity MDO technique capable of revolutionizing aircraft design.

Conclusions

- **Adjoint Based Aerodynamic Shape Optimization** has been Demonstrated on a Wide Variety of Applications
- Adjoint Methods Combine the **Efficiency** of **Inverse Design Methods** with the **Versatility** of **Numerical Optimization**
- Adjoint Methods Demonstrate a **Very Large Gain in Computational Efficiency** Over Traditional Finite Difference Methods: **10-100 Fold Reduction in CPU Time** to Calculate the Gradient
- A **Further Reduction** in Wall Clock Time is Realized through the **Use of Parallel Computing** with **Near Linear Speed Up** as a Function of Number of Processors
- Complex Geometries can be Addressed Through **Multiple Blocks** or **Unstructured Meshes**
- **Constrained Multipoint Optimization** is Demonstrated with a View Towards Eventual **MDO Problems**

FUTURE ADVANCES IN AERODYNAMIC SHAPE OPTIMIZATION

James Reuther
RIACS/NASA Ames
Mark Rimlinger
Sterling Software/NASA Ames

February 25-27, 1997

FUTURE ADVANCES IN AERODYNAMIC SHAPE OPTIMIZATION

James Reuther, RIACS/High Speed Research Branch, NASA Ames
Mark Rimlinger, Sterling Software/High Speed Research Branch, NASA Ames

February 1997

This paper presents an overview of the future direction of aerodynamic shape design as seen by HSR participants at NASA Ames Research Center. Dr. James Reuther recently completed his Ph.D. at the University of California, Davis. He is currently employed at the Research Institute for Advanced Computer Science (RIACS) situated at Ames Research Center and is devoting much of his time to the development of practical aerodynamic design tools using the latest available technologies. Mark Rimlinger is finishing his Ph.D. from Carnegie Mellon University while concurrently being employed by Sterling Software. His primary research activity at Ames is the development of advanced shape design software that will directly interface with CAD systems.

The focus of this paper will be to highlight future directions and to show some promising examples of developing technologies. Two other talks at this conference, entitled **"Improvements to the Single-Block Adjoint-Based Aerodynamic Shape Design Method, SYN87-SB"** and **"Development and Validation of a Multi-Block Adjoint-Based Design Method"**, will be referred to for past and current capabilities as well as the mathematical foundations of aerodynamic shape design. The presentation will review all the available aerodynamic shape design tools used within the HSR program and examine their limitations. Requirements will be explored for: flow solvers, design methods, geometry/mesh generation, and interactive environments.

Outline

- Currently Available Aerodynamic Shape Design Methods
- Limitations of Current Methods
- Flow Solver Requirements
- Example Navier-Stokes Calculations
- Design Method Requirements
- Geometry/Mesh Generation Requirements
- Visualization Techniques and Tools for Engineers

The aerodynamic shape design tools used within the HSR program can essentially be classified into two groups: those that are based on optimizing an aerodynamic figure of merit chosen by the user (optimization-based methods), and those that use an alternative strategy to achieve design improvement.

At Ames, exploration into the feasibility of aerodynamic shape optimization within the HSR program began in 1989 with the development of OPT3D[1]. This computer code coupled TEAM(FLO57)[2], a cell-centered Euler flow solver originally written by Antony Jameson and later enhanced by Lockheed, with QNMDIF[3], a quasi-Newton numerical optimization algorithm originally written by Gill, et al. (NPL, England) and later modified by Robert Kennelly[4] (NASA Ames). Aerodynamic sensitivities (gradients) were provided by finite-differencing flow solutions after independently perturbing each of the design variables. The TEAM(FLO57) code solve the Euler equations on a body-fitted mesh and thus captures all inviscid flow phenomena. Automatic mesh generation was provided by WBGRID, a C-H elliptic mesh generator capable of creating wing-body meshes and written at Lockheed. The initial OPT3D code was developed on the CRAY X-MP and was applicable to wing and wing-body design calculations. It was extensively tested and used during 1991-92. Proven success of the software came about with the Douglas Wing 4/Wing 5 test during the summer of 1993 that demonstrated gains of between 6% and 8% in the configuration L/D[7].

Developments that took place during 1992-93 were the addition of pseudo-nacelle effects and initial development of OPT67 which used FLO67 instead of TEAM. FLO67, also written by Antony Jameson, proved to be much faster than TEAM since it included the use of multigridding in addition to the residual smoothing and enthalpy damping available within TEAM(FLO57). This increase in speed was essential at the time due to the prohibitive cost of the finite difference-based gradients. FLO67 also used a vertex-centered scheme as apposed to the cell-centered scheme employed in FLO57. The pseudo nacelle effects which took into account the influence of the nacelles on the wing as well as the reverse represents an attempt to incorporate the nacelles and diverters into the design process. The pseudo nacelle capability was incorporated into both OPT3D and OPT67. It was also in this time frame that source for both OPT3D and OPT67 were released to Douglas so that they could develop an in-house capability based upon the initial studies at Ames.

Work on OPT67 took place at both Ames and Douglas after 1992. Douglas incorporated their own version of FLO67 and an alternate mesh generation capability (QGRID). Both the Ames and Douglas versions of OPT67 were proven to be successful in a series of wind tunnel tests on both the Boeing Ref-H configuration and the alternate Douglas M247A configuration. These tests were conducted between 1994 and 1995 and showed that the design tools could achieve significant cruise point performance improvements while including the presence of both nacelle integration effects and a limited number of constraints. Design applications were demonstrated for both fuselage as well as wing optimization cases.

More recently (beginning at the end of 1995) Douglas has switched all three elements of the design algorithm. A C-O mesh generator replaced QGRID, CFL3D replaced FLO67, and QNMDIF was replaced by DOT. The CFL3D (Euler/NS) solver developed by NASA Langley allows for more general topologies than FLO67 and hence allowed the replacement of QGRID with a more capable C-O mesh generator. DOT is a constrained quasi-Newton optimization package as opposed to the unconstrained QNMDIF. This new design tool has subsequently been named MDO3D. The changes provided significant enhancements to the mesh generation, design variable, and constraint treatment capabilities.

Currently Available Aerodynamic Shape Design Methods

Optimization Based Methods

Name	Org.	Eqn. Type	Dates	Config.	Nac/Div	Opt.	Grads.
OPT3D	Ames	Euler	89-93	W/B	Pseudo	QNMDIF	F.D.
OPT67	Ames	Euler	92-94	W/B	Pseudo	QNMDIF	F.D.
SYN87-SB	Ames	Euler	94-Pres.	W/B	Pseudo	NPSOL	Adjoint
SYN87-MB	Ames	Euler	96-Pres.	Full	Actual	NPSOL	Adjoint
TRANAIR	Boeing	Potential	91-Pres.	Full	Actual	NPSOL	Built In
MDO3D	Douglas	Euler	91-Pres.	W/B	Psuedo	DOT/NPSOL	F.D.

Alternative Methods

Name	Org.	Eqn. Type	Dates	Config.	Nac/Div	Comments
Natural Flow	Langley	Euler	93-Pres.	W/B	Pseudo	Determine Optimum Thickness Distribution Based on Calculated Cp
CDISC	Langley	Euler/NS	82-Pres.	Full	Actual	Inverse Type Method

At Ames, work on aerodynamic shape optimization proceeded into the development of SYN87-SB, starting in 1994. The FLO67 used by OPT67 was replaced with FLO87—a cell-centered scheme similar to FLO57 but with all the convergence acceleration techniques proven in FLO67. The main difference in SYN87-SB however is the addition of an adjoint solver. This tool allows for the gradients to be calculated at the cost of roughly two flow calculations as opposed to a number of flow calculations proportional to the number of design variables. Hence it significantly reduces the cost of using aerodynamic shape optimization. Since its use began in earnest in the spring of 1995, the number of design variables typically used has risen from about 25 to between 100 and 200. This capability has significantly increased the efficacy of aerodynamic shape design. During 1996, SYN87-SB was further modified to use NPSOL[5] as an alternative to QNMDIF and thereby allow for the treatment of linear and nonlinear constraints. The single-block grid generation was also enhanced significantly, as was the pseudo nacelle approximation.

The latest efforts at Ames have focused on developing a multiblock version of SYN87. This new software, SYN87-MB[9], detailed in a previous presentation, will allow future point and multipoint optimizations to be carried out on the complete configurations without resorting to pseudo nacelle effects.

Meanwhile, Boeing had been developing their own aerodynamic shape optimization capability starting from TranAir. Starting in 1991 the TranAir team led by David Young and William Huffman began to create a design version[8] of the work-horse Boeing CFD analysis tool. TranAir solves the full-potential equations by a Newton iteration procedure. Each Newton iterate is in turn solved by a preconditioned iterative technique (GMRES). The mesh used for TranAir is a Cartesian type with cell refinement taking place near solid boundaries and flow features characterized by high gradients. While the construction of the initial geometry and mesh is difficult it has the advantage of allowing arbitrarily complex configurations. To create a design tool the TranAir team elected to augment their analysis tool with transpiration boundary conditions that simulate the effect of modifying the surface shape. By employing the same solver, and adjusting the right hand side of the Newton linearized system to represent the motion simulated by transpiration, it is possible to obtain design sensitivities very inexpensively (similar in cost to adjoint-based gradients).

There are two alternative methods that have been explored within the HSR program that do not directly use optimization of a user-specified objective function. The first is the Natural Flow Method[11] developed by R. Wood and S. Bauer at NASA Langley. In essence the method shapes the wing contours by taking into consideration wing thickness constraints and the fact that Cp distributions acting on wing surfaces should correspond to the directional surface normals in such a way as to minimize drag. The technique has been validated by a wind tunnel test of an optimized version of the M247A configuration. The method currently requires the use of another design approach to incorporate the nacelles and diverters.

The second alternative design approach is the Constrained Direct Iterative Surface Curvature (CDISC[12]) method developed by R. Campbell, also from Langley. The technique is based on an inverse approach where a target pressure distribution is specified and the flow solver is driven by the design method to attain the target by relating a change in surface slope to a change in Cp for supersonic flow. The technique has been integrated with both Euler and Navier-Stokes analysis methods, and thus allows for true Navier-Stokes-based design capabilities. In order to accommodate situations where the optimal pressure distribution is not known, options are provided whereby the method attempts to construct targets by shifting the loading in the streamwise direction.

All of the methods currently available are limited in one or more ways. One major area requiring attention is the actual design of the nacelle and diverter shapes. Not only does this pose a challenge to the available design methods, with those using pseudo nacelle effects being inherently limited, but the capability will require significant effort to include many more constraints (thrust angle penalty, inlet flow quality, nacelle thickness, nacelle interior dimensions and angles, etc.). The Ames and Douglas methods used thus far employ the pseudo nacelle approximation and are therefore limited even in their ability to integrate the nacelles and diverters much less actually design them. The multiblock SYN87-MB promises the hope of accomplishing some of these integration and design challenges. The Boeing approach also will need careful reworking in that transpiration boundary conditions will have to be applied to the nacelles and diverters in addition to the wing and body. Computing intersections among these various components will prove to be an implementational challenge regardless of the approach used.

Although some work has taken place to illustrate the feasibility of viscous-based aerodynamic shape design, a robust tool that attains the level of improvements shown by the inviscid design methods while retaining their constrained design capacity has not been demonstrated. As has been seen from the latest round of TCA optimization studies, pressure drag differences can occur between viscous and inviscid calculations when designs are pushed for optimum performance. It therefore remains an open question well worth exploring as to how much additional benefit might be obtained if a true viscous design tool were used for cruise point optimization. It must be remembered that even the inviscid methods used today are computationally very demanding. Future methods using viscous flows that can treat nacelle/diverter design in conjunction with wing/body design will be even more demanding on available computer resources. As if this were not enough, it will not be long before we will have to be able to treat viscous complete configuration design capability while juggling either multiple design points or multiple disciplines, or both.

Limitations of Current Methods

- **Limited Nacelle Diverter** Shape **Design** and Integration Capability
- **No Available Viscous Capability** for Full Configuration Design
- Current Design Methods are Still Computationally Demanding
- **Multipoint** Capability has **Not** Been **Demonstrated**
- **Aeroelastic Analysis** and **Design** Capability Are **Not Mature**
- High Fidelity **Multidisciplinary Methods Do Not Exist**

A clear requirement for these future methods is a Navier-Stokes solver to serve at their cores. A Navier-Stokes solver used at the heart of an aerodynamic shape design method must satisfy certain requirements. These include: treatment of goemetric complexity, computational efficiency, computational accuracy, robustness, and adequate convergence capability. Since the goal is to treat full configuration design, any future Navier-Stokes flow solver to be considered must be able to address complete configuration analysis. Even in a design environment where an adjoint solver is used to mitigate the cost of the gradient calculations, it is absolutely essential that the computational cost of a Navier-Stokes analysis be as small as possible. Many current methods require 10-50 hours of CRAY C90 time in order to obtain one complete configuration solution. An acceptable computational cost is 1 hour of wall clock time for a single solution. This will allow several design cycles to be performed over-night using an adjoint-based approach.

Because of the large increase in the minimum number of mesh points and the high aspect ratio of many of the computational cells for a Navier-Stokes solution, the issue of switching to a higher-order dissipation scheme is of great importance. Simple scalar diffusion schemes tend to pollute the viscous layer with artificial diffusion that creates an artificial Reynolds number shift. Another deficiency of many Navier-Stoke solvers is their delicacy. Many require parameter adjustments, especially in the turbulence model, for even small geometry changes to meet convergence/solution time criteria. A solver to be used within a design algorithm must be very robust, working efficiently and consistently within the entire design space of the problem. Lastly, because the design algorithm will be looking for gains in the hundredths of a drag count range, the solver must be able to converge to the extent that it can resolve such small force increments.

Some expected guidelines for acceptable complete configuration Navier-Stokes performance are: one hour computer wall clock time for a single solution, one day to completely remesh a configuration, and one day to run a complete design run. The last two capabilities will not only hinge on the solver but also on mesh generation and design algorithm capabilities.

Flow Solver Requirements

- **Navier-Stokes** Flow Solver **Requirements** for Use in **Design**
  - **Complex Geometries**
  - **Speed**
  - **Accuracy**
  - **Robustness**
  - **Convergence**
  - **One Hour Computer Wall Time** for a Single Solution
  - **One Day Turn Around for Analysis** (Including Remeshing) — Currently it is One Week
  - **One Day Complete Design Run** — Currently Not Feasible

Many recent developments may help the situation with regards to Navier-Stokes solvers. First on the list is the continued advancement of computer technology, especially parallel systems. Parallel computing has finally reached a state where stability and portability allow it to be applied to problems such as production-type Navier-Stokes solutions. The MPI standard now available on many distributed and shared memory machines allows the same parallel source code to be compiled and run on many architechtures. Furthermore, carefully written software can be implemented such that near-linear speed-ups can be obtained on all of these platforms. These developing capabilities point to many hundreds or thousands of commodity CPUs being used in future computers or networks of computers to solve problems which are intractable today. The speed enabled by parallel computing will be truly awesome (see later in this presentation).

The advent of higher-order dissipation schemes now available in most N-S solvers allows for accuracy even in the presence of extreme aspect ratios of the computational cells. An example of one of these new schemes is the CUSP scheme developed by A. Jameson[6].

In order to obtain computational efficiency in a Navier-Stokes solver, a first step is to use all the convergence acceleration techniques that have worked well for inviscid methods. These include residual smoothing and multigridding. However, even with these techniques implemented, the performance of current production N-S solvers is not efficient when compared with comparable Euler solvers. They usually take many times the number of time steps in order to resolve a solution or fail to attain the required level of convergence often demanded by a design algorithm. The main problem seems to be a lack of the multigrid algorithm's ability to damp properly all the modes in the time-propagating solution. Unlike the multigrid Euler solvers using cells with reasonable aspect ratios, multigrid N-S solvers with their extreme aspect ratio cells convect waves at different rates in different directions. This causes some of the modes not to be damped during the iteration process. Thus a standard multigrid N-S solver often gets stuck at a convergence level well above machine accuracy. A recently developing alternative to full multigridding may alleviate this problem and allow N-S solvers to perform comparably to their Euler counterparts. The technique combines block-Jacobi preconditioning with J-coarsening multigridding. The underlying theoretical work has been done by N. Pierce[10] at Oxford University. The new method should not only drastically reduce N-S solution time but also allow for convergence to any desirable level.

Probably the bleakest topic with respect to N-S solvers is turbulence modeling, a necessary evil. While this problem may not seem as severe for supersonic cruise point design problems as in other cases such as transonic buffet, a quick look at the predicted local skin friction values from various turbulence models demonstrates that we are still in the dark ages. For the supersonic cruise point, our experience at Ames shows that while pressure drag can probably be predicted accurately by the available N-S solvers regardless of the turbulence model used, both the local and total skin friction values are yet to be trusted by any of the models. The current state of the science points to replacing the Baldwin-Lomax turbulence model with the Spalart-Almaras model. Much more work in this area is clearly needed but is probably way beyond the scope of HSR.

- **Developing Navier-Stokes** Flow Solver **Technologies**
  - Parallel Computing Technologies
    - **Portable Code** via the **MPI** Standard
    - Improvements in Both Shared and Distributed Memory Architectures
    - Close to **Linear Scaleability**
    - **Commodity CPUs**
  - Computational Accuracy
    - **Higher Order Dissipation Schemes**
  - Computational Efficiency
    - **All Previous Techniques**
      - Residual Smoothing
      - Multigridding
    - **Advanced Preconditioned Multigridding**
      - J Coarsening Multigridding
      - Block Jacobi Preconditioning
  - Turbulence Models ???

The new multiblock N-S flow solver FLO107-MB embodies most of these developing technologies. It is a general multiblock flow solver that allows arbitrary topologies though point-to-point matched meshes. A double halo is used to retain a complete stencil for both the convective and dissipative fluxes across the block boundaries. The algorithm is an extension of the existing single-block Euler and Navier-Stokes algorithms pioneered by A. Jameson and L. Martinelli. As such it retains many feature of its heritage. The time stepping is done by a multistage Runga-Kutta-like algorithm, where in the case of multiblock meshes the residuals are updated along the double fringe at each stage. The spatial discretization is a standard cell-centered finite volume scheme. Two dissipation schemes are available: the original blended 2nd- and 4th-order difference scalar dissipation scheme and the newer CUSP dissipation scheme. Convergence is accelerated with both implicit residual smoothing and full multigridding. Each coarser level within the multigridding retains the same double halo construction so that the speed-up realizable via the multigridding should not be hindered by the block boundaries. A J-coarsening multigridding scheme that also employs a block-Jacobi preconditioning iteration algorithm to accelerate convergence further is under development. One of the great advantanges of FLO107-MB is that it is implemented to take adavantage of current parallel computing technologies. It is constructed such that it may use any number of processors up to the number of blocks within the mesh to be used. A preprocessor is run to divide the blocks among the available processors in such a way as to load-balance the problem as well as possible. The communications between blocks that are outside a given processor are treated using the MPI standard routines that are now supported on most systems. Ports to the IBM SP2, SGI-R8000/SGI-R10000, CRAY J90, and HP systems have all been readily accomplished. The Baldwin-Lomax turbulence model has been implemented with the Spalart-Almaras model currently under delvelopment.

FLO107-MB Multiblock Navier-Stokes Solver

- Starting Points Are the **FLO107** Single Block Flow Solver and **FLO87-MB**.
  - General Multiblock Point-to-point Topology
  - Double Halo Block Interfacing to Maintain Convective and Viscous Fluxes Across Block Boundaries
- Natural Development From Euler to Navier-Stokes
  - Jameson Style Runga-Kutta Explicite Time Stepping
  - Cell Centered Spacial Discretization
  - 2nd and 4th Difference Scalar Dissipation Option
  - CUSP Higher Order Dissipation Option
  - Residual Smoothing
  - Full Multigridding
  - Preconditioned J-Coarsening Multigridding (under development)

- Analysis Carried Out on Parallel Computers
  - Code ported to IBM-SP2, SGI-R8000/R10000, CRAY-J90, and HP architechtures.
- Turbulence Models
  - Baldwin-Lomax
  - Spalart-Almaras (under development)

During the early fall of 1996, FLO107-MB was given a trial by fire christening as immediately after its development it was used for a massive number of Navier-Stokes calculations around configurations that represented a real transonic transport design. At the time, McDonnell Douglas Aircraft was considering the development of a new large transport configuration dubbed the MD-XX. Many design variations were being considered and multiple Navier-Stokes calculations were needed in order to sort out the benefits and drawbacks of each design. Before one particular design review it was determined that 6 alternative wing designs needed to be analyzed at 5 design points in addition to a drag creep point and a transonic buffet boundary point. In order to complete the design review on schedule for the development of the aircraft it was necessary to perform these calculations during a single weekend. Thus between September 9th and September 11th 1996 a total of 60 N-S calculations were run on the 6 competing configurations. Each mesh, which was automatically generated for the wing-body geometries, contained 48 blocks and 1.3 million computational cells. By using three different IBM SP2 machines located across the country it was possible to run up to 10 flow simulations concurrently with each calculation occupying 16 processors. Each calculation took 2 hours of wall clock time to complete 300 4-level multigrid cycles using the 16 processors. The calculations all converged roughly 4 orders of magnitude. These times turn out to be 30% more expensive than Euler calculations per grid point per cycle. Furthermore since each of the calculations used the CUSP higher order dissipation scheme a 50% additional computational cost was incurred over the standard scalar dissipation scheme. The main cost of switching to Navier-Stokes calculations is not in the additional cost of evaluating the Navier-Stokes terms but in the additional cycles required to converge the solution and in the vast increase in the number of mesh points that are required to obtain reasonably mesh-independent solutions. The demonstration that weekend both validated the flow solver and proved that it is possible to perform a large number of N-S calculations using a modern flow solver and parallel computing.

Large Transonic Transport Configuration

- Mesh A
  - Wing/Body
  - 48 Blocks
  - 1.3 Million Mesh Points
- Quick Cross-Checks for Four Designs
  - MD-XX Baseline Configuration
  - 6 Alternative Wing Designs Analyzed
  - 5 Cruise Point Checks + 1 Drag Creep Point + 1 Buffet Point
- Human Costs
  - Geometries Finalized Friday September 9th
  - 60 Navier-Stokes Solutions Completed Sunday September 11th
  - All Automatic Wing/Body Mesh Generation Focused Human Time on Monitoring Progress and Post-Processing Results

- Computational Costs
  - Up to 10 Analysis points were Calculated Concurrently Using IBM SP2 Machines Spread Across 3 Sites
  - Each Analysis was Run for 300 Multigrid Cycles and Achieved a Reduction in the Average Residual of 4 Orders
  - 16 Processors were used for Each Case and Took 2.0 Hours of Wall Clock Time
  - Navier-Stokes Calculations are Roughly 30% More Expensive than Euler Calculations
  - Higher Order Dissipation Schemes Add 50% to the Computational Costs

Low-Wing Transport Configuration: Trailing Edge

Navier Stokes Solution

Mach = 0.86 C_L = 0.6 Re = 50×10^6

1.5 Million Mesh Points 48 Blocks

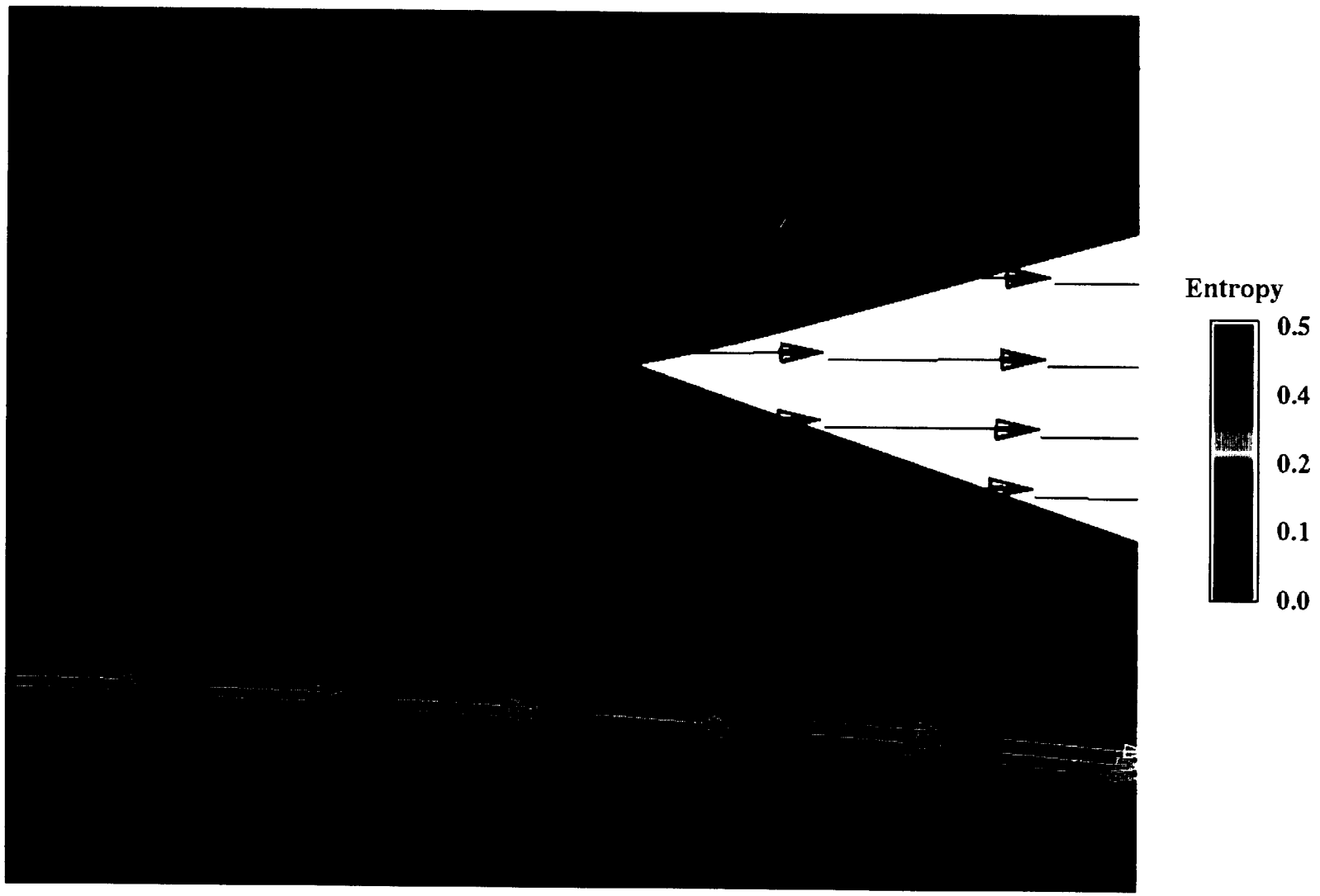

Low-Wing Transport Configuration: Leading Edge

Navier Stokes Solution

Mach = 0.86 C_L = 0.6 Re = 50×10^6

1.5 Million Mesh Points 48 Blocks

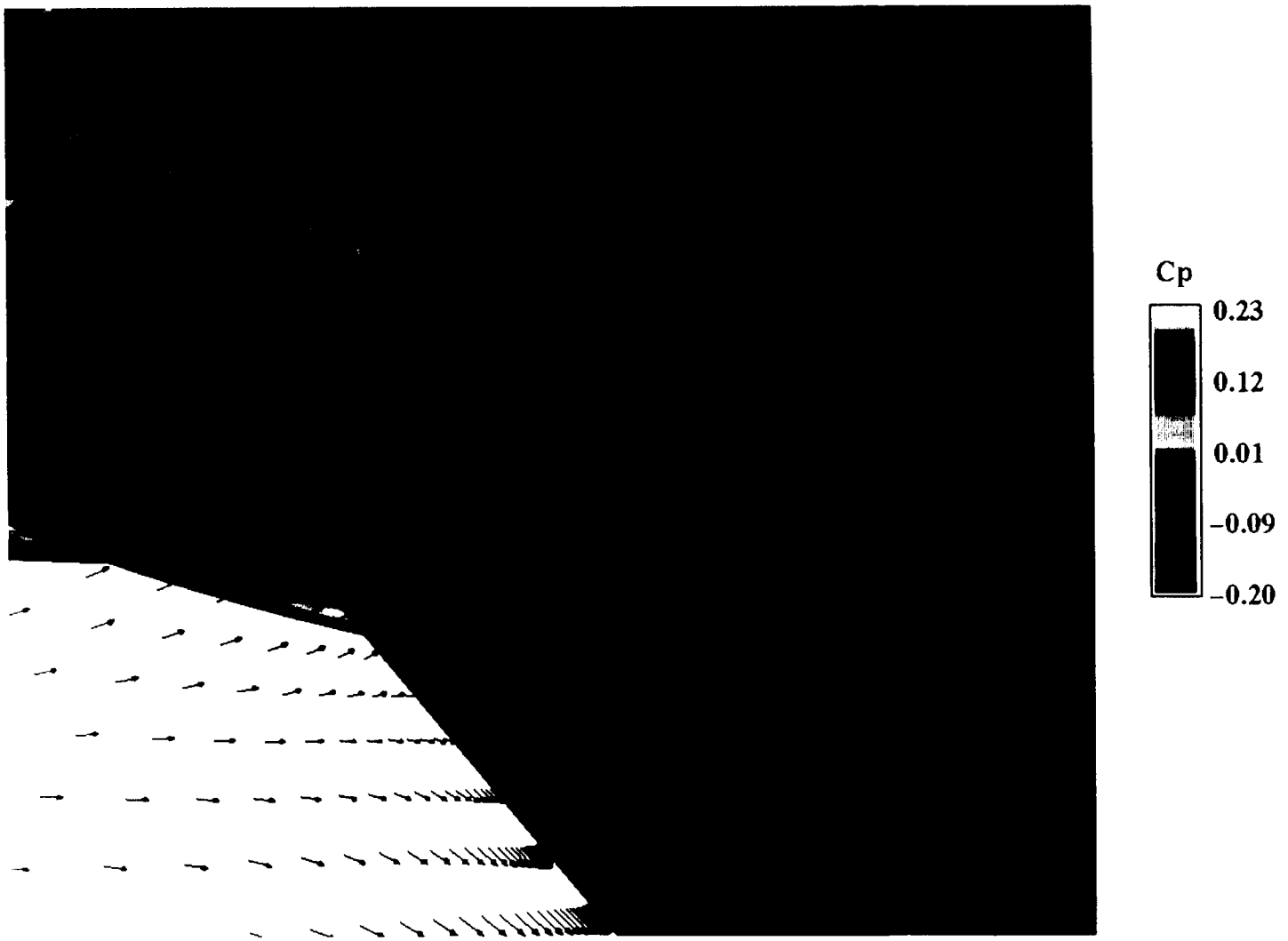

A further demonstration of the N-S analysis tool came with the need to determine the effects of the nacelles and winglets on the aerodynamic performance of the configuration presented in the previous slide. These evaluations would drive further design refinements. This time instead of a wing-body geometry the geometry consisted of wing-body-nacelle-winglets. The first mesh around the baseline configuration which was created using GRIDGEN took three weeks. It featured 234 blocks and 6.1 million computational cells. All subsequent meshes for various alternative wing designs were developed in about 6 hours by first generating the surface meshes within GRIDGEN. The volume meshes were then created using the mesh perturbation techniques outlined in the earlier presentations. Again six alternative designs needed to be analyzed at various design conditions. This time the calculations were run for 500 multigrid cycles using 32 processors. Each calculation used 5.5 hours of wall clock time and converged the average residual 4 orders of magnitude. In order to make aerodynamic design of complete configurations possible while using the Navier-Stokes equations these calculations must be able to run in about 1 hour. With the current code this could be done by using roughly 180 processors. However with enhancements that are under way to the method it may be possible to accomplish the calculation in 1 hour with just 32 processors thus opening the door to full Navier-Stokes-based design.

Large Transonic Transport Configuration, continued

- Mesh B
  - Wing/Body/Nacelle/Winglets
  - 234 Blocks
  - 6.1 Million Mesh Points
- Quick Validation of Alternative Wing Designs
  - MD-XX Baseline Configuration
  - 6 Alternative Wing Designs Analyzed
- Human Costs
  - Three Week Initial Mesh Generation Time for Baseline Configuration
  - Each of the 6 Alternative Configurations Took 6 Interactive Hours to Remesh
  - 20 Solutions Total were Calculated Over a 1 Week Period

- Computational Costs
  - Each Analysis was Run for 500 Multigrid Cycles
  - The Average Residual was Converged 4 Orders of Magnitude
  - 32 Processors were Used with a Wall Clock Time of 5.5 Hours

Large Transonic Transport Configuration
FLO107-MB Solution
Baldwin-Lomax Turbulence Model
Mach = .85 234 Blocks 6.1 Million Mesh Points

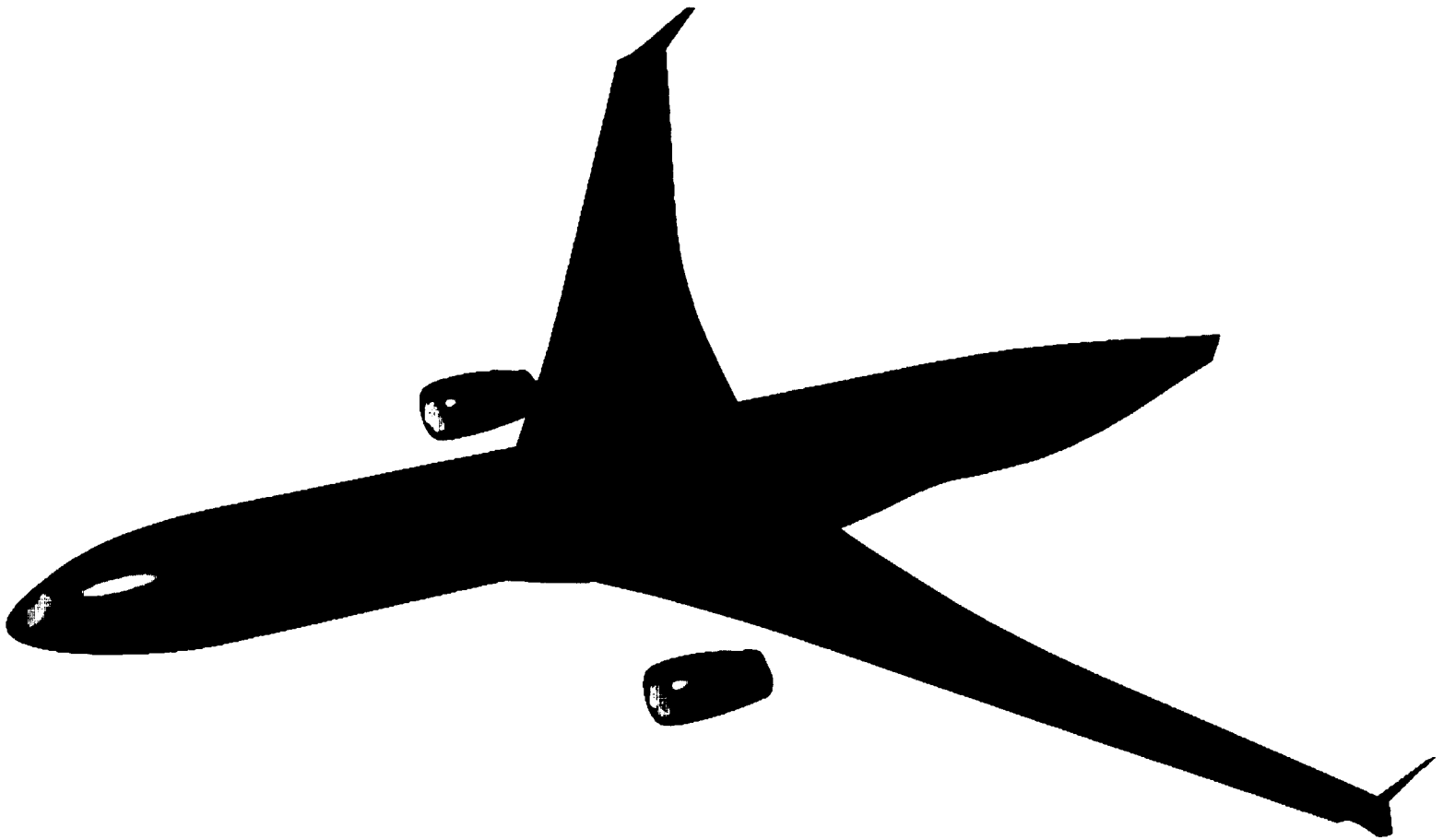

As a final example of the analysis capability of FLO107-MB, a complete configuration transonic business jet is analyzed. The mesh took 1.5 weeks of interactive time using GRIDGEN. The objective of this study was to determine the limits of current N-S capability to extend into the transonic buffet regime and to predict drag rise accurately. The configuration included wing, body, nacelle, pylon, vertical tail and horizontal tail. The mesh featured 240 blocks and 5.8 million computational cells. Each analysis was run for 300 multigrid cycles on 32 processors. The average residual was converged 4.3 orders of magnitude and took 3.25 hours of wall clock time.

Transonic Business Jet Configuration

- – Wing/Body/Nacelle/Pylon/Vertical Tail/Horizontal Tail
  - – 240 Blocks
  - – 5.8 Million Mesh Points
- Determination of Limits of Navier-Stokes Analysis Capability
  - – Validate Attached-Flow Transonic Solutions Against Wind Tunnel Data
  - – Prediction of Transonic Drag Rise Characteristics
  - – Prediction of Transonic Buffet Boundary
  - – Post-Buffet/Separated Flow Analysis
- Human Costs
  - – 1.5 Weeks Initial Mesh Generation Time

- Computational Costs
  - Each Analysis was Run for 300 Multigrid Cycles
  - The Average Residual was Converged 4.3 Orders of Magnitude
  - 32 Processors were Used with a Wall Clock Time of 3.25 Hours

Transonic Business Jet
FLO107-MB Solution
Baldwin-Lomax Turbulence Model
Mach = .82 240 Blocks 5.8 Million Mesh Points

Even if the Navier-Stokes flow solver techniques begin to meet requirements adequately, many areas of aerodynamic design are in need of attention. For instance, to date only cursory investigations on the choice of families of design variables have been explored. It may be a worthy investment for the HSR program to support more satisfactory analyses and numerical investigations studying the effectiveness of various design space parameterizations.

Another area requiring greater investigation is the sensitivity of the aerodynamic performance to the constraints that have thus far been placed on configurations such as the TCA-6. Such a study, combined with an integrated effort accomplished by the HSR Technology Integration Group, should result in weight trade penalties that could be translated back and forth with aerodynamic performance penalties and thereby incorporate some MDO design sensibility into the current aero.-only design methods.

Much further research is also needed into exploring the optimum coupling between the aerodynamic and sensitivity analysis methods and the numerical optimization method. Clearly, there is room for improvement over dense-matrix methods such as NPSOL. One possible alternative is the limited memory quasi-Newton class of methods which are less sensitive to gradient inaccuracies corrupting the approximate Hessian, and allow for a greater number of design variables by avoiding dense matrix operations. Another alternative is to do away with second-order information altogether by resorting to a steepest descent approach and coupling the flow and sensitivity analyses very closely to the design steps. This is the strategy advocated by Antony Jameson, combined with appropriate smoothing of the gradient vectors. At the other extreme is the use of a full Newton algorithm through direct calculation of the full Hessian matrix via multiple flow solutions and an adjoint solution.

Regardless of the optimization algorithm used, it will be necessary to bring Navier-Stokes adjoint methods to the level of maturity that current Euler-based adjoint methods have attained. Jameson has recently introduced such a capability although it has yet to be exercised adequately.

Perhaps the challenge most facing the recently proven design methods is their expansion to treat more complex design problems and to incorporate a limited degree of MDO capability. In the coming year, investigations will attempt to extend the design methods to become sensitive at least to multiple design points, aeroelastic effects, inlet flow quality, jet plume effects, and thrust angle losses due to nacelle orientations. It is presently not unreasonable to consider nacelle/diverter shape design. Further out on the horizon, attempts must be made to bring about a true MDO capability by incorporating structural and manufacturing considerations into the design methods, possibly leading to the use of DOC as the objective function.

However, it is the impression of the authors that, while all of the improvements and studies for both Navier-Stokes solvers and design algorithms, etc., are salient, the HSR program needs to begin a concerted effort towards achieving a better understanding of the fluid dynamics phenomena affecting the HSR design space. For instance, the differences that exist between inviscid and viscous calculations are still poorly understood. Clearly it would be beneficial to understand the differences better. Noteworthy is the fact that all of both the inviscid and viscous analysis methods applied to the TCA-6 configuration have agreed well on the pressure drag. However, when the optimized designs are analyzed, the inviscid and viscous methods show discrepancies. In the case of viscous drag, the discrepancies are considerably greater, and they are only clouded further by the trip drag and Alpha uncertainty issues apparent in all wind tunnel tests. It is well within the HSR charter to seek resolution of these issues.

Design Method Requirements

- Design Technique Enhancements Required in The Future
  - General **Design Variable** and **Constraint** Treatment
    - * Research Directly Comparing Families of Design Variables
    - * Constraint Sensitivity Study
  - Advanced **Constrained Numerical Optimization** Algorithms
    - * More Robust Algorithms
    - * Greater Coupling Between Design and Flow Analysis Algorithms?
    - * Second Order Formulations?
  - **Adjoint** Solver For **Navier-Stokes** Equations
  - Treatment of **Multiple Disciplines** in Design
    - * Aeroelastic Analysis and Design
    - * Inlet Flow Quality
    - * Jet Plume Effects
    - * Thrust Angle/Losses Due to Nacelle Orientations

Finally, as seen from a practical point of view, a constructive analytical study of relevant physical phenomena may lead to the formulation of objective functions that are better suited to supersonic design. It is fortunate that for transonic flows an intuitive understanding of the shape of the pressure distribution can lead to the development of very efficient designs. While the Natural Flow Wing technology takes a stab at this type of approach for supersonic configurations, it would be beneficial if a far more comprehensive understanding of the flow physics could be established. Such an understanding may point to new objective functions that could be posed for the supersonic design problem.

* Nacelle Shape Design
* Structures and Materials?
* Manufacturability?
* DOC as an Objective Function!?

– Greater **Emphasis** on **Understanding Fluid Dynamics**

* Difference in Performance Between Inviscid & Viscous Analysis
* New Objective Functions (Drag Distributions?)

In a view towards making the design tools both current and future to be more versatile and easy to use, improvements are needed in the areas of geometry treatment, mesh generation, and mesh perturbation.

Future design methods that work directly with CAD entities as opposed to point definitions will facilitate much more rapid interdisciplinary cross analysis and design as well as quick turn-around of wind tunnel model fabrications. Thus if a parametric form of CAD entity served to drive the design process, such CAD entities would remain in the same formats for both input and output by the design tool. However, this integration requires that CAD entities can be manipulated, intersected, and parameterized by the design tool.

With regards to the computational meshes, there are two aspects to consider: the initial mesh generation, and the subsequent mesh perturbations. Once complex configurations are considered, mesh generation invariably becomes a semi-interactive procedure. Limiting this highly labor-intensive portion of the design process will be of great importance. Fortunately, the other half of the process, mesh perturbation, has become highly automated, efficient, and reliable. The various approaches used at Boeing, McDonnell Douglas, Langley, and Ames should be compared both in terms of algorithm efficiency and resulting mesh quality so that all parties could benefit. It seems that much of the work in this area has been done independently by each organization.

As a final aside with regards to geometries and meshes, the authors would like to mention an alternative to structured multiblock meshes. One possible and very attractive alternative is the prismatic + unstructured tetrahedral approach. The prismatic meshes would extend away from solid surfaces up to the point of the height of the viscous boundary layer at which point the switch would be made to a completely unstructured tetrahedral mesh. Advances in mesh generation algorithms for such topologies seem to indicate that automated capabilities treating complex configurations will soon be in hand. Such a capability will offer even greater geometric complexity in the design process as well as reduce the number of mesh points that will be required for accurate design development.

Geometry and Mesh Requirements

- **Direct CAD — Design Interface**
  - Aerodynamic Design Methods **Must Work** with **CAD Entities**
  - **Geometry Entities** must Underly and **Drive** the **Design** Process
  - **Geometry Manipulations** and **Intersections** Must be **Automated**
- Mesh Generation/Perturbation Techniques
  - **Faster**, Less Interactive **Mesh Generation**
  - Cross Testing & Improvements in Mesh Perturbation Techniques
- Prismatic + Tetrahedral Unstructured Mesh Generator and Flow Solver
  - Possible **Alternative** to Current **Structured Mesh Design** Tools
  - Offers **Greater Geometric Complexity**
  - **Reduces** Required **Number** of **Mesh Points**
  - Automatic Mesh Generation/Perturbation Seems Feasible

One apparent realization that is clear about all of the design optimization methods currently available for HSR applications is that they are not easy to use by anyone except the developer(s) or those that are closely associated with the developer(s). To change this trend, it will be necessary to build a tool package that interfaces better with these sophisticated modern design methods. It is ironic that we are living in the era of the information revolution yet our best aerodynamic design tools fade further and further into user-unfriendliness owing to their extreme complexity. Four areas needing attention are: design space visualization, constraint space visualization, a graphical user interface (GUI) to set up the design problem, and a GUI to monitor the design progress.

Visualization Techniques and Tools for Engineers

- Design Space Visualization
- Constraint Space Visualization
- Graphic User Interface (GUI) to Set Up Design Problems
- GUI to Monitor Design Output

References

1. A. Jameson, T.J. Baker, and N.P. Weatherhill, *Calculation of Inviscid Transonic Flow Over a Complete Aircraft*, AIAA paper 86-0103, 1986.

2. P. Raj, *Computational Simulation of Free Vortex Flows Using an Euler Code*, ICAS-84-1.3.1, 14th Congress of the International Council of the Aeronautical Sciences, Sept. 1984.

3. P. Gill, W. Murray, and R. Pitfield, *The Implementation of Two Revised Quasi-Newton Algorithms for Unconstrained Optimization*, Report DNAC 11, National Physical Laboratory, Division of Numerical Analysis and Computing, 1972

4. R. Kennelly, *Improved Method for Transonic Airfoil Design-by-Optimization*, AIAA paper 83-1864, 1983

5. P.E. Gill, W. Murray, M.A. Saunders, and M.A. Wright, *User's Guide for {NPSOL} (version 4.0). A {FORTRAN} Package Nonlinear Programming*, Stanford University Technical Report SOL86-2, 1986

6. A. Jameson, *Analysis and Design of Numerical Schemes for Gas Dynamics 1 & 2*, RIACS Technical Reports 94.15 & 94.16, 1994.

7. R.M. Hicks. Shreekant Agrawal, D.L. Antani, S.E. Cliff, and J. Reuther, *An Experimental/Computational Evaluation of an Arrow-Wing HSCT Designed Using Numerical Optimization and the Euler Equations*, Unpublished.

8. D.P. Young, W.P. Huffman, M.B. Bieterman, R.G. Melvin, F.T. Johnson, C.L. Hilmes, A.R. Dusto, *Issues in Design Optimization Methodology*, BCSTECH-94-007, 1994

9. J. Reuther, A. Jameson, J.J. Alonso, M.J. Rimlinger, and D. Saunders, *Constrained Multipoint Aerodynamic Shape Optimization Using an Adjoint Formulation and Parallel Computers*, AIAA paper 97-0103, 1997.

10. N.A. Pierce, *A Preconditioned Implicit Multigrid Algorithm for Parallel Computation of Unsteady Aeroelastic Compressible Flows*, AIAA paper 97-0444, 1997

11. S.X.S. Bauer, and S.E. Krist, *The Application of the Natural Flow Wing Design Philosophy to the HSR Arrow Wing Configuration*, First NASA/Industry HSR Configuration Aerodynamics Workshop, 1996.

12. R.L. Campbell, *Efficient Constrained Design Using Navier-Stokes Codes*, AIAA paper 95-1808, 1995

NASA Ames Research Center

AN ANALYSIS OF CFD AND FLAT PLATE PREDICTIONS OF FRICTION DRAG FOR THE TCA W/B @ SUPERSONIC CRUISE

Scott L. Lawrence
NASA Ames Research Center
Moffett Field, California

OUTLINE

- MOTIVATION/INTRODUCTION
- ANALYSIS
  - -FLAT PLATE
  - -WING
  - -FUSELAGE
- ODDS AND ENDS
- SUMMARY/CONCLUSIONS

1997 High Speed Research Aerodynamic Performance Workshop
NASA Langley Research Center
February 25-28, 1997

This paper presents results of a study which attempted to provide some understanding of the relationship between skin friction drag estimates produced by flat plate methods and those produced by Navier-Stokes computations. A brief introduction is followed by analysis, including a flat plate grid study, analysis of the wing flow, an analysis of the fuselage flow. Other results of interest are then presented, including turbulence model sensitivities, and brief analysis of other configurations.

NASA Ames Research Center

SUMMARY OF TCA COMPONENT SKIN FRICTION DRAGS

Wind Tunnel Conditions: Re = 4 x 10^6/ft, 1.675% scale model

Integrated Skin Friction Drags

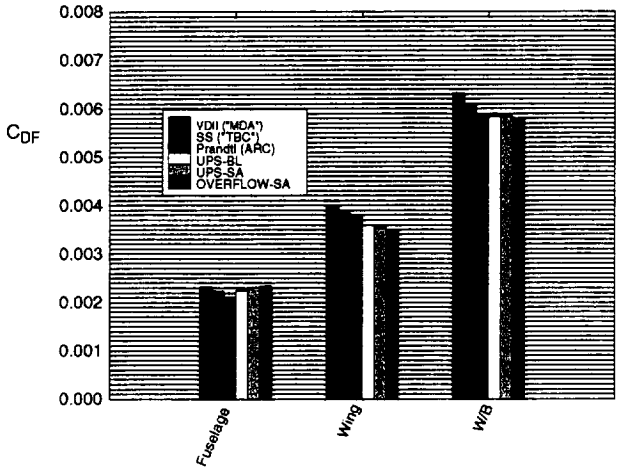

OBJECTIVES:

- -UNDERSTAND WHY N-S METHODS TEND TO UNDERPREDICT FLAT PLATE C_{Dv} ON THE WING
- -DETERMINE IF THERE IS A "BEST" FLAT PLATE METHOD(OLOGY)

This study was primarily motivated by two existing situations: 1) the substantial variation in flat plate predictions produced by the various organizations involved in the optimization effort, and 2) the substantial variation between typical Navier-Stokes predictions for friction drag and flat plate predictions.

This figure illustrates both of these issues. Friction drag is plotted for six different prediction methods, broken down by component. The flat plate methods were applied consistently within the NASA Ames friction drag code developed by Hicks, and may not represent the identical method of application used by the associated organizations. Friction drag is computed for the fuselage with a single evaluation of average skin friction for the Reynolds number based on the length of the vehicle. The wing is broken spanwise into strips and average skin friction is evaluated on each strip using the Reynolds number based on the local chord length. The flat plate wing and fuselage drag estimates have been adjusted so that the associated areas agree with the areas as demarcated in the CFD grid.

A four drag count discrepancy is observed between the highest (van Driest II) and lowest (Prandtl) flat plate predictions for the wing/body total friction drag. On a percentage basis, the discrepancy is greater on the fuselage than on the wing. This is caused by the failure of the Prandtl method at higher Reynolds numbers as will be seen in a subsequent figure.

Results of the parabolized Navier-Stokes code UPS and the OVERFLOW Navier-Stokes code are observed to fall within the spread of flat plate methods for the fuselage, but are 2-5 counts below the flat plate results on the wing. The main objective of this study was to understand this discrepancy. A secondary objective was to shed light on the spread in flat plate predictions and obtain information which might lead toward flat plate method standardization.

APPROACH

- IDENTIFY FLAT PLATE METHOD THAT AGREES WITH GRID-INDEPENDENT CFD SOLUTIONS *ON A FLAT PLATE*
  - -TURBULENT INCOMPRESSIBLE FORMULAS
  - -COMPRESSIBILITY CORRECTIONS
  - -FLAT PLATE GRID STUDY
- APPLY THE CFD-COMPATIBLE FLAT PLATE FORMULA TO THE TCA WING/BODY
  - -LINE INTEGRAL
  - -SURFACE INTEGRAL
- ATTEMPT TO ACCOUNT FOR DIFFERENCES BY QUANTIFYING VARIOUS NON-FLAT-PLATE PHYSICAL EFFECTS
  - -WING
  - -FUSELAGE

Results of the UPS parabolized Navier-Stokes code were the focus of the present analysis because of the author's familiarity with the code. Similar analysis can obviously be applied to any N-S solution.

The first step in the analysis was to try to remove what might be called bias, i.e., differences in computed and flat plate skin friction on a case for which the flat plate assumptions are valid. A wealth of flat plate methods are available from the various incompressible formula/compressibility correction permutations. A method was sought that would provide the best agreement with UPS-generated skin friction coefficients for Reynolds numbers ranging from wind tunnel conditions to flight conditions. A grid study was performed so that the comparisons would be performed on grid-independent solutions.

The UPS-compatible method could then be applied to the TCA6 wing/body using both the line-integration method described earlier as well as by surface integration of the local skin friction coefficients. The latter method allowed for point-to-point comparison with UPS results.

Finally, use of the surface integration approach allowed for some modification of the flat plate method to include some non-flat-plate effects, and this allowed these effects to be quantified to some extent.

NASA Ames Research Center

TURBULENT FLAT PLATE FORMULAS

INCOMPRESSIBLE FORMULAS:

Method	Local Skin Friction	Average Skin Friction
Prandtl	$C_f^i = 0.058/Re_x^{0.2}$	$C_F^i = 0.074/Re_x^{0.2}$
Prandtl-Schlichting	$C_f^i = 0.39/(\log Re_x)^{2.58}$	$C_F^i = 0.455/(\log Re_x)^{2.58}$
Karman-Schoenherr	$\frac{1}{\sqrt{C_f^i}} = 4.15\log(C_f^i Re_x) + 1.7$	$\frac{1}{\sqrt{C_F^i}} = 4.13\log(C_F^i Re_x)$
White	$C_f^i = 0.455/(\ln(0.06Re_x))^2$	$C_F^i = 0.523/(\ln(0.06Re_x))^2$?
Sivells-Payne	$C_f^i = 0.088\log(Re_x/233.7)/(\log(Re_x/31.62))^3$	$C_F^i = 0.088/(\log(Re_x/31.62))^2$

NOTES:

- -KARMAN-SCHOENHERR IS THE ONLY ITERATIVE APPROACH
- -THE WHITE C_F FORMULA DOES NOT APPEAR TO BE CONSISTENT WITH THE C_f FORMULA

Applied Computational Aerodynamics Branch

Lawrence-HSR/CA - 7 of 55

Compressible flat plate formulas tend to consist of an incompressible formula that is stretched and scaled with compressibility effects. The incompressible formula, to a large extent, provides the basic shape if the skin friction distribution. Some of more well known of the incompressible formulas are shown in this figure, along with a method which may not be as well known (Sivells-Payne) but which will be relevant to this study. Each method for local skin friction, C_f, can be integrated from the leading edge of the plate to x to provide a function for the average skin friction, C_F.

The Sommer-Short and van Driest II compressibility corrections are typically, though not necessarily, associated with the Karman-Schoenherr incompressible formula, the only formula requiring iteration.

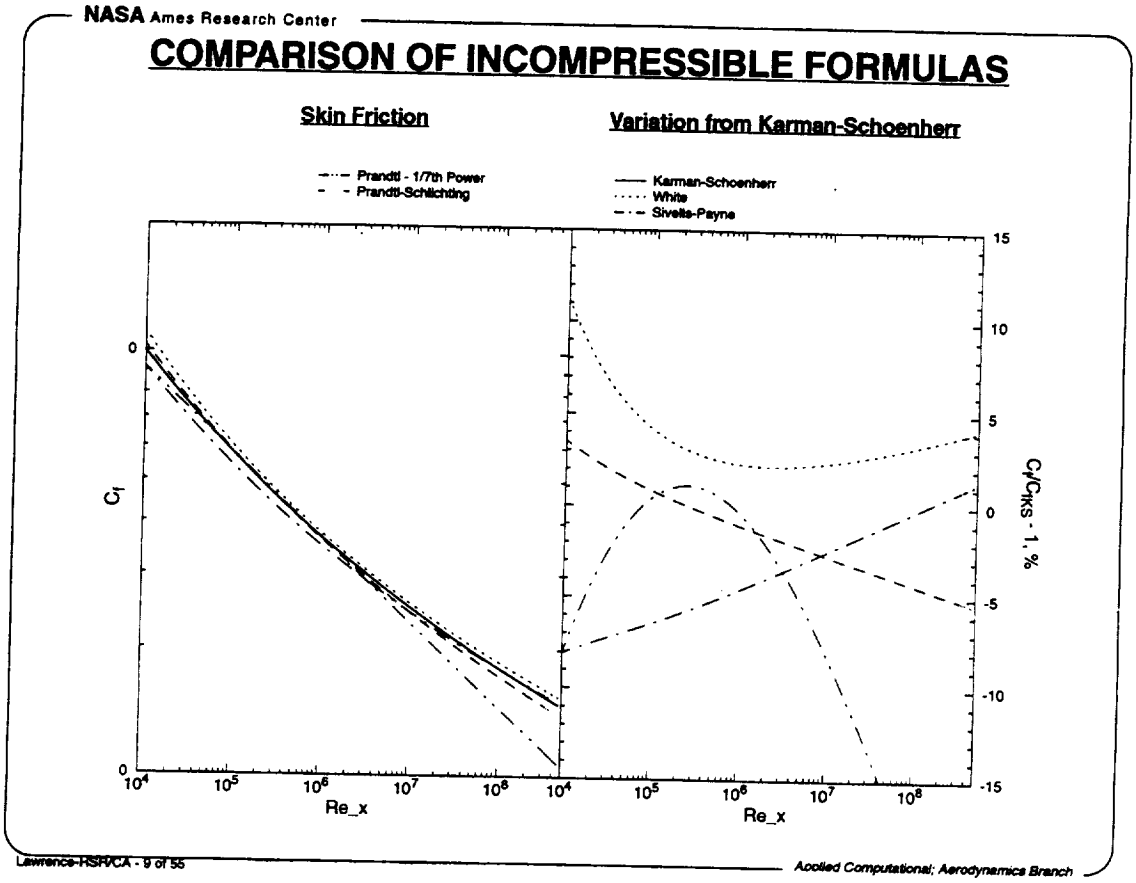

The incompressible formulas described on the previous page are plotted on the left in terms of local skin friction coefficient. On the right, the formulas are compared with the Karman-Schoenherr formula in terms of a percentage variation. Not surprisingly, the formulas compare fairly well in the "wind tunnel" Reynolds number range. The White formula is higher than the others for all Reynolds numbers. The other most notable feature of these plots is the deterioration of the Prandtl formula at high Re.

NASA Ames Research Center

COMPRESSIBLE FLAT PLATE FORMULAS

STRETCH AND SCALE INCOMPRESSIBLE FORMULA BY:

$$C_f^c(Re_x) = \frac{1}{F_c} C_f^i(F_x Re_x) \quad \text{AND} \quad C_F^c(Re_x) = \frac{1}{F_c} C_F^i(F_x Re_x)$$

SOME RELEVANT APPROACHES (*FOR ADIABATIC WALLS*):

Method	F_x	F_c
Nicolai	1	$(1 + 0.144 M_e^2)^{0.65}$
Sommer-Short	$\frac{\mu(T_e)}{\mu(F_c T_e) \cdot F_c}$	$1 + 0.1157 M_e^2$
Spalding-Chi	$\frac{(T_w/T_e)^{0.702}}{F_c}$	$\frac{T_w/T_e - 1}{\text{asin}\left(\frac{T_w/T_e - 1}{T_w/T_e}\right)^2}$
Van Driest II	$\frac{\mu(T_e)}{\mu(T_w) \cdot F_c}$	$\frac{T_w/T_e - 1}{\text{asin}\left(\frac{T_w/T_e - 1}{T_w/T_e}\right)^2}$
White-Christoff	$\frac{\mu(T_e)}{\mu(T_w) \cdot \sqrt{(T_w/T_e) F_c}}$	$\frac{T_w/T_e - 1}{\text{asin}\left(\frac{T_w/T_e - 1}{T_w/T_e}\right)^2}$

Lawrence-HSR/CA - 11 of 55

Applied Computational; Aerodynamics Branch

As stated previously, compressible skin friction formulas are generally obtained through modification of an incompressible formula. The incompressible formula can be said to be stretched (evaluated at a scaled-down Reynolds number) and scaled according to functions of the edge Mach number and wall temperature ratio. These functions are shown in this figure for some of the more well-known compressibility corrections. The formulas shown here have been simplified by assuming an adiabatic wall.

The method given in Nicolai (Fundamentals of Aircraft Design) is applied to the Prandtl incompressible formula to obtain the results ascribed to NASA Ames.

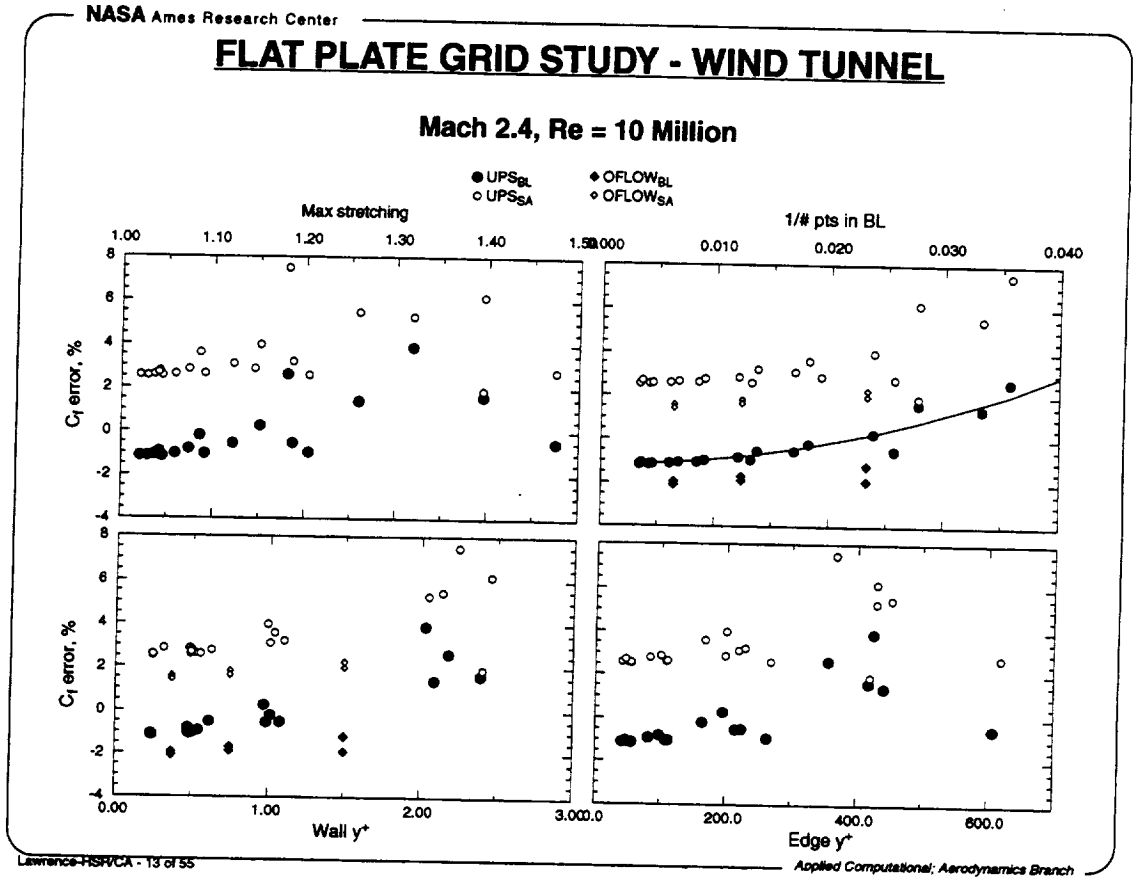

Two fairly extensive grid studies were performed to insure that a reasonably grid independent solutions were used to choose a flat plate method. The first was performed for moderate Reynolds number and the second for high Reynolds number. The wind tunnel study is shown here.

Solutions were obtained on 16 different grids using both the Baldwin-Lomax and Spalart-Allmaras turbulence models. Four families of grids distinguished by the wall-normal stretching function used were studied, with four levels of refinement within each. Then within each family, starting with a grid of 400 total points and a value of y^+ at the wall of 0.25, the wall spacing was doubled at each level of refinement and the number of points was cut in half. OVERFLOW solutions were also computed on three grids using both central-differencing and upwinding for the inviscid fluxes.

Skin friction coefficients computed at a Reynolds number of 10 million are plotted in terms of percent variation from the flat plate method of Sivells-Payne/Spalding-Chi (SP/SC), against four mesh characteristics: 1) wall-spacing in terms of y^+, 2) spacing at the boundary-layer edge in terms of at y^+, 3) maximum stretching within the boundary layer, and 4) the average grid spacing within the boundary layer in terms of boundary-layer thickness.

Some interesting trends are evident. First, the results tend to asymptote from above the grid-independent solution. Second, the S-A model generates consistently higher skin friction (3-4%) than the B-L model, at this Reynolds number. Third, OVERFLOW results tend to fall approximately 1% below UPS results for each turbulence model. Finally, the UPS skin friction predictions appear to increase quadratically with the average grid spacing in the boundary layer. This may be a function of the inviscid algorithm because the OVERFLOW upwind results (higher) show a similar behavior, whereas OVERFLOW central-differencing results (lower) appear somewhat less sensitive.

FLAT PLATE GRID STUDY - FLIGHT

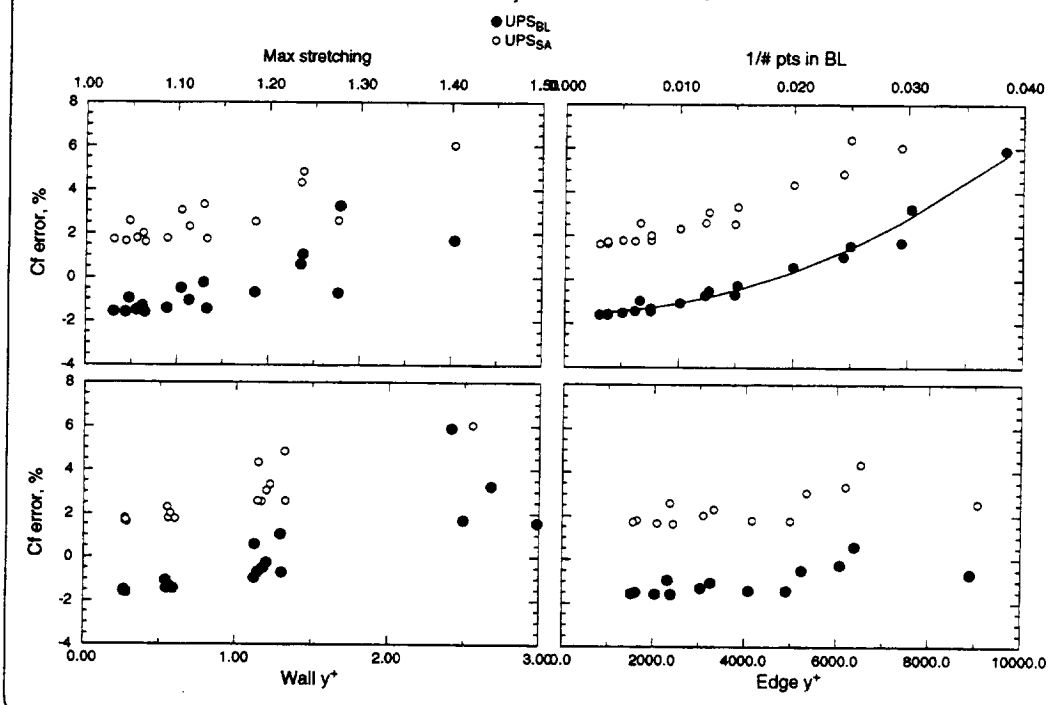

The equivalent study at a flight-like Reynolds number is shown here. A similar trend with average grid spacing is observed here to a greater extent. Note that the skin friction coefficient is virtually converged with 200 points in the boundary layer.

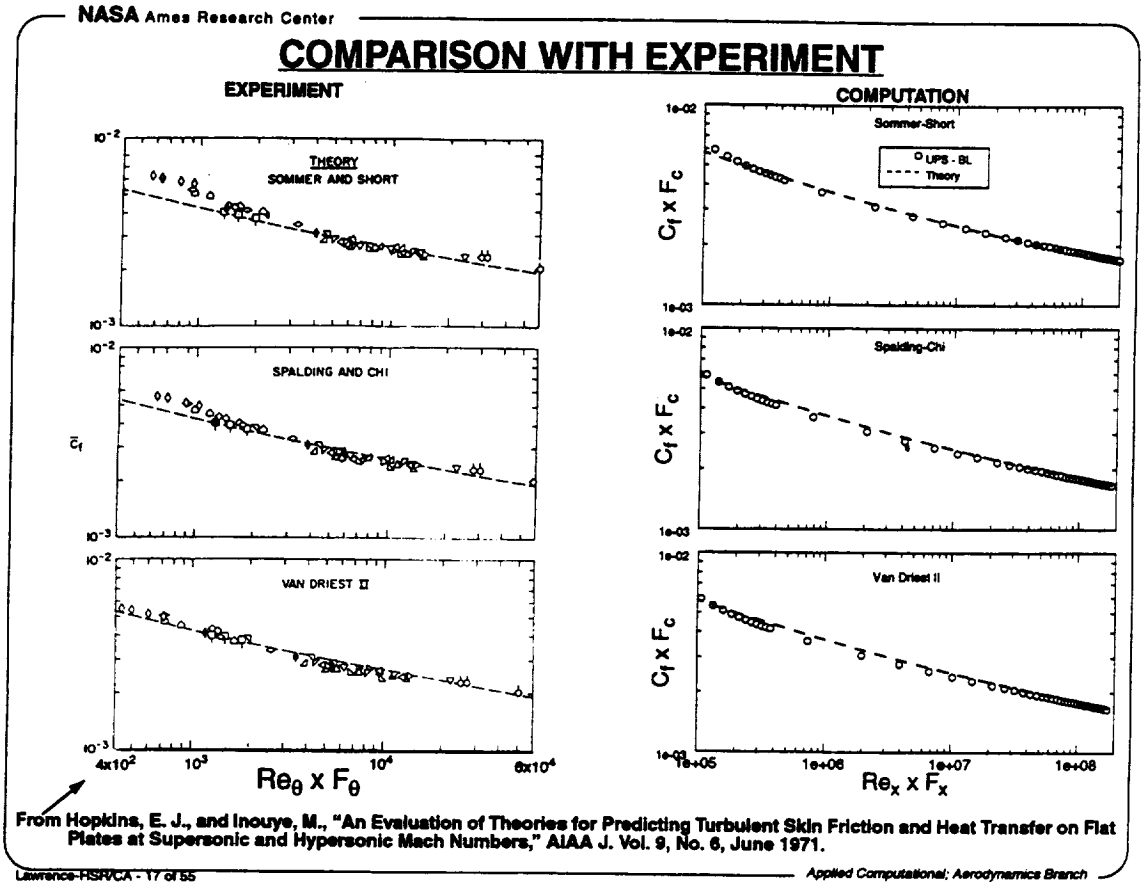

Experimental results as compiled by Hopkins and Inouye are plotted on the left in generalized form, i.e., unstretched and unscaled using three different compressibility approaches into incompressible curves. The Karman-Schoenherr formula is plotted for comparison. The data consist of adiabatic flat plate results for freestream Mach numbers ranging from 1.5 to 5.8 with the bulk taken between Mach 1.5 and 2.5. UPS results for 400 point grids with the Baldwin-Lomax turbulence model are plotted in a similar generalized form, but are plotted against Re_x rather than Re_θ.

Despite the different abscissa units, similar trends are observed in the experimental and computed data. For example, both sets show good agreement with Sommer-Short at moderate Reynolds numbers and good agreement with van Driest II at high and low Reynolds numbers. That is, both the computed and measured data indicate somewhat higher curvature than the Karman-Schoenherr formula produces. The experimental data appears to exhibit slightly more curvature than the CFD results, though it should be noted that the data at the lowest Reynolds number was taken at Mach 5.8. Recognizing that the Spalart-Allmaras model produces 3-4% higher skin friction, the scatter in the data (10% spread) makes it difficult to choose a turbulence model based on accuracy on a flat plate. Other problems experienced with Spalart-Allmaras, to be discussed later, led to the decision to focus on the Baldwin-Lomax results.

NASA Ames Research Center

CHOOSING A FLAT PLATE FORMULA

Generalized Skin Friction (Mach 2.4)

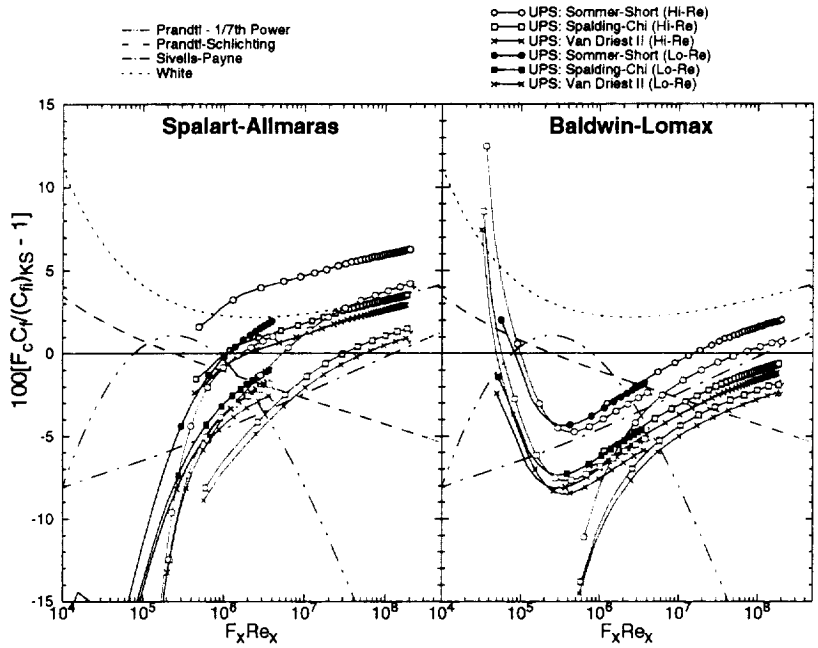

- COMPATIBLE PAIRS: (UPS_{BL} : SP/SC), (UPS_{SA} : White/SC), (OF_{BL} : SP/SS), and (OF_{SA} : SP/VD)

Given a grid-converged solution at both wind tunnel and flight Reynolds numbers, the next step is to obtain a flat plate method that gives satisfactory agreement for a wide range of Reynolds numbers. These figures show computed skin friction coefficients in generalized form, as on the previous page, but plotted in terms of a percent variation from Karman-Schoenherr.

The curvature observed on the previous page is accentuated here, and for corrected Reynolds number greater than 10^6, the computed results using Baldwin-Lomax all (including OVERFLOW results, shown in red) exhibit a common slope. Similar behavior is exhibited by the Spalart-Allmaras model. The slope in the B-L results at moderate to high Reynolds number agrees fairly well with that of the Sivells-Payne formula. The different compressibility corrections appear mainly to shift the curves by different amounts.

Finally, it can be seen that the UPS-BL results, corrected using the Spalding-Chi compressibility formula, agree with the Sivells-Payne incompressible formula to within 2% for $Re > 10^5$, and to within 1% for $5x10^6 < Re < 10^8$. Thus, the SP/SC flat plate approach was used for the remainder of the study. The best flat plate method for the S-A model appears to be Spalding-Chi applied to the White incompressible formula. For the OVERFLOW results: using B-L, Sivells-Payne with Sommer-Short compressibility, and using S-A, Sivells-Payne with van Driest II compressibility.

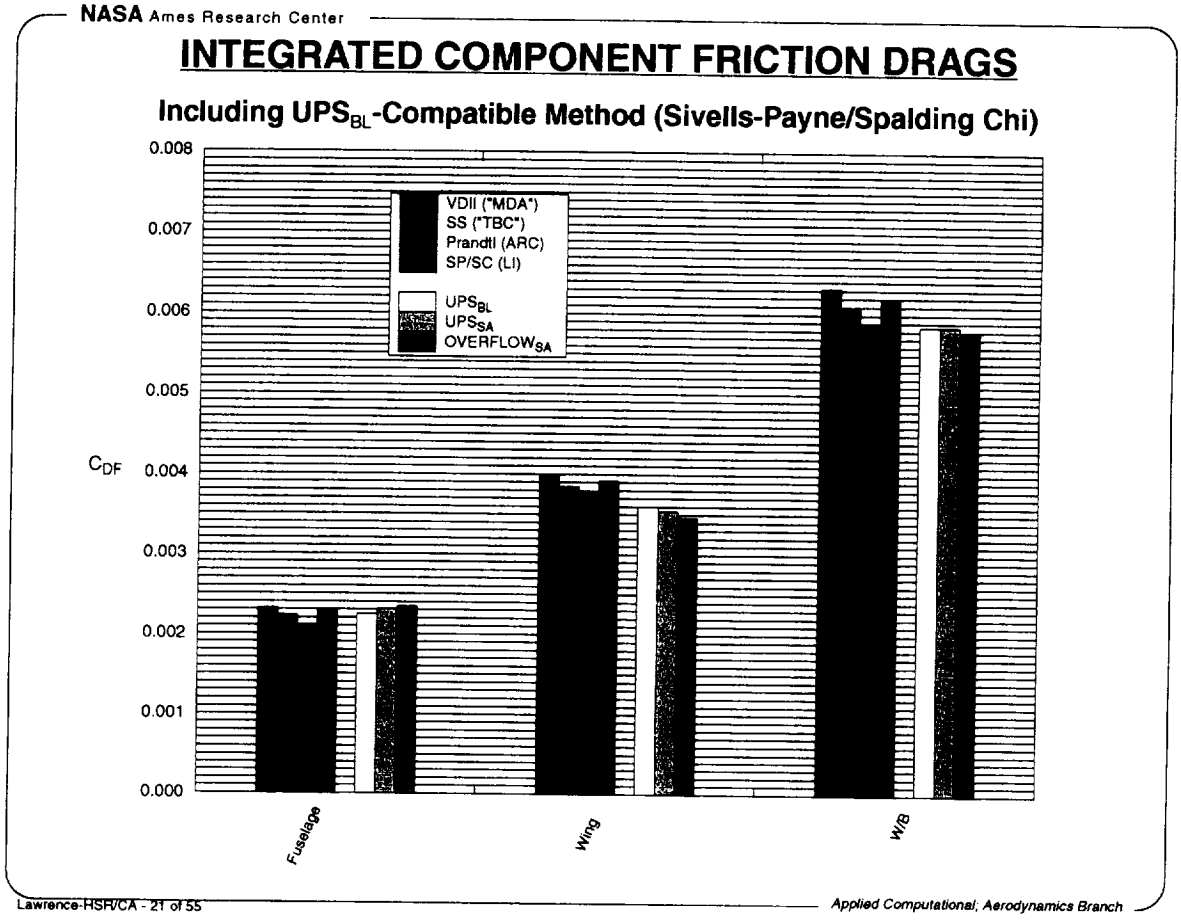

This figure shows the bar chart of Figure 2, with results of the Sivells-Payne/Spalding-Chi average skin friction formula included. It is observed to fall approximately halfway between the van Driest II and the Sommer-Short results for both the wing and fuselage.

The UPS results were computed on a four zone, axially patched mesh with a constant wall-normal spacing of 0.01 inches, airplane scale. This spacing yields y+ values at the wall of less than 0.5 over the fuselage and wing acreage and less than 3 over virtually all the surface. The average number of wall-normal points in the boundary layer is between 45 and 70 for the four zones. The total number of wall-normal points used was 120.

The Baldwin-Lomax results are less than a half count lower than SP/SC on the fuselage, but are still 3.5 counts below flat plate on the wing.

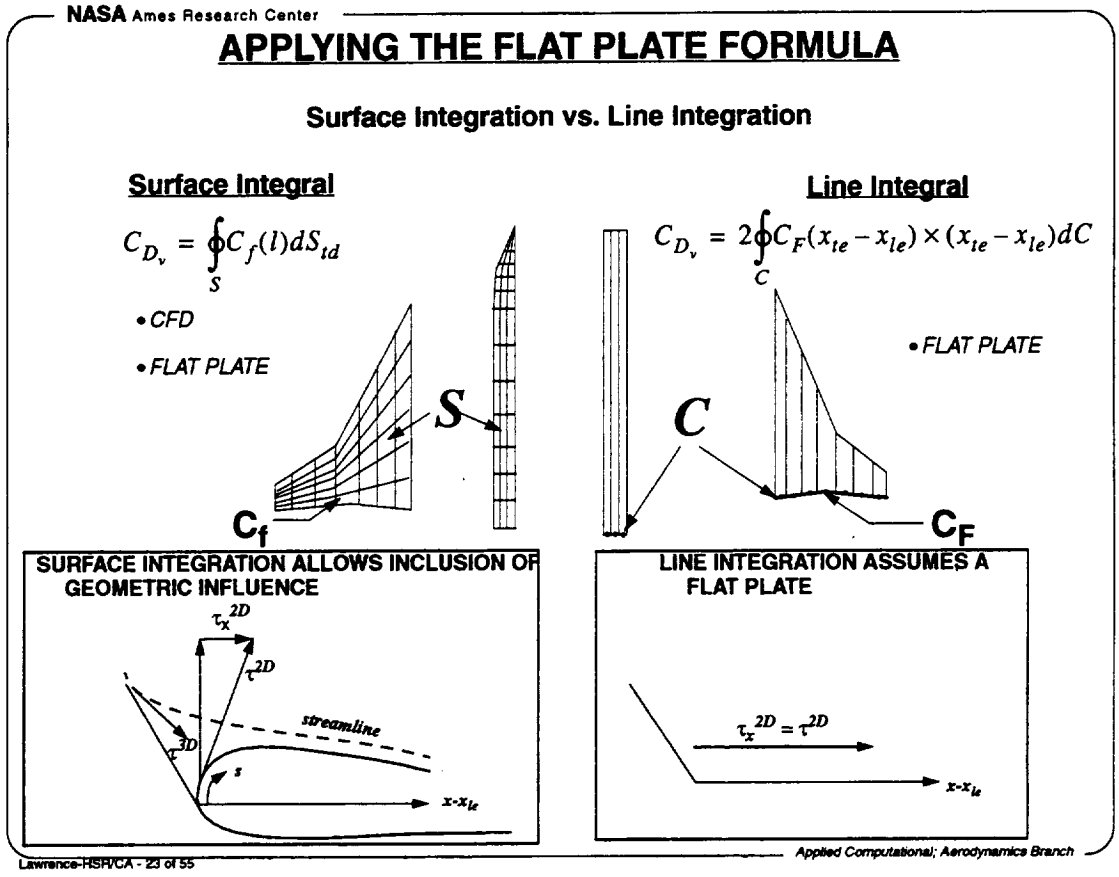

The method in which the flat plate formula is applied can significantly affect the resulting flat plate friction drag estimate. Two alternative methods are shown schematically in this figure. The line-integration approach shown on the right has been used to generate the flat plate estimates shown in the previous bar charts. As described earlier, this method uses a line integration of the *average* skin friction coefficients along the trailing edge for the wing estimate, and a single evaluation of the *average* skin friction at the aft end of the body for the fuselage estimate. The areas of the spanwise wing strips are computed using the strip's average arc length. A similar approach is taken on the fuselage, before subtracting the airfoil area of the innermost wing section.

With the surface integration method, the flat plate formula for local skin friction is used, along with a function that defines the wing leading edge (x_{le} as a function of span location), to perform an integration of local skin friction coefficient over the surface of the configuration. This is essentially the same method as that used to evaluate friction drag from a CFD solution.

There is a difficulty with the flat plate formula integration that the CFD integration doesn't have, however. Given a value of local skin friction coefficient on a surface element, it is not clear in which direction the skin friction is acting, i.e., what fraction of the surface element area should be included. The two simplest approaches are: total area ($dS_{td} = dS$), and two-dimensional ($dS_{td} = dS_{plan}$, wing and $dS_{td} = dS_r$, fuselage). These methods produce significantly different results near the wing leading edge, and the effect on integrated drag is significant as well. The first method is the most like the line-integration approach on the wing. The second method essentially assumes a chordwise flow direction. Although the assumption of chordwise flow is not accurate at the leading edge, it does seem to be the logical choice when using $x - x_{le}$ as the characteristic length. There would appear to be some cancellation of errors with this approach, as well. That is, the underestimation of the component of the surface velocity in the drag direction (especially along the leading edge) is compensated by an overestimation of the skin friction coefficient caused by assuming new boundary layer is being formed at the leading edge.

NASA Ames Research Center

FLAT PLATE APPROXIMATIONS

FLAT PLATE WALL SHEAR: $\tau_{wall}^{FP} = \rho_\infty V_\infty^2 C_f(M_\infty, Re_\infty x)$

APPROXIMATIONS:

- -(W) EDGE CONDITIONS = FREESTREAM CONDITIONS
- -(W) FLOW IS 2D, i.e., $s(x,z) = x - x_{le}$
- -(W) NO STREAMWISE PRESSURE GRADIENT
- -(W/B) NO INTERFERENCE EFFECTS
- -(B) NO BODY GROWTH IN THE AXIAL DIRECTION
- -(B) NO SPANWISE CURVATURE
- -(W/B) ETC.

SOME POSSIBLE MODIFICATIONS TO FLAT PLATE WALL SHEAR:

- MFPI: $\tau_{wall}^{MFPI} = \rho_e V_e^2 C_f(M_\infty, Re_\infty \Delta x)$, $\Delta x = x - x_{le}$
- MFPII: $\tau_{wall}^{MFPII} = \rho_e V_e^2 C_f(M_e, Re_e \Delta x)$, $\Delta x = x - x_{le}$
- MFPIII: $\tau_{wall}^{MFPIII} = \rho_e V_e^2 C_f(M_e, Re_e s)$, s = surface streamline length

In addition to the ability to account for some geometric effects, the surface integration method allows for the inclusion of local flow variations in the estimate of local wall shear.

The line-integration method forces the use of freestream quantities to evaluate compressibility effects and to convert the skin friction coefficient into wall shear (the author attempted to include some angle-of-attack effects by using oblique shock and Prandtl-Meyer theory, but the effects were found to be less than 25% of the angle-of-attack sensitivity observed in CFD solutions). This simple formula comes at the expense of neglecting: 1) the effects of local inviscid flow variations (edge conditions), 2) three-dimensionality, 3) effects of streamwise pressure gradient, 4) interference effects, 5) effects of increasing body circumference in the streamwise direction, 6) spanwise curvature effects, and probably many others. The various effects are labeled above according to whether they are believed to be more significant on the wing, on the body, or both. Although, spanwise curvature is associated with the body here, there is a significant spanwise curvature effect on the TCA wing caused by the landing gear box, as will be seen.

The first of these effects is believed to be the most significant. Fortunately, it is straightforward to include edge conditions into the flat plate formula for local skin friction. They can be included at two levels: first, the local edge dynamic pressure can be used to convert the skin friction coefficient into wall shear, and second, the local edge Mach number, Reynolds number, and temperature can be used within the calculation of the skin friction coefficient itself.

A third effect was also investigated. The effect of three-dimensional surface streamlines was studied by computing streamlines backward in time from the given location on the wing to where they encounter the leading edge. The lengths of these streamlines were computed and compared with the local $x - x_{le}$, and the skin friction coefficient adjusted accordingly. It is not practical to perform this operation for each surface element, so spot checks at three axial locations were performed to obtain a general feeling for the level of importance of this effect.

NASA Ames Research Center

INTEGRATED EFFECT OF MODIFICATIONS

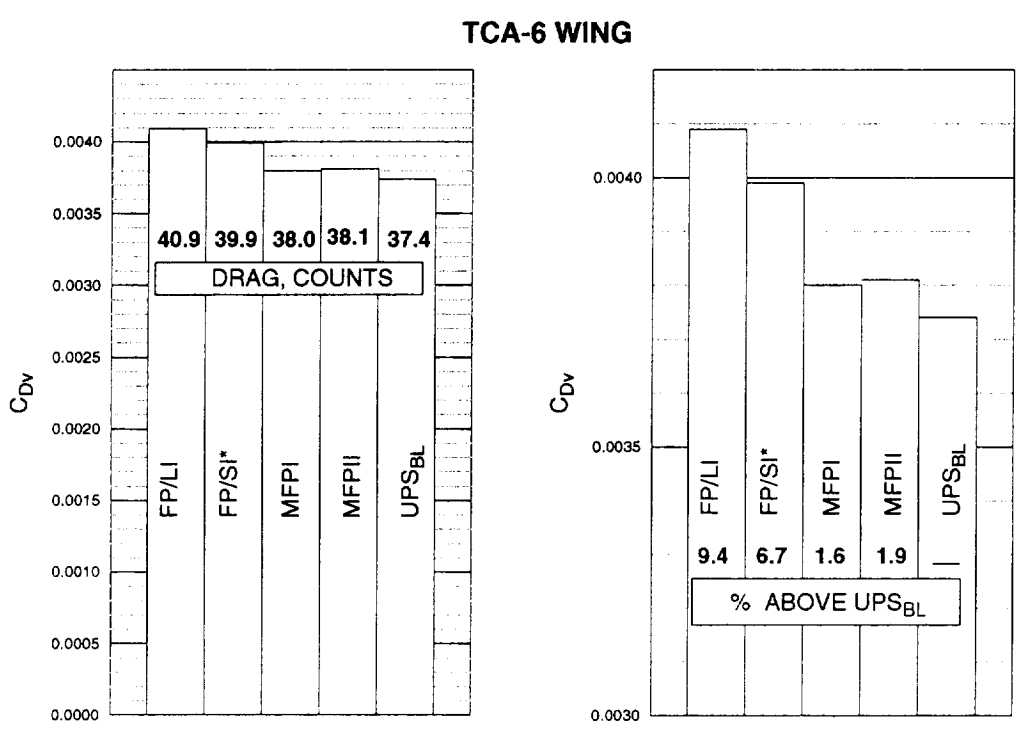

* - INCLUDES 2D GEOMETRICAL EFFECTS

Applied Computational; Aerodynamics Branch

The effects of some of the modifications discussed on the previous two pages are quantified in this bar chart of the wing friction drag. The notation is as follows:

-FP/LI is Sivells-Payne/Spalding-Chi applied using line-integration

-FP/SI is Sivells-Payne/Spalding-Chi applied using 2D surface-integration

-MFPI is FP/SI scaled locally by q_{edge}/q_{∞}

-MFPII is SP/SC(M_{edge}, Re_{edge}, T_{edge}), scaled locally by q_{edge}/q_{∞}

-UPS$_{BL}$ is UPS with Baldwin-Lomax turbulence

Significant geometric effects are observed as exhibited by the one count difference between FP/LI and FP/SI. This drop is almost entirely associated with the wing leading edge curvature.

Even more significant is the effect of boundary-layer-edge dynamic pressure, accounting for another 1.9 count reduction. The average dynamic pressure on the surface tends to be 5-10% below the freestream value and has a surface distribution very similar to the pressure, though scaled by a function of the ratio of edge to freestream Mach number. Thus, the upper surface tends to show lower wall shear than the lower surface of the wing.

The effect of including the edge conditions in the evaluation of the local skin friction coefficient is small compared with the dynamic pressure effect. Also, it is not clear to the author whether the use of local edge conditions (virtually extending a flat plate at the local flow conditions to the leading edge) provides a more physically realistic result than simply using freestream quantities.

On the right, the bar chart is scaled up, and figures are included indicating the percentage difference between the associated flat plate estimate and the CFD result. Note, nearly 80% of the difference between the original flat plate application and the CFD can be explained by geometric and inviscid flow effects. Also note, these numbers do not correspond exactly to the results present earlier because a slightly different line of demarcation was used to separate the wing and fuselage on the lower surface.

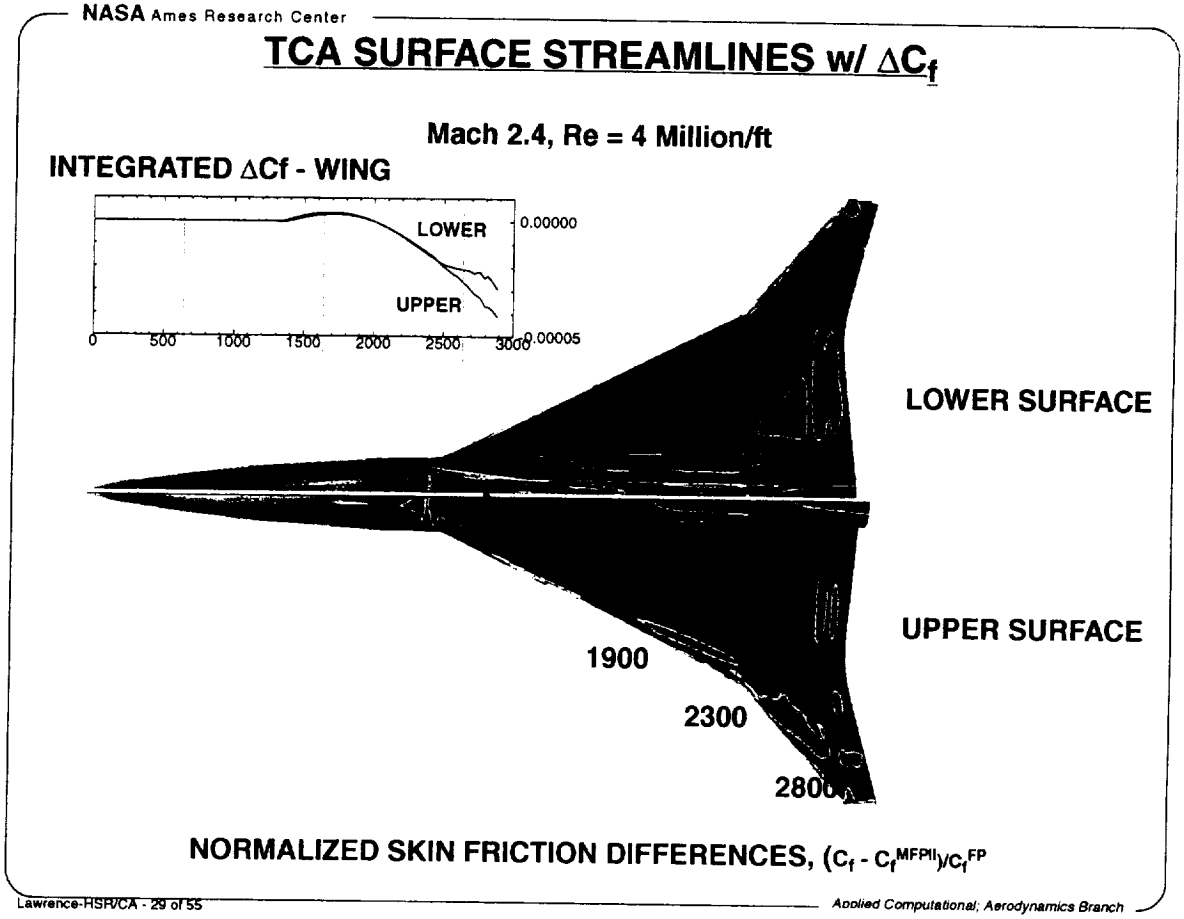

To provide a qualitative idea of the potential effects of three-dimensional flow on the wing surface, surface streamlines are plotted in this figure. The surface is colored by the normalized difference between the UPS results and the flat plate result generated by MFPII (full use of edge conditions). The color scale extends from -20% (blue) to +20% (white). A white contour line is shown for the value of zero (UPS and MFPII give the same wall shear). Values are normalized by FP/SI. Three locations are indicated where the skin friction coefficients will be examined in more detail, including an attempt to quantify three-dimensional streamline effects. Finally, a line plot is included that shows the axially accumulated difference in skin friction drag on the upper and lower wing surfaces.

Streamlines on the lower surface indicate a fairly two-dimensional flow, with a slight outboard flow in the forward part of the wing. Note that, due to the leading edge sweep, an outboard flow tends to produce a streamline length somewhat larger than $x - x_{le}$ while an inboard flow tends to produce a streamline length less than $x - x_{le}$. Inboard flow is observed on the forward part of the upper surface. Based on the streamline shown here, however, the effect of three-dimensionality would not appear to be as significant as the inviscid effects previously discussed.

The colored surface indicates regions on the upper surface associated with the recompression shock where the CFD results fall below flat plate and closer to the leading edge on the lower surface. Regions where the viscous computations give higher shear than flat plate are observed on the upper surface toward the inboard trailing edge, on the biconvex section, and near the leading edge just inboard of the break. On the lower surface, there are regions of relatively high shear toward the trailing edge and at the edge of the landing gear box. Some oscillatory behavior is seen in the UPS results toward the trailing edge. This behavior is the result of variation in the wall-normal spacing generated be the HYPGEN hyperbolic grid generator in response to streamwise clustering of the surface grid around the wing-tip corner.

The line plot indicates that 0.4 counts of the friction drag difference lies on the upper surface, while 0.3 counts lies on the lower surface. The slight rise in both curves near the front of the wing is associated with the fact that the flat plate result goes to zero at the leading edge due to the 2D assumption, whereas the CFD results indicate a significant spanwise flow at the leading edge (especially inboard).

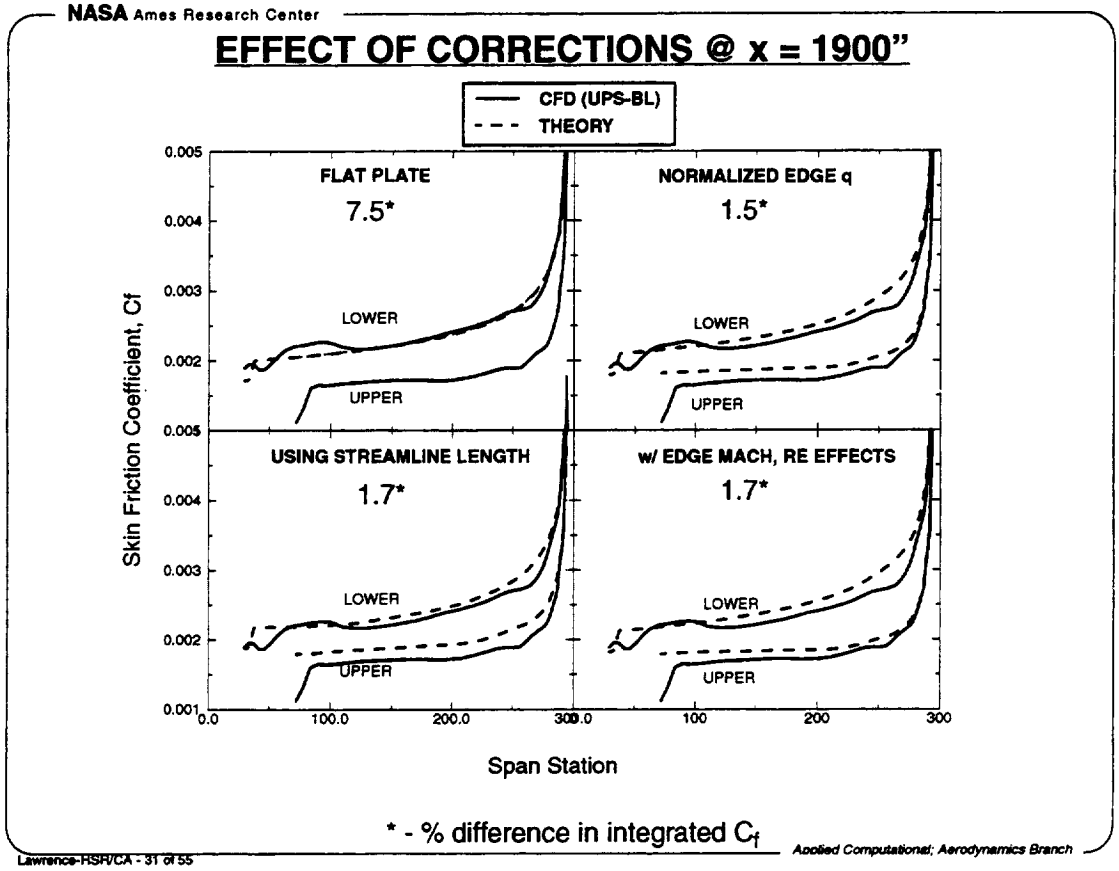

The first location to be studied is at x=1900", which is in the mid portion of the subsonic wing section.UPS results for local skin friction coefficient are plotted in comparison with four editions of the flat plate local skin friction coefficients. The upper left figure shows the flat plate method with no local flow corrections, the upper right figure shows the MFPI result, the lower right shows the MFPII result, and the lower left shows the MFPII corrected to account for local streamline length. Each figure has an associated figure in red indicating the integrated difference at this x location between the CFD result and the flat plate result.

The pure flat plate method is observed to provide good agreement with the CFD on the lower surface, at this location, but significantly overpredicts the CFD on the upper surface, where the dynamic pressure is significantly lower than freestream.The bump in the UPS results for the inboard lower surface is associated with the landing gear box.

Scaling the flat plate skin friction coefficient by the normalized edge dynamic pressure, q_{edge}/q_{∞}, provides surprisingly good agreement with the CFD results on both the upper and lower surfaces. The flat plate results fall consistently lower than the CFD results and there is a slight dip observed in the CFD results that is apparently not explained by dynamic pressure effects.

As was observed in the integrated friction drag values, very little effect is observed when local conditions are used to evaluate the local skin frictions. A slight tendency is observed toward lower values than MFPI on the upper surface and higher values on the lower surface.

Finally, adjusting for streamline length appears to have little effect on the average skin friction at this location. Some improvement in the agreement with CFD is observed on the lower surface, but agreement on the upper surface is worse.

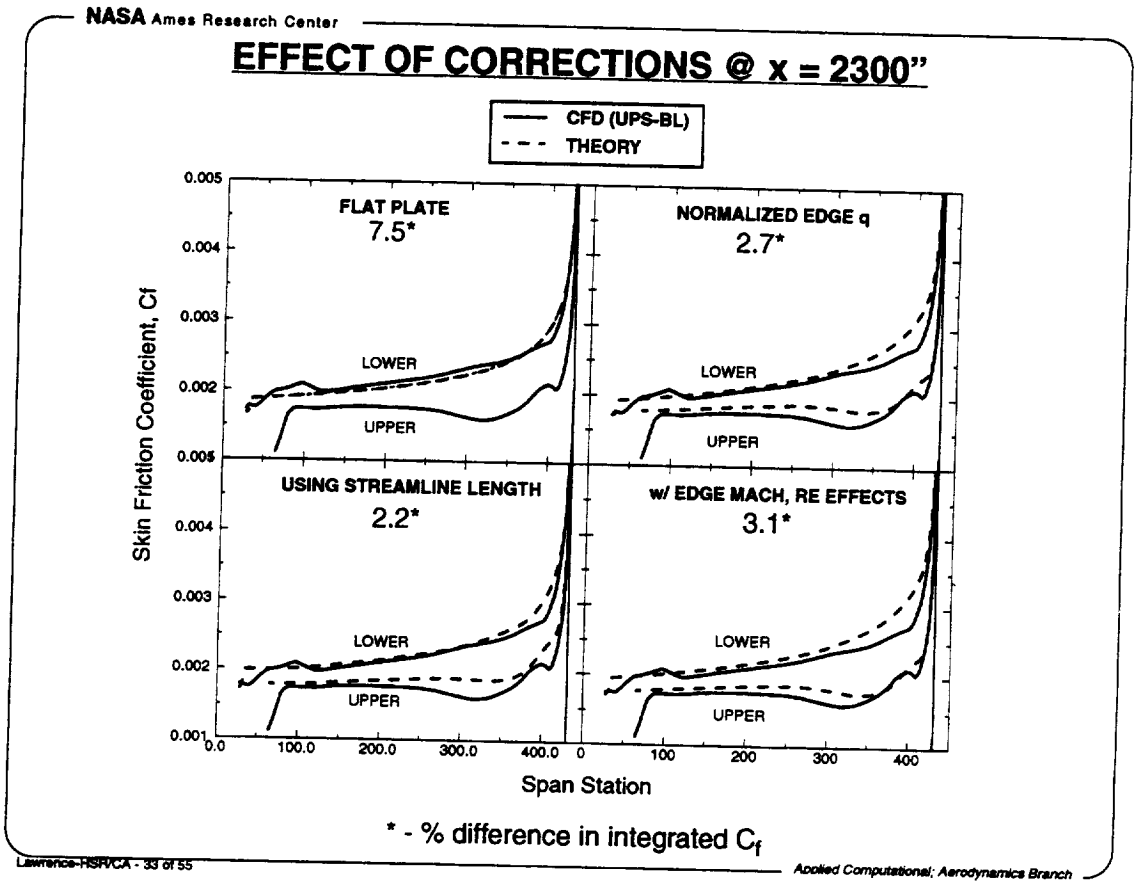

Similar results are shown downstream near the leading edge break.

Again, the pure flat plate results tend toward the lower surface CFD skin friction. The MFPI results agree better on the lower surface at this location, except toward the leading edge. On the upper surface, an inflection is observed in the CFD skin friction which is present to a much lesser degree in the flat plate result. Inboard the agreement between the theory and the computation appears to be improving. Even less influence of edge Mach, etc., is observed at this location than at x=1900". At this location, however, the integrated effect of using streamline length is significant. The influence is primarily located near the lower surface leading edge, where the outboard flow was observed in the streamline plot. The outboard flow, again, tends to increase the streamline length and, consequently, the Reynolds number at which the skin friction function is evaluated.

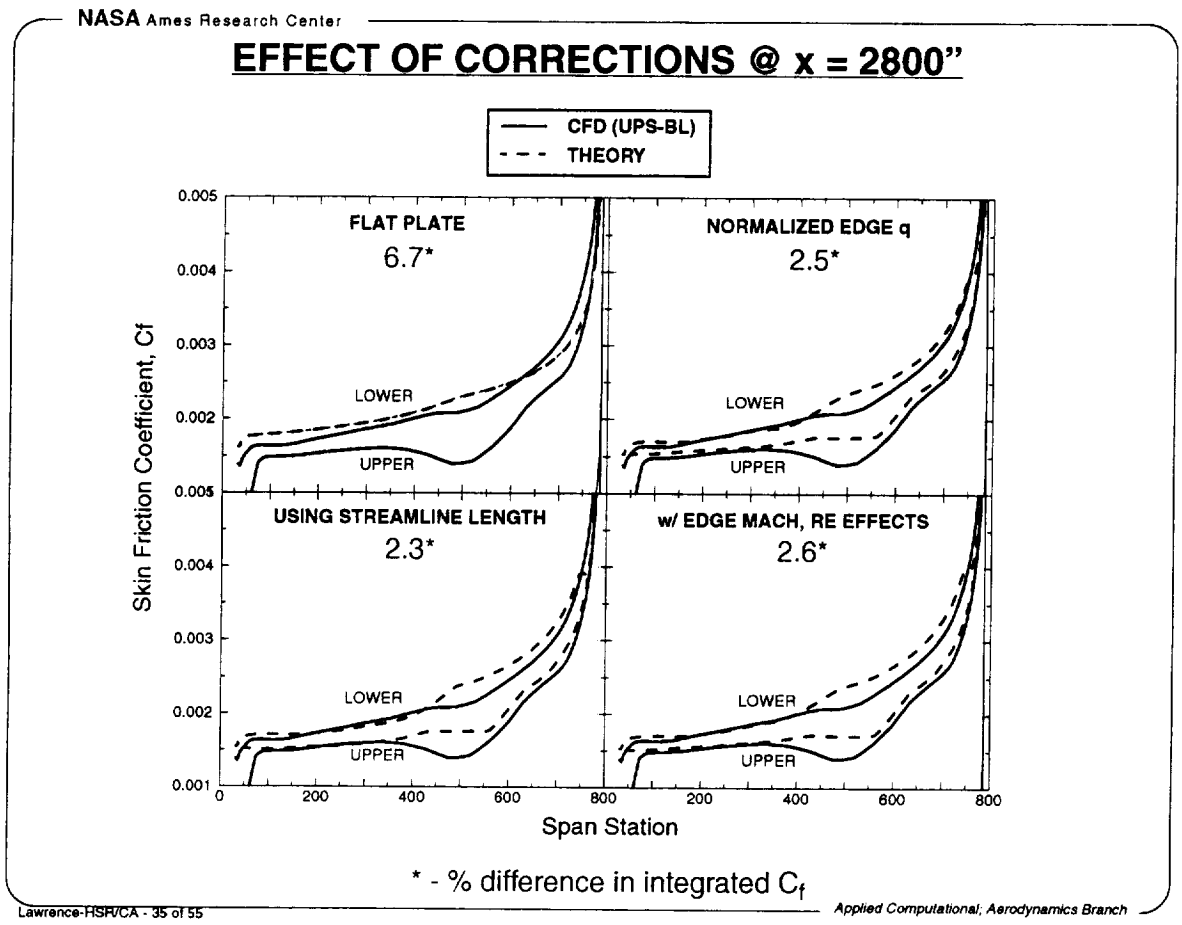

Finally, results are presented along a line which passes near the front of the wing tip. This was, perhaps, an unfortunate location to study, since it includes results from within the oscillatory region of the CFD solution. The computed skin friction data at this location appears to be slightly lower than that slightly upstream and downstream, generally, as can be seen in the following figure.

Somewhat similar trends are observed as in the previous two figures. Again, the relatively low CFD data indicated outboard of the break is believed to be anomalous to this axial station. Inboard results show good agreement between the UPS results and all three modified flat plate theories.

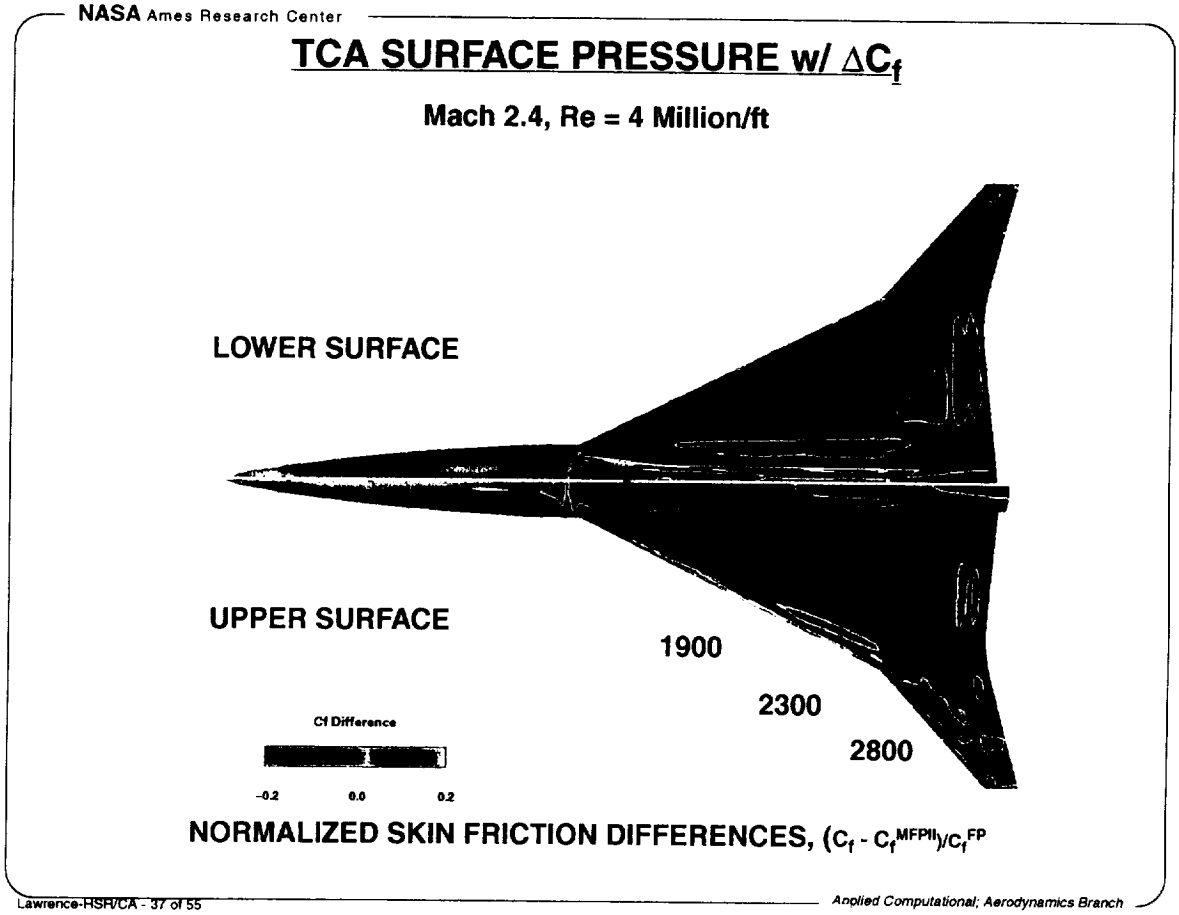

In this figure, the surface is again colored as in the streamline figure, but contours of surface C_p are overplotted.

It appears possible to qualitatively correlate regions of relatively low CFD-predicted skin friction with adverse pressure gradient regions, and regions of relatively high CFD-predicted skin friction with favorable pressure gradient regions. The primary exception to this rule is the "hot spot" along the landing gear box which is generated by the lateral convex curvature. The pressure gradient also influences the surface streamlines in such a way as to compound its effect, i.e., favorable pressure gradient near the leading edge pulls the streamlines inboard, and adverse pressure gradient near the leading edge pushes the streamlines outboard.

The effects of pressure gradient on the local skin friction coefficient have not yet been quantified.

NASA Ames Research Center

INTEGRATED SKIN FRICTION DRAGS

TCA-6 FUSELAGE

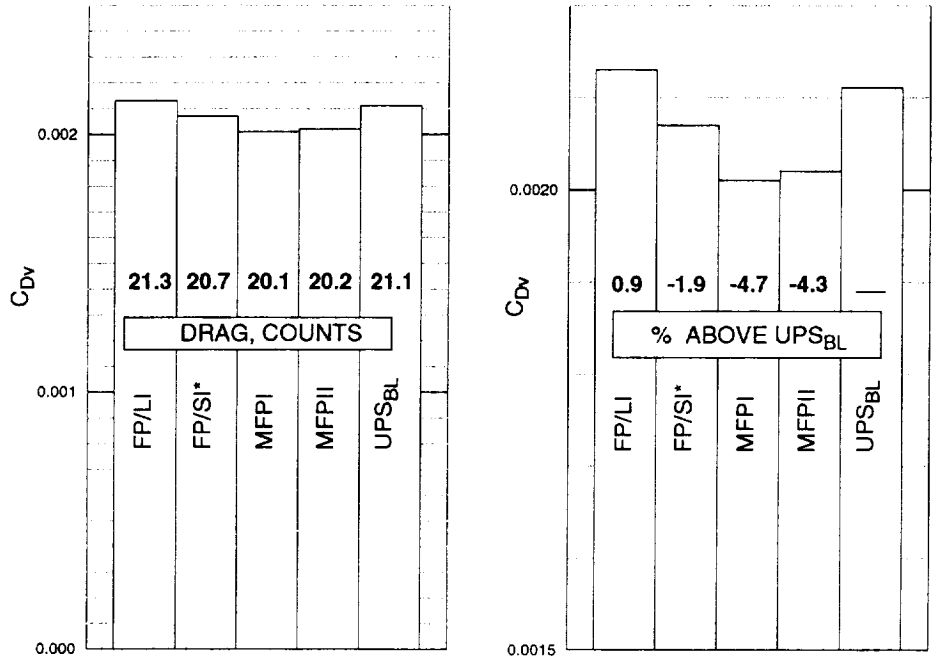

* - INCLUDES 2D GEOMETRIC EFFECTS

Applied Computational; Aerodynamics Branch

Similar analysis was performed for the TCA fuselage flow field and the "bottom-line" results are shown in this figure.

The trend for the flat plate modifications is similar to that observed for the wing. One may wonder, however, about the relatively large difference between the line-integrated and surface-integrated results, since there is no leading edge effect in the surface-integration of the fuselage. The reason for the difference is the effect of the shrinking nose circumference. The surface integration effectively produces a weighted average skin friction coefficient, with the high-local-Cf nose region weighted less because of the lower circumference. Similarly on the wing, the surface integration weights the high-local-Cf leading edge less because the flow direction is not in the drag direction.

As on the wing, the average surface dynamic pressure is lower than freestream and the edge-modified theories show a lower integrated friction drag than the freestream-based methods.

In the case of the fuselage, however, the CFD result is significantly higher than those of the modified flat plate methods, falling close to the line-integrated result. The following figures will attempt to, at least qualitatively, explain this trend.

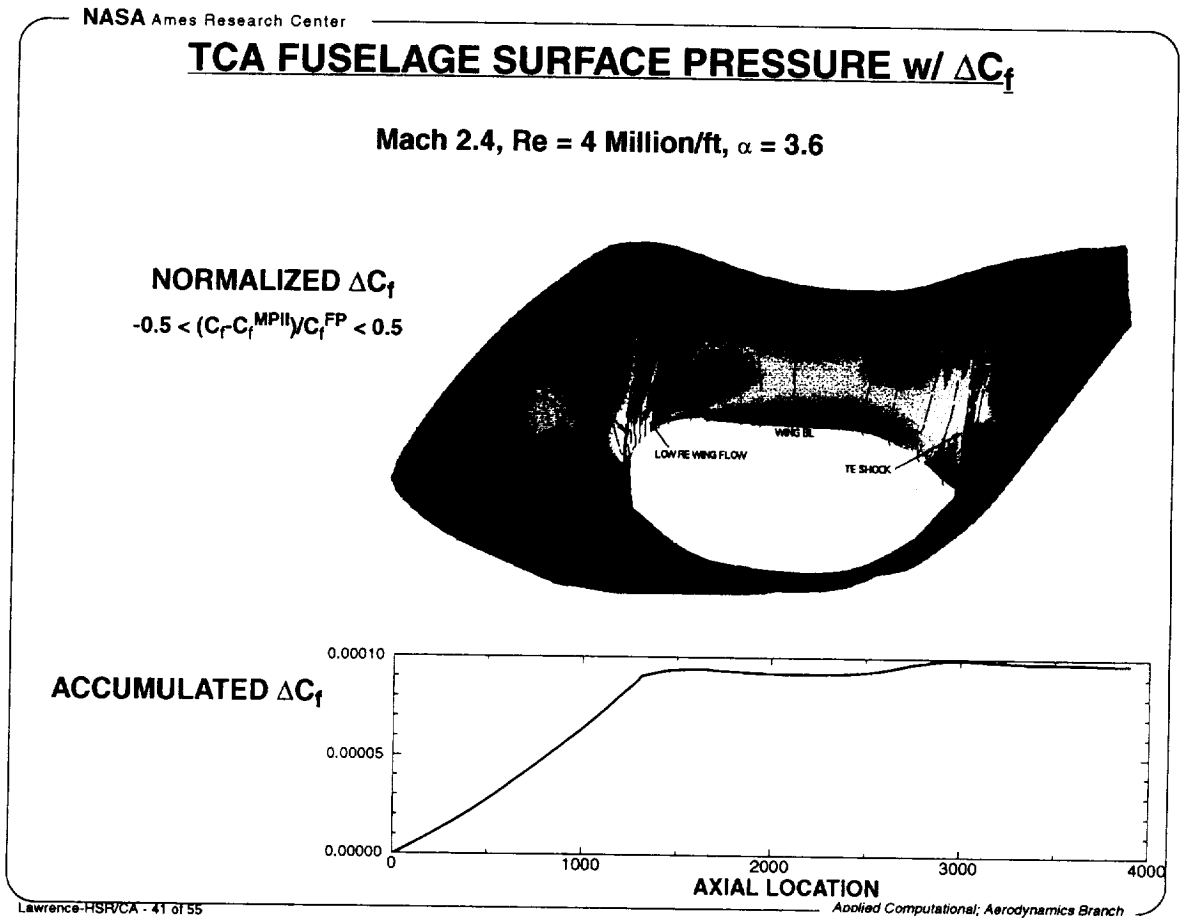

This plot shows the fuselage surface colored using the same normalized skin friction difference as shown in previous figures focusing on the wing flow field. Here, the axial distance is compressed to highlight the fuselage flow and the wing is cut out. The color scale here extends from -50% to +50%, rather than the narrower scale used in the previous figures. Surface pressure contours are overplotted. Also included is a plot of axially accumulated friction drag difference.

The line plot indicates that more than 90% of the difference between the modified flat plate and the UPS friction drag estimates is contained on the forebody, upstream of the wing. At the point of maximum fuselage radius, the curve sharply flattens.

Other "hot spots" on the fuselage are associated with the flow of wing boundary layer onto the fuselage behind the wing shock. The wing shock provides an adverse pressure gradient lowering skin friction and diverting flow away from the wing, and the aft wing expansion sweeps across the fuselage creating a relatively high C_f region. The low speed flow from the wing boundary layer is observed, superimposed on the fuselage. Finally, some colorful, and perhaps non-physical, effects are observed on the aft fuselage. Although more pronounced in this figure than the forebody coloring, it should be remembered that the normalization used here tends to accentuate differences at higher Reynolds number. Thus, the relatively small effect on accumulated friction drag observed in the line plot.

NASA Ames Research Center

RECONCILING EDGE-BASED METHODS

Flying Fuselage Test Case

PRIMARY REASON FOR 4% DIFFERENCE BETWEEN UPS-BL AND SI_{edge}:

-TURBULENT CONE FLOW EFFECT FOR ~40% OF BODY LENGTH

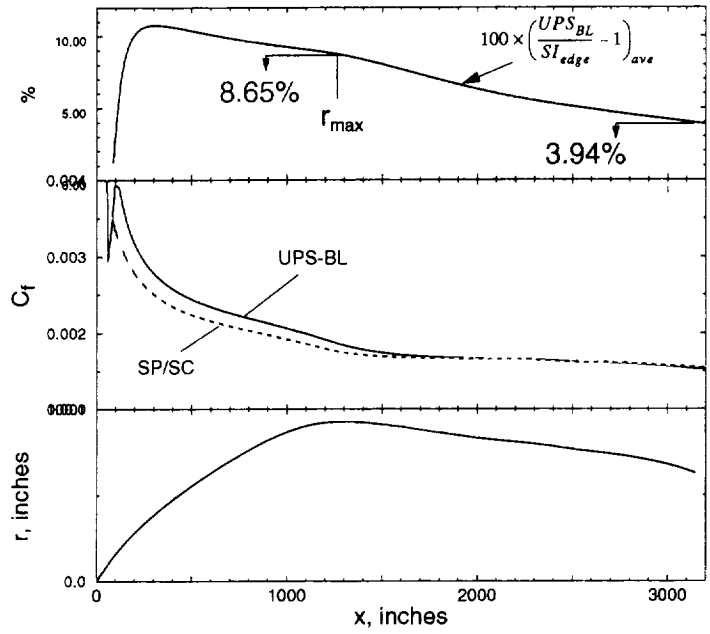

White: For turbulent flow,

$$0.087 < \frac{C_{f,cone}}{C_{f,plate}} - 1 < 0.176$$

CFD shows elevated C_f where $\frac{dr}{dx} > 0$

Applied Computational; Aerodynamics Branch

Lawrence-HSR/CA - 43 of 55

In an effort to understand the forebody flow field, an axisymmetric flow case was computed using the axial radius distribution corresponding to the TCA fuselage. This is referred to as the flying fuselage case. The radius distribution is plotted at the bottom. Skin friction computed by UPS is compared with flat plate (MFPII) in the middle plot, and the percentage difference in axially accumulated friction drag is plotted at the top.

Similar behavior is observed in this axisymmetric case as was seen in the 3D case - significantly higher C_f on the portion of the body where the radius in increasing in the axial direction. This level of excessive skin friction is consistent with that experienced in cone flow, where the growth of the body produces a boundary layer that is thin relative to a flat plate or cylinder. White (Viscous Fluid Flow, 2nd Ed) provides estimated bounds on the level of the effect of between 8.7% and 17.6% for turbulent flow. At maximum radius, the integrated CFD friction drag is observed to be 8.65% higher than the flat plate theory. This produces an overall increase for the body of 3.94%, which is in fairly good agreement with the level of 4.3-4.7% observed in the wing/body case, considering the reduced fuselage area in the wing/body case.

SENSITIVITY TO TURBULENCE MODEL

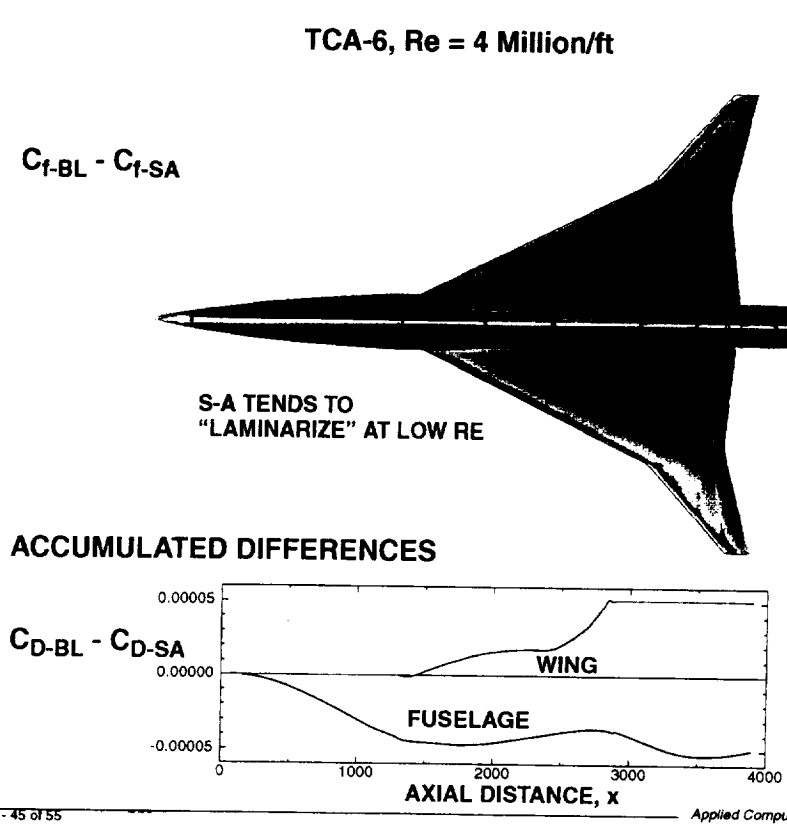

In the category of odd and ends, this figure shows the difference in skin friction produced by the UPS code using two different turbulence models: Baldwin-Lomax and Spalart-Allmaras. A black contour line at zero is included to separate regions of higher B-L skin friction from those of higher S-A. Also shown is a plot of the axially accumulated differences on the wing and fuselage.

As indicated by the flat plate study, the S-A model produces higher skin friction over most of the wing and fuselage. However, there are a few regions where the B-L model produces higher Cf, most notably near the wing leading edge. The S-A model was observed to produce a significant undershoot in Cf near the leading edge, especially on the outboard section. Some hint of this behavior was experienced in the flat plate case as well, where attempts to trip the boundary layer at arbitrarily low Reynolds numbers failed. This effect is also evident in OVERFLOW solutions of the TCA wing/body and wing/body/nacelle/diverter (low Cf rings are seen near the nacelle leading edges) to a somewhat greater degree than in the UPS solutions, perhaps because of a coarser axial grid spacing than that used in the UPS solutions. The integrated effect is observed in the wing/fuselage breakdowns shown in the first two bar charts. Interestingly, at this Reynolds number, the leading edge effect almost exactly cancels the tendency toward higher flat plate skin friction. At flight conditions, the leading edge undershoot was not observed and S-A produced higher skin friction drag on both the wing and fuselage.

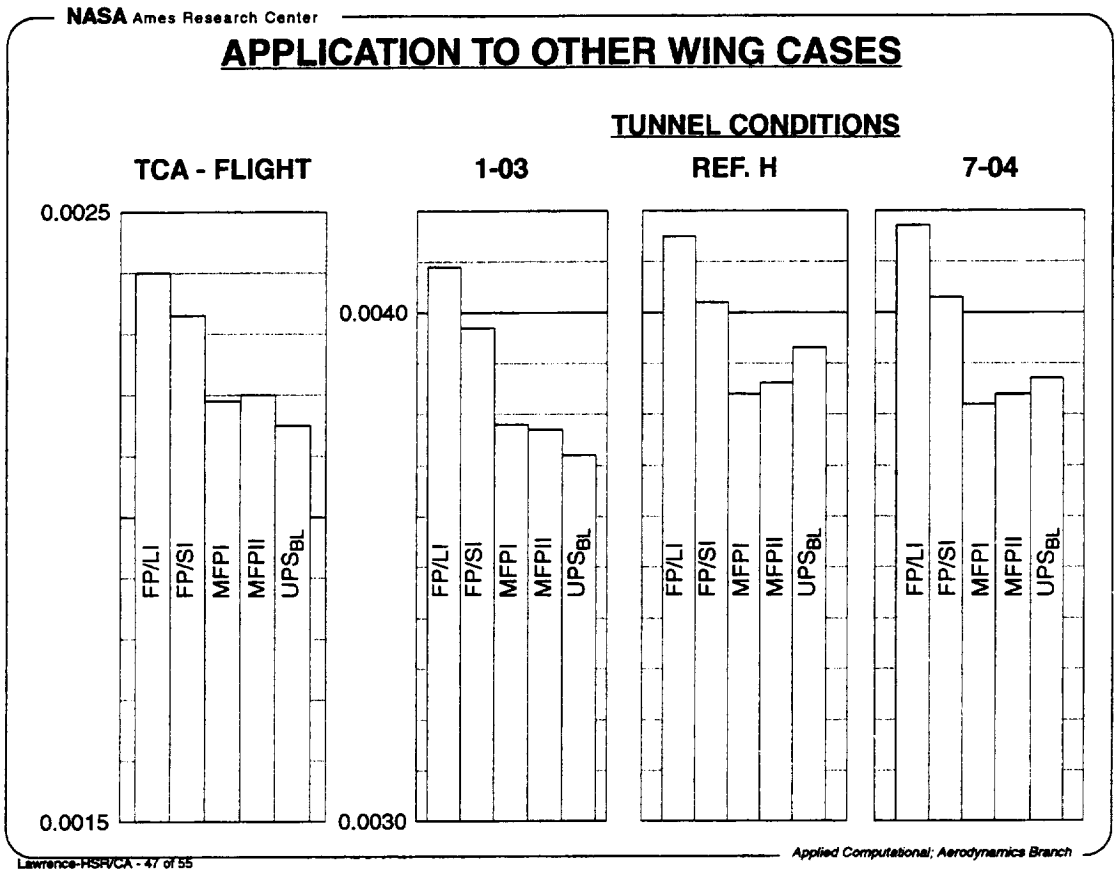

Finally, the analysis described here for the TCA was also applied to other cases. The integrated results for the TCA wing at flight conditions, the 1-03 wing, the Ref. H wing, and the 7-04 wing are shown in this bar chart.

The trends for the TCA wing at flight conditions and the 1-03 wing are very similar to the trends for the TCA wing at tunnel conditions. At flight conditions, the MFPII friction drag is 2.3% higher than the UPS result compared with 1.9% at tunnel conditions. Thus, the method appears relatively insensitive to Reynolds number.

The results for the Ref. H and Ref. H-based bodies are somewhat different in that the UPS predicts higher friction drag than the modified flat plate theories. A surface plot of skin friction differences indicates the presence of chordwise flow features produced by the UPS simulations near the wing fuselage junction. These features are reduced in intensity on the 7-04 configuration, but are not removed. At present, it is not known whether these are physical flow features associated with the higher leading edge sweep on the inboard Ref. H wing section, or whether they are numerical oddities produced by the Baldwin-Lomax model.

SUMMARY

FLAT PLATE STUDY

- S-A MODEL GIVES 3-4% HIGHER SKIN FRICTION THAN B-L
- UPS GIVES HIGHER SKIN FRICTION THAN OVERFLOW (1%)
- QUADRATIC IMPROVEMENT WITH AVERAGE BOUNDARY-LAYER Δh

UPS_{BL}-COMPATIBLE FLAT PLATE METHOD

- -SIVELLS-PAYNE INCOMPRESSIBLE FORMULA
- -SPALDING-CHI COMPRESSIBILITY CORRECTIONS

DIFFERENCES BETWEEN UPS AND FLAT PLATE QUANTIFIED (WING):

- -TOTAL DIFFERENCE = 3.5 ct
  - •LEADING EDGE GEOMETRIC EFFECT = 1 ct
  - •BOUNDARY-LAYER EDGE DYNAMIC PRESSURE = 1.8 ct

QUALITATIVE EXPLANATIONS FOR REMAINING VARIATIONS (WING AND BODY)

- -PRESSURE GRADIENT EFFECTS AND CONVEX CURVATURE (WING)
- -CONE FLOW AND INTERFERENCE EFFECTS (BODY)

TURBULENCE MODEL SENSITIVITIES OBSERVED

A summary of the present study is provided in this chart.

A flat plate study was performed to understand the grid sensitivities of the Baldwin-Lomax and Spalart-Allmaras turbulence models, and to obtain a true, grid-independent UPS solution to the flat plate problem at cruise Mach number.

The Sivells-Payne incompressible skin friction formula in conjunction with the Spalding-Chi compressibility correction was found to give good agreement with the UPS B-L results over a wide range of Reynolds numbers.

Geometric and inviscid flow effects were observed to account for approximately 80% of the difference between the flat plate and CFD friction drag estimates on the TCA wing.

The physical location of pressure gradients on the wing were observed to be correlated with the location of the most noticeable local differences between the modified flat plate theory and the CFD results. On the body, effects of the increasing body radius over the upstream 30% of the body could account for the elevated CFD prediction for fuselage friction drag.

The Spalart-Allmaras turbulence model tends to produce higher skin friction when in a fully turbulent state, but tends to revert to laminar flow at low local Reynolds number.

CONCLUSIONS

FLAT PLATE APPROXIMATIONS

-NO "BEST" METHOD

- SOMMER AND SHORT WORKS WELL FOR TUNNEL CONDITIONS
- VAN DRIEST II WORKS WELL AT FLIGHT CONDITIONS
- SIVELLS-PAYNE/SPALDING-CHI COMPARES WELL WITH CFD FOR A WIDE RANGE OF RE

FLAT PLATE APPLICATION

-80% IMPROVEMENT IN FLAT PLATE PREDICTIONS CAN BE OBTAINED USING SURFACE INTEGRATION WITH AN INVISCID SOLN

N-S SOLUTIONS NEEDED TO DETERMINE INFLUENCE OF:

-INTERFERENCE
-PRESSURE GRADIENT
-LATERAL CURVATURE
-FUSELAGE CONE-FLOW EFFECT

Some general conclusions are given here.

The study failed to determine a universally best flat plate method. Various methods work better for different conditions. For comparison with CFD, it seems appropriate to choose a method which agrees with a grid independent solution of the chosen N-S solver on a flat plate.

Flat plate method application appears to be as important as the particular method chosen. In particular, surface integration using inviscid dynamic pressures produces much better agreement with CFD than line integration. This would allow first-order friction drag sensitivities to be included within the design process.

Second-order effects which still require Navier-Stokes analysis are listed.

Preliminary Comparison of Skin Friction Measurements with CFD Predictions

Robert A. Kennelly, Jr.

Scott L. Lawrence

NASA Ames Research Center

Jeffrey D. Flamm

NASA Langley Research Center

HSR Aero Performance Workshop
Hampton, VA

February 25-28, 1997

The work to be described was performed at the NASA Langley UPWT (4-ft supersonic), test section #2, during 21-24 May 1996. The configuration being tested was the 1.675% Ref H controls model; test conditions were Ma = 2.40, Re = 3 million/ft.

This was an exploration of a new technique, and it was *not* intended to provide definitive comparison of measured and computed skin friction results. It is, however, hoped that the experience gained will make such a rigorous comparison possible in the future.

The authors are pleased to acknowledge helpful discussions on the development of the oil film technique with Dave Driver (NASA Ames Research Center), and Russ Westphal and Aaron Drake (Washington State University, Tri-Cities).

OBJECTIVES

(1) Can the oil film skin friction technique be applied to an HSCT configuration at supersonic conditions?

(2) Will the oil film technique assist verification of boundary layer trip effectiveness?

(3) Can we use skin friction visualization to better understand the impact of trip dots on drag determination?

(4) More generally, is it time to begin a dialog between experiment and computation based on *direct* assessment of viscous effects (rather than just surface pressures)?

METHOD (1)

• Use Fizeau interferometry to measure slope of thin oil film surface influenced primarily by local shear:

... Demonstration

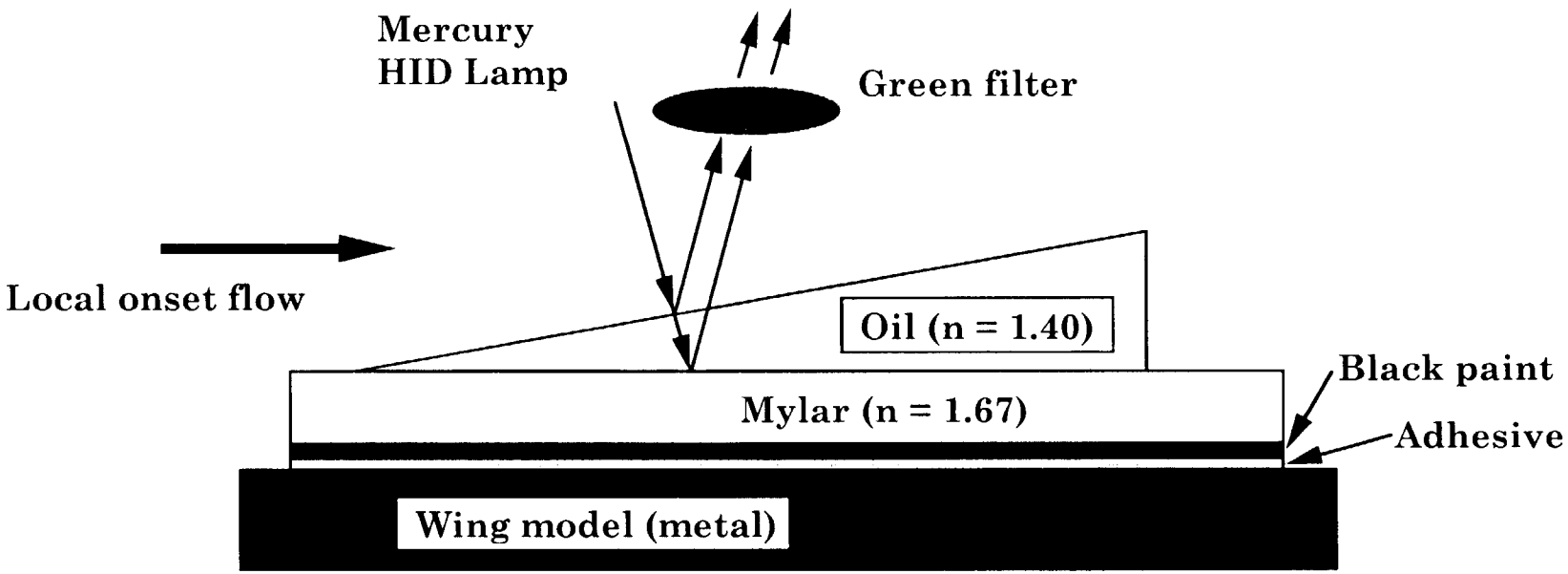

• According to theory of creeping flow, the slope will be approximately constant near the leading edge of a line of oil ($dy/dx = \mu / (\tau\, t)$).

A line or dot of transparent silicone oil (DC-200 Fluid, Dow-Corning, Midland, MI) gradually thins under the influence of surface shear. Under suitable assumptions, the constant slope of the oil surface at the leading edge of the oil is simply related to the component of local skin friction perpendicular to the edge. Optical interferometry provides a sensitive probe for measuring the film's wedge angle. The required optically-smooth surface can be inexpensively produced by a thin layer of Mylar temporarily glued to the model.

The oil is non-toxic and has a low vapor pressure. It is available in a wide range of kinematic viscosities from 10 cS to 30,000 cS (±5%, at 25 °C). We have found it necessary to calibrate the oil at several temperatures in the range of interest; there is some evidence that the viscosity drifts slowly over a period of months. (Other relevant properties such as density and index of refraction are still under inverstigation.)

The interference fringes are easily seen by eye, and are not too difficult to photograph, although a tripod is needed to permit the long exposures (typically 0.5 to 2.0 sec) and small lens openings required for adequate depth-of-field.

METHOD (2)

• Interference fringe spacing yields the component of the local skin friction coefficient perpendicular to the line of oil:

$$c_{f,\infty} = \frac{2\,(n\,\rho\,\nu)_{ref}}{\lambda \int_0^{t_{run}} q_\infty(t)\; e^{\left\{(S+R)\left[T(t) - T_{ref}\right]\right\}}\, dt}\; \Delta\xi_f$$

(for near-normal illumination)

• This is an *absolute* measurement, provided the flow history, $q_\infty(t)$, and oil temperature, T(t), are known, and assuming that c_f is constant during the run.

• References: Tanner & Blows, 1976; Monson, Mateer & Menter, 1995.

Wind tunnel run times must be long enough to render negligable the effects of startup and shutdown transients, and the oil viscosity is chosen to produce a convenient fringe spacing in that length of time. The present work used run lengths of 30 min "on condition", with startup and shutdown each taking about 5-10 min. Oil viscosity was nominally 10,000 cS, and Tzero was 125 °F. The resulting fringe spacings were on the order of 1.8 mm (laminar) and 3.0 mm (turbulent), and could be measured off a photograph to within a few percent using a caliper.

Constancy of the local skin friction *coefficient* is assumed. This is difficult to assess directly, but this source of error can be brought under control (for reasonable flows), by varying the run time: for a sufficiently long run, the effect of non-constant Cf should become negligable.

Flow conditions Tzero (used to estimate model surface temperature) and Pstatic (for freestream dynamic pressure) were recorded at 30 sec intervals from wind-on to wind-off. Except for the transients, the freestream conditions were essentially constant.

The computed skin friction coefficient is referenced to freestream conditions.

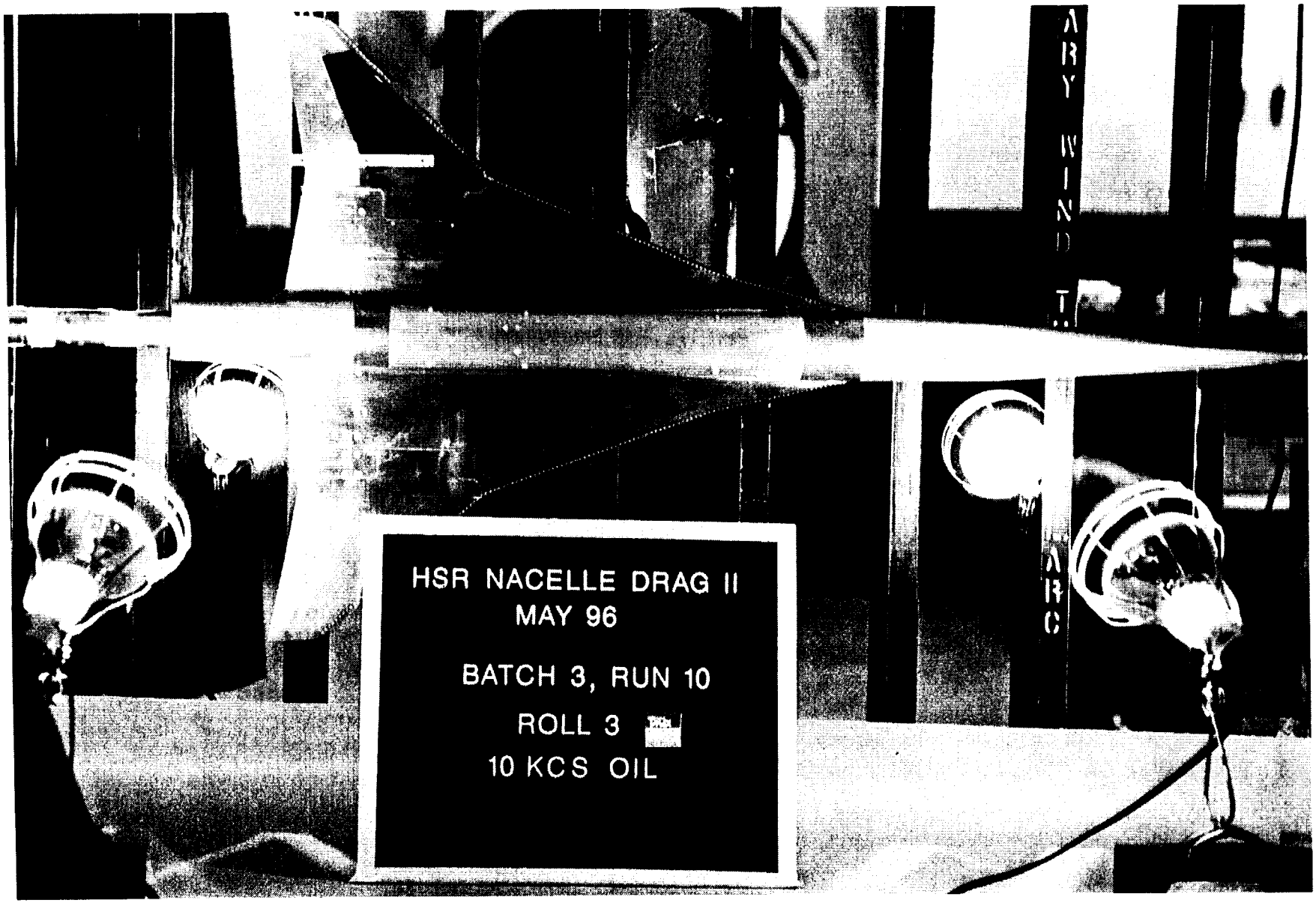
HSR NACELLE DRAG II
MAY 96
BATCH 3, RUN 10
ROLL 3
10 KCS OIL

The model is shown installed in the test section. The wings-vertical orientation proved to be advantageous during post-run photography of the fringe images, permitting near-normal illumination and viewing angles.

Three patches of black Monokote (Top Flite Models, Inc., Champaign, IL) are visible on the left wing's upper surface; in what follows, only the middle and outboard patches will be used.

The reflector lamps (Iwasaki Electric Co., Tokyo, Japan) are those used for obtaining the interference images, but in actual use their light is bounced off a large white card to provide a uniform, diffuse source against whose reflection in the mylar the interference fringes are visible. The lamps are 160 W, self-ballasted, high intensity discharge Mercury type, with a strong spectral peak at a wavelength of 546.1 nm (green). This peak was (fairly well) isolated by photographing through a green dichroic process filter. The average effective wavelength of the filtered light was found by calibration of the lamp+filter to be about 555 nm.

First of all, it needs to be established that the proposed method works at all under the conditions of production wind tunnel testing. Concerns such as tunnel cleanliness, length and severity of startup and shutdown transients, and constancy of flow conditions must be addressed. This is not as big an issue as it was a year or two ago—we have, since the first application of the technique in a production environment [Kennelly, et al., 1995], successfully demonstrated the method in several high- and low speed wind tunnels, in flight (on a Beech Bonanza), and on a rotor blade in hover.

The accompanying fringe image photograph, one of two which we'll refer to repeatedly in what follows, illustrates both good and bad aspects of the method. Interference fringes are clearly visible, having formed downstream of three spanwise oil lines. The boundary layer trip in the lower 1/3 of the photo consists of 0.015" epoxy dots, which should be more than large enough to ensure transition, while the middle 1/3 has no trip applied. A break between broadly-spaced fringes downstream of the dots, and more narrowly-spaced fringes in the presumably-laminar region is clearly visible.

Unfortunately, after two lengthy runs, the mylar has de-bonded from the black paint layer in upper 1/3 of the photograph, rendering interpretation of that portion of the image impossible. This was, however, not the usual result.

The zig-zag pattern in the fringes near the leading edge is significant—we'll return to this issue below, when the impact of dots is considered.

Note inclusion of the machinist's scale to provide a length and axis reference.

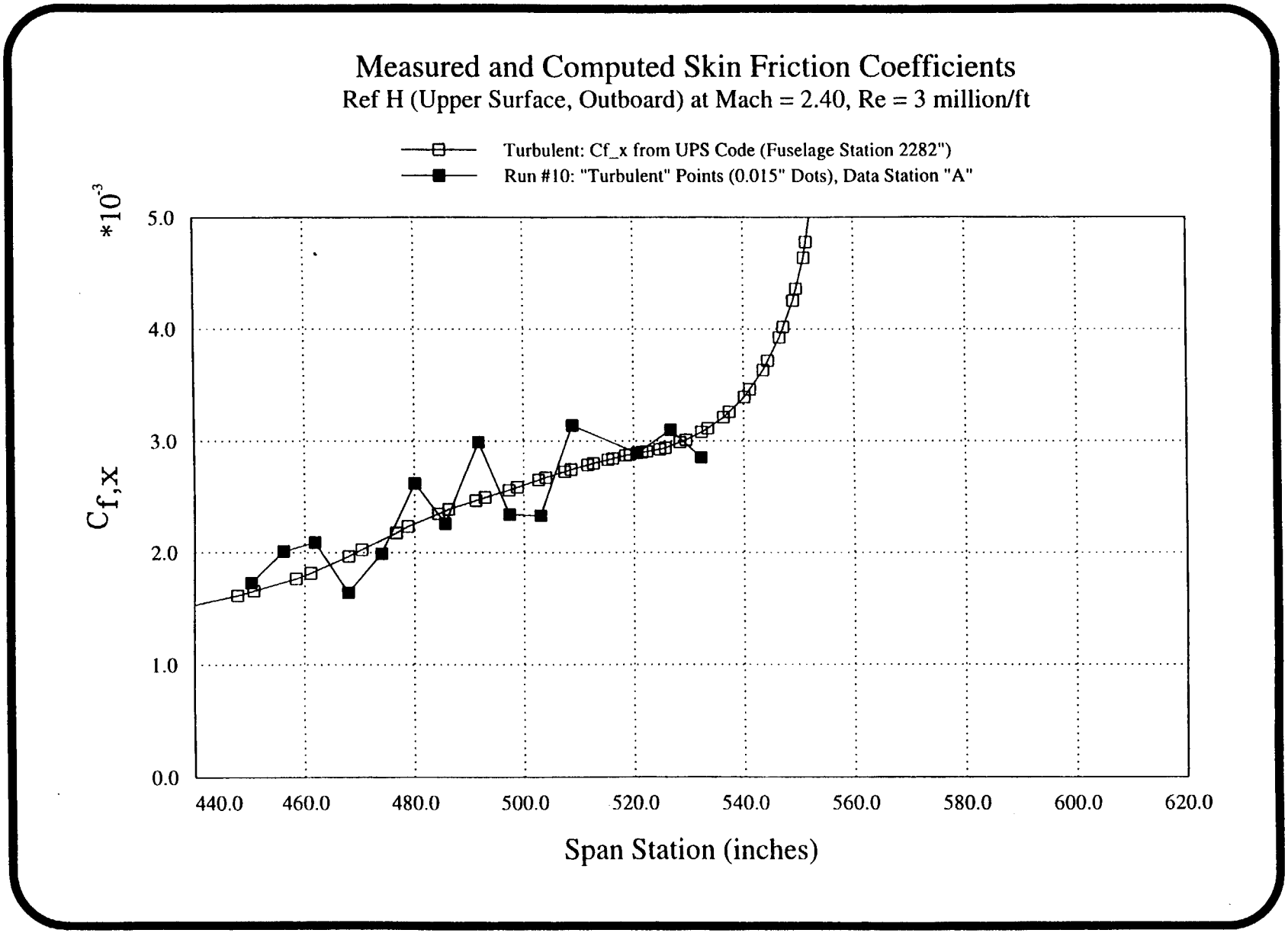
Measured and Computed Skin Friction Coefficients
Ref H (Upper Surface, Outboard) at Mach = 2.40, Re = 3 million/ft
Turbulent: Cf_x from UPS Code (Fuselage Station 2282")
Run #10: "Turbulent" Points (0.015" Dots), Data Station "A"
*10^-3
Cf,x
5.0
4.0
3.0
2.0
1.0
0.0
440.0
460.0
480.0
500.0
520.0
540.0
560.0
580.0
600.0
620.0
Span Station (inches)

Reduced fringe measurements from the upstream oil line at fuselage station 2282" are plotted together with Cf,x calculations obtained using the UPS parabolized Navier-Stokes code. The data reduction assumes a wall temperature everywhere equal to the adiabatic wall temperature based on the freestream Mach number and an assumed recovery factor of (Pr)**1/2 (laminar) and Pr**1/3 (turbulent), with Pr = 0.71 (for air at about 300 °K). Note that this is surely wrong, since the actual wall temperature varies by about ±5 °K over the region of interest (according to UPS), and the turbulent recovery factor only predicts wall temperature to about ±2 °K even for flat plates. Since the oil's viscosity is sensitively dependent on temperature, this contributes about ±0.0003 to the uncertainty in measured Cf, the dominant error source. More exacting measurements are dependent on getting the wall temperature correct to within ±1 °K, not out-of-the question with a combination of wing-mounted thermocouples and IR thermography or temperature sensitive paint.

Measured and computed Cf,x values are similar in this case, though, as will be seen, this is not consistently true.

The zig-zags in the measured Cf values are *not* indicative of sloppy measurements, but rather are a reflection of the zig-zag fringe pattern observed in the photograph. No special effort has been made to sample the peaks and valleys of the Cf,x distribution downstream of the dots, although a detailed look at the dot wakes is planned for later this year in a low-speed facility. Note that in this and the following plot, the oscillations die out as the sample point moves inboard, and thus farther downstream from the transition strip.

A similar pattern can be observed in recent, careful sublimation photographs obtained during testing of the "solid" TCA baseline model 2b in the LaRC UPWT, where streaks corresponding to higher surface shear are visible downstream of each dot. Interestingly, this effect is much more persistent on the lower surface from mid-semispan outwards, but we have as yet no corroborating oil film fringe images.

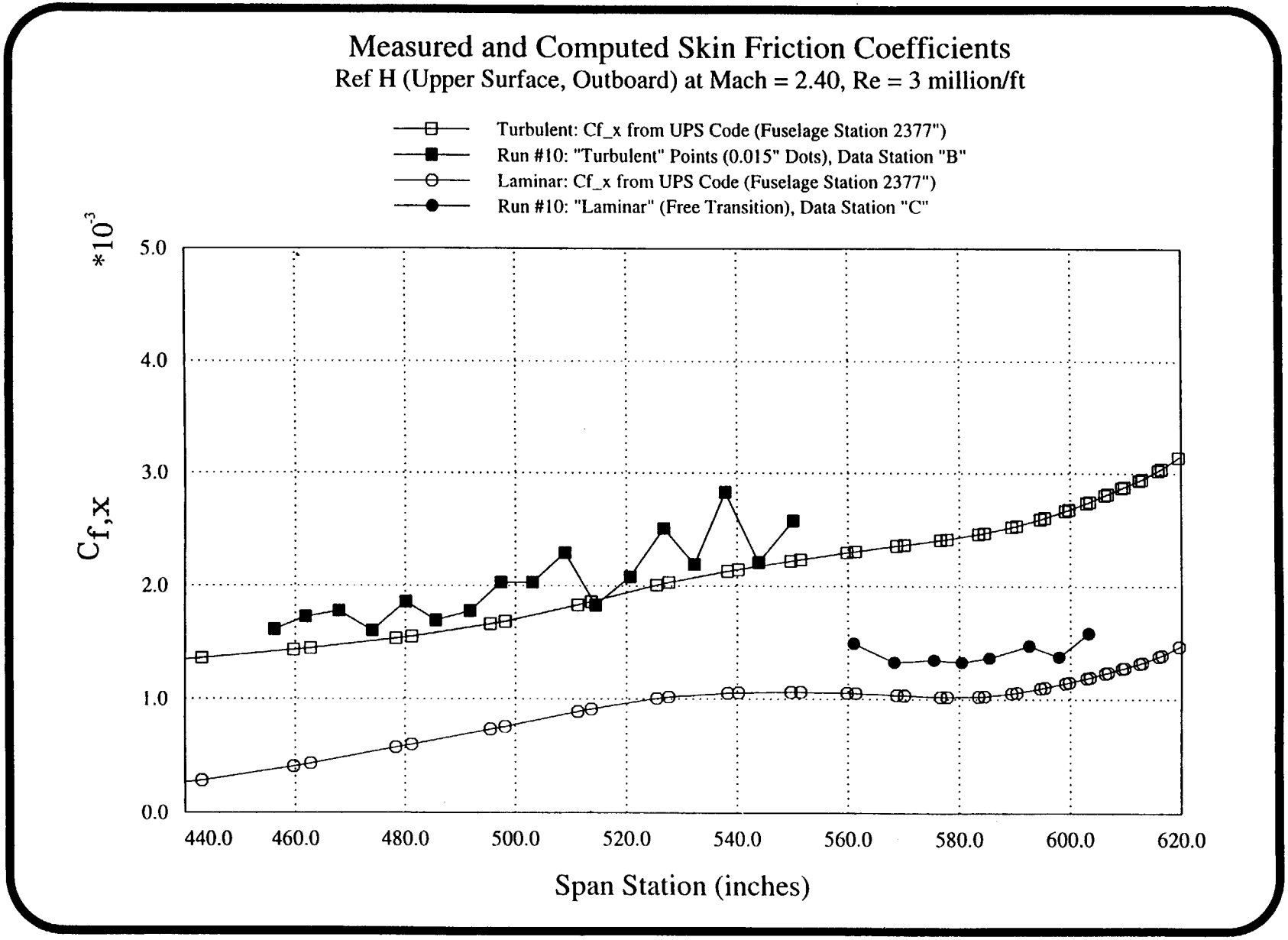
Measured and Computed Skin Friction Coefficients
Ref H (Upper Surface, Outboard) at Mach = 2.40, Re = 3 million/ft
Turbulent: Cf_x from UPS Code (Fuselage Station 2377")
Run #10: "Turbulent" Points (0.015" Dots), Data Station "B"
Laminar: Cf_x from UPS Code (Fuselage Station 2377")
Run #10: "Laminar" (Free Transition), Data Station "C"
$C_{f,x}$ *10^-3
5.0
4.0
3.0
2.0
1.0
0.0
440.0
460.0
480.0
500.0
520.0
540.0
560.0
580.0
600.0
620.0
Span Station (inches)

32 NDS
64 THS
CHESTERMAN
MADE IN ENGLAND

Here is shown the corresponding fringe image of the mid-wing, obtained during the same tunnel run. Most of the same qualitative features are present, and the mylar film remained attached everywhere. The dots on the hatched part of the leading edge (upper 1/3 of the photograph) are only 0.0095" high, but appear to have been sufficient to trip the boundary layer. Once again, note the persistent zig-zag pattern in the fringes near the leading edge.

The streaks in the oil suggest surface streamlines, but have been clearly misleading in other work. The path of an oil droplet on the dry Mylar surface is not necessarily a reliable indication; we suggest another technique such as UV fluorescent oil flow, and a completely-wetted surface, for such visualization.

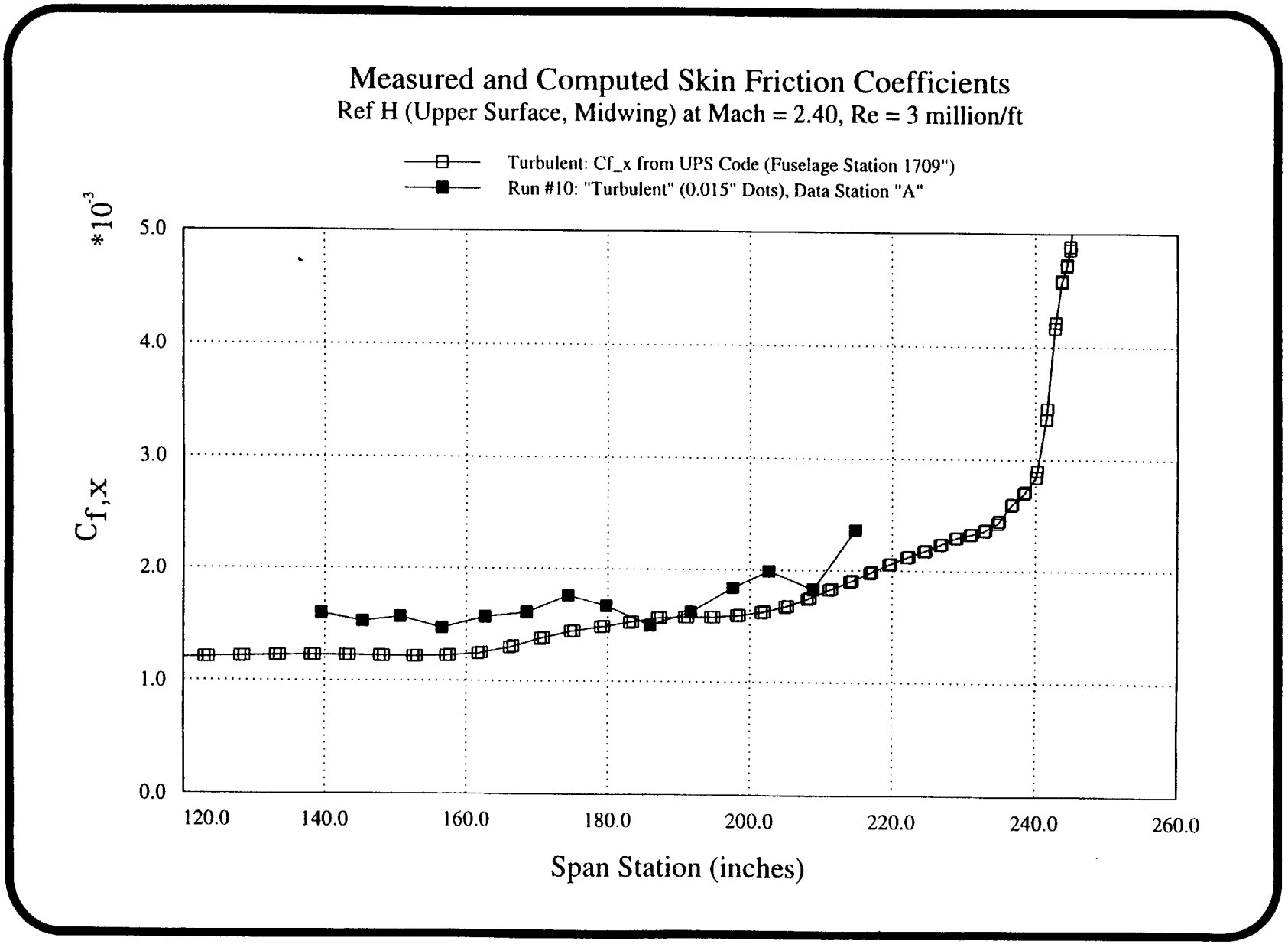
Measured and Computed Skin Friction Coefficients
Ref H (Upper Surface, Midwing) at Mach = 2.40, Re = 3 million/ft
Turbulent: Cf_x from UPS Code (Fuselage Station 1709")
Run #10: "Turbulent" (0.015" Dots), Data Station "A"
$C_{f,x}$ *10^{-3}
5.0
4.0
3.0
2.0
1.0
0.0
120.0
140.0
160.0
180.0
200.0
220.0
240.0
260.0
Span Station (inches)

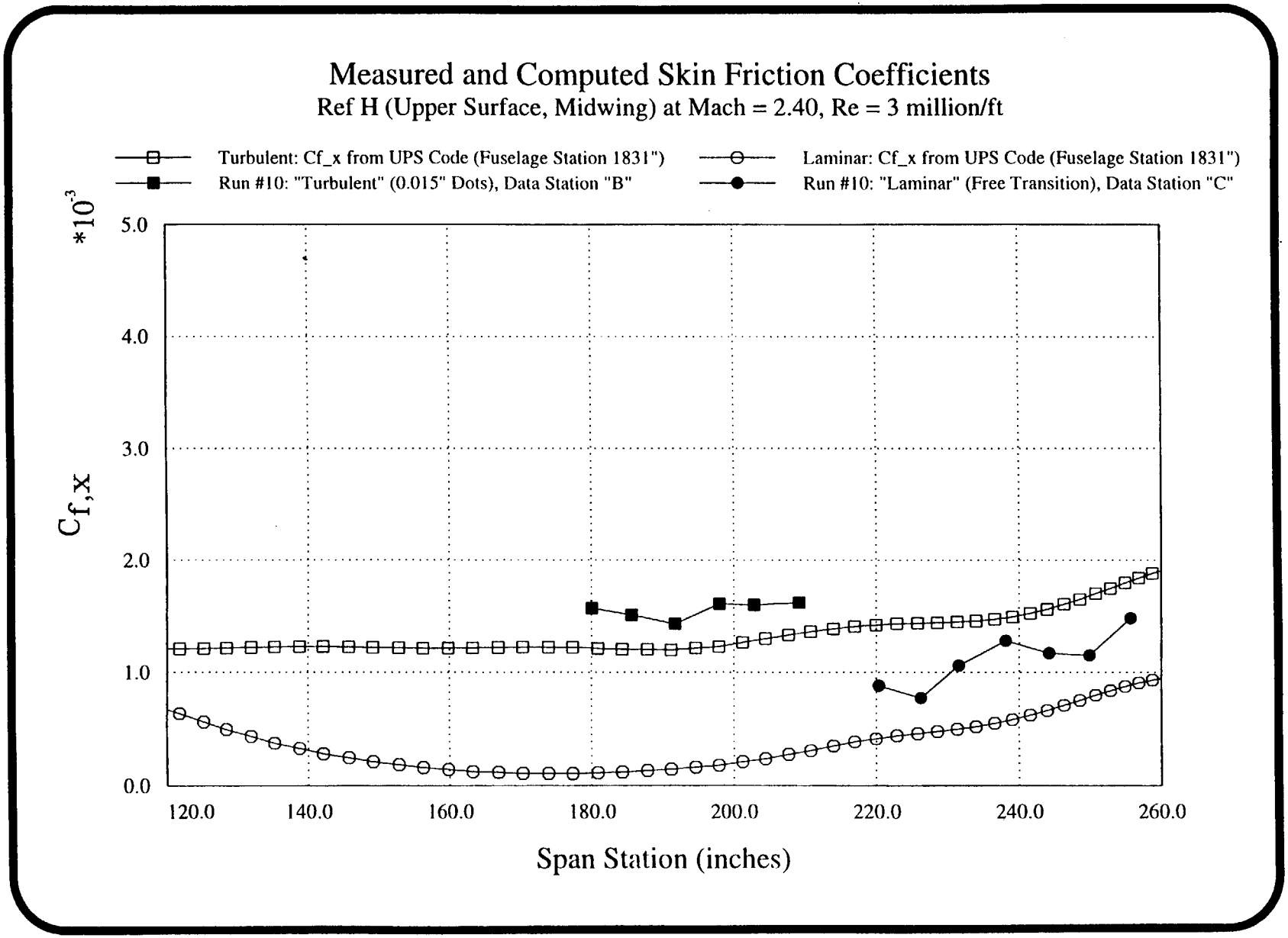
Measured and Computed Skin Friction Coefficients
Ref H (Upper Surface, Midwing) at Mach = 2.40, Re = 3 million/ft
Turbulent: Cf_x from UPS Code (Fuselage Station 1831")
Laminar: Cf_x from UPS Code (Fuselage Station 1831")
Run #10: "Turbulent" (0.015" Dots), Data Station "B"
Run #10: "Laminar" (Free Transition), Data Station "C"
*10^-3
Cf,x
5.0
4.0
3.0
2.0
1.0
0.0
120.0
140.0
160.0
180.0
200.0
220.0
240.0
260.0
Span Station (inches)

ERRORS

This "maiden voyage" effort can be improved upon:

(1) TEMPERATURE (± 15-20% uncertainty in Cf)

(2) Assumed constancy of Cf during transients (±12% ?)

(3) Fringe measurements (±5%)

(4) Illumination wavelength (±1%)

Thus our estimated errors are ±20- 25% (but can probably be reduced to ±5- 10% with modified procedures).

Rough estimates of the impact on Cf of the various error sources are collected together to guide the planning of a follow-on "real" experiment. It should be noted that, in contrast to forces and pressures, a measurement of local skin friction values to even ±20-25% is not all that bad for a first try! But it is clearly insufficient for any serious dialog with the CFD community.

The following approach is proposed, with an expected accuracy of better than ±10%:

(1) Use a combination of point measurements together with field techniques (e.g. IR thermography or temperature sensitive paint) to reduce the surface temperature error to less than 1 °K (±3-4% contribution to Cf uncertainty),

(2) Conduct a *series* of runs of different length to eliminate sensitivity to non-constant Cf during the tunnel transients (< 5% uncertainty?),

(3) Use digitized images and a curve fitting technique to improve measurement accuracy, and arrange for more-consistently normal illumination and viewing angles (2%),

(4) Employ a notch filter centered on the Hg spectral line at 546.1 nm to essentially eliminate the small uncertainty due to wavelength of illumination (0%).

The test article could be either the TCA flapped model 2a (provided temperature instrumentation could be installed), or a specially-built W/B configuration. Coordinated CFD analyses would be needed.

Concluding Remarks

The oil film skin friction technique was successfully demonstrated on an HSR configuration at Mach 2.40.

With some reservations, the method appears to be a useful complement to sublimation for verifying transition.

The *qualitative* interpretation of the fringe images obtained has helped understand the effects of trip dots. Further work is in progress.

Simultaneous, *quantitative* skin friction measurements at a number of discrete locations were obtained. Some necessary improvements have been identified which will allow routine Cf measurements on wind tunnel models, a new capability.

References

Kennelly, Jr., Robert A., Russell V. Westphal, George G. Mateer, and Julie Seelen. 1995. Surface Oil Film Interferometry on a Swept Wing Model in Supersonic Flow. In *Flow Visualization VII,* ed. J.P. Crowder. New York: Begell House.

Mateer, George G., Daryl J. Monson, and Florian R. Menter. 1995. Shear and Pressure Measurements on an Airfoil at Angle of Attack. AIAA Paper 95-2192.

Tanner, L.H., and L.G. Blows. 1976. A Study of the Motion of Oil Films on Surfaces in Air Flow, with Applications to the Measurement of Skin Friction. *J. Phys. E: Sci. Inst.* 9:194-202.

White, Frank M. 1991. *Viscous Fluid Flow,* 2nd ed. New York: McGraw-Hill.

Comparison of CFD Predictions of the TCA Baseline

Presented by
Gelsomina Cappuccio
NASA Ames Research Center

Materials from
NASA Ames Research Center
The Boeing Company
McDonnell Douglas Corporation
NASA Langley Research Center

HSR Aerodynamic Performance Workshop
February 25-28, 1997
NASA Langley Research Center

- Wind Tunnel Data
  - LaRC UPWT Test Section #2 Test 1671
    - Baseline TCA
    - Model 2a
    - Flapped Wing
    - Forces and Pressures
    - Nacelle Internal Duct
      - IGES Definition - constant area duct with short circular cross-section duct
      - WT Model - Linear Duct from Inlet to Exit
    - Nacelle Installation
      - with and without fairing
  - LaRC UPWT Test Section #2 Test 1679
    - Baseline TCA
    - Model 2b
    - Solid Wing
    - Forces Only
    - Nacelle Internal Duct Same as Model 2a
    - Nacelle Installation with Fairing

The computational fluid dynamics (CFD) comparisons being presented are compared to each other and to wind tunnel (WT) data on the baseline TCA. Some of the CFD computations were done prior to the tests and others later. Only force data (CL vs CD) from CFD will be presented as part of this report.

The WT data presented comes from the testing of the baseline TCA in the Langley Unitary Plan Wind Tunnel (UPWT), Test Section #2. There are 2 sets of wind tunnel data being presented: one from test 1671 of model 2a (flapped wing) and the other from test 1679 of model 2b (solid wing). Most of the plots show only one run from each of the WT tests per configuration. But many repeat runs were taken during the tests. The WT repeat runs showed an uncertainty in the drag of ±0.5 count. There were times when the uncertainty in drag was better, ±0.25 count.

Test 1671 data was of forces and pressures measured from model 2a. The wing had cutouts for installing various leading and trailing edge flaps at lower Mach numbers. The internal duct of the nacelles are not designed and fabricated as defined in the outer mold lines (OML) iges file. The internal duct was fabricated such that a linear transition occurs from the inlet to exhaust. Whereas, the iges definition has a constant area internal duct that quickly transitions from the inlet to exhaust cross sectional shape. The nacelle internal duct was fabricated, the way described, to save time and money. The variation in the cross sectional area is less than 1% from the iges definition. The nacelles were also installed with and without fairings. Fairings are defined as the build up of the nacelles on the upper wing surface so that the nacelles poke through the upper surface as defined in the OML iges file.

Test 1679 data was of forces measured from model 2a and 2b. The wing for model 2b was a solid wing. The nacelles were built the same way as for model 2a, except for the nacelle base pressure installation. The nacelles were only tested with the fairings for model 2a and 2b during test 1679.

Baseline TCA Model 2a
Nacelles Installed With Fairings

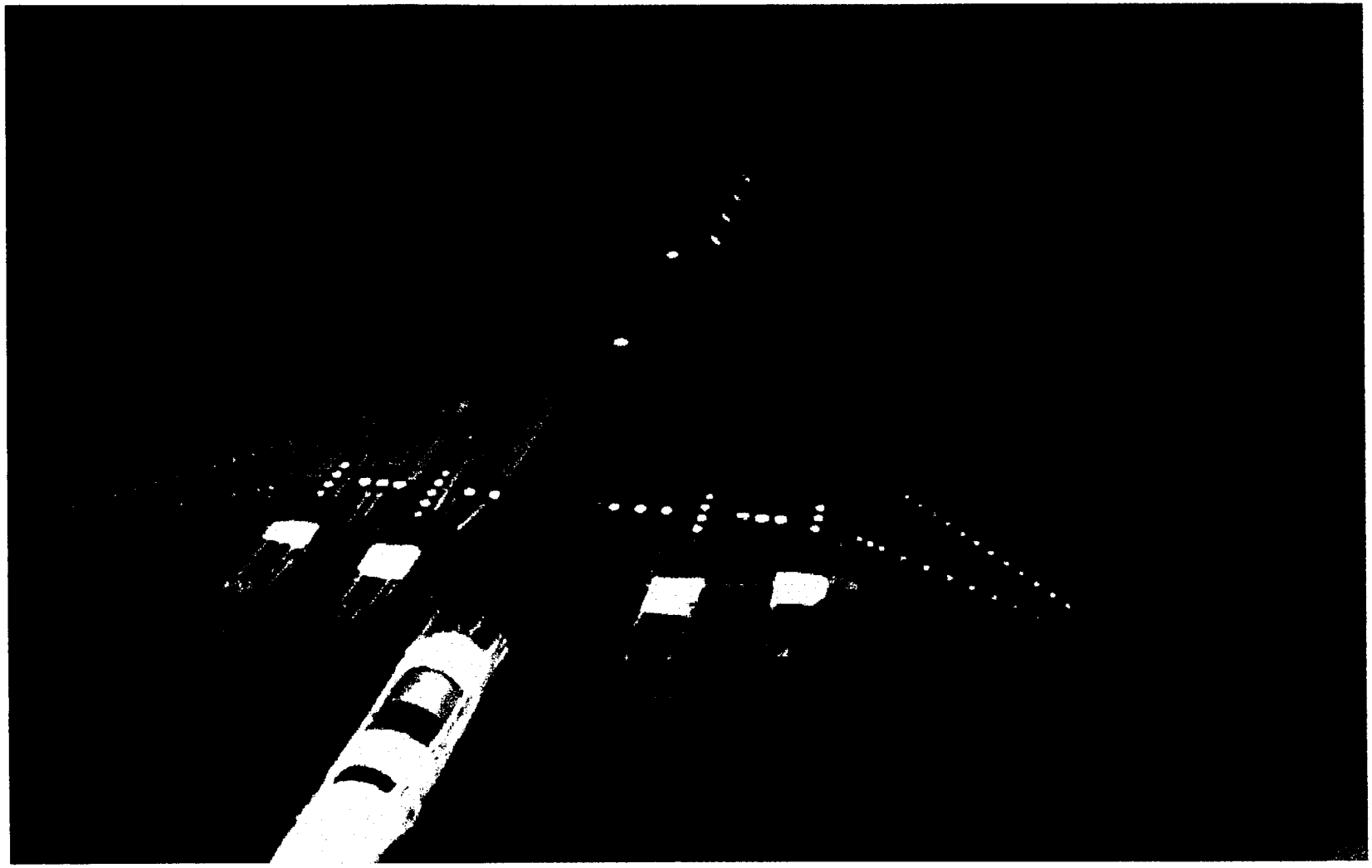

This is a figure of model 2a with nacelles installed with fairings in UPWT during test 1671. Notice the routing of the pressure instrumentation and the flap cutouts.

Baseline TCA Model 2a
Nacelles Installed Without Fairings

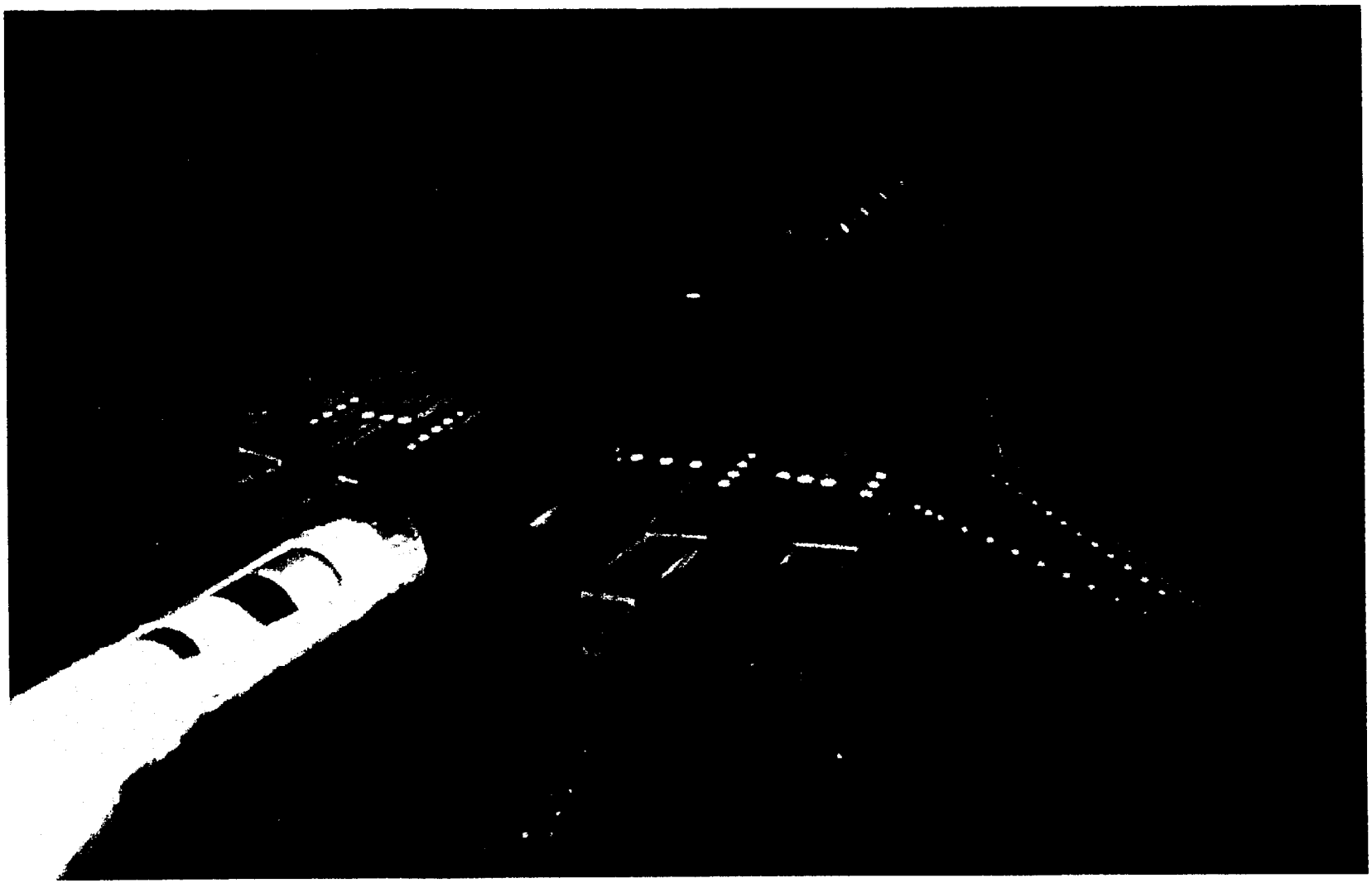

This is a figure of model 2a with the nacelles installed without fairings. The data from this test showed a drag increase of 0.4 count when the fairing was not included. There is an aft facing step due to the nacelles being trimmed to not poke through the upper wing surface.

Baseline TCA Model 2b

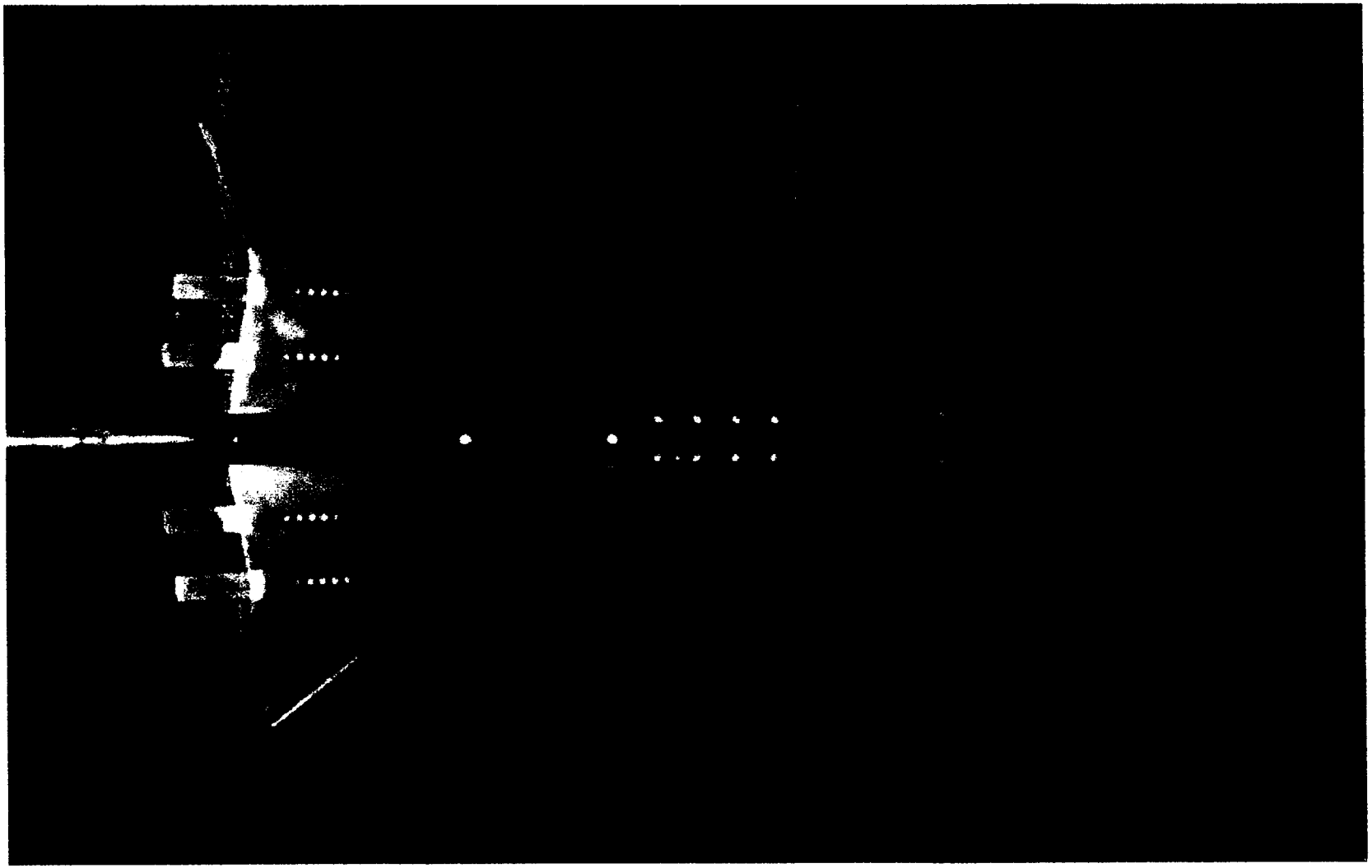

This figure is of model 2b with nacelles installed with fairings. Notice that the wing is solid. Only force data was taken. Test 1679 tested models 2a and 2b. The test also did an extensive trip drag study of the epoxy discs being used on HSR models. The study included a variation of disc heights from 0 to 0.017 inches at one location on the entire wing; a variation of disc height from 0.006 to 0.014 on the upper inboard wing while keeping 0.012 inches on the rest of the wing; 3 nacelle trip disc heights; one glass bead and grit height; and one trip disc height at another location. This study was done to get a better handle on the trip drag correction to the wind tunnel data.

Baseline TCA Model 2b
Nacelles Installed with Fairings

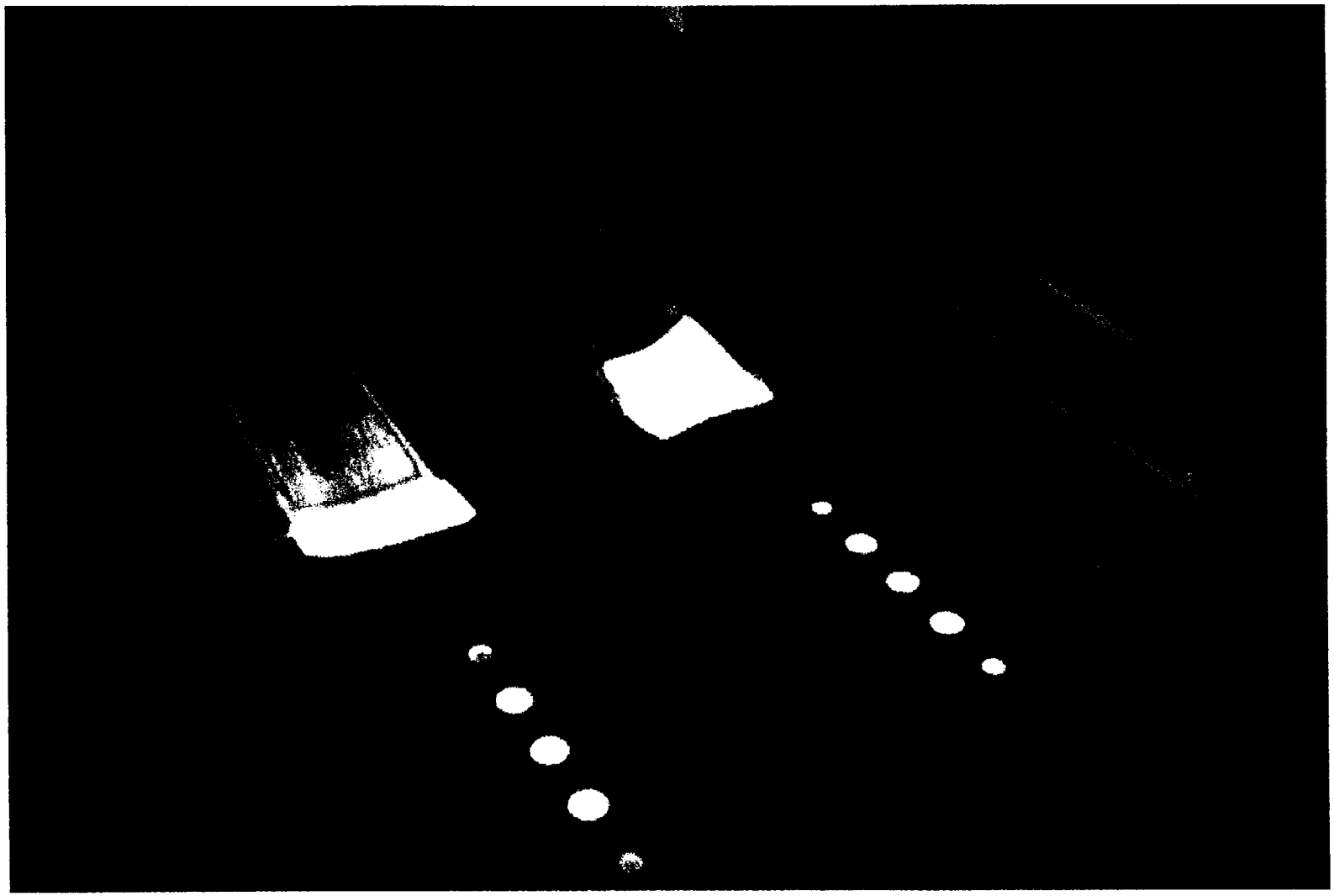

This figure is a close up of the nacelles installed on model 2b. Notice the build up of the fairings. The fairings were built up using templates to mold bondo onto the surface. This process is not very exact and takes about an hour to perform.

- WT Data Corrections
  - Fuselage Cavity
  - Nacelle Base
  - Nacelle Internal Duct - Viscous
- Post WT Data Corrections
  - Trip Drag Based on Data from M2.4-7A Opt 5 WT Test 1651
  - Trip Drag Study Being Done on Model 2b during Test 1679

Corrections were made to the wind tunnel data during the test and after. The corrections made based on measurements were the fuselage cavity pressure and nacelle base pressure forces. Static pressures were measured just behind the force balance within the fuselage cavity and averaged. This pressure was applied across the exposed fuselage cavity area. Static pressures were also measured at the base of the inboard and outboard nacelles on one side of the wing. Each nacelle set of base pressures were averaged and applied over the exposed nacelle base area.

The correction that was not based on measurements was internal nacelle drag. The internal nacelle drag correction made was only a skin friction correction based on flat plate theory. The internal nacelle, fuselage cavity, and nacelle base drag corrections were made during the WT tests.

The only other correction made to the data being presented is trip drag. The trip drag correction being made to the data is based on a previous HSR test on a similar planform, the M2.4-7A Opt5 model. The Opt5 trip drag was estimated to be 4.2 counts for the wing-body (WB) and 6.3 counts for the wing-body-nacelle-diverter (WBND). This correction is made external to the WT test and is a function of how data is analyzed to estimate trip drag. A trip drag correction will be made based on data taken on model 2b. This data is still being analyzed. Preliminary estimates show that the trip drag could be as high as 5.5 counts for the WB.

- CFD Data
  - Boeing
    - TRANAIR: Full Potential
    - OVERFLOW: Navier-Stokes
  - McDonnell Douglas
    - CFL3D: Euler and Navier-Stokes
  - NASA Ames
    - AIRPLANE: Euler (Unstructured)
    - SYN87MB: Euler
    - UPS: Parabolized Navier-Stokes
    - OVERFLOW: Navier-Stokes

The other data presented are CFD results on the baseline TCA configuration performed by Boeing, McDonnell Douglas, and NASA Ames. Boeing ran TRANAIR, which solves the full potential equations, and OVERFLOW, which solves the Navier-Stokes (N-S) equations. McDonnell Douglas ran CFL3D in Euler and N-S modes. NASA Ames ran several codes. AIRPLANE is an unstructured Euler code. SYN87MB is a structured Euler code. UPS is a Parabolized N-S code that can only analyze a WB configuration. And, finally Ames ran OVERFLOW like Boeing.

I am not going to describe each code further. Each organization has and will be presenting detailed results from their computations. This paper will only be presenting the force data (CL vs. CD). A comparison between codes and between CFD and WT data will be presented.

- CFD Codes & Modeling
  - TRANAIR
    - WBND - no fairing
    - Added Viscous Drag: Sommer-Short Method
  - AIRPLANE
    - WBND - no fairing
    - Added Viscous Drag: Nicolai Method to CA
  - SYN87MB
    - WBND - no fairing
    - Added Viscous Drag: Nicolai Method
  - CFL3D Euler
    - WBNDf - with fairing
    - Added Viscous Drag: Clutter Charts based on Van Driest II Curve Fits
  - CFL3D N-S
    - WBNDf - with fairing
    - Viscous Drag: Baldwin-Lomax
  - OVERFLOW
    - WBND - no fairing (Ames)
    - WBNDf - with fairing (BCA)
    - Viscous Drag: Spalart-Allmaras
  - UPS
    - WB Only
    - Viscous Drag: Baldwin-Lomax

Each organization was given an iges file of the baseline TCA OML that the Technology Integration ITD provided to the HSR organization. The CFD results presented were computed at the WT Reynolds number and forces were integrated up to the location the wind tunnel model ended. A configuration feature each organization modeled differently was the nacelle installation. The only two organizations that modeled the nacelle fairing was McDonnell Douglas in CFL3D and Boeing in OVERFLOW.

There are probably other features modeled differently among the codes, but the details were not all provided for a comparison to be made. Suffice it to say, that the configurations were modeled as closely as possible to the WT model.

Other key features that need to be pointed out is the methods used to compute the viscous drag. For the Full Potential and Euler codes, the methods used were external to the CFD code. This chart shows the methods used for a truncated fuselage at a wind tunnel Reynolds number of 4 Million/ft or 6.3 Million. The viscous drag gets computed internally to the Navier Stokes codes.

Wind Tunnel vs Full Potential and Euler
M=2.4, RN=4 M/ft

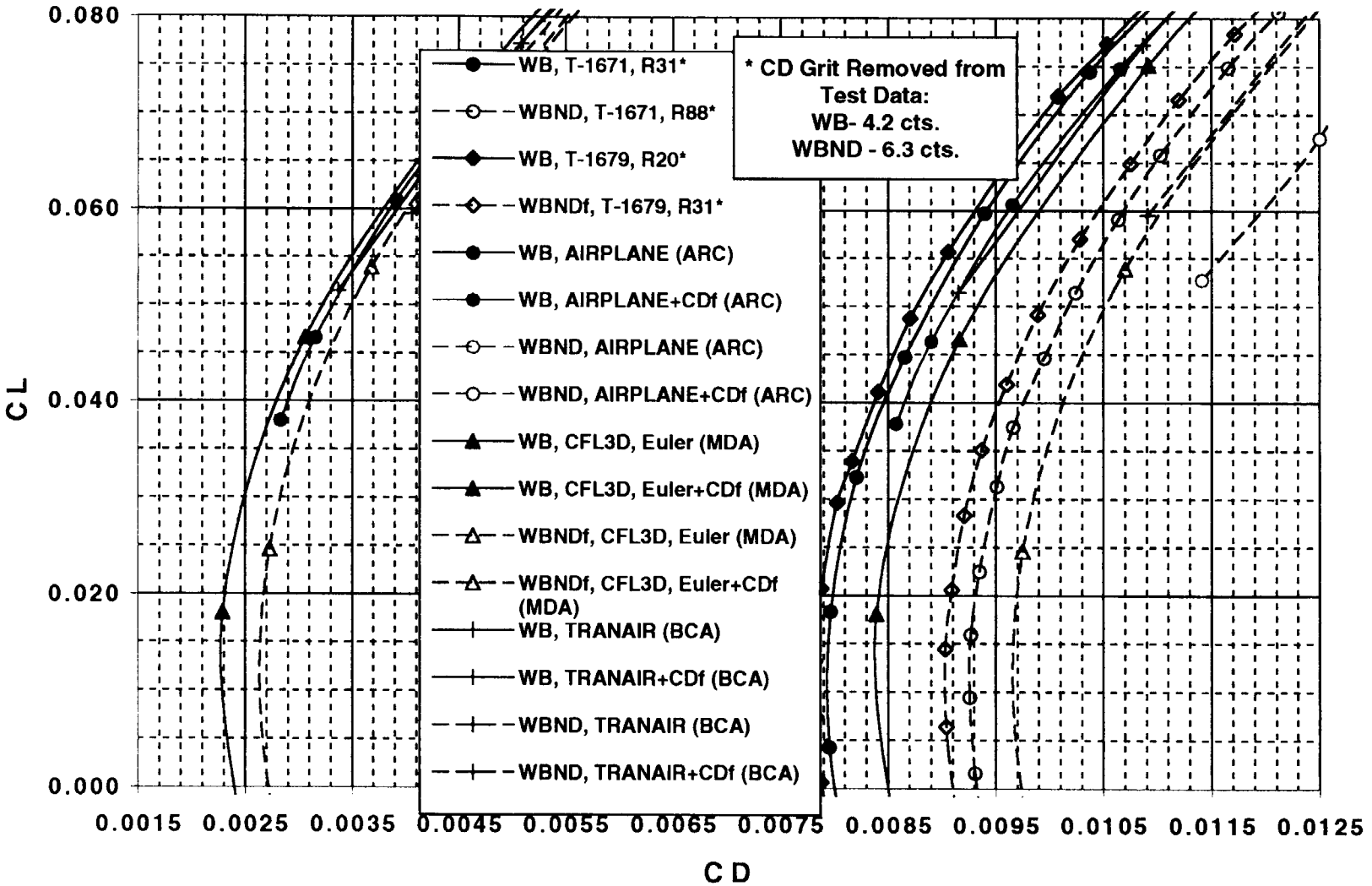

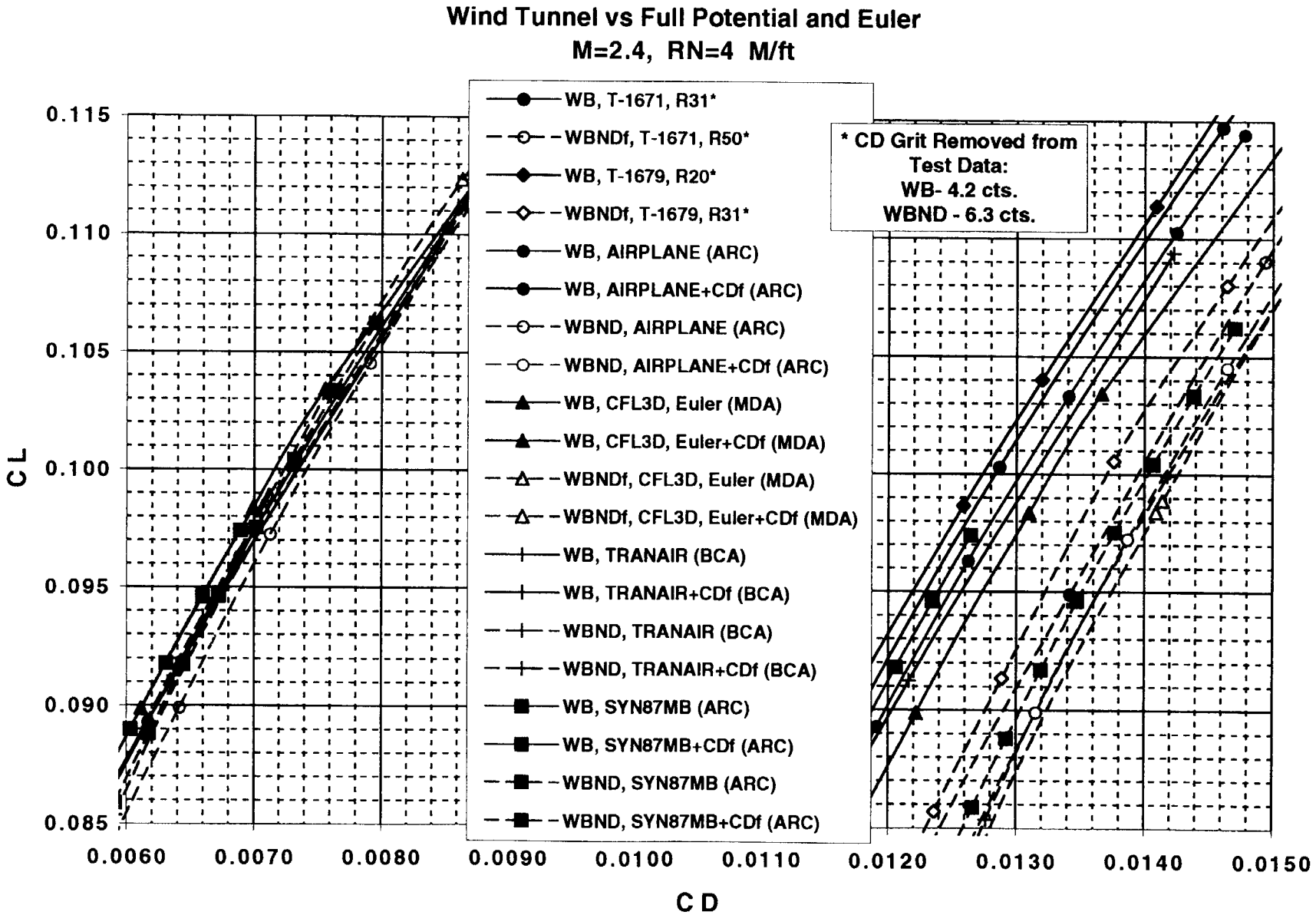
Wind Tunnel vs Full Potential and Euler
M=2.4, RN=4 M/ft
WB, T-1671, R31*
WBNDf, T-1671, R50*
WB, T-1679, R20*
WBNDf, T-1679, R31*
WB, AIRPLANE (ARC)
WB, AIRPLANE+CDf (ARC)
WBND, AIRPLANE (ARC)
WBND, AIRPLANE+CDf (ARC)
WB, CFL3D, Euler (MDA)
WB, CFL3D, Euler+CDf (MDA)
WBNDf, CFL3D, Euler (MDA)
WBNDf, CFL3D, Euler+CDf (MDA)
WB, TRANAIR (BCA)
WB, TRANAIR+CDf (BCA)
WBND, TRANAIR (BCA)
WBND, TRANAIR+CDf (BCA)
WB, SYN87MB (ARC)
WB, SYN87MB+CDf (ARC)
WBND, SYN87MB (ARC)
WBND, SYN87MB+CDf (ARC)
* CD Grit Removed from Test Data:
WB- 4.2 cts.
WBND - 6.3 cts.
CL
0.115
0.110
0.105
0.100
0.095
0.090
0.085
0.0060
0.0070
0.0080
0.0090
0.0100
0.0110
0.0120
0.0130
0.0140
0.0150
C D

This figure shows the drag polar zoomed in around cruise of CL=0.1 for comparison of Full Potential and Euler codes. There is a total difference in pressure drag of 2 counts for WB and WBND. The CFD drag polars are to the right of WT data. The CFD data shows a total drag difference of 3 counts for WB among codes and 3 counts for WBND.

The WT data ranges over 1.4 count for WB and 2 counts for WBND.

OVERFLOW Comparisons
M=2.4, RN=4 M/ft

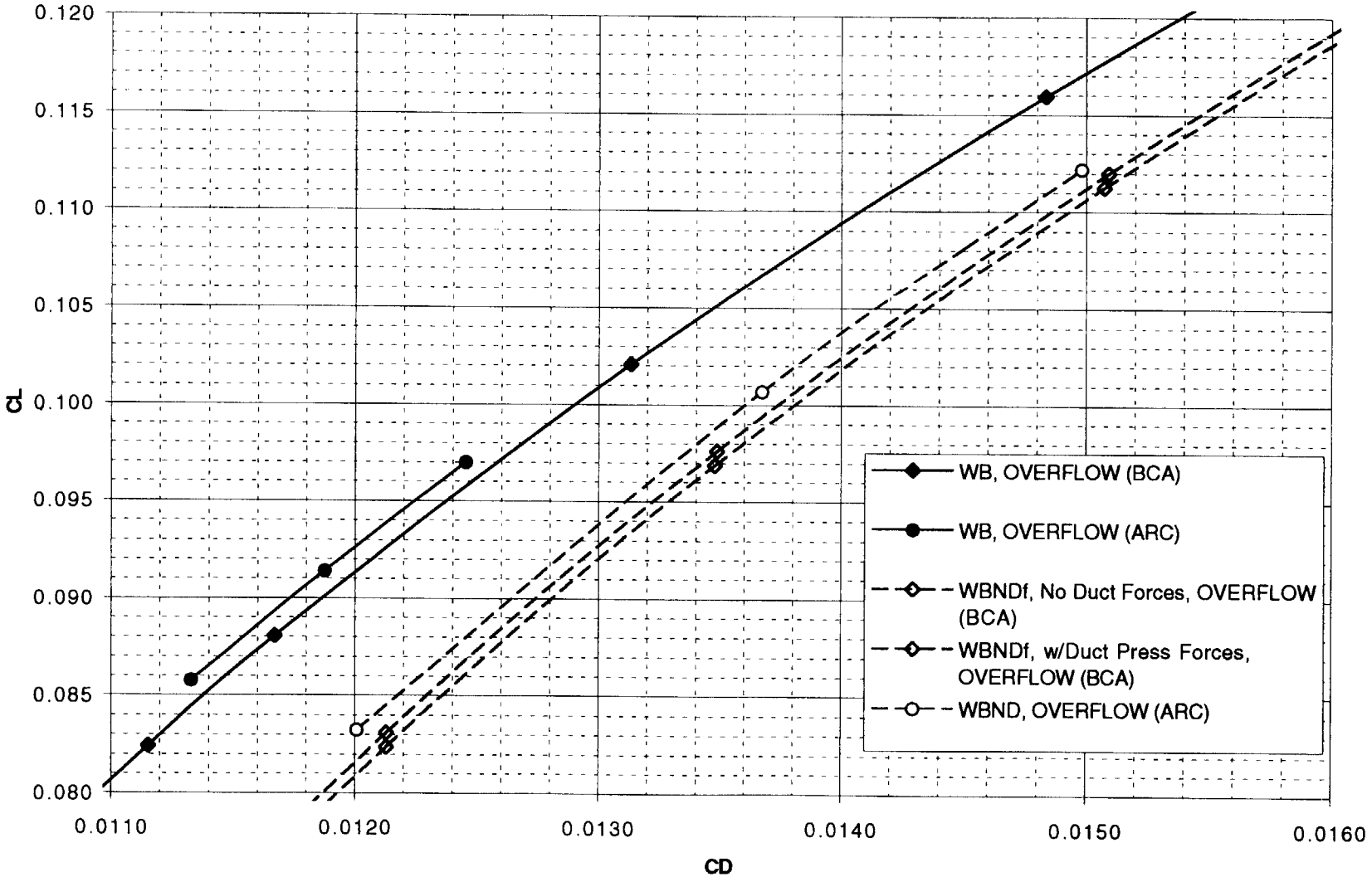

OVERFLOW was run by NASA Ames and Boeing. The major differences between the way the two organizations ran it were in the grid, geometry fidelity, and fringe spacing. Ames used single fringe spacing and Boeing used double fringe spacing. Boeing's grid had more points than the Ames grid due to the fringe spacing. Even though there were these differences, the results are very similar. The total drag difference is 1 count for WB and WBND. Boeing did an additional computation where only the viscous component of drag for the nacelle internal duct was removed. This is what the WT data has in it's correction. The effect is 0.6 drag count.

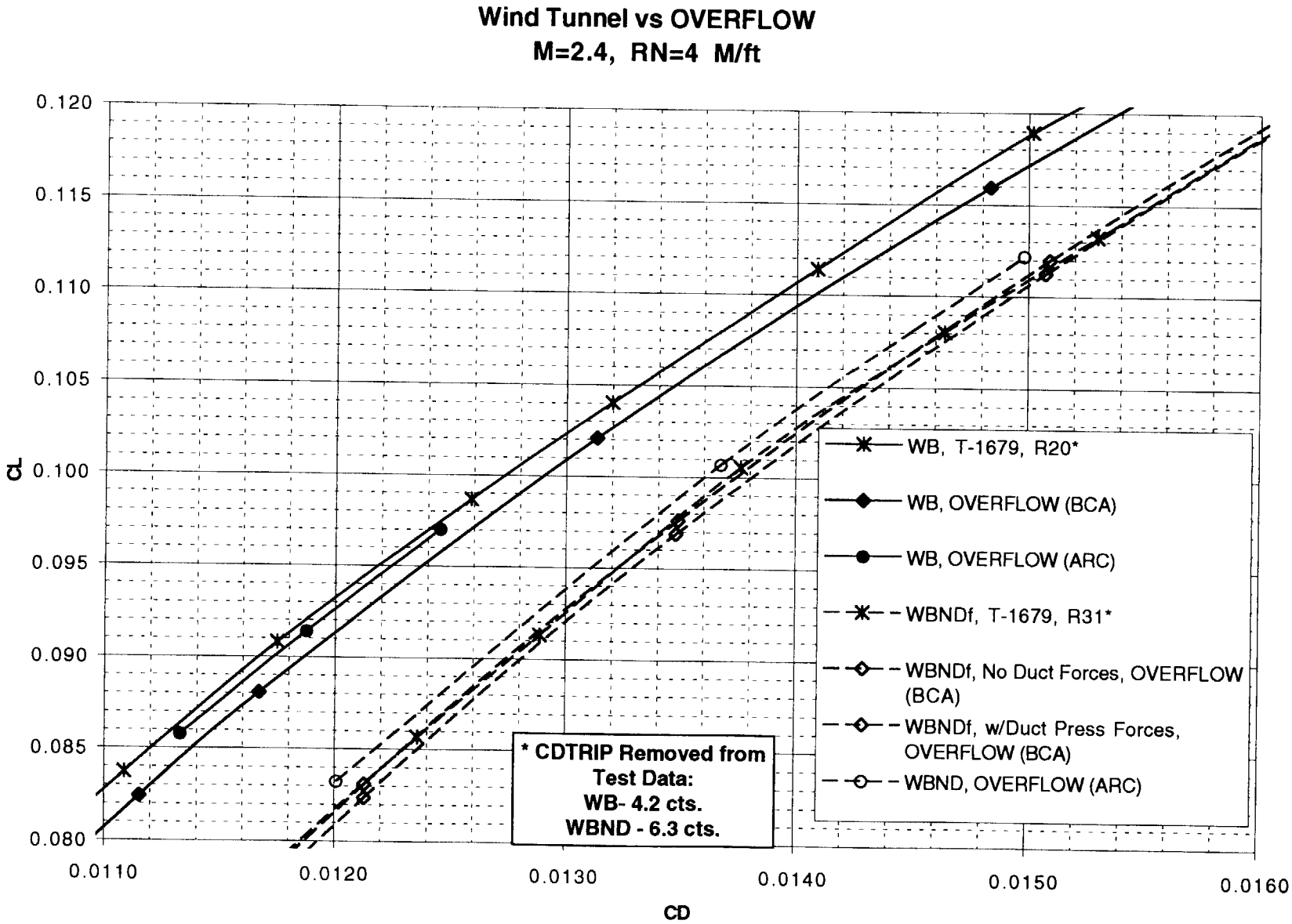
Wind Tunnel vs OVERFLOW
M=2.4, RN=4 M/ft
CL
CD
0.120
0.115
0.110
0.105
0.100
0.095
0.090
0.085
0.080
0.0110
0.0120
0.0130
0.0140
0.0150
0.0160
WB, T-1679, R20*
WB, OVERFLOW (BCA)
WB, OVERFLOW (ARC)
WBNDf, T-1679, R31*
WBNDf, No Duct Forces, OVERFLOW (BCA)
WBNDf, w/Duct Press Forces, OVERFLOW (BCA)
WBND, OVERFLOW (ARC)
* CDTRIP Removed from Test Data:
WB- 4.2 cts.
WBND - 6.3 cts.

When comparing OVERFLOW to WT, the differences are smaller than the Full Potential and Euler results. For WB, the drag from OVERFLOW/Ames is less than 1 count from WT. For WBND, the WT data is between both OVERFLOW solutions.

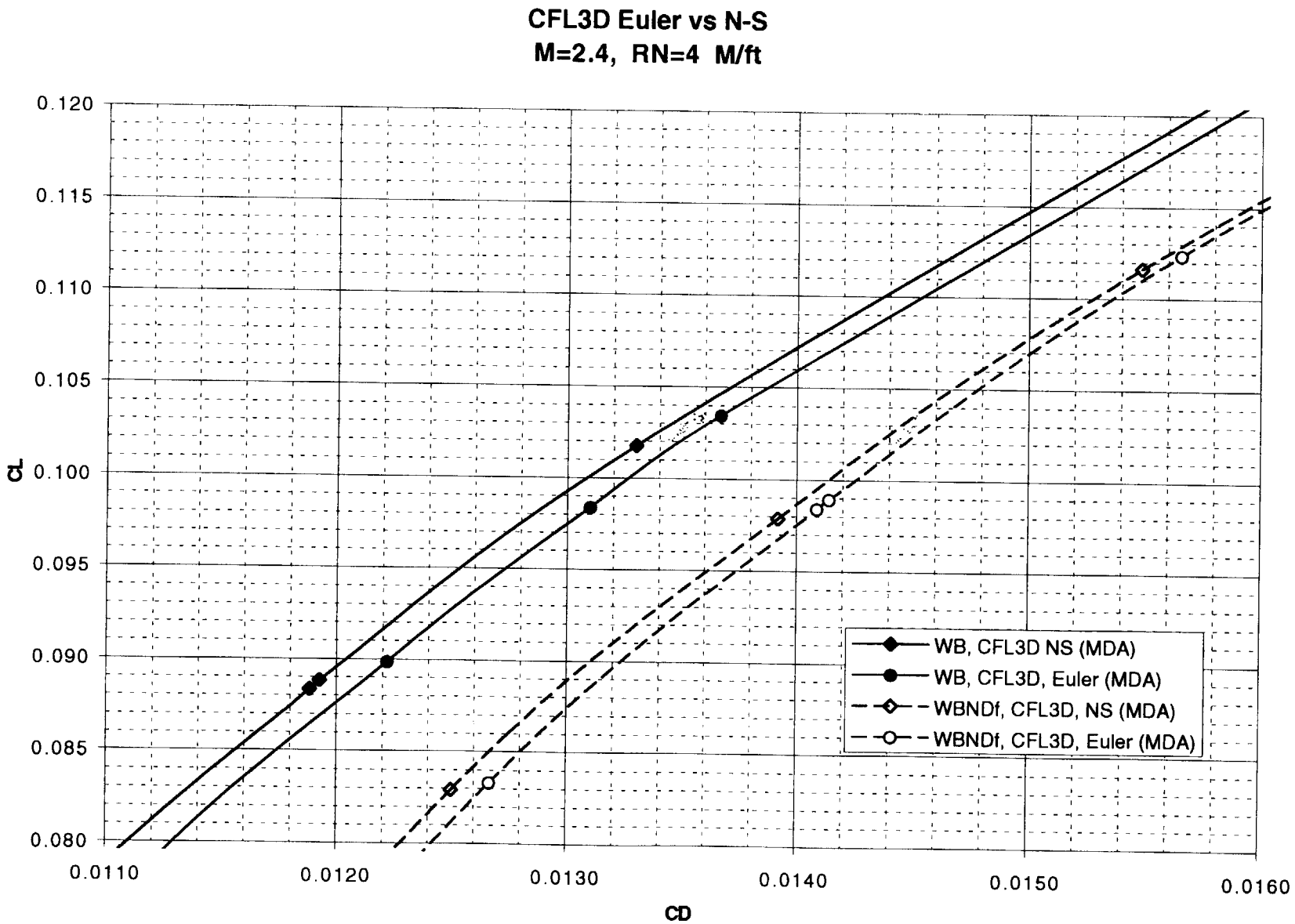
CFL3D Euler vs N-S
M=2.4, RN=4 M/ft
0.120
0.115
0.110
0.105
0.100
0.095
0.090
0.085
0.080
CL
0.0110
0.0120
0.0130
0.0140
0.0150
0.0160
CD
WB, CFL3D NS (MDA)
WB, CFL3D, Euler (MDA)
WBNDf, CFL3D, NS (MDA)
WBNDf, CFL3D, Euler (MDA)

McDonnell Douglas ran CFL3D in Euler and N-S modes. This plot shows the difference between the two methods. It is almost 2 counts for WB and 1 count for WBND.

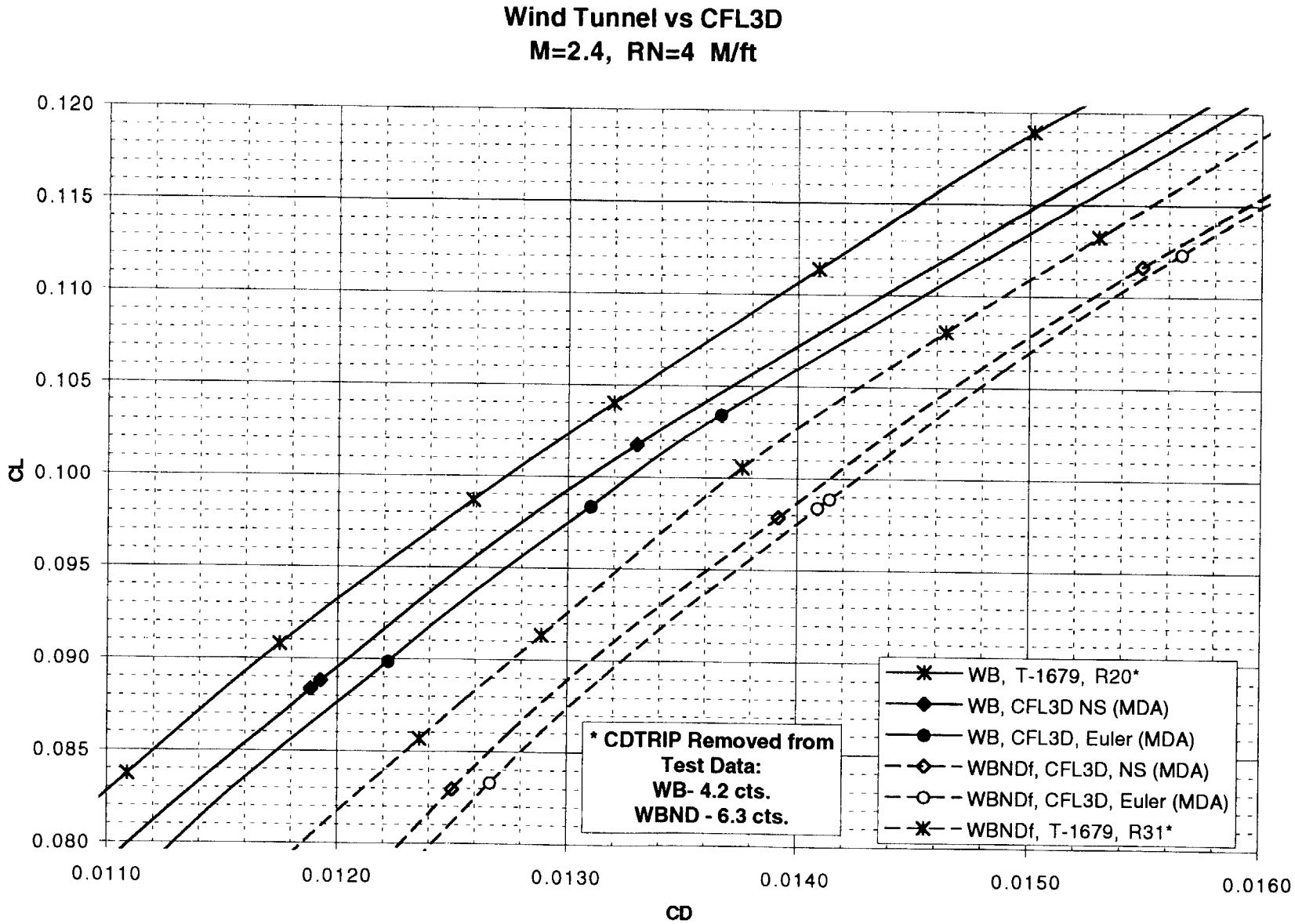
Wind Tunnel vs CFL3D
M=2.4, RN=4 M/ft
CL
CD
0.120
0.115
0.110
0.105
0.100
0.095
0.090
0.085
0.080
0.0110
0.0120
0.0130
0.0140
0.0150
0.0160
* CDTRIP Removed from Test Data:
WB- 4.2 cts.
WBND - 6.3 cts.
WB, T-1679, R20*
WB, CFL3D NS (MDA)
WB, CFL3D, Euler (MDA)
WBNDf, CFL3D, NS (MDA)
WBNDf, CFL3D, Euler (MDA)
WBNDf, T-1679, R31*

This figure compares CFL3D with WT data. CFL3D gives higher drag than WT data for both Euler and N-S by 4 counts.

Wind Tunnel vs OVERFLOW and CFL3D
M=2.4, RN=4 M/ft

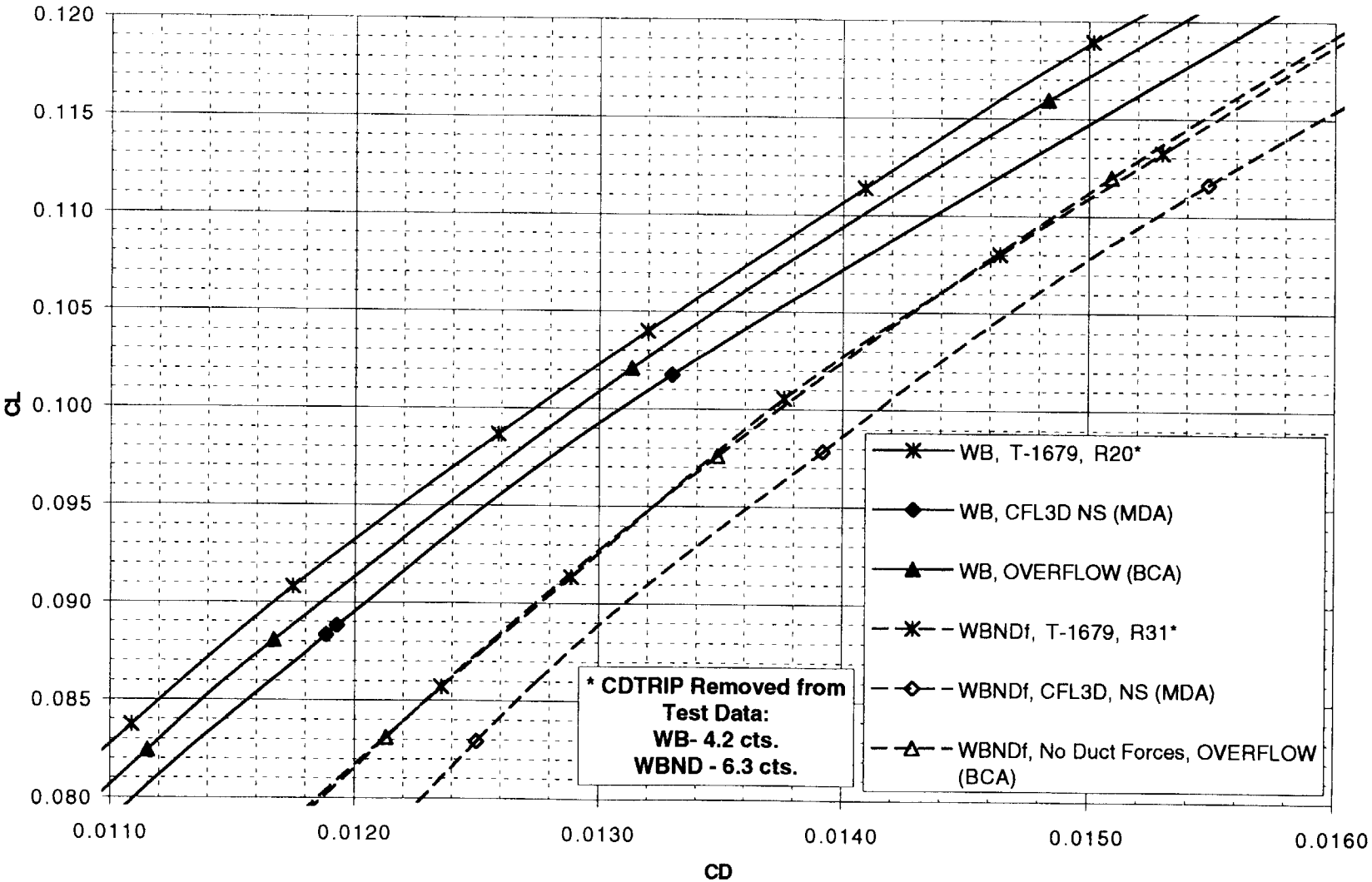

This figure shows a comparison of CFL3D, OVERFLOW/Boeing, and WT data.

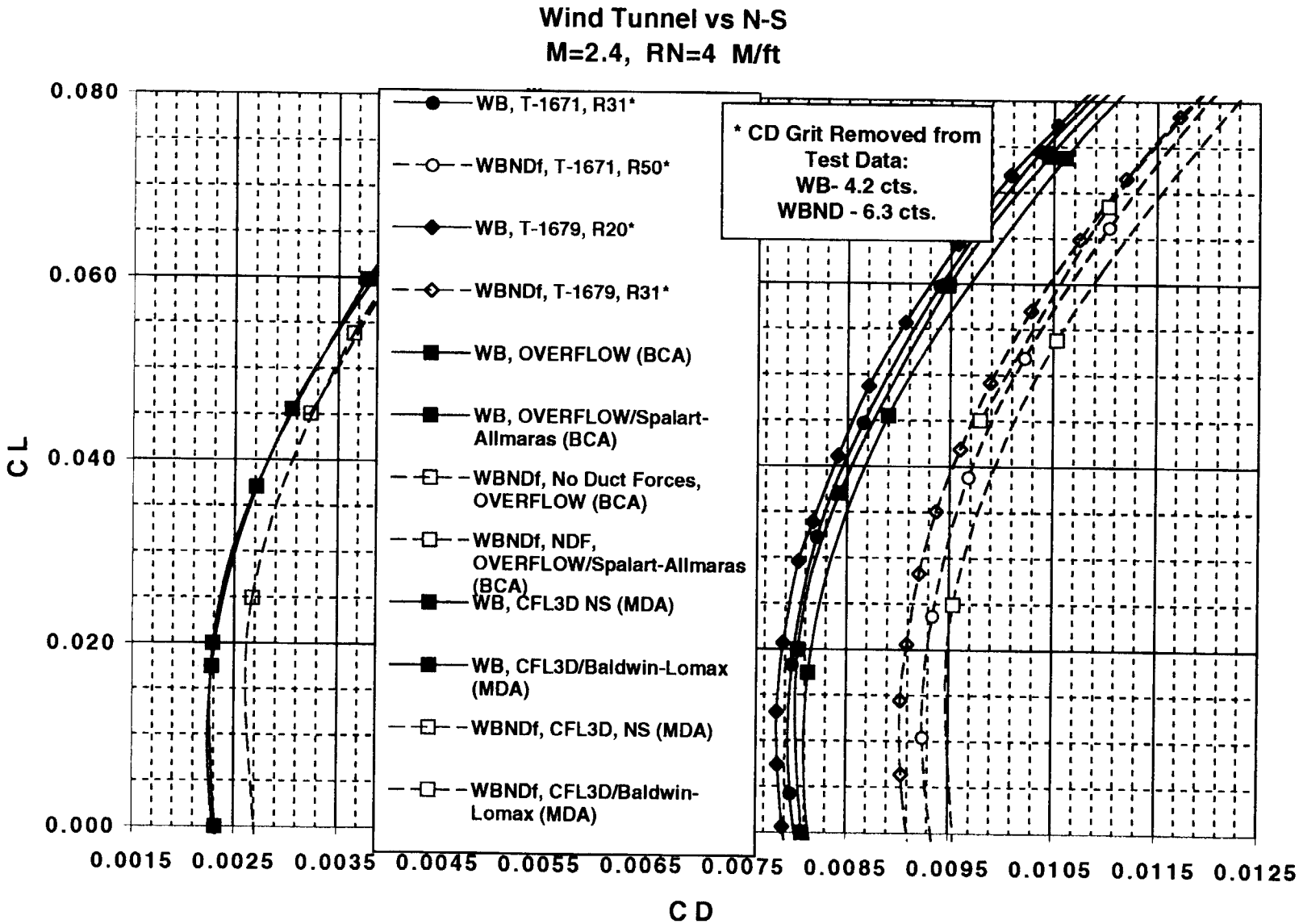
Wind Tunnel vs N-S
M=2.4, RN=4 M/ft
0.080
0.060
0.040
0.020
0.000
CL
0.0015 0.0025 0.0035 0.0045 0.0055 0.0065 0.0075 0.0085 0.0095 0.0105 0.0115 0.0125
CD
WB, T-1671, R31*
WBNDf, T-1671, R50*
WB, T-1679, R20*
WBNDf, T-1679, R31*
WB, OVERFLOW (BCA)
WB, OVERFLOW/Spalart-Allmaras (BCA)
WBNDf, No Duct Forces, OVERFLOW (BCA)
WBNDf, NDF, OVERFLOW/Spalart-Allmaras (BCA)
WB, CFL3D NS (MDA)
WB, CFL3D/Baldwin-Lomax (MDA)
WBNDf, CFL3D, NS (MDA)
WBNDf, CFL3D/Baldwin-Lomax (MDA)
* CD Grit Removed from Test Data:
WB- 4.2 cts.
WBND - 6.3 cts.

This figures shows the drag polar zoomed in around minimum drag for comparison of N-S codes. To the left of the plot is the pressure drag plotted for WB and WBND. The pressure drag for the N-S codes do not differ for WB and WBND. The CFD total drag polars are to the right of the wind tunnel data. The CFD data shows a total drag difference of 2 counts for WB among codes and 2.5 counts for WBND.

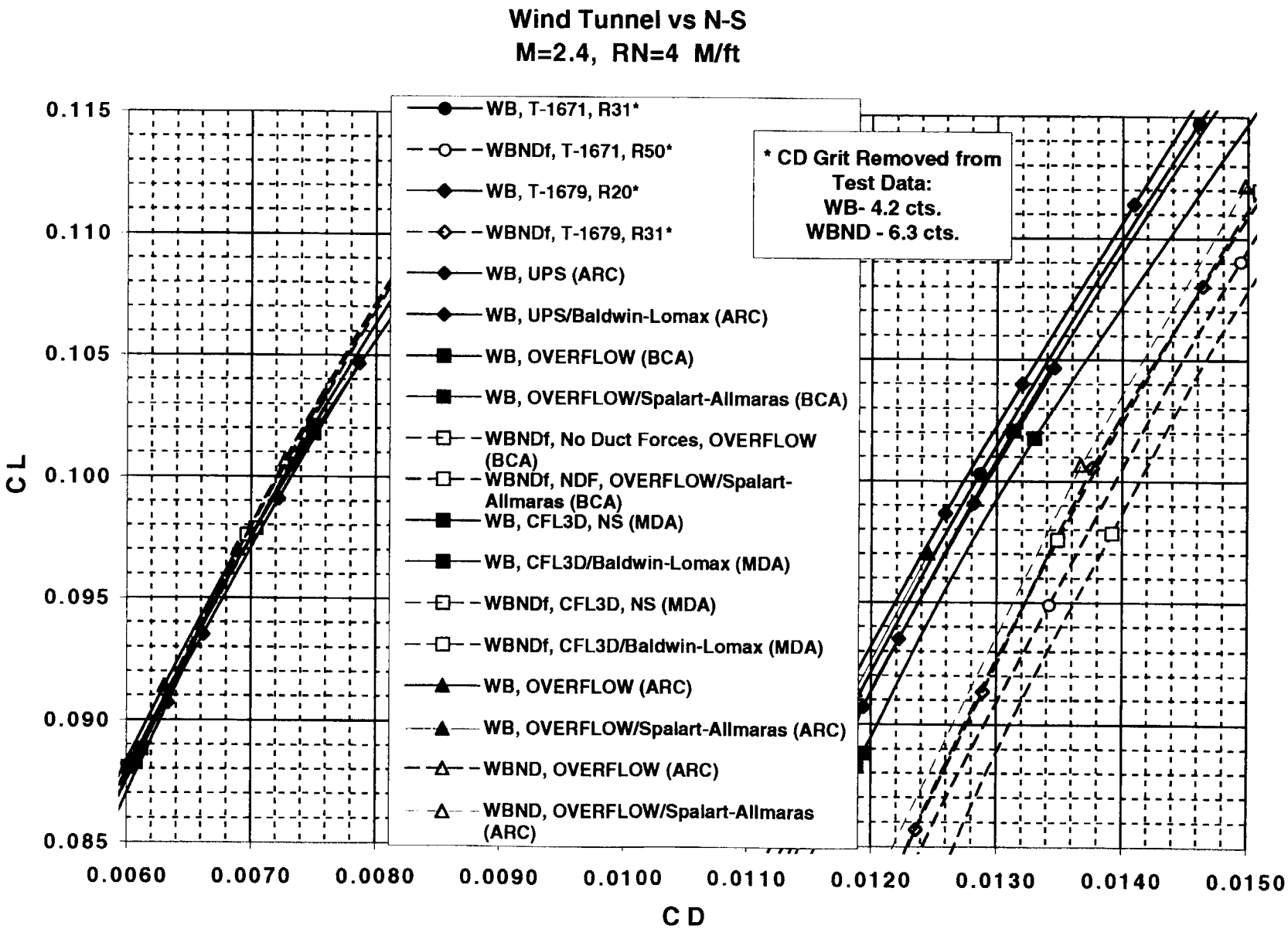
Wind Tunnel vs N-S
M=2.4, RN=4 M/ft
CL
CD
0.115
0.110
0.105
0.100
0.095
0.090
0.085
0.0060
0.0070
0.0080
0.0090
0.0100
0.0110
0.0120
0.0130
0.0140
0.0150
WB, T-1671, R31*
WBNDf, T-1671, R50*
WB, T-1679, R20*
WBNDf, T-1679, R31*
WB, UPS (ARC)
WB, UPS/Baldwin-Lomax (ARC)
WB, OVERFLOW (BCA)
WB, OVERFLOW/Spalart-Allmaras (BCA)
WBNDf, No Duct Forces, OVERFLOW (BCA)
WBNDf, NDF, OVERFLOW/Spalart-Allmaras (BCA)
WB, CFL3D, NS (MDA)
WB, CFL3D/Baldwin-Lomax (MDA)
WBNDf, CFL3D, NS (MDA)
WBNDf, CFL3D/Baldwin-Lomax (MDA)
WB, OVERFLOW (ARC)
WB, OVERFLOW/Spalart-Allmaras (ARC)
WBND, OVERFLOW (ARC)
WBND, OVERFLOW/Spalart-Allmaras (ARC)
* CD Grit Removed from Test Data:
WB- 4.2 cts.
WBND - 6.3 cts.

This figure shows the drag polar zoomed in around cruise of CL=0.1 for comparison of N-S codes. There is a total difference in pressure drag of 1 counts for WB and 0.5 count for WBND. The CFD data shows a total drag difference of 2 counts for WB among codes and 6 counts for WBND.

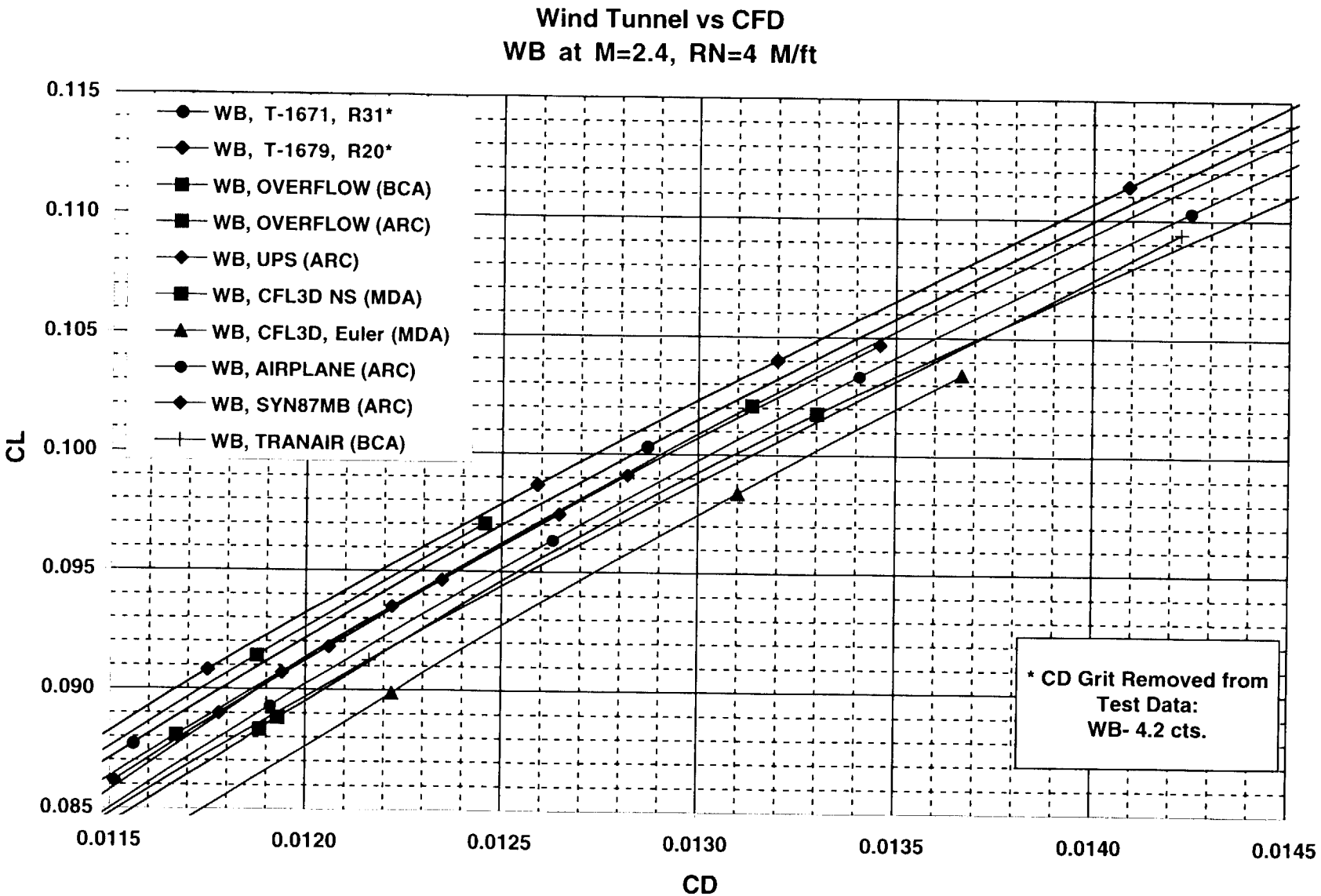
Wind Tunnel vs CFD
WB at M=2.4, RN=4 M/ft
WB, T-1671, R31*
WB, T-1679, R20*
WB, OVERFLOW (BCA)
WB, OVERFLOW (ARC)
WB, UPS (ARC)
WB, CFL3D NS (MDA)
WB, CFL3D, Euler (MDA)
WB, AIRPLANE (ARC)
WB, SYN87MB (ARC)
WB, TRANAIR (BCA)
* CD Grit Removed from Test Data: WB- 4.2 cts.
CL
CD
0.115
0.110
0.105
0.100
0.095
0.090
0.085
0.0115
0.0120
0.0125
0.0130
0.0135
0.0140
0.0145

The total drag for WB ranges over 5.5 drag counts between all the CFD and WT.

Full Potential, Euler, and N-S CFD Comparisons
WB Pressure Drag

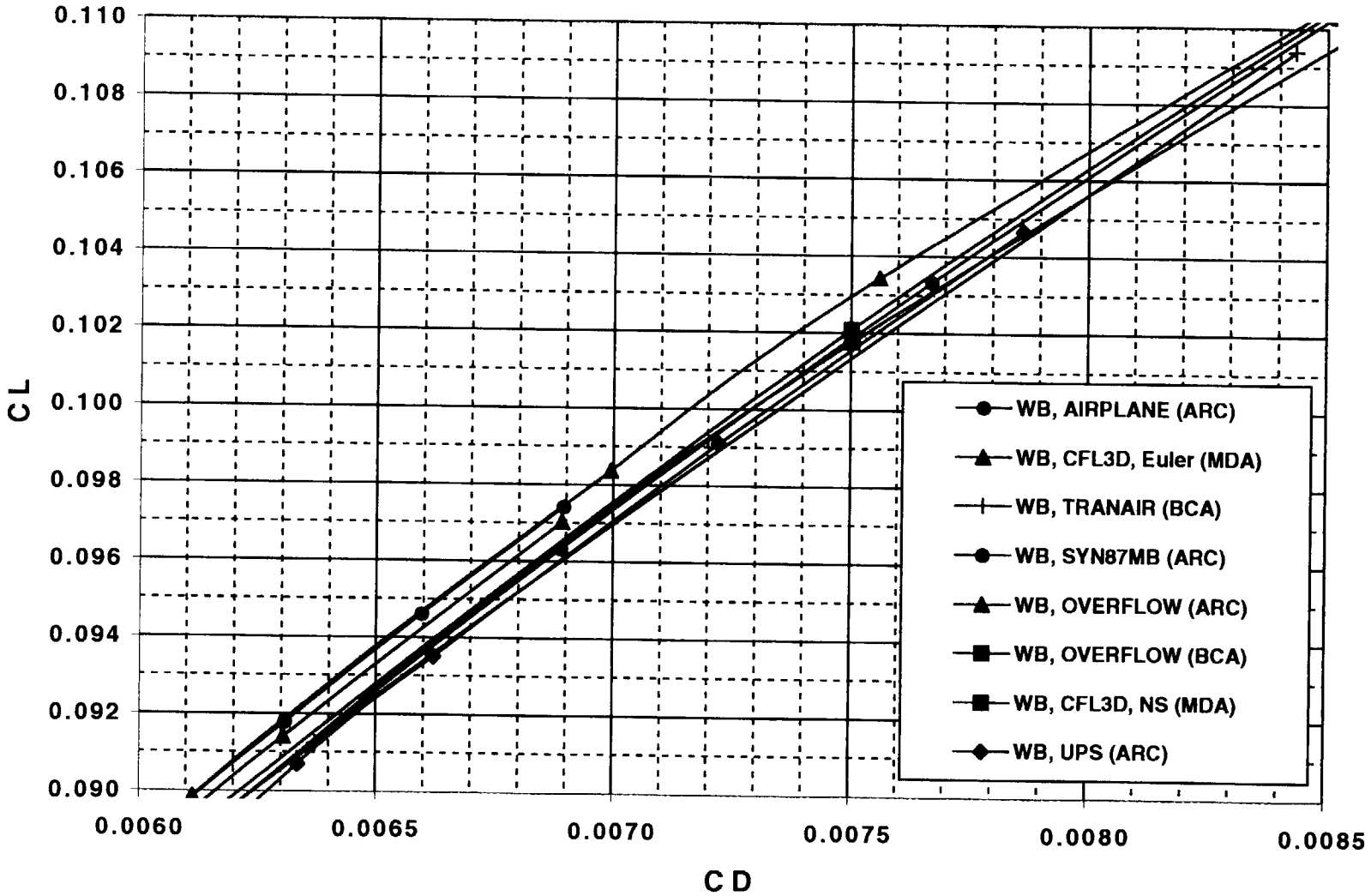

The pressure drag among all the codes are more consistent than the total drag. The pressure data for WB ranges over 0.5 drag count for N-S and 2 drag counts for Full Potential and Euler.

WB Viscous Drag Comparisons
M=2.4, RN=4 M/ft

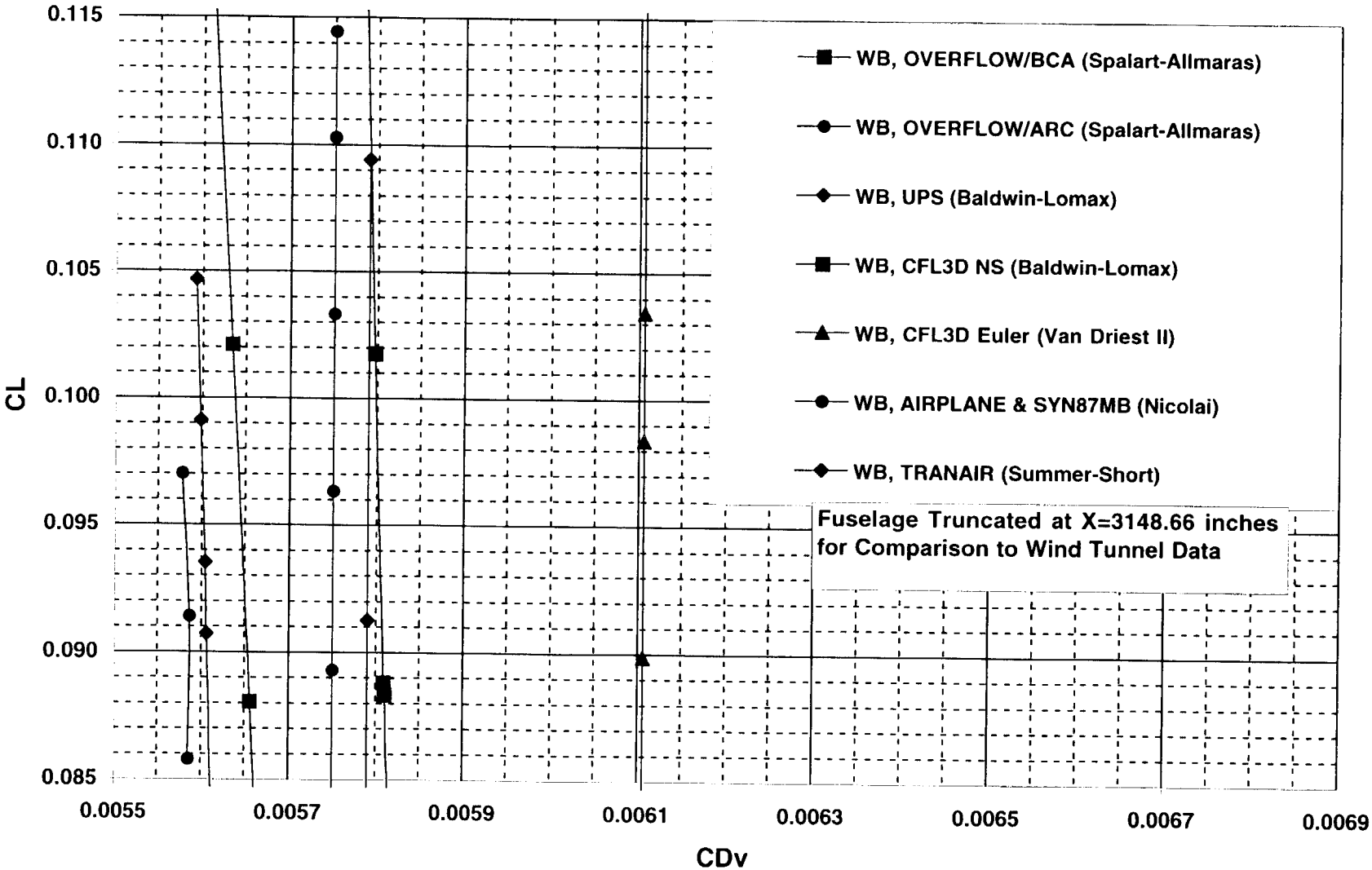

The figure shows the variation of viscous drag computation for the WB. The spread of the data is over 5.25 drag counts.

Wind Tunnel vs CFD
WBND at M=2.4, RN=4 M/ft

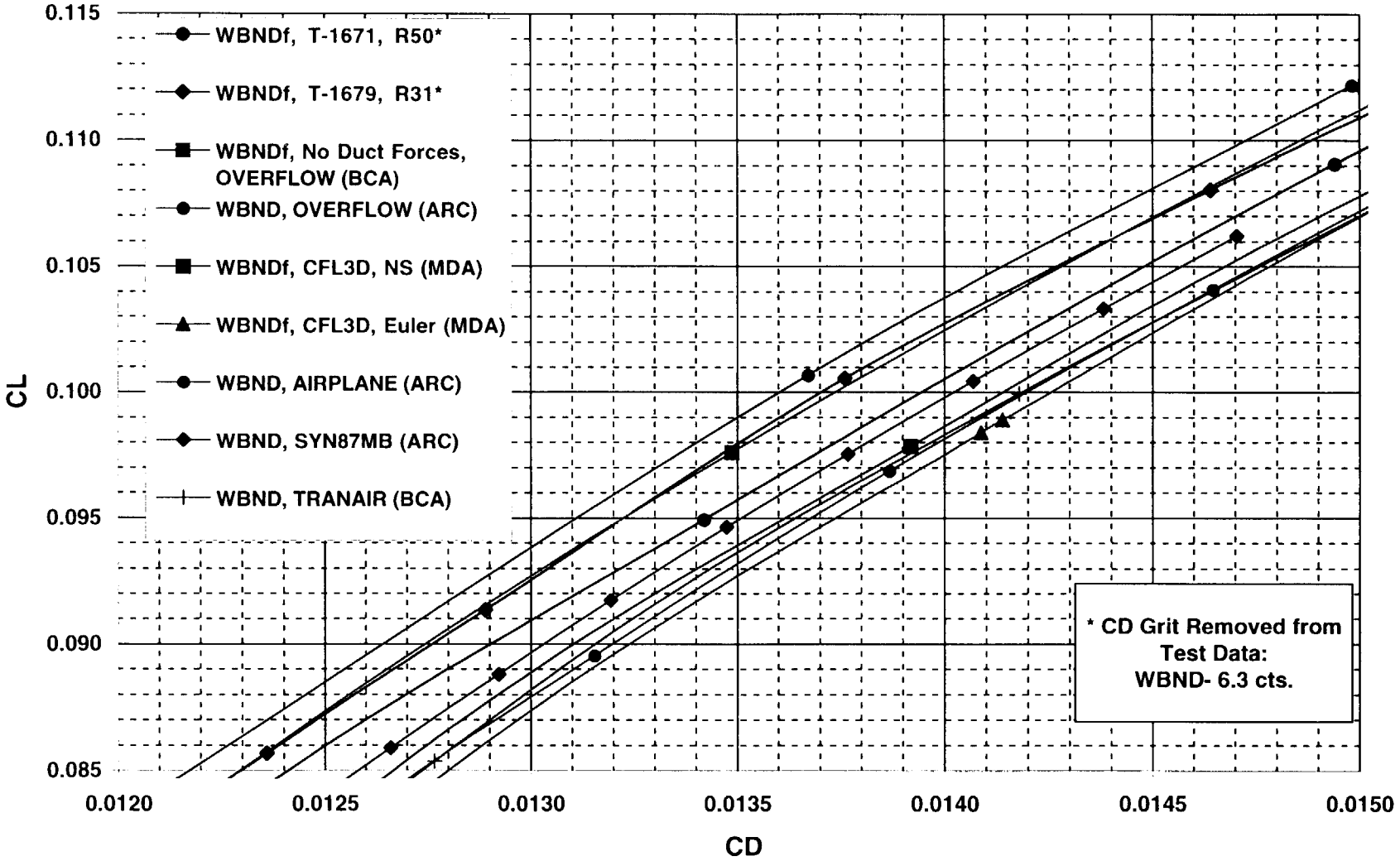

The total drag for WBND ranges over 6.5 cts between all of the CFD and WT.

Full Potential, Euler, and N-S CFD Comparisons
WBND Pressure Drag

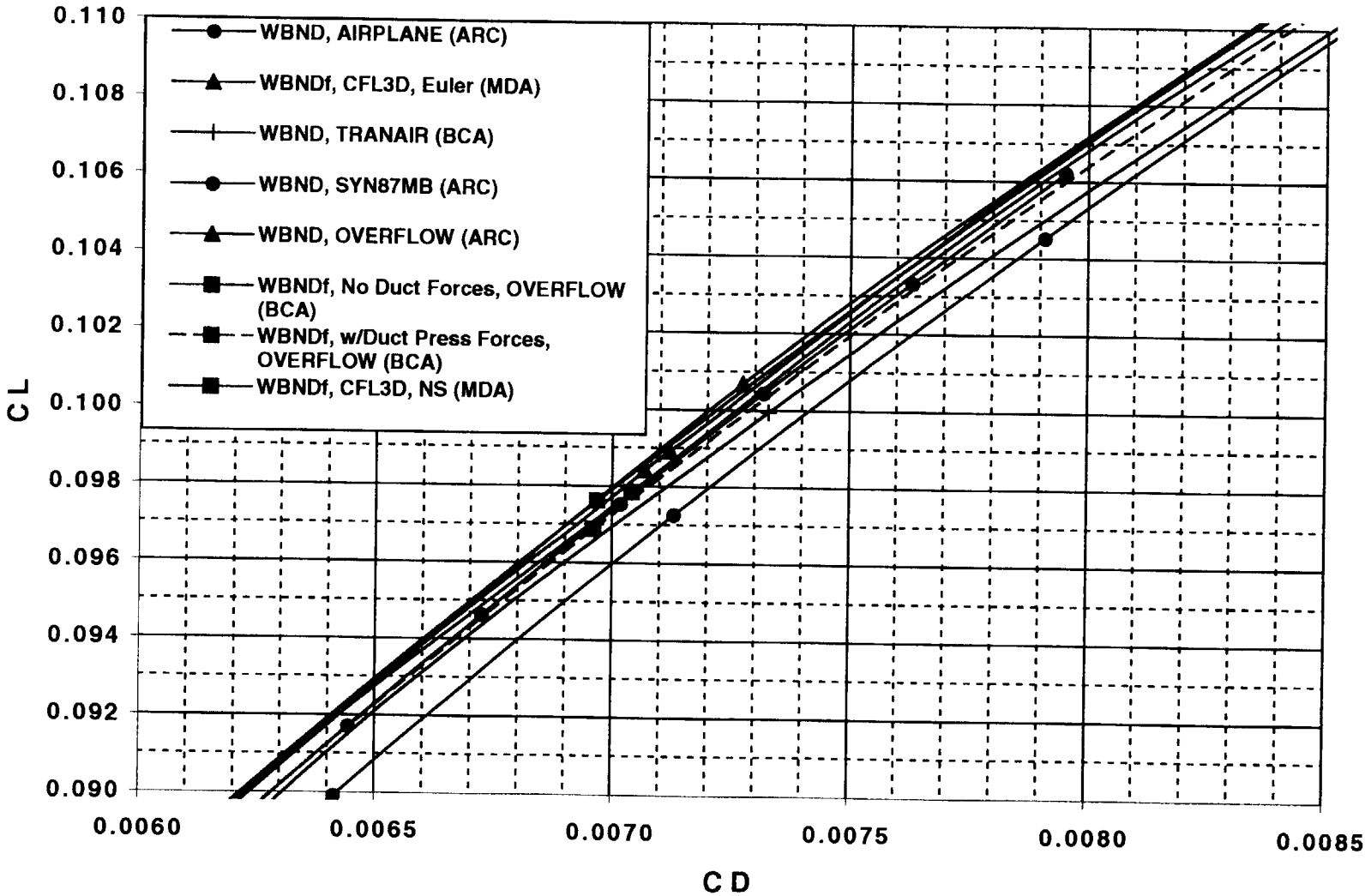

The total pressure drag for WBND ranges over all the CFD codes is 2 drag counts.

WBND Viscous Drag Comparisons
M=2.4, RN=4 M/ft

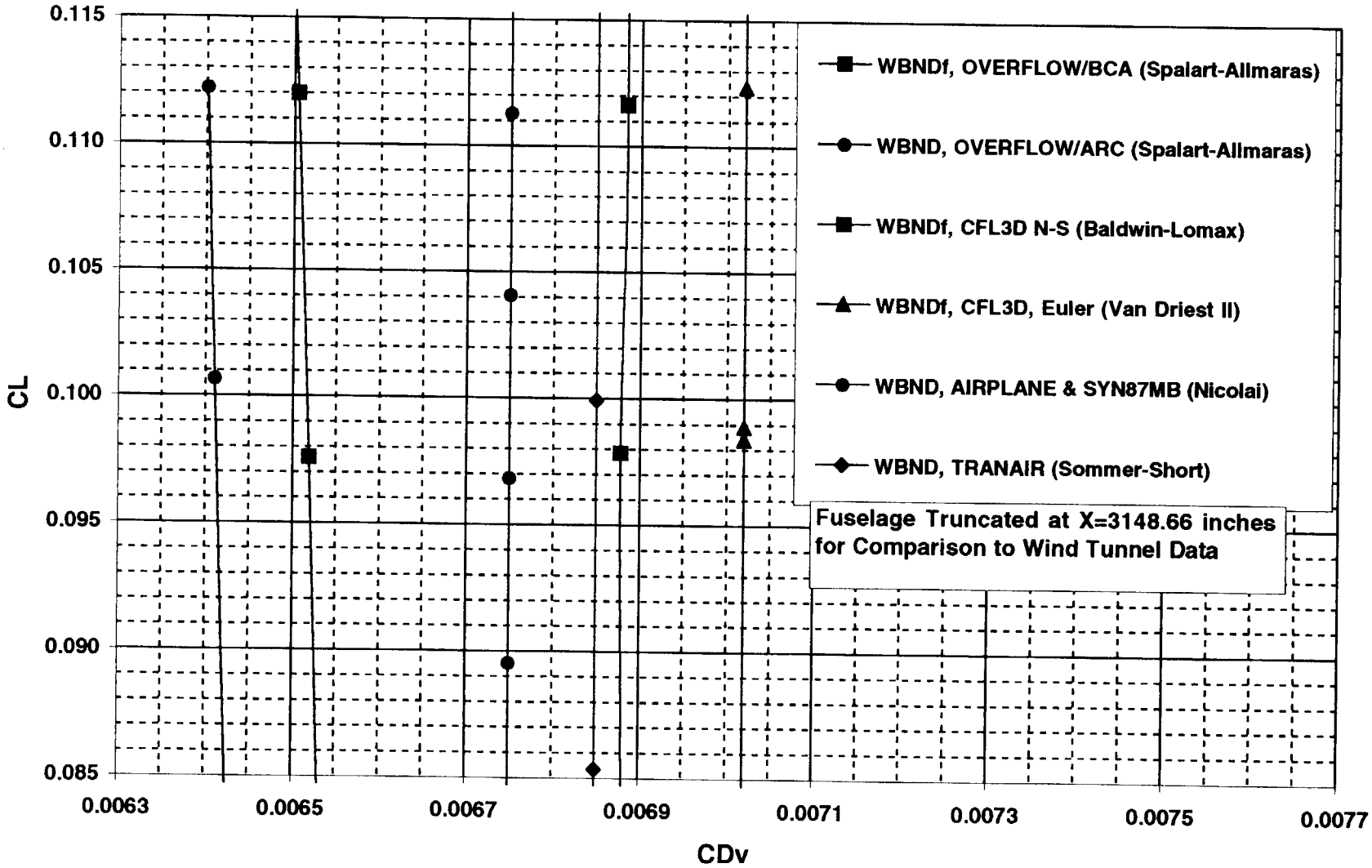

The major differences lie in the viscous drag, which is 6 counts.

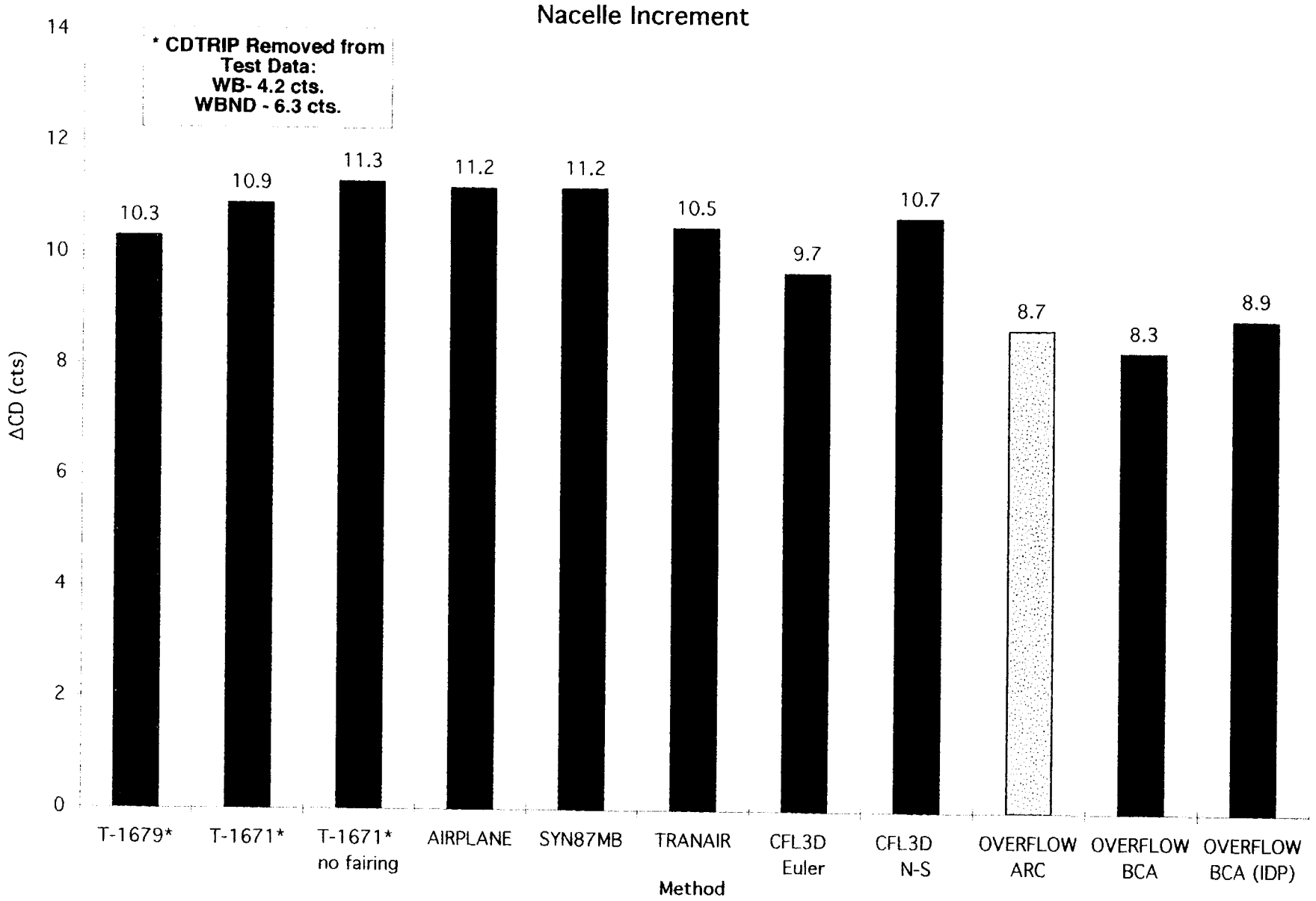

NASA ARC/Cappuccio

The difference between WB and WBND gives the drag increment for installing the nacelles. The WBND CFD force data covers all external geometry and no nacelle internal duct forces. Internal duct forces include pressure and viscous components. The wind tunnel data only corrects for the viscous component. The viscous component is estimated using flat plate skin friction theory. All of the CFD data removes both pressure and viscous drag.

Boeing computed data for the WBND with just the viscous drag removed and with both pressure and viscous drag removed. Boeing's data shows a difference between the computations of around 0.6 counts. One needs to understand that the pressure drag in the nacelle internal duct isn't measured because the instrumentation needed would impinge on the overall drag measurements. It probably means that this correction should be made to the wind tunnel data using CFD computations in addition to the viscous drag.

The bar chart shows a comparison of the drag increment for installing the nacelles between wind tunnel and CFD data. OVERFLOW shows the lowest increment of 8.3 counts. The wind tunnel data shows an increment at most of 11.3 counts. CFL3D N-S shows an increment of 10.7 counts. Over all the CFD data, nacelle increments range from 8.3 to 11.2 counts. The wind tunnel nacelle increment range measured is from 10.3 to 11.3 counts.

Recommendations

- CFD
  - Boundary Layer Trip Location
  - WT Nacelle Internal Duct
  - Viscous Drag

- Wind Tunnel
  - Boundary Layer Trip Drag
  - Nacelle Internal Duct Corrections

Recommendations for both CFD and WT data are as follows.

One item that is still not being modeled in CFD like being tested in the WT is where the boundary layer is being tripped to go turbulent. Most CFD codes are modeling fully turbulent flow which is definitely not happening in the WT.

CFD should attempt to model the wind tunnel nacelle internal duct.

Viscous drag computations is still not resolved. We need to get a higher degree of confidence in the viscous computations of N-S codes and the external computations made to correct Full Potential and Euler computations.

A better handle needs to be had on what the trip drag is, so that the correction can be made to wind tunnel data with a higher degree of confidence.

WT data needs to correct the internal nacelle duct with the same corrections CFD do on their computations.

Propulsion Induced Effects Test Program

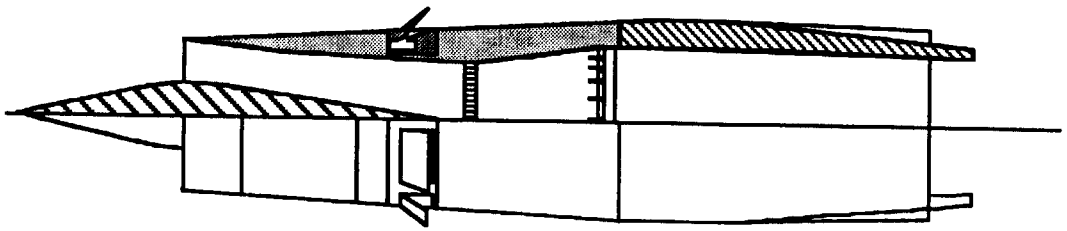

Gelsomina Cappuccio, Mark Won, and Dan Bencze
NASA Ames Research Center

HSR Aerodynamic Performance Workshop
NASA Langley Research Center
February 25-28, 1997

Overall Test Program Objectives

CA Milestone 4-14 Propulsion Induced Effects

- The objective of this milestone is to assess the propulsion/airframe integration characteristics of the Technology Concept Airplane and design variations through computational analysis and experimental subsonic through supersonic wind tunnel testing
- The Milestone will generate a comprehensive CFD and wind tunnel data base of the baseline and design variations
- Emphasis will be placed on establishing the propulsion induced effects on the flight performance of the Technology Concept Airplane with all appropriate wind tunnel corrections.

The propulsion induced effects test program is being lead by NASA Ames for Configuration Aerodynamics (CA). Representatives from CA, Technology Integration (TI), Inlet, and the Nozzle ITD's are working with Ames in defining and executing this test program. The objective of the CA 4-14 milestone is to assess the propulsion/airframe integration characteristics of the Technology Concept Airplane and design variations through computational analysis and experimental subsonic through supersonic wind tunnel testing. The test program will address the experimental part transonically and supersonically. This milestone will generate a comprehensive database. Emphasis will be placed on establishing the propulsion induced effects on the flight performance of the Technology Concept Airplane with all appropriate wind tunnel corrections.

Program Definition Approach

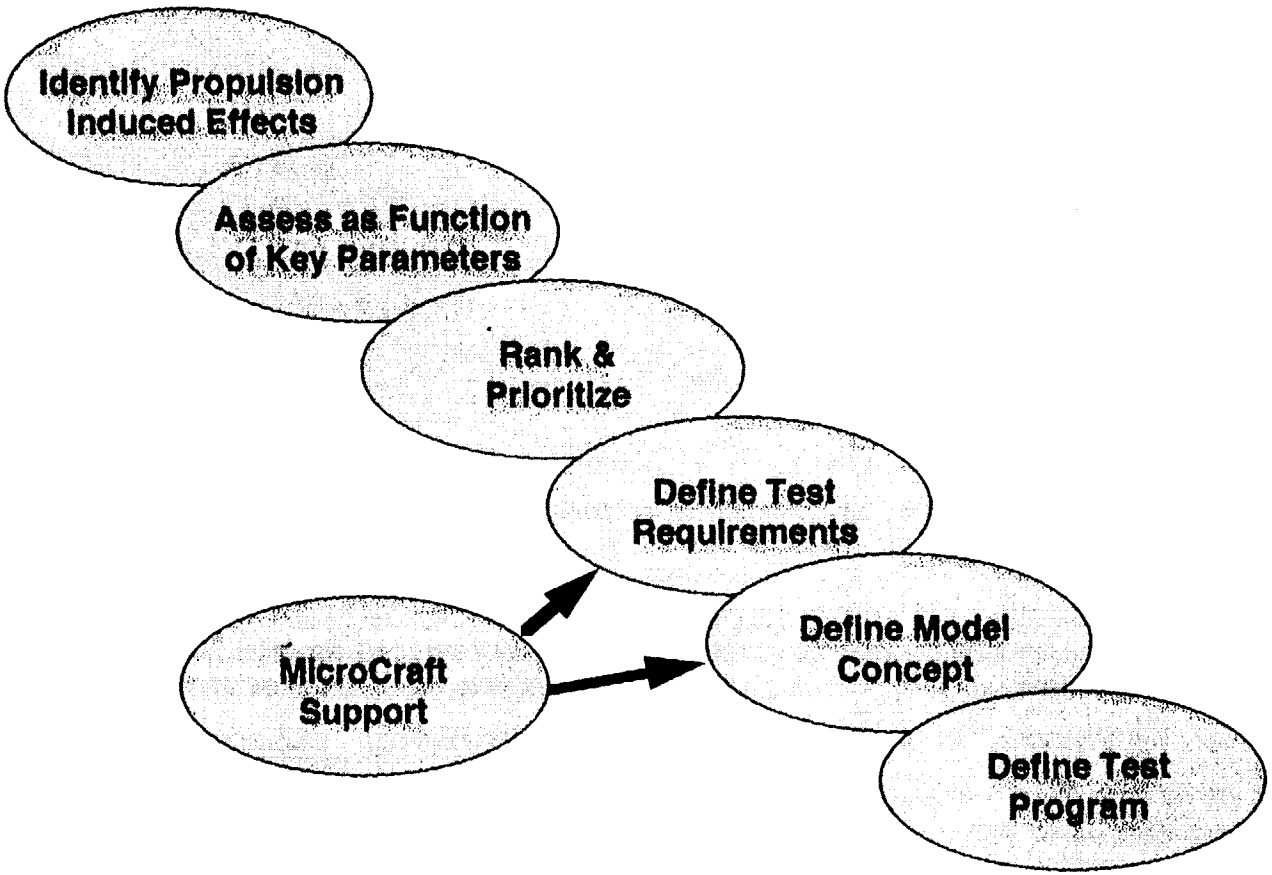

The group has been in the program definition stage for the past 10 months. The approach used was to get a large group of technical people together to define the objectives of this milestone and define the PIE technology items. These people came form the different disciplines needed to work on this task. They came from propulsion, inlet, nozzle, configuration aerodynamics, and technology integration. The group identified these PIE technology items, assessed them as a function of key parameters, ranked and prioritized them. The group chose the highest priority items for the test program.

The group then downsized to a working group level composed of Joe Koncsek from the Inlet team, Hoyt Wallace from the Nozzle team, Chet Nelson from the Technology Integration team, Fran Capone and Dan Bencze from the CA team, MicroCraft, and Mina Cappuccio and Mark Won. The group defined the test requirements and the model concept. MicroCraft took these requirements and did a preliminary design.

Once this was defined the working group made a presentation to CA on what the test program would look like, issues, and guidance on how to proceed.

Propulsion Induced Effects Technology Objectives

- Inlet Flow
  - * Inlet Spillage Drag
  - * Spillage Interference Drag
  - * Impact of Inlet/Diverter Design
  - * Ram Drag
  - * Inlet Flow Field
  - * Inlet Unstart
    - Δ Nac/Nac Interactions
    - Δ Overall F & M's
- Nacelle Flows
  - * Bleed/Bypass Drag (Isolated)
  - * Bleed/Bypass Interference Drag
- Nozzle Flows
  - * Isolated Nozzle Drag
  - * Installed Boattail Drag
  - * Impact of Nozzle Design
  - * Plume Effects
    - Δ Afterbody Interactions
    - Δ Tail Interactions
  - * Climb Ejector Interactions
  - * Inlet/Nozzle Flow Field Interactions

The technology items identified by the larger group were group in terms of inlet, nozzle, and nacelle flow. Under inlet flow came items associated with the installation of the inlet on the aircraft. They include inlet spillage drag, spillage interference drag, impact of inlet/diverter design, ram drag, inlet flow field, and inlet unstart. Under nozzle flows came items associated with the installation of the nozzle on the aircraft. They included isolated nozzle boattail drag, installed nozzle boattail drag, impact of nozzle design, plume effects on the afterbody and tail, climb/ejector interactions, and inlet/nozzle flow field interactions. Under nacelle flows came items associated with the overall installation of the nacelle. They include bleed & bypass drag (isolated) and bleed & bypass interference drag.

Technology Objective Selection Criteria

Criteria	Assessment
• Airplane * Performance Impact * S&C Inpact	0 = N/A, 1 = Low, 5 = High
• Flight Regime * Transonic (0.6 - 1.5) * Supersonic (>1.5) * Off-Design * Rn Issue	0 = N/A, 1 = Low, 5 = High
• Impact * Certification Requirements * Inlet, Nozzle Selection * ΔTOGW	Yes / No
• Approach * Exp Data BaseRequired * Exp & CFD Assessment * CFD Validation Required * Test Technique Development	√ = Priority R = Req'd to Satisfy Priority
• Risk	0 = N/A, 1 = Low, 5 = High
• Priority	(Perf+S&C) * Risk

The criteria used to select which items had higher priority than others, was based on many things. The criteria were airplane: performance and stability & control impacts; flight regime; impact on certification requirements, inlet/nozzle selection, and take off gross weight. The assessment for each of these categories were set by 1=low and 5=high. Zero meant not applicable. The impact was either a yes or a no. Once this was done, the group had to decide what was the risk of this technology item if it wasn't worked on, where 1=low and 5=high. Then the priority was established by adding the performance and S&C rank and multiplying it to the risk. Once this was done, the ranking of the priorities was established.

Propulsion Induced Effects Technology Items

		Airplane		Flight Regime				Program Impact			Approach				Milestone 4-14			
#	Technical Issue	Perf. Impact	S&C Impact	Tran-sonic M > 0.6 M < 1.4	Super-sonic M > 1.6	Off Design	RN Issue	Cert. Req.	Inlet, Nozzle, Diverter Selection	ΔTOGW	Exp. Data Base Req'd	Exp't & CFD Ass't	CFD Valid. Req'd	Test Tech. Dev.	Risk	Priority	Rank	Overall Rank
	Inlet Flows																	
1	Inlet Spillage (Isolated)	5	2	5	1	3	1	0	Y	Y		√			1	7	13	
2	Spillage Interference	5	4	5	1	3	2	0	Y	Y	R	√		R	5	45	2	2
3	Impact of Inlet/Diverter Design	5	1	2	5	1	3	0	Y	Y	R	√			4	24	6	2
4	Ram Drag	4	1	3	5	3	1	0	Y	Y		√			2	10	12	
5	Inlet Flow Field	5	2	1	5	5	3	Y	Y	Y		√			2	14	10	
	Inlet Unstart																	
6	Nacelle/Nacelle Inter.	2	5	0	5	5	3	Y	Y	Y	R	√			5	35	3	3
7	Overall F&M's	2	5	0	5	5	3	Y	Y	Y	R	√			5	35	3	3
	Nozzle Flows																	
8	Isolated Nozzle Drag	5	1	5	3	1	4	N	Y	Y		√			2	12	11	
9	Installed Boattail Drag	5	2	5	3	1	4	N	Y	Y	R		√		4	28	5	5
10	Impact of Nozzle Design	5	2	5	3	1	4	N	Y	Y	R		√		4	28	5	5
	Plume Effects																	
11	Boattail	3	1	4	2	2	4	N	Y	Y	R		√		4	16	9	5
12	Airplane Afterbody Inter.	3	4	3	4	4	1	N	N	Y	√		R		3	21	7	6
13	Tail Interactions	1	5	5	5	5	2	Y	N	N	√		R		4	24	6	6
14	Climb Ejector Inter.	5	1	5	0	0	3	Y	N	Y		√			5	30	4	4
15	Inlet/Nozzle Flow Field Inter.	2	2	2	2	2	2	N	N	Y		√			5	20	8	
	Nacelle Flows																	
16	Bleed/Bypass (Isolated)	5	2	5	5	2	3	N	N	Y	R		√	R	5	35	3.5	1
17	Bleed/Bypass Interference	5	5	5	5	5	3	N	N	Y	R		√	R	5	50	1	1

Not Applicable or Not an Issue = 0

Airplane and Flight Regime Impact: Low = 1 and High = 5

Program Impact: Y or N

√ = Priority

R = Required

Risk = What is the Risk Now? Low = 1 and High = 5

Priority = Impact of (Perf+ S&C) * Risk

Bleed and bypass interference was ranked priority one. Inlet spillage was ranked second., followed by inlet unstart, climb/ejector interactions, nozzle boattail, and afterbody and tail interactions.

Summary of Test Objectives Presented to CA

Transonic				Supersonic			
	Perf	S&C	CFD Val		Perf	S&C	CFD Val
Inlet Spillage Drag	X		X	Inlet Bleed & Bypass Interference	X	X	X
Installed Boattail Drag	X		X	Plume/Tail Interactions		X	X
Plume/Tail Interactions		X	X				

Of these items the group decided on inlet bleed & bypass interference, inlet spillage, and installed nozzle boattail as PIE items to work on under this test program. Transonically the issues are inlet spillage, installed nozzle boattail, and plume/tail interactions. Supersonically the issues are inlet bleed & bypass interference, and plume/tail interactions. The priority for each item is CFD validation and experimental data is required to meet this objective. In the case of bleed & bypass interference test technique is also a requirement to meet the objective.

Test and model objectives were defined based on these items. MicroCraft then went off with the group's guidance on the preliminary design.

Outcome of Review to CA

- Concentrate on Transonic Test
  - * Spillage
  - * Jet Effects
- Incorporate Supersonic Testing Capablities
  - * Bypass
  - * Jet Effects
- Remove Bleed from the PIE Model/Test Program
  - * MicroCraft directed to look at designing bypass doors to be interchangeable with a generic bleed system for future test
  - * Generic Bleed Test Program

A review of what the PIE team had decided on for the test program and the preliminary design by MicroCraft was presented to the CA team. The outcome of the review was to concentrate on the transonic testing of inlet spillage and jet effects on the nozzle boattail and tail interactions. CA said to incorporate the supersonic testing in the model design, which include bypass and jet effects on the nozzle boattail and tail interactions. Bleed was too large of a risk to take in the test program, so it was eliminated. But, CA asked that bleed be incorporated into a generic test program. MicroCraft was asked to make the bypass doors interchangeable to add bleed at a later date.

Current Summary of Test Objectives

Transonic				Supersonic			
	Perf	S&C	CFD Val		Perf	S&C	CFD Val
Inlet Spillage Drag	X	X	X	Inlet Bypass Interference	X	X	X
Installed Nozzle Boattail Drag	X		X	Plume/Tail Interactions		X	X
Plume/Tail Interactions		X	X				

So now these are the current test objectives. MicroCraft has been asked to remove the bleed design from the model.

Test Requirements

- Focus on Performance, Selected S&C Requirements
- Configuration Fidelity
  - * TCA Configuration
- Uncertainty
  - * C_D Transonic $\pm$1.5 cts, Incremental F&M's
  - * C_D Supersonic $\pm$0.5 cts, Incremental F&M's
  - * Mass Flow 0.25%
- Mach Regime

Req'd	Highly Preferred
0.9 < M < 1.2	0.6 < M < 2.4
M=2.4	

- α/β

Req'd	Highly Preferred
Cruise α's	$-4° < \alpha < 8°$
$\beta = 0°$	$-4° < \beta < 4°$

The test requirements that MicroCraft and the group are using as a guide for the model design and test program are to focus on performance, and selected S&C requirements. The configuration will be the baseline TCA, which includes nacelles with an axisymmetric inlet and a 2-D nozzle. The model is full span with an extended cylindrical aft body that incorporates vertical and horizontal tails. The wing has leading and trailing edge flaps for transonic conditions. The instrumentation needs to meet uncertainty levels of ±0.5 drag count supersonically, ±1.5 drag counts transonically, and mass flow accuracy of 0.25%. It is a requirement to get data at a Mach number between 0.9 and 1.2, transonically, and Mach=2.4, supersonically. Cruise angle-of-attack is most important at a side slip angle of 0 degrees.

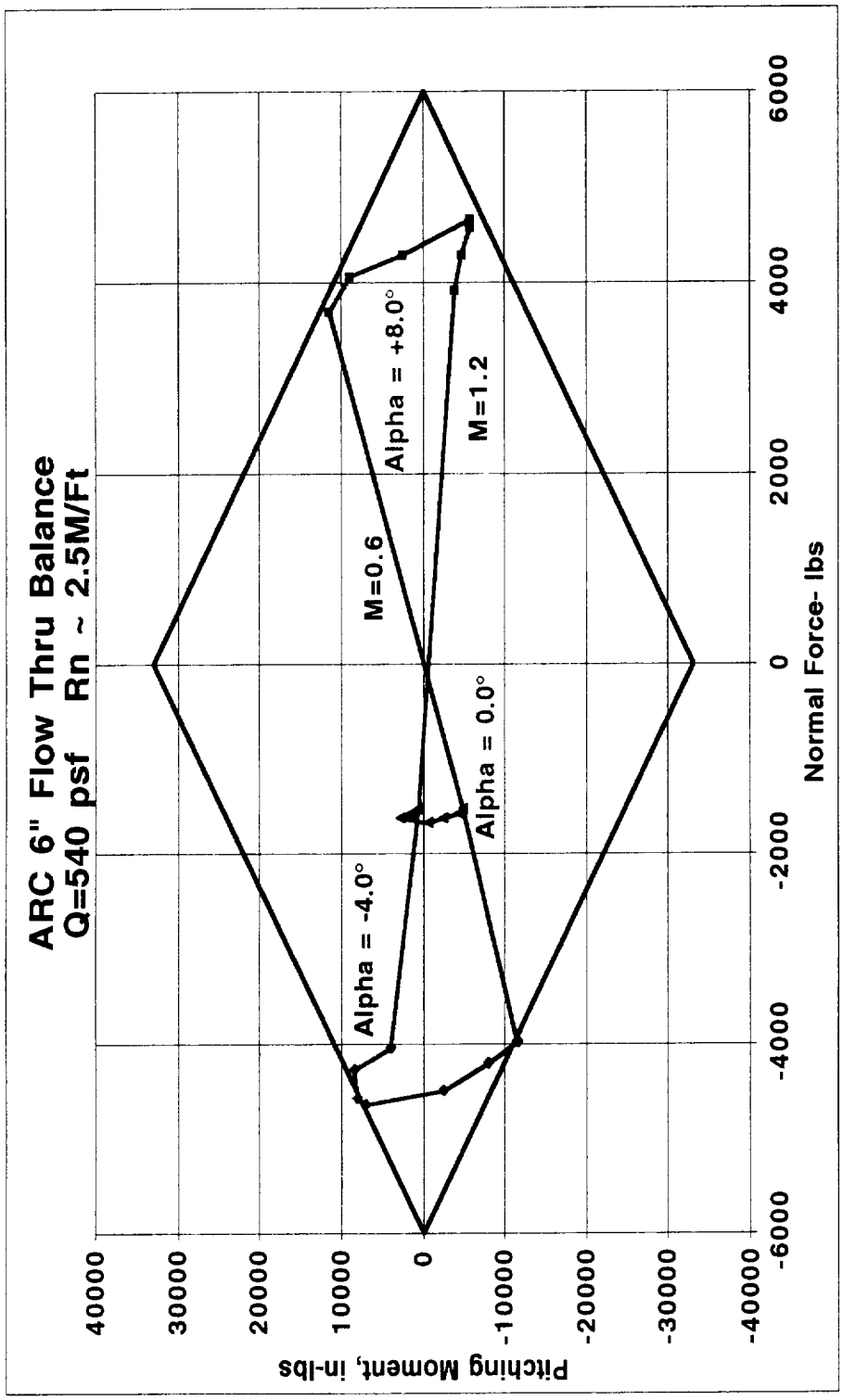
ARC 6" Flow Thru Balance
Q=540 psf Rn ~ 2.5M/Ft
Pitching Moment, in-lbs
Normal Force- lbs
40000
30000
20000
10000
0
-10000
-20000
-30000
-40000
6000
4000
2000
0
-2000
-4000
-6000
Alpha = +8.0°
Alpha = 0.0°
Alpha = -4.0°
M=0.6
M=1.2

The balance of choice at this time is the NASA Ames 6 inch diameter flow through balance. Based on the TCA performance data acquired to date, the range of data to be measured is within the balance rhombus. If data is only required at the cruise angle of attack, it would be preferable to redesign and fabricate a new balance where data could be measured over the full range of the balance to get the best data possible for PIE increments.

Preliminary Model Design

- Largest Size Permissable Incorporating Operating Propulsive Elements
- 5.7% Scale
  - * length=18.58 ft, span=7.48 ft
  - * inlet diameter=3.9 in
- Full Span, All Metric Configuration
- 4 Nacelles - Flowing Inlets and Powered Nozzles
- Tails (Aft Empennage with a Straight Sting Entry)
- On Board Model Air Delivery System to Nacelles
- Multiple Nacelle Configurations Derived from Test Technique
  - * Aero Reference Flow Through
  - * Inlet - Bypass and Spike
  - * Jet Effects - Reference and Operating Nozzles

Due to the instrumentation and airflow needed to simulate inlet and nozzle internal flow, the model was scaled at 5.7% to be able to fit in the Ames 11x11 transonic wind tunnel. The model scale is such that the data that comes out of the test would be incremental and not absolute, due to shock reflections. This scale forces the model to be tested in either the Lewis 10x10 or AEDC 16S supersonically. An alternative to the Ames 11x11 is AEDC 16T. The model is a full span model, all metric, with 4 flowing inlets and powered nozzles. Vertical and horizontal tails would be modeled on an extended cylindrical aft body with a straight sting entry. There would be leading and trailing edge flaps transonically. There would be an on board model air delivery system to the nacelles. The type of nacelles to be tested on the model are an aerodynamic reference nacelle that is flow through, an inlet nacelle that includes bypass and centerbody spike for inlet spillage, and jet effects that includes reference and operating nozzles.

Model Components

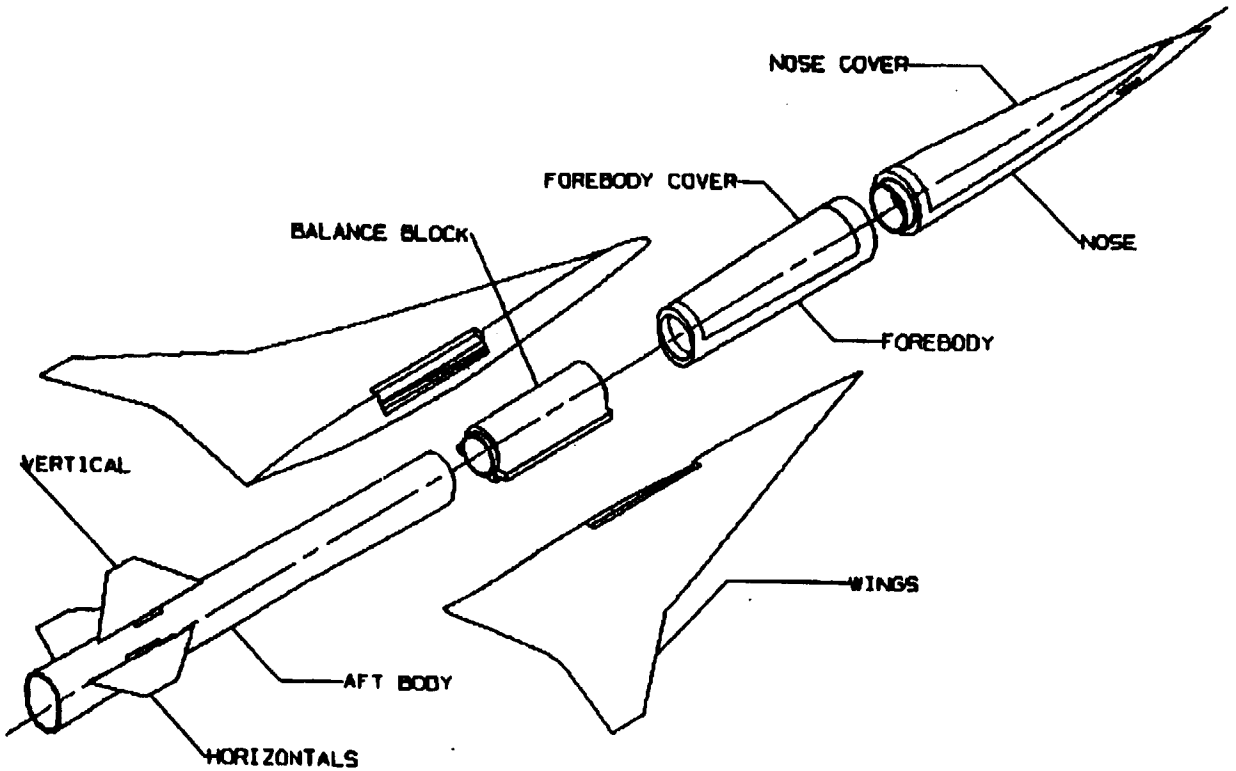

Model components would include a wing body made entirely of aluminum except for the balance block. The fuselage can hold up to 100 ESP psi modules.

Flow Through Nacelle

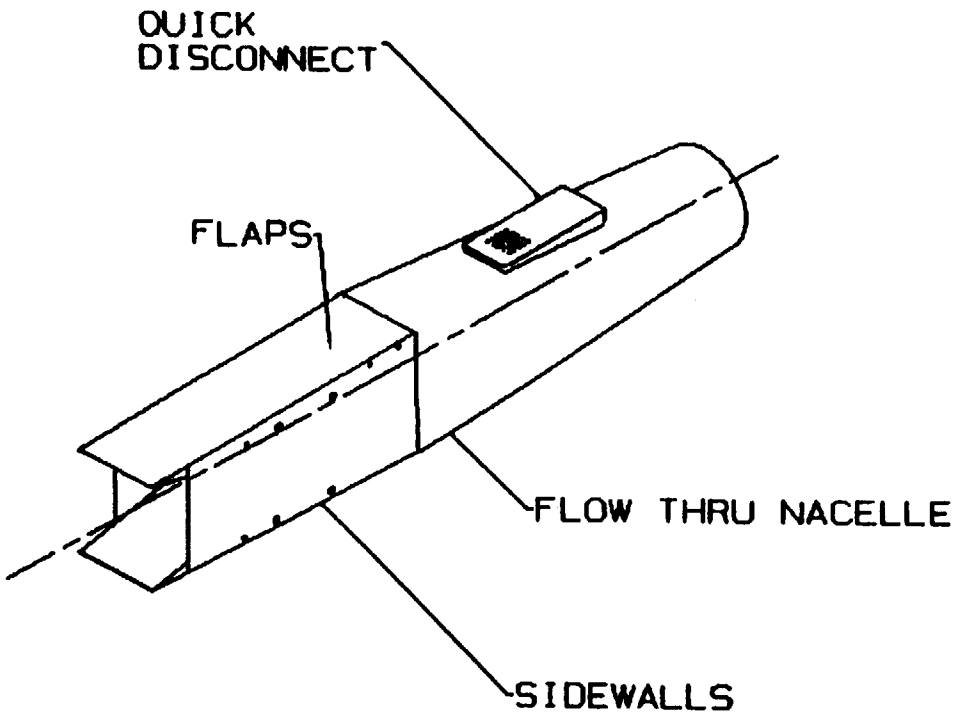

The aerodynamic flow through nacelles would model the actual nozzle flaps and side walls. They would have quick disconnects at the diverter interface to the wing so pressure instrumentation would be easy to change with nacelle configuration changes. The internal duct would have a constant area, from inlet to exhaust, as the aerodynamic performance TCA models that have been tested to date.

Inlet Nacelle

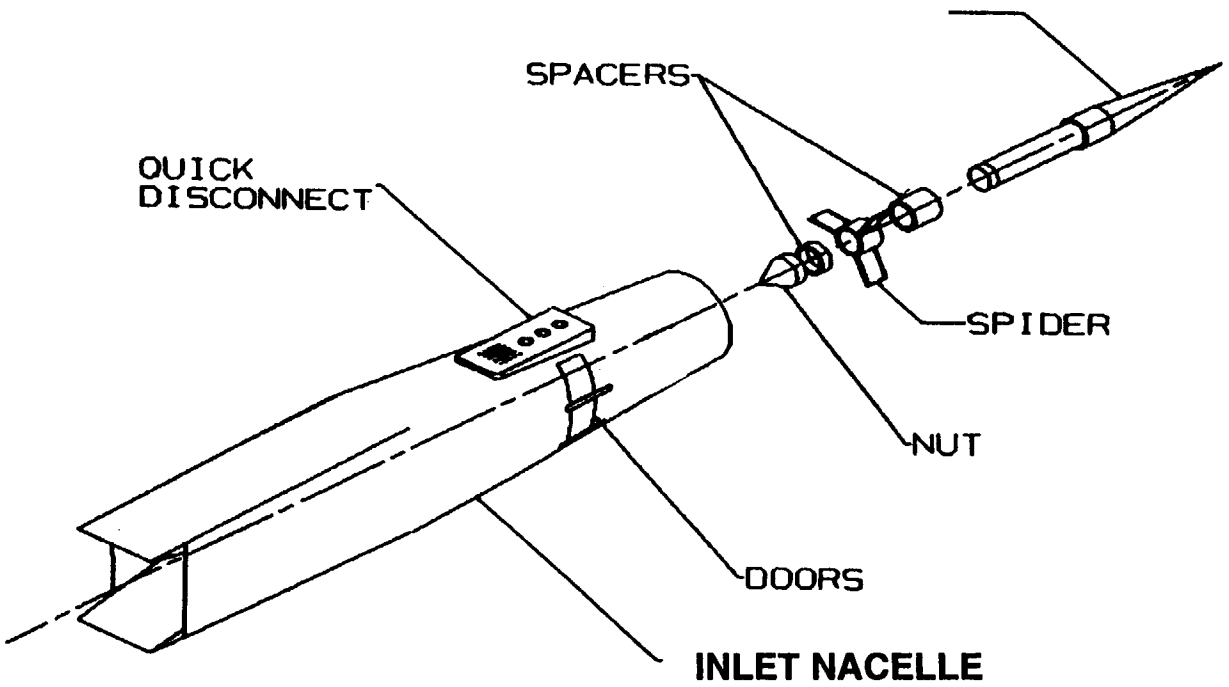

The inlet nacelle would have the same quick disconnects. The internal duct would be modified so that a centerbody spike could be installed to model inlet spillage. Basically 3 spike positions would be built: Mach < 1.65, Mach=2 and 2.4. A spacer would adjust the position of the spike. In addition to the inlet centerbody, bypass doors would be incorporated into the inlet model. These doors can be set to the different positions necessary depending on the Mach number tested at.

Propulsion Nacelle

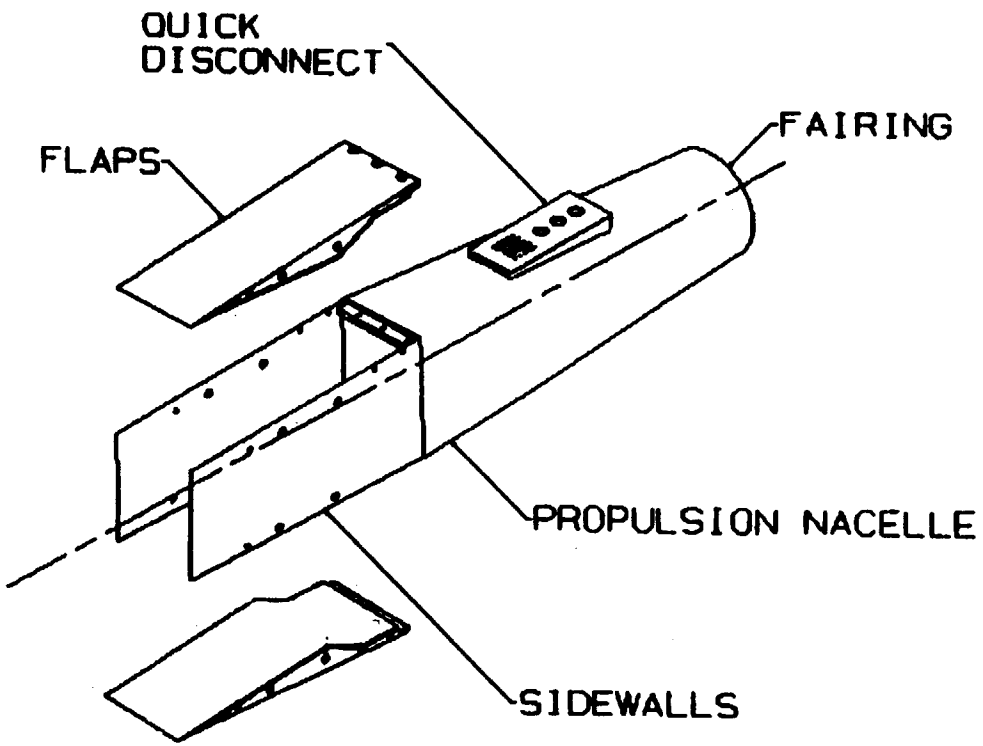

The propulsion nacelle is the one that would be used for the jet effects part of the test. This nacelle would have interchangeable nozzle parts, quick disconnects, and an inlet fairing. The nozzle team is very interested in this test program to get installed nozzle boattail drag, and to study side wall effects. They plan to participate and fund the nozzle testing on this model.

Model Air Delivery System

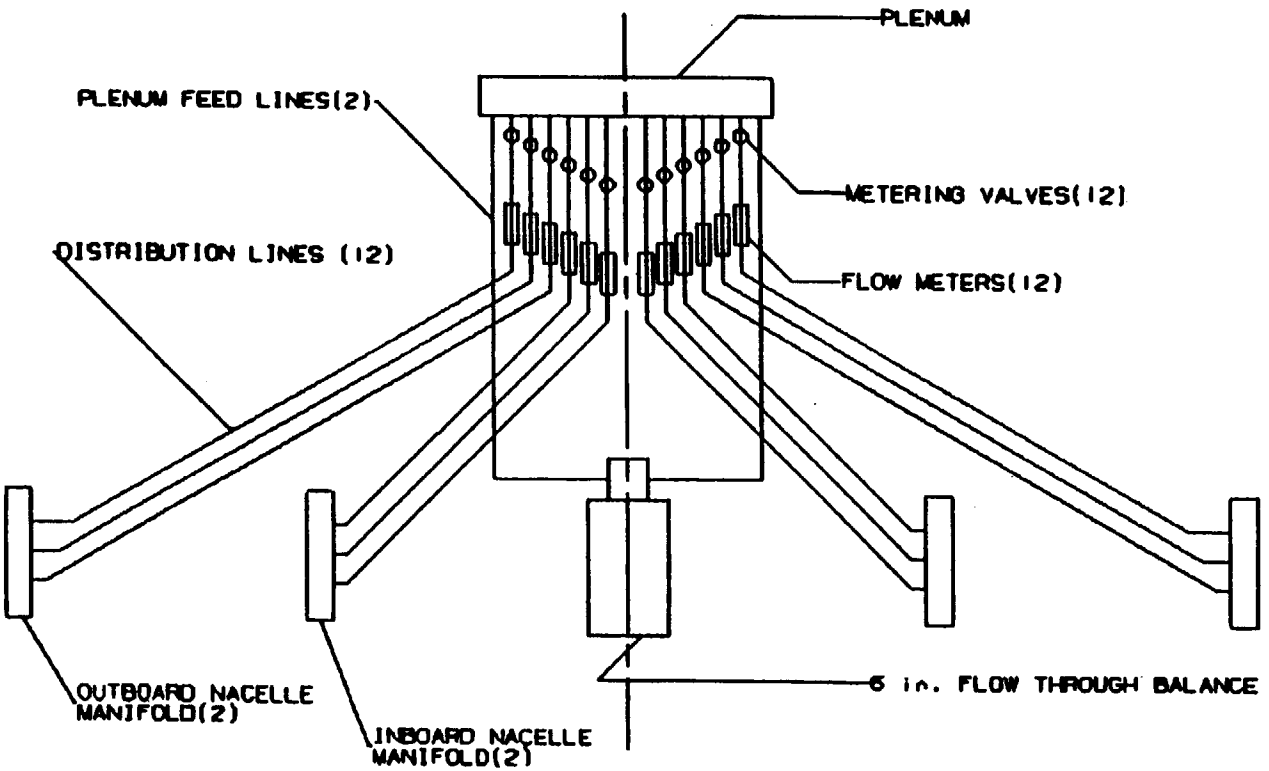

The model air delivery system will take on board high pressure air through the balance center, go through flow meters and be adjusted by metering valves. This schematic shows 3 lines being fed to each nacelle. This would be correct if we were going to be modeling bleed in addition to the bypass doors and nozzle. since bleed has been eliminated, only one line needs to be fed to each nacelle. One line per nacelles would be used to supply air through either the bypass doors or nozzle.

Nacelle Configurations

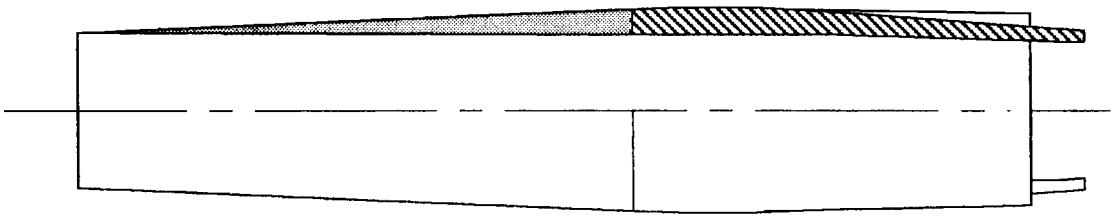

Aero Reference Nacelle

The nacelle configurations that need to be tested are the aerodynamic reference flow through nacelle. As described earlier, this nacelle would be similar to what gets tested on the aerodynamic performance TCA models.

Inlet Spillage and Bypass Nacelles

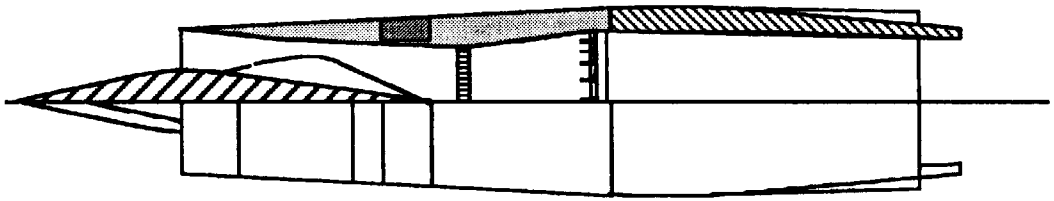

Inlet Reference Nacelle

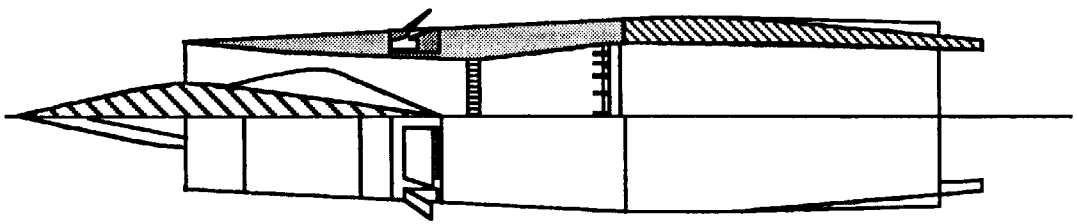

Bypass Simulation Nacelle

The inlet nacelles would include an inlet spillage configuration and an inlet spillage and bypass door configuration. In both cases, a choke plate would be installed down stream to control the mass flow through the nacelle. Total pressure rakes and static pressures would be used for measurements to compute the mass flow through the nacelle. Each nacelle would have to be calibrated in a facility outside of the wind tunnel to measure the internal drag for making corrections to the wind tunnel data.

Nozzle Boattail Nacelles

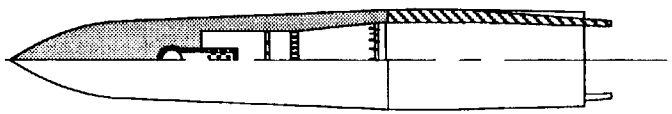

Nozzle Reference
Nacelle

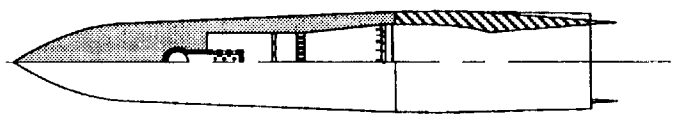

Transonic Reference
& Operating Nacelle

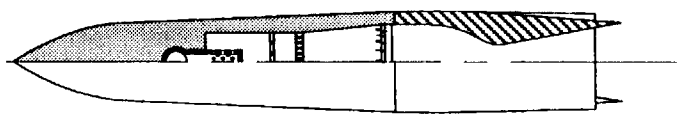

Supersonic Reference
& Operating Nacelle

The propulsion or nozzle boattail nacelles are made up of a reference nacelle to be able to increment off the aerodynamic reference flow through nacelle, a transonic and supersonic reference nacelle., and operating nacelles transonically and supersonically. In all cases, choke plates are need to get the correct nozzle pressure ratios desired. Total and static pressure would also be measured. These nozzles would need to be calibrated in a facility prior to the wind tunnel test.

Number of Nacelle Types

- Transonic
  - * Inlet Flows
    - Δ Aero Ref
    - Δ W/Center Body, 4 MFR's
  - * Nozzle Flows
    - Δ Powered Aero Ref
    - Δ 4 Operating Nozzle Shapes
- Total Transonic Nacelle Types = 10

- Supersonic
  - * Inlet Flows
    - Δ Aero Ref (Sames as Transonic Nacelle)
    - Δ 3 Centerbody Positions
    - Δ Bypass
  - * Nozzle Flows
    - Δ Powered Aero Ref
    - Δ 2 Operating Nozzle Shapes
- Total Nacelle Supersonic Types = 8

Total Number Nacelles to be Fab'd, Calibrated, & Tested = (10 + 8 -1) x 4 = 68

There would be a total of 68 nacelles that would need to be fabricated, calibrated, and tested. The table describes all of the nacelles that would have to be tested. The inlet spillage nacelle would have to be tested at 4 mass flow ratios transonically. 4 operating nozzles shapes transonically would also have to be tested. In total 10 types of nacelles would be tested transonically.

Supersonically, the inlet nacelles would include the aerodynamic reference, 3 inlet spike positions (M<1.65, M=2, M=2.4), and bypass doors. The nozzle nacelles would include a powered reference and 2 operating nozzle shapes. It turns out the supersonic nozzle shape gets tested both transonically and supersonically. This is why the total is subtracted by 1.

Issues

- Magnitude of Propulsion Induce Effects
- Major Calibration Effort Prior to Wind Tunnel Test
- Attainable Accuracies with Existing Instrumentation & Calibration Methods
- Balance Adequacy & Availability
- Configuration fidelity
  - * CFD Validation vs TCA Data Dase vs Test Technique Development
- Cost & Phasing of Funds
- Schedule

The issues for this kind of a test program are magnitude of PIE to be measured. This is one of the reasons bleed was removed from the list of objectives. Bleed is such a big unknown. Currently Northrop-Grumman is contracted under Boeing to look at this problem using CFD. The size of these holes are so small, that it might not be possible to model them at the wind tunnel scale talked about here.

There is a major calibration effort prior to the wind tunnel test. Without it , the corrections to subtract internal drag cannot be made. The wind tunnel test is anticlimactic compared to the calibration effort.

Attaining accuracy's with existing instrumentation and calibration methods will be a challenge. We need to make sure the correct instrumentation is chosen and care is taken in attaining the data to be able to measure increments due to these PIE objectives of the test program.

There is a concern that the balance is adequate and has the accuracy levels needed. We are looking into other existing balances and building a new one or two.

Configuration fidelity is also an issue. This data is going to be used in validating CFD to assess propulsion induced effects. At the same time, test techniques will be developed. CFD work needs to done in conjunction with the test program, so that the model tested can be modeled in CFD.

The cost and phasing of funds for this project are huge and daunting. The funds need to be spread out over the phasing of the project efficiently, as shown in the following charts.

Schedule

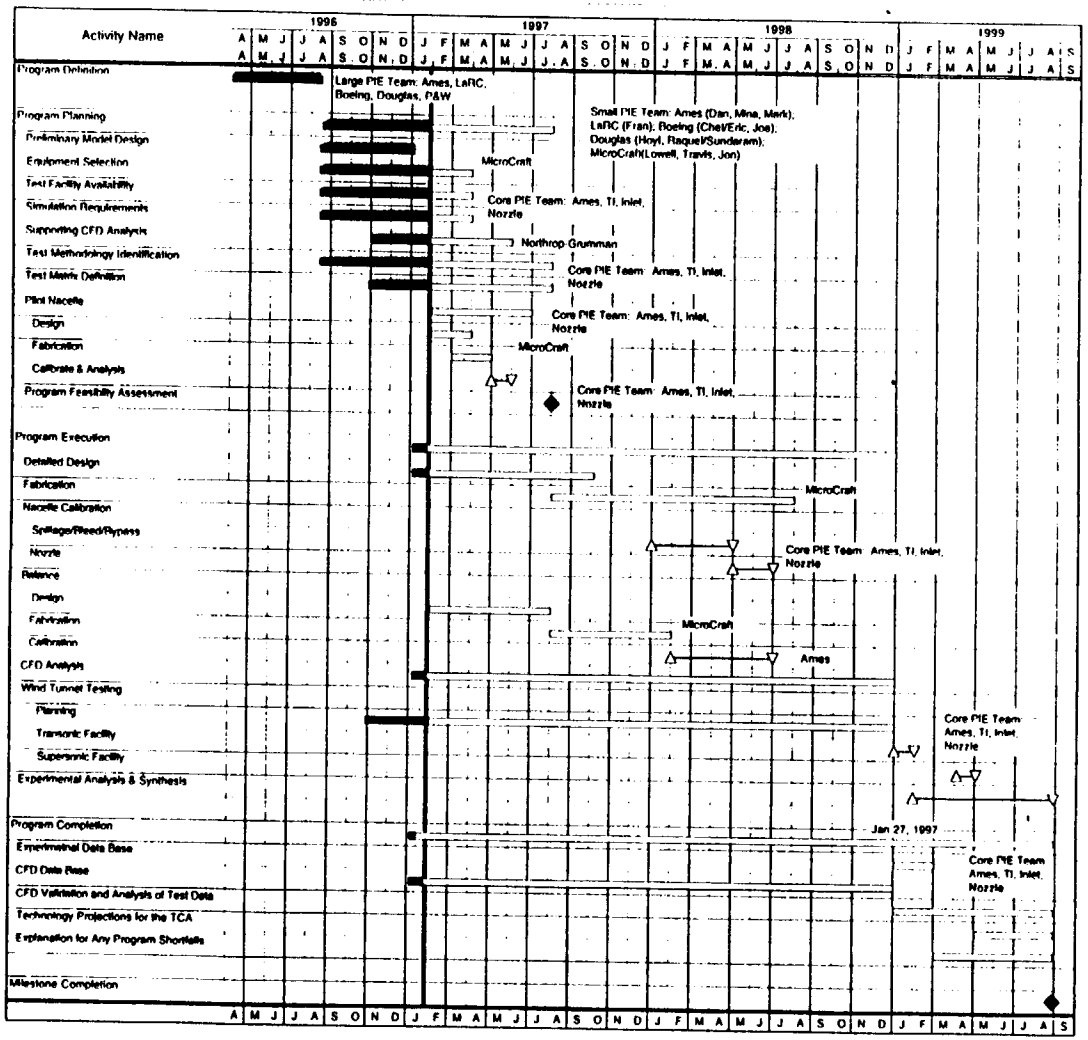
Activity Name
1996
1997
1998
1999
Program Definition
Program Planning
Preliminary Model Design
Equipment Selection
Test Facility Availability
Simulation Requirements
Supporting CFD Analysis
Test Methodology Identification
Test Matrix Definition
Pilot Nacelle
Design
Fabrication
Calibrate & Analysis
Program Feasibility Assessment
Program Execution
Detailed Design
Fabrication
Nacelle Calibration
Spillage/Bleed/Bypass
Nozzle
Balance
Design
Fabrication
Calibration
CFD Analysis
Wind Tunnel Testing
Planning
Transonic Facility
Supersonic Facility
Experimental Analysis & Synthesis
Program Completion
Experimental Data Base
CFD Data Base
CFD Validation and Analysis of Test Data
Technology Projections for the TCA
Explanation for Any Program Shortfalls
Milestone Completion
Large PIE Team: Ames, LaRC, Boeing, Douglas, P&W
Small PIE Team: Ames (Dan, Mina, Mark); LaRC (Fran); Boeing (Chet/Eric, Joe); Douglas (Hoyt, Raquel/Sunderam); MicroCraft(Lowell, Travis, Jon)
MicroCraft
Core PIE Team: Ames, TI, Inlet, Nozzle
Northrop Grumman
Core PIE Team: Ames, TI, Inlet, Nozzle
Core PIE Team: Ames, TI, Inlet, Nozzle
MicroCraft
Core PIE Team: Ames, TI, Inlet, Nozzle
MicroCraft
Core PIE Team: Ames, TI, Inlet, Nozzle
MicroCraft
Ames
Core PIE Team: Ames, TI, Inlet, Nozzle
Jan 27, 1997
Core PIE Team: Ames, TI, Inlet, Nozzle

The schedule put together for this project shows some critical milestones. One is the program feasibility assessment. This is where the group decides if the nacelles are scaled and designed properly to be able to model the PIE items of interest via a pilot nacelle. If successful, the pilot nacelle would be one of the four nacelles. If not, changes would be made for the 4 nacelles to be built. After this milestone the model will be fabricated, nacelles will be calibrated, balances will be built and calibrated, and wind tunnel tests would occur late in 1998 and in the beginning of 1999. The milestone completion date is scheduled for end of August 1999.

Cost Estimate & Phasing

	QTY	Unit Cost	Total Cost	FY 97	FY 98	FY 99	FY 00
Industry Planning Support	2 Mys	200	400	100	200	100	
Pilot Nacelle	1	150	150	150			
Model Design & Fab			1750	250	1500		
Balance Fab & Calibration			250	50	200		
Nacelle Calibrations	68 Nac's	6	408		408		
Industry Eng'g Test Support	1 My		200			200	
Model & Inst. Support	8	100	800		300	500	
		Total	3958	550	2608	800	

In addition to the 1.75 million dollars the model will cost, there would be additional costs for industry planning support, pilot nacelle, balance fabrication and calibration, nacelle calibrations, industry engineering test support, and model and instrumentation test support. The total cost would be at 4 million.

Facilities

- Transonic
  - * Estimated Requirement - 90 shifts (18 Shift Weeks)
  - * ARC - 11' x 11'
    - Δ Available in FY 99
    - Δ Level of Operations Uncertain
  - * AEDC 16'-T
    - Δ Available
    - Δ Estimated Cost - ~ $3.3M
- Supersonic
  - * Estimated Requirement - 45 shifts (9 Shift Weeks)
  - * LeRC - 10' x 10'
    - Δ Potential Conflict with HSR Inlet Testing
  - * AEDC 16'-S
    - Δ Available
    - Δ Estimated Cost - ~ $3.0M

Not included in this cost, is tunnel entry cost. If the NASA Ames 11x11 foot Transonic Wind Tunnel does not come up in time for the test, testing could be done at AEDC 16T at an estimated cost of 3.3 million. Supersonic testing could be done at 16S at an estimated cost of 3 million, if the NASA Lewis 10x10 foot Supersonic Wind Tunnel is not available. Test location is all an unknown right now. The plan is to do the transonic testing in the Ames 11x11, since this is what CA wants the PIE group to do.

What's Next?

- Meeting in Seattle on Feb. 19
  - * Boeing Calibration Facility
  - * Outcome of CA Review
  - * Work out details between MicroCraft, Inlet, and Nozzle Reps
- Detail Test Plans
- Detailed Design
- Fabricate Pilot Nacelle
- Fabricate Wing-Body

So, what is next? A meeting was held in Seattle between the group on February 19. The group was informed of the outcome of the CA review. The group went to check out the Boeing Calibration Facility for the nacelle calibrations. Individual members were going to work out details with MicroCraft on the next step of the model design.

Details of the test plan will be worked on, as well as detailed designs by MicroCraft. MicroCraft will begin to fabricate the pilot nacelle and the wing body as soon as drawings are approved.

Program Evolution

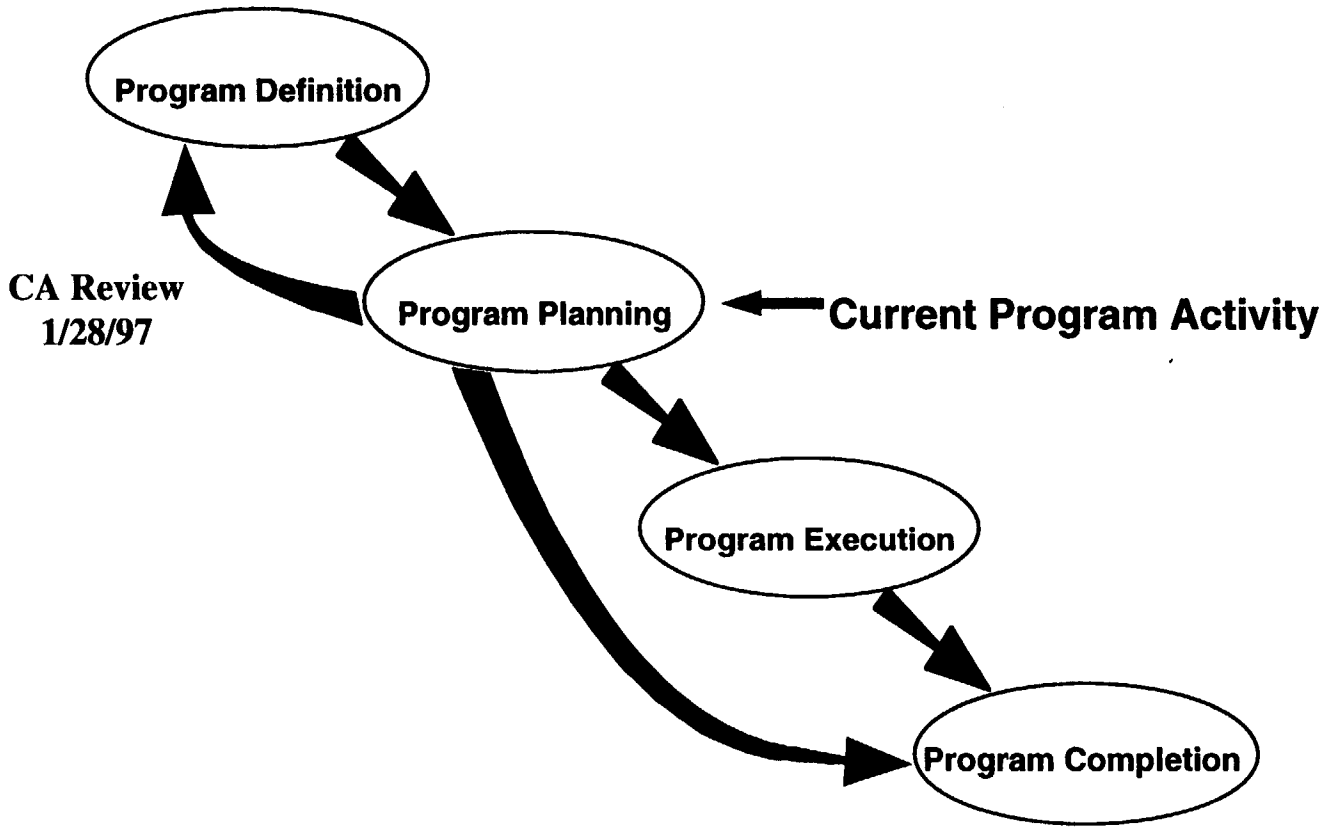

The program will evolve from the program planning stage, working it's way to program execution and completion over the next 2 years.

Program Planning

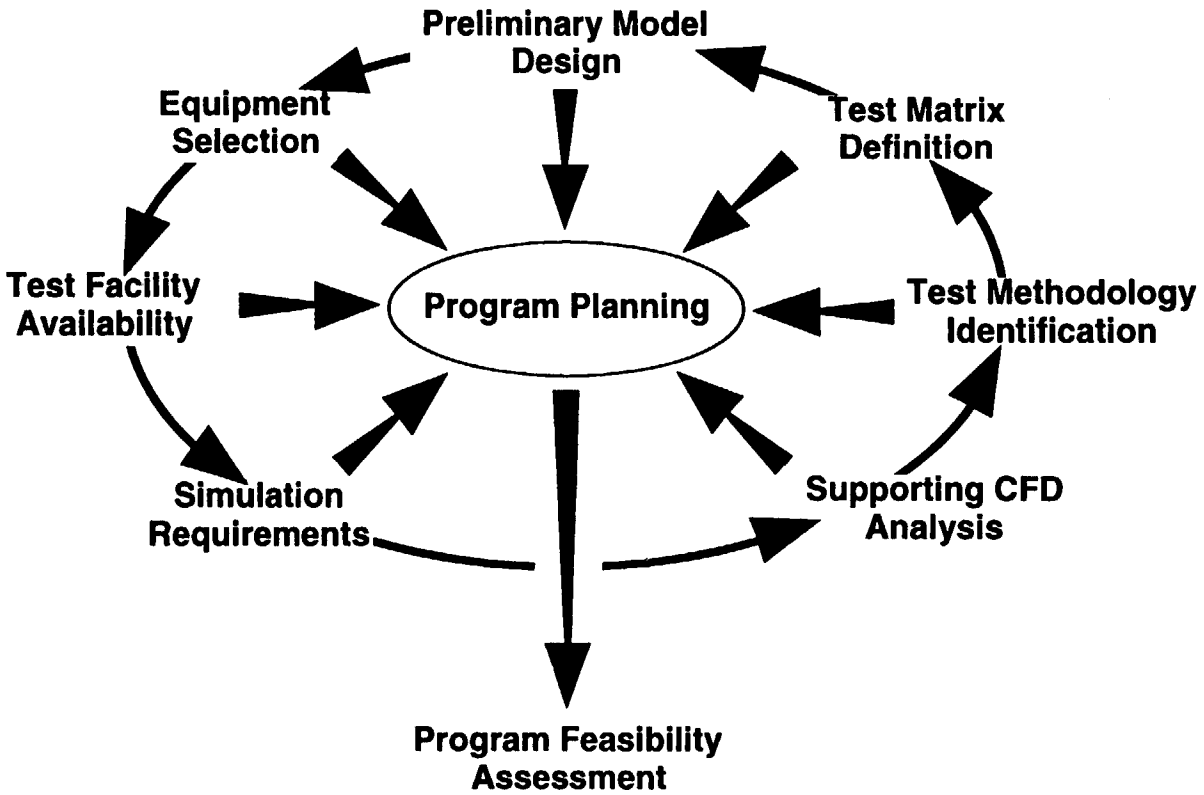

The program planning includes the preliminary model design which is done, putting together a test matrix, selecting equipment, test facilities, identifying test methodologies, supporting CFD and simulation requirement. All these items will feed into the program feasibility assessment along with the output of the pilot nacelle calibration.

This program is large in scope and effort. It will need dedicated people and support from upper management to make it a successful project within HSR.

Inlet Spillage Drag Predictions using the AIRPLANE Code

Scott D. Thomas, Sterling Software, Inc.

Mark A. Won, NASA Ames Research Center

Susan E. Cliff, NASA Ames Research Center

1997 HSR Aerodynamic Performance Workshop

February 25-27, 1997

NASA Langley Reid Conference Center

Mark set up the nacelle geometry and plug positions, Susan generated the mesh, and Susan and Scott ran the flow solver on the SP2 Metacenter and analyzed the results.

Our goal was to apply AIRPLANE to four transonic spill cases and then report the results.

Outline of the talk (no slide for the outline):

* Quick review of the AIRPLANE code.
* One flow condition, four plug positions.
* Wing-body-nacelle-centerbody-plug geometries.
* Mach/vector and pressure contours.
* Oscillatory nature of the solutions.
* Plots of lift and drag as functions of the mass flow ratio.

Inlet Spillage Drag Predictions using the AIRPLANE Code

Scott D. Thomas, Sterling Software, Inc.

Mark A. Won, NASA Ames Research Center

Susan E. Cliff, NASA Ames Research Center

February 25-27, 1997

AIRPLANE

AIRPLANE (Jameson/Baker) is a steady inviscid unstructured Euler flow solver. It has been validated on many HSR geometries. It is implemented as MESHPLANE, an unstructured mesh generator, and FLOPLANE, an iterative flow solver. The surface description from an Intergraph CAD system goes into MESHPLANE as collections of polygonal curves to generate the 3D mesh. The flow solver uses a multistage time stepping scheme with residual averaging to approach steady state, but it is not time accurate. The flow solver was ported from Cray to IBM SP2 by Wu-Sun Cheng (IBM); it could only be run on 4 CPUs at a time because of memory limitations. Meshes for the four cases had about 655,000 points in the flow field, about 3.9 million tetrahedra, about 77,500 points on the surface. The flow solver took about 23 wall seconds per iteration when using 4 CPUs. It took about eight and a half wall hours to run 1,300 iterations at a time (the queue limit is 10 hours). A revised version of FLOPLANE (Thomas) was used on up to 64 CPUs to finish up some calculations at the end. We had to turn on more communication when using more processors to eliminate noise that was contaminating the flow field; this added about 50% to the elapsed wall time per iteration when using 64 CPUs.

This study involved computing lift and drag for a wing/body/nacelle configuation at Mach 0.9 and 4 degrees pitch. Four cases were considered, corresponding to four nacelle mass flow conditions.

AIRPLANE

T. Baker, Princeton University and A. Jameson, Stanford University

MESHPLANE:

- Unstructured tetrahedral mesh
- Constrained Delaunay algorithm
- Arbitrary Complex geometries

FLOPLANE:

- Euler
- Finite volume
- Explicit Runge-Kutta time stepping
- Enthalpy damping and residual smoothing

Transonic Spillage: AIRPLANE Mesh

Wing/Body/Nacelles/Centerbodies/Plugs

The wing and body are Ref. H (orthographic view). It was convenient to treat nacelles without diverters. The nacelles were lowered a couple inches to help the mesh generator work properly. The nacelles were extended to more than twice their original lengths and flared at the back to accommodate plugs. The plugs were translated fore and aft in tandem to obtain four mass flow conditions. Plugs were used to control mass flow because FLOPLANE does not have a mass flow boundary condition feature. Fixed centerbodies were added to each inlet. The centerbodies block about 30% of each inlet area. The centerbodies and plugs are bicones with rounded middle transitions.

In this and the next picture the fuselage is red, lower wing is green, upper wing is blue. The nacelle exteriors are red and the nacelle extensions and interiors are magenta. The centerbodies are yellow and the plugs are cyan. Forces were obtained by integrating pressures only on the red, green, and blue surfaces.

The wing is fairly smooth, blunt and thick inboard, sharp and thin outboard, joined with a short ramp joining inboard and outboard portions of the wing. There are no tails on the fuselage. The outboard nacelle is placed slightly ahead of the inboard nacelle. Toe-in is evident in the front view at the top of the picture.

At zero degrees pitch you can see that both nacelles are oriented with nose-down and toe-in. When the geometry is pitched 4 degrees nose-up (not shown) the nacelle pitch and yaw angles become

	alpha	beta
inboard	0.096	1.020
outboard	-1.196	2.401

so the inboard nacelle is nose-down slightly, and outboard is nose-up with respect to the freestream velocity vector.

1610

Transonic Spillage: AIRPLANE Mesh

View of Surface from Aft

This perspective view looking forward from aft of the outboard nacelle shows the gap between the inboard nacelle and the wing. Both nacelles were disconnected from the wing. The nacelle extensions follow the lines of the original nacelles for a short distance (decreasing diameter), then they run parallel to their axes back to where they flair out at the end (flairs not shown).

Transonic Spillage
AIRPLANE Mesh

Transonic Spillage: AIRPLANE Solution

Wing and Inboard Centerbody, Nacelle, and Plug

These four pictures show final AIRPLANE solutions on vertical slices through the axis of the inboard nacelle. The four plug positions can be seen, x=15, 24, 33, and 45. The value of x is such that a plug at x=0 would close the nacelle extension. Each of the four pictures has two parts. The part on top shows the Mach number ranging from 0 to 1.2. Values off the top of the scale are all colored magenta. The bottom part shows normalized vectors colored by Mach number using the same scale. Supersonic flow at the aft plug and between the nacelle and lower wing is present in all cases. A transonic pocket is evident at the lower lip in the first three cases (low mass flow), and only the fourth one shocks at the inlet (high mass flow). The blue region under the centerbody at the x=15 plug position contains recirculating flow.

Vertical slices through the outboard nacelle (not shown) have similar features but without recirculation for the x=15 plug position.

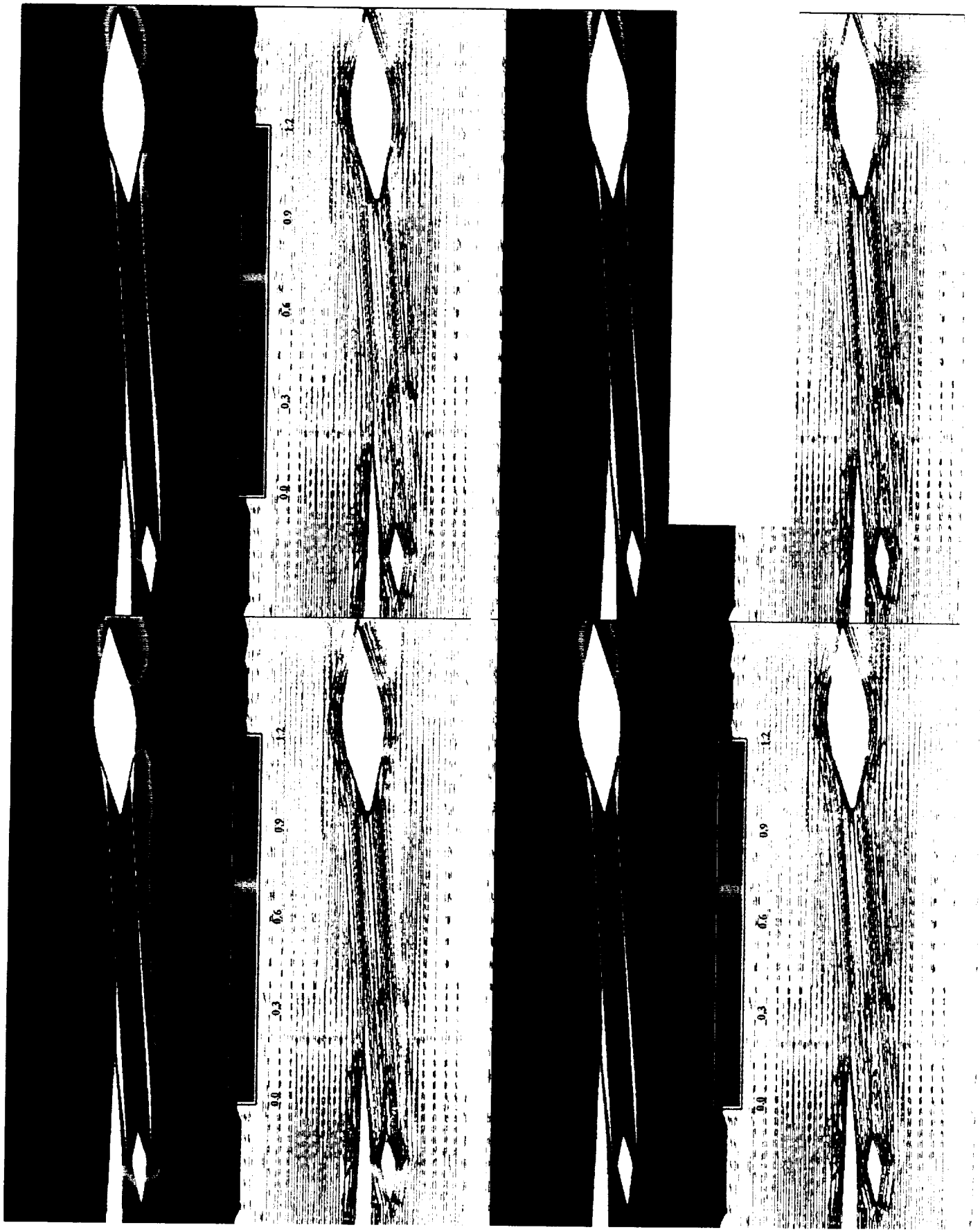
0.0
0.3
0.6
0.9
1.2

Transonic Spillage: AIRPLANE Solution

Wing and Inboard Centerbody and Nacelle

These are like the previous picture but zoomed in a little closer to the inlet. The normalized velocity vectors are colored by local Mach number with the same scale as before. This time the vectors are drawn with arrowed tips and only every tenth point is shown. Recirculating flow is evident below and aft of the centerbody in the plug position x=15 case (upper left corner). A tiny bit of low speed reverse flow can be seen in the x=45 case (lower right corner) at the upper aft end of the centerbody. There is a lot of turning in the flow field for the first three plug positions, especially near the lower lip of the inlet. Only the x=45 case shocks at the inlet.

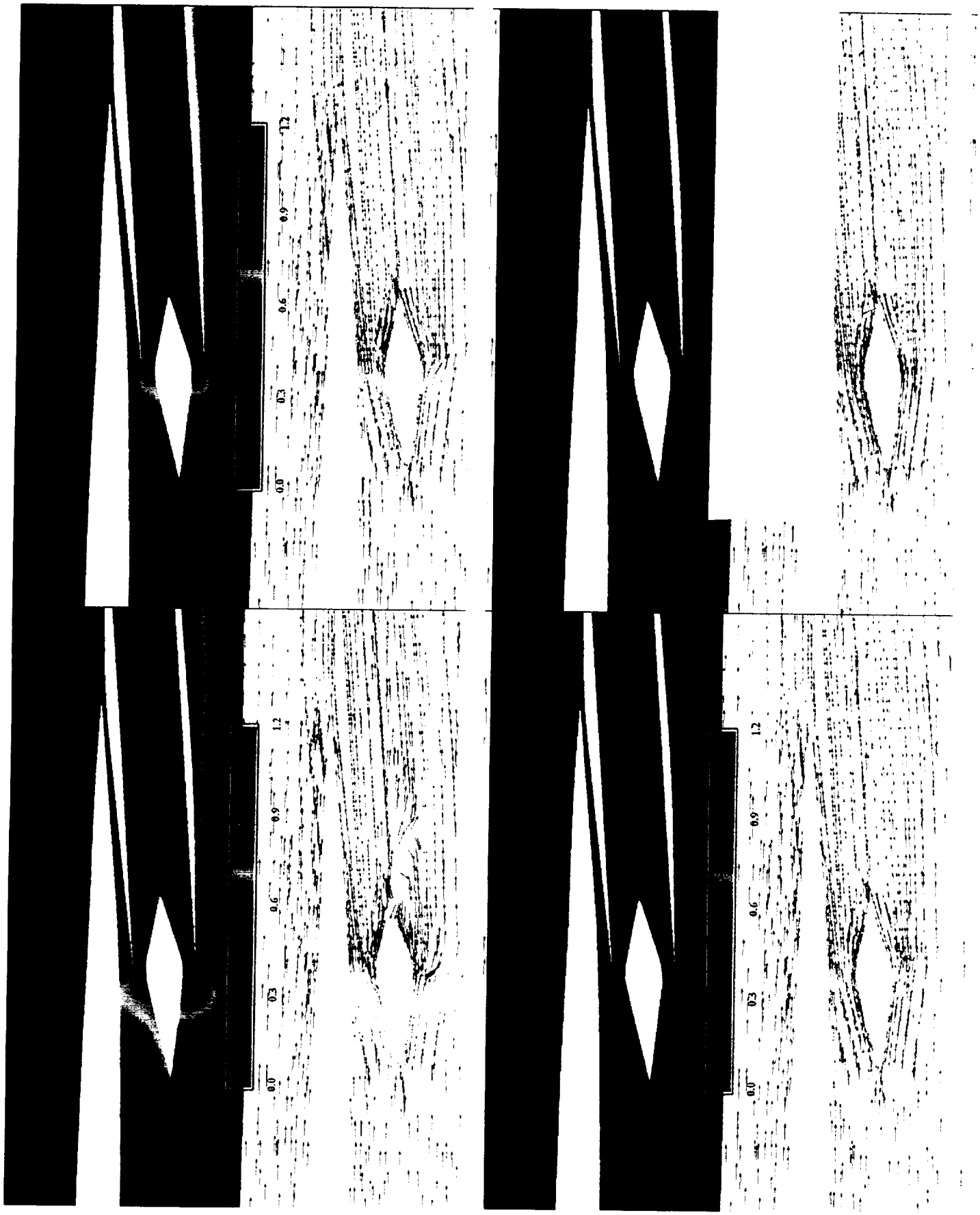
1.2
0.9
0.6
0.3
0.0
1.2
0.9
0.6
0.3
0.0
1.2
0.9
0.6
0.3
0.0

Transonic Spillage: AIRPLANE Solution

Plug Position X=15

Inboard Nacelle

This is the upper left corner of the previous picture.

Let's take a closer look at the inboard inlet for the two extreme plug positions. This one is for x=15. The recirculating region is quite evident. The vectors are normalized in length, the color indicates the magnitude, only every tenth vector is shown. This region under the aft centerbody is stagnant and we observed reversals in flow direction in the last few restarts of the flow solver (alternately running forward and backward). The flow may actually be emerging from the inlet at this instant. We know that AIRPLANE is not time accurate and we cannot claim to fully understand what is happening here.


1.2
0.9
0.6
0.3
0.0

Transonic Spillage: AIRPLANE Solution

Plug Position X=45

Inboard Nacelle

This is the lower right corner of the picture shown before the previous slide.

This is like the previous slide but for plug position x=45. The flow does not turn as much as before. There is one vector pointing forward at the aft end of the centerbody, but its magnitude is very small (blue). The flow shocks at both inboard and outboard inlets only for this high mass flow plug position. The outboard inlet is not shown.


1.2
0.9
0.6
0.3
0.0

Transonic Spillage: AIRPLANE Solution

Plug Position X=15

Inboard Nacelle

This is a graph of mass flow ratio (MFR) for the inboard nacelle, plug position x=15, along the axis for iterations 27,000 to 32,200 with 1,300 iterations between flow solver restarts.

Let's talk about flow solver convergence. None of the cases converged in the usual sense. In each case the residual dropped a little and then buzzed forever (that is, small amplitude regular oscillations). This is an indication of unsteadiness in the flow field. We had to select an alternate measure of convergence.

Since we were interested in computing the mass flow ratio from the 3D flow field, we established a convergence criterion based on the flatness of these curves.

This graph shows mass flow ratio for the inboard nacelle at 5% intervals down its axis from 5% to 95% of the nacelle-plus-extension length. The five curves represent solutions at iterations ranging from 27,000 to 32,200 in increments of 1300. You can see there is still a lot a variation along the nacelle axis. The final curve, solid squares, deviates as much as 10% from the average value. A converged steady-state solution should have no deviation.

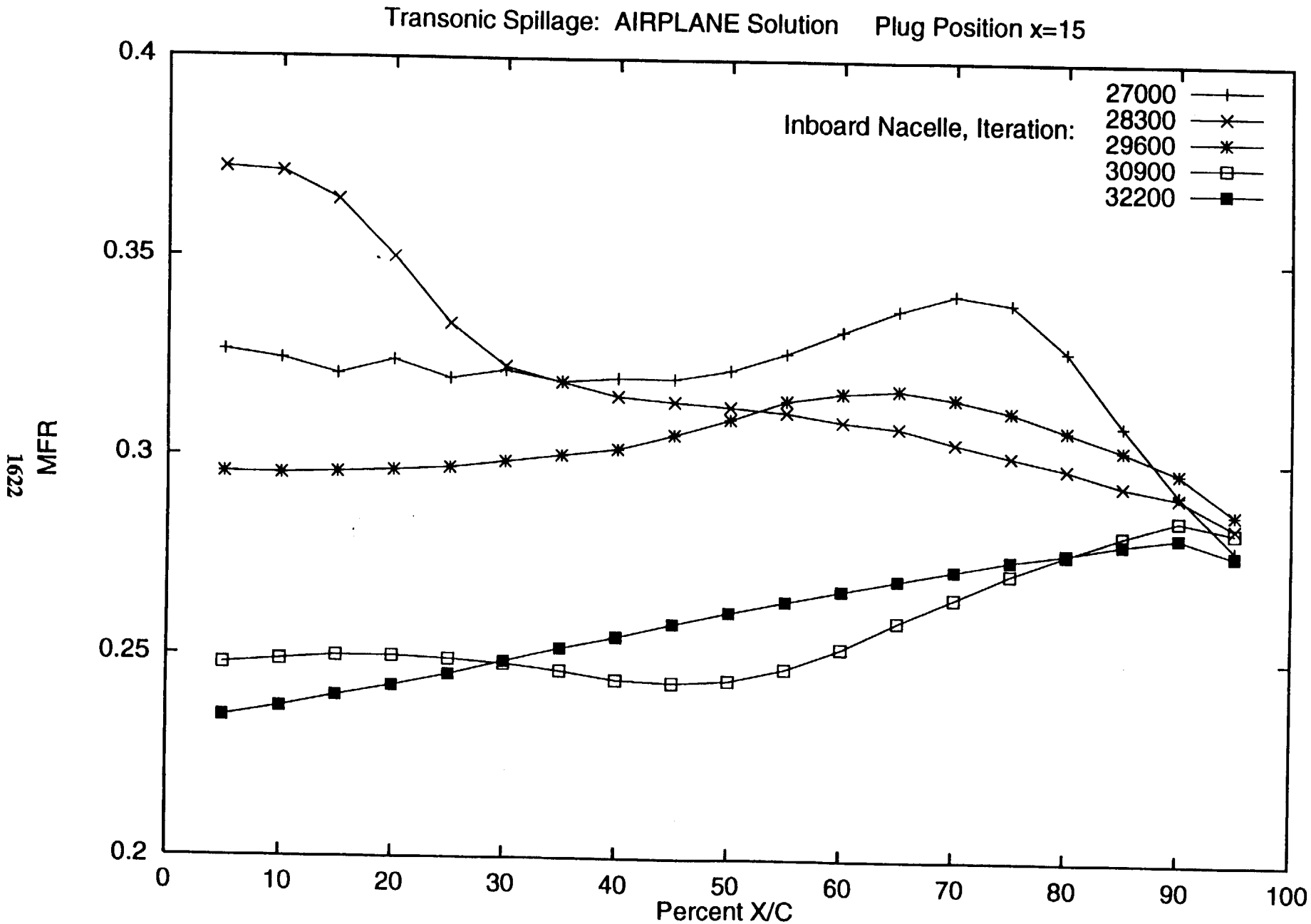
Transonic Spillage: AIRPLANE Solution Plug Position x=15
Inboard Nacelle, Iteration:
27000
28300
29600
30900
32200
MFR
1622
0.4
0.35
0.3
0.25
0.2
0
10
20
30
40
50
60
70
80
90
100
Percent X/C

Transonic Spillage: AIRPLANE Solution

Plug Position X=15

Outboard Nacelle

This is a graph of mass flow ratio (MFR) for the outboard nacelle, plug position x=15, along the axis for iterations 27,000 to 32,200 with 1,300 iterations between flow solver restart.

This is the same thing as the previous slide but for the outboard nacelle. The variation is not as large. The MFR for the final curve, solid squares, deviates about half a percent from the average value for the final solution.

In a steady flow field these numbers should all come out to be the same because of conservation of mass. Our convergence criterion was that we should see less that a 2% deviation from the average value of MFR down each inlet on two subsequent runs. We only achieved this for the three highest mass flow cases (X=24, 33, and 45 plug positions).

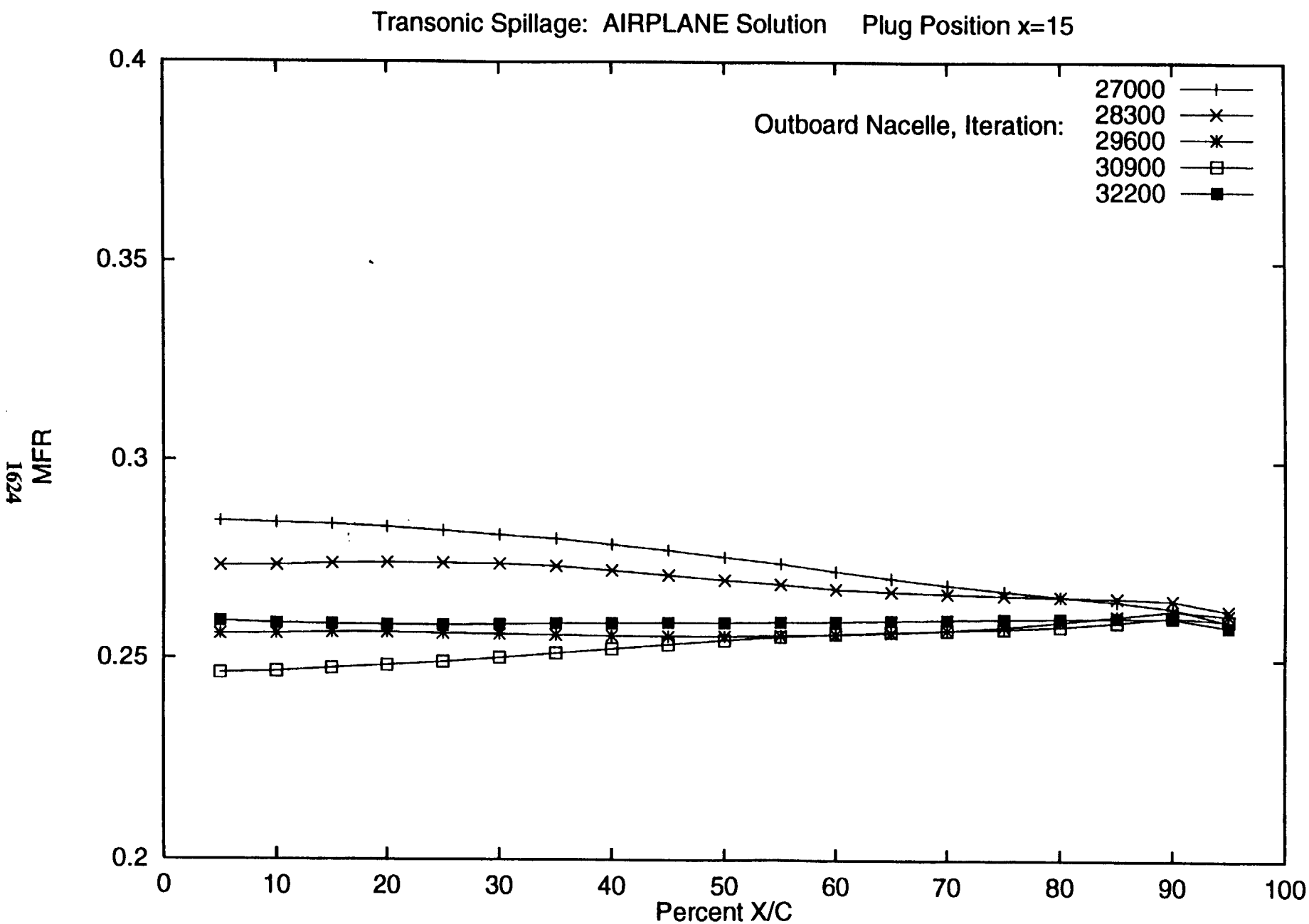
Transonic Spillage: AIRPLANE Solution Plug Position x=15
Outboard Nacelle, Iteration:
27000
28300
29600
30900
32200
MFR
1624
0.4
0.35
0.3
0.25
0.2
0
10
20
30
40
50
60
70
80
90
100
Percent X/C

Transonic Spillage: AIRPLANE Solution

Four Plug Positions

Inboard Nacelle

This shows the MFR down the inboard nacelle axis for each of the four plug positions. MFR for the three largest plug positions look very flat. The deviation of the x=15 curve is about 10%. We decided to stop the solver for the low mass flow case before the MFR curve flattened out.

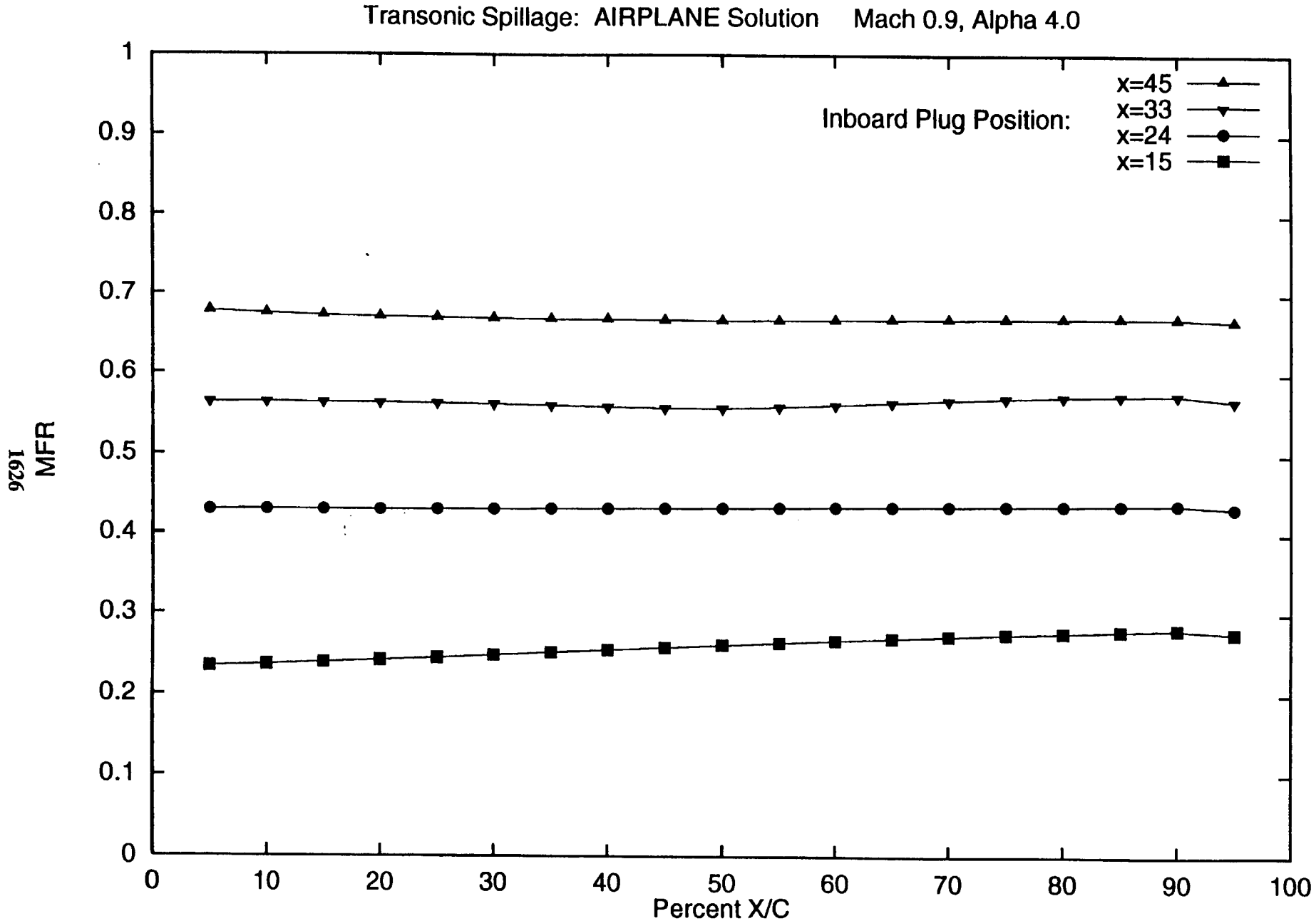
Transonic Spillage: AIRPLANE Solution Mach 0.9, Alpha 4.0
Inboard Plug Position:
x=45
x=33
x=24
x=15
MFR
Percent X/C
0
0.1
0.2
0.3
0.4
0.5
0.6
0.7
0.8
0.9
1
0
10
20
30
40
50
60
70
80
90
100

Transonic Spillage: AIRPLANE Solution

Four Plug Positions

Outboard Nacelle

This shows the MFR down the outboard nacelle axis for all plug positions. These curves are all flat: the deviation of MFR from the average value is below 2% in each case. The low mass flow (x=15) case deviates from its average by less than one percent, but we didn't run enough iterations to determine whether this would have happened again.

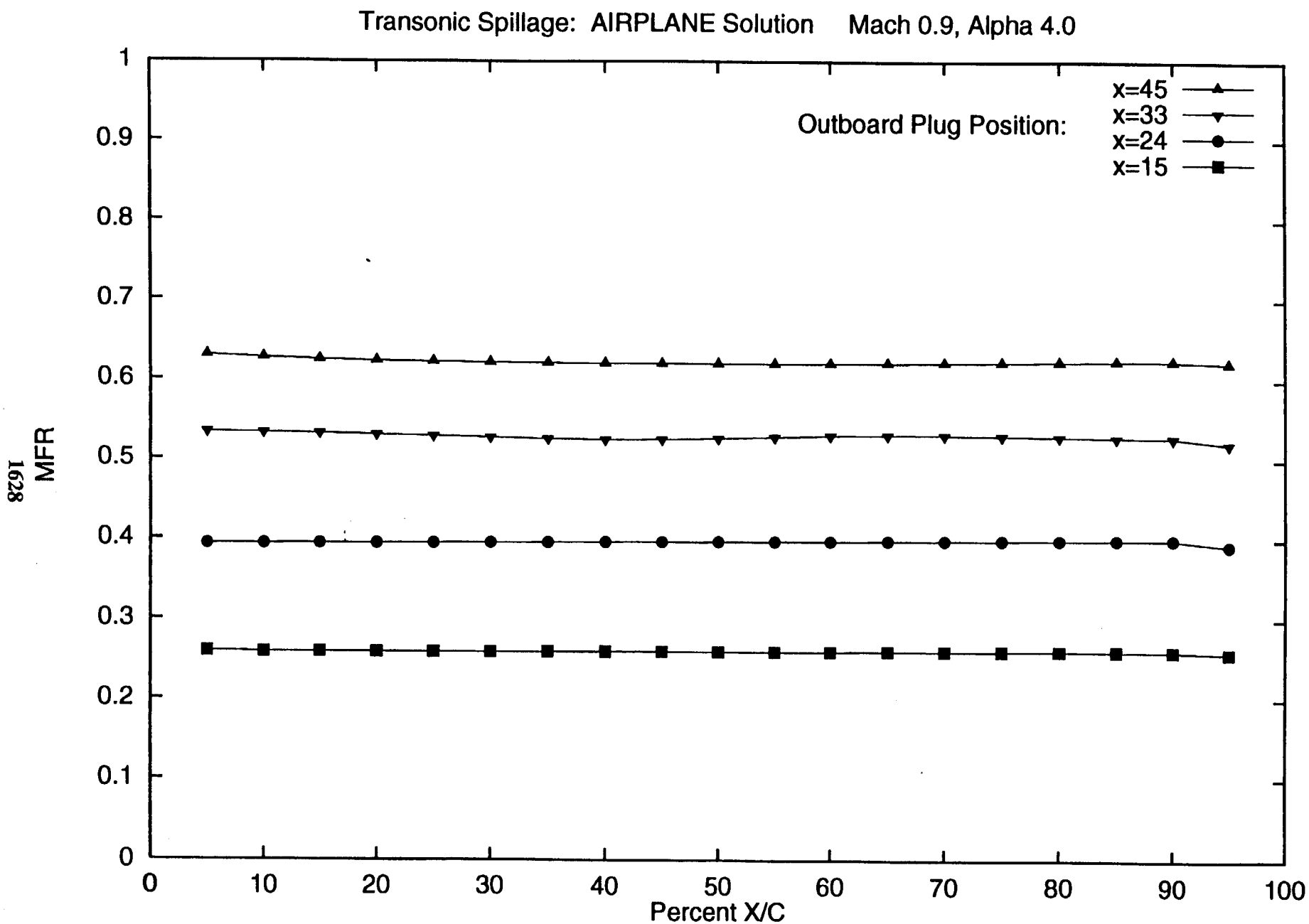
Transonic Spillage: AIRPLANE Solution Mach 0.9, Alpha 4.0
Outboard Plug Position:
x=45
x=33
x=24
x=15
MFR
Percent X/C
0
0.1
0.2
0.3
0.4
0.5
0.6
0.7
0.8
0.9
1
0
10
20
30
40
50
60
70
80
90
100

Transonic Spillage: AIRPLANE Solution

Average MFR as Functions of Iteration

Four Plug Positions

This shows the average of inboard and outboard average MFRs for each plug position as functions of iteration. If we think of iterations as measuring pseudotime then we can say that the flow field is pseudounsteady. At any rate, the average MFR oscillates for each plug position.

We seem to have enough restarts to capture the period of oscillation. Mean values of average MFR, shown to the right of each curve, were obtained by fitting exponential decay envelopes through a few of the points (dashed lines). This kind of model fits the decaying amplitude of a damped spring. The amplitude for the low mass flow case decays slowly. There's no point going beyond three periods.

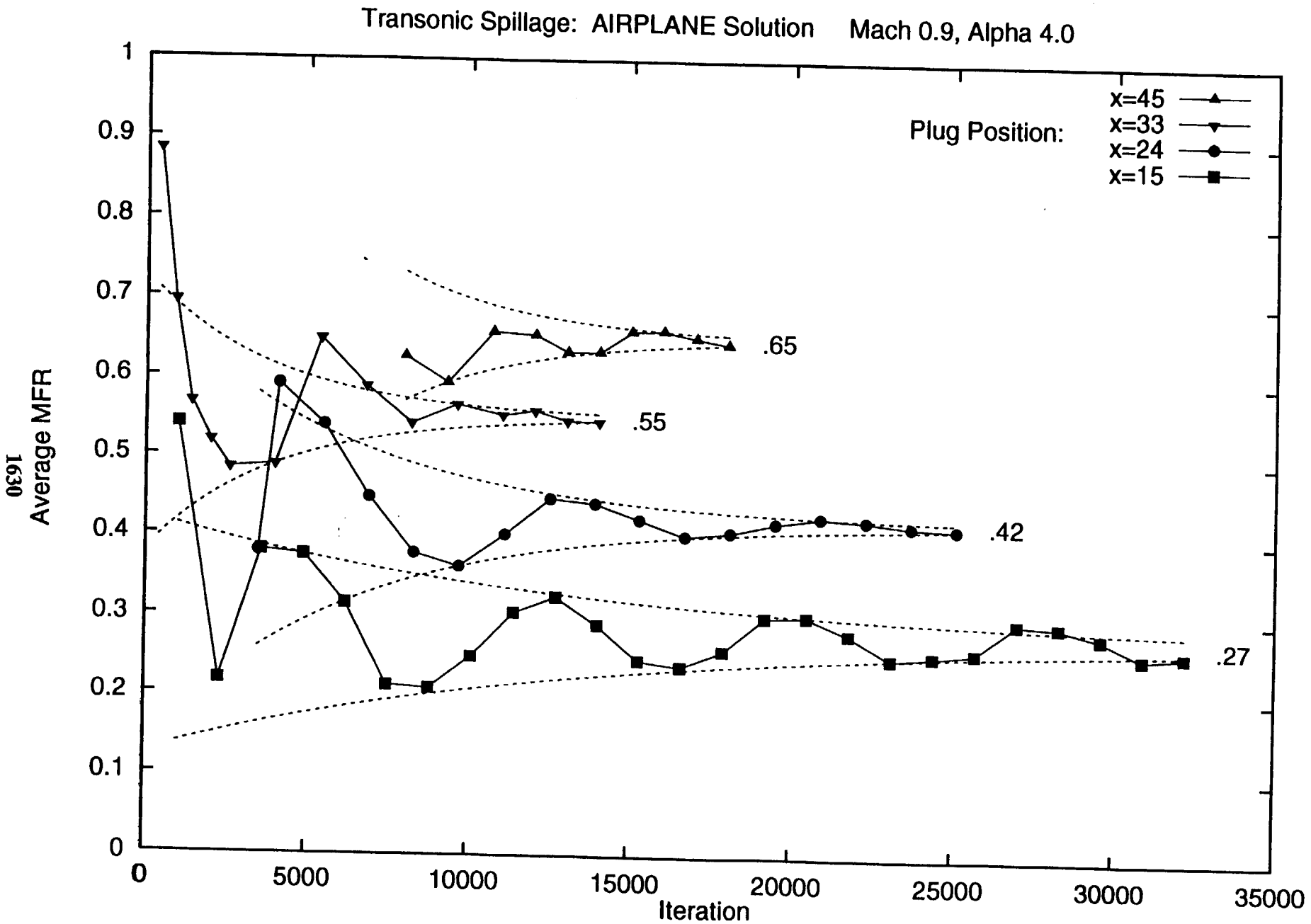
Transonic Spillage: AIRPLANE Solution Mach 0.9, Alpha 4.0
Plug Position:
x=45
x=33
x=24
x=15
.65
.55
.42
.27
Average MFR
Iteration
0
0.1
0.2
0.3
0.4
0.5
0.6
0.7
0.8
0.9
1
0
5000
10000
15000
20000
25000
30000
35000

Transonic Spillage: AIRPLANE Solution

Cp on Lower Surface for Four Plug Positions

This shows coefficient of pressure (Cp) on the wing-body-nacelles surfaces for all four plug positions. This is the surface of integration for computing lift and drag. Again, the starboard side has the nacelles removed only to make the lower wing visible. The flow solver was applied to a half model (port side). No calculations were done for wing-alone geometry. The range of Cp values is -1.0 to 0.5. Surfaces with Cp lower than -1 are all colored blue and surfaces with Cp higher than .5 are colored magenta. The sharp leading edge is painted magenta in the upper right corners of each picture; a little of the blunt inboard leading edge is visible on the left.

The effect of large spill (low mass flow) for x=15 is evident. Spillage increases the high pressure on the wing ahead of the inlets and decreases the low pressure behind the inlets. Since the interior of the inlets are not shown we can see the inlet upper lips near the lower wing surface. Increased suction at the inlet lower lips for the first three plug positions is quite evident. Suction is not as pronounced for the upper inlets as for the lower inlets.

Average mass flow ratios are listed on the slide for each plug position. For plug positions 15, 24, 33, and 45, the MFR values turn out to be 0.274, 0.419, 0.551, and 0.652, respectively. The MFR values listed are the averages of the inboard and outboard values. MFR is almost the same as the capture area ratio. The centerbody blocks about 30% of the circular inlet area so we expect the MFR to be no larger that 70%, which is what we observe.

For one nacelle MFR is computed as follows. Let Si be a surface that spans the inside of the nacelle.

MFR = {integral over Si of (rho*V) dot (dA)} / (rhoinf*Vinf*Aref)

where (rho*V) is the local momentum vector and (dA) is the vector associated with each element of area on Si. rhoinf*Vinf is the magnitude of the freestream momentum vector and Aref is a reference area. In the present case this is the area of the inlet, assumed to be a circle of radius 28.3854 inches, so Aref = 2531.2784 square inches.

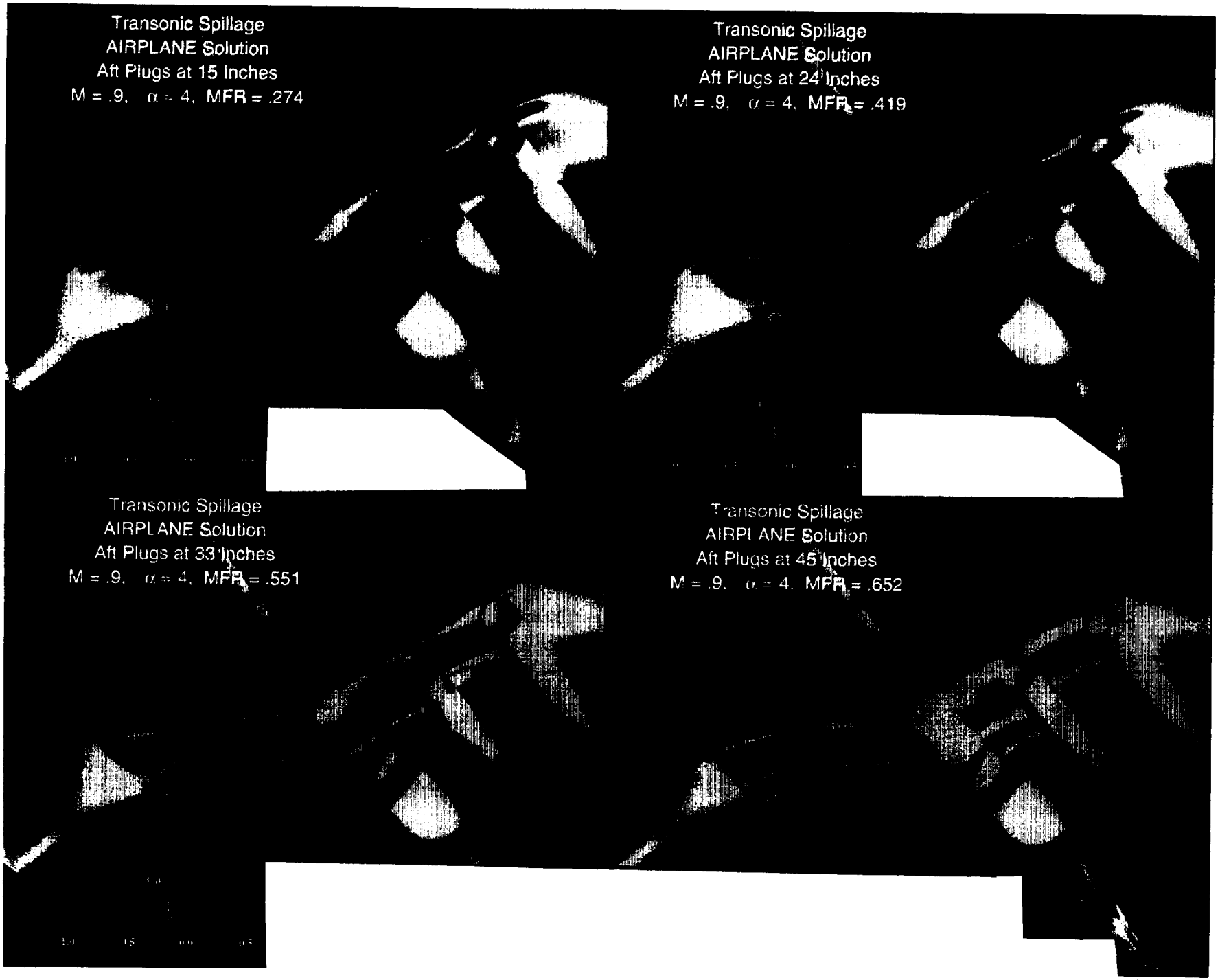
Transonic Spillage
AIRPLANE Solution
Aft Plugs at 15 Inches
M = .9, α = 4, MFR = .274
Transonic Spillage
AIRPLANE Solution
Aft Plugs at 24 Inches
M = .9, α = 4, MFR = .419
Transonic Spillage
AIRPLANE Solution
Aft Plugs at 33 Inches
M = .9, α = 4, MFR = .551
Transonic Spillage
AIRPLANE Solution
Aft Plugs at 45 Inches
M = .9, α = 4, MFR = .652

Transonic Spillage: AIRPLANE Mesh

At 4 Degrees Pitch: Magenta Faces Forward, Blue Faces Aft

This is the same point of view as before, and the color is based purely on the geometry.

The color gives us an idea of how pressure on the surface will affect drag. Each triangular face on the surface has been colored with a value that indicates its orientation with respect to the freestream vector. An inner product between Vinf/|Vinf| and each surface normal determines cos(theta), where theta is the angle formed by the two vectors. As cos(theta) ranges from -.01 to .01, theta ranges from 89.427033 to 90.572967 degrees (a range of about 1.15 degrees). Magenta indicates the parts that face forward and blue indicates the parts that face aft. You can see that most of the forward parts of the nacelles face forward. The inside part of the outboard nacelle (which is yawed 2.4 deg, toe-in) faces aft. The outside part of the aft end of the outboard nacelle actually faces forward.

Lip suction evident in the previous slide will contribute negatively to drag because most of the forward parts of the inlets face forward.

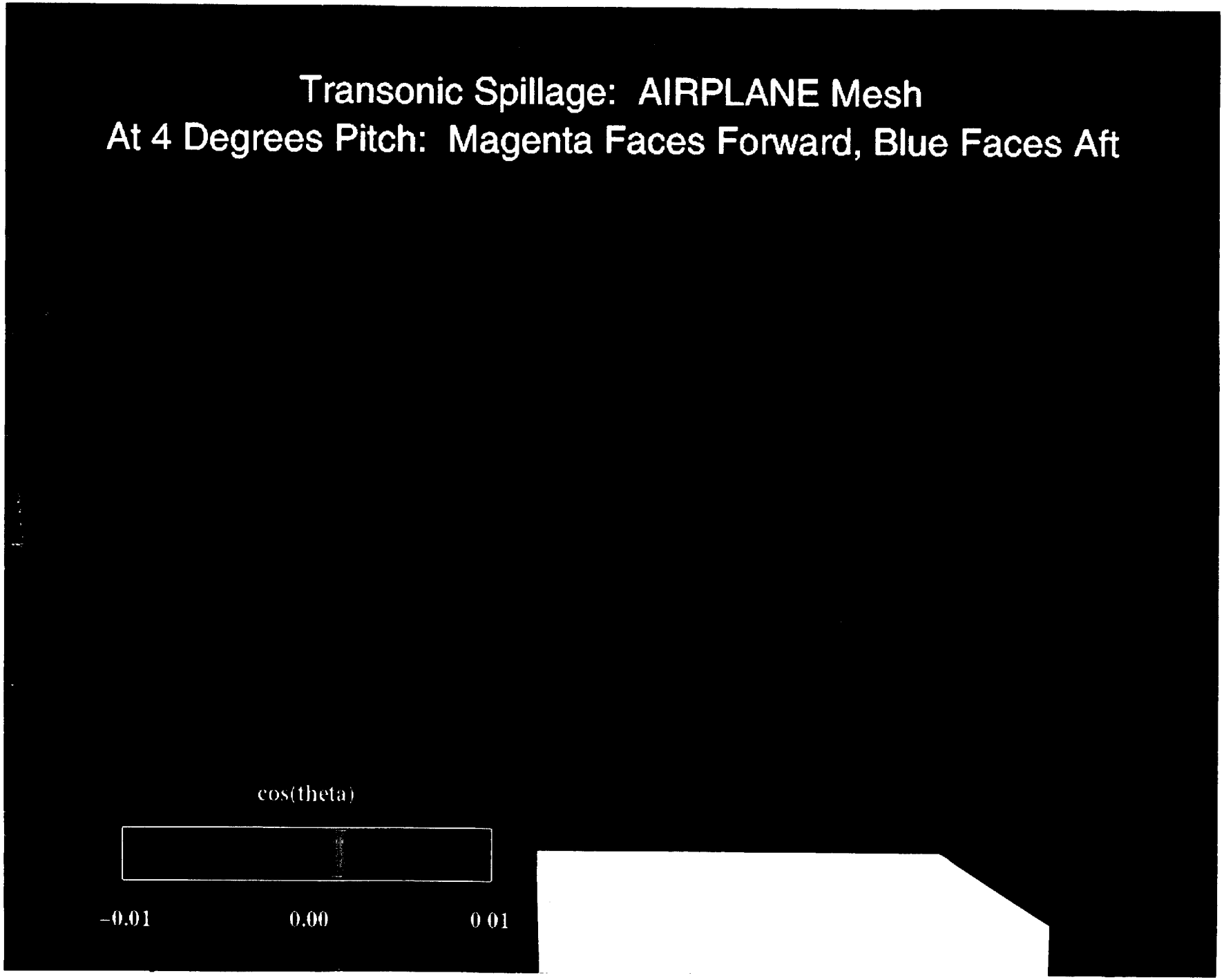
Transonic Spillage: AIRPLANE Mesh
At 4 Degrees Pitch: Magenta Faces Forward, Blue Faces Aft
cos(theta)
-0.01
0.00
0.01

Transonic Spillage: AIRPLANE Solution

Cp on a Chordwise Wing Cut at ZCUT=203

This is a graph of Cp at ZCUT=203.072 on the wing (inboard inlet center).

Let's look at Cp curves for each plug position along chordwise cuts that correspond to the centers of the inlets. Since the inlets are toed in slightly, these curves correspond only approximately to the vertical Mach slices shown above.

This and the next three plots use the same horizontal and vertical scales. Our span direction is Z, and the inboard nacelle's center is about at Z=203. This graph is just for the wing. We see a monotonic rise and fall in Cp ahead of the inlet as plugs close up. The upper surface is hardly affected.

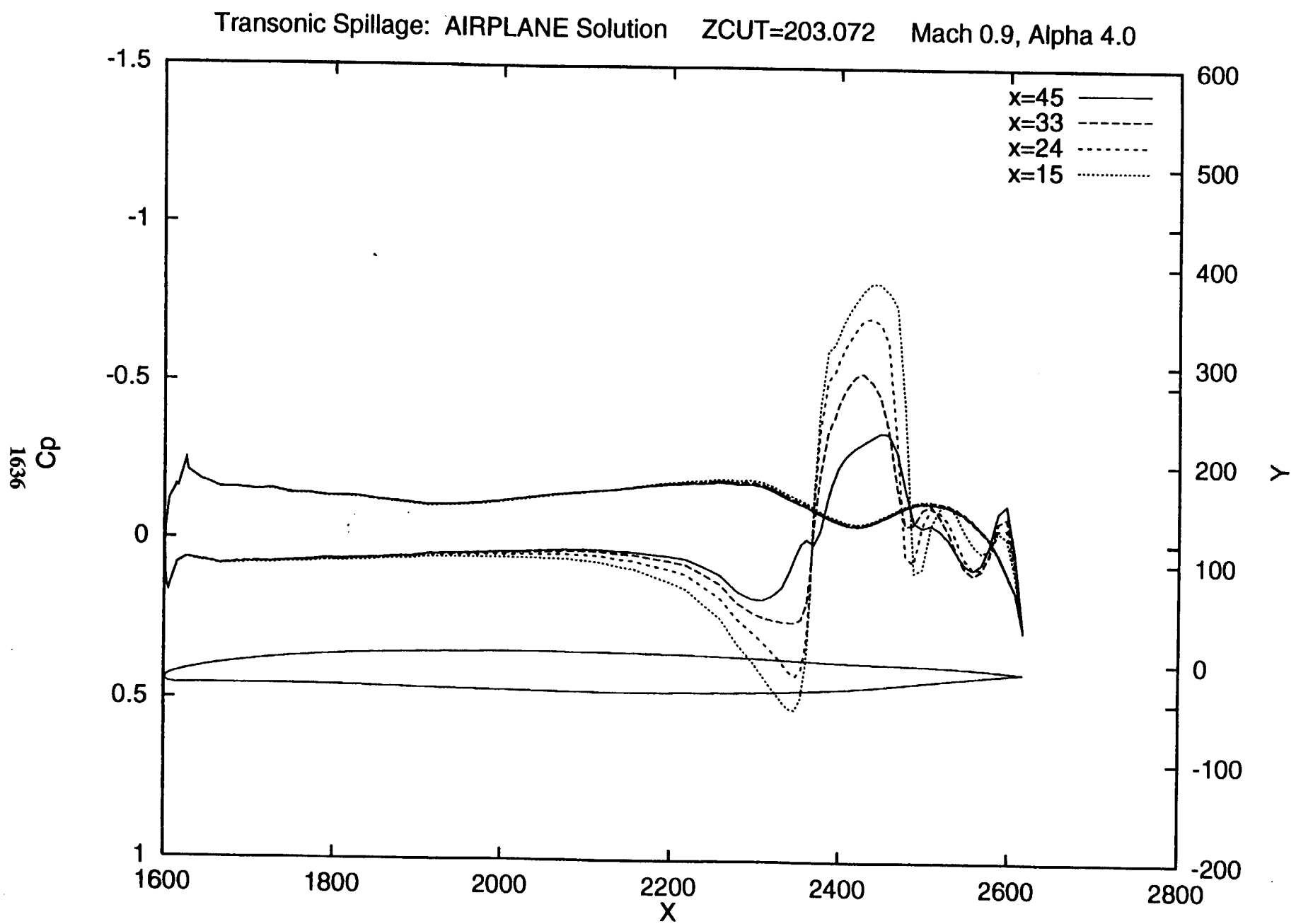
Transonic Spillage: AIRPLANE Solution ZCUT=203.072 Mach 0.9, Alpha 4.0
x=45
x=33
x=24
x=15
Cp
Y
X
-1.5
-1
-0.5
0
0.5
1
600
500
400
300
200
100
0
-100
-200
1600
1800
2000
2200
2400
2600
2800

Transonic Spillage: AIRPLANE Solution

Cp on a Chordwise Wing Cut at ZCUT=359

This is a graph of Cp at ZCUT=358.842 on the wing (outboard inlet center).

This is for the outboard nacelle at about Z=359, just showing the wing. The behavior is similar to what we observe inboard. The double shock here in the gap between the nacelle and the wing lower surface is nearly balanced for the two smaller plug positions.

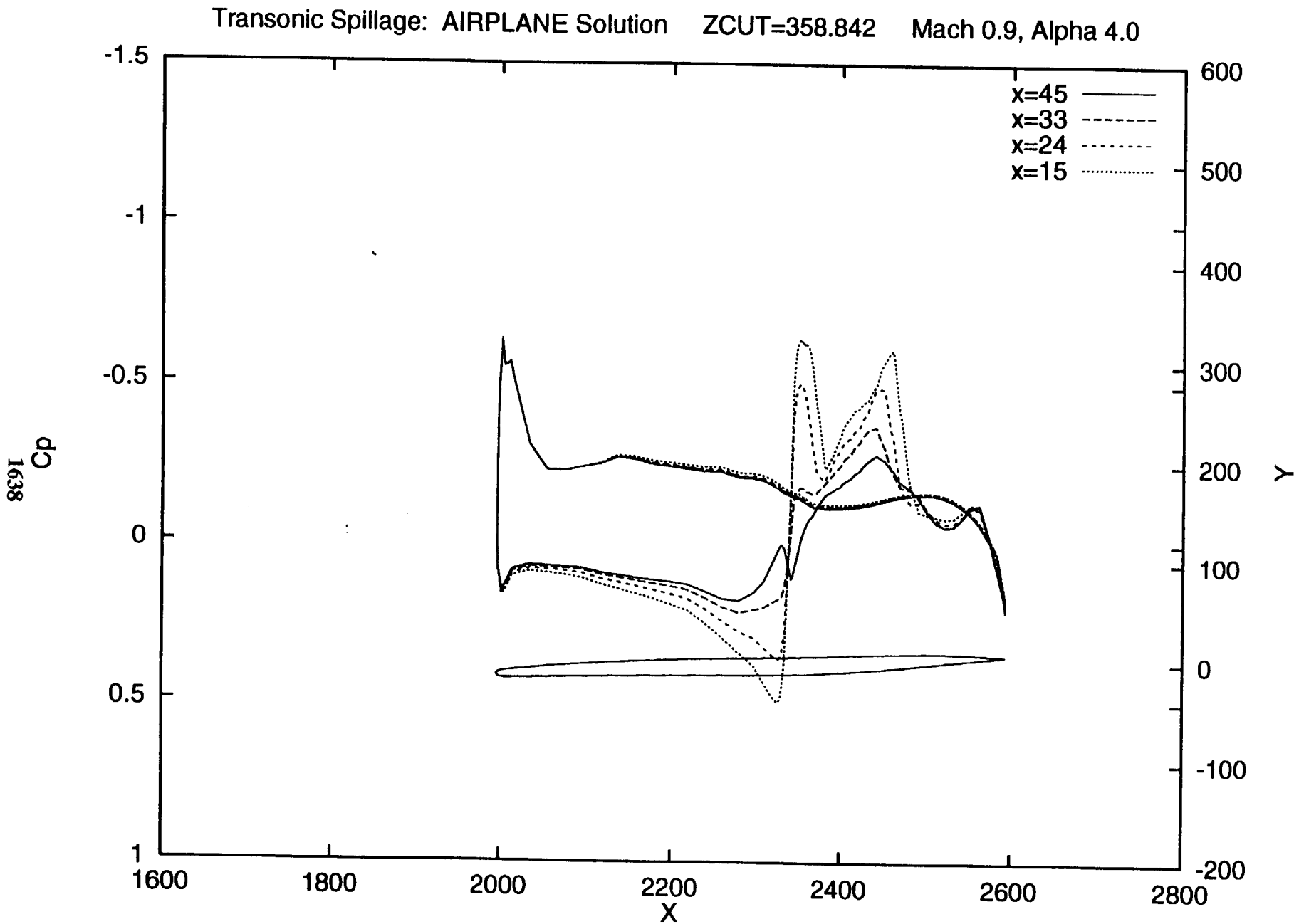
Transonic Spillage: AIRPLANE Solution ZCUT=358.842 Mach 0.9, Alpha 4.0
x=45
x=33
x=24
x=15
Cp
Y
X
-1.5
-1
-0.5
0
0.5
1
600
500
400
300
200
100
0
-100
-200
1600
1800
2000
2200
2400
2600
2800

Transonic Spillage: AIRPLANE Solution

Cp on a Chordwise Nacelle Cut at ZCUT=203

This is a graph of Cp at ZCUT=203.072 on the nacelle (inboard inlet center).

The extreme peak in negative pressure on the lower lip of the inboard inlet is evident here, just like in the color Cp slide (number 14). It increases monotonically as the plug closes. On the upper side this is observed as well. The Cp's for all four cases look about the same aft of the trailing edge of the wing.

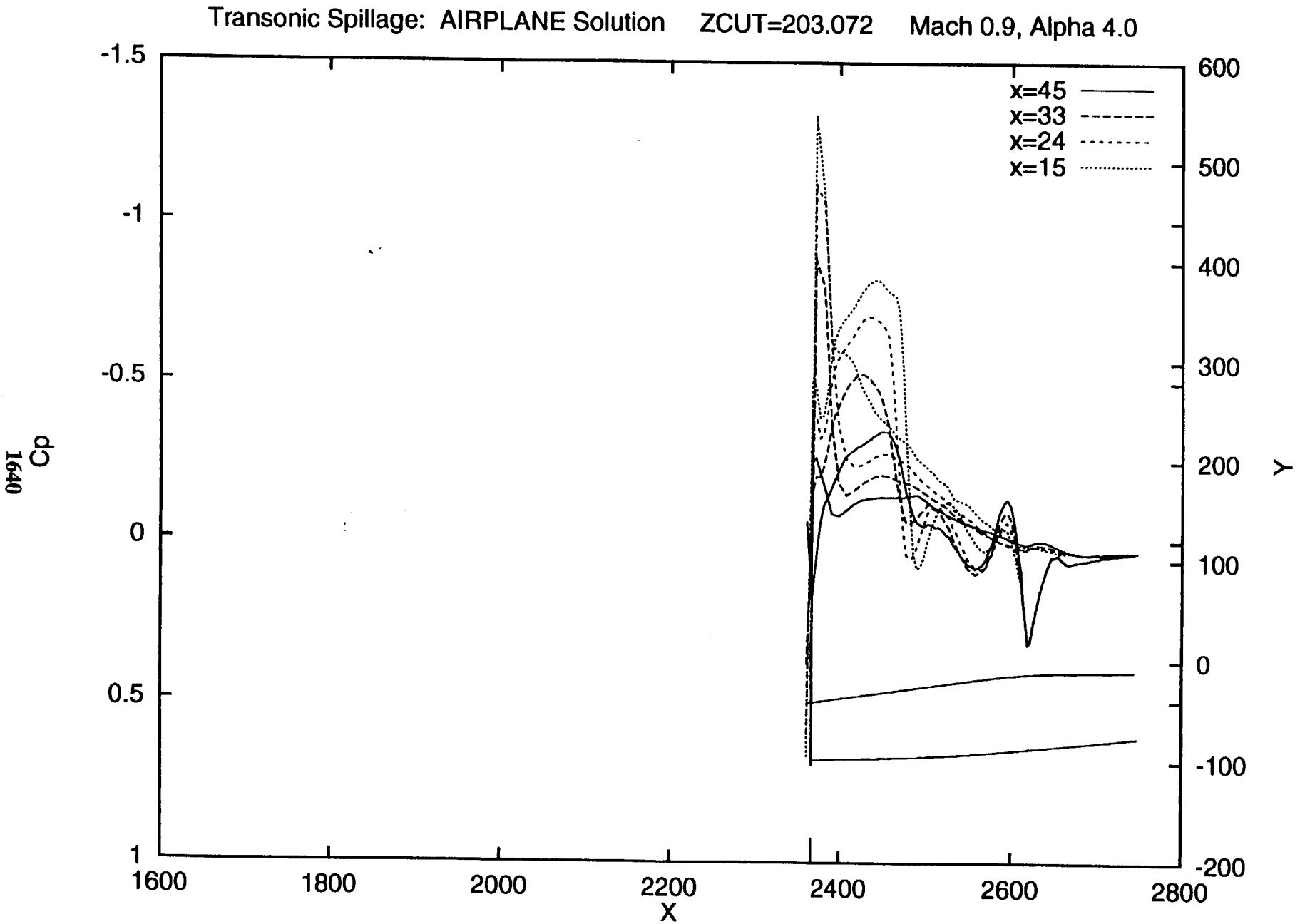
Transonic Spillage: AIRPLANE Solution ZCUT=203.072 Mach 0.9, Alpha 4.0
x=45
x=33
x=24
x=15
-1.5
-1
-0.5
0
0.5
1
Cp
1640
600
500
400
300
200
100
0
-100
-200
Y
1600
1800
2000
2200
2400
2600
2800
X

Transonic Spillage: AIRPLANE Solution

Cp on a Chordwise Nacelle Cut at ZCUT=359

This is a graph of Cp at ZCUT=358.842 on the nacelle (outboard inlet center).

The outboard nacelle is positioned slightly ahead of the inboard one. The curves seem to move monotonically again with little difference aft of the wing trailing edge. The balanced shocks observed on the wing for the smaller two plug positions are reflected here on the upper surface of the nacelle.

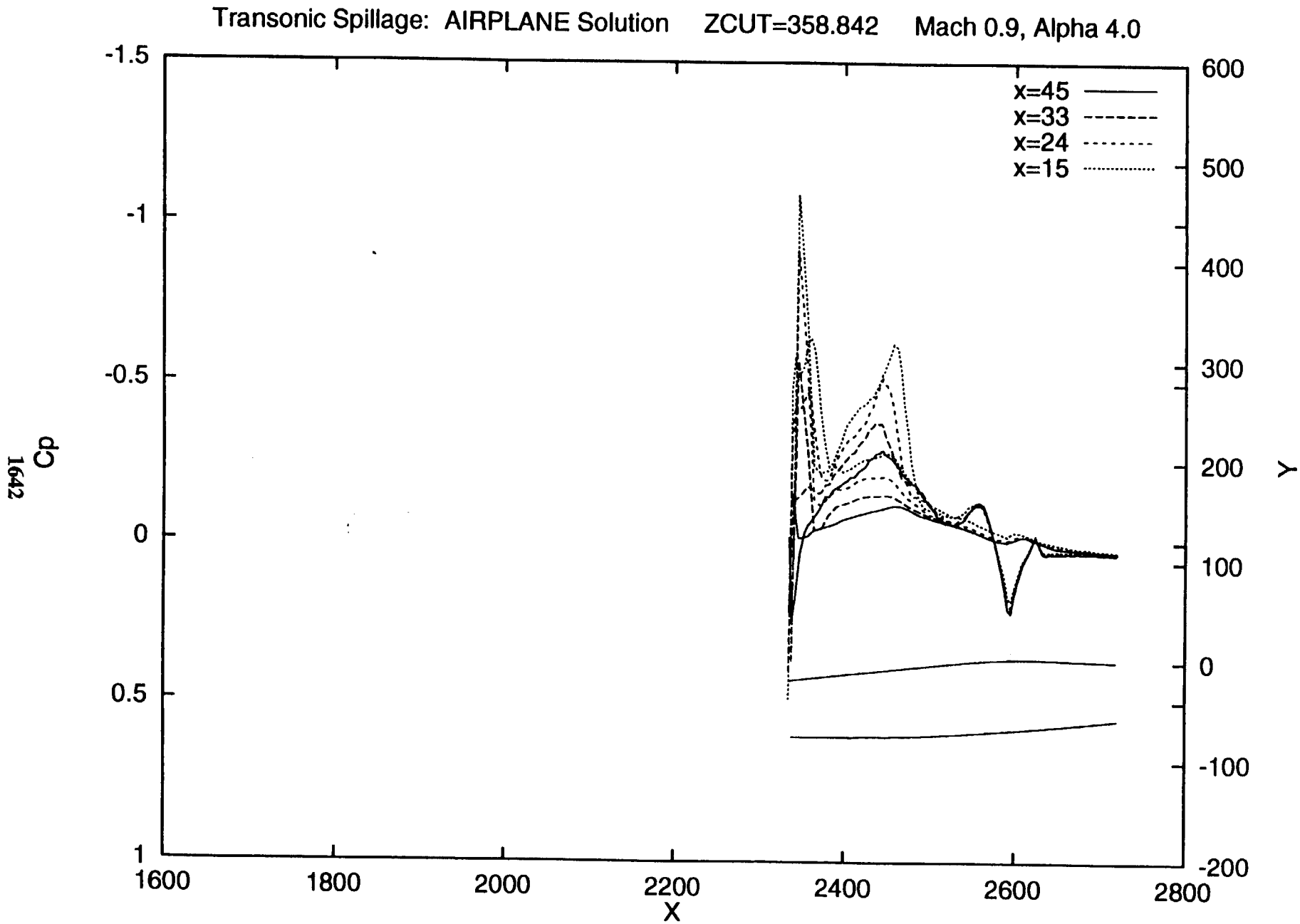
Transonic Spillage: AIRPLANE Solution ZCUT=358.842 Mach 0.9, Alpha 4.0
x=45
x=33
x=24
x=15
-1.5
-1
-0.5
0
0.5
1
Cp
1642
600
500
400
300
200
100
0
-100
-200
Y
1600
1800
2000
2200
2400
2600
2800
X

Transonic Spillage: AIRPLANE Solution

Lift as a Function of MFR

This shows lift as a function of MFR with ten counts between tic marks on the left. The MFR range on the lower axis is zero to one. The open symbols connected by dashed lines show how CI(MFR) varies with iteration count for the last five x=15 restarts. This gives us a way to measure our confidence in the lift prediction.

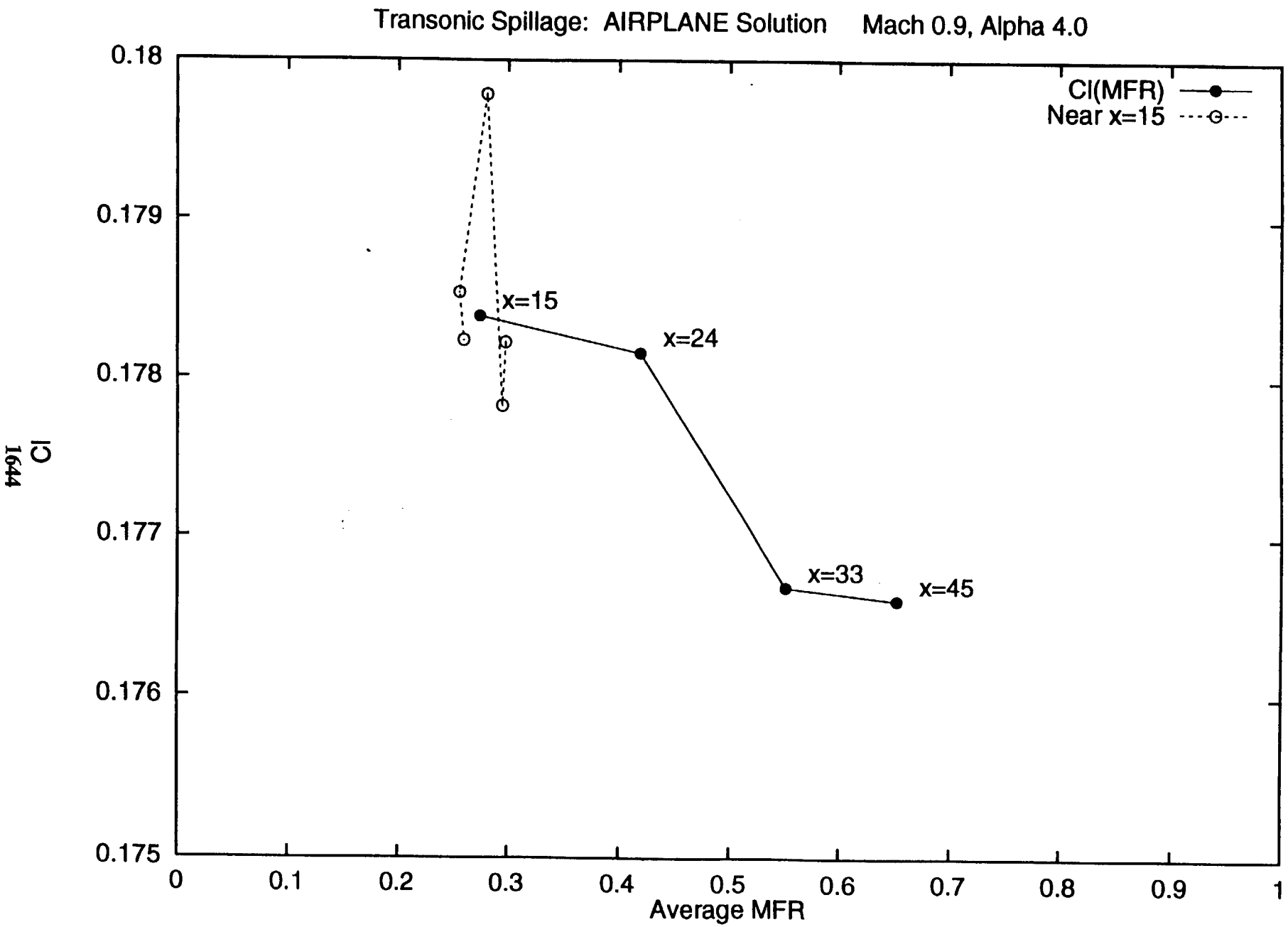
Transonic Spillage: AIRPLANE Solution Mach 0.9, Alpha 4.0
0.18
0.179
0.178
0.177
0.176
0.175
Cl
0
0.1
0.2
0.3
0.4
0.5
0.6
0.7
0.8
0.9
1
Average MFR
Cl(MFR)
Near x=15
x=15
x=24
x=33
x=45

Transonic Spillage: AIRPLANE Solution

Drag as a Function of MFR

This shows drag as a function of MFR with one drag count between tic marks on the left. The MFR range is the same as before. The open symbols and tic marks show how Cd(MFR) varies with iteration count for the last five x=15 restarts. This leads us to assert that there really is a corner in the drag curve here at the low end of mass flow ratio. This might be a nacelle leading edge suction effect since there is a lot of spill near that forward facing surface.

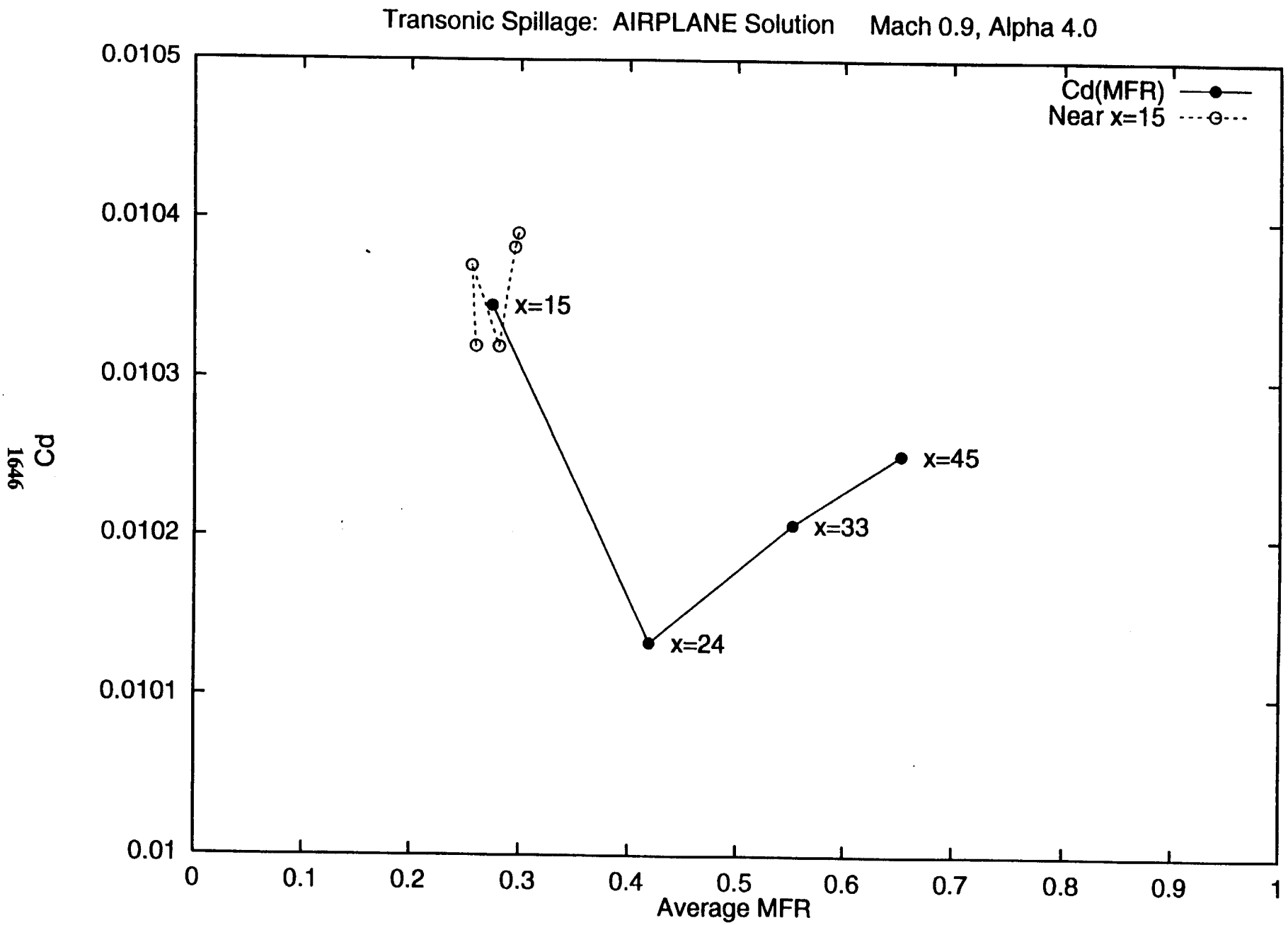
Transonic Spillage: AIRPLANE Solution Mach 0.9, Alpha 4.0
Cd(MFR)
Near x=15
x=15
x=24
x=33
x=45
Cd
Average MFR
0.0105
0.0104
0.0103
0.0102
0.0101
0.01
0
0.1
0.2
0.3
0.4
0.5
0.6
0.7
0.8
0.9
1

Transonic Spillage: AIRPLANE Solution

Lift and Drag as Functions of MFR

Let's put these last two plots in perspective by plotting them together. The lift scale on the left and the drag scale on the right both use ten counts (0.001) between tic marks. The contributions of the wing and body (W/B) are shown with open symbols and dashed lines. The lift and drag for the complete configuration (W/B/N) are shown with solid symbols and solid lines. The nacelle contributions can be seen as the difference between the dashed and solid curves. We did not run any nacelle-off computations; this just gives us an idea of what the nacelles contribute to lift and drag.

We see that the effect of integrating lift over the nacelles is to add lift, shifting the lift curve up. The effect of integrating drag over the nacelles is to add thrust, lowering and slightly rotating the drag curve.

When plotted to this scale, the drag as a function of MFR looks very flat. The range is about two and a half counts. It would be a challenge to measure this limited range in an experiment.

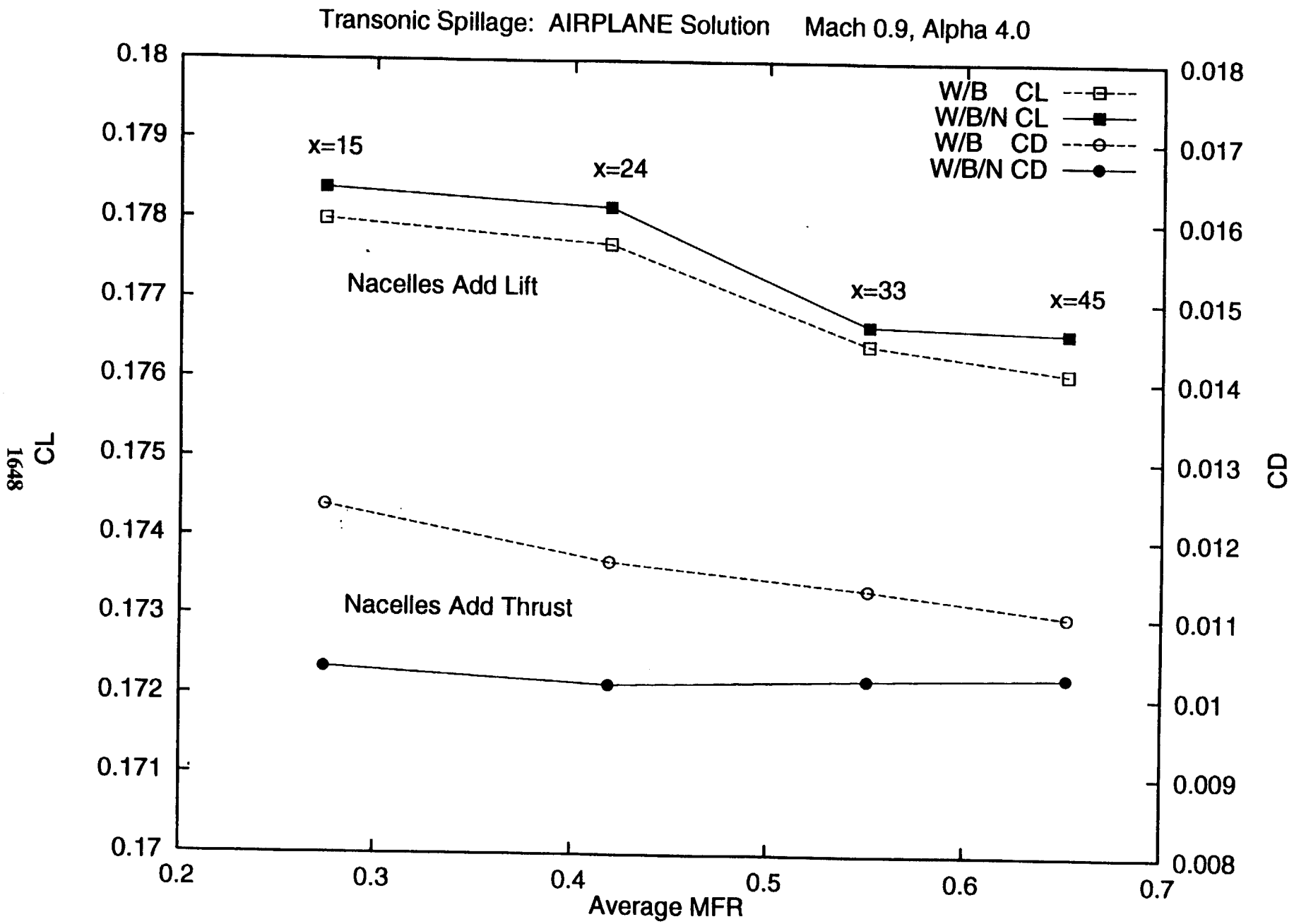
Transonic Spillage: AIRPLANE Solution Mach 0.9, Alpha 4.0
W/B CL
W/B/N CL
W/B CD
W/B/N CD
x=15
x=24
x=33
x=45
Nacelles Add Lift
Nacelles Add Thrust
CL
CD
Average MFR
0.18
0.179
0.178
0.177
0.176
0.175
0.174
0.173
0.172
0.171
0.17
0.018
0.017
0.016
0.015
0.014
0.013
0.012
0.011
0.01
0.009
0.008
0.2
0.3
0.4
0.5
0.6
0.7

Use of CFD Results in the Excrescence Drag Estimation

Sasan Yaghmaee
HSCT Aerodynamics
Boeing Commercial Airplane Group
Seattle, WA

1997 HSR Aerodynamic Performance Workshop
February 25-28, 1997
NASA Langley Research Center, Hampton, VA

A Navier-Stokes based method has been developed to assess the excrescence drag contribution to the flight polar build-up process. A major step in the method is the estimation of the local boundary layer thickness and edge conditions from the calculated CFD solution. Initial application of the method has been successful in identifying drag critical areas of the surface, where deviations from the aerodynamically designed smooth sealed surface should be avoided. The drag of a generic excrescence item is also presented. The developed method can be used for accurate and timely assessment of weight/drag trade-off's for manufacturing concepts. The detailed boundary layer data extracted from the viscous Navier-Stokes solution can be a valuable tool in understanding fluid dynamics.

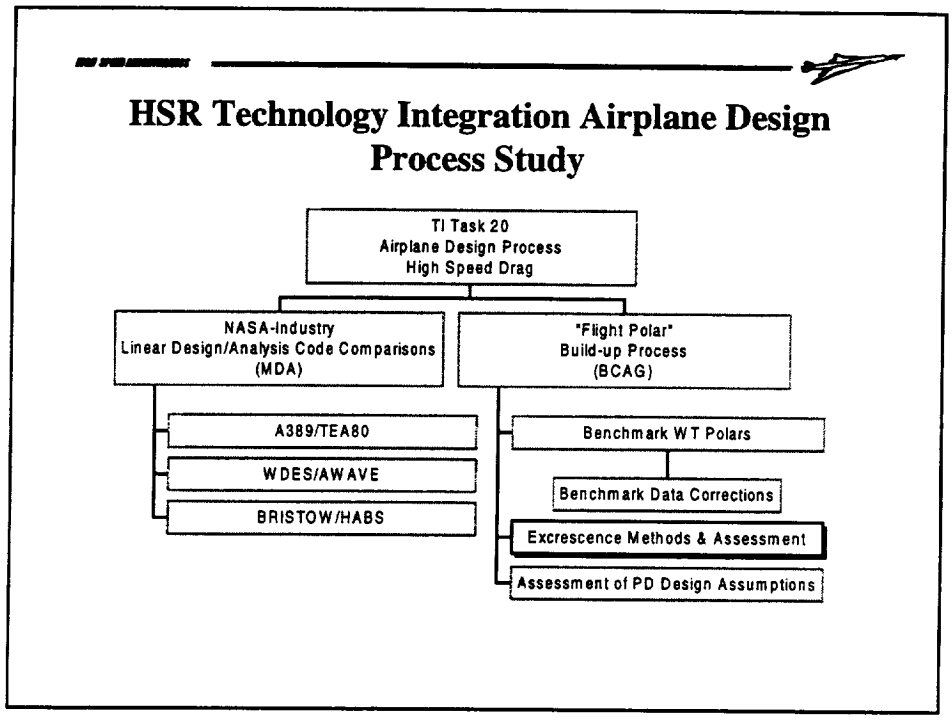

This presentation reports on the progress made in developing a methodology to assess excrescence drag contributions to flight polar build-up process in the Technology Integration (TI) task 20. The flight polar build-up sub-task was assigned to Boeing Commercial Aircraft Group (BCAG).

Definition of Excrescence Drag

The excrescence drag is

- defined as the sum of all deviations from an aerodynamically smooth sealed external surface
- minimized by good manufacturing techniques and design practices
- generally due to surface imperfections smaller than local boundary layer thickness
- traditionally normalized by the total skin friction drag of the airplane

Technically, excrescence drag is the additional drag on the airplane due to the sum of all deviations from a smooth, sealed, aerodynamically designed external surfaces. As defined, accurate manufacturing techniques can significantly reduce the excrescence drag. Design can also reduce excrescence drag by proper placement of non-aerodynamic surfaces.
The excrescence drag is generally due to surface imperfections that are much smaller than the boundary layer thickness. The drag of an imperfection is often represented as a function of the local skin friction. Thus, to correlate the data on various airplanes, the excrescence drag is traditionally normalized by the total skin friction of the aircraft.

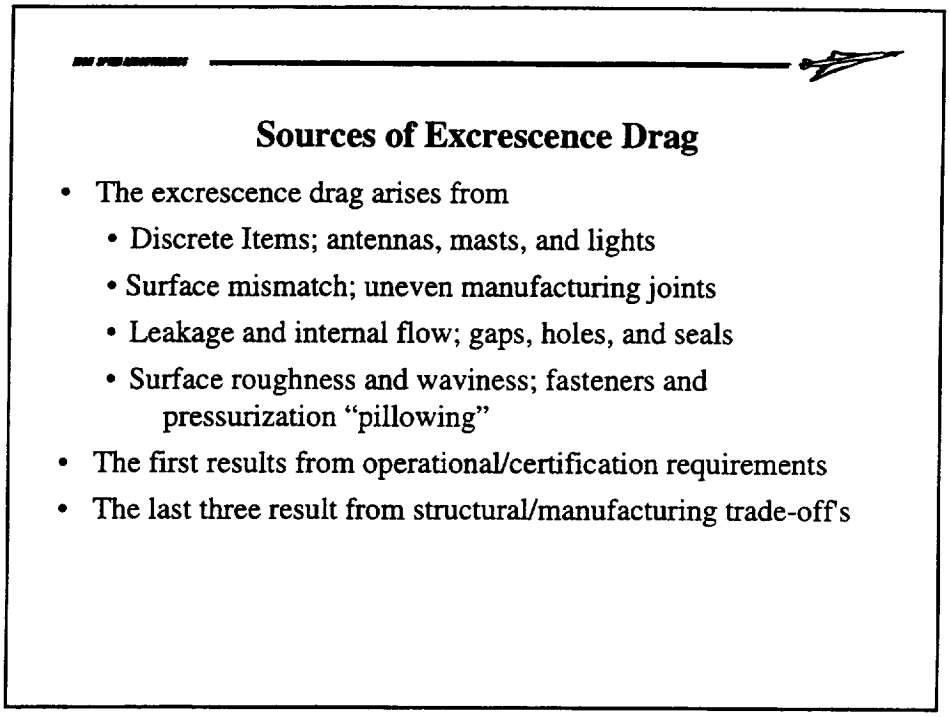

The sources of excrescence drag can be grouped into four categories, drag of discrete items, drag due to surface mismatch at manufacturing joints, drag of surface roughness, and drag due to leakage. Of the four categories, the first usually arises from operational/certification requirements, while the last three result from manufacturing cost/weight/drag trade-off's.

Discrete items refer to antennas, masts, etc. that are exposed to the external stream. The drag of the discrete items is determined by their size, shape, location, and orientation on the airplane. A detailed knowledge of the external flow during the design phase, can be used to optimize the placement of the item and in some cases the shape of the protuberance.

Surface mismatch refers to the steps that occur at skin joints, around windows, control surfaces, access panels, etc. A drag force is associated with a pressure on a forward facing area and/or suction on a backward facing area.

The internal flow caused by leaks reduces the available useful energy and causes additional drag force.

Surface roughness refers to the effects of distributed disruptions related to fastener flushness and surface finish smoothness and waviness. The effect is generally to increase the skin friction force caused by the air flowing over the airplane surface.

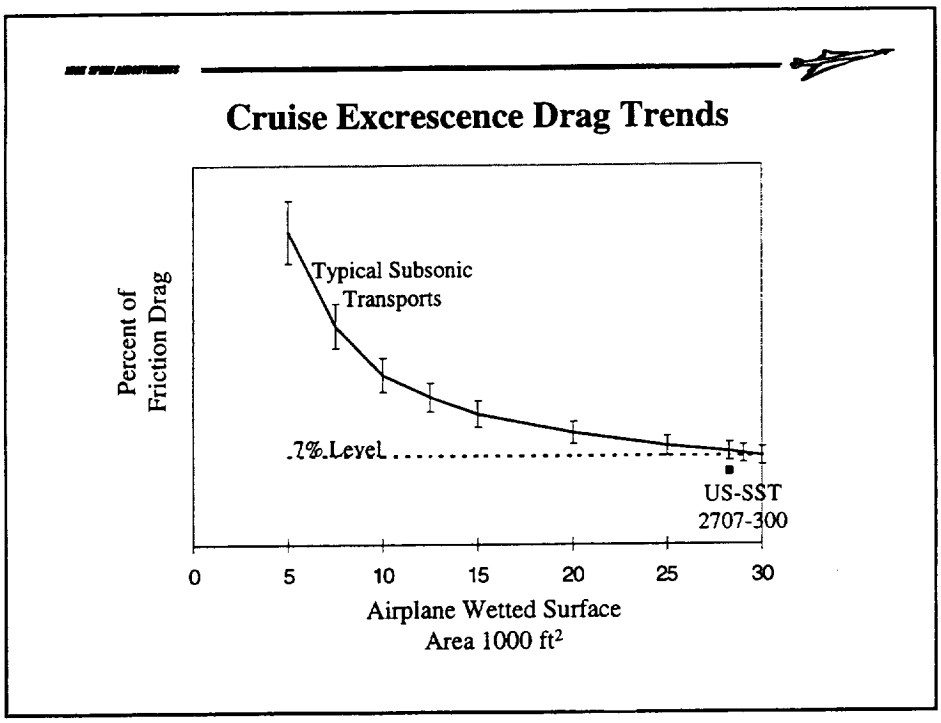

The Excrescence contribution to total drag decreases with an increase in wetted surface area for subsonic transports. The data suggests an excrescence level of 7% of skin friction for large transports. A detailed estimate of the excrescence drag of the 1970 US-SST 2707-300 configuration led to a 6% level, which is slightly better than today's subsonic transport trend.

The 2707 estimates already included some of the design details for low excrescence that we currently assume in our "technology projection", confirming that 7% is a reasonable excrescence level for a current technology "status" airplane.

Excrescence Drag Estimation

The excrescence drag of a protuberance is traditionally defined as

$$CD = CD_{\pi} (A_{\pi}/S_{ref}) q_e/q_l \, m$$

CD_{π}	Measured drag of isolated excrescence (Empirical)
A_{π}	Area used in CD_{π}
S_{ref}	Wing surface reference area
q_e	The equivalent q experienced by the protuberance
q_l	Local boundary layer edge velocity
m	Drag magnification factor correcting for the variation of the local q from that of the free stream

The excrescence drag of a discrete protuberance is traditionally defined as, see reference 1,

$$CD = CD_{\pi} \ (A_{\pi}/S_{ref}) \, q_e/q_l \, m$$

where CD_{π} is the empirical data on the drag of individual isolated protuberances, and A_{π} is the area used in CD_{π} Tabulation. S_{ref} is wing surface reference area. The factor q_e/q_l corrects for the average dynamic head experienced by excrescence on the surface when CD_{π} is measured for the isolated excrescence exposed to a uniform stream. For many excrescence geometries of interest the drag, CD_{π}, is measured in presence of flat plate turbulent boundary layer. In this case the dynamic head correction is set to unity. The factor m is known as the magnification factor, which corrects for the variation of the local q_l from that of the free stream.

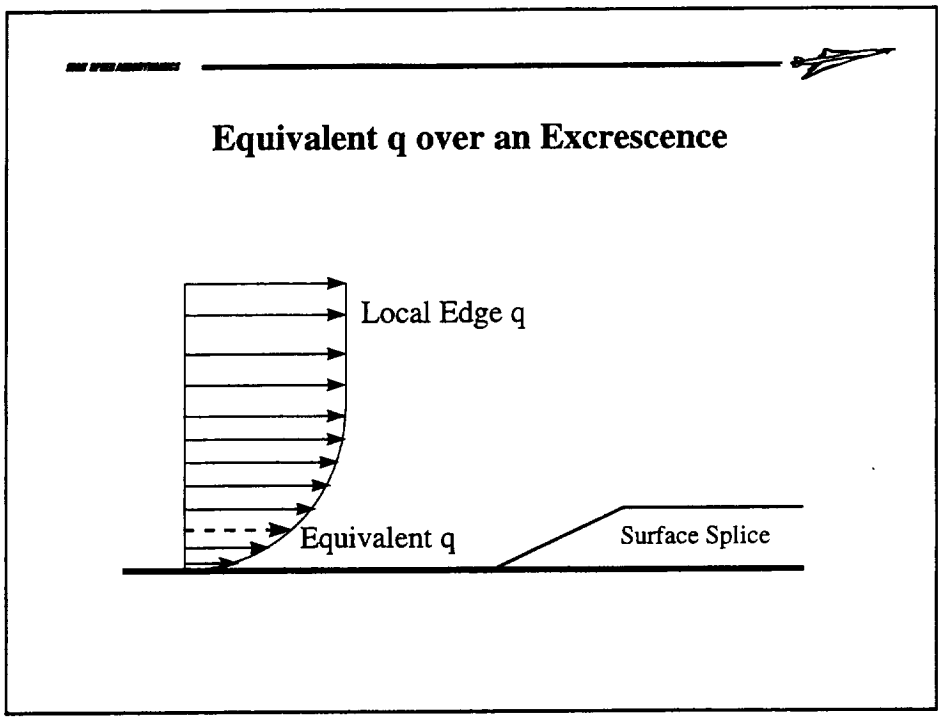

The equivalent q is defined as the average dynamic head experienced by the protuberance. Assuming a power law velocity profile and corresponding temperature distribution for the compressible turbulent boundary layer, the definition becomes

$$\frac{q_e}{q_i} = \frac{\delta}{h}\int_0^{\frac{h}{\delta}} \frac{(\frac{y}{\delta})^{\frac{2}{n}}}{1 + r\frac{(\gamma-1)}{2}M_e^2(\frac{y}{\delta})^{\frac{2}{n}}} d(\frac{y}{\delta})$$

where γ is the ratio of specific heats, δ is the boundary layer thickness, h is the height of the protuberance, M_e is the local boundary layer edge Mach number, n is the power law exponent, and r is the recovery factor.

The equivalent q is a function of the power law exponent n and rM_e^2. The exponent n is between 7 and 10 depending on the Reynolds number. For typical HSCT flight Reynolds numbers of about 200 million the appropriate value is 10.

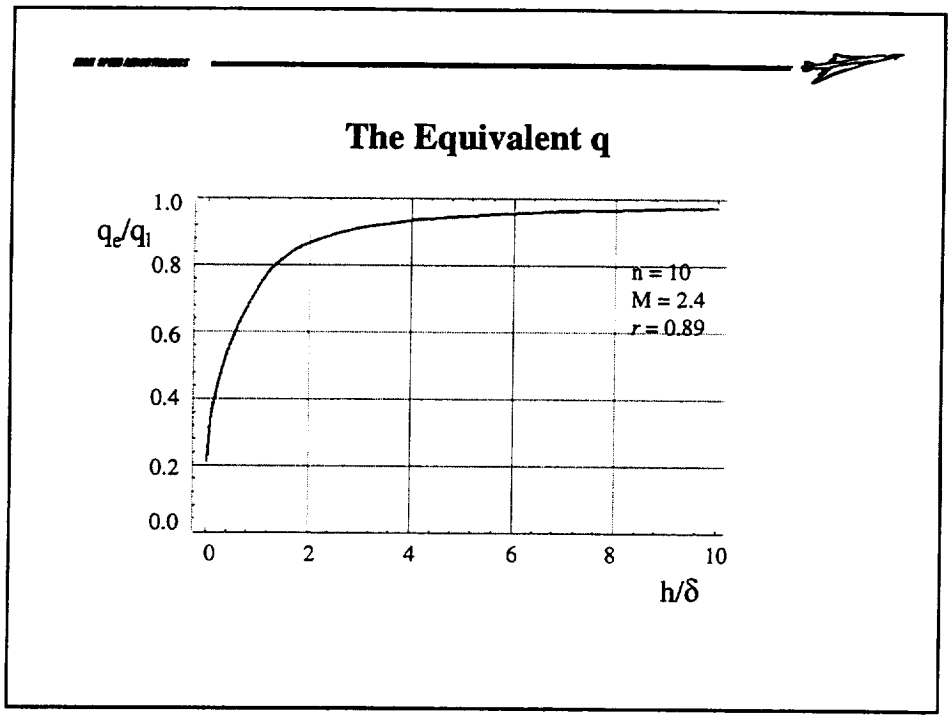

The figure above shows the variation of effective dynamic head, q_e/q_l, with the protuberance height, h/δ. The value asymptotes to one as h/δ increases. The assumptions that have gone into the above universal curve are based on the flat plate turbulent boundary layer theory. This should approximate the local boundary layer flow about the slender TCA geometry at low a lift level with reasonable accuracy.

An alternative approach is to numerically integrate the product of calculated CFD velocity squared and density profile at a surface location for a given protuberance height. This method may be more accurate, however, it is considerably more time consuming and is not suited for preliminary design activities.

The Magnification Factor

- Accounts for the pressure gradients from excrescence location to the downstream far field
- Scales the effects of the excrescence on the subsequent viscous flow on the surface
- Equals unity for flat plate flow
- For compressible flow is defined by

$$m = \left(\frac{M_\infty}{M_{TE}}\right)^{(1-M_\infty^2)} \times \left(\frac{1+0.2M_\infty^2}{1+0.2M_{TE}^2}\right)^{(2+0.5M_\infty^2)} \times \left(\frac{M_L}{M_\infty}\right)^{(4.2-0.6M_\infty^2)} \times \left(\frac{1+0.2M_\infty^2}{1+0.2M_L^2}\right)^{(2.1-0.3M_\infty^2)} \times \left(\frac{\theta_L}{\theta_{TE}}\right)^{0.2}$$

The magnification factor approximates the effects of the excrescence drag on the subsequent development of the flow on the surface. More specifically, the drag of the excrescence significantly effects the subsequent development of the momentum thickness associated with the boundary layer on a surface that experiences a non-uniform pressure field . Nash and Bradshaw (Ref. 2) developed an approximation for this effect for two dimensional incompressible flow by representing the effect of excrescence by a sudden change in momentum thickness. For compressible flow (Ref. 3) the approximation for the magnification factor is

$$m = \left(\frac{M_\infty}{M_{TE}}\right)^{(1-M_\infty^2)} \times \left(\frac{1+0.2M_\infty^2}{1+0.2M_{TE}^2}\right)^{(2+0.5M_\infty^2)} \times \left(\frac{M_L}{M_\infty}\right)^{(4.2-0.6M_\infty^2)} \times \left(\frac{1+0.2M_\infty^2}{1+0.2M_L^2}\right)^{(2.1-0.3M_\infty^2)} \times \left(\frac{\theta_L}{\theta_{TE}}\right)^{0.2}$$

Reference 4 compared the predictions based on the compressible form with subsonic experimental data and concludes the for sub-critical conditions the difference is within 10%. However, for supercritical conditions the comparison significantly deteriorates due to the presence of shock waves. For transonic flows, Reference 5, limits the validity of the approximation to shock free conditions. The range of validity of the approximate form for supersonic flows has not been established yet. However, it is expected that outside of the non-linear transonic flow range, where small perturbations can have significant effects on the inviscid pressure distributions, the approximation should be valid. This assumption, however, needs to be verified.

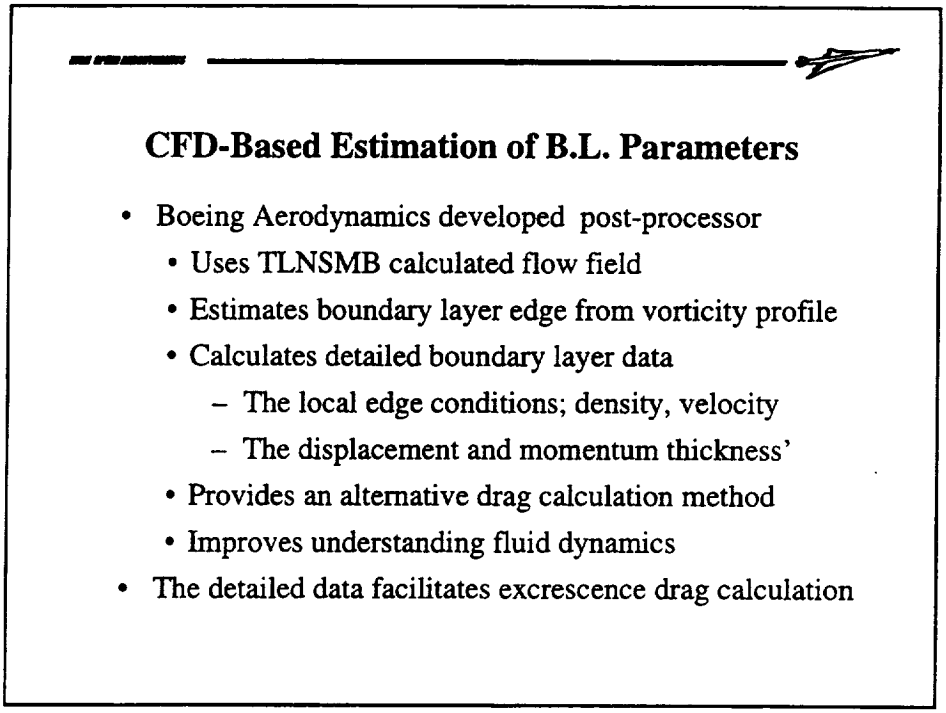

Boeing Aerodynamics Research has developed a program to post-process the TLNSMB calculated flow field. The post-processor judges the boundary layer edge based on the local vorticity profile and calculates detailed boundary layer data. The data contains the local boundary layer edge conditions, such as density and velocity vector, as well displacement and momentum thickness'. The detailed data is used to provide an alternative drag calculation method to the traditional force integration. A further benefit is improved understanding of the flow field and increased confidence in the calculated drag.

The detailed data made available by the post-processor can be used in the excrescence drag calculation.

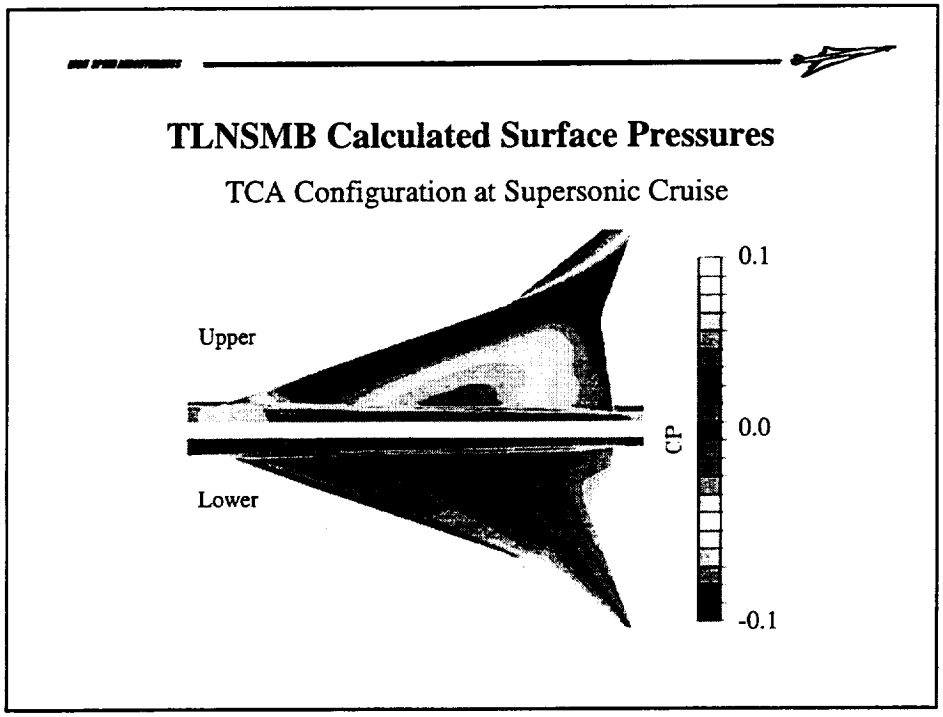

This plot shows the TLNSMB calculated contours of surface pressure for TCA configuration at supersonic cruise Mach number of 2.4 and 3.5° angle of attack. The salient features are the glancing shock on the inboard upper surface of the wing, and the leading edge shock on both surfaces of the outboard wing.

Estimated Boundary Layer Thickness from TLNSMB Solution

Full Scale TCA Configuration at Supersonic Cruise

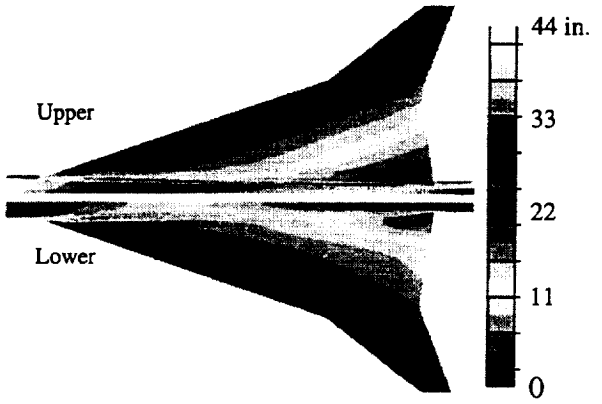

This plot shows the contours of estimated boundary layer thickness for the TCA configuration at supersonic cruise Mach of 2.4 and 3.5° angle of attack. The calculations were made at wind tunnel Reynolds number of 6 million per mac to flight Reynolds of number 200 million per mac. The dimensions are in inches full scale . For comparison, a flat plate of length of the mean aerodynamic chord of 1140 in. would have an estimated boundary layer thickness of 15 in.

The boundary layer on the body crown is seen to be very thick. This is a classical feature of conical fore-body flows at an angle of attack, where the inviscid pressure differential pushes the retarded boundary viscous layer from the keel to crown.

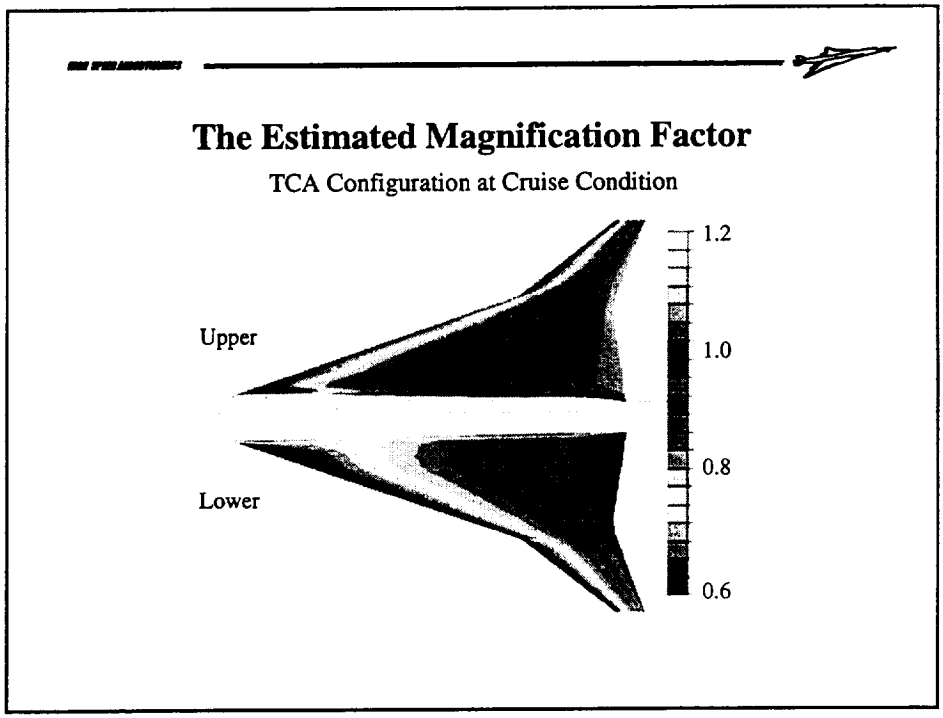

This plot shows the contours of estimated magnification factor for the TCA configuration at supersonic cruise Mach of 2.4 and 3.5° angle of attack. The magnification factor is seen to be close to unity for the most part. This results from the slender TCA geometry being at low a lift level, that leads to small deviations from a flat plate flow.

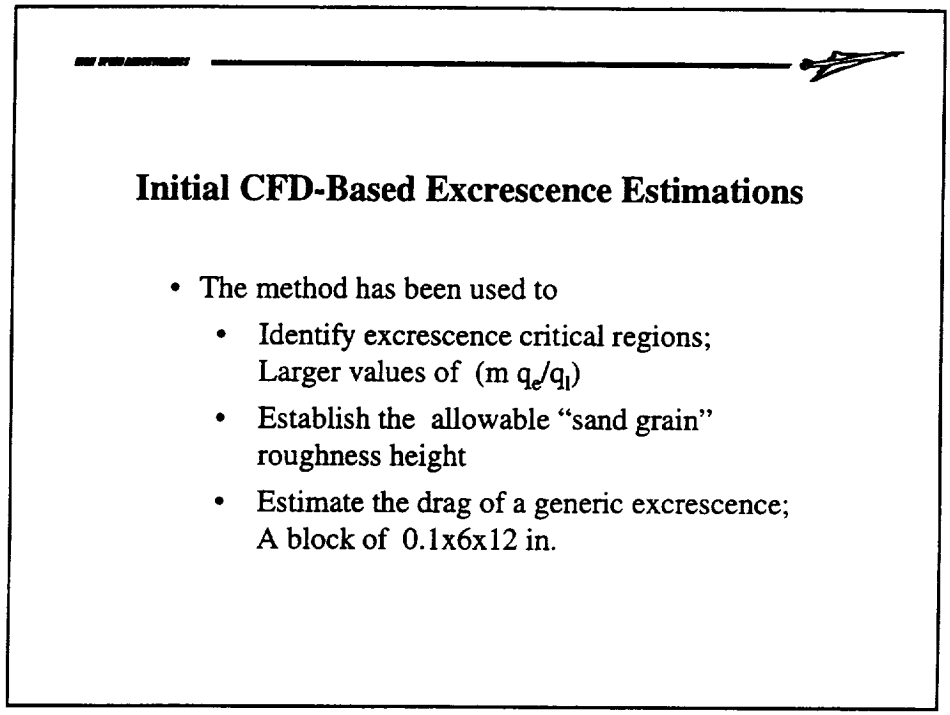

The method has been used to identify excrescence critical regions, establish allowable "sand grain" roughness height, and estimate the drag of a generic excrescence.

The excrescence critical region is judged as the areas where the term "m q_e/q_l" is large, since the term scales the isolated drag. The q_e/q_l component of the term depends on the height of the excrescence, and a height of 0.1 in. was used in the initial calculations.

This allowable height is the limit below which the surface would be classified as hydraulically smooth. This height is of the order of laminar sub-layer and is defined by

$$y^+ = h\, v^*/\nu < 5$$

where $v^* = (\tau/\rho)^{0.5}$, τ is shear stress, and ρ is the density. All fluid properties are evaluated at wall.

To validate the calculation, the drag of a 0.1 in. high block was estimated. The block was 6 in. long and 12 in. wide. For the sake of excrescence drag calculation, the block was represented by the sum of a forward-facing and an aft-facing steps of 0.1" height. The experimental data on the isolated drag of these geometries in supersonic flow are found in Ref.6.

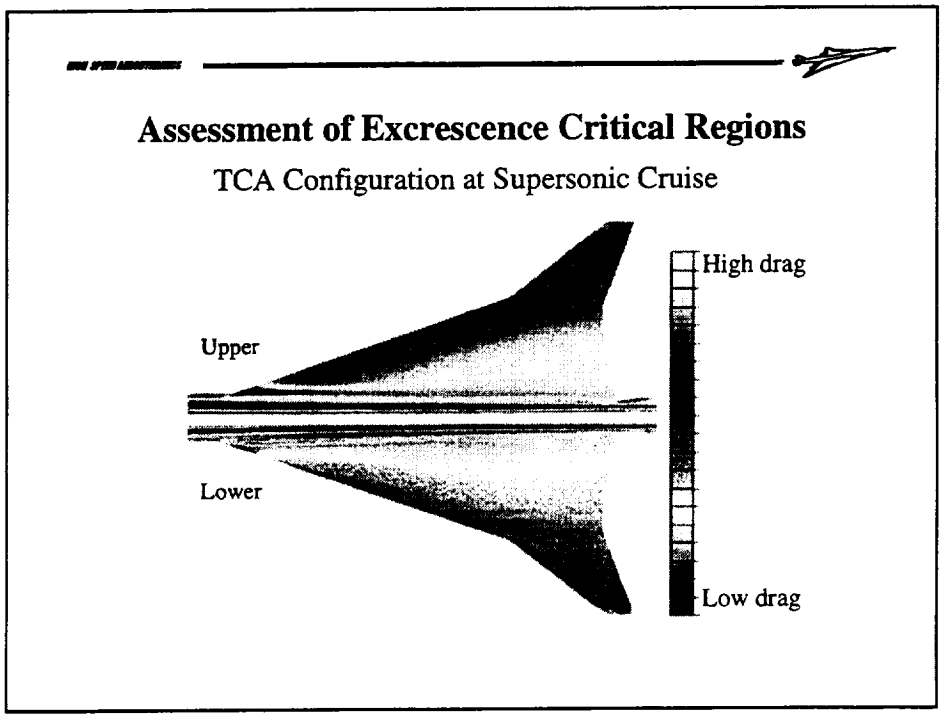

This plot shows the contours of the quantity ($m\ q_e/q_l$) the TCA configuration at supersonic cruise Mach of 2.4 and 3.5° angle of attack for a generic excrescence of 0.1 in. height. The higher levels of drag define the critical regions. The outboard wing is identified as excrescence critical. On the upper surface of the wing, the area upstream of the shock wave is also excrescence critical.

The low drag area near in the wing body juncture, especially near the leading edge on the upper surface, should be viewed with suspicion, since the assumption of excrescence estimation may be grossly violated. The juncture flow is highly three dimensional. At the leading edge, the introduction of an excrescence may effect the shock propagation and associated wave drag.

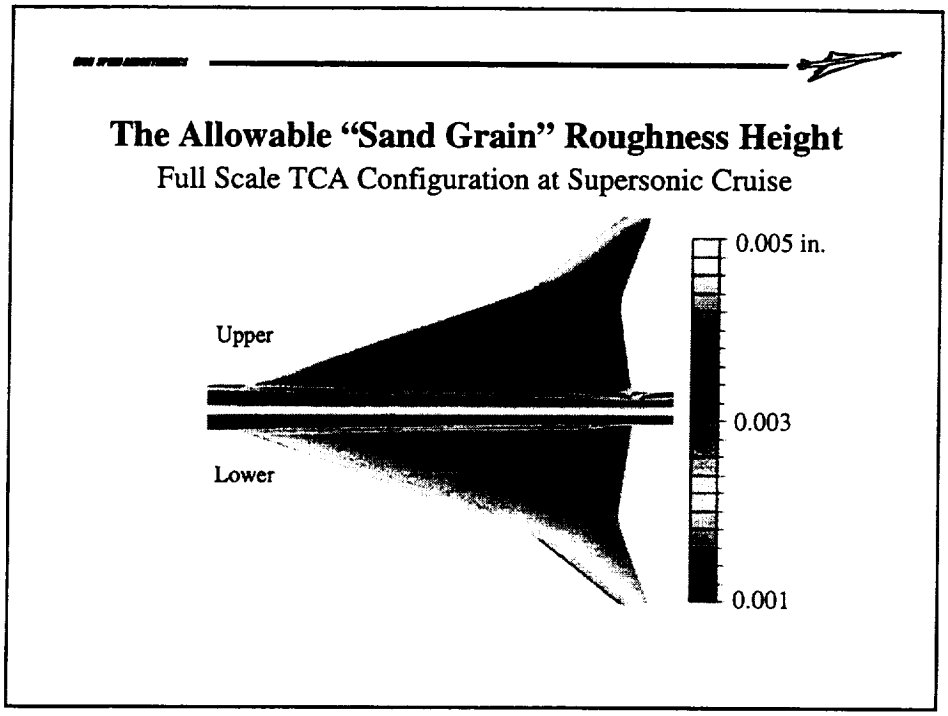

This plot shows the contours of estimated allowable sand grain roughness height for the TCA configuration at supersonic cruise Mach of 2.4 and 3.5° angle of attack. The admissible roughness height is seen to about 0.003 in. outside the leading edge. This is consistent with estimations based on flat plate turbulent boundary layer flows (at a distance of 600 in. admissible roughness is .004 in.).

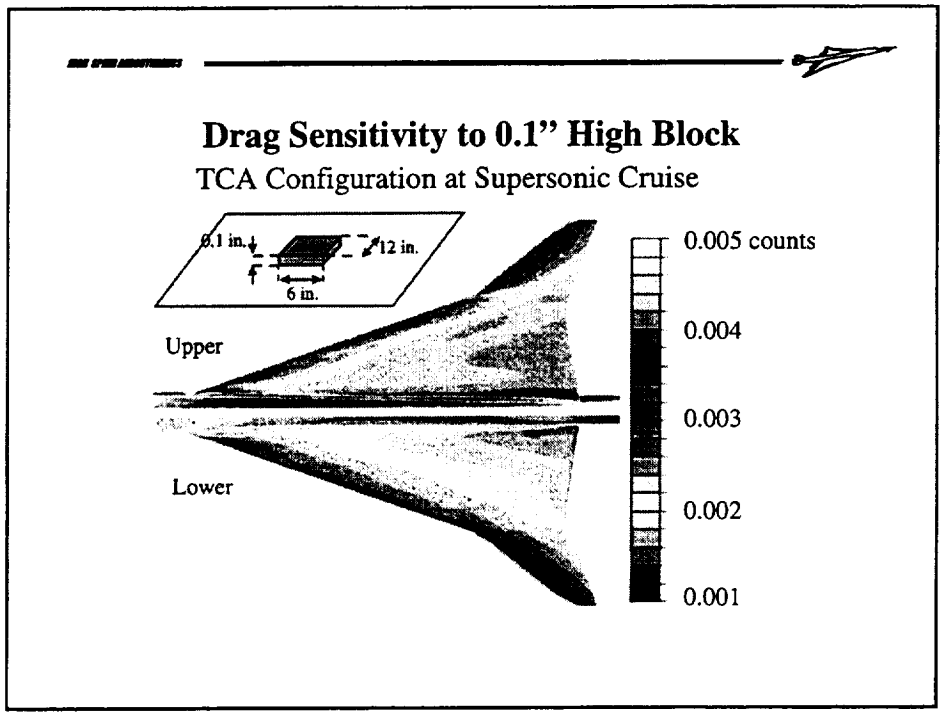

This plot shows the estimated the drag of a 0.1x6x12 in. block centered at a location on the TCA configuration at supersonic cruise of Mach 2.4 and 3.5° angle of attack. This generic excrescence will add about a thousandth of a count per foot in the non-critical region.

Summary and Future Work

- Progress made
  - Validated CD_{Exc} value of 7% of C_F as reasonable
  - Developed a Navier-Stokes based excrescence drag estimation process
    - Identified the excrescence critical regions
    - Estimated allowable "sand grain" roughness height
    - Estimated the drag of a generic excrescence
- Future work
  - Estimate drag due to surface skin waviness and pressurization pillowing
  - Utilize in weight and drag trade-off's
  - Update of technology projections for excrescence drag

A Navier-Stokes based method has been developed to assess the excrescence drag contribution to the flight polar build-up process. Initial application of the method has been successful in identifying drag critical areas of the surface, where deviations from the aerodynamically designed smooth sealed surface should be avoided. The drag of a generic excrescence item is also presented. There has been much progress on this sub-task, however, there are a few items left to complete the study. The drag due to surface skin waviness and pressurization pillowing will be estimated in the near future. The method will be utilized in weight and drag trade-off's in evaluation of structural and manufacturing concepts. As the drag of typical excrescence items are estimated, an update on the technology projections for excrescence drag will be made.

References

1. ESDU, An introduction to aircraft excrescence drag, Item No. 90029, Engineering Sciences Data Unit, London, March 1993.
2. Nash, J. F., and Bradshaw, P., The Magnification of Roughness Drag by Pressure Gradients, Journal of the Royal Aero. Society, Jan., 1967.
3. ESDU, Calculation of excrescence drag magnification using the Nash and Bradshaw formula adapted to compressible flow and a modified BDGK computer program, ESDU Memor. No. 63, 1987.
4. AGARD, Aircraft Excrescence Drag, AGARDograph No.264, AGARD-AG-264, 1981.
5. ESDU, Calculation of excrescence drag magnification due to pressure gradients at high subsonic speeds, Item No. 87004, Engineering Sciences Data Unit, London, November 1989.
6. Gaudet, L., Winter, K. G., Measurements of the Drag of Some Characteristic Aircraft Excrescences Immersed in Turbulent Boundary Layers, RAE TM Aero 1538, Bedford, October, 1973.

Trip Drag Corrections to Performance Polars Using Excrescence Methods

Kevin M. Mejia
HSCT Aerodynamics
Boeing Commercial Airplane Group
Seattle, WA

1997 HSR Aerodynamic Performance Workshop
February 25-28, 1997
NASA Langley Research Center, Hampton, VA

ABSTRACT

This paper presents an alternative method for the calculation of wind tunnel model trip drag increments for application to the build-up of full scale airplane flight polars. Under Technology Integration Task 20, a benchmark data set of Reference H wind tunnel data was created for test-theory comparisons and increments. Several corrections were applied to increase the fidelity of the benchmark data, one of which was a correction for model trip disk drag.

A technique for the estimation of model trip drag is derived based on traditional excrescence drag methods. The method relies on both the experimentally determined drag coefficient of a cylinder and CFD estimations of the boundary layer thickness and magnification factor. For the proper application to full scale airplane predictions, a laminar flow correction is also derived and incorporated. Validation of the proposed method is done by comparison to the Braslow variable roughness size method using wind tunnel test data from both the NASA 2.7% Reference H model and preliminary data from a recent 1.7% TCA test.

Agreement between experimental and excrescence methods is best at the baseline trip height of both models, but diverge as trip height is increased. Possible sources for the differences include: test data uncertainty, curve extrapolation, data applicability, magnification factor estimate, and/or boundary layer characteristic estimates. Recommendations are made for additional work to validate the excrescence and other trip drag estimation methods at other test conditions and suggestions are made for additional checks and assessments.

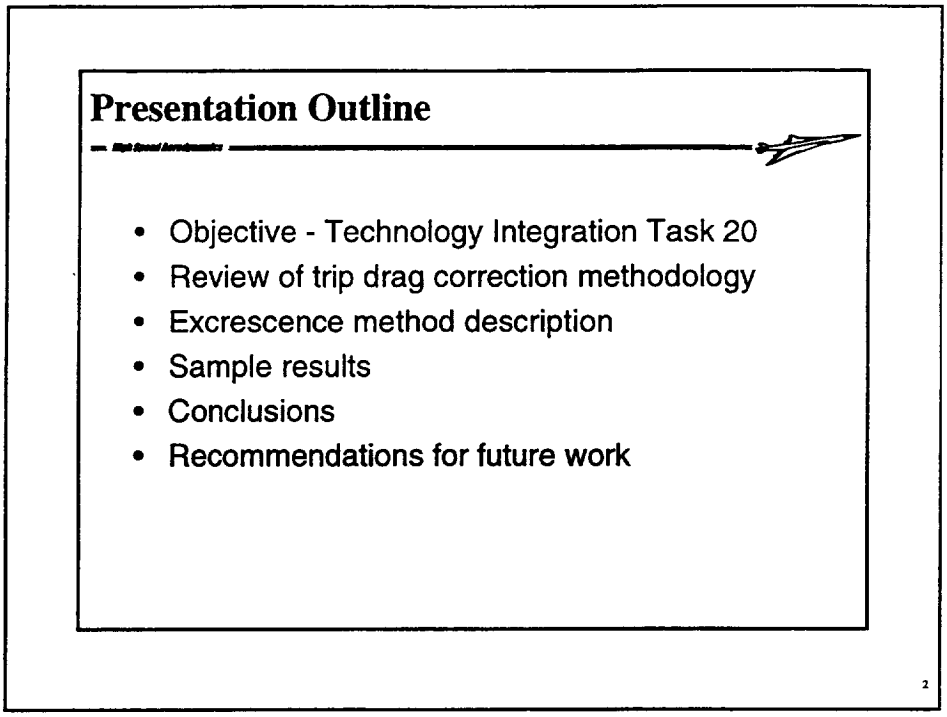

The content of this presentation is organized in the following manor. First a description of the 1996 Technology Integration task under which the current work was performed is reviewed. Next, a brief discussion of the current experimental methods available for determining trip drag is covered, reviewing the pro's and con's of each. The emphasis of the presentation is then devoted to the review of excrescence methodology and its application to the problem of trip drag. Each term in the excrescence equation is reviewed in detail and sample results are presented. Based on the results of this exercise important conclusions and insights are drawn from the data and possible sources of error are identified. Finally, conclusions about the significant findings of the study are made and recommendations for future work are identified.

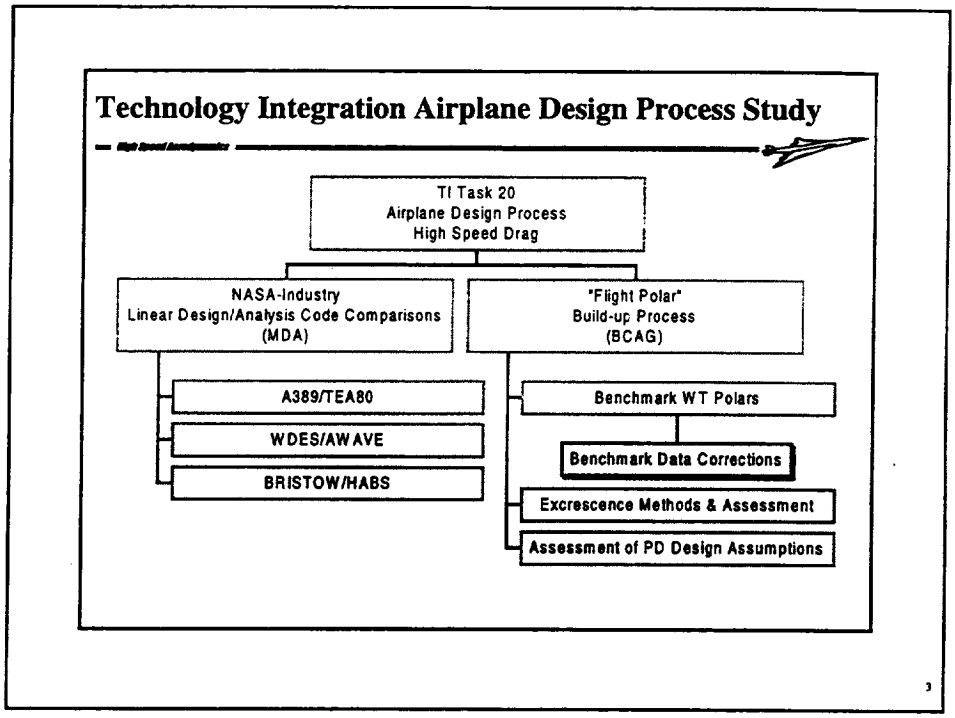

The FY 1996 Technology Integration Airplane Design Process Study (Task 20) was composed of two separate sub-tasks. The first was a comparison of linear design and analysis codes conducted by McDonnell Douglas Aerospace. For this task, MDA compared the capabilities of the three major linear theory analysis codes used by NASA, Boeing, and MDA. The process involved design of a linearly optimized TCA and then a reanalysis and evaluation of the resulting configuration in each of the three codes under consideration.

The second sub-task, conducted by Boeing Commercial Airplane Group, was a detailed assessment and improvement of the prediction process of full scale flight performance of the TCA. To calibrate these prediction methods, a single set of corrected wind tunnel data was created to serve as a common "benchmark" for calibration of prediction methods. Several corrections were made to the benchmark data to account for wind tunnel to flight differences, one of the most significant being a correction for model trip drag.

TCA wind tunnel data was not available until late in fiscal 1996, therefore the benchmark data for this task is based on Reference H data taken between 1993 and 1995. ADP work at Boeing in FY97 will include updating TI's performance polars for refined technology projections and TCA wind tunnel test data, as well as improving the capability of predicting the drag of multi-surface control concepts.

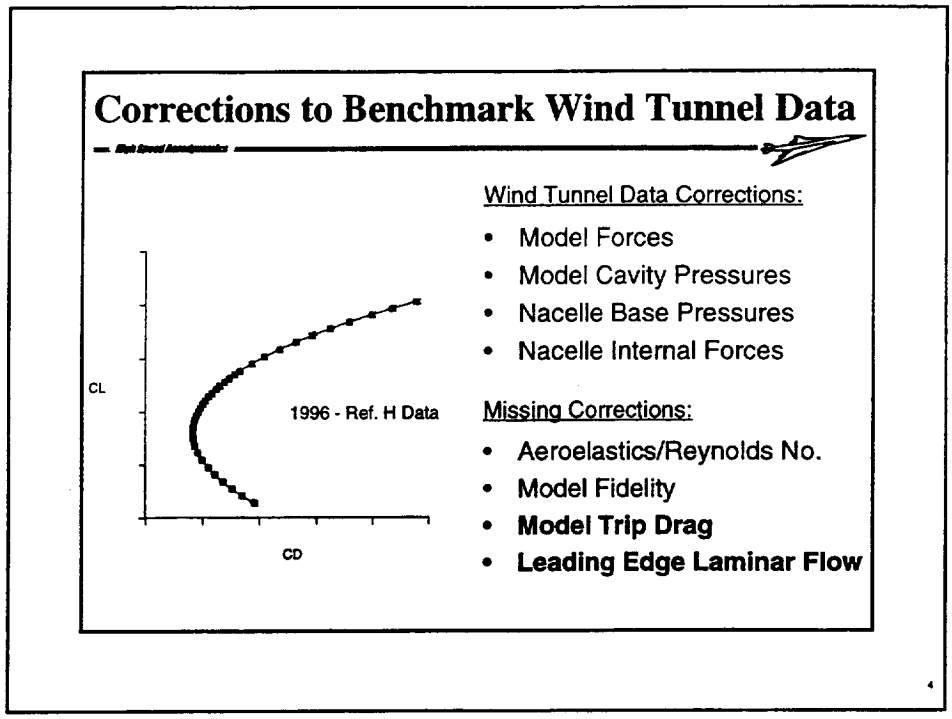

Before wind tunnel results can be applied to full scale flight performance predictions, the benchmark data tables must be corrected for all significant wind tunnel induced effects. This step is required because the limitations in either analysis capability or testing capability (model fidelity, test flexibility, facility Reynolds number capability, etc.) often introduce differences between the tested model and the analyzed configuration. Force data from a test is corrected for angle of attack, cavity and nacelle base pressures, and nacelle internal forces. Corrections not applied to test data, but required for full scale airplane performance predictions include:

- Model aeroelastics/Reynolds number
- Model fidelity and facility selection
- Effect of boundary layer tripping devices

To more accurately represent the flow experienced by the full scale vehicle at flight Reynolds number, it is common practice in wind tunnel testing to artificially transition the flow to fully turbulent using a boundary layer trip. In recent years, the trend in testing has been to use transition disks made of epoxy resin instead of the traditional "grit" composed of finely screened sand particles. Trip disks are easier to apply, measure, and maintain and are more durable than their grit predecessors. Their disadvantage is that they introduce a significant drag increment into the data which to date has never been satisfactorily quantified. The goal of this study is to quantify the trip drag of transition disks using excrescence methods. A proper accounting for leading edge laminar flow is also necessary to correctly evaluate trip drag.

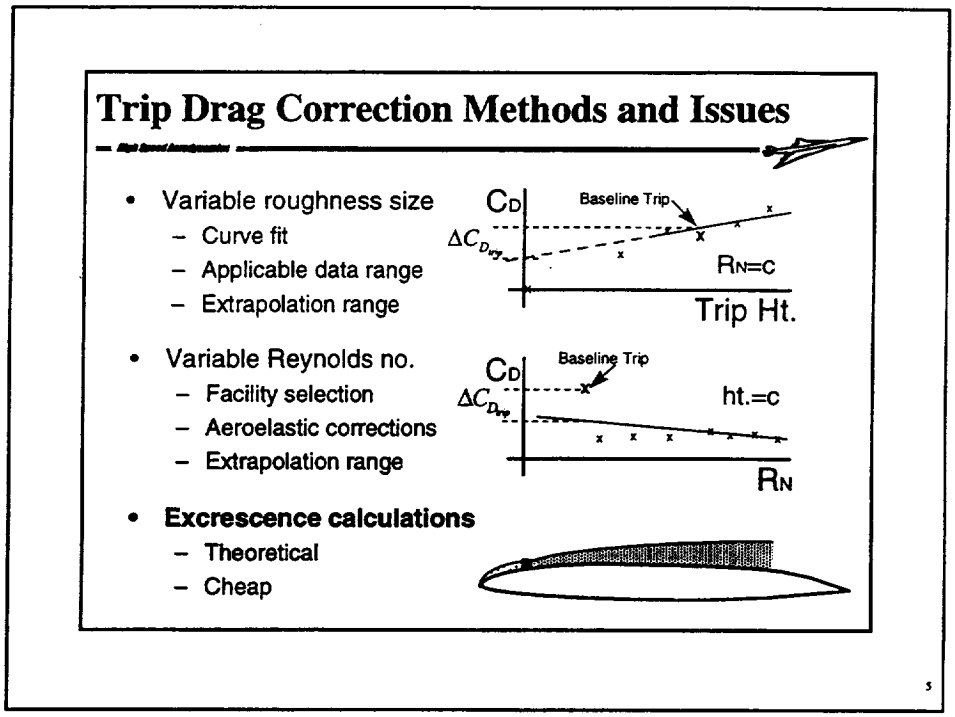

To date, calculation of drag increments for transition disks on HSR models have followed a methodology outlined by Braslow (Reference 1) known as the variable roughness size method. This method is based on grit type trips and their second order variation of drag based on the characteristic "area" of a grit (k^2), where k represents the height (or width) of the grit. Lines (Reference 2) describes a method similar to Braslow's variable roughness size method except he proposes a characteristic area (k), based on disk height. This linear variation in drag with trip height was proposed to better represent disk type trips in transonic flow which extend beyond the edge of the laminar boundary layer.

A second method proposed by Braslow known as the variable Reynolds number method, offers an alternative method for the calculation of trip drag. This method relies on extrapolation of data taken for a constant height trip over a large Reynolds number range where the value for fully turbulent flow is known.

These experimental determinations of the trip disk drag increment lend insight into the magnitude of the trip drag correction, but remain inconclusive because of their inherent uncertainties. Uncertainties in the variable roughness method include: which characteristic "area" is appropriate for a cylinder in supersonic flow (hence, which order curve fit was most appropriate for the C_D vs. roughness height curves,) large extrapolation regions, and what range of heights are appropriate to curve fit for accurate results. The variable Reynolds number method is limited by facility, extrapolation range, and model loading.

Calculation of trip drag using excrescence methods is proposed as an alternative to the experimental methods above without the aforementioned uncertainties.

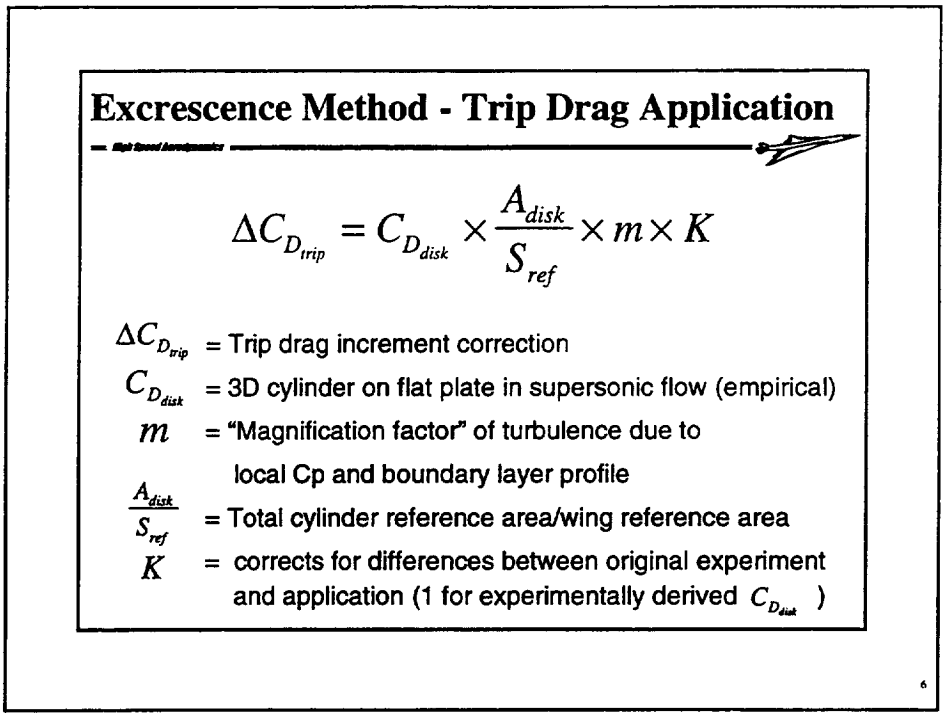

The generalized excrescence equation, discussed in Reference 3, can be rewritten to represent the incremental drag caused by wind tunnel model trip disks in transonic or supersonic flow and is presented above as ΔC_{Dtrip}. C_{Ddisk} is the drag coefficient of a cylinder on a flat plate based on local q and total disk reference area, A_{disk}. S_{ref} is the model reference area and m is the drag magnification factor due to the non-uniform pressure distribution effects on the boundary layer downstream of the roughness element.

The factor K, applied to C_{Ddisk}, allows for the differences between the geometry and orientation of the excrescence as originally tested in the wind tunnel and as located on the wind tunnel model. If there are no differences, then C_{Ddisk} is truly representative and $K = 1$. The original wind tunnel test experiment used to derive the drag coefficient of a three dimensional cylinder appears to properly capture dynamic pressure effects and should accounts for the shock off of the portion of the cylinder which extend beyond the edge of the boundary layer into the freestream. Therefore, for HSCT class wind tunnel models and the excrescence method proposed for calculating C_{Ddisk}, the cylinder data is applicable and K is assumed to equal 1.

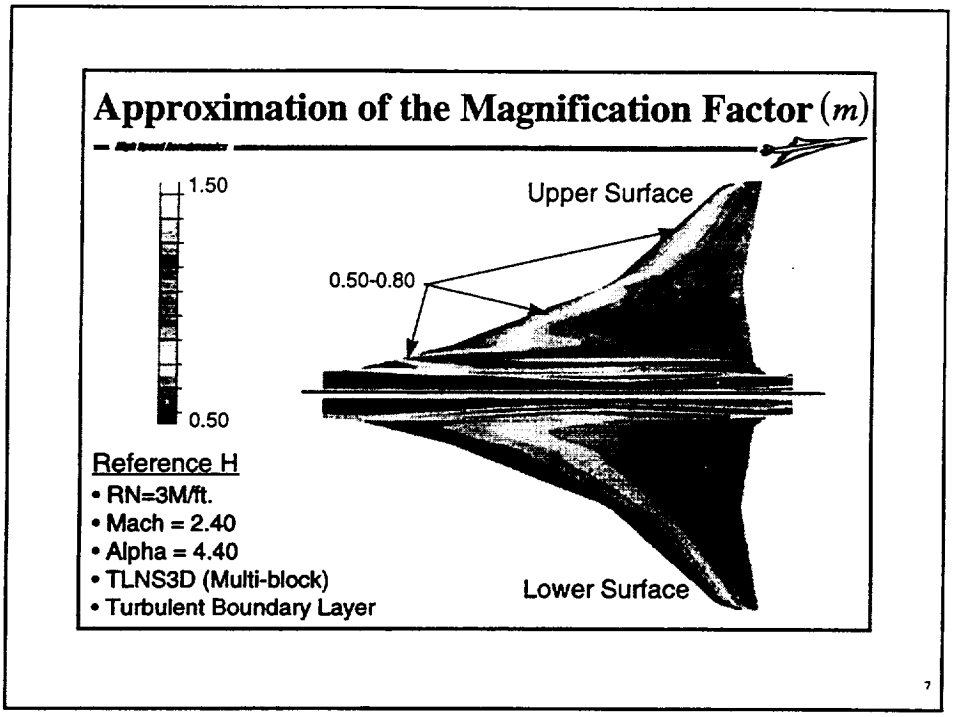

Presented above is CFD solution of the drag magnification factor for the Reference H configuration at wind tunnel conditions. The viscous drag magnification factor, m, for an excrescence in compressible flow is defined in Reference 4 as

$$m = \left(\frac{M_\infty}{M_{TE}}\right)^{(1-M_\infty^2)} \times \left(\frac{1+0.2M_\infty^2}{1+0.2M_{TE}^2}\right)^{(2+0.5M_\infty^2)} \times \left(\frac{M_L}{M_\infty}\right)^{(4.2-0.6M_\infty^2)} \times \left(\frac{1+0.2M_\infty^2}{1+0.2M_L^2}\right)^{(2.1-0.3M_\infty^2)} \times \left(\frac{\theta_L}{\theta_{TE}}\right)^{0.2}$$

The subscripts L, TE, and ∞ indicate local, trailing edge, and free stream conditions, respectively. This formula is a compressible flow adaptation of the Nash and Bradshaw method (Reference 5) for prediction of magnification of roughness drag by pressure gradients for incompressible flow. This parameter can be easily calculated using local flow parameters from existing Euler or Navier-Stokes computational solutions for the geometry under consideration.

TLNS3D (multi-block Navier-Stokes CFD code) was run to calculate the turbulent flow magnification factor for both the upper and lower surface of the full scale Reference H configuration at wind tunnel Reynolds numbers. Typical turbulent boundary layer magnification factors at the location of the trip disks ranged from 0.50 to 0.80.

Drag of a Cylinder in Supersonic Flow $\left(C_{D_{disk}}\right)$

$$C_{D_{disk}} = \left(\frac{\delta}{h}\right)C_{D_\delta} + \left(1-\frac{\delta}{h}\right)C_{D_\infty}$$

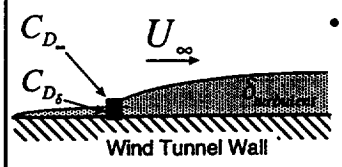

- Supersonic - Gaudet & Winter (1973)
- Transonic - Pallister (1974)
  - Finite length cylinders
  - Turbulent boundary layer
  - Flat plate
  - 2-D flow
  - $\frac{h}{\delta} = 0.5 \rightarrow 2.0$

The generalized equation for C_{Ddisk} presented above is based on the measurements made by Gaudet and Winter (Reference 6) and Pallister (Reference 7.) Their experiments measured the drag of various forms of excrescence over a Mach number range of 0.2 to 2.8. The data is known to be valid for the following conditions: finite length cylinders, a turbulent boundary layer ahead of the excrescence, zero pressure gradient, two dimensional flow, and h/δ ranging from 0.5 to 2.0.

For circular cylinders which extend into the free stream (h≥δ) the drag is calculated by pro-rating the submerged and exposed areas with the applicable drag coefficient and then summing the two components. $C_{D\delta}$ and $C_{D\infty}$ represent the drag of the finite and infinite length cylinder, respectively. Both $C_{D\delta}$ and $C_{D\infty}$ can be obtained using plots created by Gaudet and Pallister, given Reynolds number based on cylinder diameter (R_d) and Mach number. These plots are shown later is this paper. The above equation was derived for cylinder heights which were equal to or greater than the flat plate turbulent boundary layer they were immersed in. For cylinders immersed in the boundary layer

$$C_{D_{disk}} = C_{D\delta} - FC_f$$

Where F can be determined from the plots of Reference 6.

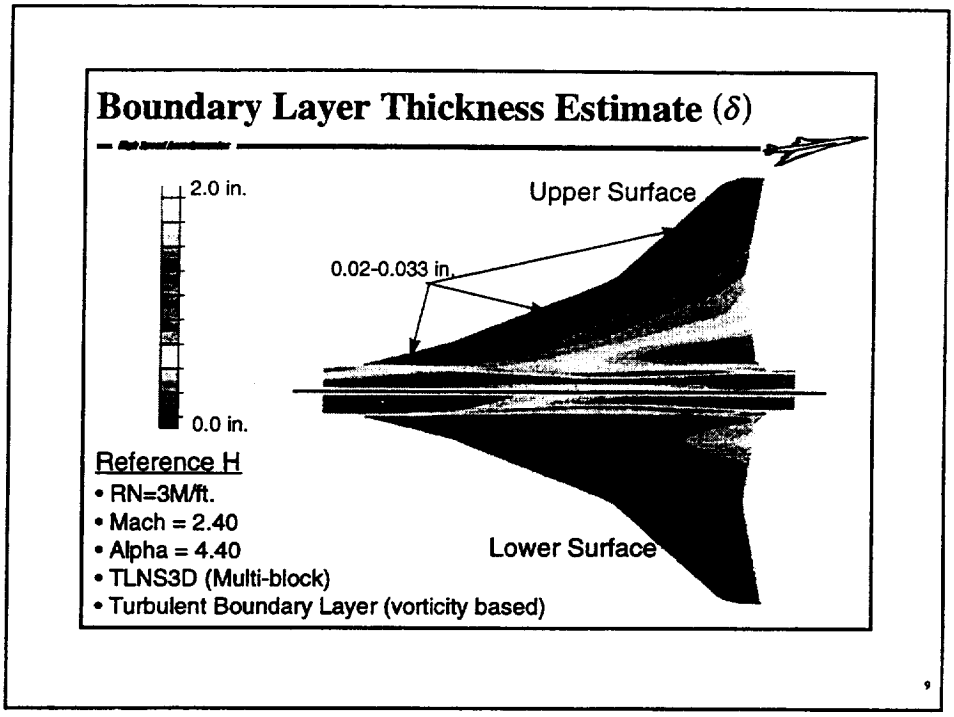

Presented above is CFD solution of the turbulent boundary layer thickness for the Reference H configuration at wind tunnel conditions. TLNS3D (multi-block Navier-Stokes CFD code) was run to calculate the boundary layer height for both the upper and lower surfaces.

Typical 2.7% model scale turbulent boundary layer heights at the location of the trip disks range from 0.02 to 0.033 inches.

Laminar Boundary Layer Height Correction

- Experimental determination of disk drag coefficient based on turbulent flow upstream of cylinder
- Model disks have laminar flow upstream
- Need to scale estimated δ_{turb} to laminar boundary layer thickness

$$\delta_{lam} = \delta_{turb}\left[\frac{13.158}{R_x^{0.3}}\right]$$

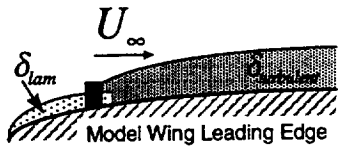

10

For HSCT class wind tunnel models, it has been observed using flow visualization techniques that because of the low Reynolds numbers and model scales being tested, there exists a laminar boundary layer on the portion of the wing ahead of the trip disks. In order to use the equation proposed for C_{Ddisk} in this analysis one significant assumption must be made. Calculation of C_{Ddisk} using the results of Gaudet and Pallister is applicable as long as the laminar boundary layer height on the leading edge of the wing of the wind tunnel model is approximately simulated.

For this study, only turbulent boundary layer height estimates were available. Following the above assumption, the CFD estimate must then be corrected to an approximate laminar height by using the ratio of the incompressible, flat plate laminar and turbulent boundary layer height equations. The simplified form is presented above.

It is acknowledged that the laminar boundary layer assumption is not entirely appropriate for the methodology outlined here because the original data used to generate the drag coefficient of a cylinder was taken in a turbulent boundary layer. However, it is proposed that proper modeling of the trip to boundary layer height ratio is the most important factor in the C_{Ddisk} equation in order to correctly estimate the disk drag coefficient. Also, the primary source of drag for an excrescence comes from the pressure drag on the aft face of the disk. Therefore using a laminar boundary approximation would not significantly affect this flow phenomena for the disk Reynolds numbers tested. Finally, no other data has been found which directly expresses the supersonic drag of a cylindrical excrescence in a laminar boundary layer.

Laminar Boundary Layer Correction (cont.)

- A drag correction is required to account for the velocity profile differences between laminar and turbulent boundary layers
- A 7% correction to $C_{D\delta}$ was derived from experimental data

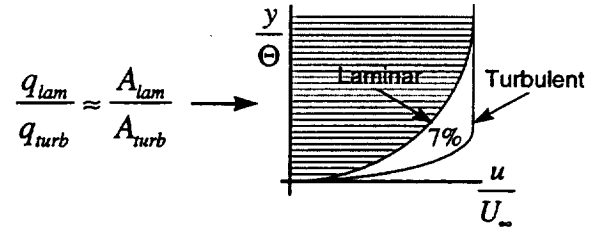

Resulting Equation: $C_{D_{disk}} = 0.93\left(\frac{\delta_{lam}}{h}\right)C_{D_\delta} + \left(1 - \frac{\delta_{lam}}{h}\right)C_{D_\infty}$

11

To compensate for the differences in velocity profile (hence, dynamic pressure) associated with the use of a laminar boundary layer in place of a turbulent one, a small correction factor should be applied to the calculation of C_{Ddisk}. This q correction is assumed to be proportional to the area ratio of the two velocity profiles. Based on experimentally determined velocity profile data contained in Reference 8 at Mach=2.40 and similar Reynolds number, a correction of approximately 7% was determined.

This correction may be different for the transonic Mach numbers because both boundary layer thickness and velocity profile ratios will change. As applied currently, this correction does not vary with trip height for trips inside the boundary layer and is only applicable for drag predictions where $h \geq \delta$. A formulation would have to be derived before any future trip drag predictions can be made for trips immersed in the boundary layer ($h < \delta$).

The equation for C_{Ddisk} is rewritten above to denote the laminar boundary layer height and velocity profile correction factor.

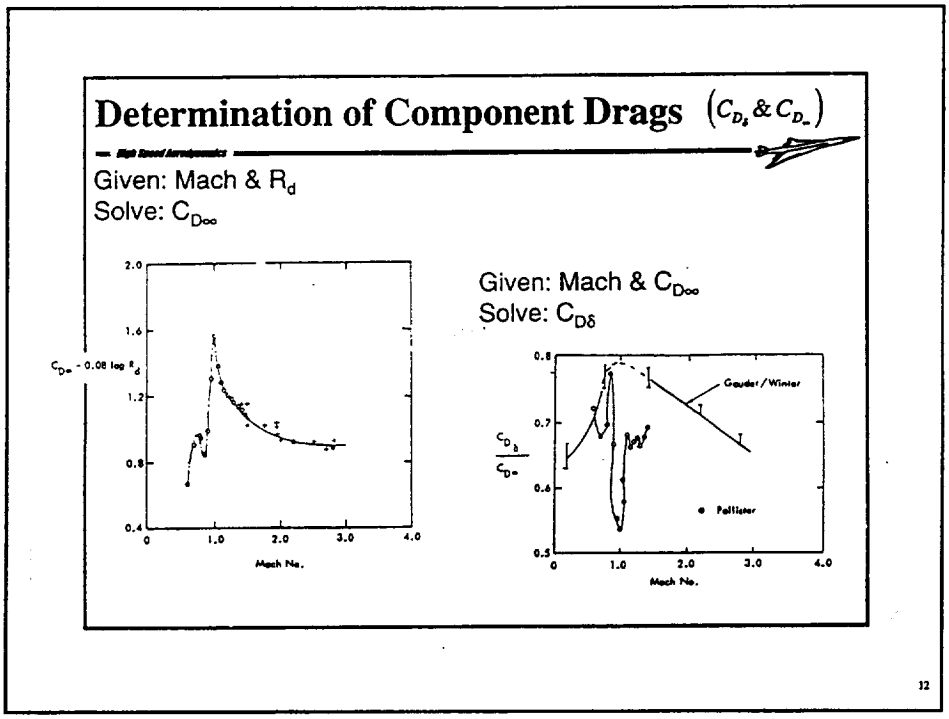

Knowing Mach number and the Reynolds number based on disk diameter (R_d), $C_{D\delta}$ and $C_{D\infty}$ can be obtained from the Figures above. With δ_{lam}, and $C_{D\delta}$ and $C_{D\infty}$ now available, C_{Ddisk} can then be calculated.

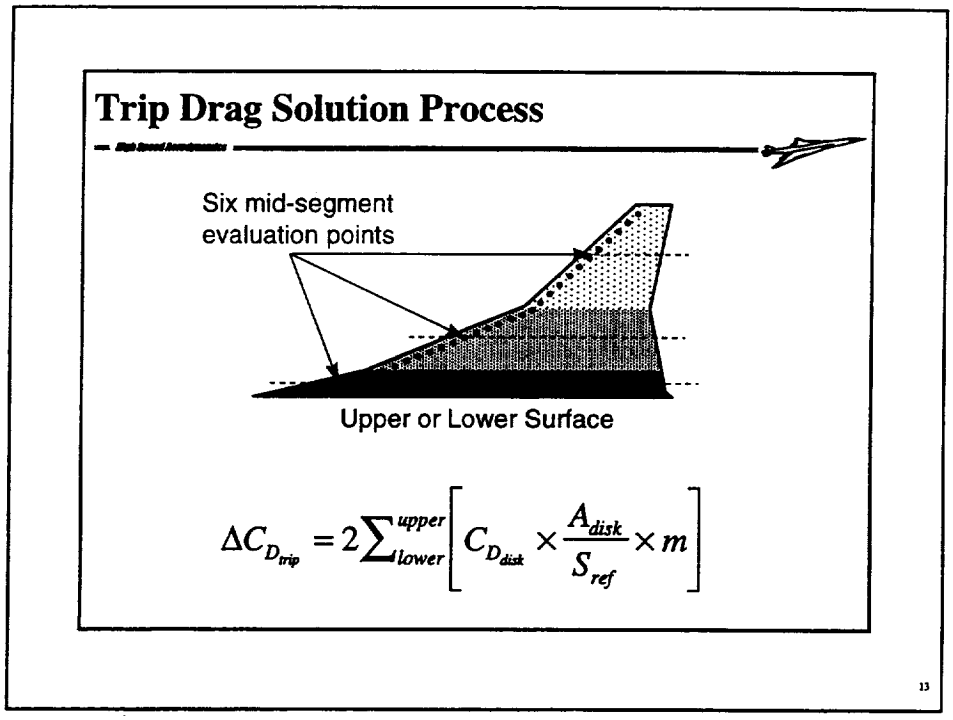

To simplify the analysis about the entire wing, the necessary components within the excrescence equation were calculated only at the midpoint of each wing segment (inboard, mid-wing, and outboard) for both the upper and lower surface. The excrescence drag was then calculated at each of the 6 wing segments shown above and the segment incremental trip drags were then summed to represent the trip drag for both wings. A_{disk} at each segment represented only the frontal area associated with the number of trips present in that segment.

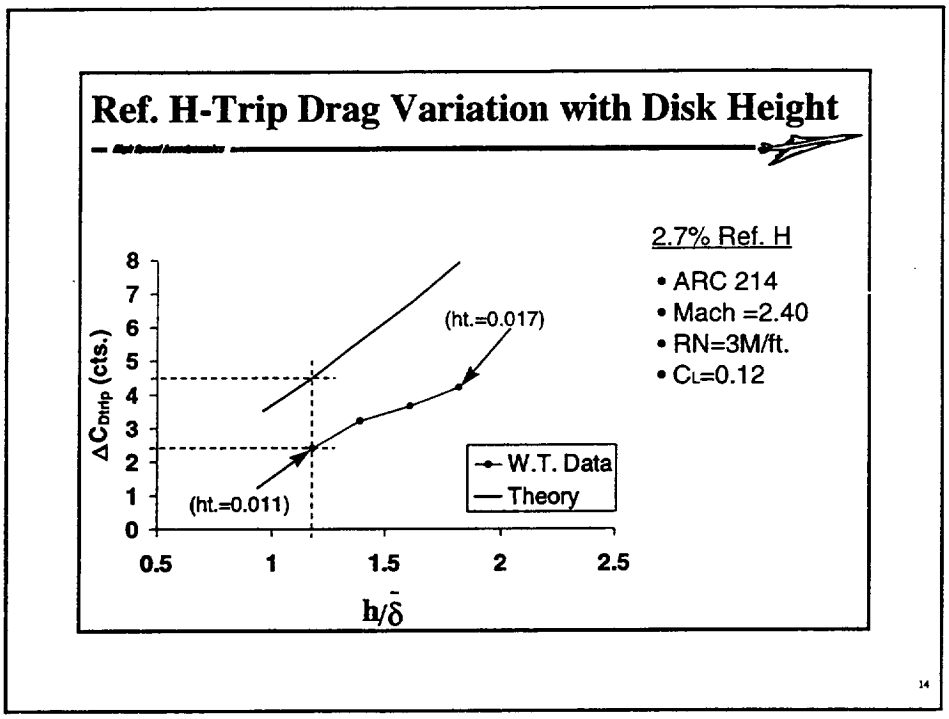

The comparison between excrescence method results and wind tunnel data utilizing the variable roughness height method (with a linear fit) for the Reference H configuration at wind tunnel conditions is presented above. A significant offset (approximately 3 cts., average) can be seen between the two methods with the excrescence method consistently predicting trip drags approximately double that of the experimental method. For the baseline wind tunnel trip height (0.011 in.) the variable roughness height calculates a trip drag correction of 2.5 cts. while the excrescence method predicts a correction of 4.5 cts. The two methods show similarities in trip drag trend and slope, with the excrescence method again predicting a slightly greater slope.

Although there appears to be little agreement between the two methods, neither of the two method can be dismissed as "incorrect" because of the uncertainties associated with the experimental data and the assumptions used in the excrescence method. Additional comparisons are made in following slides and an assessment of each of the significant components of both methods is also presented later.

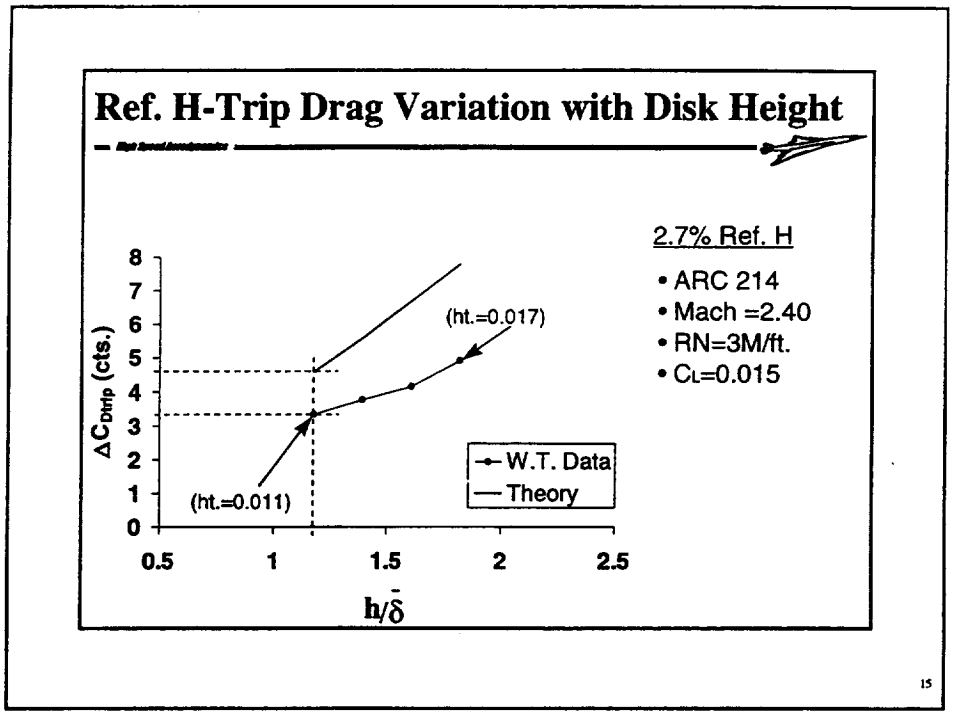

Presented above is a comparison of excrescence and variable roughness height methods for a lift coefficient corresponding to the minimum drag coefficient (C_L=0.015) on the Ref. H drag polar. As observed previously, the excrescence method predicts a higher trip drag than the experimental method while the slope trend with $h/\bar{\delta}$ (trip disk height/average boundary layer height) of the two curves is similar.

As seen in other trip drag assessments, the variable roughness method shows a significant trip drag variation with changing lift coefficient. When compared to the cruise condition (C_L=0.12, previous slide) at the baseline trip height, the variable roughness height method shows a 0.9 ct. increase in trip drag (2.5 cts. vs. 3.4 cts.) The excrescence method, however, shows that trip drag has only a slight dependence, 0.1 ct, on lift coefficient (4.5 cts. vs. 4.6 cts.)

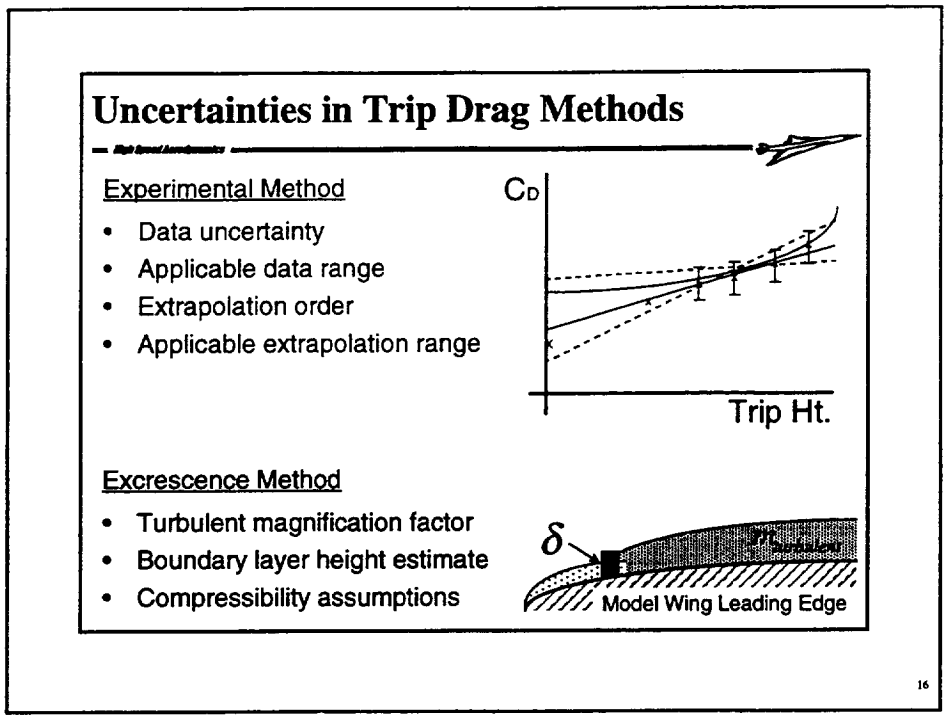

To fully understand the problems in determining trip drag using either the excrescence or variable roughness height methods, the uncertainties of each method must be carefully reviewed. The primary uncertainties in each method are listed above and explained below.

Variable Roughness Height Method

• There exists scatter in each data point taken due to tunnel repeatability issues. Extrapolation to zero trip height can vary on the order of ~±0.5 ct. due to data.

• No firm guidelines exist for selecting data points to fit. Selection of various combinations of trip data can vary the extrapolation results on the order of ~±1 ct.

• There is little experience in selection of order of curve fit for trip disks in supersonic flow. The effect on extrapolation is on the order of ~±2 cts.

• It difficult to understand how a curve fit of drag data for disks extending into the freestream can properly approximate disks immersed in the boundary layer. Effect on extrapolation: ~±? cts.

Excrescence Method

• Boundary layer transition on a wind tunnel model does not immediately begin at the trip location for the entire model. Perhaps correlation would improve with a magnification factor calculated for a laminar boundary layer.

• Method fidelity could be improved by calculating directly the laminar boundary layer height using CFD tools.

• Compressible formulations for the turbulent to laminar boundary layer height and skin friction corrections would be more accurate.

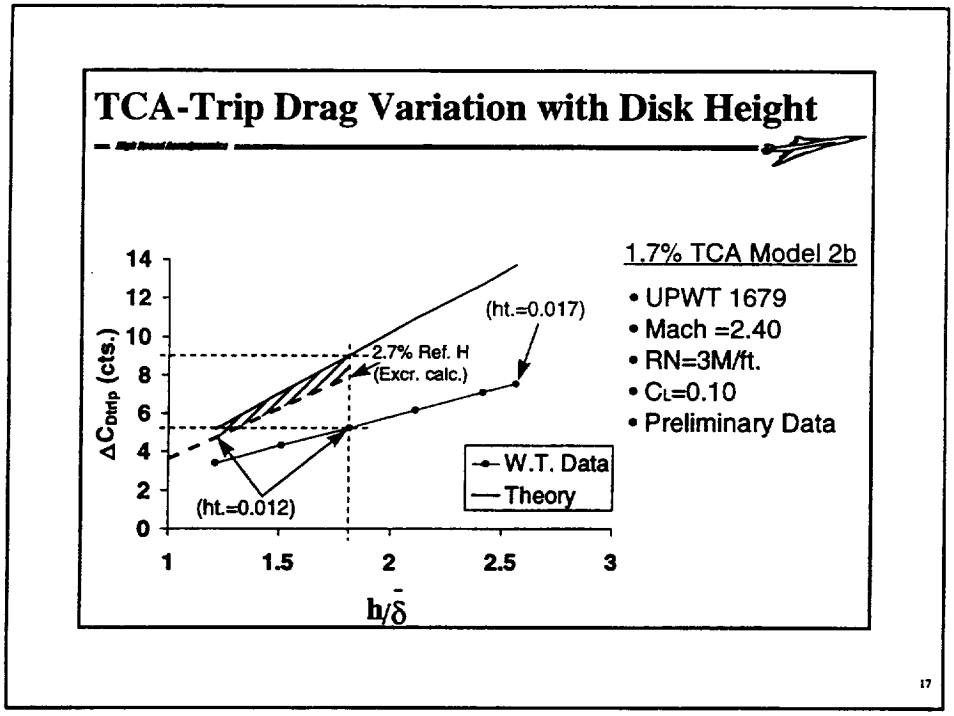

Another comparison between methods is presented above for the TCA configuration based on preliminary trip drag estimates for the TCA (UPWT 1679). The comparison between the two methods show similar trends as for the Reference H configuration. An offset (an average of 5 cts.) can again be seen between the two methods with the excrescence method consistently predicting trip drags approximately double that of the experimental method. A slight slope difference can also be seen between the two methods. For the baseline wind tunnel trip height (0.012 in.) on the TCA, the variable roughness height calculates a trip drag correction of 5.2 cts. while the excrescence method predicts 8.9 cts.

At first glance, application of the excrescence method appears to only further cloud the trip drag issue, but this "analogy" allows us to begin to understand the flow mechanisms affecting trip drag (represented by each term in the excrescence equation). To aid in understanding, the plot of the 2.7% Ref. H calculation is also included. Comparisons of the full scale boundary layer height and magnification factor calculations between the two models showed no significant differences. Remaining sources for trip drag differences then only include A_{wet} and C_{Ddisk}. Because TCA has more wing area than the Ref. H, it is known that there is approximately 11% more disk A_{wet} on the TCA, which can explain some of the increased drag over the Ref. H model. Also, because the TCA is a smaller scale model than the Ref. H, the baseline trip $h/\bar{\delta}$ ratio is greater, leading to a larger value of C_{Ddisk} and a higher trip drag located further up the curve. If the trip were reduced to a height known to trip ($h/\bar{\delta} \cong 1.2$), the trip drag could be reduced to drag ranges previously predicted by both methods for the Ref. H configuration.

Currently there is no explanation for the absolute drag level difference between the two methods.

Leading Edge Laminar Flow Correction

- Application of wind tunnel data for prediction of full scale flight performance polars requires a correction for model leading edge laminar flow
  - Flow visualization techniques have shown significant regions of laminar flow on wind tunnel models
- Approximately equal to 2 to 3 cts.

$$\Delta C_{D_{lam\_flow}} = \frac{A_{L.E.}}{S_{ref}}\left[\left(\frac{0.074}{R_x^{0.2}}\right) - \left(\frac{1.328}{R_x^{0.5}}\right)\right]$$

A final correction must be used on the outlined methodology for accurate application of wind tunnel data to full scale flight conditions. It has been verified in the wind tunnel that laminar flow occurs ahead of the trip disks on the model over the entire span of the wing (hence, the need for trips.) This region of laminar flow on the model represents approximately 6.5% (Reference H) to 8.2% (TCA) of the projected wing reference area. This is a significant percentage of the wing reference area that should not be neglected.

Using the incompressible Blausius and Prandtl flat plate boundary layer skin friction equations as an approximation, a drag increment can be calculated to represent the turbulent skin friction difference between a leading edge laminar flow (model) and turbulent flow (full scale.) The equation representing this correction is shown above. The magnitude of this correction is on the order of 2 to 3 cts.

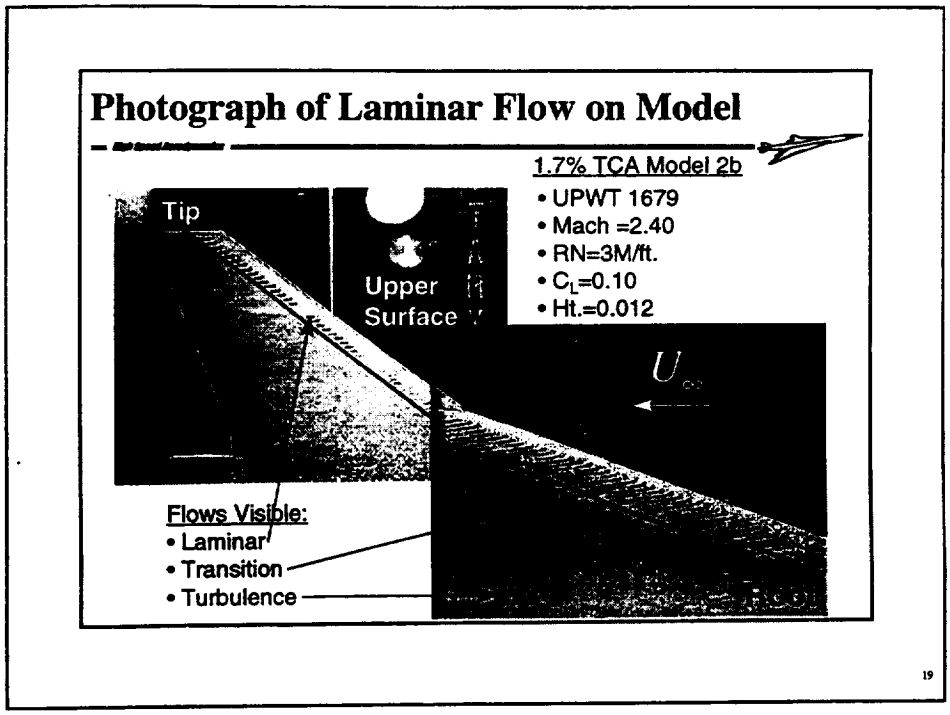

Presented above are sample images of a sublimation run done on the 1.7% TCA model 2b (UPWT 1679) to illustrate the extent of laminar flow present on typical HSCT wind tunnel models. The sublimation technique shows areas of laminar and turbulent flow by using the relative skin friction (scrubbing power) of each flow to sublime Flourine powder off of the wing's surface. In this image lighter colored areas represent laminar flow and grayer areas represent turbulent flow.

In this example, the outboard wing transitions to turbulent flow at the trip disks. The inboard section of the wing trips immediately at the disks but takes approximately 0.75 inches to transition to fully turbulent flow. The two large wedges of laminar flow seen in the pictures are where trip disks have been intentionally removed to observe natural transition. The black streaks behind the inboard trip disks represent additional scrubbing due to the shed vortices of the disks themselves.

Summary of Corrections to Benchmark Data

- Excrescence method trip drag corrections were applied to benchmark Ref. H data over a range of Mach numbers
  - Correction for model leading edge laminar flow included
    - No variation with C_L was included
  - "Engineering judgment" used to fill in benchmark corr. table
    - Only a select number of CFD solutions were available
    - Relative magnitude of correction values between Mach numbers compared against wind tunnel estimates

Trip Drag Correction Table - Ref. H

Mach	0.90	0.90 (w/ flap)	1.20	2.40
Correction	-0.00008	-0.00011	0.0	-0.00025

20

The methodology previously outlined was employed to generate a table of values to be added directly to the benchmark wind tunnel data to correct the data for drag due to model transition disks. Because boundary layer heights and magnification factors had to be taken from expensive Navier-Stokes CFD solutions, only a select number of conditions were run. The table above shows the conditions for which the trip disk drag increments were actually calculated.

Corrections at the specified Mach numbers were calculated for the cruise condition and all intermediate steps matched the tunnel conditions of the benchmark data. The corrections were assumed to be constant throughout the range of $C_{L's}$ covered by the data and input as such in the tables. For Mach numbers or configurations within the benchmark data which lied between the calculated values, the data were linearly interpolated between the two nearest applicable conditions. There are two exceptions to this statement. First, data at M=0.95 and 0.98 were input as twice (2x) the data calculated at M=0.90. This assumption was made based on the results of a test conducted by McDonnell Douglas Aerospace on their model M2.4-7A Opt 5 (Reference 9) in September, 1994. Second, corrections for trip disk drag at M=1.07 and 1.10 were assumed to be the same as that calculated at M=1.20. Because the transonic assumptions were based on the results of a model M2.4-7A test, they should be verified for the TCA or Reference H configurations when data becomes available.

The application the trip drag corrections to the benchmark data is shown below.

$$C_{D_{benchmark}} = C_{D_{wind\_tunnel}} + \left(-\Delta C_{D_{trip}} + \Delta C_{D_{lam\_flow}}\right) + \Delta C_{D_{other}}$$

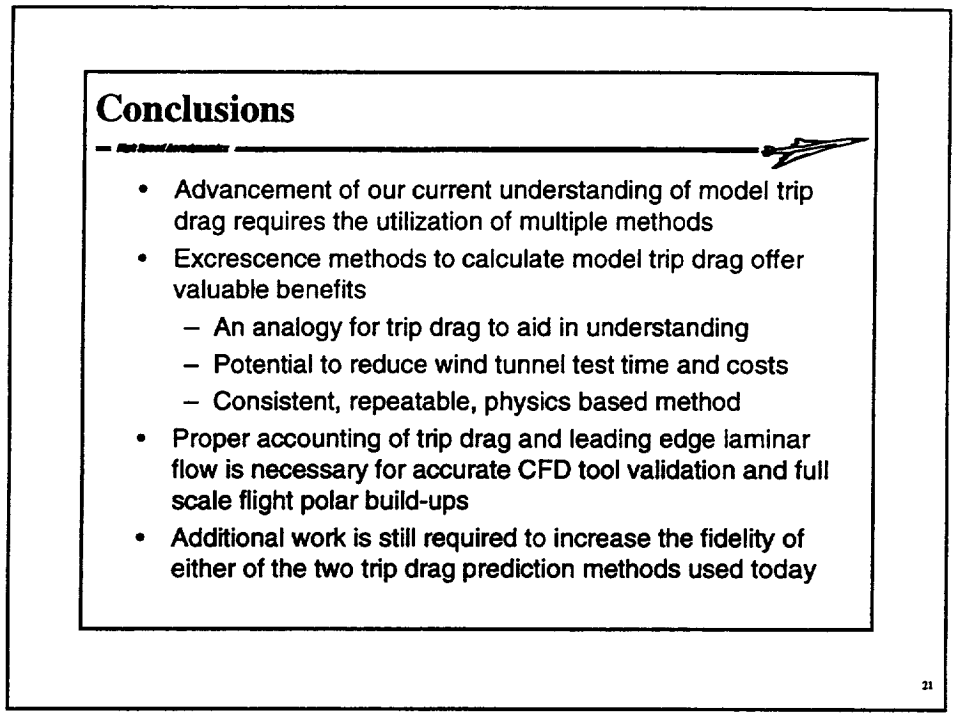

For application to FY 96 Technology Integration Task 20, the results of the previously outlined excrescence methodology were used to correct Reference H based benchmark wind tunnel data for trip drag effects. Comparison of excrescence method results to the experimentally based variable roughness size method show significant differences, but the uncertainties in the experimental methods raise many other questions. Until a better understanding of the trip drag phenomena can be acquired, multiple trip drag estimation methods should continue to be explored.

Application of the excrescence method to the problem of model trip drag provides a valuable analogy, based on boundary layer flow phenomena, to help understand the mechanisms involved in boundary layer transition. Also, it has the potential to reduce the need for expensive and lengthy wind tunnel testing for trip drag determination. Finally, because the method is flow phenomena based, an accurate solution should be possible once all component uncertainties are resolved.

Almost as important as trip drag in wind tunnel to flight or CFD correlations is the proper accounting for the laminar flow which exists in wind tunnel data. Current predictions/correlations do not account for this drag component and could be in error by as much as 2 to 3 counts at wind tunnel conditions.

It is apparent that currently no one method is mature enough to fully quantify the trip drag problem, therefore additional work on the topic is recommended.

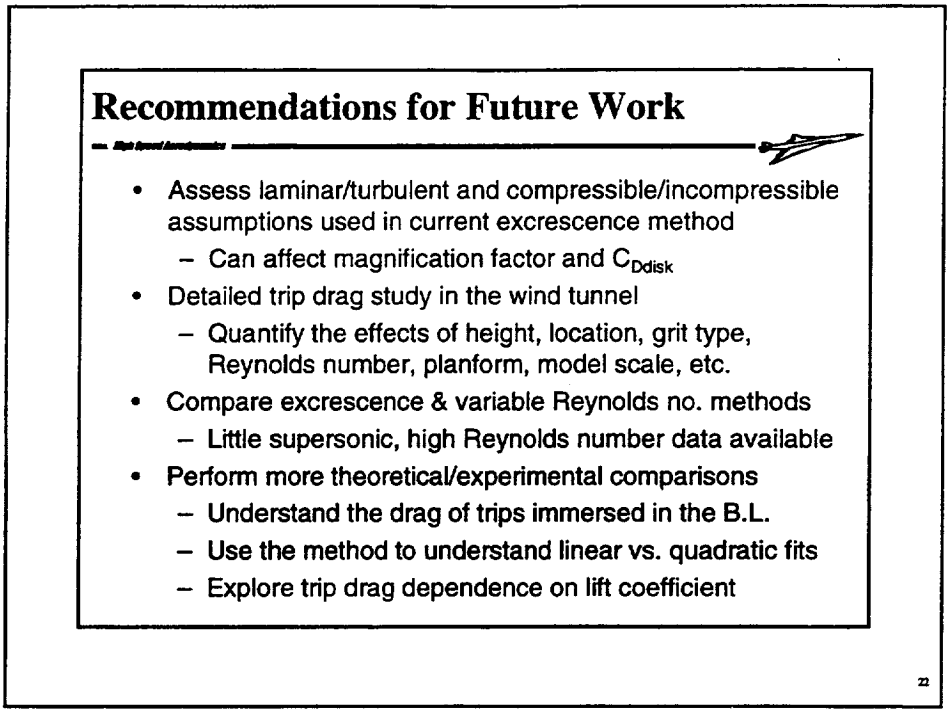

The above items detail some topics for additional work which should be completed to better understand the trip drag phenomena at transonic and supersonic conditions.

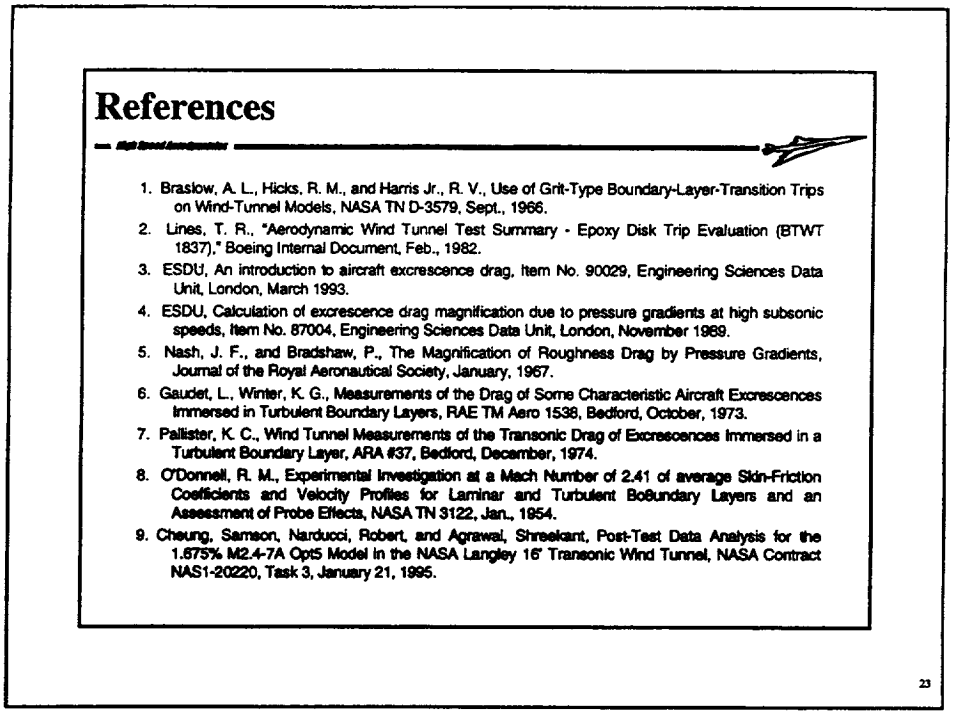

The references listed above were used in the development of the trip disk excrescence methodology.

REPORT DOCUMENTATION PAGE

Form Approved
OMB No. 0704-0188

1. AGENCY USE ONLY *(Leave blank)*	2. REPORT DATE	3. REPORT TYPE AND DATES COVERED
	December 1999	Conference Publication

4. TITLE AND SUBTITLE
1997 NASA High-Speed Research Program Aerodynamic Performance Workshop
Volume I—Configuration Aerodynamics

5. FUNDING NUMBERS
WU 537-07

6. AUTHOR(S)
Daniel G. Baize, Editor

7. PERFORMING ORGANIZATION NAME(S) AND ADDRESS(ES)
NASA Langley Research Center
Hampton, VA 23681-2199

8. PERFORMING ORGANIZATION REPORT NUMBER
L-17916C

9. SPONSORING/MONITORING AGENCY NAME(S) AND ADDRESS(ES)
National Aeronautics and Space Administration
Washington, DC 20546-0001

10. SPONSORING/MONITORING AGENCY REPORT NUMBER
NASA/CP-1999-209691/
VOL1/PT2

11. SUPPLEMENTARY NOTES

12a. DISTRIBUTION/AVAILABILITY STATEMENT
Unclassified–Unlimited
Subject Category 02 Distribution: Nonstandard
Availability: NASA CASI (301) 621-0390

12b. DISTRIBUTION CODE

13. ABSTRACT ***(Maximum 200 words)***

The High-Speed Research Program and NASA Langley Research Center sponsored the NASA High-Speed Research Program Aerodynamic Performance Workshop on February 25–28, 1997. The workshop was designed to bring together NASA and industry High-Speed Civil Tranport (HSCT) Aerodynamic Performance technology development participants in area of Configuration Aerodynamics (transonic and supersonic cruise drag prediction and minimization), High-Lift, Flight Controls, Supersonic Laminar Flow Control, and Sonic Boom Prediction. The workshop objectives were to (1) report the progress and status of HSCT aeroydamic performance technology development; (2) disseminate this technology within the appropriate technical communities; and (3) promote synergy among the scientist and engineers working HSCT aerodynamics. In particular, single- and multi-point optimized HSCT configurations, HSCT high-lift system performance predictions, and HSCT Motion Simulator results were presented along with executive summaries for all the Aerodynamic Performance technology areas.

14. SUBJECT TERMS	15. NUMBER OF PAGES
High-Speed Research; High-Speed Civil Transport	941
	16. PRICE CODE: A99

17. SECURITY CLASSIFICATION OF REPORT	18. SECURITY CLASSIFICATION OF THIS PAGE	19. SECURITY CLASSIFICATION OF ABSTRACT	20. LIMITATION OF ABSTRACT
Unclassified	Unclassified	Unclassified	UL